JAERI-Conf
96-008

INDC(JPN)-175/U

PROCEEDINGS OF THE 1995 SYMPOSIUM ON NUCLEAR DATA

November 16-17, 1995, JAERI, Tokai, Japan

March 1996

(Eds.) Tetsuo IGUCHI* and Tokio FUKAHORI

日本原子力研究所
Japan Atomic Energy Research Institute

本レポートは，日本原子力研究所が不定期に公刊している研究報告書です。
入手の問合わせは，日本原子力研究所技術情報部情報資料課（〒319-11 茨城県那珂郡東海村）あて，お申し越しください。なお，このほかに財団法人原子力弘済会資料センター（〒319-11 茨城県那珂郡東海村日本原子力研究所内）で複写による実費頒布をおこなっております。

This report is issued irregularly.
Inquiries about availability of the reports should be addressed to Information Division, Department of Technical Information, Japan Atomic Energy Research Institute, Tokai-mura, Naka-gun, Ibaraki-ken 319-11, Japan.

編集兼発行　日本原子力研究所
印　　刷　㈱原子力資料サービス

JAERI−Conf 96−008

INDC(JPN)-175/U

Proceedings of the 1995 Symposium on Nuclear Data
November 16-17, 1995, JAERI, Tokai, Japan

(Eds.) Tetsuo IGUCHI * and Tokio FUKAHORI

Japanese Nuclear Data Committee
Tokai Research Establishment
Japan Atomic Energy Research Institute
Tokai-mura, Naka-gun, Ibaraki-ken

(Received February 21, 1996)

The 1995 Symposium on Nuclear Data was held at Tokai Research Establishment, Japan Atomic Energy Research Institute (JAERI), on 16th and 17th of November, 1995. This symposium was organized by Japanese Nuclear Data Committee and Nuclear Data Center, JAERI. In the oral sessions, presented were 18 papers on integral testing of JENDL-3.2, photonuclear data, activities of nuclear data research in Malaysia, Vietnam and Russia, special purpose files for activation cross section and intermediate energy nuclear data for IFMIF project, nuclear data needs and usage and topics on new measurements. In the poster session, presented were 40 papers concerning experiments, evaluations, benchmark tests and on-line database on nuclear data. Those presented papers are compiled in this proceedings.

Keywords: Nuclear Data, Symposium, Proceedings, Nuclear Reaction, Photonuclear Data, Activation, JENDL-3.2, IFMIF Project, Experiment, Evaluation, Benchmark Tests, Cross Section.

* Nuclear Engineering Research Laboratory, University of Tokyo

1995年核データ研究会報文集

1995年11月16日～17日，東海研究所，東海村

日本原子力研究所東海研究所
シグマ研究委員会
（編）井口　哲夫*・深堀　智生

（1996年２月21日受理）

1995年核データ研究会が，1995年11月16日と17日の両日，日本原子力研究所東海研究所において開催された。この研究会は，日本原子力研究所のシグマ研究委員会と核データセンターが主催して開いたものである。口頭発表では，JENDL-3.2 の積分テスト，光核反応データ，マレーシア，ベトナム，ロシアにおける核データ研究，放射化断面積及びIFMIF計画用高エネルギー核データに関する特殊目的ファイル，核データの利用及びニーズ，トピックスとして新しい実験・測定の18件の報告があった。ポスター発表では，40件の発表があり，それらは，核データの測定，評価や評価済核データのベンチマークテスト，オンラインデータベース等に関するものであった。本報文集は，それらの論文をまとめたものである。

東海研究所：〒319-11　茨城県那珂郡東海村白方白根2-4
* 東京大学工学部附属原子核工学研究施設

Program Committee

Tetsuo IGUCHI (Chairman)	University of Tokyo
Satoshi CHIBA	Japan Atomic Energy Research Institute
Tokio FUKAHORI	Japan Atomic Energy Research Institute
Hideki IIMURA	Japan Atomic Energy Research Institute
Shin IWASAKI	Tohoku University
Ken NAKAJIMA	Japan Atomic Energy Research Institute
Yutaka NAKAJIMA	Japan Atomic Energy Research Institute
Shigeaki OKAJIMA	Japan Atomic Energy Research Institute
Makoto SASAKI	Mitsubishi Atomic Power Industries, Inc.
Etsuro SAJI	Toden Software Inc.
Hiroshi TAKADA	Japan Atomic Energy Research Institute
Yasushi TAMURA	Japan Atomic Energy Research Institute
Naoki YAMANO	Sumitomo Atomic Energy Industries, Ltd.

プログラム委員会

井口　哲夫（委員長）	東京大学
千葉　敏	日本原子力研究所
深堀　智生	日本原子力研究所
飯村　秀紀	日本原子力研究所
岩崎　信	東北大学
中島　健	日本原子力研究所
中島　豊	日本原子力研究所
岡嶋　成晃	日本原子力研究所
佐々木　誠	三菱原子力工業（株）
佐治　悦郎	東電ソフトウェア（株）
高田　弘	日本原子力研究所
田村　康志	日本原子力研究所
山野　直樹	住友原子力工業（株）

Contents

目　　次

1. Introduction

The 1995 symposium on nuclear data was held at Tokai Research Establishment, Japan Atomic Energy Research Institute (JAERI), on 16th and 17th of November, 1995. The symposium was organized by Japanese Nuclear Data Committee and Nuclear Data Center, JAERI. The program of the symposium is listed below. In the second and fifth oral sessions, four invited talks were addressed on integral testing of JENDL-3.2. Three papers related to photonuclear data research were reported in the third session as results of discussion at the photonuclear data work shop held just before this symposium. As an international session, nuclear data research activities in Malaysia, Vietnam and Russia were presented. In the other sessions, total 8 papers were presented on special purpose files, nuclear data application and needs and topics on new measurements. In the poster session, presented were 40 papers concerning nuclear data experiments, evaluations, benchmark tests and on-line database on nuclear data. Those papers are compiled in this proceedings.

Program

Oral Presentation

Nov. 16 (Thu.)

10:00-10:10

1. Opening Address (Hosei Univ.) R. Nakasima

10:10-11:50

2. Benchmark Test of JENDL-3.2 (I) Chairman: (KHI) T. Watanabe

2.1 Present Status of Libraries Processed from JENDL-3.2 [50] (SAEI) N. Yamano

2.2 Analysis of JUPITER Critical Experiments by JENDL-3.2 [40] (PNC) M. Ishikawa

11:50-13:00 Lunch

13:00-14:55

3. Photonuclear Reaction Data Chairman: (NFD) T. Murata

3.1 Japanese Evaluation of Photoreaction Data [40] (JAERI) N. Kishida

3.2 Photonuclear Data: Analysis of Discrepancies and Evaluation [40] (Moscow Univ.) V.V. Varlamov

3.3 From User of Photoreaction Data [30] (JAERI) Y. Asano

14:55-15:10 Coffee Break

15:10-16:45

4. Topics (I) Chairman: (JAERI) Y. Kikuchi

4.1 Nuclear and Atomic Data Activities in Malaysia [30] (National Univ. of Malaysia) A.S. Abdullah

4.2 Current Status of Russian Evaluated Neutron Data Libraries [30]
(IPPE) A.I. Blokhin

4.3 Nuclear Data Activities in Vietnam [30] (JAERI) Vuong Huu Tan

16:45-17:50

5. Benchmark Test of JENDL-3.2 (II) Chairman: (Toshiba) M. Kawai

5.1 Reactor Physics Experiment and Benchmark Analysis of STACY [40]
(JAERI) Y. Miyoshi

5.2 Report of Task Force on JENDL-3.2 Spreading Method [15]
(JAERI) Y. Kikuchi

18:00-20:00 Reception at Akogi-ga-Ura Club

Nov. 17 (Fri.)

9:10-10:50

6. Poster Session
at Lobby of Main Meeting Room and ABC Meeting Room

10:50-11:55

7. Special Purpose File Chairman: (Tohoku Univ.) S. Iwasaki

7.1 JENDL Activation Cross Section File [30] (JAERI) Y. Nakajima

7.2 JENDL High Energy File for IFMIF [30] (JAERI) T. Fukahori

11:55-13:00 Lunch

13:00-14:05

8. Topics (II) --- Application and Needs of JENDL-3 Nuclear Data Chairman: (TSI) E. Saji

8.1 Nuclear Data Usage for Research Reactors [30] (JAERI) Y. Nakano

8.2 Nuclear Data Library for WIMS-ATR Code [30] (PNC) T. Ihara

14:05-16:20

9. Topics (III) --- New Experiments Chairman: (TIT) M. Igashira

9.1 Present Status and Future Plan of the Research Using HIMAC of NIRS [40]
(NIRS) K. Kawachi

9.2 Measurement and Analysis of Delayed Neutron Ratio, β eff [30]
(JAERI) T. Sakurai

9.3 Status of Neutron Induced α-production Cross Sections [30]
(Tohoku Univ.) M. Baba

9.4 The First Data of Double Differential Cross Section of $^{12}C(p,p')$ at 300 MeV with a Stacked NaI(Tl) Spectrometer [30]
(Kyushu Univ.) H. Murohka

16:20-16:35

10. Summary Talk (Kyushu Univ.) Y. Kanda

Poster Presentation

1. Measurement of Fission Cross Section with Pure Am-241 Sample using Lead Slowing-Down Spectrometer
   (Kyoto Univ.) K. Kobayashi, M. Miyoshi, S. Yamamoto, Y. Fujita, I. Kimura, I. Kanno, S. Kanazawa and N. Shinohara
2. Measurement of keV-Neutron Capture γ Rays of Fission Products (II)
   (TIT) M. Igashira
3. Verification of Dosimetry Cross Sections Based on Measurement of Reaction Rates in Fission Neutron Field
   (SRI) N. Odano and A. Yamaji
4. Benchmark Calculation of JMTRC Core Using JENDL-3
   (JAERI) Y. Nagao, S. Shimakawa, Y. Komori and N. Ooka
5. Benchmark Test of FP Nuclear Data in JENDL-3.2 and Consideration of Resonance Self-Shielding Effects for Neutron Strong Absorber Nuclei
   JNDC FPND Working Group, (KHI) T. Watanabe, M. Kawai, T. Nakagawa, Y. Nakajima, T. Sugi, S. Chiba, A. Zukeran, H. Matsunobu, H. Takano and H. Akie
6. Measurements of Double-differential Neutron Emission Cross Sections for 18 and 11.5 MeV Neutrons
   (Tohoku Univ.) D. Soda, S. Matsuyama, M. Ibaraki, M. Baba, S. Iwasaki and N. Hirakawa
7. Development of Wide Range Charged Particle Spectrometer for Ten's MeV Neutron
   (Tohoku Univ.) Y. Nauchi, M. Baba, S. Matsuyama, N. Hirakawa and S. Tanaka
8. Measurement of (n,2n) Cross-Sections for Cu, Zn, Ag and Sn between 12 to 20 MeV with Activation Technique
   (Tohoku Univ.) S. Iwasaki, S. Matsuyama, D. Soda, Y. Nauchi, H. Fukuda, M. Kitamura and N. Odano
9. Helium Production Cross Section Measurement by Helium Atoms Measurement System
   (Kyushu Univ.) Y. Takao, Y. Kanda, M. Miwa, H. Etoh, K. Yamaguchi, T. Yonemoto and K. Nagae
10. Measurement of Formation Cross Sections Producing Short-lived Nuclei by 14 MeV Neutrons - Pr,Ba,Ce,Sm,W,Sn,Hf -
    (Nagoya Univ.) S. Murahira, Y. Satoh, N. Honda, A. Takahashi, T. Iida, M. Shibata, H. Yamamoto and K. Kawade
11. Measurement of Beta-decay Half-lives of Short-lived Nuclei by Using Spectrum Multi-Scaler (SMS)
    (Nagoya Univ.) T. Hirose, T. Shibuya, S. Murahira, H. Yamamoto, T. Iida, A. Takahashi and K. Kawade
12. Calibration for Absolute Detection Efficiency of γ-ray Detector in High Energy Region with ^{56}Co
    (Nagoya Univ.) A. Yoshida, H. Miyahara and C. Mori
13. Application of the Slowing Down Time Method for Neutron Spectrum Measurement in the Energy Region of eV in Various Neutron Field
    (JAERI) F. Maekawa and Y. Oyama

14. The Evaluation of Multigroup and Pointwise Cross section Libraries for Monte Carlo Calculation of 14 MeV Neutron Streaming Through Fusion Reactor Penetration
(Univ. of Tokyo) A. Jirkin
15. Investigation of Shielding Design Margin Evaluation in Fusion Reactors
(Hitachi Ltd.) K. Maki, K. Hayashi, C. Konno, H. Maekawa and F. Maekawa
16. Processing of PKA Spectrum File for FENDL from JENDL Fusion File
(JAERI) T. Fukahori, S. Chiba and M. Kawai
17. Damage Energy Cross Section of Charged Particles from Light Nuclides Irradiated with High Energy Neutrons
(JAERI) T. Aruga, S. Chiba, M. Harada, H. Kashimoto, Y. Watanabe and M. Kawai
18. Measurements of Neutron Spectra from Stopping-Length Target Bombarded with Light Ions
(JAERI) S. Meigo, H. Takada, H. Nakashima, T. Sasa, S. Tanaka, K. Shin and S. Ono
19. Evaluation of Neutron Production Rate in Electron Accelerator Facility
(PNC) Y. Shigetome, H. Harada, T. Noguchi and T. Yamazaki
20. High Energy Resolution Measurement Method of Photonuclear Reaction Cross Section
(PNC) H. Harada, Y. Shigetome and Y. Wada
21. Measurement of Double-Differential Neutron-Induced α-Particle Emission Cross-Sections of ^{58}Ni and ^{nat}Ni
(Tohoku Univ.) T. Sanami, M. Baba, S. Matsuyama, T. Kawano, T. Kiyosumi, Y. Nauchi, K. Saito and N. Hirakawa
22. Measurement of Neutron Spallation Cross Sections
(Tohoku Univ.) E. Kim, T. Nakamura, A. Konno, M. Imamura, N. Nakao, T. Shibata, Y. Uwamino, N. Nakanishi, Su. Tanaka, H. Nakashima and Sh. Tanaka
23. Gamma Rays Emission Cross Section From Proton-Incident Spallation Reaction
(Kyushu Univ.) K. Iga, K. Ishibashi, N. Shigyo, T. Nakamoto, K. Maehata, N. Matsufuji, S. Meigo, H. Takada, S. Chiba, M. Numajiri, T. Nakamura and Y. Watanabe
24. Measurement of Nuclear Reaction Cross Sections of Therapeutic Heavy Charged Particles
(NIRS) A. Fukumura, T. Hiraoka, T. Tomitani, T. Kanai, T. Murakami, S. Minohara, H. Tomura, N. Matsufuji, T. Kohno and T. Nakamura
25. Evaluation of the Dependencies without Systematic Errors
(Moscow Univ.) N. Efimkin
26. Nuclear Data Evaluation for ^{12}C in the Energy Region More than 20 MeV and Kerma Factor Calculation
(Kyushu Univ.) M. Harada, Y. Watanabe and S. Chiba
27. Semi-Classical Distorted Wave Model Analysis of (p,p'x) and (p,nx) Reactions at Intermediate Energies
(Kyushu Univ.) Y. Watanabe, H. Shinohara, M. Higashi and M. Kawai

28. Fragmentation Cross Sections by HETC
(Kyushu Univ.) N. Shigyo, T. Nakamoto and K. Ishibashi
29. Semi-gross Theory of Nuclear β-decay II
(Waseda Univ.) H. Nakata, T. Tachibana and M. Yamada
30. Determination of Shell Energies - Nuclear Deformations and Fission Barriers
(Waseda Univ.) H. Koura, T. Tachibana and M. Yamada
31. A Simple Method for Evaluation of Uncertainties in Fission Product Decay Heat Summation Calculations
(Nagoya Univ.) H. Ohta, K. Oyamatsu and K. Tasaka
32. Direct Radiative Capture Mechanisms and the Structure of Light Nuclei
(RIKEN) A. Mengoni
33. Future Prospects of Superfine Structure of Neutron Resonance Levels
(JAERI) K. Ideno
34. Nuclear Level Density Formula with Energy-dependent Shell and Pairing Corrections
(FEC) H. Nakamura
35. Neutron Resonance Level Clusters and Localized Crystalline Structures
(JAERI) M. Ohkubo
36. Intelligent Pad for Exchanging and Reusing Nuclear Reaction Data Information as Shared Resources
(Hokkaido Univ.) M. Chiba
37. Nuclear Data Information System for Nuclear Materials
(NRIM) M. Fujita, T. Noda and M. Utsumi
38. An User-Interface for Retrieval of Nuclear Data (Demonstration)
(NRIM) M. Utsumi, M. Fujita and T. Noda
39. World Wide Web of JAERI Nuclear Data Center
(JAERI) T. Nakagawa
40. A Simple Method to Evaluate the Differences of Fission Yields of Various Fissiles
(Nagoya Univ.) K. Oyamatsu and M. Sagisaka

2. Papers Presented at Oral Session

2.1 Benchmark Test of JENDL-3.2

2.1.1 Present Status of Libraries Processed from JENDL-3.2

Naoki YAMANO
Department of Nuclear Design
Sumitomo Atomic Energy Industries, Ltd.
2-10-14 Ryogoku, Sumida-ku, Tokyo 130
E-mail: saei@taurus.bekkoame.or.jp

Data libraries processed from JENDL-3.2 were produced by JAERI for use of typical applications in the area of nuclear reactor and shielding. These libraries had the distinction of being free of restrictions on distribution. The other data libraries for decay, activation, dosimetry, nuclide transmutation, burn-up, PKA, KERMA and DPA calculations are now being accumulated. The current status on the development of these libraries has been described. A discussion is presented about how to disseminate and share the products of JNDC activities.

1. Introduction

Version 3.2 of the Japanese Evaluated Nuclear Data Library (JENDL-3.2)[1] was released in June 1994. To validate the data accuracy and applicability, secondary data libraries processed from JENDL-3.2 were produced by JAERI for use of typical applications in the areas of thermal, fast, fusion reactors and shielding. These libraries were named as SRACLIB-J32, JFS-3-J32, MVPLIB-J32, MGCL-J3.2, BERMJ3, JSSTDL-295/J32 and FSXLIB-J3R2. These had the distinction of being free of restrictions on distribution. The other data libraries for decay, activation, dosimetry, nuclide transmutation, burn-up, PKA, KERMA and DPA calculations are now being accumulated through the compilation works of JNDC Nuclear Data Library[2] and JENDL Special Purpose Files[3]. In this present paper, the current status on the development of these invaluable libraries is described. A discussion is also given about how to disseminate and share the products of JNDC activities.

2. Status of Libraries based on JENDL-3.2

Data libraries processed from JENDL-3.2 are summarized in Table 1. This table shows only for typical applications such as fission, fusion, shielding, nuclide transmutation and safety analyses in nuclear fuel cycle. Most of these libraries were produced by JAERI, and tested with numerous benchmarks[4,5]. In this table, "status" means the current status on compilation of the library. "distribution" shows whether or not the library is available to use as free of restrictions. "contact" indicates e-mail address where questions about the library should be addressed.

The other data considering more fundamental purpose are available from WWW (World Wide Web) server located at Nuclear Data Center in JAERI. On this server, point-wise cross sections at 0 and 300K, thermal cross sections (2200 m/s value), resonance integral, Maxwellian average cross sections, Fission spectrum average cross sections, 14 MeV cross sections, 30 keV Maxwellian average cross sections and one-group cross sections for typical BWR/PWR/HCLWR/FBR core conditions are stored for all isotopes (340 materials) in JENDL-3.2. Data transfer with ftp service is only available to domestic users at this time. The URL (Uniform Resource Locator) of this server is (http://cracker.tokai.jaeri.go.jp/index.html) and the IP address is (133.53.24.51). Questions on this service should be addressed to www-admin@cracker.tokai.jaeri.go.jp.

Table 1 Data libraries processed from JENDL-3.2 for typical applications.

SRACLIB-J32: SRAC code system library (JAERI)
Fast (10MeV-0.414eV): 74 groups, Thermal (up to 3.93eV): 48 groups, Resonance (1keV-0.414eV): ultra-fine groups. 268 materials. Self-shielding table temp.: 4(max.). Thermal temp.: 10(max.). Pseudo FP(P67) based on Takano's 65-FP chains considered.
status: completed. distribution: available from JAERI. contact: Takano, H. (JAERI) takano@mike.tokai.jaeri.go.jp
WIMSD-J32: WIMS-D code library (Reactor Integral Test WG in JNDC)
69 groups (up to 10 MeV). 16 materials (H,O,Al,Cr,Fe,Ni,Zr,Sn,U-235,238,Pu-238,239,240,241,242,Am-241).
status: generation in progress. distribution: to be considered. contact: Takami, M. (CRC) m-takami@crc.co.jp
WIMS-D4 code library (PNC)
174 groups. 98 materials for ATR application. (Pu-243,244 retrieved from ENDF/B-V)
status: generation in progress. distribution: no distribution planned. contact: Ihara, T. (PNC) ihara@oec.pnc.go.jp
MVPLIB-J3.2: MVP code library (JAERI)
point-wise (up to 20 MeV). 98 materials(300K), 34 materials(600K), 24 materials(900K), 7 materials(1500K), 6 materials(1800K) and 37 materials will be added for burn-up calculation in FY 1995 (scheduled). KERMA factor for 54 materials prepared.
status: completed. distribution: available from JAERI. contact: Mori, T. (JAERI) mori@mike.tokai.jaeri.go.jp
JFS-3-J32: JAERI Fast Set (JAERI)
JFS-3 type: 70 groups. 106 materials, 185 FP materials, 6 Lumped FP (Gas release: 0%, 100%) for Th-232,U-233,235,238,Pu-239,241.
status: completed. distribution: available from JAERI. contact: Takano, H. (JAERI) takano@mike.tokai.jaeri.go.jp
FSXLIB-J3R2: MCNP4A code library (JAERI)
point-wise (up to 20 MeV). 340 materials (300K). 66 materials include Gamma-ray production data. 61 reactions in JENDL Dosimetry File, KERMA factor for 47 materials considered.
status: completed. distribution: available from RIST. contact: Maekawa, F. (JAERI) fujio@fnshp.tokai.jaeri.go.jp Kosako, K. (SAEI) saei@taurus.bekkoame.or.jp

Table 1 Data libraries processed from JENDL-3.2 for typical applications. (continued)

JSSTDL-295/J32: JSSTDL library (JAERI)
Neutron: 295 groups (up to 19.64MeV), Gamma-ray: 104 groups (up to 50MeV). 63 materials (300K). KERMA factor for 40 materials considered.
status: completed. distribution: available from JAERI. contact: Nakagawa, T. (JAERI) nakagawa@cracker.tokai.jaeri.go.jp
JSSTDL-175/125/42: JSSTDL Collapsed library (JAERI)
Neutron: 175/125/42 groups, Gamma-ray: 42/40/21 groups. 63 materials (300K).
status: generation in progress. distribution: to be considered. contact: Maekawa, F. (JAERI) fujio@fnshp.tokai.jaeri.go.jp
BERMJ3: BERMUDA code system library (JAERI)
Neutron: 125 groups (up to 16.5MeV). 30 materials (300K).
status: completed. distribution: available from RIST. contact: Nakashima, H. (JAERI) nakasima@shield1.tokai.jaeri.go.jp
MGCL-J3.2: JACS code system library (KENO-IV/V code) (JAERI)
137 groups (up to 16.487 MeV). 177 materials (293K).
status: completed. distribution: to be considered from RIST. contact: Naitoh, Y. (JAERI)
ORIGEN2 code library (PWR/BWR) (JAERI)
one-group burn-up dependent effective cross sections. 340 materials. PWR: 2.1wt%(20GWd/t), 3.2wt%(33GWd/t), 3.4wt%(39GWd/t), 4.1wt%(48GWd/t), 4.7wt%(55GWd/t). BWR: 3.0wt%(void fraction 40%), 4.0wt%(void fraction 0/40/70%), 5.0wt%(void fraction 40%).
status: generation scheduled in FY 1996. distribution: to be considered. contact: Kurosawa, M. (JAERI) kurosawa@s4a.tokai.jaeri.go.jp
ORIGEN2 code library (FBR) (PNC)
one-group burn-up dependent effective cross sections. 340 materials. Large-scale FBR (1000MWe) homogenized core/blanket retrieved Pu/U from LWR/FBR for oxide/metal fuels.
status: start to generation. distribution: to be considered. contact: Yoshida, T. (Toshiba) yos@rcg.nel.rdc.toshiba.co.jp

Table 1 Data libraries processed from JENDL-3.2 for typical applications. (continued)

Nuclide Equilibrium Transmutation library (PWR/BWR/FBR/GCR) (Titeck)
one-group effective cross sections in nuclear equilibrium state. FBR(sodium cooled oxide/metal fuels), PWR, GCR. 129 heavy materials (Tl-206 to Fm-255), 1238 FP materials (H-3 to Lu-172)
status: completed (FBR oxide fuel, PWR). the other in progress. distribution: available from Tokyo Institute of Technology. Data will be supplied "as is". contact: Sekimoto, H. (Titech) hsekimot@nr.titech.ac.jp

3. Status of Libraries based on JNDC Nuclear Data Library and JENDL Special Purpose Files

In the products of JNDC activities, JNDC Nuclear Data Library for FP decay data and several kinds of JENDL Special Purpose Files have been released. Data libraries processed from these files are summarized in Table 2. This table contains information only for decay, dosimetry, activation, fusion and PKA files. These libraries were produced by JAERI. In this table, "status", "distribution" and "contact" indicate the same meaning as shown in Table 1.

Table 2 Data libraries processed from the other files compiled by JNDC.

Decay Data Library of ORIGEN2 (JAERI) [processed from JNDC Decay Data Library]
decay data and the release energy were updated to meet The AESJ/JNDC decay heat standards. An easy replacement with the original ORIGEN2 decay library is considered.
status: completed. distribution: to be considered. contact: Katakura, J. (JAERI) katakura@cracker.tokai.jaeri.go.jp
Dosimetry library (JAERI) [processed from JENDL Dosimetry File]
61 reactions in 42 nuclides. point-wise and the SAND-II group structure (640 groups). reevaluation work of JENDL Dosimetry File is being proceeded. covariance data for 30 nuclides will be included in the next revision. library for the MCNP4A code is available.
status: completed. the revised version will be released in FY 1996 (scheduled). distribution: available from WWW server of Nuclear Data Center in JAERI. contact: Nakagawa, T. (JAERI) nakagawa@cracker.tokai.jaeri.go.jp
Activation library (JAERI) [processed from JENDL Activation File]
1158 reactions in 225 nuclides. 175/125 group cross sections.
status: to be completed in FY 1995. distribution: to be considered. contact: Ikeda, Y. (JAERI) ikeda@fnshp.tokai.jaeri.go.jp

Table 2 Data libraries processed from the other files compiled by JNDC. (continued)

FSXLIB-JFF: MCNP4A code library (JAERI) [processed from JENDL Fusion File]
point-wise (up to 20 MeV). 72 materials (300K). (Li-6,7,C-12 retrieved from JENDL-3.2)
status: evaluation in progress. distribution: to be considered. contact: Maekawa, F. (JAERI) fujio@fnshp.tokai.jaeri.go.jp Kosako, K. (SAEI) saei@taurus.bekkoame.or.jp
PKA library generated with ESPERANT code (JAERI)
PKA cross sections up to 50 MeV. 177 nuclides. PKA library up to 20 MeV was completed for F-19 to Bi-209. KERMA/DPA library will be generated in FY 1996.
status: completed (PKA up to 20 MeV), in progress (KERMA/DPA). distribution: available from JAERI. contact: Fukahori, T. (JAERI) fukahori@cracker.tokai.jaeri.go.jp

4. Discussion and Conclusion

From the previous sections, we could understand that the products of JNDC were applicable in various areas of nuclear design applications. How we can disseminate and share the JNDC products much more? We would recognize that three problems blocking the dissemination exist. One is the JNDC products are recorded in the ENDF-5/6 format. New users may not be familiar with the ENDF/B format and many design engineers require data in the formats close to each target application. We should pay much attention to generating data library which is directly applicable to the design tools. The second problem is accessibility. Multi-media and internet communication tools are rapidly growing. RSIC in Oak Ridge National Laboratory added CD-ROM media using a 650-MB recordable disk for distribution from September 1995[6]. OECD Publications started distribution service on a JEF-PC package[7] for personal computers which provided the ability to display selected data from the JEF-2.2 library in both numerical and graphical form. We should consider the JENDL-3.2 distribution in a user-friendly manner. Moreover, ftp service is essentially needed not only to domestic users but also to international users. On-line sign-on procedure will be needed as authentification when the user gets libraries distributed from the authorized organization, since maintenance and upgrade costs may be required in the future. The third problem is how to share technical information with each other. The technical information on the data reliability for typical applications will be important to users who wish to use the JNDC products. A final document such as JAERI report is most suitable, but it takes considerable time to prepare and publish it. Many evaluation and validation works would be available from published Journals, Reports, Proceedings, Memos...., but these are not classified into each nuclide/application. We propose a compilation work to collect sources and classify into several groups, then the compiled information should be stored in the WWW server on Nuclear Data Center in JAERI, because the internet communication tool such as WWW is suitable to distribute information.

Acknowledgements

The author wishes to thank members of JNDC whose useful comments on the status of data libraries were essential for preparing this manuscript.

References

[1] Kikuchi Y.: "JENDL-3 REVISION-2 -JENDL-3.2-," Proc. Int. Conf. on Nuclear Data for Science and Technology, May 9-13, 1994, Gatlinburg, USA, p.685 (1994, ANS, Inc.).

[2] Tasaka K. et al.: "JNDC Nuclear Data Library of Fission Products –Second Version–," JAERI–1320 (1990).
[3] Nakagawa T. and Kikuchi Y.: "JENDL Special Purpose Files," Proc. Int. Conf. on Nuclear Data for Science and Technology, May 9–13, 1994, Gatlinburg, USA, p.709 (1994, ANS, Inc.).
[4] Takano H., Akie H. and Kikuchi Y.: "Benchmark Tests of JENDL–3.2 for Thermal and Fast Reactors," ditto., p.809.
[5] Yamano N., Hasegawa A., Ueki K. and Kawai M.: "Status on Testing of JENDL–3.2 Iron Data with Shielding Benchmarks," ditto., p.812. see also Yamano N., Hasegawa A., Ueki K. and Kawai M.: "Status on Neutron Data Testing of JENDL–3.2 with Shielding Benchmarks," Proc. 8th Int. Conf. on Radiation Shielding, April 24–28, 1994, Arlington, USA, p.824 (1994, ANS, Inc.), Yamano N. and Ueki K.: Journal of Nucl. Sci. Technol., Vol. 32, p. 614 (1995).
[6] RSIC Newsletter No. 370, September 1995, Oak Ridge National Laboratory.
[7] Konieczny M., Potet B. and Rockey J.: "A PC Program for Displaying Data from the Joint Evaluated File(JEF) Library," Proc. Int. Conf. on Nuclear Data for Science and Technology, May 9–13, 1994, Gatlinburg, USA, p.754 (1994, ANS, Inc.).

2.1.2 Analysis of JUPITER Critical Experiments by JENDL-3.2

Makoto ISHIKAWA
O-arai Engineering Center, Power Reactor and Nuclear Fuel Development Corporation (PNC)
4002 Narita-cho, O-arai-machi, Ibaraki-ken 311-13, e-mail: ishikawa@oec.pnc.go.jp

Applicability of the JENDL-3.2 library to large FBR cores was evaluated using JUPITER experimental data. The nuclear characteristics treated in the present report include criticality, reaction rate ratio, space dependency of C/E values, sodium void reactivity and Doppler reactivity. As a conclusion, JENDL-3.2 is judged to be a well-balanced library for prediction of large FBR core parameters. The unification of integral experimental information from JUPITER and differential nuclear data of JENDL-3.2 will enhance the accuracy and reliability of large FBR core design.

1. Introduction

A series of critical experiments for large FBR core study, JUPITER, was analyzed with a JENDL-3.2-based 70-group constant set, JFS-3-J32, referred to as J3.2 hereafter. The C/E values of JUPITER were compared with those of the earlier JENDL-2 and JENDL-3.1-based libraries (J2 and J3.1), and their physical consistency was evaluated by extensive use of the cross-section sensitivity method. Further, J3.2 was preliminarily adjusted using these C/E values from JUPITER experiments and the results were compared with those of J2.

2. Outline of JUPITER Experiment

The JUPITER critical experiment[1] was a joint research program between US DOE and PNC of Japan, using the ZPPR facility at ANL-Idaho from 1978 to 1988. The aim of JUPITER was to study the nuclear characteristics of large LMFBR cores with variant core concepts and structures, which were divided into four series of experiments.

The first series was JUPITER-I (ZPPR-9 through 10D/2), a set of critical experiments for conventional two-zone homogeneous cores of 600 to 800 MWe-class FBRs, including a clean benchmark core and six engineering mockup cores with control rods or control rod positions. The second set was performed as JUPITER-II (ZPPR-13A through 13C), and studied six radially-heterogeneous cores of 650 MWe-class. For the third series, half of JUPITER-III (ZPPR-17A through 17C) was dedicated to the investigation of three axially-heterogeneous cores of 650 MWe-class. Finally, the ZPPR-18A through 19B cores, both the latter half of JUPITER-III and Io series, consisted of five 1,000 MWe-class homogeneous cores with enriched uranium in the outer core region. The JUPITER program is the largest critical experiment in the FBR history so far, and the data include much valuable information for large FBR core study.

3. Analytical Methods of JUPITER

The standard calculational flow of fast reactor analysis[2] is divided into three parts as depicted in Fig.1. The first step is to generate homogenized effective cross-sections from a basic 70-group constant set such as J3.2, by means of one-dimensional heterogeneity cell models. The preceding J2 and J3.1 constant sets were also used for comparison here. In JUPITER analysis, there are some features in this homogenizing procedure: (a) each plate is stretched in height to make a one-dimensional model from as-built structure, where total atomic numbers of the plate are conserved (Plate-stretch model), (b) the background cross-section to take the plate-heterogeneity into account is based on Tone's method[3], which can treat the resonance shielding effect of mutual nuclides in plural plates more precisely than the traditional Dancoff coefficient, and (c) effective transport cross-sections are evaluated by current($1/\sigma_t^2$)-weighted self-shielding factors, which are regarded as more physically reasonable than flux($1/\sigma_t$)-weighted ones.

Next, to obtain basic analytical values, reactor characteristics are calculated using three-dimensional XYZ diffusion theory with Benoist's anisotropic diffusion coefficients[4], which can treat the streaming effects of the plate structure. Here, the number of energy groups is 18 or 70, depending on the complicatedness of target core parameters. The standard mesh size is approximately 5 cm. The compositions of drawers are homogenized for each core region and each drawer type.

As the last step, the basic analytical values are corrected for many aspects to obtain the most detailed-modeling results. The correction factors considered in the present study are: the transport effect using three-dimensional XYZ model[5], the mesh effect for extrapolating to zero-mesh-sized values, the number-of-energy-group effect if needed, an all-master model to reflect the slight difference of drawer-wise compositions, a multi-

drawer model to treat the interference between fuel and blanket regions, and the cell-asymmetry effect that is needed only for JUPITER-I experiment.

Besides the standard calculational procedure above, some new detailed analytical methods have been applied recently. One is the continuous energy Monte Carlo method[6,7], which enables us to simulate the complicated as-built structure without any approximations, although much computing time is needed to get small statistical errors. The other is the ultra-fine energy structure calculation[8] over 150,000-energy groups, which can handle individual resonance peaks precisely unlike the coarse 70-group analysis.

Further, one special feature of the present study is the wide use of cross-section sensitivity analysis, only from which the physical consistency of various C/E (calculation/experiment) values can be judged quantitatively against both different cores and nuclear characteristics. An attempt to adjust J3.2 by a set of 84 data from JUPITER was preliminarily performed in this context. The detail of the cross-section adjustment method applied here is described elsewhere[8,9].

4. Evaluation

In this chapter, the analytical results of JUPITER experiments by J3.2 are summarized and evaluated from the viewpoint of applicability to large FBR cores. The nuclear characteristics evaluated here include criticality, reaction rate ratio, space dependency of C/E values, Na void reactivity and Doppler reactivity.

(1) Criticality

The final C/Es of JUPITER criticality using J3.2 are summarized and compared with those from J2 and J3.1 in Fig.2. The analytical values based on J3.2 slightly underestimate the criticality by the order of -0.5%dk, while the C/E dependency on core heterogeneity is reduced from that of J2. Although the C/E values seem rather closer to those of J2 than J3.1, sensitivity analysis indicated that the nuclide-reaction-wise contributions were extremely complicated and canceled with each other as shown in Fig.3. This means that these C/E values of JUPITER cannot be easily applied to other cores with different compositions or cross-section sensitivities by the simple bias method.

In order to verify the performance of the standard JUPITER analytical method, Table 1 compares the results for ZPPR-9 criticality with those of Monte Carlo codes. The standard JUPITER method can be judged to be quite accurate for the criticality evaluation, since it agrees with the Monte Carlo method only in the difference of approx. 0.1%dk.

The change of criticality C/Es from the cross-section adjustment of J3.2 is shown in Fig.4, compared with that of J2. All adjusted C/Es for both libraries become almost unity in spite of the wide variety of core concepts in JUPITER. Further, although the C/Es before adjustment were a little different between J3.2 and J2, they agreed almost identically after adjustment. This fact is quite satisfying from the reliability viewpoint of the adjusted library.

(2) Reaction Rate Ratio

Figure 5 shows the C/Es for the reaction rate ratio of U-238 capture to Pu-239 fission (C28/F49) in JUPITER cores. Apparently the C/Es of C28/F49 by J3.2 are overestimated by 4-6%, which is just the same as the previous J2 case. On the other hand, the recent result at FCA showed good agreement between experiment and analysis for this reaction[10], which is not consistent with the JUPITER's results. Since the difference of cross-section sensitivity or analytical methods between JUPITER and FCA could not explain the inconsistency of C28/F49, it seems that experimental methods of JUPITER need some reviewing. After adjustment of cross-sections in Fig.6, the C/E values improved by 3%, but are still overestimated consistently in JUPITER cores.

For the reaction rate ratio of U-235 fission to Pu-239 fission (F25/F49), the C/Es of J3.2 seemed to be improved by 2% from J2 as seen in Fig.7. The adjusted C/Es in Fig.8 were lowered by 2% in both cases of J3.2 and J2.

Figures 9 and 10 show the C/Es of the reaction rate ratio of U-238 fission to Pu-239 fission (F28/F49) before and after adjustment, respectively. In JUPITER, however, the C/Es of F28 reaction cannot be used for nuclear data evaluation since the scattering of measured values was too large.

(3) Space Dependency of C/E Values

The past analytical results of JUPITER by J2 indicated the C/Es of control rod worth and reaction rate distribution systematically changed with the radial positions in cores[11]. Figure 11 shows the C/E dependency of control rod worth on radial positions in the ZPPR-9 core for various libraries. The persistent 'C/E space dependency' of J2 was found to be largely alleviated by using J3.2, though it still exists in some degree. The results of the other cores are shown in Fig.12 with similar improvement by J3.2, except for ZPPR-19B case that has different characteristics due to the presence of enriched uranium in the outer core region. The nuclide-wise contributions of this improvement for space dependency in ZPPR-10A are examined in Fig.13. We find this change comes from the combination of many nuclides and reactions as in the case of criticality. The C/Es of

control rod worth can be further improved by the adjustment as shown in Fig.14, especially for the case of ZPPR-19B.

A similar tendency for the F49 distribution is found in Fig 15. The J3.2 set improved the C/E space dependency from J2 except for the ZPPR-19B case. Figure 16 shows the adjusted results for the F49 distribution. Although the C/Es seem to be excessively corrected by the adjustment, the values are deviated only by less than 2%, which is within the experimental and analytical errors of JUPITER. The results of reaction rate distribution are considered as consistent with those of control rod worth.

Although the problem of C/E space dependency was almost solved by the adoption of J3.2 and the cross-section adjustment, there still remain other concerns about the space-dependent characteristics of large FBR cores, that is, the underestimation of reaction rate in blanket regions. Figure 17 shows the C/Es of F49 reaction rate distribution in the radially heterogeneous core, ZPPR-13A, where the C/E values are obviously lower in the internal blanket rings and radial blanket region. To reduce the underestimation of reaction rate in blanket regions, a correction was tried using a continuous energy Monte Carlo calculation. The correction was found to improve the C/Es in the blanket regions to a degree as shown in Fig.17. From this fact, there might be possibilities to solve the problem by applying some modified analytical methods such as the direction-flux-weighted group-constant generation technique as proposed by R.N.Hill, et al[12].

(4) Sodium Void Reactivity

One of the large concerns about the former J2 library in FBR application was the well-known extreme overestimation of sodium void reactivity[11]. The C/Es of sodium void reactivity by J3.2 were in the range of 0.95-1.15 and greatly improved from the J2 case as seen in Fig.18. The leakage and non-leakage components of sodium void reactivity from J3.2 and J2 are compared in Fig.19 for various void region sizes. The improved J3.2 prediction comes from rather small changes of the non-leakage term. Figure 20 shows the nuclide-wise contributions of sodium void reactivity changes from J2 to J3.2. It is found that sodium inelastic and Pu-239 capture reactions, which were not considered important before, mainly contributed to this improvement, although many other nuclide-reactions have opposite effects and canceled with each other, as in the case of criticality.

From the viewpoint of nuclear data evaluation, there might occur a question about why U-238 inelastic reactions did not contribute to the sodium void reactivity changes as shown in Fig. 20, in spite of the large difference of the evaluated inelastic cross-sections between J3.2 and J2. Figure 21 gives the answer, that is, the changes of scattering matrix components from J3.2 to J2 canceled with each other for sodium void reactivity, although the effect of each matrix component is very large for the reactivity value. This fact means we need to consider not only the total cross-sections of inelastic reactions but also matrix-wise to improve the prediction capability of a library. We are going to include the treatment of inelastic matrix-wise components in the next step of the cross-section adjustment study.

As seen in Fig.22, the adjustment of J3.2 made the C/Es of sodium void reactivity move closer to unity for the inner-blanket voiding case of ZPPR-17A as well as for core-regions, which is preferable from the viewpoint of physical consistency.

(5) Doppler Reactivity

In JUPITER, Doppler reactivity was measured as a kind of sample worth. Figure 23 shows the C/Es of Doppler reactivity for various temperature ranges in ZPPR-9 core. Relatively, the C/Es of J3.2 improved by 4% from those of J2 due to the extension of the U-238 unresolved resonance region in J3.2. The absolute values of Doppler reactivity are, however, still significantly underestimated.

Since the Doppler reactivity by the sample worth experiment was found very sensitive for the modeling methods of reactor analysis as designated in Table 2, it seems we need to study further the analytical method from the reactor physics viewpoint for such as the interference effect between Doppler sample and core fuel, as well as the treatment of the resonance region in nuclear data evaluation.

5. Conclusion

As a conclusion of the present study, the J3.2 library is judged to be a well-balanced library for applicability to large FBR cores, especially from the viewpoint of the C/E space-dependency and the sodium void reactivity, although there is room to further improve the performance. On the other hand, the sensitivity analysis of JUPITER indicated that the C/E values should not be simply applied to reactor design works without reflection of sensitivity difference between experiments and design cores, since the components of prediction changes by different libraries were found to be exceedingly complicated. Therefore the unification of integral experimental information from JUPITER and differential nuclear data of J3.2, by the cross-section adjustment, is considered as the most promising policy to enhance the accuracy and reliability of large FBR core design.

Acknowledgment

The present work has been performed as a part of efforts to develop a standard data base for FBR core nuclear design, working group members of which are: Masayuki Saito(CRC), Wakaei Sato and Ken-ichi Ibato(NESI),

Kazuteru Sugino(PNC), and Toshio Sanda(Hitachi). The author deeply appreciates their collaborations for the numerous analyses and discussions.

References

[1] Shirakata K., et al.: Proc. Int. Conf. on Nucl. Data for Sci. and Tech., Mito, 53 (1988)
[2] Ishikawa M., et al.: J. Atomic Energy Soc. of Japan,**36**, 11, 1031 (1994)
[3] Tone T.: J. Nucl. Sci. Technol.,**12**[8], 467 (1975)
[4] Benoist P.: Nucl. Sci. Eng.,**34**, 285 (1968)
[5] Yamamoto, T., et al.: Proc. Int. Conf. on Math. Methods and Computation, Portland, 470 (1995)
[6] Blomquist R.N., et al.: OTNL/RSIC-44 (1980)
[7] Mori T., et al.: JAERI-Data/Code 94-007 (1994)
[8] Ishikawa M., et al.: 1992 Symp. on Nucl. Data, JAERI-M 93-046, 36 (1993)
[9] Ishikawa M., et al.: Proc. Int. Conf. on Math. Methods. and Supercomputing, Karlsruhe, 593 (1993)
[10] Sakurai T., et al.: 1994 Symp. on Nucl. Data, JAERI-Conf 95-008, 53 (1995)
[11] Yamamoto M., et al.: Proc. Topical Meeting on Reac. Phy. and Shielding, Chicago, 773 (1984)
[12] Hill R.N., et al.: Nucl. Sci. Eng.,**103**, 12, 25 (1989)

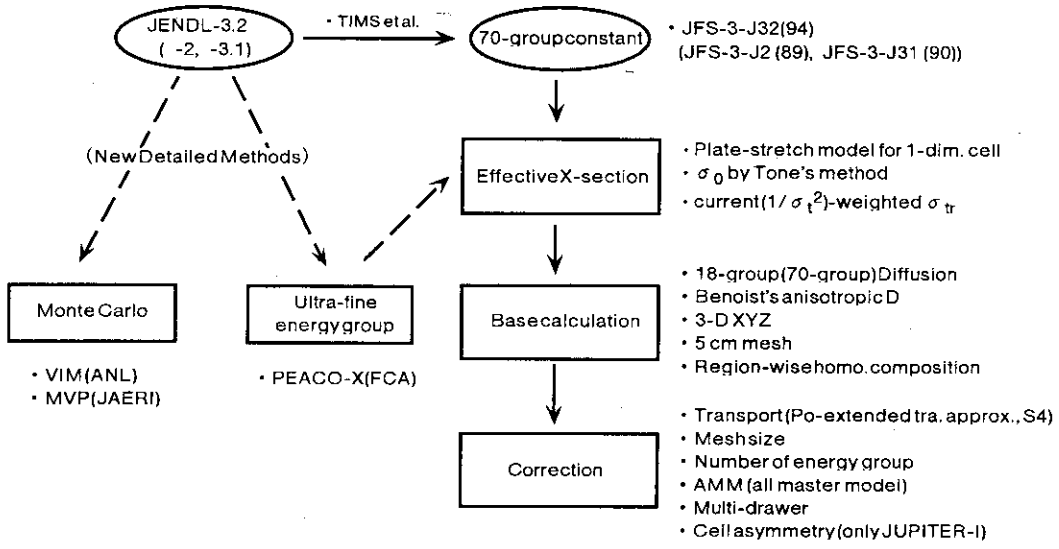

Fig.1 Analytical Method of JUPITER Experiments

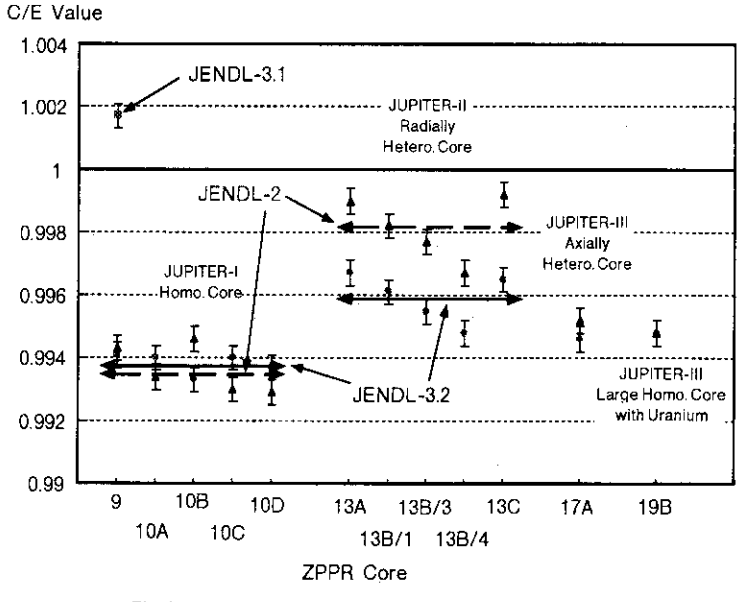

Fig.2 Criticality Analysis of JUPITER Experiment

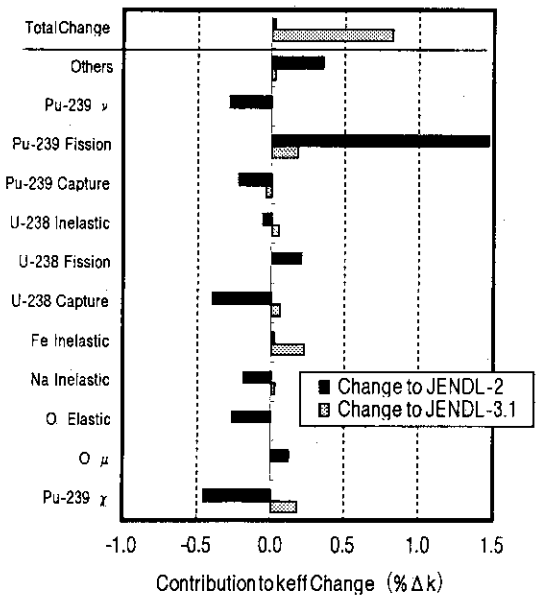

Fig. 3 Components of keff Dependency on Libraries (ZPPR-9 core、Difference with JENDL-3.2)

Table 1 ZPPR-9 Criticality Evaluation by Monte Carlo Method

Method	Orgnization	JENDL-2	JENDL-3.1	JENDL-3.2
Finite Difference (3D-transport, various corrections)	PNC	0.9943	1.0017	0.9941
Finite Difference (2D-transport)	JAERI (H.Takano)	0.9991	1.0063	0.9986
Monte carlo code - MVP (730,000 history)	JAERI (H.Takano)			0.9952 ±0.00047
Monte carlo code - VIM (1,200,000 history)	PNC		1.0004 ±0.0006	

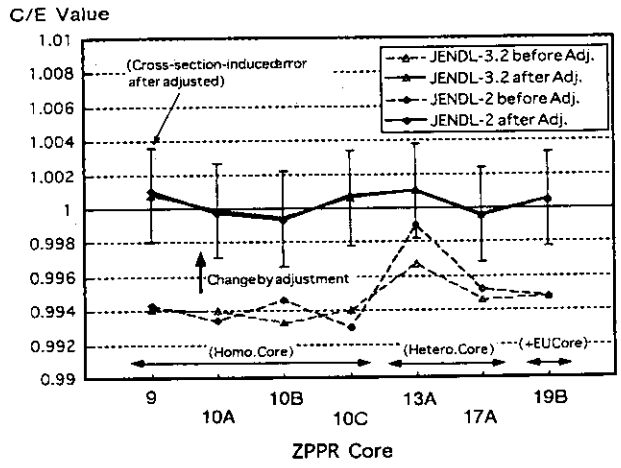

Fig. 4 Cross-section Adjustment by JUPITER - Criticality-

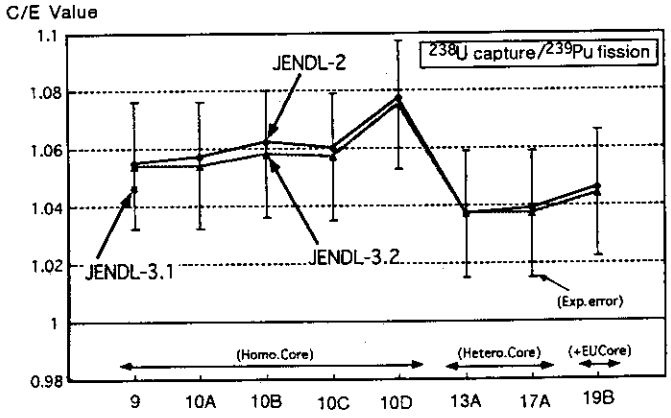

Fig. 5 C28/F49 Analysis of JUPITER Experiment

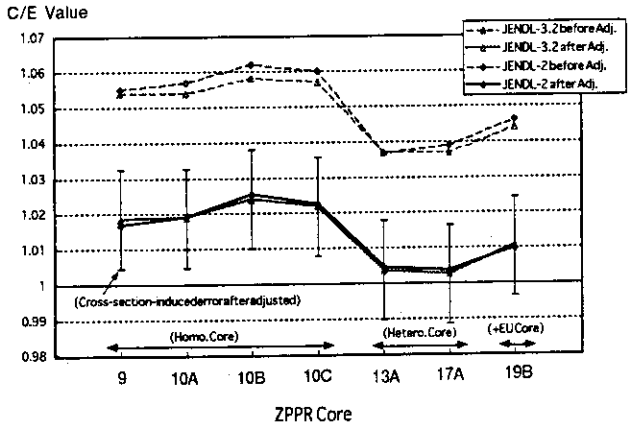

Fig.6 Cross-Section Adjustment by JUPITER - C28/F49 -

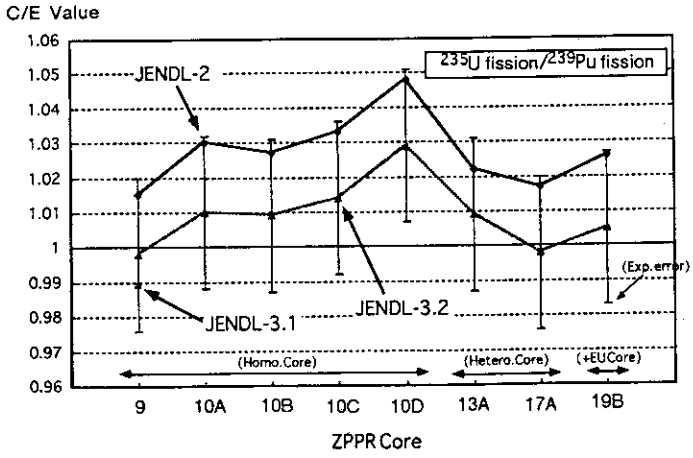

Fig.7 F25/F49 Analysis of JUPITER Experiment

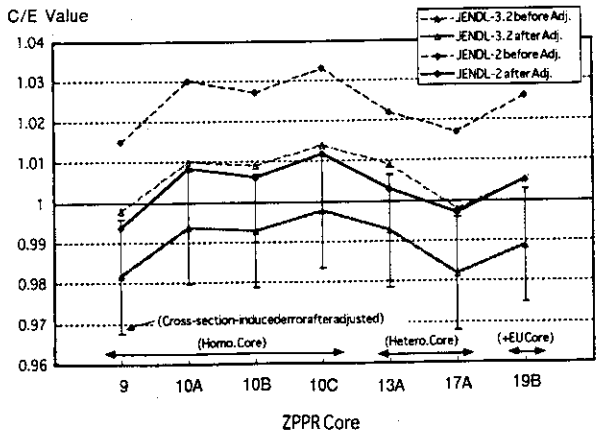

Fig.8 Cross-Section Adjustment by JUPITER - F25/F49 -

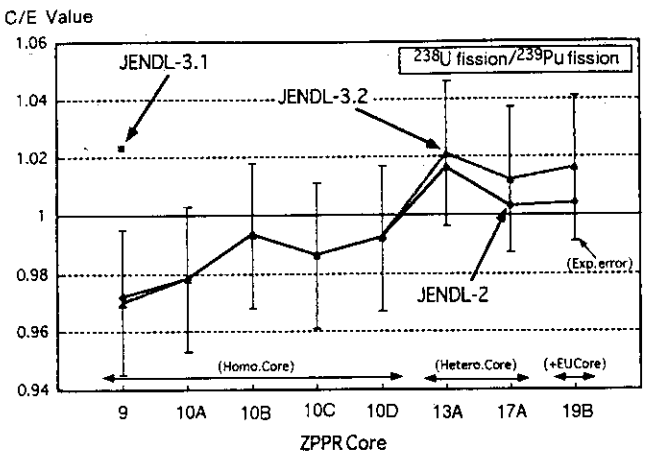

Fig.9 F28/F49 Analysis of JUPITER Experiment

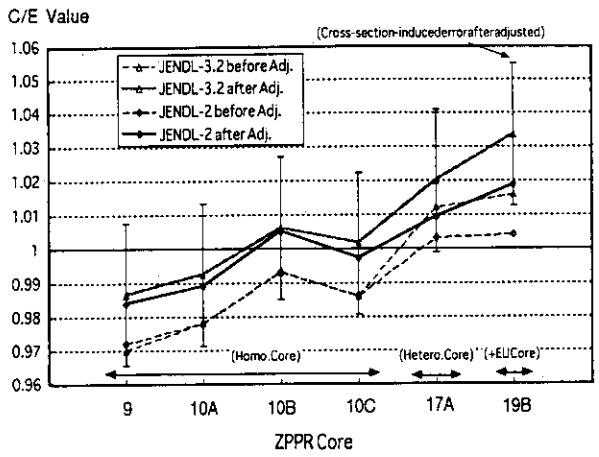

Fig.10 Cross-Section Adjustment by JUPITER - F28/F49 -

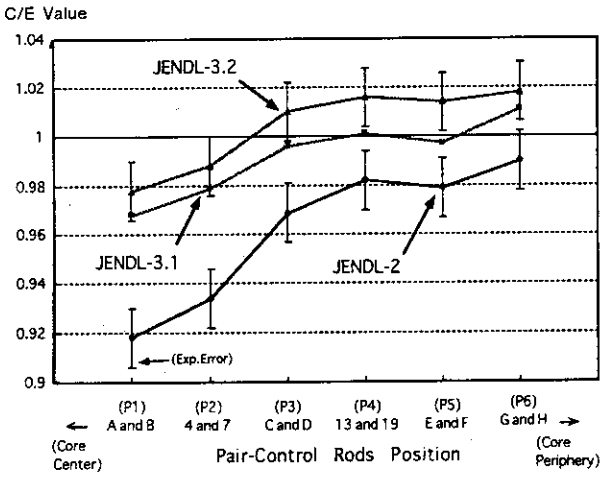

Fig. 11 Control Rod Worth Analysis of ZPPR-9 Core

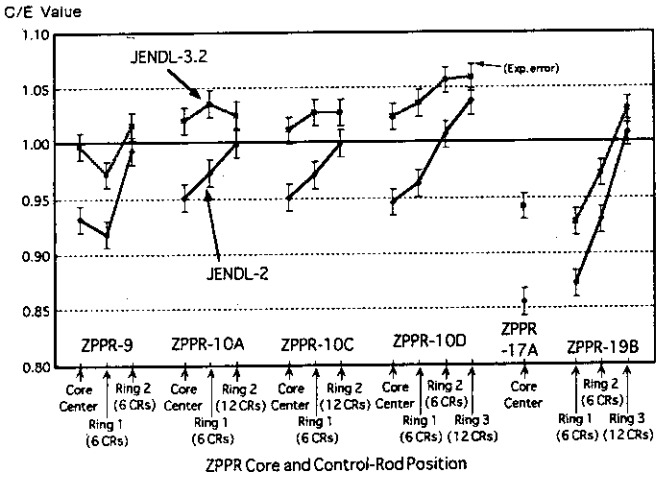

Fig.12 Control Rod Worth Analysis of JUPITER Experiment

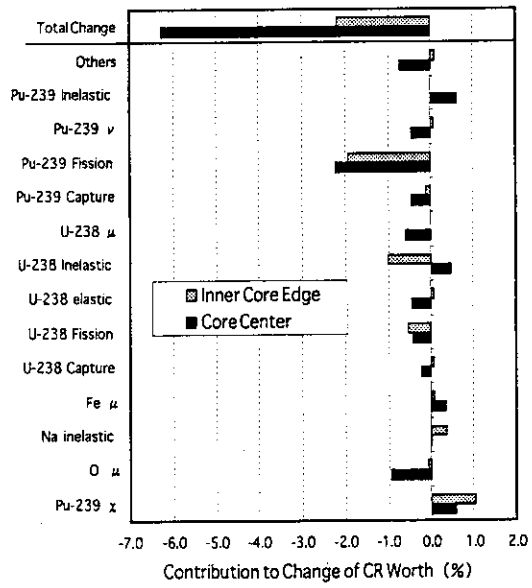

Fig.13 Nuclide-wise Contribution to Control Rod Worth Change (ZPPR-10A Core, From JENDL-3.2 to JENDL-2)

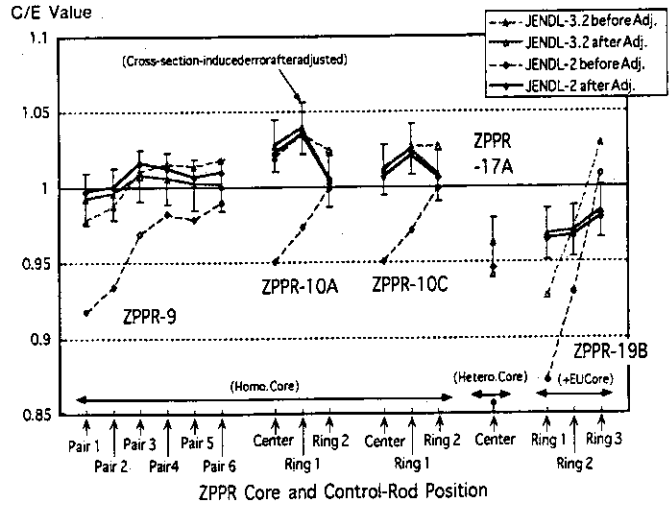

Fig. 14 Cross-Section Adjustment by JUPITER - CR Worth -

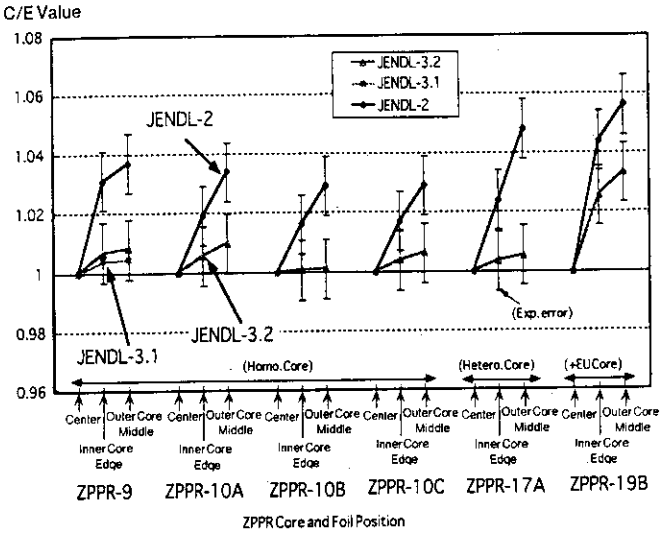

Fig. 15 F49 Distribution Analysis of JUPITER Experiment

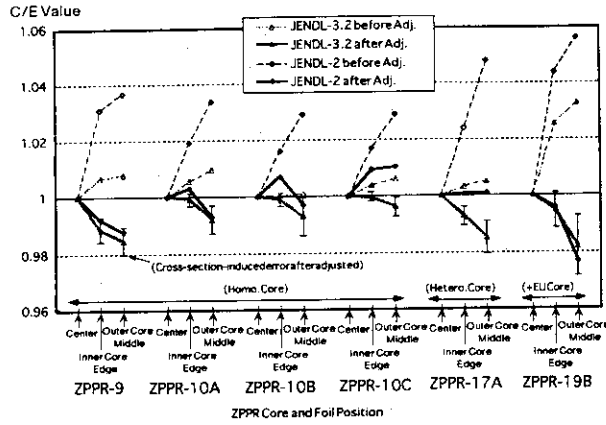

Fig. 16 Cross-Section Adjustment by JUPITER - F49 Distribution -

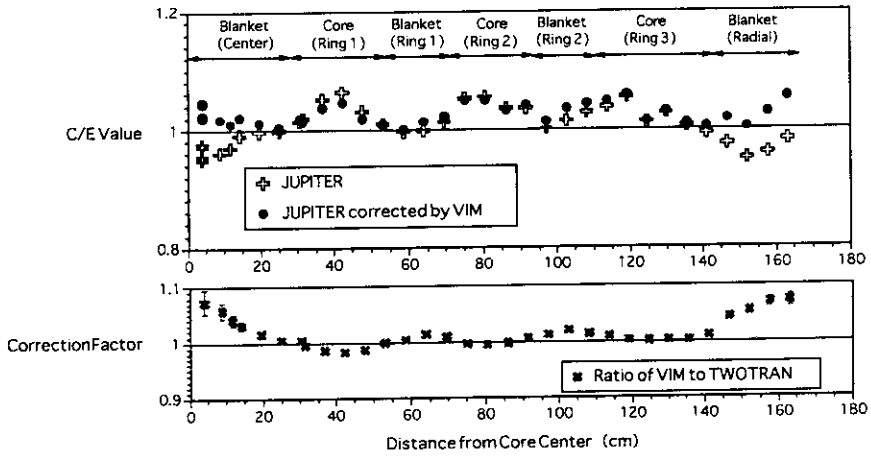

Fig. 17 F49 Distribution Analysis corrected by Monte Carlo Method
(Radially Heterogeneous Core - ZPPR-13A -)

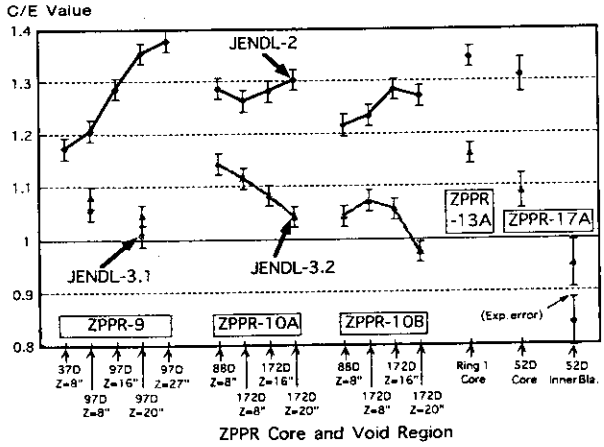

Fig.18 Na Void Reactivity Analysis of JUPITER Experiment

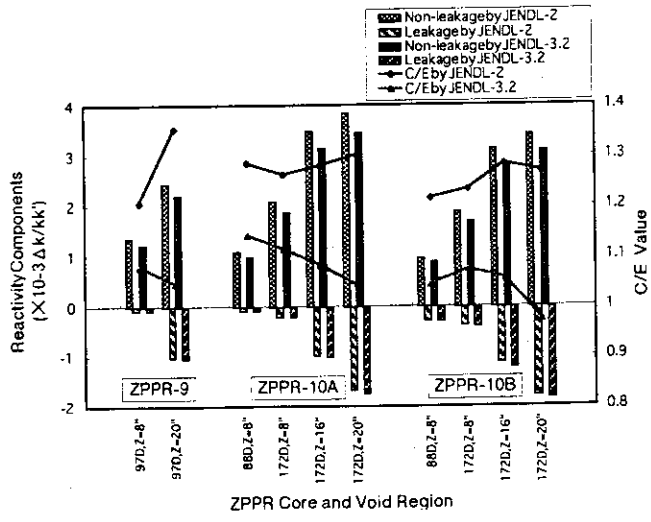

Fig. 19 Components of Na Void Reactivity

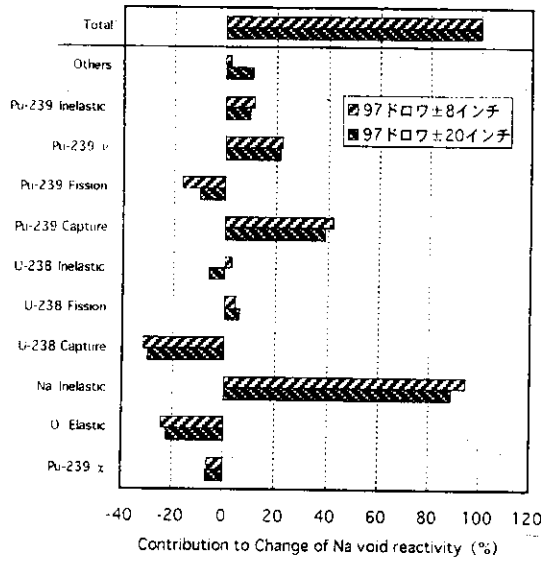

Fig. 20 Nuclide-wise Contribution to Na Void reactivity
(ZPPR-9 Core, Difference between JENDL-3.2 and JENDL-2)

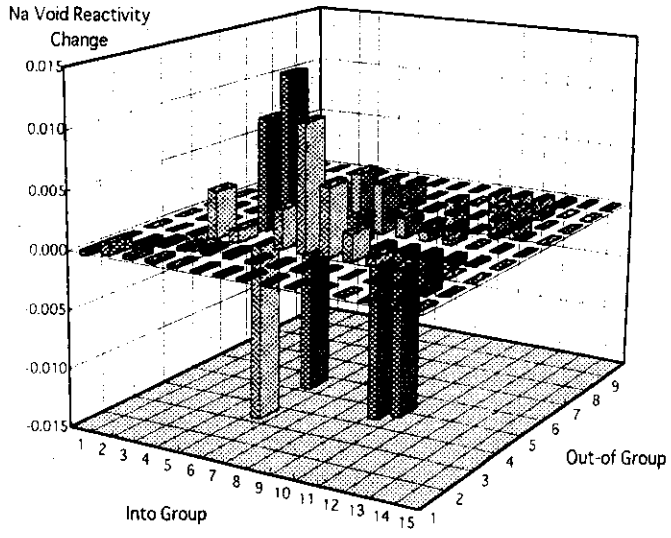

Fig. 21 U-238 Inelastic Scattering Contribution to Na Void Reactivity
(ZPPR-9 Core, Change from JENDL-3.2 to JENDL-2)

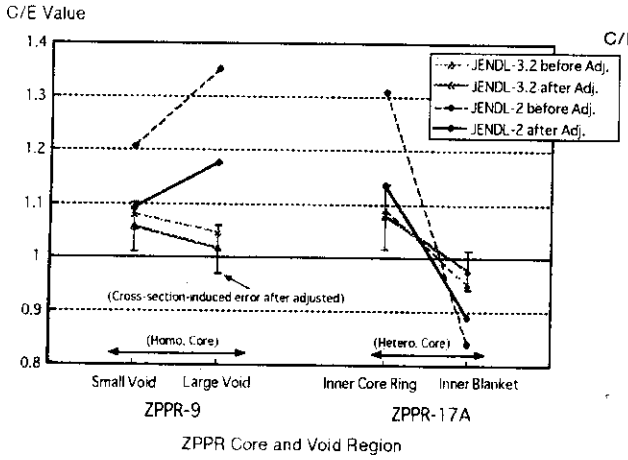

Fig.22 Cross-Section Adjustment by JUPITER - Na Void Reactivity -

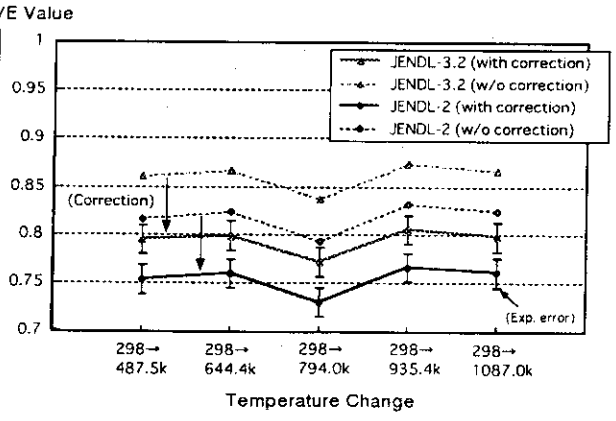

Fig. 23 Doppler Reactivity Analysis of JUPITER Experiment
(ZPPR-9 Core)

Table 2 Correction Factor for ZPPR-9 Doppler Reactivity

Diffusion, Isolated lump model (JENDL-3.2-based 70 group) :	C/E = 0.86
● Transport & Mesh correction :	-3%
● Cell asymmetric correction :	-5%
After Corrected :	C/E = 0.79
< Other Effects >	
● Cell heterogeneity model and Definition of σ tr for core fuel : (Tone, Current ($1/\sigma_t^2$) - weighted σ_{tr} → Dancoff, Flux ($1/\sigma_t$) - weighted σ_{tr})	+2%
● Core modeling for flux and adjoint calculation : (Sample included → Not included)	+3%
● Resonance Interference Effect by PEACO-X : (JENDL-3.1-based 151,700 group, FCA, S.Okajima)	+5 - +7%

2.1.3 Reactor Physics Tests and Benchmark Analyses of STACY

Yoshinori MIYOSHI, Takuya UMANO

Department of Fuel Cycle Safety Research
Japan Atomic Energy Research Institute

1. INTRODUCTION

The Static Experiment Critical Facility, STACY in the Nuclear Fuel Cycle Safety Engineering Research Facility, NUCEF is a solution type critical facility to accumulate fundamental criticality data on uranyl nitrate solution, plutonium nitrate solution and their mixture [1,2].

A series of critical experiments have been performed for 10 wt% enriched uranyl nitrate solution using a cylindrical core tank.

In these experiments, systematic data of the critical height, differential reactivity of the fuel solution, kinetic parameter and reactor power were measured with changing the uranium concentration of the fuel solution from 313 gU/ℓ to 225 gU/ℓ.

Critical data through the first series of experiments for the basic core are reported in this paper for evaluating the accuracy of the criticality safety calculation codes.

Benchmark calculations of the neutron multiplication factor keff for the critical condition were made using a neutron transport code TWOTRAN in the SRAC system [3] and a continuous energy Monte Carlo code MCNP 4A[4] with a Japanese evaluated nuclear data library, JENDL 3.2.

2. CRITICAL FACILITY

STACY consists of the core tank containing fuel solution, solution transfer system, fuel storage system, solution adjusting system, and water reflector system [5,6]. The fuel solution is fed from the storage tank to the core tank through a critical approach. The core tank has a cylindrical geometry with a diameter of 60 cm, which is made of stainless steel SUS 304.

Solution height in the core tank is measured with contact type height gauge. This height gauge has an accuracy of ±0.2 mm. Two B10 counters and four gamma compensated ionization chambers were positioned around the core tank to measure in the source range and power range, respectively. The maximum power is limited up to 200 watt. The external neutron source, Am-Be, is inserted below the bottom of the core tank at the beginning of the operation. Reactivity is controlled by adjusting the solution height in the core tank without control rods.

3. EXPERIMENT

Main experimental items through the first series of experiments are listed in Table 1.

3.1 Critical solution height

The cylindrical core tank was settled in a reflector pool and the light water was supplied into the reflector pool before the operation. The side reflector and lower reflector are more than 30 cm in thickness. The height of the water reflector was 20 cm more than the upper plate of the core tank. The vertical cross section of the core tank is shown in Figure 1. The initial critical approach for a water reflected core was performed on February 23, 1995 using the uranyl nitrate solution containing 310.1 gU/ℓ and 2.2 mol/ℓ free nitric acid, and the measured critical height was 41.5 cm. The uranyl nitrate solution had an enrichment of 9.97wt%. Additional four experimental channels composed of three He3 proportional counters and one B10 counter (Channel 1-4) are positioned around the core tank. The lowest uranium concentrations for the water reflected and unreflected cores were 225 gU/ℓ and 242 gU/ℓ, respec-

tively under the limitation for the maximum critical height of 140 cm. Measured critical heights are summarized in Table 2.

3.2 Tests on nuclear limitations

The nuclear limitations such as maximum reactivity and maximum reactivity addition rate are fundamental quantities for safe operation of the critical assembly. The differential reactivity was evaluated using an inhour equation by measuring the reactor period at a slightly super critical state after attaining criticality. The dependence of differential reactivity on the solution height is determined by the shape of the fundamental mode of the neutron flux along the vertical direction.

The neutron flux distribution along the vertical direction was measured by activation of gold wires attached on the outer surface of the core tank. Activity of the gold wire was measured with a NaI(Tl) scintillation counter using the beta-gamma coincidence counting technique. Four cylindrical safety rods containing B_4C pellets are positioned at the upper part of the core tank, and are dropped by gravity in an emergency shutdown condition.

Reactivity worth of safety rods were measured using a rod drop method to evaluate the shutdown margins in both conditions of all-rod insertion and one-rod stuck insertion.

Power calibration was made using an analysis of fission products in the fuel solution which was sampled after the operation. The gamma activities were measured with a Germanium detector for fission products such as Ce143 and Ba140, and Np239, which is produced by capture reaction of U238,. In addition, the activation method of Au foil attached to the outer surface of the core tank was applied to the experimental core, and the validity of this method was confirmed by comparison with the calibrated power by FP analysis method. In the irradiation of gold foil, the integral power of the operation was estimated by combining the activity of the Au foil and activation rate calculated by MCNP4A, a continuous neutron Monte Carlo code.

4. CALCULATION AND DISCUSSION

4.1 Calculation method

The calculations were performed with SRAC code system developed at JAERI and MCNP 4A. SRAC code system is composed of neutron cross section library with 107 groups called a public library, diffusion code CITATION and transport codes, ANISN and TWOTRAN. Among these codes, ANISN and TWOTRAN were adapted to the calculations on account of their geometrical capability and feasibility. The former was used for energy collapse from 107 to 16 group and the latter was used for calculation of the effective multiplication factors of experimental cores. The thermal cut-off energy was 0.6825 eV. The narrow resonance approximation was adapted for energy group collapse calculation. The number of neutron particles is usually 1,000,000 (=5000X200) in the calculations with a continuous energy Monte Carlo code MCNP 4A. The multigroup nuclear data library in the SRAC system and the MCNP nuclear data library were both prepared from the latest Japanese evaluated nuclear data library JENDL3.2 which was completed in JAERI.

4.2 Calculation model

Two types of geometrical models were adapted in the benchmark calculations. Simple two dimensional R-Z models were used for TWOTRAN, which does not include the upper part above solution height. Therefore, the heights of the core tank and water reflector changes according to the critical solution height in this simple model. Three dimensional model including the water reflector above the core tank were used in the calculations with MCNP 4A. The thickness of side water reflector and bottom water reflector were fixed 30 cm and that of the top reflector was fixed 20 cm. The calculation model for each code is shown in Figure 2.

4.3. Benchmark calculations

The results of the benchmark calculations for experimental cores with TWOTRAN and MCNP 4A are summarized in Table 3. When using JENDL 3.2, the average values of calculated k_{eff} with TWOTRAN for water reflected and unreflected cores were 1.00796 ±

0.00145 and 1.00630 ±0.00131, respectively. The average values with MCNP 4A for reflected and unreflected cores were 1.00795 ±0.00197 and 1.00380 ±0.00173, respectively. The variation of calculated keff with the critical solution heights for reflected and unreflected cores are shown in Figure 3 and 4.

Fluctuation of calculated keff with MCNP 4A was small for both water reflected and unreflected cores. However, calculated keff is slightly larger than the experimental value of 1.0. The further investigation of the discrepancy of the average keff between reflected and unreflected cores are necessary. However, in the calculations with MCNP 4A, the fuel region, the core tank and reflector region of sufficient thickness were all considered and no apparent bad approximation were found.

The first feature of TWOTRAN calculation is that the variation in keff with the critical heights for unreflected cores is relatively smaller than that for water reflected cores. The second feature is that the calculated values of TWOTRAN are always larger than those of MCNP about 0.25 %ΔK. It is mainly due to that the differences of infinite multiplication factors between two methods. The discrepancy between TWOTRAN and MCNP is almost constant, which implies that both MCNP and TWOTRAN evaluated the leakage effect comparatively. The discrepancy between calculated and experimental values is mainly due to the nuclear data library JENDL 3.2. This is because the calculations with the combination of TWOTRAN and JENDL 3.1 gave smaller keff as seen in Table 3. The calculated infinite multiplication factor for typical fuel concentrations are seen in Figure 5. Calculated infinite multiplication with ANISN are always about 0.25 %ΔK larger than those with MCNP 4A.

In the case of the water reflected cores, the calculated keff with TWOTRAN has a tendency of increasing with critical height. In comparison with the results of MCNP 4A, the values with TWOTRAN were smaller in the lower range of the solution height and larger in the range of solution height more than 70 cm.

Taking account of the conventional R-Z model used in TWOTRAN calculations, the negligence of the above parts of water reflector above the fuel solution height probably effected negative, especially in low height cases. This negative effect becomes smaller with increasing in the solution height, the differences of infinite multiplication factors between two code systems gradually become dominant.

The ratio of the group wise production rate to the total absorption rate is shown in Figure 6. It can be seen from this figure that most of all production reaction occurred under 0.1 eV neutron energy range, and neutron multiplication is dominated by the neutrons in the 15th. and 16th. energy groups.

5. SUMMARY

As the STACY started steady operations, systematic criticality data on low enriched uranyl nitrate solution system could be accumulated. Main experimental parameters for the cylindrical tank of 60 cm in diameter were uranium concentration and the reflector condition. Basic data on a simple geometry will be helpful for the validation of the standard criticality safety codes and for evaluating the safety margin included in the criticality designs.

Calculations with TWOTRAN and MCNP 4A using JENDL 3.2 overestimated the effective multiplication factor for critical configuration, which is mainly due to the nuclear data library. However, further investigation is necessary to the discrepancy between the calculation and experimental values.

ACKNOWLEDGMENT

Reactor physics tests on the STACY were promoted in cooperation with staffs in the Criticality Technology Division of Department of NUCEF Project. The authors are grateful

to them for their continuous support of operating critical facility, fuel treatment and chemical analysis during the first series of the critical experiments.

REFERENCES

[1] Y. Miyoshi et al., "Neutronic Design of Criticality Facilities (STACY and TRACY) at JAERI for Criticality Safety Research" Proc. of 1988 International Reactor Physics Conference, Jackson Hole, Vol. II 493- 504 (1988)

[2]Y. Miyoshi et al., Critical Experiment Programs for Fuel Solution with STACY and TRACY" , OECD Criticality Safety Expert Meeting, Albuquerque (1995)

[3] K. Tsuchihashi et al., "Revised SRAC Code System", JAERI 1302 (1986)

[4] J.F. Briesmeister, Ed., "MCNP General Monte Carlo N-Particle Transport Code , Version 4A," ,LA-12625 (1993)

[5] N. Izawa et al., "Design of Solution Criticality facility of NUCEF" Proc. on International Seminar on Nuclear Criticality Safety (ISCS'87) , Tokyo, 38-43 (1987)

[6] K. Tonoike et al, "New critical facilities toward their first criticality, STACY and TRACY in NUCEF", Proc. of the Fifth International Conference on Nuclear Criticality Safety, Al buquerque, Vol. II 10.25- 10.32. (1995) criticality

Table 1 Main items of reactor physics test and their requirements

No.	Experimental Item	Limit value	Measurement	Instrumentation
1	Critical height	40-140 cm	Inverse multiplication	B10 counter, He3 counter
2	Maximum reactivity	0.8$	Reactor period measurement	Compensated Ionization Chamber (CIC)
3	Maximum reactivity addition rate	3 cent/sec		
4	Reactivity of driving mechanism	≦30 cent		
5	Shutdown margin at all-rod insertion	Keff≦0.985	Rod drop method	B10 counter, He3 counter
6	Shutdown margin at one-rod stuck	Keff≦0.995		Multi-Channel Scaler (MCS)
7	Reactor power	Power ≦200 watt	Neutron source introduction method	B10 counter ,CIC, Am-Be source
			Gamma activity of fission products and Np239	Ge(Li) detector, γ -ray spectroscopy
			Activation of gold foil	NaI(Tl) Scintillation , β - γ coincidence system
8	Kinetic parameter β eff/l	-	Reactor noise method	Fast Fourier Analyzer, CIC, Analog Data Recorder
		-	Pulsed neutron method	Pulsatoron, B10 counter, MCS
9	Neutron flux	-	Activation of gold wire	NaI(Tl) Scintillation counter
		-	Scanning of neutron counter	Counter driving system

Table 2 Experimental results of critical solution heights

Run No.	Reflector	Uranium Concentration (g/l)	Acidity (moll/l)	Core Temperature (℃)	Critical Height (cm)	Density (g/cc)	Date
1	Water	310.1	2.17	23.1	41.53	1.48266	1995/2/23
29		290.4	2.23	24.8	46.70	1.45717	1995/5/30
33		270.0	2.20	24.7	52.93	1.43479	1995/6/9
34		253.6	2.24	24.8	64.85	1.40902	1995/6/12
46		241.9	2.27	24.6	78.56	1.39357	1995/7/6
51		233.2	2.28	22.4	95.50	1.38480	1995/9/20
54		225.3	2.28	23.3	130.33	1.37220	1995/9/26
14	None	313.0	2.25	23.8	46.83	1.48807	1995/4/11
30		290.7	2.23	25.4	54.20	1.45711	1995/6/1
32		270.0	2.20	25.8	63.55	1.43389	1995/6/7
36		253.9	2.23	25.8	83.55	1.41018	1995/6/21
49		241.9	2.27	23.4	112.27	1.39410	1995/7/13

Table 3 Results of the benchmark calculations

Reflector	Run No.	Uranium Conc. (g/l)	Acidity (moll/l)	Effective multiplication factor		
				TWOTRAN JENDL 3.2	TWOTRAN JENDL 3.1	MCNP 4A JENDL 3.2
Water	1	310.1	2.17	1.00547	0.99810	1.00751 ± 0.00068
	29	290.4	2.23	1.00763	1.00054	1.00848 ± 0.00068
	33	270.0	2.20	1.00625	0.99948	1.00669 ± 0.00066
	34	253.6	2.24	1.00925	1.00276	1.01044 ± 0.00058
	46	241.9	2.27	1.00949	1.00323	1.00799 ± 0.00054
	51	233.2	2.28	1.00873	1.00266	1.00754 ± 0.00053
	54	225.3	2.28	1.00889	1.00299	1.00702 ± 0.00055
None	14	313.0	2.25	1.00424	0.99669	1.00278 ± 0.00070
	30	290.7	2.23	1.00678	0.99957	1.00403 ± 0.00066
	32	270.0	2.20	1.00564	0.99878	1.00300 ± 0.00065
	36	253.9	2.23	1.00817	1.00161	1.00533 ± 0.00062
	49	241.9	2.27	1.00666	1.00033	1.00385 ± 0.00067

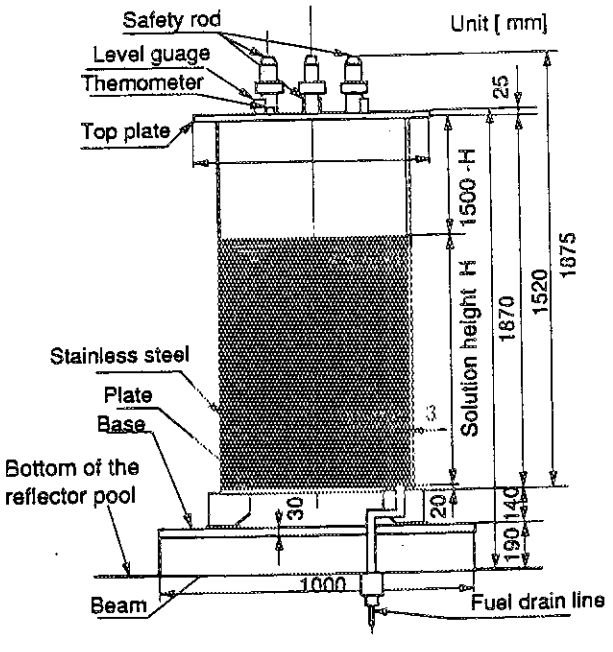

Figure 1 Vertical cross section of the core tank

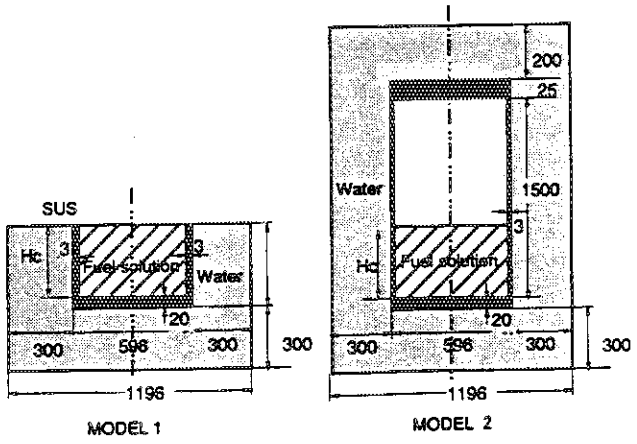

Figure 2 Calculation model

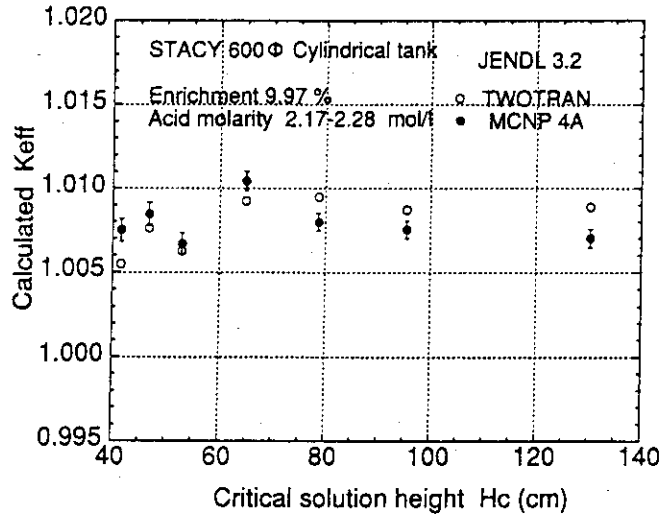

Figure 3 Calculated Keff for water reflected cores

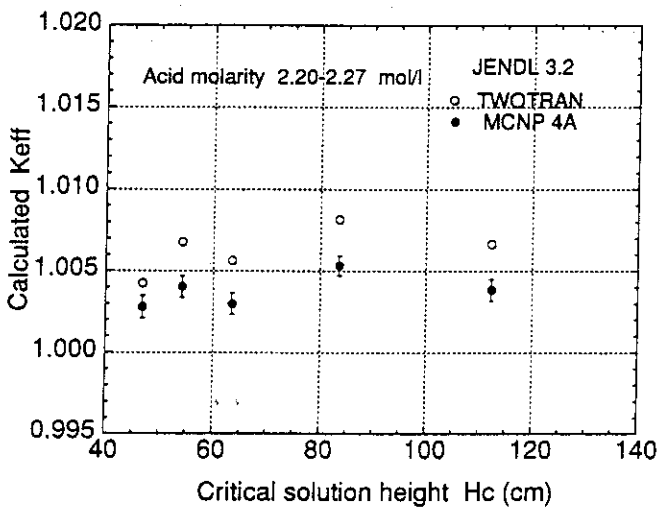

Figure 4 Calculated Keff for unreflected cores

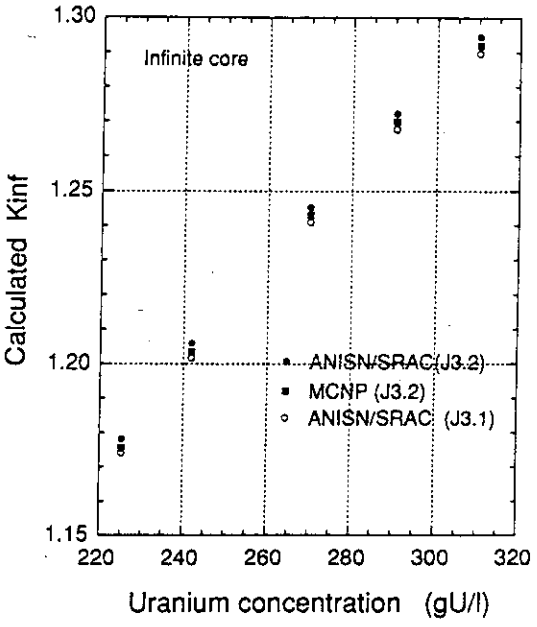

Figure 5 Calculated infinte multiplication

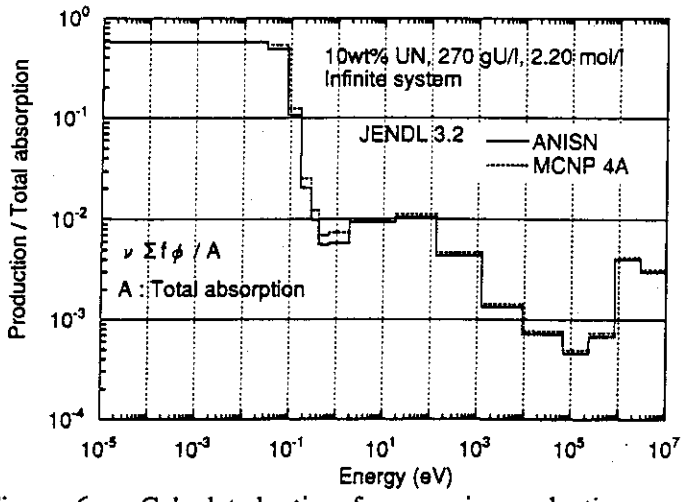

Figure 6 Calculated ratio of group wise production rate to total absorption rate

2.1.4 How to Disseminate JENDL-3.2
Recommendation of Subcommittee on Dissemination of JENDL-3.2

Yasuyuki KIKUCHI
Japan atomic Energy Research Institute
Tokai-mura, Naka-gun, Ibaraki-ken 319-11
e-mail: kikuchi@cracker.tokai.jaeri.go.jp

A special small subcommittee was established in JNDC to discuss how to disseminate JENDL-3.2. The subcommittee discussed on various matters and made the following recommendation: a) Offer of Standard Group Constants, b) Publication of Data Book, c) Further Benchmark Tests, d) Adoption in Licensing Procedure, e) Utilization of Multi-media, f) Internet Service.

1. Introduction

JENDL-3.2 satisfies most of conventional data needs. So it will be frozen for several years so as to avoid the version confusion and most of efforts will be devoted to disseminate it not only in Japan but also in the world. A special small subcommittee was established in JNDC to discuss how to disseminate JENDL-3.2. The subcommittee had met 5 times, discussed on various matters and made the following recommendation.

2. Subcommittee Members

Itsuro Kimura	(Kyoto Univ.)
Tadashi Yoshida	(Toshiba Co.)
Atsushi Zukeran	(Hitachi Ltd.)
Naoki Yamano	(Sumitomo Atomic Energy Industries, Ltd.)
Makoto Sasaki	(Mitsubishi Heavy Industries, Ltd.)
Kensuke Kitao	(Data Engineering)
Toshio Wakabayashi	(PNC)
Makoto Ishikawa	(PNC)
Norio Kishida	(JAERI)
Hideki Takano	(JAERI)
Tsuneo Nakagawa	(JAERI)
Tokio Fukahori	(JAERI)
Yasuyuki Kikuchi	(JAERI), Chairman

3. Analysis of the Present Status

For the LWR design, the nuclear data consist of a part of the large design code system. Hence it is not easy to replace the data independently. However, when the design method is

changed in future, the nuclear data will be also updated.

For th new reactor design, JENDL-3.2 will be used soon, if its reliability has been confirmed with benchmark tests and advertised widely. Most of individual users cannot process the new data, even if the new data are better than the old ones. For them, it is essential to provide the processed library.

Utilization of multi-media is indispensable to disseminate JENDL-3.2 to wider users. Particularly dissemination through INTERNET is the most important issue in future. JAERI Nuclear Data Center has already started the service by WWW and a-FTP. This must be more encouraged.

4. Recommendation

a) Offer of Standard Group Constants

The group constants for standard code systems should be provided to the users. For the following libraries widely used in JAERI as the standard, JENDL-3.2 was already processed or to be processed. They will be released after validation.

JFS-3J32	: 130 nuclides + 5 lumped FP
SRAC-J32	: 130 nuclides + 3 lumped FP
JSSTDL	: 63 nuclides
MVP	: 98 nuclides
MCNP	: 340 nuclides
MGCL	: 59 nuclides
FPGS	: 66 nuclides

JSSTDL cannot be used by itself and some group-collapsing code system must be also provided. It is also desirable to provide the library in VITAMIN-J form.

On the other hand, the libraries for the following codes which are widely used in the world must be also provided. The work has been started.

ORIGEN-2	: in progress
WIMS-D	: in progress
VIM	: under consideration.

b) Publication of Data Book

Various data books have so far been published on the basis of JENDL. Most of them are, however, for nuclear data scientists. Data books for general users must be published. In such data books, some additional values should be given. For example, in a data book for radioactive analyses, it is required to contain not only the cross section values but also the emitted gamma-ray strength and spectrum. It is to be noted that the newly revised " Radioisotope Notebook Ver. 9" adopts the JENDL-3.2 data in its tables.

It is also recommended to check published textbooks and handbooks whether the referred data are out-of-dated and to urge the authors and publishers to update them with JENDL data.

c) Further Benchmark Tests

The benchmark tests should be continued. The future tests should be done not only on the conventional facilities but also on new facilities such as MONJU, HTTR, NUCEF and so on.

The results of the benchmark tests should be discussed not only in JNDC but also in all Japan such as Reactor Physics Committee or AESJ Reactor Physics Division.

The results of the benchmark tests must be kept as a database.

d) Adoption in Licensing Procedure

One of the successful example is JNDC FP Decay Library, which is now adopted in the ECCS calculation. It is noted, however, that it needed long leading time. For JENDL-3.2, experiences in NUCEF or Monju must be accumulated.

e) Multi-media

In data distribution, not only the conventional media such as MT or FD, but also new media such as CD-ROM, OD and DAT must be utilized. Particularly CD-ROM containing data and retrieval software such as MOSAIC will be very useful.

f) Internet

WWW and a - FTP services were already started in Nuclear Data Center and have been very successful. Not only JENDL-3.2 data but also pointwise data, figures, group constants and processing codes will be provided. Of course security problems should be considered carefully.

2.2 Photonuclear Reaction Data

2.2.1 Japanese Evaluation of Photonuclear Data

Norio Kishida†
Center for Promotion of Computational Sci. and Eng.
Japan Atomic Energy Research Institute
2-28-2, Honkomagome, Bunkyou-ku, Tokyo 113
E-mail : kishida@koma.jaeri.go.jp

and

Photonuclear Data Working Group
Nuclear Data Center
Japan Atomic Energy Research Institute
Tokai-mura, Naka-gun, Ibaraki-ken 319-11

The present status of evaluation work for photonuclear data is described. The photonuclear data working group aims to evaluate the photonuclear cross sections for every natural isotopes, some transuranic nuclei and several fission products up tp 140 MeV. The photonuclear data file is to be made using ENDF-6 format. The following kinds of the cross sections are evaluated: absorption, photoneutron, photoproton, photoneutron yield, photoproton yield, neutron energy spectra, proton energy spectra and nuclide production cross sections. Theoretical evaluation as well as experimental data evaluation are employed. Nuclear model calculation based on pre-equilibrium and evaporation model is carried out and reproduce experimental data quite well. Evaluation for d, ^{12}C, ^{14}N, ^{16}O, ^{23}Na, ^{24,25,26}Mg, ^{27}Al, ^{28,29,30}Si, ^{40,48}Ca, ^{46,48}Ti, ^{51}V, ^{52}Cr, ^{55}Mn, ^{54,56}Fe, ^{59}Co, ^{58,60}Ni, ^{63,65}Cu, ^{64}Zn, ^{90}Zr, ^{92,94,96,98,100}Mo, ^{93}Nb, ^{133}Cs, ^{181}Ta, ^{186}W, ^{197}Au, ^{206,207,208}Pb, ^{209}Bi and ^{235,238}U have been completed. A photonuclear data index like CINDA was made and is bibliographic references to the data which have been published since 1950.

1. Introduction

The photonuclear data evaluation task started at 1989. Various kinds of photonuclear reaction cross sections have been being evaluated by each member of the group. We purpose to evaluate photonuclear data for all natural isotopes, several transuranic nuclides and some fission products. From a survey of many literatures, we reached the conclusion that it is difficult to construct the photonuclear data file if we adhere to evaluation method to use measured cross sections only, for there are not sufficient experimental data necessary for the evaluation. For instance, there scarcely exist energy spectra and DDX for emitted particles which were measured using quasi monoenergetic gamma-rays. We are therefore proceeding the evaluation work with the help of theoretical calculation based on statistical nuclear reaction models.

2. Evaluated Cross Sections

The photonuclear cross sections that are to be contained in the forthcoming data file are as follows: photonuclear absorption cross sections not to include elastic cross sections, photoneutron cross sections, photoproton cross sections, yield cross sections for photoneutrons, photoprotons, photodeuterons, phototritons, photo-^{3}He-particles and photo-alpha-particles, single neutron emission cross sections, double neutron emission cross sections, energy spectra, angular distributions and DDX for photoneutrons and photoprotons, and nuclide production cross sections. The maximum energy of incident photons is 140 MeV because the evaluation work becomes very hard once the pion production channel opens. The photonuclear data file is planned to be constructed using ENDF−6 format. Now we have evaluated the photonuclear cross sections for d, ^{12}C, ^{14}N, ^{16}O, ^{23}Na, ^{24,25,26}Mg, ^{27}Al, ^{28,29,30}Si, ^{40,48}Ca, ^{46,48}Ti, ^{51}V,

†Permanent Address
CRC Research Institute Inc.
2-7-5, Minamisuna, Koutou-ku, Tokyo 136
E-mail : nkishida@crc.co.jp

^{52}Cr, ^{55}Mn, ^{54,56}Fe, ^{59}Co, ^{58,60}Ni, ^{63,65}Cu, ^{64}Zn, ^{90}Zr, ^{92,94,96,98,100}Mo, ^{93}Nb, ^{133}Cs, ^{181}Ta, ^{186}W, ^{197}Au, ^{206,207,208}Pb, ^{209}Bi and ^{235,238}U have been completed.

3. Experimental Data

The EXFOR file for photonuclear reaction data was obtained from NEA Data Bank and includes the monoenergetic photoneutron cross sections that Dietrich and Berman[1] have compiled. In evaluation for the nuclides that we can not obtain sufficient quantities of the cross sections from the file, we read values of the cross sections from the figures in literatures. In order to seek the literatures, the abstract sheets[2] edited at NIST are utilized. In addition, Computer Index for Photonuclear Reaction Data[3] like CINDA is being made by one of the group members to aid our evaluation work. The literatures which were published between 1950 and 1990 and treat the photonuclear reactions are registered on the index file.

4. Evaluation of Photoabsorption Cross Sections

4.1 Data Evaluation for Photoabsorption Cross Sections

It is thought that nuclear photoabsorption process up to 140 MeV mainly takes place via excitation to the giant electric dipole resonance (GDR) or via disintegration of a proton-neutron pair (quasideuteron) in a nucleus. The latter process has been originally proposed by Levinger[4] and is called the quasideuteron model (QDM) at present. The former process is dominant for incident photon energies in the range up to about 40 MeV, while the latter process is dominant in the energy range from 40 MeV to 140 MeV.

It is widely recognized that experimental excitation functions of photoabsorption cross sections for GDR region can be well reproduced by superposition of Lorentz resonance curves:

$$\sigma_{abs}^{GDR}(E) = \sum_{i=1}^{n} \frac{\sigma_i^{abs}}{1 + \left[\left(E^2 - E_i^2\right)^2 / E^2\Gamma_i^2\right]}, \tag{1}$$

where the Lorentz parameters E_i, σ_i^{abs} and Γ_i are the i-th resonance energy, its peak cross section and its full width at half-maximum, respectively, E is the incident photon energy, and n is the number of resonances. Strictly speaking, σ_i^{abs} and Γ_i are not constant, but energy dependent. Furthermore, σ_i^{abs} is divided into many factors: the ground state spin, that of GDR, its total width, its partial width for de-excitation to the ground state, the wave length of the incident photon and some other physical constants.

The QDM photoabsorption cross section $\sigma_{abs}^{QDM}(E)$ is expressed in terms of the free deuteron photodisintegration cross section $\sigma_d(E)$,

$$\sigma_{abs}^{QDM}(E) = \frac{L}{A} NZ\sigma_d(E) f(E), \tag{2}$$

where L is the Levinger parameter, $f(E)$ is the Pauli-blocking function. The meanings of A, N and Z seem to be obvious. Recently, Chadwick *et al.*[5] have proposed a new derivation of the Pauli-blocking function. As a result, it become possible to calculate the QDM cross sections without free parameters. They also showed that the calculated photoabsorption cross sections are in good agreement with experimental data.[5]

On the basis of the facts mentioned above, we have decided to express the photoabsorption cross section $\sigma_{abs}(E)$ as the sum of $\sigma_{abs}^{GDR}(E)$ and $\sigma_{abs}^{QDM}(E)$,

$$\sigma_{abs}(E) = \sigma_{abs}^{GDR}(E) + \sigma_{abs}^{QDM}(E). \tag{3}$$

In case of existence of the measured photoabsorption cross sections with high accuracy, a least-squares fitting procedure, in which Eq. (3) is the fitted expression and E_i, σ_i^{abs}, Γ_i and L are the fitted parameters, is employed to determine the evaluated photoabsorption cross sections. Although Chadwick *et al.*[5] derived the value $L = 6.5$ without theoretical ambiguity and use of its value indeed reproduced very well many experimental data for nuclides heavier than Sn, we found that this value failed to reproduce the measured values for nuclides lighter than Al and always underestimated those values in the present evaluation. We therefore treat L as a free parameter at present.

4.2 Evaluation of Photoabsorption Cross Sections

In a large number of nuclides, it is usual that photoabsorption cross sections have not been measured, but those of photoneutrons have been measured. Thus we need the evaluation methods to estimate the photoabsorption cross sections $\sigma_{abs}(E)$ from the photoneutron cross sections $\sigma_{(\gamma,nx)}(E)$. In fact we can carry out such evaluation if we obtain the branching ratios for the photoneutron reactions. Then the absorption cross sections are derived from

$$\sigma_{abs}(E) = \frac{\sigma_{(\gamma,nx)}(E)}{R_{(\gamma,nx)}(E)}, \tag{4}$$

where $R_{(\gamma,nx)}(E)$ represents the branching ratio.

In this evaluation method the evaluated photoneutron cross sections are indispensable. From Eq. (3) and (4) the photoneutron cross sections are expressed as

$$\sigma_{(\gamma,nx)}(E) = \sigma^{GDR}_{(\gamma,nx)}(E) + R_{(\gamma,nx)}(E)\sigma^{QDM}_{abs}(E), \tag{5}$$

where $\sigma^{GDR}_{(\gamma,nx)}(E)$ represents the photoneutron cross sections with excitation to GDR and it is written by the expression that σ^{abs}_i of Eq. (1) is replaced with $\sigma^{(\gamma,nx)}_i$. We have been obtaining the evaluated photoneutron cross sections by fitting Eq. (5) to those obtained by experiment. In addition, since the branching ratios must be known before the fitting, we calculate those ratios using evaporation and pre-equilibrium nuclear model codes, ALICE–F[6] and MCPHOTO[7] , which is modified versions of ALICE–P[8] and MCEXCITON,[9] respectively.

5. Theoretical Evaluation

We need to perform theoretical evaluation as well as the data evaluation, because it is evident that we cannot make the evaluated photonuclear data file via experimental data evaluation only,

Wu and Chang[12] have first applied a pre-equilibrium reaction model to analysis of the photonuclear reactions. They showed that the model can reproduce neutron and proton energy spectra resulting from irradiation by bremsstrahlung gamma-rays. In 1983, Blann *et al.*[13] have revealed that the model can also reproduce excitation functions of various kinds of photoneutron cross sections, which had been measured using quasi-monoenergetic photons. Then it was made clear to be able to apply the model to the photonuclear reactions.

From the viewpoint of a microscopic nuclear theory, the excitation process of GDR is considered as production process of a particle−hole excited state. On the other hand, QDM assumes that an incident photon excites one neutron and one proton above the Fermi level and leaves two holes in the Fermi see. It is therefore thought that pre-equilibrium, especially exciton models can describe the de-excitation process of photonuclear reactions. Consequently, reaction branching ratios, energy spectra, nuclide production cross sections and other quantities can be obtained from model calculations by ALICE–F and MCPHOTO.

We make the exciton model calculation initiate from a one particle and one hole (1p–1h) configuration in excitation to GDR and from a 2p–2h or a 2p-1h configuration in the quasi-deuteron process. Use of the 2p–1h initial configuration was originally proposed by Blann *et al.*[13] The reason is because the two holes produced from a quasi-deuteron are correlated so that they jointly provide one degree of freedom rather than two. In fact, results of two types of calculations do not present large difference. A level density parameter necessary in evaporation calculation following the pre-equilibrium stage is adjusted in such a way to reproduce the ratio of single neutron emission cross sections and those of double neutron emission if those cross sections have been measured.

6. Some Evaluation Results

6.1 Result for ^{27}Al Nucleus

In Fig. 1 the evaluated results for ^{27}Al are shown together with the experimental data on photoabsorption,[14] photoneutron[15, 16] and photoproton[17, 18, 19] cross sections. The measured photoabsorption and photoneutron cross sections except for those of photoprotons were simultaneously fitted into by Eq. (3) and Eq. (5). The photoproton cross sections were not used in the fitting procedure because the author did not feel that they have high accuracy. Then the branching ratios of the photoneutron reactions

were obtained from calculation by the MCPHOTO code. The evaluated photoproton cross sections were also obtained from the calculation.

6.2 Result for ^{100}Mo Nucleus

In Fig. 2 the evaluated photoneutron cross sections for ^{100}Mo are shown together with the experimental data.[20] The measured photoneutron cross sections were fitted into by Eq. (5). Then the branching ratios of the photoneutron reactions were obtained from calculation by MCPHOTO. The evaluated single, double and triple neutron emission cross sections were also obtained by the calculation. It is clearly seen that the calculated cross sections except for those of triple emission reproduce the experimental data rather well. The reason why the calculation fails to reproduce those of triple neutron emission is because the employed value of the level density parameter was probably inadequate for ^{97}Mo.

Acknowledgements

We would like to thank Dr. F. Fukahori for permitting use of ALICE–F.

References

1) S. S. Dietrich and B. L. Berman : *Atomic Data and Nuclear Data Tables* **38** (1988) 199.

2) E. G. Fuller and H. M. Gerstenberg : "Photonuclear Data – Abstract Sheets 1955 – 1982," *NBSIR 83-2742*, National Bureau of Standards(1983–1985).

3) T. Asami : private communication.

4) J. S. Levinger : *Phy. Rev.* **84** (1951) 43.

5) M. B. Chadwick, P. Obložinský, P. E. Hodgson and G. Reffo : *Phy. Rev.* **C37** (1991) 814.

6) T. Fukahori : private communication.

7) N. Kishida and H. Kadotani : private communication.

8) S. Pearlstein : *Astrophysi. J.* **346** (1989) 1049.

9) N. Kishida and H. Kadotani : in *Proc. Int. Conf. on Nuclear Data for Science and Technology*, ed. S. Igarasi (Saikon, Tokyo, May/June 1988), p. 1143.

10) P. Carlos, R. Bergère, H. Beil, A. Leprêtre and A. Veyssière : *Nucl. Phys.* **A219** (1974) 61.

11) J. S. Levinger : *Ann. Rev. Nucl. Sci.* **4** (1954) 13.

12) J. R. Wu and C. C. Chang : *Phys. Rev.* **C16** (1977) 1812.

13) M. Blann, B. L. Berman and T. T. Komoto : *Phys. Rev.* **C28** (1983) 2286.

14) J. Ahrens, H. Borchert, K. H. Czock, H. B. Eppler, H. Gimm, H. Gundrum, M. Kröning, P. Riehn, G. Sita Ram, A. Zieger and B. Ziegler : *Nucl. Phys.* **A251** (1975) 479.

15) S. C. Fultz, J. T. Caldwell, B. L. Berman, R. L. Bramblett and R. R. Harvey : *Phys. Rev.* **143** (1966) 790.

16) A. Veyssière, H. Beil, R. Bergère, P. Carlos, A. Leprêtre and A. de Miniac : *Nucl. Phys.* **A227** (1974) 513.

17) R. E. Chrien and A. H. Benade : *Phys. Rev.* **119** (1960) 748.

18) J. Halpern and A. K. Mann : *Phys. Rev.* **83** (1951) 370.

19) K. Shoda, K. Abe, T. Ishizuka, N. Kawamura and M. Kimura : *J. Phys. Soc. Japan* **17** (1962) 735.

20) H. Beil, R. Bergère, P. Carlos, A. Leprêtre, A. de Miniac and A. Veyssière : *Nucl. Phys.* **A227** (1974) 427.

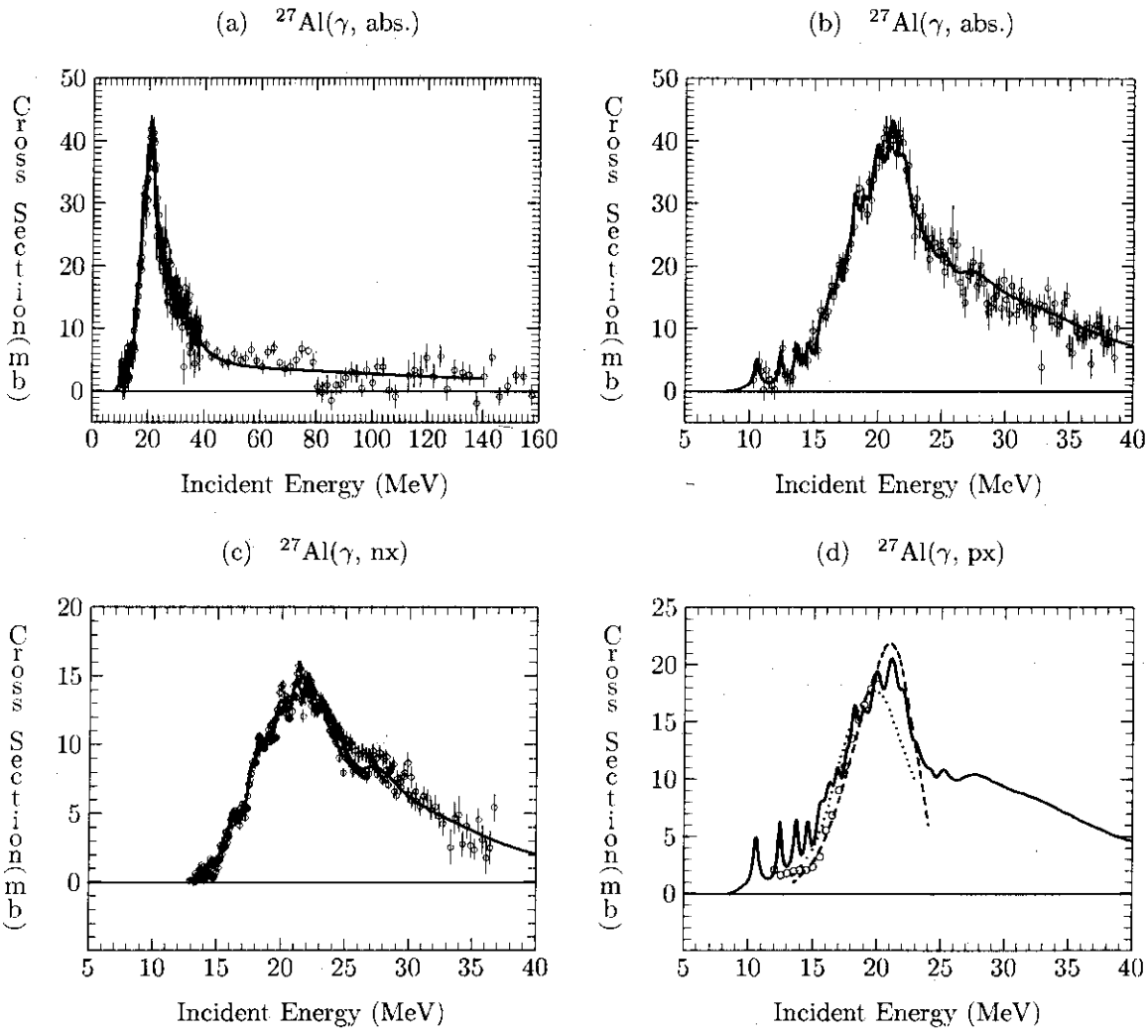

Fig. 1 The evaluated (a), (b) photoabsorption, (c) photoneutron and (d) photoproton cross sections for ^{27}Al are compared with the experimental data. The solid lines show the evaluated cross sections.

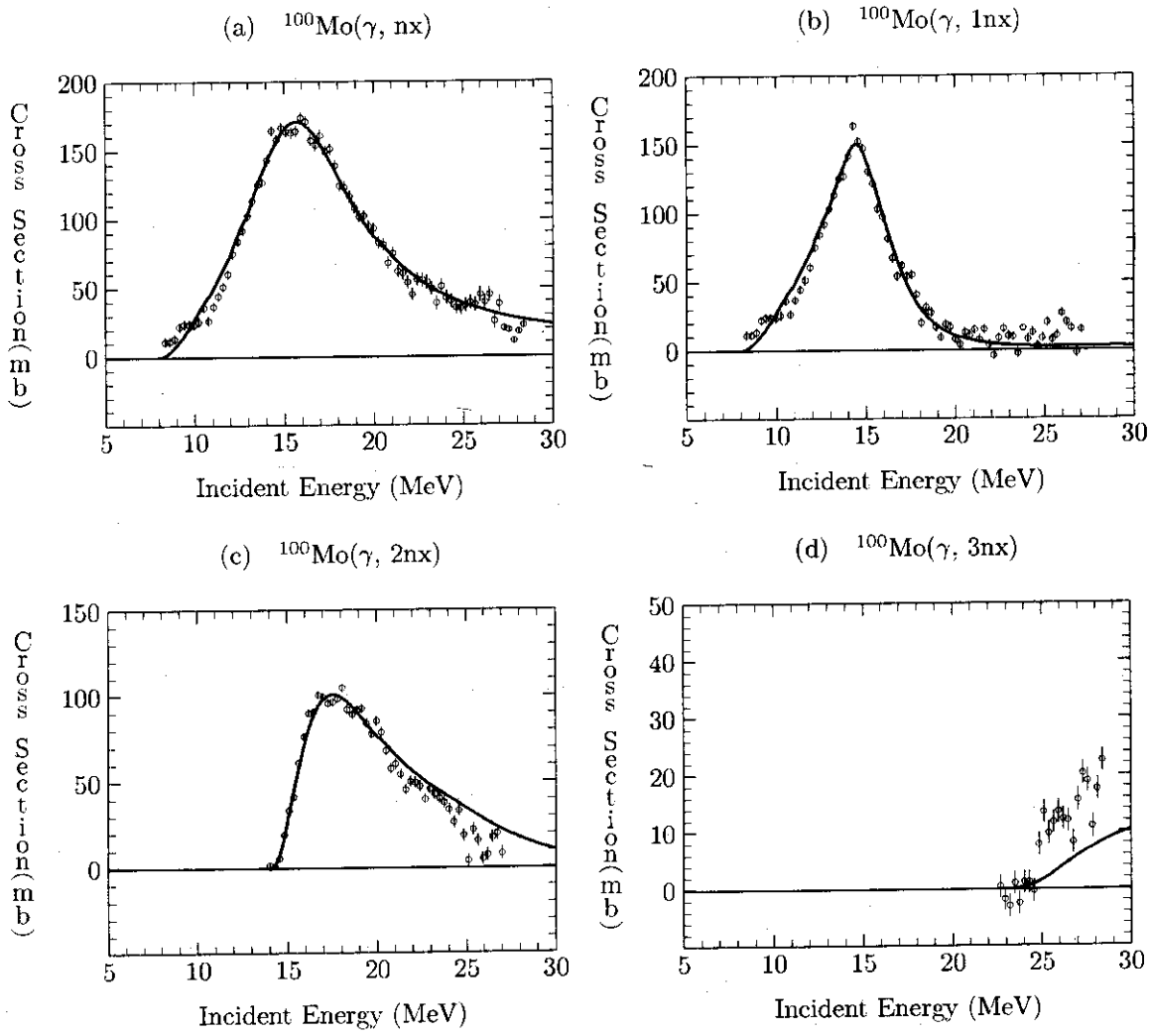

Fig. 2 The evaluated (a) photoneutron, (b) single neutron emission, (c) double neutron emision and (d) triple neutron emission cross sections for ^{100}Mo are compared with the experimental data. The solid lines show the evaluated cross sections.

2. 2. 2 Photonuclear Data: Analysis of Discrepancies and Evaluation

V.V.Varlamov, N.G.Efimkin, M.E.Stepanov
Centre for Photonuclear Experiments Data
Institute of Nuclear Physics Moscow State University
Moscow 119899, Russia

Possible reasons for the discrepancies in shapes and amplitudes of the cross sections obtained using different photon beams and experiment methods are the differences in apparatus functions (the effective shapes of incoming photon spectra) with which the data have been measured and smoothly energy dependent errors of cross section data energy calibration and normalization. The method of reduction is proposed for evaluation of photonuclear reaction cross sections obtained at significant systematic uncertainties. The evaluation procedure consists of using the real apparatus function of each individual experiment to reduce data to the most reasonably achievable monoenergetic representation generated by another apparatus function of better quality and to take into account the each experiment uncertainties of calibration and normalization procedures.

1. Introduction

Because of absence of sufficiently intensive beams of monoenergetic photons the experimenters must use various methods for creation of special conditions in which the effective photon energy spectrum in any approach can be interpreted similar to the monoenergetic one. The considerable number of such methods results [1] in certain systematic disagreements between the experimental results, which sometimes are significant.

The most known example of systematic disagreements of data under discussion is the difference in intermediate structure and value of photonuclear reaction cross sections obtained using bremsstrahlung (BR) and quasimonoenergetical (QME) photon beams: as a rule, QME - cross sections are smoother and have the smaller amplitudes than BR - ones. The character of such kind disagreements is illustrated in Fig. 1. where the total photoneutron reaction (γ,xn) cross section data [2-4] for ^{16}O are presented.

The detailed comparative analysis [8] of the parameters of clearly identified resonances in $^{18}O[(\gamma,n)+2(\gamma,2n)]$ reaction cross section in BR [6] and QME [7] experiments gives the possibility to make two obvious conclusions:

- practically all QME resonances have in the average the smaller amplitudes than BR ones: $\langle A_{BR}\rangle/\langle A_{QME}\rangle=1.17$;
- the majority of QME resonances have in the average width larger than BR ones: $\langle \Gamma_{BR}\rangle/\langle \Gamma_{QME}\rangle=1.25$.

The systematics on three characteristics of experimental (γ,xn) reaction cross sections for large number of nuclei from ^{6}Li to ^{238}U were studied [8]:

- the ratios of integrated cross sections for (γ,xn) reaction $R=\int \sigma(k)dk \Big/ \int \sigma_l(k)dk$,

where σ are the cross sections obtained in various laboratories and σ_l are the Livermore's ones;

- the ratios S/S_l (S were calculated for the data obtained in different laboratories and S_l in Livermore) of special parameter of structureness S which describes the integrated deviation of individual cross section from very smoothed one:

$$S = \sum \left(\sigma_i - \langle \sigma_i \rangle\right)^2 \Big/ N \left\langle \langle \sigma_i \rangle \right\rangle^2$$

- the differences between the centres of gravity $E_{c.g.} = \int_D \sigma(k) k dk \Big/ \int_D \sigma(k) dk$ of (γ,xn) reaction cross section and appropriate average value $\langle E_{c.g.} \rangle$.

The following conclusions [8] have been done on the base of these results:

- for R values all data are clearly separated into two parts, one of which consists of Livermore data and the other one - of all other data (average value is $\langle R \rangle = 1.122 \pm 0.243$);
- for S values all data are clearly separated into two parts: QME data (average value 1.22) and BR data (average value 4.35);
- for $E_{c.g.}$ values as a rule the centers of gravity of cross sections have been obtained in various experiments are displaced against each other on value which can reach $\Delta E_{c.g.} \approx 200$ keV (standard deviation is ±83.6 keV).

It was underlined also [1,9] that the differences in energy positions of resonances and structures in the cross sections depend on the photon energies [9].

It was shown [1,5,8] that the main reason for the data disagreements of such kind is the difference of individual experiment apparatus functions (effective photon spectra). The apparatus functions for several widely used methods of "monoenergetic" spectrum condition creation are shown in Fig 2.

It is obvious that joint analysis and evaluation of photonuclear reaction cross sections in conditions described above are possible only for the data which are transformed to the view as being obtained for some unique apparatus function and for identical or maximally close cross section and energy scales.

2. The Photonuclear Reaction Cross Section Evaluation Technique

2.1. The Method of Reduction Brief Description

As it follows from the above none of the experimental results estimates the cross section σ(k) as a function of photon energy k in literal way, since their apparatus functions are not the δ-function. In fact each of the results is the reaction yield $y(E_j)$ and should be considered in terms of apparatus function (effective photon spectrum) $W(E_j,k)$:

$$y(E_j) = \alpha \int_{E_{th}}^{E_l} W(E_j, k) \sigma(k) dk + \nu_j,$$

where ν_j is a statistical uncertainty (additive noise), described by means of covariance matrix Σ.

To solve it the method of reduction [10,11] was applied.

The experimentally measured reaction yield $y(E_j)$ for which $W(E_j,k)$ means as well any of effective photon spectrum can be written in operator form

$$y = \hat{A}\sigma + \nu, \tag{1}$$

In the method of reduction (MR) [10,11] the experimental yield y (1) is transformed to the vector $\sigma' = \hat{U}\sigma + \nu'$, which is interpreted as a result of experiment, the apparatus function

(photon spectrum) of which $u(E_i,k)$ described by means of operator $\hat{U}$ has the desired properties, e.g. it might be ordered to be as monoenergetic as possible.

To solve this problem the linear operator $\hat{R}$ should be found so that the vector

$$\sigma' = \hat{R}y, \tag{2}$$

could be interpreted as the least square estimator of vector $\hat{U}\sigma$. The condition of solution existence should be satisfied:

$$\hat{R}\hat{A} = \hat{U}, \tag{3}$$

since only in this case the vector σ' and its uncertainty can be found without a priori information about the unknown σ:

$$\sigma' = \hat{R}y = \hat{R}\hat{A}\,\sigma + \hat{R}v = \hat{U}\sigma + \left(\hat{R}\hat{A} - \hat{U}\right)\sigma + \hat{R}v \tag{4}$$

The total uncertainty $M\left\|\hat{R}v\right\|^2$ of the vector σ' is minimum [10,11] if:

$$\hat{R} = \hat{U}\left(\Sigma^{-1/2}\hat{A}\right)^{-}\left(\Sigma^{-1/2}\right), \tag{5}$$

where $\left(\hat{X}\right)^{-}$ is pseudoinversion of the operator $\hat{X}$, $\left\|\hat{X}\right\|$ is norm of operator $\hat{X}$, M is assembly averaging.

The covariance matrix G, characterising the uncertainty $v' = \hat{R}v$ of the vector σ', equals

$$G = \hat{R}\Sigma\hat{R}^{*}. \tag{6}$$

If the operator $\hat{U}_0$ to be the desired apparatus function having, e.g., a Gaussian line shape, we must find an operator $\hat{U}$, closest to $\hat{U}_0$, as the product $\left(\hat{K}\hat{A}\right)$ of an arbitrary operator $\hat{K}$ with operator $\hat{A}$ (to satisfy condition (3)), and use $\hat{K}$ to minimise the difference between $\hat{U}$ and $\hat{U}_0$ as given by the following form: $\left\|\hat{U} - \hat{U}_0\right\|_{l2}^2 = tr\left(\left(\hat{U} - \hat{U}_0\right)\left(\hat{U} - \hat{U}_0\right)^{*}\right)$, where $\left\|\hat{X}\right\|_{l2}^2$ means the Hilbert-Schmidt norm of the operator $\hat{X}$. Then

$$\hat{U} = \hat{U}_0\hat{A}^{-}\hat{A} \tag{7}$$

and $\hat{U}$ is determined only by the operator $\hat{A}$ of the experiment and the operator $\hat{U}_0$. The discrepancy between $\hat{U}$ and $\hat{U}_0$ is characterised by the value of $\left\|\hat{U} - \hat{U}_0\right\|_{l2}^2$.

So the expressions (2,6) under conditions (3,7) define the solution of the equation (1).

The method described is not the method of "unfolding" or reconstruction of the cross section $\sigma(k)$ from experimental yield y. It just transforms the data obtained with some apparatus function $\hat{A}$ to the form they would have being measured by means of apparatus function $\hat{U}$. The reduction of the data obtained in different experiments to the same presentation provides the principal opportunity for their joint analysis and simultaneous evaluation.

2.2. Recalibration-Renormalization Procedure

The other two kinds of disagreements were pointed out above, the systematic uncertainties in normalization and energy calibration, are smooth functions [8,9] of energy and their possible values are known.

In the case when researcher can easily identify the shape of the curve and "guess" which regions of different curves should coincide it is possible to order the limits of corresponding regions and to fit the parameters a_i (additive adjustment), b_i (normalization adjustment), c_i (energy shift): $a+(1+b)\sigma(E+c)$, where $i=2-M$, and M - number of curves, $a_1=b_1=c_1=0$, to minimise the sum of square differences between each of the curves and one of them chosen arbitrarily and marked by index 1. Afterwards the weighted averages are computed and subtracted from found parameters: $\hat{a}=a_i-\langle a\rangle$ etc. Therefore the adjustments $\hat{a}_i$, $\hat{b}_i$, $\hat{c}_i$ corresponding to energies c_i are found. These adjustments should be applied to achieve the coincidence of marked regions of the curves.

In the case when the curves have only one or two broad maxima the similar but modified procedure was used.

As an example of the action of procedures described above, the photoneutron cross sections for ^{16}O reduced to the resolution 600 keV before and after the application of recalibration - renormalization procedures are presented in Fig. 3.

3. The Results of Evaluation

The method described has been used for evaluation of various photonuclear reaction cross section for a number of nuclei from Li to Pb. As an examples the data obtained for Pr and Pb are presented in Fig. 4 and Fig 5 in comparison with the data obtained experimentally using the beams of tagged photons [12].

In Fig. 6 the result of our evaluation of the $^{28}Si(\gamma,xn)$ reaction cross section is compared with the result of evaluation [13] using the statistical nuclear reaction model calculations.

4. Conclusion

The numerous data on total photoneutron reaction cross section obtained by different experimental methods have been used for analysis of the reasons of well known systematical discrepancies. A method of reduction technique was proposed for data evaluation. This one makes possible to take into account three types of errors and to obtain the evaluated cross section with the covariance matrix.

Acknowledgements

I would like to thank Prof.Y.Kikuchi (Japan JAERI) for the possibilities of participation the 1995 Symposium on Nuclear Data and Dr. N.Kishida (Japan JAERI) for very fruitful discussions of various problems concerned.

References

[1] Efimkin N.G. and Varlamov V.V.: "The Method of Reduction as Photonuclear Data Evaluation Tool". International Symposium on Nuclear Data Evaluation Methodology". World Scientific. ISBN 981-02-1285-2, 1993, p. 585.

[2] Ishkhanov B.S., Kapitinov I.M., Lazutin E.V., Piskarev I.M., Sopov V.S. and Shevchenko V.G.: Yadernaya Fizika, 12, 892 (1970).

[3] Veyssiere A., Beil H., Bergere R., Carlos P., Lepretre A. and De Miniac A.: Nucl.Phys., A227, 513 (1974).
[4] Bramblett R.L., Caldwell J.T., Harvey R.R and Fultz S.C.: Phys.Rev., 133, B869 (1964). Caldwell J.T.: Ph.D. Thesis, LRL, University of California, 1967.
[5] Varlamov V.V., Efimkin N.G., Lenskaja N.A. and Chernjaev A.P.: "Investigation of the Reasons for Discrepancies in Results of Photonuclear Experiments at the Beams of Bremsstrahlung and Quasimonoenergetic Gamma-Quanta. The Problem of Interpretation", MSU INP Preprint-89-66/143, 1989.
[6] Pywell R.E., Thompson M.N. and Berman B.L.: Nucl.Instr. & Meth., 178, 149 (1980).
[7] Woodworth J.G., McNeil K.G., Jury J.W., Alvarez R.A., Berman B.L., Faul D.D. and Meyer P.: Phys.Rev., C19, 1667 (1979).
[8] Varlamov V.V., Efimkin N.G., Ishkhanov B.S., Sapunenko V.V. and Stepanov M.E.: "The Analysis and Evaluation by the Method of Reduction of Total Photoneutron Reaction Cross Sections in the Range of Giant Dipole Resonance", MSU INP Preprint-93-8/300, 1993.
[9] Fuller E.G.: Physics Reports, 127, 187 (1985).
[10] Pyt'ev Yu.P.: Vestnik Moskovskogo Universiteta. Fizika. Astronomia, 25 (1984) 53.
[11] Efimkin N.G., Ishkhanov B.S., Pyt'ev Yu.P., Varlamov V.V.: "The Energy Resolution Improvement by the Method of Reduction in Photonuclear Experiments", MSU INP Preprint-91-35/239, 1991.
[12] Young L.M., Ph.D. Thesis, University of Illinois, 1972.
[13] Kishida N., Japan JAERI, Private information.

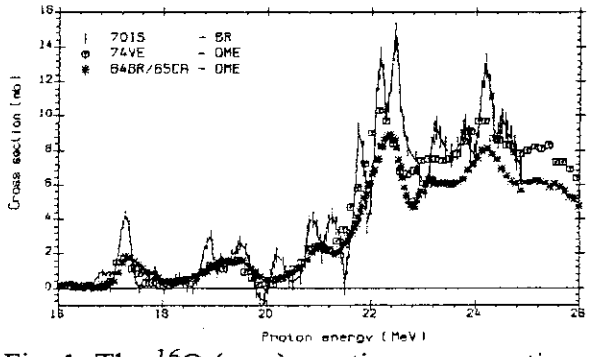

Fig. 1. The ^{16}O (γ,xn) reaction cross sections obtained in various experiments.

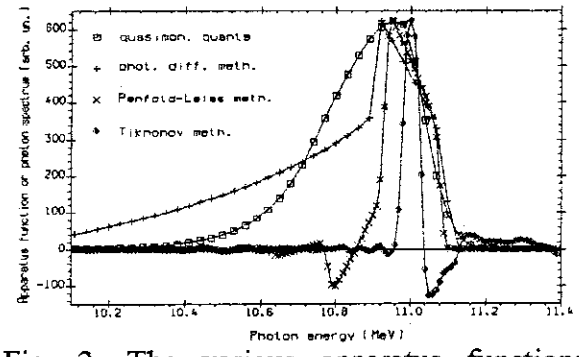

Fig. 2. The various apparatus functions (effective photon spectra).

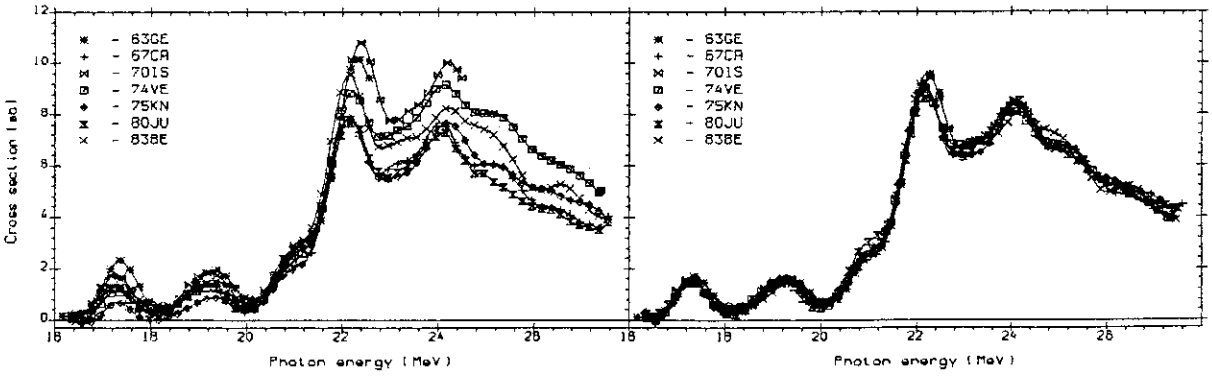

Fig. 3. The photoneutron reaction cross sections (600 keV resolution) for Oxigen before (left) and after (right) recalibration-renormalisation procedure.

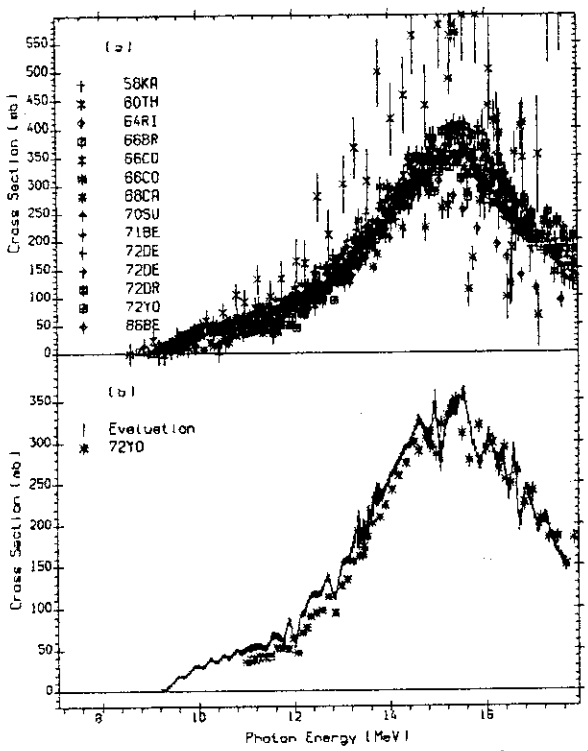

Fig. 4. The data base of initial experimental photoneutron reaction cross section for Praseodymium (a) and the evaluation result with the resolution 120 keV (b). The tagged photon data [12] are presented for comparison.

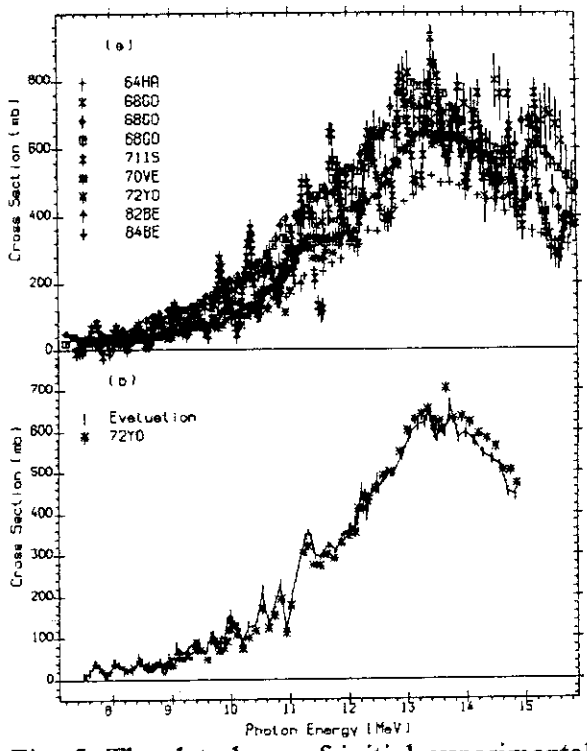

Fig. 5. The data base of initial experimental photoneutron reaction cross section for Lead (a) and the evaluation result with the resolution 120 keV (b). The tagged photon data [12] are presented for comparison.

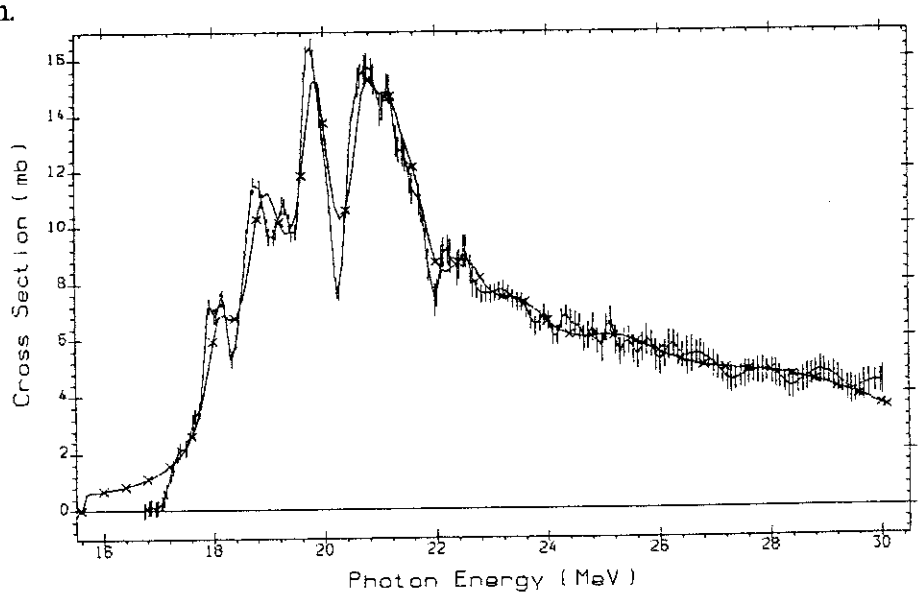

Fig. 6. The comparison of the $^{28}Si(\gamma,xn)$ reaction cross section evaluated using the method of reduction (dots with error bars) and calculated [13] using statistical nuclear reaction model (crosses).

2.2.3 From User of Photoreaction Data (Application to shielding calculation of SR beamline)

Yoshihiro Asano
Department of Synchrotron Radiation Project
Japan Atomic Energy Research Institute

Photoneutron production-yield has been calculated by using the data of track-length distribution caused by gas bremsstrahlung and photoreaction cross-section on a insertion device beamline of SPring-8. The track-length distribution and gas bremsstrahlung spectra were calculated by the Monte Carlo code EGS4. About 1.7 μSv/h has been obtained for the total photoneutron dose-equivalent rate at 1 m from the center of a thick target of Pb by assuming that the target is a point source and neutron emission is isotropic. The benchmark calculations of photoneutron production presented at the SATIF2 meeting have been also discussed.

1. Introduction

A generation of photoneutrons in a beamline is one of the serious problems of safety on synchrotron radiation beamlines, which requires an additional shielding. The photoneutrons are produced through interactions between beamline components and gas bremsstrahlung generated in an accelerator storage ring. At HASYLAB of DESY[1], the shielding against the photoneutrons has actually been a significant item of radiation protection on beamlines. In the third generation facilities, such as ESRF[2], APS[3] and SPring-8[4], the intensities of gas bremsstrahlung and photoneutrons are seriously high because of the introduction of insertion devices onto very long straight sections in a high- energy and high-current storage ring. Therefore the photoneutron production process is significant in the shielding calculation for the beamline.

2.Insertion-device beamline of SPring-8

SPring-8, an 8 GeV class synchrotron radiation facility of Japan, is now under construction and the beamlines are in the design stage. The first beam will be emitted by October in 1997. The machine of SPring-8 is composed of an electron/positron linear accelerator (linac), a booster synchrotron injector, and a storage ring. The linac is about 140 m long and accelerates electrons or positrons to 1 GeV. The booster synchrotron accelerates electrons or positrons from the linac up to 8 GeV, of which a circumference is about 400 m. Electrons or positrons will then be injected into the storage ring, which is capable of storing circulating currents up to 100 mA at 8 GeV. The storage ring is

about 1500 m of circumference with 38 straight sections (34 standard sections are 19 m in length and the others are 40 m in length). The electrons or positrons emit synchrotron radiation as they are deflected in the fields of the ring-bending magnets or specially arranged magnets called insertion devices, which are placed in the straight sections. The synchrotron radiation is introduced to experimental floor with the beamline through ratchet-shaped bulk shielding walls of storage ring. The beamlines receive the synchrotron radiation of extremely high brilliance and high power density. The shields of the beamlines for radiation safety must be designed safety under very severe conditions.

Main components of the beamline for safety shielding are a main beam shutter, down stream shutter, gamma stop, beam stop, optics and experimental hutch. The main beam shutter is installed inside the bulk shielding wall to control the introduction of synchrotron radiation beams and the down stream shutter is operated to control the beams downstream of optical components. The beam stop is set to prevent the dose outside the hutch from being high. The gamma stop made of lead is a standard beamline component of the SPring-8 to prevent the bremsstrahlung from expanding to the downstream of the beamline. It is one of the important functions of the hutch to shield the scattered photons of synchrotron radiation. In the shielding calculation of the beamline, the following 4 radiations must be considered; (a)neutrons, photons and muons due to electron beam loss, (b)synchrotron radiation, (c)bremsstrahlung from the residual gas-molecules in the straight section of the storage ring and (d)photoneutrons generated from a gamma stop struck by gas bremsstrahlung.

In this paper, we consider the gas bremsstrahlung and photoneutrons in the insertion-device beamline from user of photoraction data.

3. Calculation of gas bremsstrahlung and associated photoneutron production

3.1 Gas bremsstrahlung

The gas bremsstrahlung is generated by an interaction of the stored electron or positron with residual gas molecules or ions in a storage-ring vacuums-chamber. It becomes important especially in the

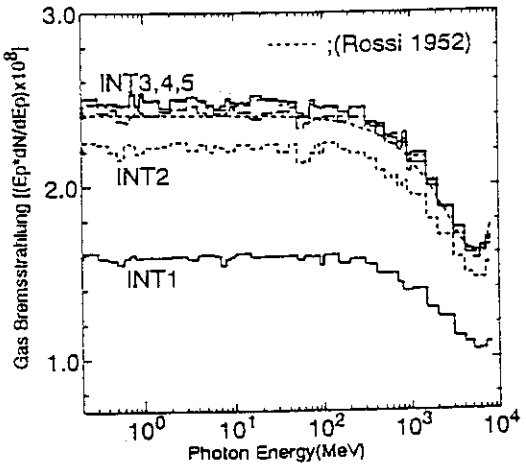

Fig.1 Gas bremsstrahlung spectra depending on the number of the interactions (generated by EGS4) resulting from 0.1A 8GeV electrons interacting with residual air-gas in the SPring-8 normal straight section. The EGS4 calculations were performed with $0.1205 g/cm^2$ air and in scaling to $3.01\times10^{-14} g/cm^2$ air (INT1;single interaction, INT2;double interactions, INT3.4.5; triple interactions or more, ---;theoretical curve(5),(6))

straight section because of its invation into the beamline.

The residual gas pressure is needed in real operation to be below 0.133 μPa (10^{-9} torr) and the calculated gas bremsstrahlung is shown in Fig.1 by using EGS4[7]. As seen in Fig.1, the gas-bremsstrahlung generated through single interaction between the electrons and 0.1205 g/cm^2 air molecules is about 60% of the total. The gas bremsstrahlung is nearly saturated within triple interaction or more. In case of the interaction with 0.01205 g/cm^2, the gas bremsstrahlung generated through single interaction is nearly equal to a saturated one. In order to avoid an over-estimation to be occurred in scaling from 0.1205g/cm^2 air molecules to 3.01×10^{-14}g/cm^2, the result of gas bremsstrahlung through single interaction was used. The emitted angle of the bremsstrahlung is almost within 0.1 mradian.

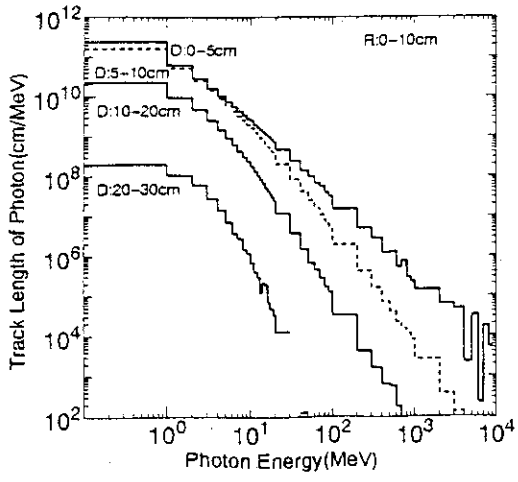

Fig.2 Photon track-length distribution within lead gamma-stop due to gas bremsstrahlung (R:radius, D:depth)

3.2 Photoneutron production yield

The track-length distribution of gas bremsstrahlung within the lead gamma stop (20 cm in radius and 30 cm in length) were calculated on the standard insertion device beamline by using the Monte Carlo code EGS4 as shown in Fig.2. The neutron yield, $N(En)$, is given by,

$$N(En) = \int dL(E\gamma)/dE\gamma \cdot \sigma(E\gamma, xEn) \cdot dE\gamma \quad (1)$$

where $dL(E\gamma)/dE\gamma$ is the photon track-length distribution and $E\gamma$ the photon energy. $\sigma(E\gamma, xEn)$ is the photoneutron production cross-section which produces the x number of neutrons with En energy. The cross-sections obtained from Dietrich and Berman[8] were used in the calculation. Figure 3 shows the neutron yield distribution within the gamma stop. In the figure, neutron production from the quasi-deuteron and photopion reactions which can be induced by photons higher than about 40 MeV was ignored.

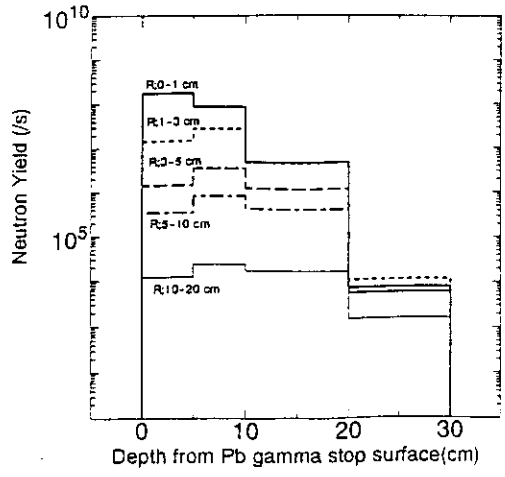

Fig.3 Neutron production distribution due to gas bremsstrahlung in lead gamma-stop (R:radius).

The energy spectra of the total neutron yield were obtained by using the Lorentz fitting from the Dietrich and Berman's data for neutron production and the maxwellian[9] for the neutron emission energy. The results are shown in Fig.4 together with the data by using other photoneutron production cross-sections generated with MCPHOTO[10] and PICA[11] up to 400MeV photon energy.

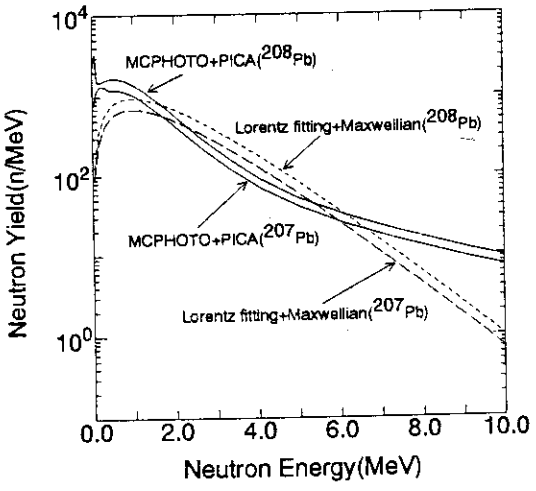

Fig.4 Calculated results of photoneutron production spectra by using track-length distribution and photoneutron production cross-section (Lorentz fitting+Maxwellian and MCPHOTO +PICA)

3.3 Dose of photoneutron

The effective dose equivalent, D, is given by,

$$D = \int K(En) \cdot N(En) \cdot dEn \qquad (2)$$

where $K(En)$ is the neutron fluence to effective dose equivalent conversion factor given by ICRP[12] ranging from the thermal neutron energy to 14 MeV and that Yoshizawa[13] above 20 MeV. On the assumption that the target is a point source and the neutron emission is isotropic, the effective dose equivalent rates at 1 m from the center of the gamma stop are 1.72 μSv/h, 1.24 μSv/h 1.45μSv/h and 1.95 μSv/h for ^{208}Pb(Lorentz fitting+Maxwellian), ^{207}Pb(Lorentz fitting+Maxwellian), ^{207}Pb(MCPHOTO +PICA code) and ^{208}Pb(MCPHOTO +PICA code), respectively.

The estimated photoneuton doses for the third generation synchrotron radiation facilities are summarized in Table 1, along with the measured data in HASYLAB. It is recommended in APS to reduce the dose equivalent rate to less than 1.25 μSv/h at 30cm from the surface of the gamma stop[15]. At HASYLAB, the neutron dose was measured by using the Anderson-Braun type rem-counter and the uncertainty of gas pressure was pointed out because of difficulty in the measurement at the midpoint of the straight section[16].

4. Benchmark calculation presented at SATIF2 meeting

In order to get the knowledge of the accelerator shielding, the "Specialist Meeting on Shielding Aspects of Accelerators, Targets and Irradiation Facilities" were held at Arlington (SATIF1) in 1994 and at Geneva (SATIF2) in 1995. In the SATIF2 meeting, the benchmark calculations for photonuclear reaction experiments, which were performed by Eyss and Luhrs[17], were picked up by Nakashima et al.[18] and Degtyarenko[19]. The former reported that the EGS4 calculations underestimated the measurements by a factor of 3.3 for all the primary electron energies ranging from 150 to 270 MeV and reproduced the shape of the measurements. The photoneutron production cross-sections generated by the MCPHOTO and

PICA codes were used in the calculation. The latter reported that DINREG and GEANT calculations reproduced the measurements with an accuracy of the order of 50% in the wide range of the initial electron and photon energies. The difference between the two benchmark calculations is thought to be mainly due to the differences in the used data of photoneutron production cross-section and neutron multiplicity. It is desired to measure the photonuetrons produced by electron beams of several hundred MeV or more and the cross-sections to validate the verification, because there are a few experimental data.

5. Concluding remarks

The dose due to the photoneutrons generated by gas bremsstrahlung onto SPring-8 insertion device beamline has been calculated with the Monte Carlo code EGS4, MCPHOTO and PICA. From user of photoreaction data, the followings can be pointed out.

(1) Photoneutron production process is significant in safety analysis on the beamlines of the third generation synchrotron radiation facilities.

(2) Well evaluated photoreaction data are strongly needed not only for shielding calculation but also for effective dose calculation.

(3) The photoreaction data library is desired to be accessible for wide application.

Acknowledgments

The author thanks Dr.N.Sasamoto, Dr. H.Nakashima of JAERI, Dr.Y.Namito of KEK, Dr.T.Sugita of SSL and Dr. H.Takahashi of CRC for useful discussions and informations. Gratitude is also expressed to Dr.S.Hashimoto of SPring-8 for his help.

Table 1 Estimation for neutron dose equivalent due to gas bremsstrahlung on the beamline of the third generation synchrotron radiation facilities. The measurement data of HASYLAB are also presented.

	ESRF[2] (Grenoble)	APS[3] (Argonne)	SPring-8[4] (Harima)	HASYLAB[1] (Hamburg)
Storage ring Electron Energy	6.0GeV	7.0GeV	8.0GeV	4.5GeV
Current	300mA	300mA	100mA	30mA
Straght section	10m	15m	19m	8.2m
Gas pressure	0.133 μPa (10^{-9}torr)	0.133 μPa (10^{-9}torr)	0.133 μPa (10^{-9}torr)	1.06 μPa (8×10^{-9}torr)
Neutron Dose	—	6 μSv/h[14] at 1.2m	~1.7 μSv/h at 1m	2.7±1.3[16] μSv/h at 1m

Reference

(1) P.Gürtler, G.Materlik and J.R.Schneider: "Experimental Stations at HASYLAB" Hamburger Synchrotronstrahlungslabor HASYLAB at Deutsches Elektronen-Synchrotron DESY Germany (1994).
(2) European Synchrotron Radiation Facility: "The Red Book Draft B" Grenoble France (1987)
(3) Argonne National Lab: "7 GeV Advanced Photon Source Conceptual Design Report" ANL-87-15 Argonne USA (1987)
(4) JAERI-RIKEN SPring-8 Project Team: "SPring-8 Project Part1 Facility Design" Tokyo Japan (1991)
(5) B.Rossi: "High-Energy Particles" Prentice-Hall Inc. Englewood N.I (1952)
(6) J.C.Liu W.R.Nelson and K.R.Kase: SLAC-PUB-6532 (1994)
(7)W.R.Nelson, H.Hirayama and D.W.O.Rogers, SLAC-265 (1985)
(8) S.S.Dietrich and B.L.Berman: Atomic Data and Nuclear Data Tables, 38 (1988)
(9) W.P.Swanson, IAEA TEC/DOC No.188 (1979)
(10) N.Kishida, BNL 12-16 Oct. (1992)
(11)T.A.Gabriel et.al., ORNL-4687, (1971)
(12) International Commision on Radiological Protection: ICRP Pub.51, Pergamon Press (1987)
(13) N.Yoshizawa et al.,: Proc. Int.Conf. Rad. Shielding on Apr., 1994, Arlinton, USA(1994)
(14) N.E.Ipe and A.Fasso: Nucl.Inst.and Meth.in Phys.Rearch A351 (1994)
(15) P.K.Job, D.R.Haeffner and D.Shu: ANL/APS/TB-20 (1994)
(16) K.Tesch: Private communication
(17) Eyss H.J. and Luhrs G.: Z.Physik 262 (1973)
(18) H.Nakashima et al.,: Proc. SATIF2 on Oct 12-13,1995,Geneva,Switzerland (1996 OECD/NEA)
(19) P.Degtyarenko: Proc. SATIF2 on Oct.12-13,1995,Geneva,Switzerland (1996 OECD/NEA)

2.3 Special Purpose File

2.3.1 Status of the JENDL Activation File

Yutaka NAKAJIMA

Japan Atomic Energy Research Institute,
Tokai-mura, Ibaraki-ken 319-11, Japan
e-mail : nakajima@cracker.tokai.jaeri.go.jp

and

Japanese Nuclear Data Committee activation-cross-section data working group [1]

The preliminary JENDL activation file was acomplished in February 1995 and has been used in the Japanese Nuclear Data Committee and as one of the data sources for the Fusion Evaluated Nuclear Data Library in IAEA. Since there are already big activation libraries in western Europe and United States, we are aiming at more accurate evaluation of important reactions to application to nuclear energy development rather than aiming at as many reaction data as in these big libraries. In the preliminary file 1,158 reaction cross sections have been compiled for 225 nuclides up to 20 MeV.

1. Introduction

Evaluation on activation cross section data for the JENDL activation file is going on based on the JENDL-3.2 [1] and supplemented by the calculation of the Nuclear Cross-Section Calculation System with Simplified Input-Format Version II(SINCROS-II)[2]. Since there are already big activation libraries REAC-ECN-4[3] and UKACT1[4] in western Europe and USACT-88[5] in the United States respectively, we are aiming at more accurate evaluation of important reactions for application to nuclear energy development rather than aiming at compilation of as many reaction data as in these big libraries.

The preliminary JENDL activation file was accomplised in February 1995 ,and has been used in the Japanese Nuclear Data Committee and as one of the sources for the Fusion Evaluated Nuclear Data Library in IAEA. In the file 1,158 reaction cross sections have been compiled for 225 nuclides up to 20 MeV in the ENDF-5 format.

II. Selection of activation reactions

All elements lighter than Bi(Z=83) were examined thoroughly from the point of the application to the nuclear energy development, and categorized into three groups according to their importance in the application. The priority decided are shown for each element in Table 1. Activation cross section data for the elements of the priority 1 and 2 will be compiled into the JENDL activation file. The cross sections for the elements of the priority 1 were especially carefully evaluated.

In the selection of the activation cross sections the following items and criteria have been employed:

(1) the half life of target nuclide: longer than 1 day, however for the version 1 only the data for the stable

---

[1] Members of the activation-cross-section-data working group

T. Asami*, M. Hachiya, Y. Ikeda, S. Iwasaki, K. Kobayashi, Y. Nakajima, Y. Seki, N. Yamamuro*, M. Yano, T. Yoshida, T. Watanabe*, (S. Iijima*).

*Evaluators

nuclide will be compiled in the file,

(2) the half life of product nuclide: longer than 1 day and shorter than 10^7 years,

(3) the threshold energy: lower than 18 MeV,

(4) the reactions: (n,γ), (n,n'), (n,2n), (n,3n), (n,p), (n,d), (n,t), (n,np), (n,nd), (n,nd), (n,nt), (n,2p), (n,α), (n,^{3}He), (n,nα).

The data for the following reactions were also included in the file: the reactions whose product nuclides have the half life shorter than 1 day and longer than 1 minute and which are important to the applications, and the reactions which produce the nuclides whose daughters have the half life longer than 1 day.

III. Evaluation method

Evaluation was made so as to reproduce reliable experimental data. The JENDL-3.2 data were compared with experimental data. When the agreement was reasonable, the JENDL-3.2 data were compiled as the data of the JENDL activation file. When the agreement was not good, the cross sections were calculated with the SINCROS-II so as to reproduce the experimental data. When the reaction cross sections are no available in JENDL-3.2, the cross sections were calculated with the SINCROS-II. When reactions produce isomeric states, the isomeric ratio was calculated with the SINCROS-II and the cross sections to the ground state and the isomeric states were obtained by multiplying the total reaction cross section by the isomeric ratio.

IV. Examples of the results

Some results of the evaluation are shown in Figs. 1 ～ 11, comparing experimental data.

1. ^{23}Na(n,2n)^{22}Na

Measured data are divided into two groups as shown in Fig. 1. While ENDF/B-VI is in agreement with the group larger values, JENDL-3.2 follows ther group with smaller values. The most recent measured data [6,7], which are not shown in Fig. 1, support the group with smaller values. So we adopt JENDL-3.2 as the activation data.

2. ^{59}Co(n,2n)^{58}Co and ^{58}Ni(n,p)^{58}Co

For both reactions the calculation with SINCROSS does not reproduce the measured gorund and isomeric state cross sections as shown in Figs. 2 and 3, while the total reaction cross section is in good agreement each other. This means that branching ratio and/or transiton probability of the γ-rays used for the calculatiion are not correct. The calculated cros sections have been normalized to repoduce the reliable experimental data as shown in Fig. 4 for the ^{59}.Co(n, 2n) reaction.

3. ^{64}Zn(n,p)^{64}Cu and ^{66}Zn(n,p)^{66}Cu

The evaluation was made with the SINCROS-II. The evaluated data are in good agreement with experimental data. For ^{64}Zn(n,p)^{64}Cu the data of Smith et al.[8] are very low compared with other measured data and the present evaluation from 5 to 10 MeV(Fig. 5), however for ^{66}Zn(n,p)^{66}Cu their measured data[9] are in good agreement with our evaluation(Fig. 6). The reason of the disagreement is not clear.

4. ^{95}Mo(n,p)^{95}Nb and ^{98}Mo(n,α)^{95}Zr

The evaluation was carried out with the SINCROS-II independently of the JENDL general purpose file and the present evaluation is in a little better agreement with measured data than JENDL-3.2. The detailed description already has been given by Yamamuro[10], so brief explanation will be given here..

For ^{95}Mo(n,p)^{95}Nb data measured by Lieskin et al.[11] have the different energy dependence from the present evaluation(Fig.7). As pointed out by Yamamuro these reaction data were contaminated by ^{96}Mo(n,d+np)^{95}Nb, because Lieskin et al. measured the cross sections using natural targets. For ^{98}Mo(n, α)^{95}Zr the evaluated data reproduce measured data including the Lieskin et al's data(Fig. 8). This is because there is no other reaction to produce ^{95}Zr even

for the natural targets of Mo.

5. $^{151}Eu(n,2n)^{150}Eu$

The cross sections to the ground and isomeric states were also evaluated from JENDL-3.2 by multiplying the isomeric ratio calculated with SINCROS-II. Both cross sections are in good agreement with values measured near 14.7 MeV(Fig. 9).

6. $^{185}Re(n,\gamma)^{186}Re$

The total capture cross section was calculated with CASTHY[12]. The cross sections to the ground and isomeric states were evaluated by multiplying the isomeric ratio calculated with SINCROS-II. For the ground state cross section measured data were reproduced by the evaluated data excellently(Fig. 10)., while the validity of the isomeric cross section has not been confirmed as there are no available measured data.

7. $^{206}Pb(n,2n)^{205}Pb$

The cross section was evaluated with the SINCROS-II. The evaluated cross section reproduces measured data excellently(Fig. 11) , while the evaluated data are larger than JENDL-3.2 by 15 %.

V. Conclusions

The evaluation of the activation cross sections for the JENDL activation file have been almost completed. The evaluated data reproduce the reliable experimental values very well. The validation test has been started using integral data measured with FNS[13]. The version 1 of the JENDL activation file will be released by the end of this year.

References

1) Nuclear Data Center, Japan Atomic Energy Research Institute.
2) Yamamuro, N.: JAERI-M 90-006(1990).
3) Kopecky, J.: INDC(NDS)-223/GF 62(1989).
4) Forrest, R. et al.: Proc. of Int. Conf. on Nucl. Data for Sci. and Technol., Mito, Japan, 1061(1988).
5) Mann, F.: Proc. of Int. Conf. on Nucl. Data for Sci. and Technol., Mito, Japan, 1013(1988).
6) Sakuma, M. et al.: JAERI-M 92-027, 278(1992).
7) Uwamino, Y. et al.: Nucl. Sci. Eng **111**, 391(1992).
8) Smith, D. L. and Meadows, J. W.: Nucl. Sci.. Eng., **58**, 314(1975).
9) Smith, D. L. et al.: Nucl. Sci. Eng., **76**, 61(1980).
10) Yamamuro, N.: Nucl. Sci. Eng., **109**, 128(1991).
11) Lieskin, H., et al.: Appl. Radiat. Isot., **41**, 83(1990).
12) Igarasi, S. and Fukahori, T.: JAERI 1321(1991).
13) Ikeda, Y.: Private communication.

Table 1. Priority of materials required for JENDL activation file

Z	Element	Priority	Z	Element	Priority	Z	Element	Priority
1	H	1	29	Cu	1	57	La	3
2	He	2	30	Zn	2	58	Ce	3
3	Li	1	31	Ga	2	59	Pr	3
4	Be	1	32	Ge	2	60	Nd	3
5	B	1	33	As	2	61	Pm	3
6	C	1	34	Se	3	62	Sm	2
7	N	1	35	Br	3	63	Eu	1
8	O	1	36	Kr	3	64	Gd	1
9	F	2	37	Rb	3	65	Tb	2
10	Ne	2	38	Sr	2	66	Dy	2
11	Na	1	39	Y	2	67	Ho	2
12	Mg	2	40	Zr	1	68	Er	2
13	Al	1	41	Nb	1	69	Tm	2
14	Si	1	42	Mo	1	70	Yb	3
15	P	2	43	Tc-99	1	71	Lu	3
16	S	2	44	Ru	3	72	Hf	1
17	Cl	2	45	Rh	2	73	Ta	1
18	Ar	1	46	Pd	2	74	W	1
19	K	2	47	Ag	1	75	Re	1
20	Ca	1	48	Cd	1	76	Os	2
21	Sc	2	49	In	1	77	Ir	2
22	Ti	1	50	Sn	1	78	Pt	2
23	V	1	51	Sb	1	79	Au	1
24	Cr	1	52	Te	3	80	Hg	2
25	Mn	1	53	I	2	81	Tl	3
26	Fe	1	54	Xe	3	82	Pb	1
27	Co	1	55	Cs	3	83	Bi	1
28	Ni	1	56	Ba	1			

Priority 1: 39 elements
Priority 2: 28 elements
Priority 3: 16 elements

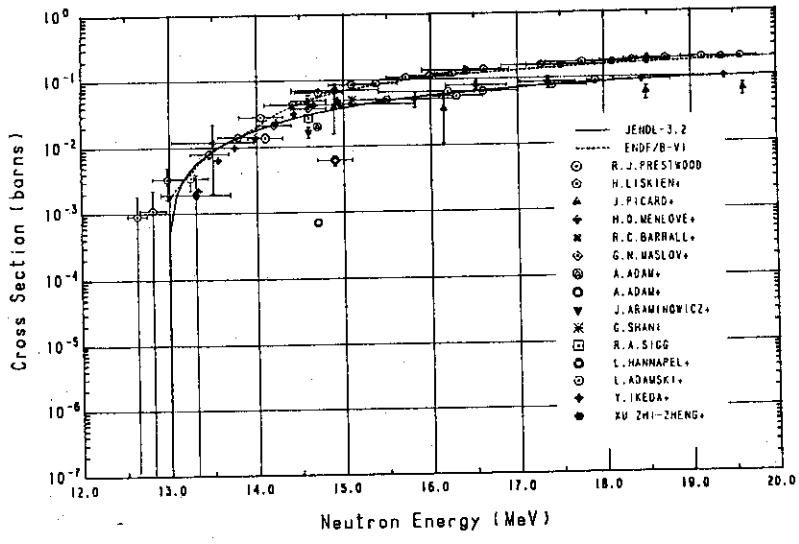

Fig. 1 $^{23}Na(n,2n)\ ^{22}Na$ cross section.

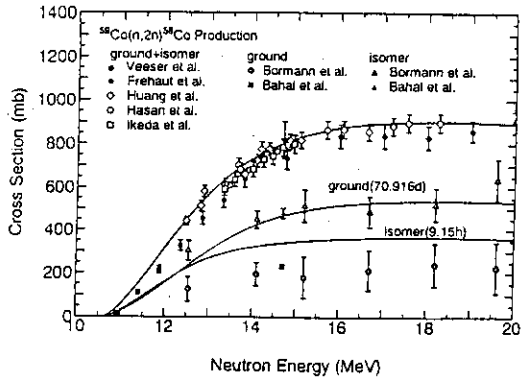

Fig. 3 ^{58}Ni(n,2n) ^{58}Co cross section(calculated data with SINCROSS-II).

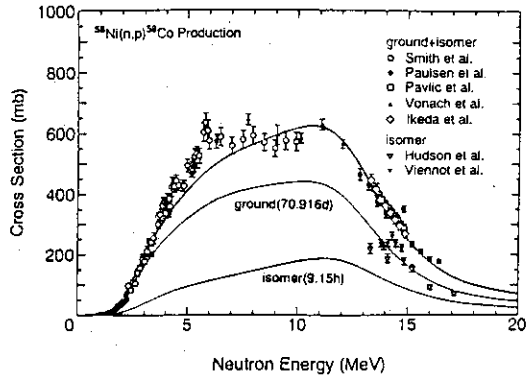

Fig. 2 ^{59}Co(n,2n) ^{58}Co cross section(calculated data with SINCROSS-II).

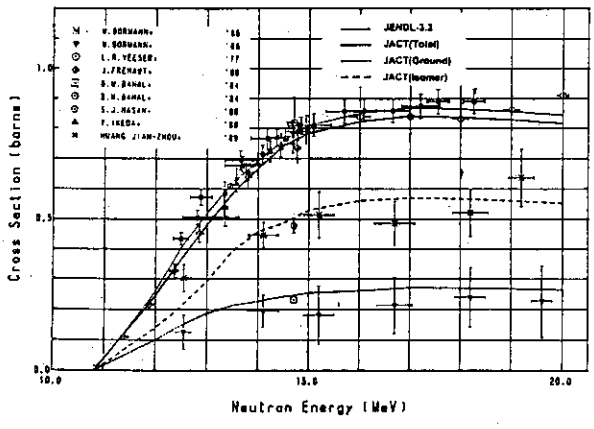

Fig. 4 ^{59} Co(n, 2n) ^{58}Co cross section(normalized).

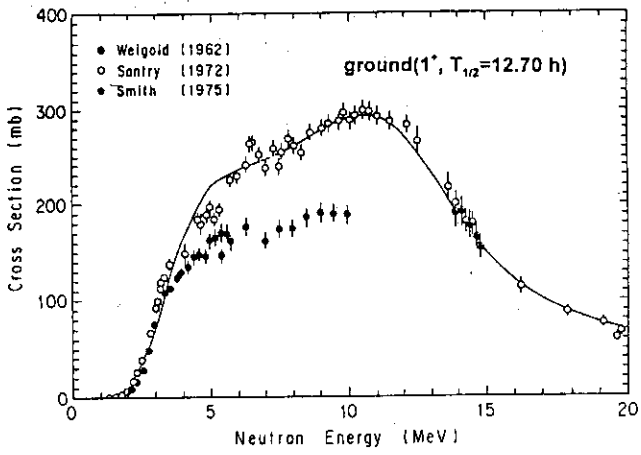

Fig. 5 ^{64}Zn(n,p) ^{64}Cu cross section.

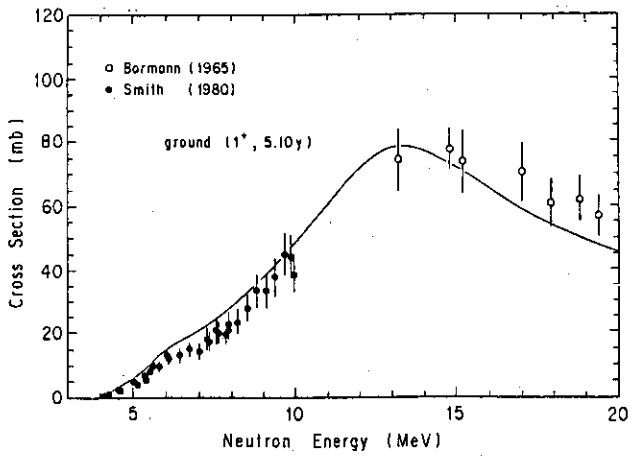

Fig. 6 ^{66}Zn(n,p) ^{66}Cu cross section.

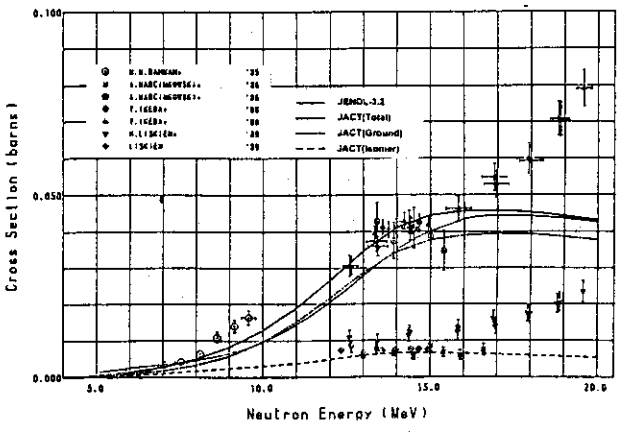

Fig. 7 ^{95}Mo(n,p) ^{95}Nb cross section.

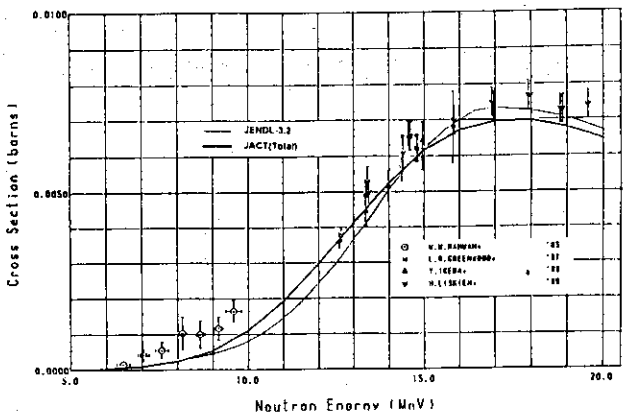

Fig. 8 ^{98}Mo(n,α) ^{95}Zr cross section.

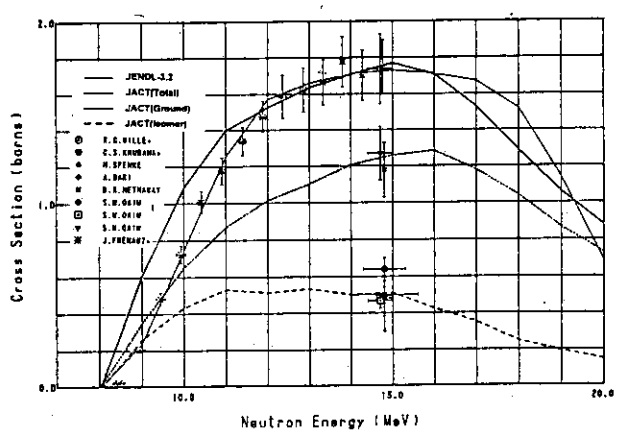

Fig. 9 ^{151}Eu(n,2n) ^{150}Eu cross section.

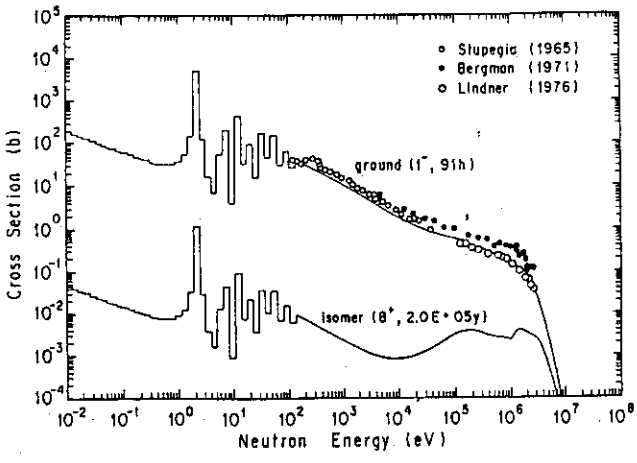

Fig. 10 ^{185}Re(n,γ) ^{186}Re cross section.

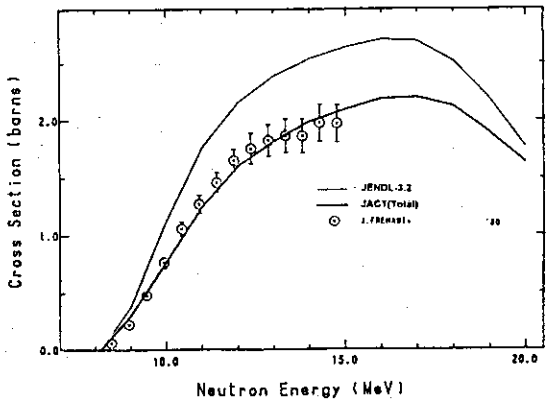

Fig. 11 ^{206}Pb(n,2n) ^{205}Pb cross section.

2.3.2 Status of JENDL High Energy File for IFMIF

T. Fukahori
Nuclear Data Center, Dept. of Reactor Engineering,
Japan Atomic Energy Research Institute,
Tokai-mura, Naka-gun, Ibaraki-ken, 319-11 Japan
fukahori@cracker.tokai.jaeri.go.jp

The JENDL High Energy File for IFMIF is a neutron nuclear data file of the phase-I of JENDL High Energy Files. The 27 elements from H to W are included in the JENDL High Energy File for IFMIF. The evaluated quantities are the total, elastic scattering, reaction, fission and isotope production cross sections, and double differential particle and γ-ray emission cross sections. The considered outgoing particles are neutron, proton, deuteron, triton, ^{3}He and α-particles. The present status of the JENDL High Energy File for IFMIF, and preliminary results for several nuclides are reported as well as their format.

1. Introduction

The JAERI Nuclear Data Center has started to generate evaluated high energy nuclear data files in cooperation with Japanese Nuclear Data Committee (JNDC) in order to give basic information to a lot of applications such as accelerator engineering, space physics and engineering and medical usage. The files considered here are JENDL High Energy File, JENDL PKA/KERMA File and JENDL Photonuclear Data File. The outlines of these files are summarized in **Table 1**.

The JENDL High Energy File will include nuclear data for proton- and neutron-induced reactions. The evaluation work is separated into two phases. The energy range of the phase-I is up to 50 MeV. The nuclear data in this energy range are needed mainly for the International Fusion Material Irradiation Facility (IFMIF)[1] which is an FMIT-type accelerator facility using Li(d,n) neutron source for an irradiation test of fusion reactor materials. The neutron spectrum of IFMIF has a high energy tail up to 50 MeV. The energy range for the phase-II is up to a few GeV mainly for an accelerator-driven radioactive waste transmutation system (OMEGA project).

The JENDL PKA/KERMA File is generated to give the primary knock-on atom (PKA) spectra, damage energy spectra, DPA (displacement per atom) cross section and kerma factor by neutron-induced nuclear reactions as basic information for estimation of material radiation damage. Incident neutron energy below 50 MeV is considered. The JENDL photonuclear data file consists evaluated gamma-ray induced nuclear reaction data below 140 MeV.

In this paper, the present status of the JENDL High Energy File for IFMIF, and preliminary results for several nuclides are reported as well as their format.

2. JENDL High Energy File for IFMIF

The JENDL High Energy File for IFMIF is a neutron nuclear data file of the phase-I of JENDL High Energy Files. The elements included in the JENDL High Energy File for IFMIF are summarized in **Table 2**. The evaluated quantities are total, elastic scattering, reaction and isotope production cross sections, and double differential particle and γ-ray emission cross sections. The outgoing particles considered are neutrons, protons, deuterons, tritons, ^{3}He and α-particles. For the evaluation, SINCROS-II is mainly used, except for light mass nuclei because of not enough experimental data.

SCINFUL/DDX code is used for the evaluation of the light mass nuclei by considering break-up reactions. Below 20 MeV, the data of JENDL Fusion File and/or JENDL-3.2 are adopted basically for all the nuclei.

A review step after calculation step finished is newly adopted. Materials for data review (Review Kit) are numerical file of evaluated result, results of format and physical checking by using FISCON, PSYCHE, CHECKR and DOUBLEP codes, plots comparing with experimental data, index list of experimental data and list of produced isotopes. After re-evaluating according to the suggestion of reviewer, data is finally compiled and is sent to some benchmark tests.

3. FORMAT

For the JENDL High Energy File for IFMIF, ENDF-6 format must be selected fundamentally. MF and MT numbers in ENDF-6 format are assigned in **Table 3**. The major applications of intermediate energy nuclear data need isotope production cross section and double differential light particle, gamma-ray, meson and PKA spectra for neutron-, proton- and photo-induced reactions, fundamentally. Though it is necessary to include individual product nuclides for isotope production cross sections, it seems that composite particle spectra, which are not identified the emitted reaction and summing up the same particle from all the reaction channels, might be enough to use for each application. It is no meaning to separate the energy region in consideration of format.

For conservation of consistency, some rules should be promised inside the format, for instance, sum rule. The evaluation information and comments are included in MF=1. If fission reaction channel is included, the fission-related quantities, for example, fission neutron spectra (MF=5, MT=18), average prompt neutron number (MF=1, MT=452,455,456), fission product distribution (MF=6, MT=18), etc., should be compiled. For sum rule, 1) (MF=3, MT=1) = (MF=3, MT=2) + (MF=3, MT=3), 2) (MF=3, MT=3) = (MF=3, MT=5) + (MF=3, MT=18), 3) For MF=3, MT=201, 203, 204, 205, 206 and 207, the contributions of elastic scattering, discrete inelastic scattering and fission channels are not included. For the angular distributions of elastic and discrete inelastic scattering channels, it can be compiled both in MF=4 and in MF=6, LAW=2. For fission neutron spectrum, both MF=5 and MF=6 can be used. Other detail of rules for MF=6 are listed below:

MF=6, LAW=0: in the case of only the isotope production ratio (MT=5) to MF=3, MT=5 is included (unknown distribution).
MF=6, LAW=1: for MT=201-207, using Legendre coefficients or Kalbach systematics.
MF=6, LAW=2: for MT=2, 51-90 (discrete two-body scattering), using Legendre coefficients or tabular expression.
MF=6, LAW=5: for MT=2 of charged particle (charged particle elastic scattering).
MF=6, LAW=7: for MT=201-207, using table type format, and
MT=5 in the case including the isotope production ratio to MF=3, MT=5, and the PKA spectra.

4. STATUS OF EVALUATION

Preliminary evaluations have been almost finished for neutron-induced reactions of elements listed in **Table 2** up to 50 MeV. Reviews of the results are now in progress.

For neutron-induced ^{1}H total and elastic scattering cross sections up to 1 GeV, the evaluation was performed by fitting experimental data below 500 MeV with the least squares method and by calculating from phase-shift data above 500 MeV. The evaluated result of ^{1}H total cross section is shown in **Fig. 1** with experimental data. The phase-shift data was also converted to elastic scattering angular distribution. Nucleon inelastic scattering cross sections, which are pion production cross section and so on, are also evaluated. For ^{6}Li, ^{7}Li and ^{12}C, evaluations were performed by SCINFUL/DDX[2] with considering break-up reactions. The primary knock-on atom (PKA) spectra

were also calculated simultaneously. The results of light particle spectra are in good agreement with the experimental data. In **Fig. 2**, evaluated spectra for proton, deuteron and α-particle from $n+^{12}C$ reaction is compared with the experimental data. EXIFON[3], which is a multistep statistical model code with preequilibrium process corrections of FKK theory and Iwamoto-Harada cluster particle emission, is used to evaluation for ^{14}N and ^{16}O.

For evaluation of the other elements, SINCROS-II[4] is basically adopted and modified. As the example of evaluated result with SINCROS-II the isotope production cross sections for $^{nat}Cr(n,x)^{49}Cr$, $^{nat}Cr(n,x)^{52}V$, $^{nat}Cu(n,x)^{61}Cu$ and $^{nat}Cu(n,x)^{62}Cu$ reactions are shown in **Figs. 3-6** with experimental data measured by Uwamino et al.[5]. The calculated results are almost in good agreement with the experimental data. Hence, other results are expected to reproduce the isotope production cross sections.

5. SUMMARY

Neutron File, Phase-I of JENDL High Energy File, is now compiling in the energy region below 50 MeV for IFMIF. The compilation will be finished in 1996. The present status of evaluation of JENDL High Energy File for IFMIF was reviewed as well as the preliminary results and format description. These files are compiled in the ENDF-6 format. In addition, the review process is newly introduced for compilation of JENDL High Energy File. The first version of IFMIF File will be released in 1997 for 21 elements, 57 isotopes, after tested.

Acknowledgements

The evaluation and review work for the JENDL High Energy File is being performed by members of Japanese Nuclear Data Committee and Nuclear Data Center of JAERI, especially done by Dr. T. Asami. The author would like to thank them.

References

[1] Noda K.; "International Fusion Material Irradiation Facility (IFMIF) Program", *Proc. 1994 Symposium on Nuclear Data, Tokai, Ibaraki, Nov. 17-18, 1994, JAERI-Conf 95-008*, p.112 (1995).

[2] Kashimoto H., et al.: "Study of the ^{12}C Breakup Process and Carbon Kerma Factor", *Proc. 1992 Symposium on Nuclear Data, Tokai, Ibaraki, Nov. 26-27, 1992, JAERI-M 93-046*, p.287 (1993).

[3] Kalka H.: "Statistical Multistep Reaction Model for Nuclear Data", *Proc. Int. Conf. on Nuclear Data for Science and Technology, Julich, May 13-17, 1991*, p.897, Springer-Verlag, Berlin, Heidelberg (1992).

[4] Yamamuro N.: "A Nuclear Cross Section Calculation System with Simplified Input-Format Version II (SINCROS-II)", *JAERI-M 90-006* (1990).

[5] Uwamino Y., Sugita H., Kondo Y. and Nakamura T.; *Nucl. Sci. Eng.*, **111**, 391 (1992).

Table 1 The Outline of Evaluated High Energy Nuclear Data Files

File Name / Incident Particle / Energy Range	priority	release
JENDL High Energy File		
Phase-I (< 50 MeV)		
neutron (for IFMIF)	1	1997
proton	2	1998
Phase-II (< a few GeV, for the OMEGA Project)		
neutron	3	1999
proton	3	1999
JENDL PKA/KERMA File(< 50 MeV)		
neutron	2	1998
JENDL Photonuclear Data File(< 140 MeV)		
gamma	1	1996

Table 2 The elements to be included in the JENDL High Energy File for IFMIF.

21 elements, 57 isotopes
H, Li, C, N, O, Na, Mg, Al, Si, K, Ca, Ti, V, Cr, Mn, Fe, Ni, Cu, Y, Mo, W

Underline: high priority

Table 3 The MF and MT Numbers Defined in ENDF-6 Format

MT	MF	quantities
1	3	total (only for neutron-induced reaction)
2	3,6	elastic scattering
3	3	total reaction
5	3,6	isotope production by spallation and evaporation processes
18	3,6	fission
51-91	3,6	discrete inelastic scattering (not always)
102	3,6	capture
103-107	3,6	(n,z) reactions
151	2	resonance information
201	3,6	neutron production
202	3,6	gamma production
203	3,6	proton production
204	3,6	deuteron production
205	3,6	triton production
206	3,6	^{3}He production
207	3,6	α production

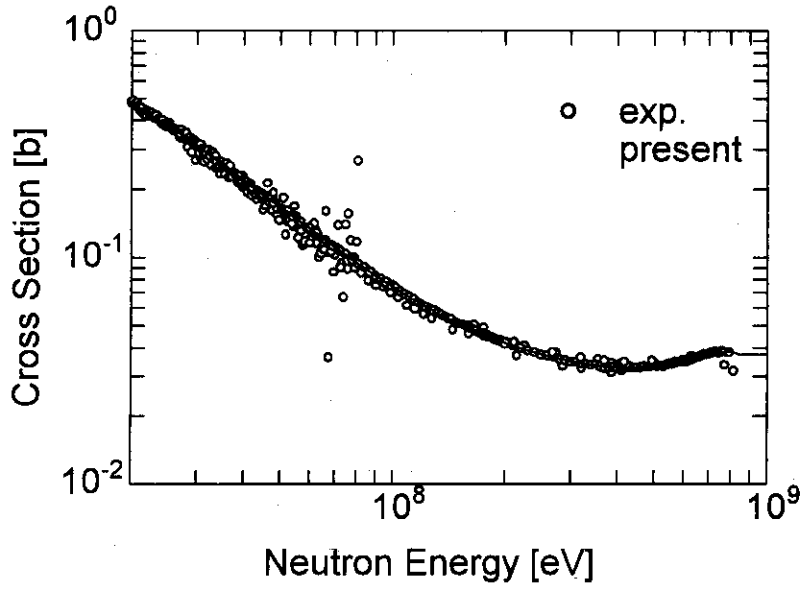

Fig.1 Neutron Total Cross Section of ^{1}H

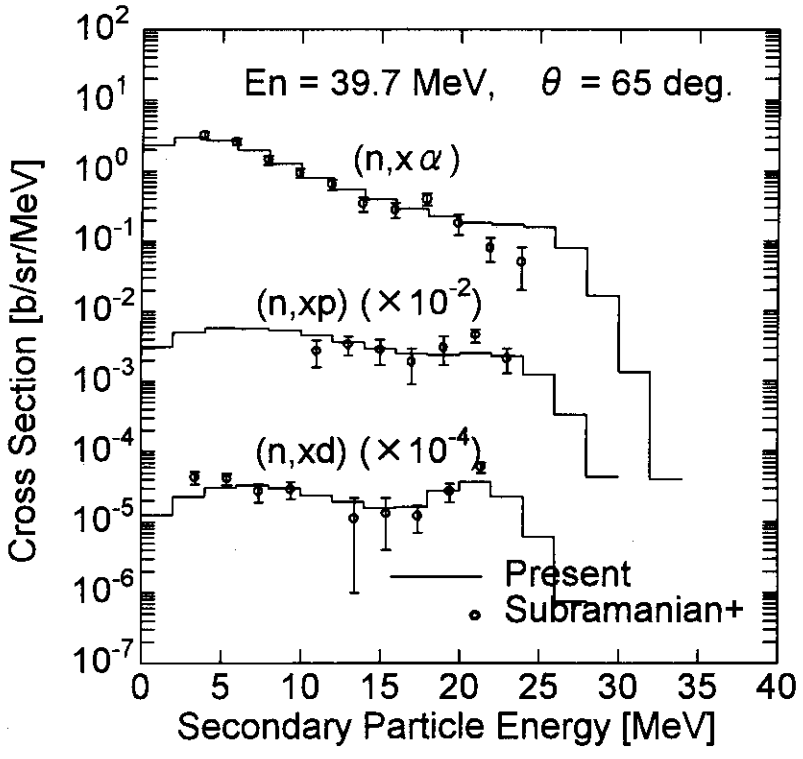

Fig.2 Double Differential Cross Section of n+^{12}C Reaction

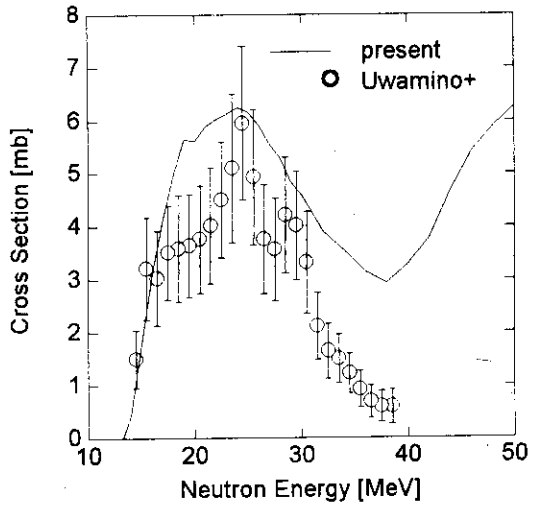

Fig.3 Cross Section of Cr-nat(n,x)Cr-49 Reaction

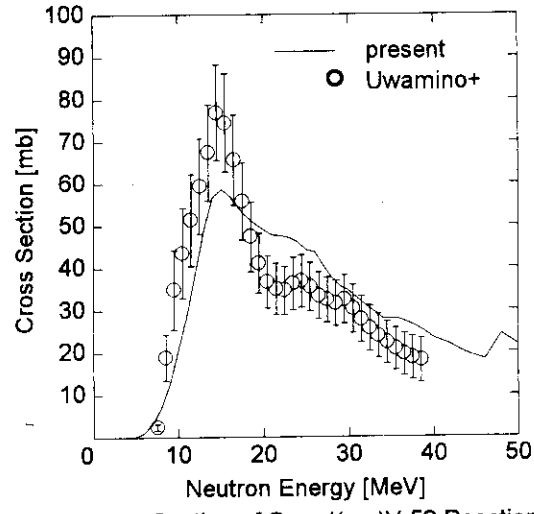

Fig.4 Cross Section of Cr-nat(n,x)V-52 Reaction

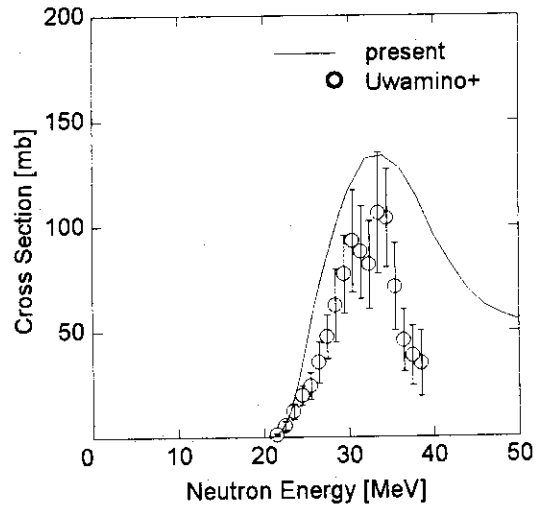

Fig.5 Cross Section of Cu-nat(n,x)Cu-61 Reaction

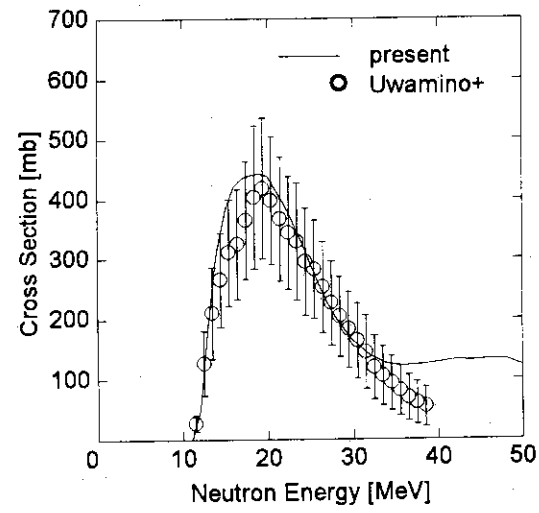

Fig.6 Cross Section of Cu-nat(n,x)Cu-62 Reaction

2.4 Topics

2.4.1 NUCLEAR AND ATOMIC DATA ACTIVITIES IN MALAYSIA

Ahmad Suhaimi
Department of Nuclear Science, National University of Malaysia
43600 Bangi, Selangor Darul Ehsan, Malaysia

Gui Ah Auu
Malaysian Institute for Nuclear Technology Research
43000 Kajang, Selangor Darul Ehsan, Malaysia

Abstract

Nuclear and atomic data measurements and calculations in Malaysia are mostly done at the National University of Malaysia (UKM) and Malaysian Institute for Nuclear Technology Research (MINT). At UKM, (n,t) reactions for ^{6}Li, ^{10}B and reactor structural materials have been investigated using liquid scintillation counting and gas phase β^- anticoincidence counting. Tritium productions via ternary fission in ^{235}U and ^{232}Th are measured using vacuum extraction and β^- counting of accumulated tritium. In addition, γ-ray attenuation coefficients on cooking oil, petroleum products, building materials, natural rubber and tropical woods have also been measured. Calculations to determine μ-value according to Hubbel method are initiated. Some collaborative works between UKM and Jülich Research Centre of Germany have been completed while others are in progress namely; (n,t) reactions study on ^{9}Be, ^{10}B, ^{14}N and also measurement of excitation functions and isomer ratios of fast neutron induced reactions on Zn, Ga and Ge. At MINT, the 1-D diffusion code TRIGAM and the 2-D EXTERMINATOR code are used for neutronic analyses of TRIGA Reactor. The radiation shielding calculation have been carried out by using ANISN, a 1-D discrete ordinates code. Some preliminary calculations for the fuel transfer cask using ORIGEN2 and MERCURE-4 have been performed. Response functions for neutrons and the associated secondary photons for neutron skyshine analyses have been generated using the MCNP code.

Introduction

The dream that the Malaysian Goverment would say yes to nuclear power as well as the need of many nuclear scientists for a planned Nuclear Research Center triggered us to form the Department of Nuclear Sciences at the National University of Malaysia in 1979. Shortly after that, the Tun Dr. Ismail Nuclear Research Center (PUSPATI) was established with its nuclear reactor TRIGA MkII. Now the center is known as Malaysian Institute for Nuclear Technology Research (MINT).

In 1981, a committee for nuclear data was set up with the cooperation of IAEA. Unfortunately nothing was heard afterward about the committee. However, a small number of nuclear scientist in our country are still interested in nuclear data works. We are doing some nuclear data measurements and testing. However due to budget contrain the so-called nuclear data group remains small and not very active. In this paper our activities in nuclear data measurement and utilization will be presented.

Tritium Production

Tritium production data are required mainly for the benefit of fusion reactor technology as well as for the calculation of tritium release to the environment. At UKM, the production of tritium at the TRIGA reactor was studied via (n,t) reactions and ternary fission. The tritium produced were measured using two methods. The first method was by tritium extraction in the gas phase followed by anti-coincidence β^- counting. The second method was the tritium assaying method in the liquid phase followed by tritium counting with the liquid scintillation counter.

Cross sections for the $^{10}B(n,t)2\alpha$ reactions were determined by the tritium extraction and tritium assaying methods respectively for thermal neutrons and the fission neutron spectrum at the Rotary Rack, PAUS system and the Central Thimble of the TRIGA reactor. At thermal neutron energy, the cross section values for the $^{10}B(n,t)2\alpha$ and the $^{6}Li(n,t)\alpha$ are (13±2) mbarn and (939±65) barn respectively. These values are in good agreement with other reported values [Ref.1&2]. Fission neutron spectrum cross section for the $^{10}B(n,t)2\alpha$ reaction of between 22 mbarn and 39 mbarn was obtained. Whereas, the $^{6}Li(n,t)\alpha$ reaction has cross section values of between 314 barn and 902 barn for the fission neutron spectrum (see Table 1). We have also performed calculations based on TRIGA Reactor neutron spectrum and cross section values to estimate for the total tritium emission in various TRIGA Reactor facilities.

Table 1: $^{10}B(n,t)2\alpha$ and $^{6}Li(n,t)\alpha$ reaction cross sections in thermal neutrons and fission neutron spectrum

	$\sigma[^{10}B(n,t)2\alpha]$ mbarn	$\sigma[^{6}Li(n,t)\alpha]$ barn
Rotary Rack	22 ± 4	902 ± 40
PAUS System	27 ± 5	724 ± 37
Central Thimble	39 ± 7	314 ± 15
Thermal Column	13 ± 2	939 ± 65

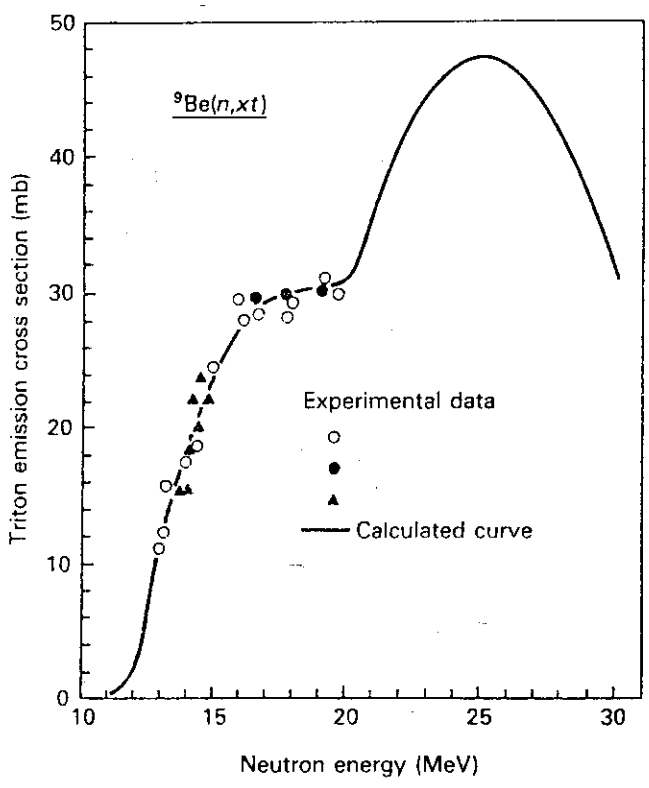

Fig. 1: Excitation function of the (n,xt) process on ^{9}Be.

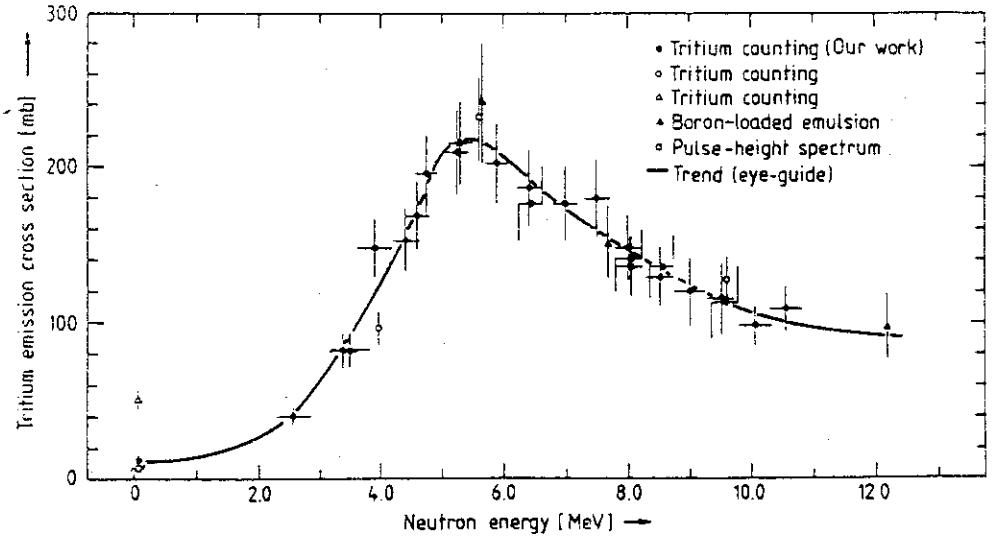

Fig.2: Excitation function of ^{10}B(n,t)2α process.

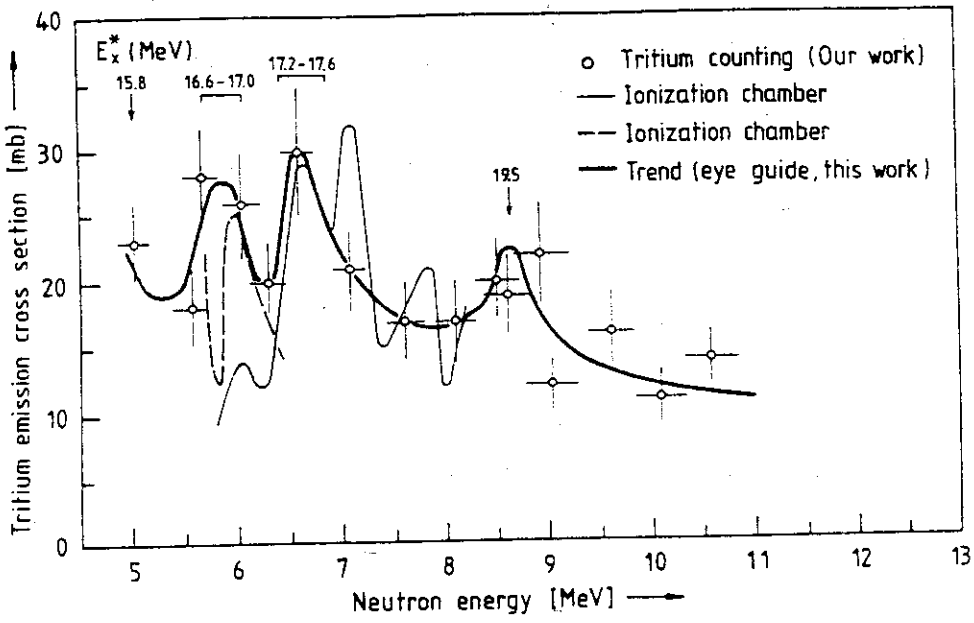

Fig.3: Excitation function of $^{14}N(n,t)^{12}C$ process.

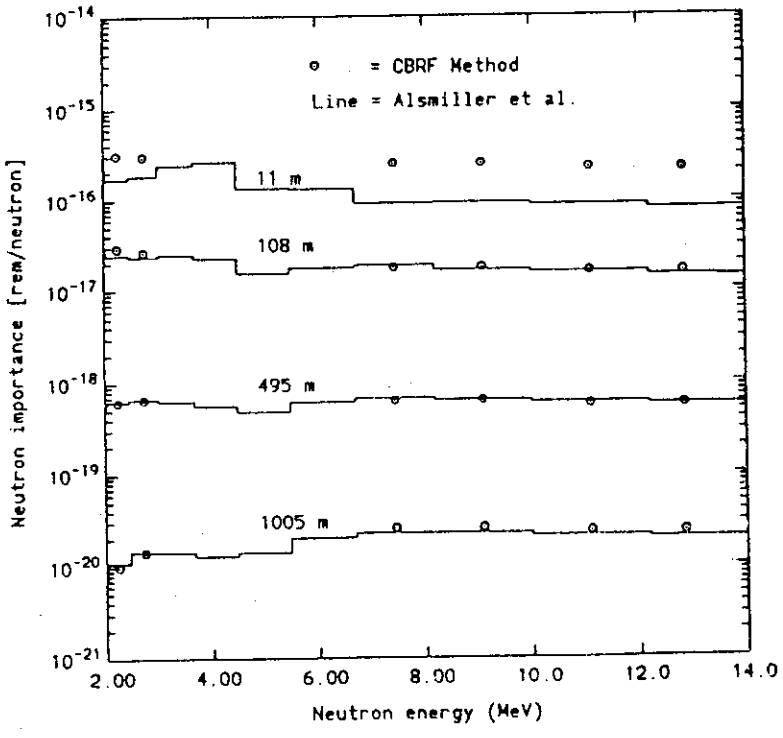

Fig.4: Comparison of the integral conical-beam method results with that of Alsmiller et al. [Ref. 22] for an air-over-ground skyshine problem. The source neutrons are emitted uniformly within the polar cosine interval, cos θ, of 0.8-1.0.

Tritium produced via (n,t) reactions for reactor structural materials such as control rod, concrete, aluminum, stainless steel (SS-304) and graphite were determined by the extraction method in the gas phase. Basically, the tritium produced in structural material depends on the lithium and boron content in the material. Tritium extracted from the material were in the range of $8x10^4$ dps/g and $2x10^{10}$ dps/g of the sample for 6 hours irradiation in the Rotary Rack.

Tritium produced via ternary fission for UO_2 and ThO_2 was measured by the gas phase extraction method. The study is still in progress. Preliminary results show that a value of one tritium atom produced for $(7.30\pm1.04)x10^4$ thermal neutron fissions of ^{235}U and (10.74 ± 2.70) x 10^4 fast neutron fissions of ^{232}Th. These values are within an order of results reported by IAEA [Ref.3].

UKM also make some collaborative works with Julich Research Center (KFA), Germany. Two of UKM's researcher have been involved in nuclear data research. Determination of the excitation function of the reactions $^9Be(n,xt)$, $^{10}B(n,t)2\alpha$ and $^{14}N(n,t)^{12}C$ has been completed [Ref.4-7]. Calculated excitation function of the (n, xt) process for ^9Be by using the LSQ code, and the experimental data measured by using monoenergetic neutrons up to 20 MeV is shown in Fig.1. The $^{10}B(n,t)2\alpha$ cross sections for the neutron energy range of 0.025 eV to 10.6 MeV lie between 12 and 215 mbarn with the maximum cross section occurs at about 5.5 MeV (see Fig.2). The $^{14}N(n,t)\ ^{12}C$ cross sections for the neutron energy range of 5.0 to 10.6 MeV lie between 11 and 30 mbarn (see Fig.3). The excitation function shows a fluctuation which is attributed to the decay properties of the compound nucleus ^{15}N. Detailed Hauser-Feshbach calculations using HELGA code [Ref.8] show that the statistical model cannot satisfactorily described the (n,t) cross section of light nuclei. Literature review also reveals that it is necessary to develop newer calculational methods to estimate for the total tritium emission rate.

Other Measurements

At KFA, measurement of excitation functions and isomer ratios of fast neutron induced reactions on Zn, Ga and Ge is still in progress under the supervision of Dr. S.M. Qaim. Measurements of gamma-ray linear attenuation coefficient has been carried out by UKM, Universiti Sains Malaysia and Universiti Pertanian Malaysia. At UKM, μ-values were measured for cooking oil, petroleum products, building materials, natural rubber and tropical woods, by using 59.54 keV photon of ^{241}Am and an intrinsic Ge detector [Ref.9]. We have also performed calculation to determine the μ-values based on Hubbel method [Ref.10]. The other groups measured μ-values on tropical wood [Ref.11] and natural rubber [Ref.12]. The data are useful for on-line density determination, hence provide quality control of the products.

Neutronic Analyses

At MINT, the 1-D diffusion code TRIGAM, a modified version the the TRIGAC code [Ref.13], is used for routine neutronic analyses of MINT TRIGA Reactor. However, for detailed analyses, the 2-D EXTERMINATOR code [Ref. 14] is used instead. Both codes use the nuclear data prepared by WIMS-D4 [Ref.15]. Usually, the 69-group neutron data in WIMS-D4 are collapsed into two energy groups for TRIGAM and EXTERMINATOR calculations. TRIGAM has been used to calculate the k_{eff} of the first critical core of MINT Reactor and that of the nine subsequent operational cores. The TRIGAM core excess values are within ±0.5% of the measured results thus justifying the use of TRIGAM for neutronic analyses of MINT Reactor.

As part of the activities in the MINT Reactor power upgrading program (initiated in 1991 and is expected to complete in 1997), TRIGAM was used to obtain a tentative loading pattern for a 2 MW core. To improve upon the tentative core, TRIGAM was used to study the favourable core locations for the 12 w/o (weight percent) and 20 w/o (LEU) fuel elements, the reactivity requirements of the core, the effects of the water gap, air follower, and control rod on power distribution. Based on these analyses, the tentative 2 MW core was modified and was analysed by using the EXTERMINATOR code. As a result of the refinements, a 2 MW core which satisfies the power peaking requirement was obtained. The results of these analyses have been reported by Gui et al. [Ref.16].

Radiation Shielding

Parallel to the neutronic analyses of MINT Reactor core, shielding analyses are needed to determine the sufficiency of the present reactor shield when the maximum reactor power is increased from 1 MW(t) to 2 MW(t). The shielding analyses will be carried out by using ANISN [Ref.17], a 1-D discrete ordinates code.

Although the present fuel racks in the reactor tank are enough to hold the spent fuel elements, it is envisaged that a fuel storage pool will be required to store spent fuel elements and to be used as an interim storage for fuel elements if for some reasons, all the fuel elements are to be removed from the reactor core. A fuel element transfer cask is also needed to transfer fuel elements between the reactor tank and the fuel element storage pool.

ANISN will also be used to perform criticality calculations in the design of the proposed fuel storage pool. Photon shielding calculations for the fuel transfer cask will be carried out using the MERCURE-4 Monte Carlo point kernel integration code [Ref.18]. The source term for the fuel element will be calculated using ORIGEN2 code [Ref.19]. Currently, some preliminary calculations for the fuel transfer cask using ORIGEN2 and MERCURE-4 have been performed.

Response functions for neutrons and the associated secondary photons for neutron skyshine analyses have been generated using the MCNP code [Ref.20] by a MINT staff for his dissertation [Ref.21]. These response functions are generated for use with the integral line-beam and the integral conical-beam methods. For the integral conical-beam method, the effect of the ground on the skyshine dose is corrected using the ground correction factors (GCF) generated using MCNP. All the response functions and the GCFs are generated using the ENDF/B-V nuclear data and are approximated by simple empirical formulas to facilitate their use. Fig. 4 compares the results obtained using the integral conical-beam method with those of Alsmiller et al. [Ref.22] for the air-over-ground skyshine problem. In future the MCNP code will be used to perform criticality calculations for the fuel storage pool, shielding calculations to evaluate the reactor shield, and neutron flux density distribution calculations to determine the neutron flux densities in the experimental facilities.

Spectrum Unfolding Studies

In a collaborative work between UKM and MINT, the neutron spectrum in the MINT Reactor experimental facilities have been measured using several activation foils such as Au (bare and cadmium-covered), Fe, Ni, In, Ti and Al. The activities of the foils were unfolded using the SAND II code [Ref.23] to give the neutron spectrum [Ref.24].

In the work to determine the excitation function of the ^{9}Be(n,xt) process mentioned earlier, we performed unfolding studies in two steps: the required set of neutron spectra were obtained first; following which the (n,xt) excitation function for ^{9}Be was determined. For the former, we used a modified version of the SAND-II iterative code [Ref.25] which permitts input of individual errors of the flux monitor excitation functions for each energy channel and each measured activity. A total of 29 energy channels with ΔE = 1 MeV were used. To unfold the (n, xt) excitation function, we used the SAND-II code as well as a generalized least-squares method (LSQ) [Ref.26].

Conclusions

Although no official nuclear data center exists in Malaysia yet however there is a small group of researcher doing significant amount of measurements and calculations in nuclear data related activities. We have also managed to gather several nuclear reaction model codes such as GNASH, DWUCK-5 and ECIS-88 from IAEA. In a meeting between the Dean of Physical and Applied Sciences of UKM and the Deputy Director General of MINT on 28 Oct., 1995, I was asked to prepare a working paper on setting up a Malaysian Nuclear Data Center. I hope with the assistance of JAERI and IAEA we can make the Malaysian Nuclear Data Center a reality.

References

[1] Suhaimi, A.: "Studies of (n,t) reactions on light nuclei", Jul-2196, ISSN 0366-8885 KFA Julich GmbH.

[2] Swinhoe, M.T. and Utley, C.A., Nucl. Sci. Eng. 89, 261-272 (1985).

[3] Drapchinkij, L.V., Khlebnikov, S.V. and Kovalenko, S.S.: " Neutron physics and nuclear data measurements with accelerators and research reactors", IAEA-TECDOC-469, 40-48 (1988).

[4] Wölfe, R., Suhaimi, A, and Qaim, S.M., Nucl. Sci. Eng. 115, 71-75 (1993).

[5] Suhaimi, A., Wölfle, R., Qaim, S.M. and Stöcklin, G., Radiochimica Acta 40, 113 (1986).

[6] Qaim, S.M., Suhaimi, A., Wölfle, R. And Stöcklin, G.: "Measurement of (n,t) cross sections an light nuclei", Proc. Int. Conf. On Nuclear Data for Sci. and Tech., May 30 - Jun 3, 1988, Mito, Japan, p.225-228.

[7] Suhaimi, A., Wölfle, R., Qaim, S.M., Warwick, P. and Stöcklin, G., Radiochimica Acta 43, 133-138 (1988).

[8] Klapdor, H.V., Reiss, H. And Rosner, G., Nucl. Phys. A262, 157(1976).

[9] Suhaimi, A., "Photon attenuation studies on various commercial products", submitted to Jur. Sains.

[10] Hubell, J.H., Int. J. Appl. Radiot. Isotopes 33(12) 1269-1290 (1982).

[11] Bradley, D.A, Tajuddin, A. A., Che Wan Ahmad, C.W.S. and Bauk, S., Int. J. Appl. Radiat. Isotopes 42(8), 771-773(1991).

[12] Sion, E., Sulaiman, Z.A. and Sulaiman, M.Y.; "Rubber characterization using gamma-ray attenuation technic", Proc. Conf. On Science and Nucl. Technology ,UKM (1990), p. 196-203.

[13] Mele, I. And Ravnik, M. *TRIGAC-A New Version of TRIGAP Code*, Institute Josef Stefan, Ijubjana, Yugoslavia (1992).

[14] Fowler, T.B., Tobias, M.L. and Vondy, D.R. *EXTERMINATOR-2: A FORTRAN IV Code for Solving Multigroup Neutron Diffusion Equations in Two Dimensions*, Report ORNL-4078. Oak Ridge National Laboratory, Tenn. (1967)

[15] Marshall, M.J., LWR-WIMS, *A Computer Code for Light Water Reactor Lattice Calculations*, Report AAEW-R 1498, United Kingdom Atomic Energy Authority, 1982.

[16] Gui, A.A., Ibrahim, J.K., Kassim, M.S., Idris, F.M., Akhir, K.M. and Ravnik, M. "Neutronic Analysis of MINT TRIGA Reactor Core", Submitted to *5th Asian Symposium on Research Reactors*, Taejon, Korea, 1996

[17] Engle Jr., W.W. *A User Manual for ANISN, a One dimensional Discrete Ordinates Transport Code with Anisotropic Scattering*, Union Carbide Corp., Nuclear Division, K-25 Report K-1693, 1967.

[18] Dupont, C., Nimal, J.C. *MERCURE-4: A 3-DIM. Monte Carlo Programme for Point Kernel Integration*, Report SERUA/T/No.436, Centre D"ETUDES NUCLEAIRES DE SACALAY, 1980.

[19] Croff, A.G., *A User's Manual for the ORIGEN2 Computer code,* ORNL/TM-7175, Oak Ridge National Laboratory, TN, 1980.

[20] Briesmeister, J.F., (ed.), *MCNP: A General Monte Carlo Code for Neutron and Photon Transport, Version 3A,* Report LA-7396-M, Rev. 2, Los Alamos National Laboratory, Los Alamos, NM, 1991.

[21] Gui, A.A., *Response Functions for Neutron Skyshine Analyses,* PHD Dissertation, Kansas State University, Manhattan, KS 66506, 1994.

[22] Alsmiller, R.G., Jr., Barish, J., and Childs, " Skyshine at Neutron Energies ≤ 400 MeV", *Particle Accelerators,* 11, 131-141 (1981).

[23] McElroy, W.N., Berg, S., Crockett, T., Hawkins, R.G. *A Computer Automated Iterative Method for Neutron Flux Spectra Determination by Foil Activation,* Report AFWL-TR 67-91, 1967.

[24] Nesaraja, C.D. and Suhaimi, A. "Determination of the Fast Neutron Spectrum At the TRIGA Reactor Using Threshold Foil Method", *J.Sains Nuklear Malaysia, vol.11, No.2,* 1993.

[25] Oster, C.A., McElroy, W.N. and Marr, J.M. : "A Monte Carlo programme for SAND-II error analysis", HEDL-TIME 73-20, Hanford Engineering Development Laboratory (1973).

[26] Perey, F.G., "Least squares dosimetry unfolding: The Programme STAY'SL", ORNL/TM-6062, Oak Ridge National Laboratory (1977).

2.4.2

CURRENT STATUS OF RUSSIAN EVALUATED NEUTRON DATA LIBRARIES

A.I.Blokhin, A.V.Ignatyuk, V.N.Manokhin, M.N.Nikolaev
Institute of Physics and Power Engineering
249020 Obninsk, Kaluga Region, Russia

ABSTRACT

The status of Russian Evaluated Data Libraries is discussed. The last modifications of the BROND-2 files and their relations to the additional files of the FOND library and the ABBN-90 group constants are considered. The main characteristics of new libraries for the photoneutron data, dosimetry and activation reaction cross sections and transmutation cross sections for intermediate energies are described briefly.

1. Introduction.

The problems of nuclear industry development in combination with economical questions and environmental aspects of nuclear wastes require a permanent improvement of nuclear data used in all projects of advanced nuclear technologies. In this report we want discuss main directions of modifications of Russian Nuclear Data Libraries recommended for practical applications.

2. BROND-2 - General purpose library.

In the elaboration process of the second version of the recommended general purpose files (the BROND-2 library) we tried to take into account all advanced nuclear reactor requirements for neutron data. The selection of evaluated data for the BROND-2 library, their analysis and handling were completed in 1990. The evaluated data for principal reactor materials developed by former soviet specialists have been included into the library. In the case of the materials used as neutron standards, the data recommended by the IAEA were accepted. As to the construction materials we paid much attention to the files of the natural mixture of isotopes. The files for separated isotopes were constructed as it seems to be necessary. The evaluations included in BROND-2 are briefly described in Refs.[1,2]. All files were checked by the ENDF utility codes and BROND-2.2 version with some technical errors corrected was distributed at the end of 1992. In the following years some improvements of the BROND files recommended for the FENDL-1 library [3] were performed. New files for zinc and Pa-231, 233 isotopes were made and some corrections in the evaluated cross sections for the americium isotopes were included. The list of modern BROND-2.2 files is given in Table 1.

3. ABBN-90 - the nuclear group constant library.

It should be noted that the full amount of the general purpose files used in practical applications exceeds the one included in Tab. 1. The additional files selected as a rule from ENDF/B-6 and JENDL-3 libraries are included in the FOND library. The list of such files is given in Table 2. These files were used in the working out ABBN-90 Russian group

constant set [4]. It is necessary to note that for some isotopes marked by asterisks in Tab. 2 foreign files were preferred to the BROND ones during the ABBN-90 constants preparation. It referred to the cases when the corresponding evaluations were performed much later and were based on updated experimental data (for example, oxygen and copper) or when the group constants have been calculated before the final processing of the BROND-2 files. In many cases the files included in the FOND were a little modified to improve the evaluated data important for nuclear reactor designs.To transform the files into the group constants the GRUCON code [5] was used as a rule. For the last years the NJOY code has been applied intensively for such tasks too. The errors found during this processing have been corrected.

Now the ABBN-90 group constants are verified for the large number of critical assemblies and other integral experiments with different neutron spectra starting with hard spectra like the GODIVA assembly and finishing with thermalized spectra of critical plutonium and uranium aqueous solutions. No essential discrepancies which require group constant corrections for the main reactor materials were found.

4. Special purpose files.

4.1. RDF-94 -the Russian Dosimetry File.

The Russian Dosimetry File (RDF-94) was formed last year. It contains 46 reactions, 36 of them are the new evaluations performed in the Nuclear Data Center (CJD). The list of reactions recommended both for the neutron spectra dosimetry and neutron measurement standards is given in Table 3. The uncertainties for all reactions have been included and the covariance matrices have been prepared for the most of them. This file is being checked and tested nowadays.

4.2 BOFOD - the evaluated photonuclear data library.

Since 1990 the evaluated photoneutron data library (BOFOD) has been under development. Corresponding data include the single and double neutron emission cross sections, spectra of emitted neutrons and the photo-fission cross sections for transuranium isotopes [7].The list of isotopes considered is given in Table 4. During 1993 the photoneutron cross section evaluations were also performed for the following fission products: Sr-90, Zr-93, Zr-96, Nb-94, Tc-99, Sn-121, Sn-126, Pd-107, Ag-108, Cs-135, Cs-137, I-129, Ho-166, Sm-147, Sm-148, Sm-151, Tb-158. The files of these isotopes in the ENDF-6 format are under preparation now.

4.3 ADL - the Activation Data Library

The new version of the Activation Data Library (ADL-3) has been prepared recently [8]. It contains the evaluated cross sections for more than 20000 reactions on stable and radioactive nuclei including the nuclei in isomeric states. The cross sections for the threshold reactions were calculated on the basis of the optical-statistical approach taking into account the angular momentum conservation law as well as direct and preequilibrium processes contribution. The fitting of calculated excitation functions to experimental data or some cross section systematics for 14-MeV neutrons were used for the reactions where the corresponding data were available. Nowadays this library is tested intensively on the fusion neutron benchmarks.

4.4 ASIYAD - the fission product yield library.

The ASIYAD fission product yield library includes the independent fission product yield data for nuclei:

U-232 - 239, Np-236 - 239, Pu-236, 239 - 243, Am-241 - 243, Cm-245.

This library was realized since 1992.

4.5 MENDL -the library of the evaluated transmutation cross sections

The MENDL library of the evaluated transmutation cross sections for neutrons and protons with energies up to 100 MeV is under formation now [9]. The first version of MENDL is realized since 1994. It contains the cross sections of the most important neutron and proton induced reactions for more than 500 stable and long-lived radioactive isotopes which could be important for different nuclear waste transmutation projects. Most of the data have been obtained on the basis of the geometry dependent hybrid model taking into account the preequilibrium processes.

5. Conclusion.

A free access to modern versions of the libraries prepared in different laboratories creates favorable opportunities for international cooperation on testing and analysis of the data recommended for various practical applications. The evaluated neutron data for principal reactor materials used in different countries have only minor discrepancies. So the task to select the best versions from the evaluations available is more important now than to prepare the new ones. Of course the search for cases where we can not come to an agreement of evaluations remains an important problem. New challenges for data intercomparision arise for the new nuclear technologies: fusion reactors, transmutation of nuclear wastes, various medical applications and so on. A search for new experiments and benchmarks for corresponding data tests is a necessary condition of successful development of these technologies.

REFERENCES:

[1] A.I.Blokhin, A.V.Ignatyuk, B.D.Kuzminov et al., "Library of Evaluated Neutron Data Files,"*Nuclear Data for Science and Technology,* Ed. S.M.Qaim, Springer-Verlag, 1992, p.800.

[2]. A.I.Blokhin, B.I.Fursov, A.V.Ignatyuk et al." CURRENT STATUS OF RUSSIAN EVALUATED NEUTRON DATA LIBRARIES" Proceedings of the International conference "Nuclear data for Science and Technology",Editor J.K.Dickens, 1994, v.2, p.695.

See also: "BROND-2. Library of Recommended Evaluated Neutron Data," *VANT, Ser. Nucl. Const.*, 1991, N 2-3.

[3] "Summary Report of Consultants Meeting on FENDL," Ed. A.Pashchenko, D.Muir, Vienna, 1990, INDC(NDS)-241.

[4] M.N.Nikolaev, A.M.Tsibulya et al., "New Nuclear Constants ABBN-90 and its Tests on Basis of Macroscopic Experiments," *Proc. Conf. on Nuclear Data for Science and Technology,* Julich, 1991.

[5] V.V.Sinitsa , A.A.Rineisky, "GRUCON - Package of Applied Computer Programs," IAEA, Vienna, 1993, INDC(NDC)-344.

[6] G.N.Manturov, M.N.Nikolaev, N.Yu.Semenov, A.M.Tsibulia, "Testing of BROND-2, JENDL-3 and ENDF/B-VI Neutron Data through Integral and Reactor Experiments," Proceedings of the International conference "Nuclear data for Science and Technology",Editor J.K.Dickens, 1994, v.2, p.803.
[7] A.I.Blokhin, N.N.Buleeva, S.M.Nasyrova et al., "The formation of the BOFOD evaluated photoneutron data library." *VANT, Ser. Nucl. Const.*,1992, **3-4,** p.3-54; A.I.Blokhin, S.M.Nasyrova, "Plots of Experimental and Evaluated Photoneutron Cross Sections," IAEA, Vienna, 1991, INDC(CCP)-337.
[8] O.T.Grudzevich, A.V.Zelenetsky, A.V.Ignatyuk , A.B.Pashchenko, "Catalog of the ADL-3 Library," *VANT, Ser. Nucl. Const*, 1993, **3-4.**
[9] A.Yu.Konobeev, Yu.A.Korovin, V.P.Lunev, V.S.Mas-terov, Yu.N.Shubin, "Cross Section Library for Study of Transmutation of Materials Irradiated by Neutrons and Protons with Energy up to 100 MeV," *VANT, Ser. Nucl. Const.*, 1992, **3-4**,p.55.

Table 3. **The list of reactions included in the RDF-94.**

7-Li(n,t)*	52-Cr(n,2n)	93-Nb(n,n')m
10-B(n,α)	55-Mn(n,2n)	93-Nb(n,2n)m
19-F(n,2n)	55-Mn(n,γ)	115-In(n,2n)
23-Na(n,γ)	54-Fe(n,2n)	127-I(n,2n)
24-Mg(n,p)	54-Fe(n,p)	139-La(n,γ)
27-Al(n,p)	56-Fe(n,p)	141-Pr(n,2n)
27-Al(n,α)	59-Co(n,2n)	181-Ta(n,γ)
45-Sc(n,2n)	58-Ni(n,2n)	197-Au(n,2n)
45-Sc(n,2n)m	58-Ni(n,p)	197-Au(n,γ)*
45-Sc(n,2n)g	60-Ni(n,p)	232-Th(n,γ)*
46-Ti(n,p)	63-Cu(n,2n)	232-Th(n,f)*
46-Ti(n,2n)	63-Cu(n,γ)	235-U(n,f)*
47-Ti(n,x)	65-Cu(n,2n)	238-U(n,γ)*
48-Ti(n,x)	89-Y(n,2n)	238-U(n,f)*
48-Ti(n,p)	90-Zr(n,2n)	237-Np(n,f)*
51-V(n,α)		

* The reactions taken from IRDF-90

Table 4. **The list of isotopes included in the BOFOD-90**

Bc-9	Sr-88	Pb-000	Am-241,243
Na-23	Zr-000,90,91,92,94,96	Bi-209	
Cr-50,52,54	Mo-92,94,96,98,100	Th-232	
Mn-55	Sn-114,116,117,118,119,120,122,124	U-233,234,235,236,238	
Fe-54,56,58	Te-120,122,124,126,128,130	Np-237	
Ni-000,56,58,60,62,64	W-182,184,186	Pu-239,241	

Table 1. **The list of the original files in the BROND-2.**

Isotopes	Eval./rev.	Authors
H-2,3	1988	Nikolaev M.N.
He-3,4	1988	Nikolaev M.N.
He-4	1976	Nikolaev M.N. et al.
Li-6	1989	Nikolaev M.N.
Li-7	1984	Bondarenko I.M.
N-14,15	1988/93	Blokhin A.I. et al.
O-16	1977	Nikolaev M.N. et al.
F-19	1990	Blokhin A.I. et al.
Na-23	1978	Nikolaev M.N. et al.
Si-000	1985/93	Hermsdorf D., Blokhin A.I. et al.
P-31	1989	Koscheev V.N.
Cl-000	1990	Nikolaev M.N. et al.
Cr-000	1984/88	Pronyaev V.G. et al.
Cr-50,52,53,54	1987	Blokhin A.I. et al.
Fe-000	1985/94	Pronyaev V.G. et al.
Fe-54,56,57,58	1985	Pronyaev V.G. et al.
Ni-000	1984	Blokhin A.I., Ignatyuk A.V. et al.
Ni-58,60,61, 62,64	1985	Blokhin A.I., Ignatyuk A.V. et al.
Cu-000	1981	Nikolaev M.N. et al.
Zn-000	1989	Nikolaev M.N., Zabrodskaya S.V.
Sr-90	1990	Grudzevich O.T., Zelenetsky A.V.
Zr-000	1988	Grudzevich O.T., Zelenetsky A.V.
Zr-90,91, 92,94,96	1988/93	Grudzevich O.T. et al./Blokhin A.I.
Zr-93,95	1989	Grudzevich O.T., Zelenetsky A.V.
Nb-93	1988/93	V.G.Pronyaev et al.
Nb-95	1990	Grudzevich O.T., Zelenetsky A.V.
Tc-99	1984	Ignatyuk A.V., Kravchenko I.V.
Ru-101,102, 104,106	1984	Ignatyuk A.V., Kravchenko I.V.
Rh-103	1985	Ignatyuk A.V., Kravchenko I.V.
Pd-105,107	1985	Ignatyuk A.V., Kravchenko I.V.
Pd-106,108	1987	Belanova T.S., Ignatyuk A.V.
Ag-109	1985	Ignatyuk A.V., Kravchenko I.V.
Sn-000	1990/93	V.G.Pronyaev et al.
I-129	1985	Ignatyuk A.V., Kravchenko I.V.
Xe-131	1985	Ignatyuk A.V., Kravchenko I.V.
Cs-133,135	1985/91	Ignatyuk A.V., Kravchenko I.V.
Ce-140,142,144	1990	Ignatyuk A.V., Ulaeva M.V.
Nd-143,145	1985	Ignatyuk A.V., Kravchenko I.V.
Pm-147	1985	Ignatyuk A.V., Kravchenko I.V.
Sm-000,144,154	1989	Belanova T.S. et al.
Sm-147,149,151	1985	Ignatyuk A.V., Kravchenko I.V.
Sm-148,150,152	1987	Zakharova S.M., Ignatyuk A.V.
Eu-153	1985	Ignatyuk A.V., Kravchenko I.V.
Gd-000,152,154, 155,156,157,158,160	1989	Blokhin A.I.
Er-162,164,166, 167,168, 170	1976	Zakharova S.M. et al
Ta-181	1988	Manturov G.N., Korchagina G.A.
W-182,183,184, 186	1983	Abagyan L.P., Manturov G.N.
Re-000	1988	Nikolaev M.N. et al.
Os-000	1990	Nikolaev M.N.
Ir-000	1990	Nikolaev M.N., Zabrodskaya S.V.
Pb-000	1984/94	Hermsdorf D., Blokhin A.I.
Pb-204,206, 207,208	1990/93	Blokhin A.I. et al.
Bi-209	1990/93	Blokhin A.I. et al.
Th-232	1983	Nikolaev M.N. et al.
Pa-231,233	1994	Blokhin A.I. et al.
U-233	1990	Sukhovitsky E., Klepatsky A.
U-235,236	1986	Konshin V.A. et al.
U-238	1980	Nikolaev M.N. et al.
Pu-238	1987	Sukhovitsky E., Klepatsky A.
Pu-239,240, 241,242	1980	Konshin V.A. et al.
Am-241,242, 242m,243	1990/94	Blokhin A.I., Maslov V.M.
Cm-242,244	1987	Sukhovitsky E., Klepatsky A.

Table 2. **Additional files included in the FOND**

Elem	Eval/Rev	Origin	Comments
*H	1989/93	ENDF/B-6	Capture data were modified.
Be	1983/93	-"-	Thermal capture was corrected.
B	1989	-"-	B-10,11 files were used.
*N	1983/90	-"-	N-14,15 files were used.
*O	1990	-"-	
*F	1990	-"-	
Mg	1987	JENDL-3	
Al	1988	JENDL-3	
*Si	1989	JENDL-3	
*S	1979/93	ENDF/B-6	INT law for MT=103 was corrected.
*Cl	1979/93	ENDF/B-6	INT law for MT=103-107 was corrected.
Ar	1979	JEF-1	
K	1987	JENDL-3	
Ca	1987/93	JENDL-3	Γ_{compet} were added for res.
Sc	1988	JENDL-3	
Ti	1988/93	JENDL-3	Threshold for 1-st inelastic level was corrected.
V	1982	ENDL-83	
Mn	1988	ENDF/B-6	
Co	1989	ENDF/B-6	
*Ni	1989/93	ENDF/B-6	Ni-58,60,61,62,64 files were used and missed p-res. were added.
*Cu	1987	JENDL-3	
Ga	1982	ENDL-83	
Ge	1974	ENDF/B-6	Ge-70,73,74,76 files were used, res. param. for Ge-70 were modifyed.
As	1982	ENDL-83	
Se	1974/93	ENDF/B-6	Data in resonance and fast regions were revised.
Br	1974/92	ENDF/B-6	Br-79 and Br-81 files were used and (n,2n) reactions were added.
Br	1974/84	ENDF/B-6	Kr-78,80,82,83,84,86 files were used.
Rb	1984	JEF-1	Rb-85,87 files were used.
Sr	1984/92	ENDF/B-6	Sr-84,86,87,88 were used, (n,2n) reactions were added.
*Zr	1977	JENDL-3	
Mo	1989	JENDL-3	Mo-nat,95,97,98,100 files were used.
Ru	1990	ENDF/B-6	Ru-96,98,99,100 files were used, others - from BROND-2.
Pd	1980/91	ENDF/B-6	Pd-102,104 files were used, others - from BROND-2.
Ag	1977	JENDL-3	Ag-107 was used, Ag-109 - from BROND-2.
Cd	1975/91	ENDF/B-6	Cd-nat and Cd-113 files were used. Energy spectra (n,2n) reaction were corrected.
In	1974/79	ENDF/B-6	In-113,115 files were used.
Sb	1974/79	ENDF/B-6	Sb-121,123,125 files were used.
Te	1974/80	ENDF/B-6	Te-120,122,123,124,125,126, 128,130 files were used.
I	1980	ENDF/B-6	
Xe	1978	ENDF/B-6	Xe-124,126,128,129,130, 132,134,136 files were used.
Cs	1974/78	ENDF/B-6	Cs-134,137 files were used.
Ba	1978	ENDF/B-6	Ba-134,135,136,137,138 files were used. Ba-130,132 were considered as Ba-134.
La	1977	JENDL-3	
Pr	1984/91	ENDF/B-6	
Nd	1974/80	ENDF/B-6	Nd-142,144,146,148,150 files were used. Nd-143,145 - from BROND-2.
Eu	1986	ENDF/B-6	Eu-151 was used, Eu-153 - from BROND-2.
Tb	1980	ENDF/B-6	
Dy	1974/80	ENDF/B-6	Dy-160,161,162,163,164 files were used with res. param. modifyed. Dy-156,158 consider as Dy-160.
Ho	1974/80	ENDF/B-6	
Lu	1967/80	ENDF/B-6	Lu-175 and Lu-176 files were used.
Hf	1989	JENDL-3	Hf-nat,174,176,177,178,179 and Hf-180 files were used.
*Ta	1989	JENDL-3	
Pt	1982/91	ENDL-83	Some errors were found and removed.
*Pb	1989	JENDL-3	Selection is based on integral experiments.
Th	1981	JENDL-3	Th-228,229 files were used.
	1982/93	ENDF/B-6	Th-230 was used. Thermal cross sections were corrected.
*Pa	1977/78	ENDF/B-6	Pa-231,233 were files used.
*U	1978/89	ENDF/B-6	U-232,234,235 files were used.
Np	1978/90	ENDF/B-5	Np-237 was used and (n,2n) cross sections were modified.
	1989	JENDL-3	Np-239 file was used.
*Pu	1987/93	JENDL-3	Pu-239 was used; LIPAR-5 library was used below 100 ev.
Pu	1976/78	ENDF/B-6	Pu-243 and Pu-244 files were used.
Cm	1976/78	ENDF/B-6	Cm-243,245,246,247,248 files were used.
	1987	JENDL-3	Cm-249,250 files were used.
Bk	1986	ENDF/B-6	Bk-249 file was used.
Cf	1975/86	ENDF/B-6	Cf-249,250,251,252,253 files were used.
Es	1975	ENDF/B-6	Es-253 file was used.

2.4.3 NUCLEAR DATA ACTIVITIES IN VIETNAM

Vuong Huu TAN
Nuclear Data Sector
Nuclear Research Institute
13 Dinh Tien Hoang, Dalat, Vietnam

This paper briefly describes nuclear data activities in Vietnam. They consist of nuclear data measurements with 14-MeV-neutrons, gamma radiation and filtered reactor keV-neutrons using the 120 kV DT-neutron generator, Microtron and the Dalat nuclear reactor. Besides, related theoretical calculations are also included in this presentation. The information presented is based mainly on the results of research Contracts of National Research Programs on Nuclear Science and Technology (50A, KC-09), Fundamental Sciences (KT-04) and the IAEA research Contract No.3515/RB.

1. Introduction

Nuclear energy will play a significant role in the growing economy and energy demands of developing countries. It is essential for any country which has any reactor program to maintain a nuclear data group who can provide reliable data for input to their reactor group, even when the reactors are commercially supplied with fixed period guarantees or are copies of well tested working model put up with technical collaboration. With this policy, Vietnam National Atomic Energy Commission (VINATOM) and The Vietnam National Center for Natural Sciences and Technology (VNCNST) have supported nuclear data activities in Vietnam in the framework of the National Research Contracts. As to majority of developing countries, in Vietnam due to the lack of experimental facilities and limited availability of funds many physicists were generally more attracted to work in the areas of theoretical research, so we have had some active groups in basic theoretical research in nuclear physics, particle physics, high energy physics,.... This is a good potential for development of nuclear data activities, especially in the field of nuclear theory and corresponding calculation codes. Nuclear data activities which will be presented in this paper consist of nuclear data measurements with 14-MeV neutrons, gamma radiation and filtered reactor keV-neutrons using the 120 kV DT-neutron generator, Microtron and the Dalat nuclear reactor. Besides, related nuclear reaction theoretical calculations are also included in this presentation. The basic theoretical research in nuclear physics, particle physics, high energy physics and reactor physics will not be included in this presentation.

2. Nuclear data measurements on the 120 kV DT-neutron generator and Microtron

2.1. A Study of the isomeric ratio for the (n,2n) and (γ,n) reactions/1/:

Measurements are made of the isomeric ratio for the (n,2n) and (γ,n) reactions on the neutron-deficient nuclei ^{92}Mo, ^{90}Zr, ^{86}Sr and ^{74}Se. The neutron source used in the experiments was the 120 kV DT-neutron generator with an output of 10^{10} n/s. The energy of neutrons incident to the target (E_n) was (14.5+-0.2) MeV. The experiment on the (γ,n) reaction was performed on a Microtron with a maximum bremsstrahlung energy (E_γ) of 14.5 MeV. Targets of Mo, Zr and SrO had a natural isotope composition, whereas for the ^{74}Se reaction an enriched target was used with 41% ^{74}Se. The isomeric ratio measured by the activation method were given in Table 1 and 2. A method was developed for calculating the isomeric ratio for a low excitation energy of the residual nucleus.

2.2. Activation cross sections with 14 MeV neutrons/2,3,4,5/:

In the framework of a Coordinated Research Programme "Measurement and analysis of 14 MeV neutron nuclear data needed for fission and fusion reactor technology" supported by the International Atomic Energy Agency measurements of 14 MeV neutron activation cross sections for important reactor structural materials were carried out at the Istitute of Physics (VNCNST) using up-to-date measuring system and data processing techniques. Irradiation was performed using a 120 kV DT-neutron generator. The 14 MeV neutron yield is 10^{10} n/s. The neutron energy calculated for the irradiation geometry was 14.8+-0.2 MeV. Neutron flux was monitored by a glass scintillation detector connected to the ND-66B multichannel analyzer working in multiscaling mode. The count numbers in each channel were used to correct the time variation of neutron flux.

A 62 cm^3 coaxial high purity Ge detector (ORTEC) with resolution 2.1 keV at the 1332 keV line of ^{60}Co was used to measure activities of irradiated samples. In order to decrease uncertainties each sample was measured with different cooling times (except the case of very short half-lives such as ^{53}V, ^{54}V, ^{46m}Sc and ^{50}Sc). For each nuclide having multiple lines the weighted mean activity of all identified photopeaks with relative intensities greater than 20% was used to obtain the corresponding cross section. Tables 3, 4 and 5 give the cross section values obtained in comparison with data of other authors in the range 14.6-14.8 MeV.

2.3. The exciton model calculations of the (n,p) cross section/6/:

Preequilibrium emission of protons and isotopic effect in the fast neutron-induced (n,p) reactions on heavy elements have been studied. The (n,p) cross sections, contributions of both evaporation and preequilibrium exciton mechanisms and the emitted proton spectra have been calculated for series of Sm, Dy and Er isotopes. By fitting the experimental data the exciton model free parameter K characterizing the transition rate between exciton states has been determined for each isotope chain (see Fig.1), they are in good agreement with the "overall best-fit" value K=700 MeV^3. It has been found that more than 85% of the preequilibrium protons are emitted from the exciton state n=3. On the basic of this result a rather simple formula has been found and can be used for the evaluation of the (n,p) cross section on heavy nuclei.

3. Nuclear data measurements at the Dalat reactor

3.1. Filter neutron beams:

Since the pioneer work of Sympson and his co-workers /7/, neutron transmission filters have been successfully used to produced quasi-monoenergetic neutrons for nuclear physics experiments. At the Dalat reactor single crystal silicon (980 mm long), aluminum (1023 mm long), iron (200 mm long) and sulfur (45 g/cm^2) filters with possibility for insertion of additional filters like ^{10}B, Ti have recently been installed to produce neutrons of 24 keV, 25 keV, 55 keV, 75 keV, 144 keV as well as thermal neutrons /8/. Characteristics of filtered neutron beams are given in Table 6. In the near future other types of filters using Sc, U, Pb and polyethylene permitting transmission of 2 keV, 186 eV, 1.2 MeV and 2 MeV neutrons will expectly be installed.

3.2. Total neutron cross sections:

Total neutron cross sections of ^{238}U and some reactor structural materials in the keV energy region have been measured using filtered neutron beams. Figure 2 shows our experimental data for ^{238}U on the filtered neutron beams of 55 keV (σ_t=13.38+-0.07 b) and 144 keV (σ_t=11.45+-0.10 b) /9,10/ obtained by fitting using Monte-Carlo IBM program/11/ with the account of both Porter-Thomas and Wigner distributions and Dopler-broading together with data of other authors taken from /12/.

3.3. Average neutron radiative capture cross sections:

The average neutron radiative capture cross sections of ^{238}U and ^{98}Mo on the filtered neutron beams have been measured by activation method. ^{197}Au was used as standards. Figure 3 shows our experimental data/13/ for ^{238}U on the 55 keV ($\sigma_{n\gamma}$=292.3+-8.5 mb) and 144 keV neutrons ($\sigma_{n\gamma}$=152.5+-4.6 mb) together with data of other authors taken from /14/. In the frame of experimental errors our data are in good agreement with the results of the work/15/, but the accuracy of our data is better (approximately 3%). A modification of the statistical approach to the neutron capture problem /22/ and the code for analyze of average neutron radiative capture cross sections /23/ allowing estimate the average radiative width and neutron strength functions from experimental data of $\sigma_{n\gamma}$ were developed.

3.4. Gamma spectra from neutron capture for reactor materials:

Capture gamma ray spectra for materials like Si, Ti, C, Al, Fe, Cr on the filtered keV-neutron beams have been measured using the Compton-suppressed and pair spectrometer /16/ that consists of HPGe-90 cc detector and 3 NaI(Tl)-scintillators. The obtained results /17/ show that the intensities and energies of the keV neutron capture gamma rays change substantially as neutron energy increases.

3.5. The energy dependence of isomeric ratio/18,19/:

The isomeric ratio of some isotopes formed in nuclear reactions with filtered neutron beams have been studied. Figure 4 shows the decay of the 828 keV gamma line of ^{82g,m}Br after irradiation of NH_4Br-sample on the filtered 144 keV neutron beam together with calculation curves for different values of ratio σ^m/σ^g. On the basic of this result the isomeric ratio of ^{82}Br can be obtained. Experiments for the other nuclei and on the other filtered neutron beams are going on.

3.6. Average resonance capture (ARC)/18,19/:

Average resonance capture is one method to determine level scheme of nuclei. At the Dalat reactor ARC investigations are being carried out on the filtered neutron beams using the Compton-suppressed and pair spectrometer. Figure 5 shows relative reduced gamma transition intensities from neutron capture resonances to

low lying levels of ^{239}U in the reaction $^{238}U(n,\gamma)^{239}U$ on the filtered 55 keV neutron beam. Other ARC experiments are being carried out at the Dalat reactor.

3.7. The (n,2γ) Reaction/18,19/

The (n,2γ) reaction was studied by the method of summation of amplitudes of coinciding pulses (SACP) from two Ge(Li) detector to obtain the spectroscopic information for high excited levels. The scheme of the SACP spectrometer designed by ourselves is given in figure 6. Besides, the SACP spectrometer is also used to study complex decay schemes of radioactive nuclei and in neutron activation analysis thanks to its very low gamma backgrounds.

3.8. The thermal neutron macroscopic absorption cross section/20,21/:

We have developed the new approach to determine the thermal neutron macroscopic absorption cross section for small samples by poisoning method. The experiments were carried out in the thermal column of the Dalat reactor where the neutron flux in the sample center was measured by activation Au-foils at different values of absorption cross section Σ_a obtained by poisoning with suitable chemicals. The absorption cross section of the unknown sample is found from the intersection of the measured curve of relative fluxes Φ/Φ_0 and the line $\Phi/\Phi_0=1$.

4. Conclusion

To further promote nuclear data activities in Vietnam, it is necessary to join all physicists working in the field of nuclear data from different institutes and universities in the country and to improve international collaboration with the advanced nuclear data centers like JAERI Nuclear Data Center. We consider a regional nuclear data center for Asia and Pacific being the most important promotion in nuclear data activities in the region. Under the circumstances the scientists from developing countries in the region like Vietnam can make active contributions in the international nuclear data activities.

Acknowledgments

The author thanks Drs. N.V. Do, L.B. Bach (Nuclear Physics Center, Institute of Physics, VNCNST, Hanoi) and Dr. H.D. Luc (The Hanoi Institute of Nuclear Science and Technology, VINATOM) for providing their experimental data with 14 MeV neutrons for this paper. The author also acknowledges with thanks the support of JAERI under STA Scientists Exchange Program and helpful cooperation with JAERI Nuclear Data Center staff.

References

[1]. F.Z.Hien et al.: "A study of the isomeric ratio for the (n,2n) and (γ,n) reactions on ^{92}Mo, ^{90}Zr, ^{86}Sr and ^{74}Se", INDC(VN)-1/L, January 1982.

[2]. P.N.Ngoc et al.: " Neutron activation cross section for $^{56}Fe(n,p)$ and $^{87}Rb(n,2n)$ reactions", INDC(VN)-2/GI, November 1983.

[3]. H.D. Luc.: " Progress report on nuclear data activities in Vietnam", INDC(VN)-003/GI, September 1984.

[4]. H.D. Luc et al.: " Determination of some (n,p), (n,n'p) and (n,α) reaction cross sections induced by 14.8 MeV neutron on Cr and Ti isotopes", INDC(VN)-5/GI, september 1986.

[5]. L.B. Bach.: "Study of 14 MeV neutron activation cross sections on some isotopes", Ph.D. thesis, Hanoi, 1993.

[6]. P.Z. Hien et al.: "Preequilibrium emission of protons and isotopic effect in the fast neutron-induced (n,p) reactions on heavy elements", INDC(VN)-006/L, December 1987.

[7]. Sympson O.D., Muller L.G.: Nucl. Ins.Meth., 61, 245-250 (1968).

[8]. P.Z.Hien et al.: "Filtered neutron beams at the Dalat nuclear research reactor", Proc. 4th National Conf. on Phys., Oct. 15-18, 1993, Hanoi, p.63.

[9]. P.Z. Hien et al.: " Total neutron cross sections of U-238 as measured on the filtered neutron beams of 55 keV and 144 keV", INDC(NDS)-265, October 1992.

[10]. V.H. Tan et al.: "Analysis of transmission data of U-238 on the filtered 55 keV and 144 keV neutron beams", Proc. Int. Conf. on Nucl. Phys., Mar. 13-18, 1994, Hanoi.

[11]. G.M. Novosolov et al. Preprint of the Kiev Institute for Nuclear Research, KINR-89-25, Kiev, 1989.

[12]. V. Mclane et al.: "Neutron Cross Section, V2: Neutron Cross section Curves", Academic Press, Inc. 1988.

[13]. V.H. Tan et al.: "Average neutron radiative capture cross sections of U-238 on the filtered neutron beams of 55 keV and 144 keV", Proc. Int Conf. on Nucl. Phys., Mar. 13-18, 1994, Hanoi.

[14]. F.H. Frohner. Nucl. Sci. & Eng. 103, 119-128 (1989).

[15]. S. Kobayashi et al. Proc. Int. Conf. on Nuclear Data for Science and Technology, May 13-17, 1991, Forschungszentrum Julich, FRG, p. 65.
[16]. V.H. Tan et al.: "The Compton-suppressed and pair spectrometer at the Dalat reactor", Proc. 4th National Conf. on Physics, Oct. 15-18, 1993, Hanoi, p.68.
[17]. V.H. Tan et al.: "The gamma spectra from average resonance capture for some reactor materials on the filtered keV neutron beams", Proc. 4th National Conf. on Physics, Oct. 15-18, 1993, Hanoi, p.73.
[18]. V.H. Tan.: " Utilization of filtered neutron beams at the Dalat reactor: Status and Prospects", Proc. Int. Conf. on Nucl. Phys., Mar. 13-18, 1994, Hanoi.
[19]. V.H. Tan.: " Exploitation of the Dalat Nuclear Research Reactor", The report of the National Research Contract KC-09-08, Dalat, 1995.
[20]. V.D. Bang et al. Proc. Int. Workshop RCM on Nucl. Tech. in Exploration of Natural Resources, April 15-19, 1991, Debrecen, Hungary.
[21]. V.H. Tan et al.: "Measurement of thermal neutron macroscopic absorption cross sections for small samples at the Dalat reactor", Proc. 5th Asian Sym. on Research Reactors, May 25-29, 1996, Korea.
[22]. V.H. Tan and G.A. Prokopets. Proc. Int. Conf. on Nuclear Data for Science and Technology, May 13-17, 1991, Forschungszentrum Julich, FRG, p. 980.
[23]. V.H. Tan et al.: "Analysis of average neutron radiative capture cross sections in the keV energy region", Proc. 4th National Conf. on Physics, Oct. 15-18, 1993, Hanoi, p.75.

Table 1: Experimental isomeric ratios (α) for the (n,2n) reaction and the parameter of nuclear level density spin dependence (σ)

Target nucleus	$\alpha=\sigma_m/\sigma_g$	σ(h)	σ/σ_{rig}	Data in literature
^{91}Mo	0.063+-0.006	5.4+-0.8	0.98	0.04+-0.01 [14.7]
				0.067+-0.007 [14.8]
				0.094+-0.003 [14.8]
				1.08+-0.1 [14.8]
				1.04+-0.01 [14.8]
^{90}Zr	0.166+-0.004	4.7+-0.4	0.87	0.25+-0.05 [14.7]
				0.198+-0.02 [14.8]
				0.22+-0.05 [14.8]
				0.22+-0.02 [14.8]
				0.220+-0.007 [14.52]
				0.300+-0.035 [14.8]
^{86}Sr	0.22+-0.02	4.8+-0.7	0.9	0.24+-0.05 [14.7]
				0.201+-0.023 [14.8]
				0.40+-0.08
				0.402+-0.053 [14.06]
				0.44+-0.05 [15.62]
^{74}Se	0.80+-0.07	4.2+-0.8	0.87	0.22+-0.07 [14.4]
				0.175+-0.021 [14.17]
				1.15+-0.29 [14.82]

Table 2: The isomeric ratio for the (γ,n) reaction

Target nucleus	α_{exp}	α_{theor}	Data in literature
^{92}Mo	1.54+-0.15	1.36	1.32+-0.15 [70]
			1.03+-0.21
			0.35+-0.07 [30]
^{90}Zr	1.52+-0.04	1.49	0.50+-0.15 [30]
^{86}Sr	0.70+-0.07	0.86	0.63+-0.14 [30]
^{74}Se	7.5+-1.0	8.6	

Table 3: The (n,p) and (n,n'p) cross sections with 14 MeV neutrons

Reaction	This work(mb)	References	Reaction	This work(mb)	References
$^{24}Mg(n,p)^{24}Na$	173.5+-8.4	122+-5 172+-8.5	$^{56}Fe(n,p)^{56}Mn$	108.6+-2.2	110.6+-5.6 98+-7
$^{46}Ti(n,p)^{46m}Sc$	58.6+-3.2	48+-8 55.0+-2.2	$^{65}Cu(n,p)^{65}Ni$	29.3+-1.5	27+-5 27+-3
$^{47}Ti(n,p)^{47}Sc$	103+-10	110+-14 169.5+-6.9	$^{66}Zn(n,p)^{66}Cu$	69+-8	73+-5 65+-13
$^{48}Ti(n,p)^{48}Sc$	60+-4	60.6+-1.5 71.7+-2.6	$^{87}Rb(n,p)^{87}Kr$	10.7+-1.2	7+-1 10+-2
$^{50}Ti(n,p)^{50}Sc$	17+-4	15.4+-0.63 12+-2	$^{90}Zr(n,p)^{90m}Y$	11.9+-0.8	9.0+-0.8 8+-1
$^{51}V(n,p)^{51}Ti$	30.0+-2.5	33+-2 25+-3	$^{91}Zr(n,p)^{91m}Y$	23.3+-1.3	18.6+-1.0 14.2+-1.2
$^{52}Cr(n,p)^{52}V$	81.5+-6.2	80+-6 72.5+-3.2	$^{97}Mo(n,p)^{97}Nb$	17.5+-1.8	17.7+-1.5 18.2+-1.7
$^{53}Cr(n,p)^{53}V$	45.7+-3.1	40+-7 48+-7	$^{98}Mo(n,p)^{98}Nb$	5.5+-1.0	4.2+-0.55 6.63+-0.39
$^{54}Cr(n,p)^{54}V$	14+-2	15.3+-0.7 18.3+-3.0	$^{49}Ti(n,np)^{48}Sc$ $^{53}Cr(n,np)^{52}V$	6.3+-1.0 14+-3	
$^{47}Ti(n,np)^{46m}Sc$ $^{48}Ti(n,np)^{47}Sc$	8.1+-1.0 12.6+-1.5		$^{54}Cr(n,np)^{53}V$	6.5+-1.5	

Table 4: The (n,α) cross sections with 14 MeV neutrons

Reaction	This work(mb)	References	Reaction	This work(mb)	References
$^{51}V(n,\alpha)^{48}Sc$	16.5+-1.7	16.1+-0.9 21+-1	$^{54}Cr(n,\alpha)^{51}Ti$	12.5+-1.5	14.0+-1.2 11.0+-0.5
$^{90}Zr(n,\alpha)^{87m}Sr$	4.5+-0.6	4.1+-0.3 2.8+-0.4			

Table 5: The (n,2n) cross sections with 14 MeV neutrons

Reaction	This work (mb)	Reaction	This work (mb)
$^{64}Zn(n,2n)^{63}Zn$	179+-15	$^{100}Mo(n,2n)^{99}Mo$	1489+-86
$^{90}Zr(n,2n)^{89m}Zr$	131+-7	$^{90}Zr(n,2n)^{89}Zr$	796+-53
$^{87}Rb(n,2n)^{86}Rb$	1390+-117		

Table 6: The charecteristics of filtered neutron beams at the Dalat reactor

Neutron	Filter combination	Flux (n/cm^2/s)	R_{Cd} or FWHM
Thermal	98cmSi + 10cmTi + 35g/cm^{2}S	1.8×10^7	143
144 keV	98cmSi + 10cmTi + 0.2g/cm^{2}B^{10}	1.2×10^7	22 keV
55 keV	98cmSi + 35g/cm^{2}S + 0.2g/cm^{2}B^{10}	4.0×10^6	8 keV
25 keV	102.3cmAl + 0.2g/cm^{2}B^{10}	1.2×10^6	
24 keV	20cmAl + 20cmFe + 25g/cm^{2}S + 0.2g/cm^{2}B^{10}	1.0×10^6	
75 keV	45g/cm^{2}S + 0.2g/cm^{2}B10	1.1×10^6	

Figure1: Comparison of experimental data (ϕ) on isotopes of Sm, Er, Dy with predictions of the preequilibrium + evaporation models (+).

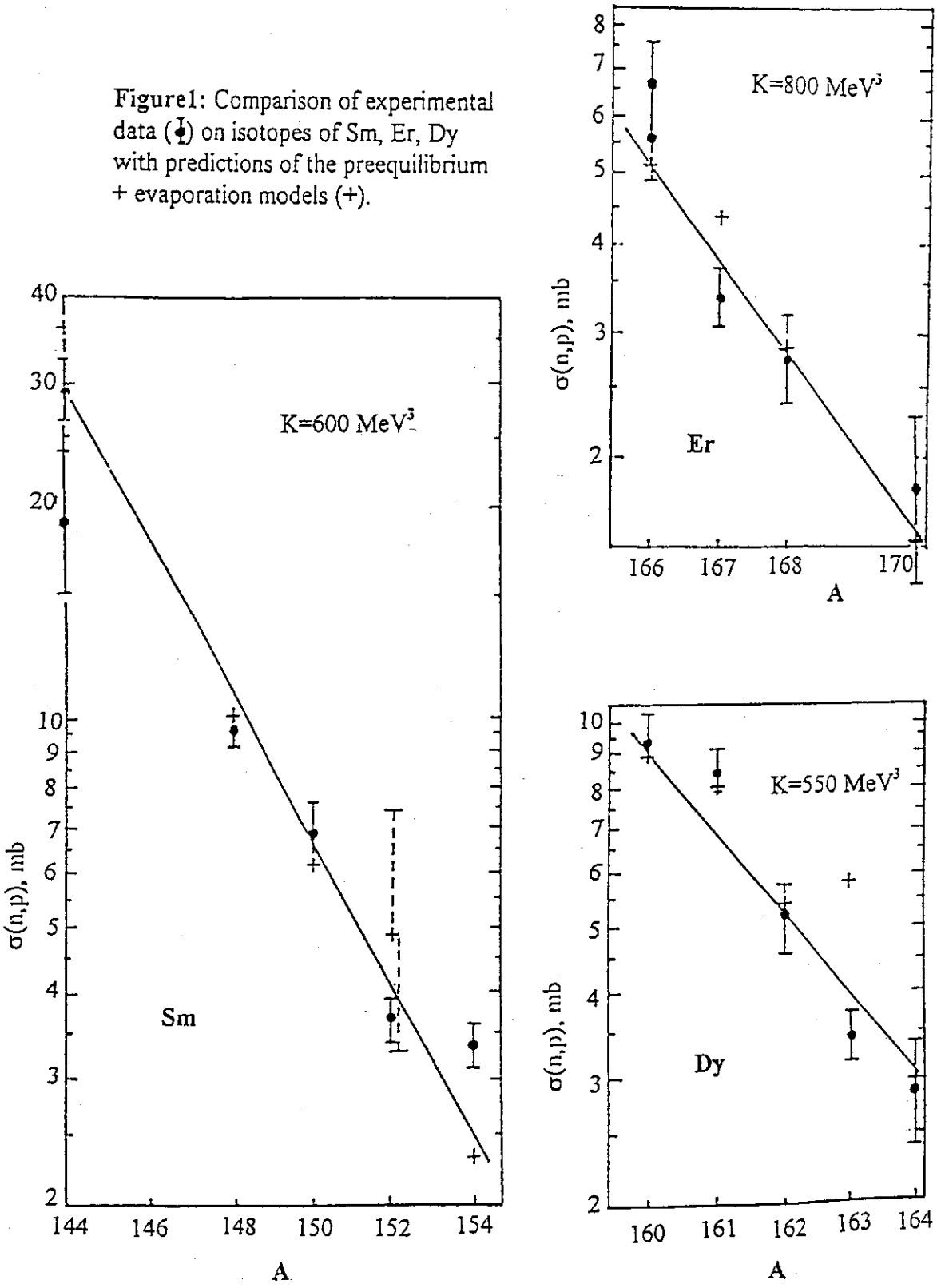

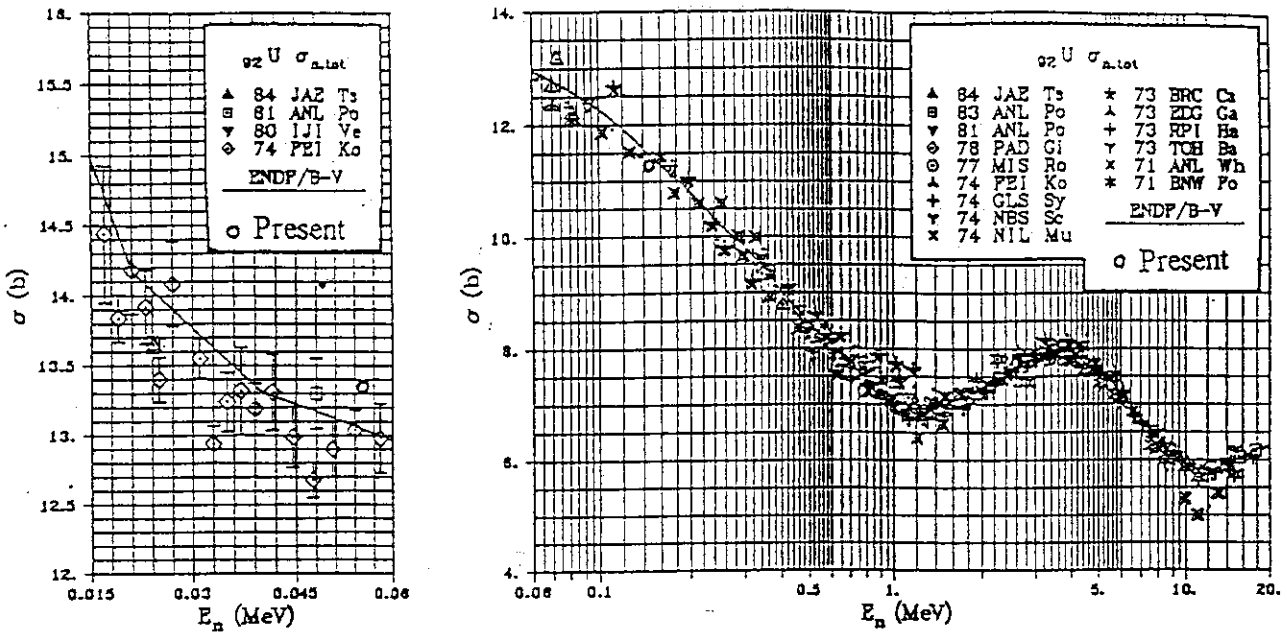

Figure 2: The total neutron cross sections of uranium

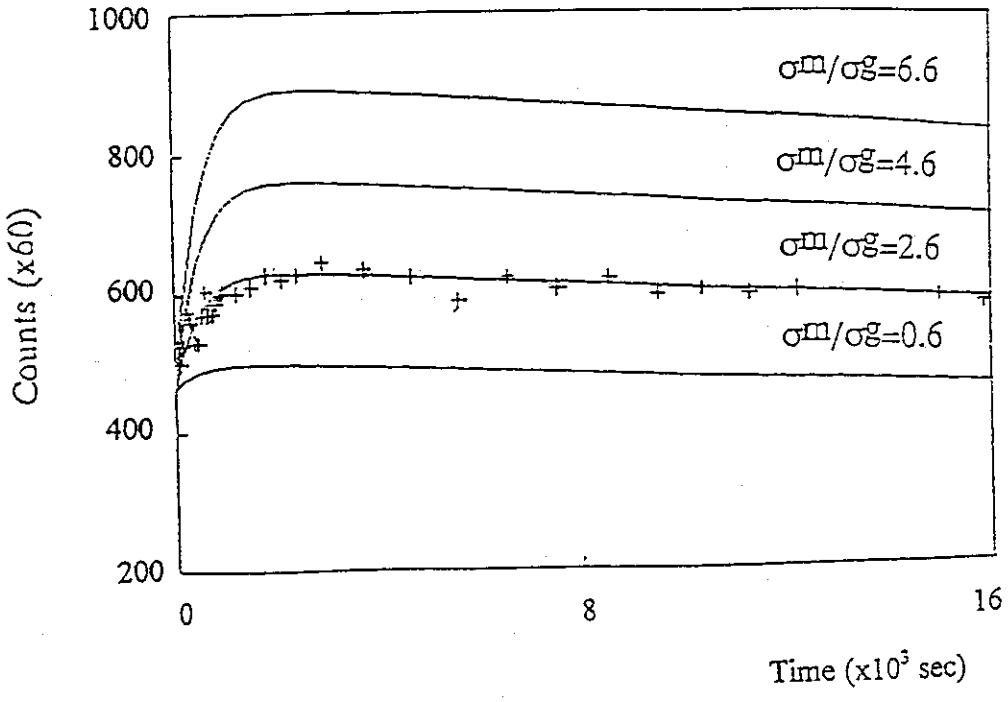

Figure 4: The time decay of the 828 keV gamma ray intensity of ^{82g,m}Br after irradiation of the NH_4Br-sample on the filtered neutron beam of 144 keV

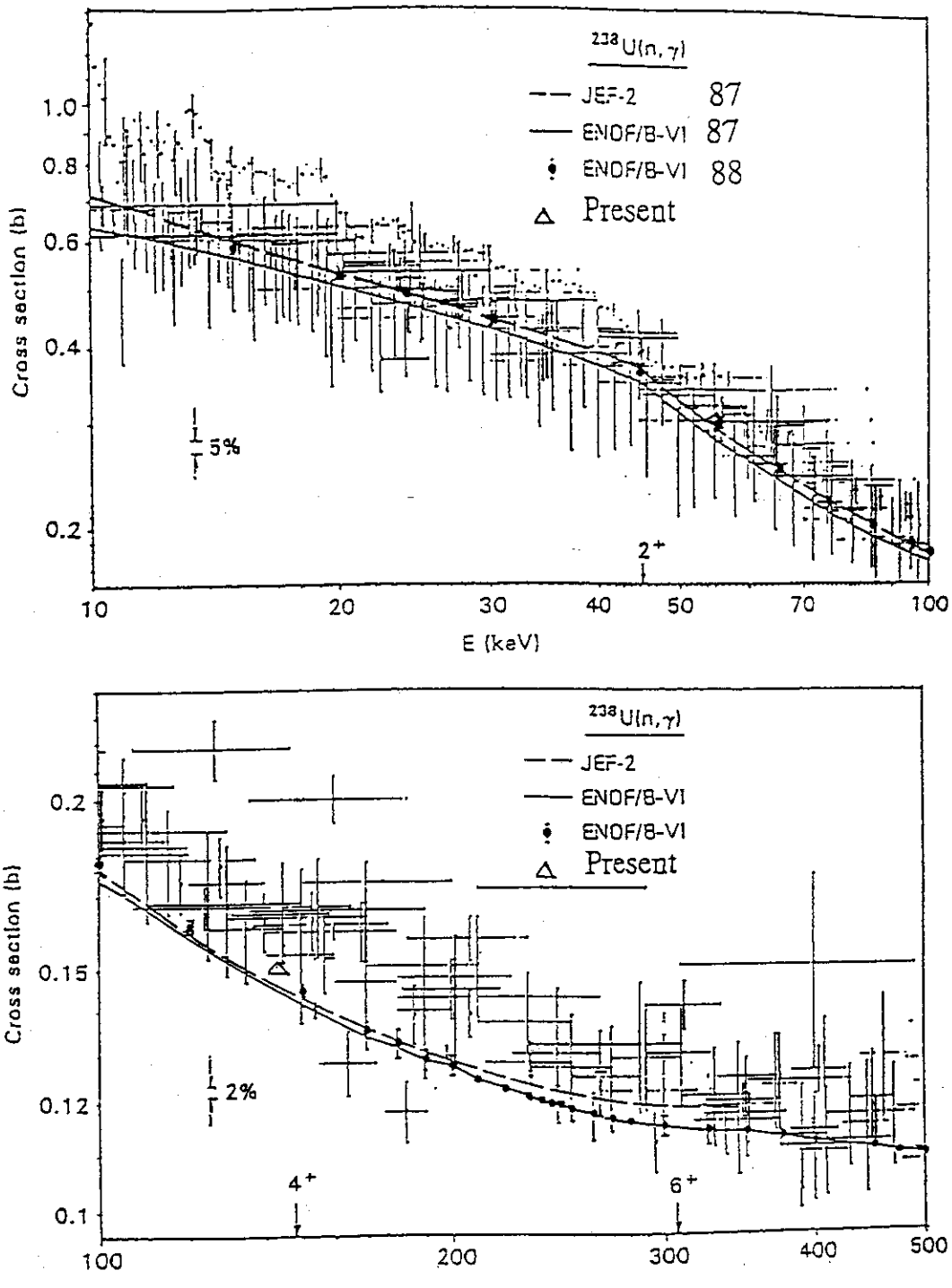

Figure 3: Average neutron radiative capture cross sections of U-238

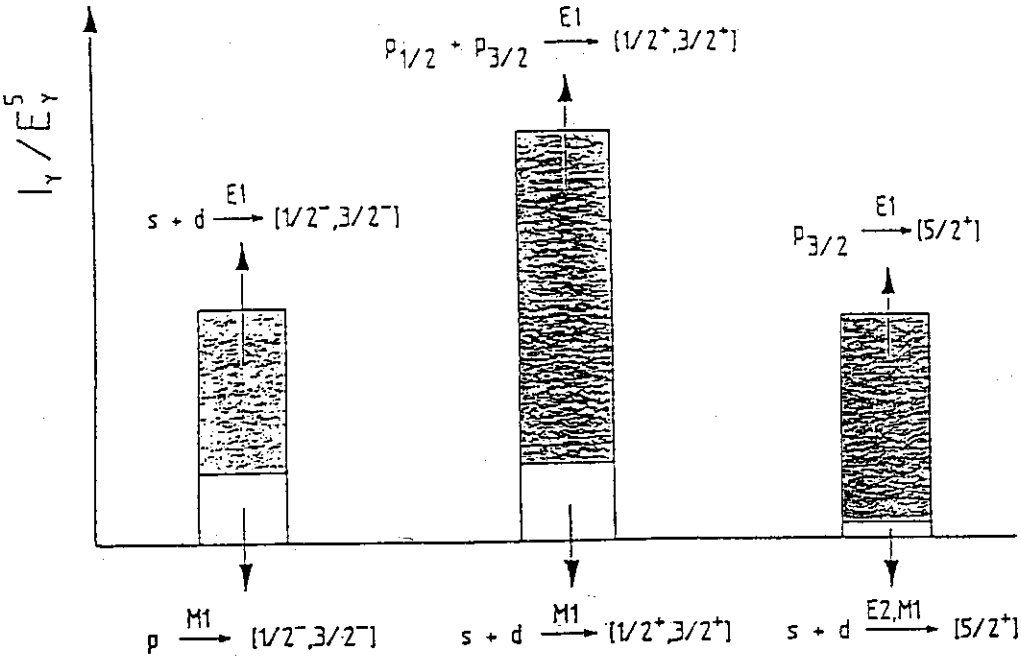

Figure 5: The relative reduced gamma transition intensities of ^{239}U from the $^{238}U(n,\gamma)$-reaction on the filtered neutron beam of 55 keV

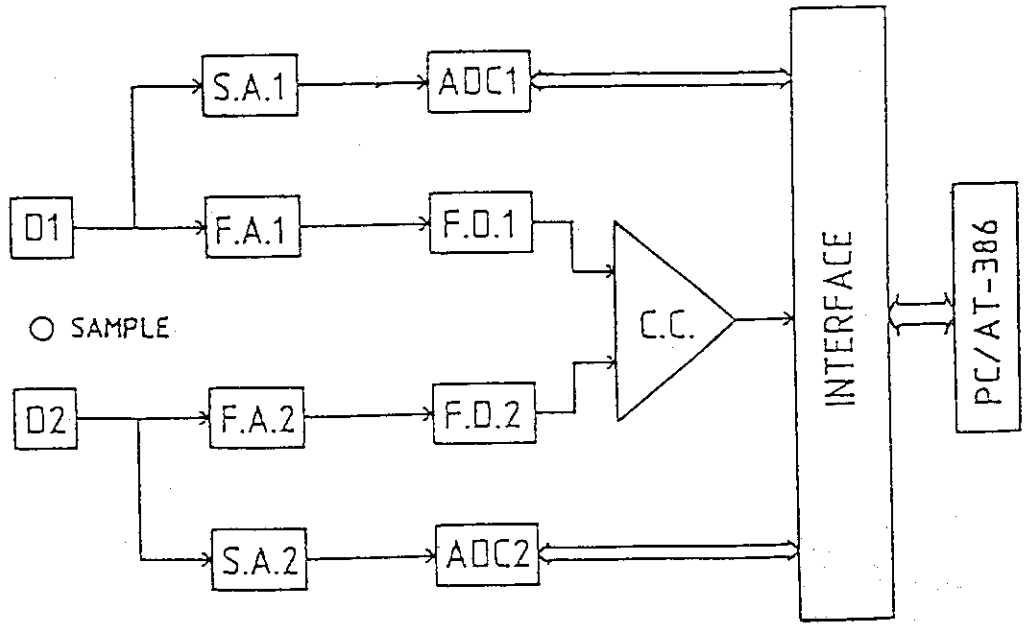

Figure 6: The scheme of the SCAP spectrometer at the Dalat reactor

D - HPGe-detector.
F.A. - Fast Amplifier.
C.C. - Coinciding Circuit.
S.A. - Spectroscopy Amplifier.
F.D. - Fast Discriminator.
A.D.C. - Analog Digital Convertor.

2.4.4 Nuclear Data Usage for Research Reactors

Yoshihiro NAKANO, Kazuhiko SOYAMA and Toshio AMANO

Research Reactor Technology Development Division
Department of Research Reactor
Japan Atomic Energy Research Institute
Tokai-mura, Naka-gun, Ibaraki-ken 319-11

Abstract

In the department of research reactor, many neutronics calculations have been performed to construct, to operate and to modify research reactors of JAERI with several kinds of nuclear data libraries. This paper presents latest two neutronic analyses on research reactors. First one is design work of a low enriched uranium (LEU) fuel for JRR-4 (Japan Research Reactor No. 4). The other is design of a uranium silicon dispersion type (silicide) fuel of JRR-3M (Japan Research Reactor No. 3 Modified). Before starting the design work, to estimate the accuracy of computer code and calculation method, experimental data are calculated with several nuclear data libraries. From both cases of calculations, it is confirmed that JENDL-3.2 gives about 1 %Δk/k higher excess reactivity than JENDL-3.1.

1. General Description of Research Reactors

1.1 JRR-4

JRR-4 is a swimming pool type, light water cooled and moderated research reactor with maximum thermal output of 3.5 MW. Present core configuration is shown in Figure-1. The reactor core consists of 20 fuel elements, graphite reflector elements, irradiation pipes, a neutron source, control rods and backup rods. The fuel element now in use is aluminum cladded plate type, 93% ^{235}U enriched and fuel meat material is U-Al alloy. The new fuel has same dimensions but the fuel meat material is U_3Si_2-Al and ^{235}U enrichment is reduced to about 20%. Figure-2 shows the horizontal cross section of the fuel. The fuel consists of 15 fuel plates. An outside plate of each side contains half of other thirteen plates because of a request from thermal-hydraulics. Uranium density of the inner plate will be 3.8 g/cm^3.

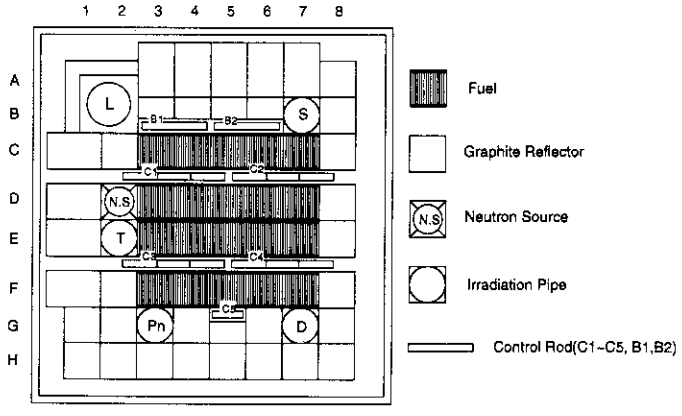

Fig.-1 JRR-4 Present Core Configuration

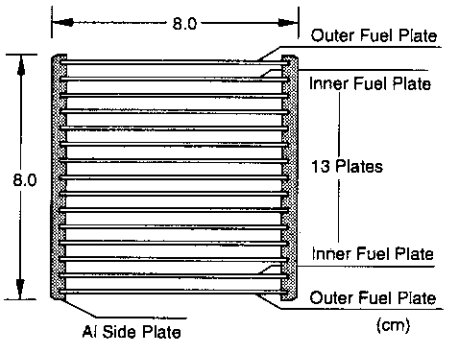

Fig.-2 Horizontal Cross Section of the Fuel Element

1.2 JRR-3M

JRR-3M is the latest research reactor in Japan. It achieved first criticality in March 1995 after the modification of old JRR-3. It is a swimming pool type, light water cooled and moderated research reactor with maximum thermal output of 20MW. The core consists of 26 standard fuel elements, 6 control elements with follower fuel elements, irradiation elements, beryllium reflector, heavy water reflector tank and neutron beam tubes. Figure-3 shows horizontal cross section of the core. The reactor uses ETR type fuel element with 20 fuel plates. The fuel meat is 20% enriched uranium aluminum dispersion type fuel (aluminide fuel) cladded with aluminum. It will be changed to 20% enriched uranium silicon dispersion type fuel (silicide fuel) with about 1.5 times of uranium loading and burnable poison to suppress the excess reactivity. Higher uranium loading enables higher burnup of discharged fuel and decreases the number of spent fuels.

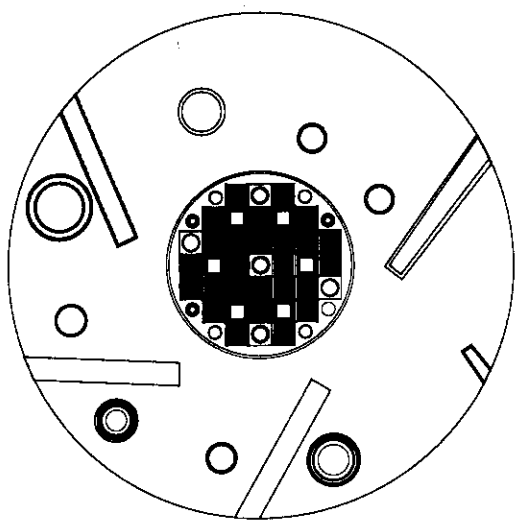

Fig.-3 JRR-3M Core Configuration

2. Calculation

Computer codes used in the calculation are SRAC Code System[1] and MVP Code[2]. Nuclear data libraries are ENDF/B-IV[3], JENDL-2[4], JENDL-3.1[5] and JENDL-3.2[6]. For the calculation of JRR-4, SRAC and MVP codes are used. Before starting the design calculation of LEU fuel, JRR-4 HEU core at the commissioning test is analyzed to estimate the accuracy of the codes and methods. It is also big purpose to see how much is the change when nuclear data library is changed. For the JRR-3M calculation, experimental data of initial critical test is analyzed with MVP code to estimate the accuracy of the code and method.

2.1 Calculation of JRR-4

2.1.1 Calculation with SRAC

The first step of the calculation is cell calculation of fuel element. Collision probability method is used in this step. Figure-4 shows calculation model of the fuel plate cell. One dimensional fixed source problem is solved with 107 group energy structure. Homogenized cross section of the plate cell is obtained. The next is cell calculation of the fuel element. Two dimensional fixed source problem is solved. The cross section of plate cell obtained in the previous calculation is used for this calculation. The number of energy group is 107. Figure-5 shows calculation model of the fuel element. From this calculation, homogenized cross section of the fuel element is obtained and energy group structure is collapsed from 107 to 6 or 8

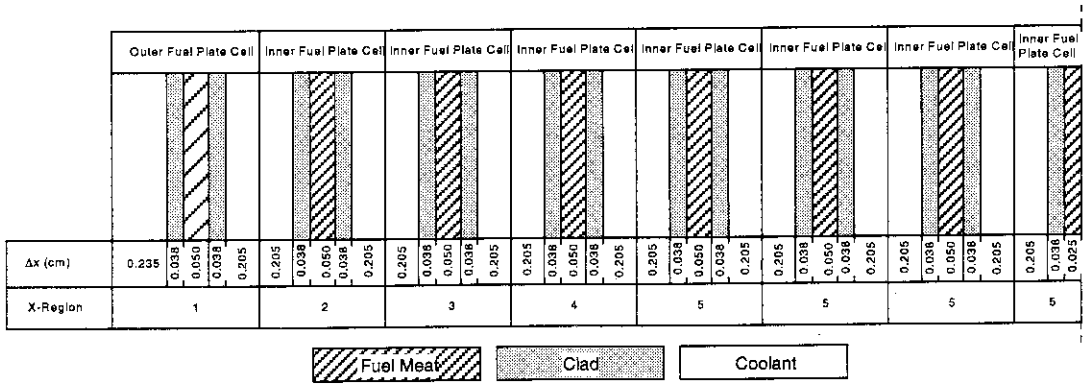

Fig.-4 Plate Cell Calculation Model

group.

The second step is generation of few group cross section of reflector, irradiation pipe and other reactor core elements. To obtain the neutron spectra as weighting functions for the energy group collapsing, two dimensional diffusion calculation of the core is performed with 107 energy group. From this calculation, element and space dependent neutron spectra are obtained. Cross sections of the elements are collapsed using the spectra.

The third step is whole core calculation using three dimension diffusion theory. Effective multiplication factor, control rod worth, neutron flux and so on are obtained from this step.

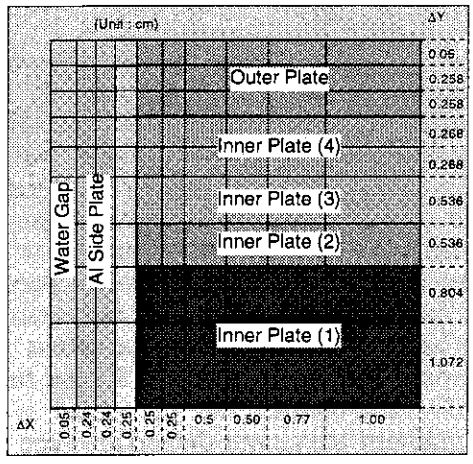

Fig.-5 Element Cell Calculation Model

2.1.2 Calculation with MVP

MVP is a continuous energy monte carlo code. It can treat JRR-4 core with fewest geometrical approximations. Active part of the fuel element is described exactly in the calculation. Other parts of the fuel elements and other core elements are divided into several horizontal planes and homogenized by atom number density in order to reduce geometrical complexity. Calculation is continued until small enough deviation is obtained.

2.2 Calculation of JRR-3M

2.2.1 Calculation with MVP

Active part of the fuel element is treated exactly. Other parts of the fuel element are divided into several horizontal planes and homogenized by atom density. Irradiation elements in the core, irradiation facilities in the D2O reflector tank, detectors in the core and reflector, beam tubes in the D2O reflector tank and other core elements are taken into account for the calculations as exactly as possible.

3. Results

3.1 JRR-4

Table-1 is the excess reactivity(k_{eff}, effective multiplication factor) of A-12 core calculated with MVP. A-12 core is the first critical core of JRR-4. The core consists of twelve A-type fuels. There are two kinds of HEU fuel for JRR-4. JRR-4 have been operated with maximum thermal output of 2.5MW using A-type HEU fuel elements for 10 years since the initial criticality. When the maximum power increased to 3.5 MW, B-type fuel elements were adopted and have been used since 1976. Table-1 shows MVP with JENDL-3.1 slightly underestimates the experimental value and gives a good C/E value. The combination of MVP and JENDL-3.2 overestimates the experimental value for 0.6%Δk/k and gives about 0.9%Δk/k higher excess reactivity than JENDL-3.1.

Table-2 is the results of criticality calculation of A-4+B-12 core. The core consists of four A-type elements and twelve B-type elements. JENDL-3.1 underestimates experimental data for about 0.6%Δk/k and JENDL-3.2 overestimates it for about 4%Δk/k. Difference between two libraries is about 1.0%Δk/k.

Table-3 is the results of excess reactivity of silicide core. SRAC code gives about 0.4%Δk/k lower reactivity than MVP. JENDL-3.2 gives about 0.8%Δk/k higher reactivity than JENDL-3.1.

Table-4 is results of excess reactivity calculation of a different kind of silicide core. This is a temporary core under the parameter survey calculation to decide the final uranium density. Uranium density of the inner plate of the core is 4.0g g/cm^3. (Final uranium density of the inner plate is 3.8 g/cm^3) From the table, it can be seen that ENDF/B-IV and JENDL-3.1 shows good agreement. JENDL-2 gives higher reactivity than other two libraries.

Table-1 Excess Reactivity of JRR-4 A-12 Core Calculated with MVP

	JENDL-3.1	JENDL-3.2	EXPERIMENT
k_{eff}	0.9948 (0.120%)	1.0035 (0.086%)	0.9972
C/E	0.9976	1.0063	-----
Δρ(J3.2-J3.1)	0.877 %Δk/k		-----

Table-2 Criticality of JRR-4 A-4+B-12 Core Calculated with MVP

	JENDL-3.1	JENDL-3.2	EXPERIMENT
k_{eff}	0.9933 (0.136%)	1.0030 (0.125%)	0.9995
C/E	0.9938	1.0035	-----
Δρ(J3.2-J3.1)	0.974 %Δk/k		-----

Table-3 Excess Reactivity of JRR-4 Silicide Core

CODE	SRAC		MVP	
LIBRARY	JENDL-3.1	JENDL-3.2	JENDL-3.1	JENDL-3.2
k_{eff}	1.1043	1.1144	1.1091 (0.103%)	1.1197 (0.104%)
Δρ(J3.2-J3.1)	0.821%Δk/k		0.852%Δk/k	
SRAC/MVP	0.9957	0.9953	-----	-----

Table-4 Excess Reactivity of JRR-4 Silicide Core (II)

	ENDF/B-IV	JENDL-3.2	JENDL-3.1
k_{eff}	1.1191	1.1266	1.1184
JENDL/ENDF/B-IV	-----	1.0067	0.9994

3.2 JRR-3M

Table-5 is excess reactivity of initial critical core calculated with MVP. Calculation with JENDL-3.1 slightly overestimates the experimental value. JENDL-3.2 gives more than 1%Δk/k higher excess reactivity than JENDL-3.1. It has been known that resonance absorption cross section of U-235 of JENDL-3.2 may be too small[7]. To confirm that the difference between two libraries is caused from U-235 or not, a calculation with JENDL-3.2 library but only the data of U-235 is changed to JENDL-3.1. As a result of the calculation, difference from the JENDL-3.1

calculation cannot be seen and it is confirmed that the dominant reason of the difference between two libraries is the data of JENDL-3.2.

Table-6 is results of criticality calculation of initial full core of JRR-3M. It shows same tendency as Table-5. JENDL-3.1 overestimates the experimental data and JENDL-3.2 gives about 1%Δk/k higher reactivity than JENDL-3.1. Combined library of JENDL-3.2 and U-235 of JENDL-3.1 shows good agreement with JENDL-3.1.

Table-5 Excess Reactivity of JRR-3M First Critical Core Calculated with MVP

NUCLEAR DATA	JENDL-3.1	JENDL-3.2 + ^{235}U of JENDL-3.1	JENDL-3.2	EXPERIMENT
k_{eff}	1.0018 (0.087%)	1.0022 (0.092%)	1.0132 (0.095%)	0.9988
C/E	1.0030	1.0034	1.0144	-----
Δρ(J3.2-J3.1)	-----	0.040%Δk/k	1.123%Δk/k	-----

Table-6 Criticality of JRR-3M Initial Full Core Calculated with MVP

NUCLEAR DATA	JENDL-3.1	JENDL-3.2 + ^{235}U of JENDL-3.1	JENDL-3.2	EXPERIMENT
k_{eff}	1.0056 (0.080%)	1.0059 (0.101%)	1.0156 (0.091%)	0.9993
C/E	1.0063	1.0066	1.0163	-----
Δρ(J3.2-J3.1)	-----	0.030%Δk/k	0.979%Δk/k	-----

4. Conclusions

Calculations on JRR-4 and JRR-3M cores with JENDL-3.1 and JENDL-3.2 libraries have been performed and followings were shown.

JENDL-3.1 gives good C/E value in almost of the calculated cases. JENDL-3.2 gives about 1%Δk/k higher reactivity than JENDL-3.1. JENDL-3.1 shows good agreement with ENDF/B-IV. JENDL-2 gives higher reactivity than ENDF/B-IV and JENDL-3.1.

In case of JRR-4, JENDL-3.1 underestimates the experimental data and JENDL-3.2 overestimates it.

In case of JRR-3M, both of JENDL-3.1 and JENDL-3.2 overestimate the experimental value. Calculations with JENDL-3.2 but only the data of U-235 is changed to JENDL-3.1 have been done. The results are not different from the results of calculations with JENDL-3.1 for all nuclides. It is confirmed that difference between two libraries is caused from the U-235 data of JENDL-3.2.

5. Acknowledgments

The authors wish to give their great thanks to Dr. K. Tsuchihashi, Dr. T. Mori and Mr. K. Okumura for their great help to use computer codes, SRAC and MVP. Thanks are also due to the stuff of Research Reactor Technology Development Division for their valuable discussions through the course of the work.

References

[1] K. Tsuchihashi, et. al., "Revised SRAC Code System", JAERI-1302 (1986).
[2] T. Mori, et. al., "MVP/GMVP: General Purpose Monte Carlo Codes for Neutron and Photon Transport Calculations based on Continuous Energy and Multigroup Methods", JAERI-Data/Code 94-007 (1994).
[3] (Ed.) D. Garber: "ENDF/B Summary Documentation," BNL-17541, 2nd Edition (1975).
[4] (Ed.) T. Nakagawa: "Summary of JENDL-2 General Purpose File," JAERI-M 84-103 (1984).
[5] K. Shibata, T. Nakagawa, T. Asami, T. Fukahori, T. Narita, S. Chiba, M. Mizumoto, A.Hasegawa, Y. Kikuchi, Y. Nakajima and S. Igarasi: "Japanese Evaluated Nuclear Data Library, Version-3, -- JENDL-3 --," JAERI 1319 (1990).
[6] T.Nakagawa, K.Shibata, S.Chiba, T.Fukahori, Y.Nakajima, Y.Kikuchi, T.Kawano, Y.Kanda, T.Ohsawa, H.Matsunobu, M.Kawai, A.Zukeran, T.Watanabe, S.Igarasi, K.Kosako, T.Asami: "Japanese Evaluated Nuclear Data Library Version 3 Revision-2: JAENDL-3.2", to be published as J. Nucl. Sci. Technol., 32, 1259 (1995).
[7] T. Nakagawa, Private Communication.

2.4.5 Present Status and Future Plan of the Research Using HIMAC of NIRS

Kiyomitsu KAWACHI
Division of Accelerator Physics and Engineering
National Institute of Radiological Sciences
9-1, Anagawa 4-chome, Inage-ku, Chiba-shi 263

The Heavy Ion Medical Accelerator in Chiba (HIMAC) was completed in 1993, and since June of 1994 heavy ion therapy has made a new start at this facility after closed-down of the BEVALAC accelerator at LBL in Berkeley, California in 1992. The HIMAC is also opened for the researchers of outside of NIRS as well as the clinical trial of the heavy ion therapy. In this report, I will describe on the present status of HIMAC facility, the beam characteristics and the future developments of HIMAC.

1. Introduction

Two years have passed since the completion of HIMAC (Heavy Ion Medical Accelerator in Chiba) facility at NIRS (National Institute of Radiological Sciences). During these two years, there have been several improvement of facility and progress of the operational techniques, such as increasing of highly charged particles at ion sources, improvements of transmission ratios at injector system, increasing the varieties of ion species and energies of the available beams, and progress of the beam extraction technique at synchrotron et. al.. These improvements and progress have conferred a great benefit on the users of the HIMAC beams as well as the clinical trials of heavy ion therapy.

In the field of medical applications of heavy ion beams, the atomic and nuclear data are very important and directly related to the treatment planning and the evaluation of the results. Several research works have been continued in the field related nuclear data, such as track structure measurements, fluence spectra measurements of fragmented particles caused by spallation reaction between heavy ions and some tissue equivalent materials, measurements of radial deviation of the heavy ions in the various materials and so on.

2. Present Status of Accelerator Performance

Performance of ion sources.

HIMAC is equipped with a PIG and an ECR ion sources. A PIG ion source is operated in a very short pulse with a relatively long time interval. Such an operation increases appreciably an arc impedance resulting in a high arc voltage. This feature improved the performance of the PIG ion source, such as the life time of the hot cathode and the yields of highly charged ions. The out put beam intensities and emittance of both sources are satisfactory for the treatment, however the ECR ion source is preferable in the daily operation for the clinical treatment, because of the easiness of the source operation.

Performance of Injector Linacs.

An RFQ linac accelerates heavy ions with $q/A \geq 1/7$ from 8 keV/u to 800 keV/u. The beam transmission efficiencies through the low energy beam transport line and RFQ linac are attained to be around 80% and 90%, respectively, in daily operation. An Alvarez type linac (DTL) also accelerates heavy ions with $q/A \geq 1/7$ from 800 keV/u to 6 MeV/u. Both linacs are operated with the same frequency of 100 MHz and with a very low duty factor of 0.3% at maximum. At the output end of the DTL, a 100 μ g/cm^2 thick carbon stripping foil is inserted to improve a charge to mass ratio of the ions. Only one stripping stage is adopted at a relatively higher ion energy of 6 MeV/u because of the reliability of the system and of the advantages for future expansion to the acceleration of heavier ions.

Table 1. Performance of the HIMAC ion sources (emA)
(Upper line for PIG, and Lower line for ECR)

Ion Species	Charge State 1+	2+	3+	4+	5+	6+	7+	8+	9+	10+	necessary Intensity
^{4}He	12.0	3.0									0.65
	3.9	2.1									
^{12}C	1.0	5.0	(3.0)	0.7	0.02						0.16
		0.47		0.43	0.06						
^{14}N		3.2	2.5	1.2	0.2						
		0.79	0.59	0.34	0.18	0.02					
^{16}O		2.0	2.3	(3.0)	0.3	0.03					
		0.66	0.47	(0.44)	0.28	0.13	0.02				
^{20}Ne	0.45	2.0	3.8	1.75	(0.4)	0.02					0.12
		0.62	0.7	0.7	(0.6)	0.22	0.05	0.01			
^{28}Si			0.4	(0.6)	0.3	0.15	0.01				0.13
^{40}Ar	0.05	0.45	1.5	2.0	(1.9)	1.1	0.5	0.2			0.34
				0.38	0.34	0.35	0.27	0.24	0.09	(0.04)	

Table 2. Typical beam performance of Injector

Ion species	He^{1+}	C^{4+}	Ne^{4+}	Ar^{8+}
(q/A)	(1/4)	(1/3)	(1/5)	(1/5)
Ion source	PIG	ECR	PIG	ECR
Intensity (e A)	480	140	250	105
Transmission efficiency (%)				
LEBT	45	93	48	71
RFQ	93	92	92	93
DTL (Alvarez)	92	96	91	86
Stripping efficiency (%)	100	93	90	18
(Charge State)	1→2	4→6	4→10	8→18
Transmission efficiency (%)				
MEBT	96	93	100	81
Output Intensity (e μ A)	357	152	180	20

Performance of Synchrotron

The two synchrotron rings are operated independently from each other except that the magnets must be excited with the phase difference of 180°. The accelerated ion species and energies with the upper ring and the lower ring (referred as U-ring and L-ring, respectively) are summarized in Table 3.

Improvement of beam extraction pattern.

At the beginning stage of synchrotron operation, the large beam intensity fluctuation was observed in the extracted beam structure from the synchrotron. This fluctuation was caused by a current ripple of the synchrotron magnets, and there was no feedback system in the magnet power supplies to stabilize the extracted beam intensity. High frequency components of the ripple in the extracted beam structure are appreciably suppressed after careful tuning of the synchrotron magnet power supplies. At the flat top, voltage ripples of the power supplies of QF and bending magnets are kept extremely low values of less than 1×10^{-6} and 1×10^{-5}, respectively (50 Hz). A beam ripple, however, has still remained at high level. By reducing the sextupole fields for chromaticity correction, the beam spill was satisfactorily improved. This fact means that the field fluctuation of the bending magnet may affect strongly on the beam intensity ripple through the sextupole fields.

Table 3. Accelerated ion species and energies
(Upper line for U-ring, and Lower line for L-ring)

Ions	Energy(MeV/u)									
$^{4}He^{2+}$	150	230								
	150	230								
$^{12}C^{6+}$	80	100	135	150	230	290	330	350	400	430
		100		150	230	290		350	400	430
$^{16}O^{8+}$		290								
	230									
$^{20}Ne^{10+}$			290	400		600				
	100	230	290	400	430	600				
$^{22}Ne^{10+}$	290									
	290	400								
$^{28}Si^{14+}$	800									
	800									
$^{40}Ar^{18+}$				650						
	100	290	550	650						

3. Present status of HIMAC operation:

After clearing the radiation safety investigation of the facility, physical and biological experiments were performed for a few months using 290 MeV carbon beams which were expected to use for the first clinical trials of head and neck cancer treatments as well as a careful beam tuning of accelerator. After confirming the reliability of the total system, the first clinical trial started on June 21, 1994. In this early stage of the accelerator operation, all devices were turned off over night except for the vacuum system and the control system. After turning on in the morning, it took only 4 hours to get the accelerated beam in a treatment room. Most part of the time are spent in tuning of the ion source and low energy beam transport (LEBT) elements.

After October 1994, HIMAC is operated day and night from Monday 7 p.m. to Saturday 7 p.m. In the day time of every Monday, weekly maintenance is scheduled. Accelerator Engineering Corporation (AEC) is responsible for the machine operation and the weekly maintenance. Major activities of the accelerator group of NIRS are set toward the improvements of the beam performance. The machine time from 9 a.m. to 7 p.m. of the weekday is scheduled for the clinical trials and from 7 p.m. to the next 7 a.m. is opened for users with carbon ions. From Friday 7 p.m. to Saturday 8 p.m., various kind of ion species are accelerated for users in physics and other fields of researchers.

Total of 37 weeks per year are available as machine time, other 2 weeks are for beam tuning and 13 weeks are scheduled shut down for machine maintenance etc. About 1,500 hr. per year was spent by the clinical trials and about 2,500 hr. of machine time is assigned to the basic experiments and beam tunings.

4. Physical Studies for heavy ion therapy

Depth dose distributions

The depth dose distributions for monoenergetic carbon beams were measured by the ionization chamber for the nominal incident energies of 290, 350 and 400 MeV/u. Fig. 1 shows a depth dose distribution for monoenergetic incidence of 290 MeV/u carbon beam. The closed triangles indicate the relative ionization in water, which is converted from the data of the measurement in Lucite to the water equivalent thickness in this figure. A solid line in the figure shows a calculated depth dose distribution which has been taken the contributions of secondary and tertiary particles into account.

Several ridge filters to make the Spread-Out Bragg Peak (SOBP) for carbon beams were designed by using the calculated depth dose distribution and LET distribution of the monoenergetic beams, and the biological responses of HSG cells for carbon beams. The typical depth dose distributions for several thickness of SOBP are shown in Fig. 2.

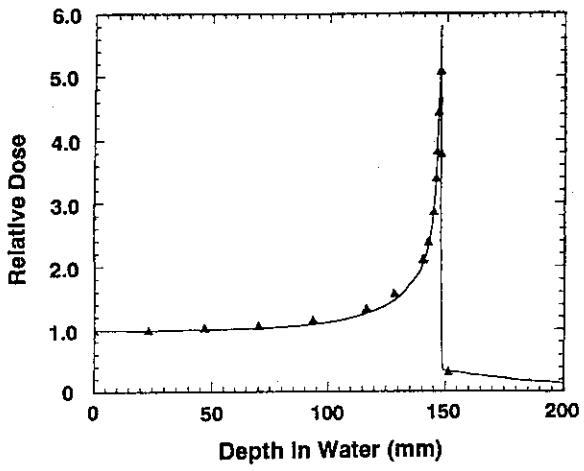

Fig. 1. Physical depth dose distribution for carbon 290 MeV/u beams.

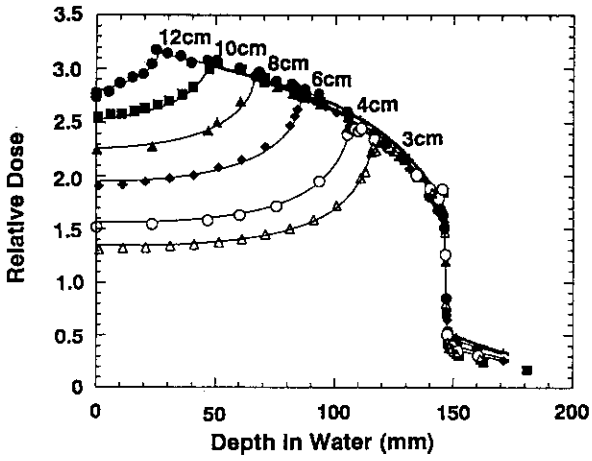

Fig. 2. Physical dose distribution for SOBP of carbon 290 MeV/u beams

Determination of absorbed dose.

Three different methods are applied to the determination of absorbed dose for heavy ion beams at HIMAC. Those are an ionization chamber method, a fluence measurement method and a silicon diode detector method. The fluence measurements have been done using a plastic scintillator and CR-39 track detector. The data of plastic scintillator were compared with those of a CR-39 track detector. The results by the use of both detectors agree within 1.2%. The measured fluence was converted to the dose by multiplying the stopping power which corresponded to the energy at each depth by the measured fluence.

At the beginning stage of the fluence measurements, the beam intensity has to be reduced about 1 x 10^6 particles per pulse from synchrotron because of the spiked beam structure which causes to produce a piled-up signal at high intensity. However, the recent fluence measurements is performed with the same intensity at the treatment. Because the extracted beam spill from synchrotron is considerably improved as above mentioned. Furthermore, a new counting technique of the tracks on the CR-39 was developed by the use of an atomic force microscope (AFM). This method is possible to observe more than 10^7 tracks/cm^2 etch pit density on CR-39 and to analyze within a minute.

Silicon diode detectors are also excellent charged particle detectors and suitable for the determination of relative absorbed dose, especially for in vivo dosimetry. Because they are stable, linear in their energy response to all charged particles, and can be made small. The absorbed dose for heavy ions was derived by the product of the measured ionization current with the silicon diode by the calibration factor.

Table 4 shows the results of the comparison of the three methods. The results show that the three methods agree within 5 %. In case of ion chamber dosimetry, there is very large uncertainty in the W value for the high energy carbon ion. If the W value in air were 33.7 eV, which was suitable for high energy electrons and gamma-rays, the result of ionization chamber would give 4.5% higher value.

Table 4. Comparison of the three dosimetry

(Fluence measurements at the intensity below 6.4 x 10^5 cpp)

Detector	p/cm^2/monitor
CR-39	(2.050 ± .017) x 10^5
Plastic Scintillator	(2.074 ± .047) x 10^5

(Ratio of the dose by the three dosimetry methods)

Dosimetry method	Ratio
Ionization Chamber	1.0
Fluence Measurement	0.958
Silicon Diode	0.973

Physical beam characteristics for heavy ions. (LET distribution, Fragmentation)

Fluence spectra of fragmented particles caused by spallation reactions between carbon ions and polymethyl methacrylate (PMMA) target were measured with E-Δ E counter telescope method for the energies of 290 MeV/u and 400 MeV/u at HIMAC. Fig. 3 illustrates a typical result of the scatter plot of the residual energy E and the energy loss Δ E for 290 MeV/u carbon beam in PMMA at the depth of 120.7 mm. The abscissa represents the residual energy E measured by the BGO scintillator and the ordinate the energy loss Δ E from the plastic scintillator. Fragmented particles are clearly separated to some groups and filled in Fig. 3.

Fluence spectra of each element were derived from the number of particles in each group by normalizing with the total number of incident particles because of the flatness and the broadness of the incident beam. Fig. 4 displays the fluence spectra at the incidence of 290 MeV/u carbon beam. In this figure, dose represents the results of this work and lines are calculational results by Sihver et al. for the sake of comparison.

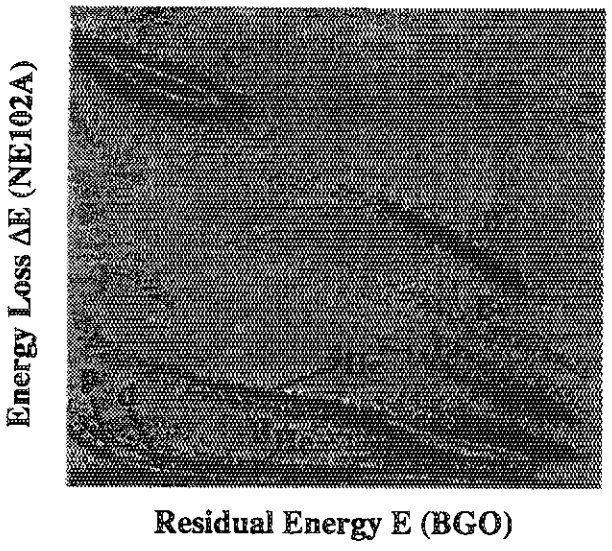

Fig. 3. The scatter plot of the residual energy E and the energy loss Δ E in PMMA.

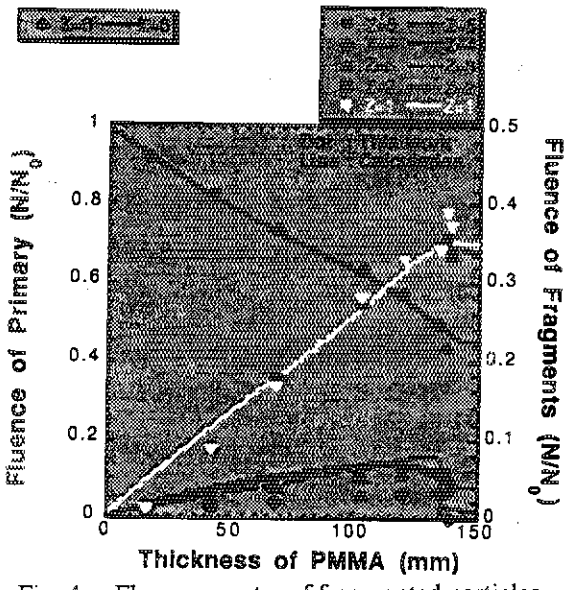

Fig. 4. Fluence spectra of fragmented particles for 290 MeV/u carbon beams.

5. Biological studies for heavy ion therapy

Determination of RBE values:

The relative biological effectiveness (RBE) of heavy ions varies not only biological variables, but also physical parameters such as ion species, energy, LET from a large reservoir of beams which can be obtained by HIMAC. Although the carbon beams were selected at the beginning stage of the clinical trials, it is very important to know the biological dose distributions at SOBP of carbon beams as well as physical dose distributions for clinical trials. These biological data were obtained by the use of five cell lines originated human carcinoma before starting the clinical trials. They were Hela S3 epitheloid carcinoma, HT1080 fibrosarcoma, T98 glioblastoma, HSGc-C5 salivary gland carcinoma and HK human keratinocytes. These cell lines cultured in vitro were irradiated by single dose of 290 MeV/u carbon beams with 6 cm width SOBP. The RBE for 10% cell survivals is depending on the cell lines, and ranging between 1.2 and 2.3 at proximal SOBP (40 keV/μ m) and increases between 2.0 and 2.7 at distal SOBP (82 keV/μ m). It was found that the biological dose of each point was uniformly distributed within the SOBP of 290 MeV/u carbon beams from these experiments. Normalizing the relative biological dose at entrance, a mean value within 6 cm SOBP was 1.9 and the data were in a range between 1.6 and 2.2, within 15% of the mean value. (Fig. 5)

RBE difference between single irradiation and multi-fractionated irradiation.

Biological doses for skin reaction at 42, 45, 48, 55, 65 and 80 keV/ m, which correspond to the edge of proximal SOBP, 1 cm downstream of proximal edge, 2 cm, 3 cm, 4 cm and 5 cm, respectively, were also calculated from figure and plotted against path of SOBP where we normalized physical doses to proximal SOBP.

As shown in Fig. 6, uniform distribution was obtained for skin reaction after fractionated irradiations, but not for single irradiations. The biological dose distribution for single irradiation was similar to physical dose distributions in such that biological dose of 2.0 at proximal SOBP decreased down to 1.7 at distal SOBP (i.e., 1 cm upstream of distal fall off). The fractionated irradiation experiments have been done not only for isoeffect dose of skin dry desquamation but also that of skin shrinkage. The distributions of biological doses within SOBP were fairly uniform after fractionated irradiation or small dose per fraction for both experiments, however those were declined at mid through distal peaks after single irradiation or large dose per fraction.

Fractionated irradiations of heavy ion beams would improve dose localization. Normal tissue is irradiated by entrance with low LET, and may repair radiation damage more efficiently than tumors which are irradiated by high LET at SOBP. We have to continue these experiments until delivering the best fractionation for heavy ion treatment.

1) How many fractionation are the best for the treatment.
2) What inter-fractionation intervals are the best for.
3) Dependency for ions, LET, tumors, size and depth.

As no single method could answer all these questions at ones, it may be effective to start a research program to which several groups join and draw conclusions.

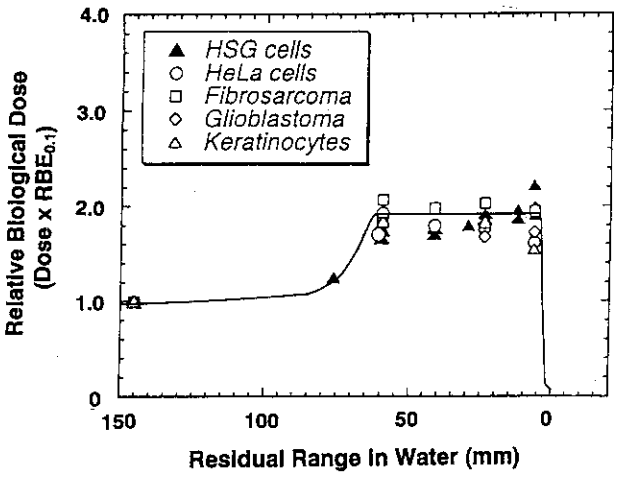

Fig. 5. Normalized biological dose distribution for 6 cm SOBP carbon 290 MeV/u beams.

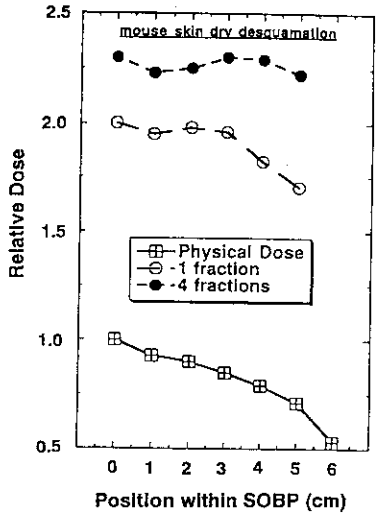

Fig. 6. Physical and biological dose distributions within 6 cm SOBP.

6. Future up-grade of HIMAC

As the future plan of HIMAC up-grade, we are considering the following items in near future:

1) Adding ECR ion source of 18 GHz for heavier particle acceleration than Ar.
2) Time-sharing acceleration of the different ion species from pulse to pulse by injector. This feature will make possible to allow plural groups to use different ions at same time.
3) Construction of the secondary beam lines.

Furthermore, we are intensively studying the developments of a fast extraction, of a junction line between upper and lower rings, and a synchrotron operation by a storage-ring mode. These future plans will be widely come up to the users requests.

References

[1] Kawachi K.: "HIMAC - A new start for heavy ions": Ion Beams in Tumor Therapy (ed. Linz U.) Chapman & Hall, Weinheim, p. 325-332 (1995)
[2] Yamada S. et.al.: "Present status of the medical accelerator HIMAC", JAERI-Conf 95-021, p. 5-7 (1995)
[3] Kanai T. et.al.: "HIMAC beam delivery system - Physical characteristics -", NIRS-M-103/HIMAC-008, p. 26-31 (1994)
[4] Matsufuji N. et.al.: "Beam quality measurements on heavy ion therapeutic beam of HIMAC", JAERI-Conf 95-021, p. 451-453 (1995)

2.4.6 Measurements and Analyses of effective delayed neutron fraction β eff

Takeshi SAKURAI and Tatsuo NEMOTO
Japan Atomic Energy Research Institute
Tokai-mura, Naka-gun, Ibaraki-ken 319-11
email sakurai@fca001.tokai.jaeri.go.jp

Measurements and analyses of effective delayed neutron fractions β eff, which is important as a scale of reactivity worth, were performed. The measurements were made by ^{252}Cf source technique at two assemblies of the MASURCA facility of CEA Cadarache : (a)a 30% enriched uranium core of R2 and (b) a 25% enriched MOX core of Zona2. The analyses of the measurements were made with JFS-3-J3.2 group constants set based on JENDL-3.2 nuclear data library. Calculation overestimated experimental β eff by more than 4% at the R2 core. On the other hand, the calculated value of β eff was in good agreement with the experimental one at the Zona2 core when Tomlinson delayed neutron yield set was used.

1. Introduction

The effective delayed neutron fraction β eff is an important parameter as a scale of reactivity worth of a nuclear reactor. A current uncertainty on prediction of β eff for a Fast Breeder Reactor(FBR) is estimated to be about $\pm 5\%(1\sigma)$ by French CEA group[1]. To reduce the uncertainty on β eff, an international β eff benchmark experiment, supported by OECD, was held at the MASURCA facility of CEA with participation of six organizations(six countries)[2]. In this paper, measurements and analyses of β eff by JAERI/FCA team at the R2 and Zona2 cores[3] are presented.

2. Cores at MASURCA facility

The R2 core[3] was fueled with 30% enriched uranium. The Zona2 core[3] was fueled with 25% enriched MOX fuel. Characteristics of these cores are summarized in Table 1. Two dimensional cylindrical model of these cores are shown in Fig.1.

3. Measurement

3.1 Measurement technique

Experimental values of β_{eff} were determined by a ^{252}Cf technique[4] as :

$$\beta_{eff} = \frac{S_{Cf}}{\rho_{Cf}\,\bar{\nu}\,R_f\,F}\left(\frac{\phi^{+}_{Cf}}{\phi^{+}_{f}}\right), \qquad (1)$$

where

ρ_{Cf} : the pseudo-reactivity in dollar unit due to emission of spontaneous fission neutrons from a ^{252}Cf source,

S_{Cf} : the source strength (n/s),

R_f : the fission rate of core material at the core center (/s cm^3),

$\bar{\nu}$: the averaged number of neutron emission per fission at the core center,

F : the normalization integral (cm^3) defined as :

$$F=\frac{\int dv\int dE\,\chi_f\phi^+\int dE\nu\Sigma_f\phi}{\int dE\,\chi_f\phi^+_{center}\int dE\nu\Sigma_f\phi_{center}}\ , \qquad (2)$$

$\left(\frac{\phi^+_{Cf}}{\phi^+_f}\right)$: the importance ratio of source neutrons to reactor fission neutrons.

The values of $\bar{\nu}$, F and $\left(\frac{\phi^+_{Cf}}{\phi^+_f}\right)$ are evaluated by a calculation. The value of $\left(\frac{\phi^+_{Cf}}{\phi^+_f}\right)$ usually becomes close to unity. A correction is applied to the calculated value of F.

3.2 Measured quantities

The pseudo-reactivity of the ^{252}Cf source was determined from an inverse kinetic method when the source was introduced into the core center through a radial penetration hole. The source strength was calibrated by a manganese bath technique at National Physical Laboratory in Great Britain.

The fission rate at the core center was measured by a foil activation technique with fission foils of ^{235}U, ^{238}U and ^{239}Pu. Calibrations of a γ-ray detector system were made by using the fission foils and absolute fission chambers[5] of ^{235}U, ^{238}U and ^{239}Pu. A minor contribution of higher plutonium isotopes and ^{241}Am to the central fission rates in the Zona2 core was estimated by a calculation.

3.3 Calculated quantities

The values of F , $\bar{\nu}$ and $\left(\frac{\phi^+_{Cf}}{\phi^+_f}\right)$ was calculated by a 70 energy group diffusion theory with a two dimensional cylindrical model and homogeneous atom densities. The group constants set of JFS-3-J3.2[6] were used.

The correction for F was obtained by a comparison of fission rates and fission importance distributions between calculation and measurement. A typical example of calculation to experiment ratios(C/E s) of the distributions is shown in Fig.2 for ^{239}Pu fission rate at the Zona2 core. Small discrepancies between calculation and measurement were observed near the boundary of core and blanket. The correction factors were deduced to be 1.015 and 1.002 at the R2 and Zona2 cores by taking account of these discrepancies.

4. Analysis

The values of β eff were calculated by the 70 energy group diffusion theory with the two dimensional cylindrical model and the homogeneous atom densities. The group constants set of JFS-3-J3.2 was used. Three delayed neutron yield sets of Keepin[7], Tomlinson[8] and JENDL3.2 were tested in the present analysis. In every case, delayed neutron emission spectra evaluated by Saphier[9] were adopted.

5. Results and discussions

The experimental values and the C/Es of β eff are given in Table 2. An experimental error of β eff was $\pm 3\%$. Components of the error are summarized in Table 3. Significant differences up to 9% between the delayed neutron yield sets were obtained in the calculated β eff of the Zona2 core as shown in Table 2. These large differences are caused by : (a) a large contribution of ^{238}U to β eff of this assembly as shown in Table 1 and (b) large differences of delayed neutron yield of ^{238}U between the delayed neutron yield sets as shown in Table 4. Good agreement between the calculated and the experimental β eff was obtained at the Zona2 core when the delayed neutron yield of ^{238}U evaluated by Tomlinson was used. On the other hand, the calculation overestimated the experimental β eff by more than 4% at the R2 core.

6. Conclusion

Measurements and analyses of β eff were performed by JAERI/FCA team at the two cores of the MASURCA facility. When Tomlinson delayed neutron yield set was used, the calculated β eff was in good agreement with the experimental one at the MOX core of Zona2. On the other hand, the experimental β eff at the uranium core of R2 was overestimated by the calculation with any of the three delayed neutron yield sets.

Acknowledgments

The authors are grateful to MASURCA staff for their support in the experiments. Thanks are also due to Mr. K. Kurosawa of JAERI for preparing some experimental devices and Mr. S. Okajima of JAERI for valuable discussions in preparing this document.

References

[1] Filip A. and D'Angelo A., : "ON THE MEASUREMENT OF THE DELAYED NEUTRON YIELDS IN "EFFECTIVE INFINITE" CRITICAL MEDIA," Proc. Topical Meeting on Advances in Reactor Physics (Charlestone, USA, 1992).

[2] Bertrand P., et al. : "THE BERNICE PROGRAM An international benchmark for the reduction of the delayed neutron fraction uncertainty," Proc. Topical Meeting on Advances in Reactor Physics (Knoxville, USA, 1994).

[3] Martini M., et al. : "NEACRP BENCHMARK MEASUREMENT AT MASURCA PROPOSAL FOR THE EXPERIMENT PROGRAM," NEACRP-A 1064 (1990).

[4] Fisher E. A., : "Integral Measurements of the Effective Delayed Neutron Fractions in the Fast Critical Assembly SNEAK," Nucl. Sci. Eng. 62, 105 (1977).

[5] Ōbu M. : "Preparation and Characteristics of Fission Chambers with Actinide Nuclides," JAERI-M 9757, (1981), (in Japanese).

[6] Takano H., et al. : "BENCHMARK TESTS OF JENDL-3.2 FOR THERMAL AND FAST REACTORS," Proc. Int. Conf. Nuclear Data for Science and Technology, (Gatlinburg, USA, 1994).

[7] Keepin G. R., : "PHYSICS OF NUCLEAR KINETICS," Addison-Wesley Publishing Company, inc.

[8] Tomlinson L., : "DELAYED NEUTRONS FROM FISSION A Compilation and evaluation of experimental data," AERE-R-6993, (1972).

[9] Saphier D., et al. : " Evaluated Delayed Neutron Spectra and Their Importance in Reactor Calculations," Nucl. Sci. Eng. 62, 660 (1977).

Table 1 Main characteristics of the β eff cores at the MASURCA facility[3]

Core	R2	Zona2
Core volume	455 litter	482 litter
Fuel	U metal	PuO_2-UO_2
Fuel enrichment	30 %	25 %
Moderator	Sodium	Sodium
Breakdown of β eff by isotope *		
^{235}U	77%	2%
^{238}U	23%	48%
^{239}Pu		43%
^{240}Pu		4%
^{241}Pu		3%
^{241}Am		0.2%

* Calculated results by JAERI.

Table 2 Comparison between experimental and calculated β eff by JAERI/FCA team at MASURCA

Core		R2	Zona2
Expt.		697 pcm ±3%	346 pcm ±3%
C/E	Keepin*	1.04	0.95
	Tomlison**	1.05	0.99
	JENDL3.2***	1.07	1.04

** Calculated results by using Keepin delayed neutron yields
* * Calculated results by using Tomlinson delayed neutron yields
* ** Calculated results by using JENDL3.2 delayed neutron yields

Table 3 Components of the experimental errors (1 σ)

Component	Error
Neutron emission rate of ^{252}Cf source	±0.7%
Pseudo reactivity worth due to ^{252}Cf source neutrons	±2.0%
Fission rate at the core center	±1.5%
Normalization integral	±1.5%
β eff total	±3%

Table 4 Evaluated delayed neutron yield per fission

Delayed neutron yield set	^{235}U	^{238}U	^{239}Pu
Keepin	0.0165	0.0412	0.0063
Tomlinson	0.0165	0.044	0.00639
JENDL3.2	0.0165	0.0481*	0.00641**

* evaluation based on Evance(1973) and Tuttle(1975)
** evaluation mainly based on Tuttle(1979)

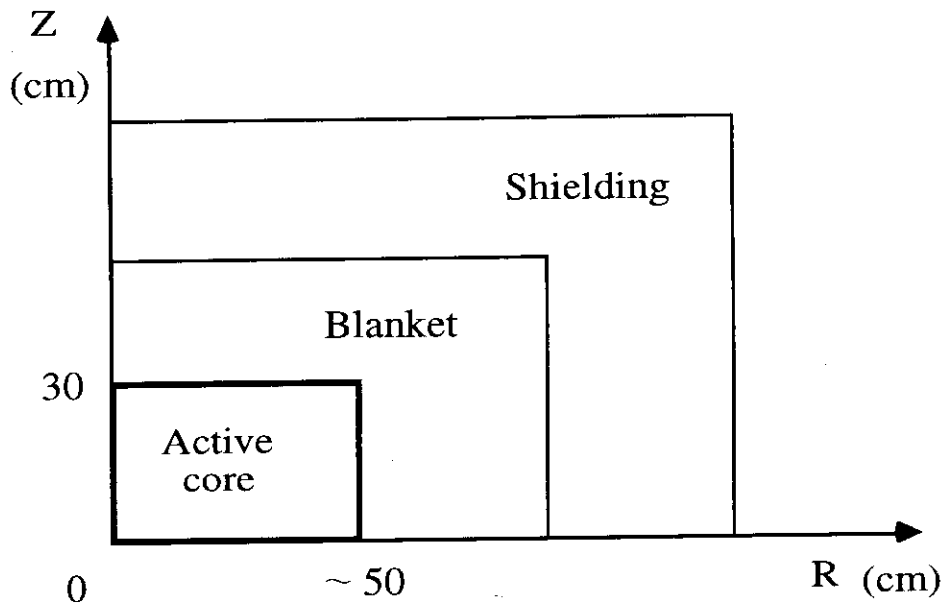

Fig.1 Two dimensional cylindrical model of the MASURCA cores

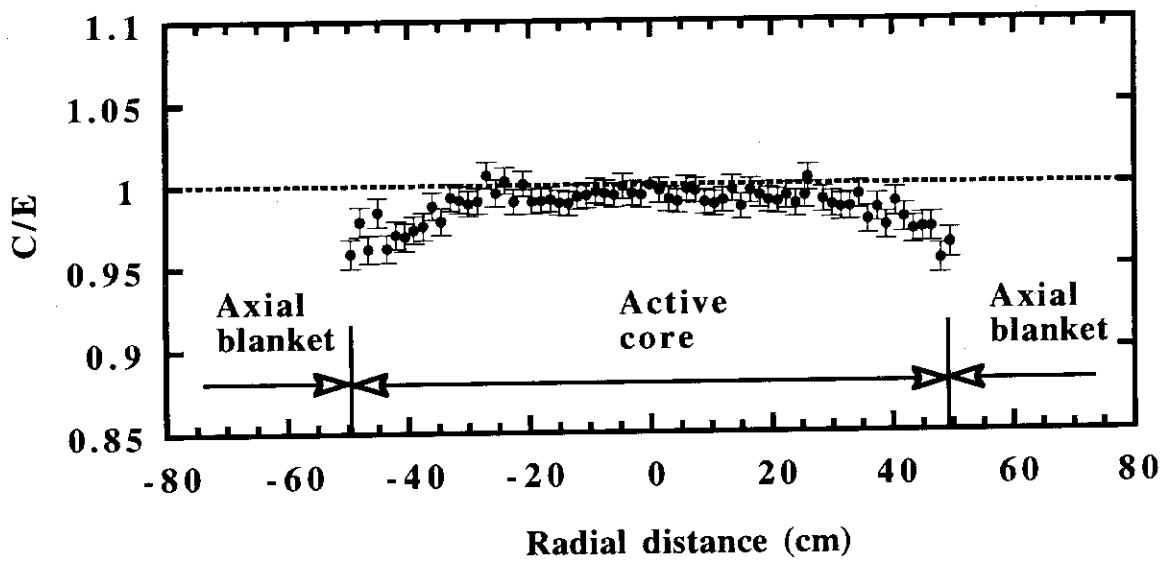

Fig.2 Radial C/E distribution of ^{239}Pu fission rate at the MASURCA Zona2 core

2.4.7 Status of Neutron Induced α-production Cross Section Data

Mamoru BABA

Department of Nuclear Engineering, Tohoku University
Aoba-ku, Sendai 980-77, Japan
E-mail: baba@rpl.nucle.tohoku.ac.jp

Recent progress in experimental techniques and the data status are reviewed on neutron-induced α-production cross sections.

1. Introduction

Neutron induced α-production reactions play a crucial role in radiation damage, nuclear heating and biological effects by fast neurons. For assessment of the effects, therefore, detailed knowledge is required on neutron-induced α-production cross sections and the energy-angular distributions (DDX) of α-particles.

However, experimental (n,xα) data were scanty and discrepant each other, because direct α-particle detection is difficult and the conventional activation technique is applicable only in limited cases [1]. Further, theoretical prediction is very uncertain because calculation results are very sensitive to the level density parameters and formula, and the optical model potentials (OMP) which are not known well for α-emission channels [2]. As a consequence, as shown in Fig.1, there are large discrepancies among evaluations even for major structural elements, Fe, Cr and Ni. Therefore, new experimental data had been required to improve the accuracy of (n,xα) cross section data.

To improve the situation, new experimental programs on (n,xα) reactions were initiated at several laboratories during recent years, and the IAEA Coordinated Research Program (CRP) was organized in 1992 to facilitate cooperative research in measurements, theoretical calculations and evaluations of neutron-induced α-production cross sections of fusion reactor structural elements, Fe, Cr and Ni [1,3]. The first CRP meeting (Research Coordination Meeting: RCM) was held in Debrecen, October 1992, the second RCM in Beijing, China, November 1994, and the third (final) RCM in Sendai, September 1995, and summarized the progress and the data status.

Owing to the efforts, various experimental data have been obtained recently by newly developed α-spectrometers, and the update of the helium accumulation and activation methods. Cooperated with theoretical and evaluation works under CRP, the data status and the knowledge on α-production reactions gained a great progress although works are expected still to be continued and extended.

This paper presents a brief review on 1)recent experimental development, 2)the data status and 3)expected future works on neutron-induced α-production reactions, mainly on the basis of the results reported in the RCMs. The summary report and proceedings of the 3rd RCM will be published from IAEA.

2. Progress in experimental techniques for (n,xα) reactions

2.1 Large solid angle spectrometers

An α-spectrometer having a very large solid angle has been developed at Tohoku University [4-6], IPPE Obninsk [7] and other laboratories using a gridded-ionization-chamber (GIC). Figure 2

illustrates GIC developed at Tohoku University. A sample foil in the central cathode plate is bombarded by a collimated neutron beam, and α-particles are detected with an almost 4π geometry. Provided that α-particles from the sample are stopped by a counting gas before reaching the grid, the anode signal *Pa* and the cathode signal *Pc* are given by $Pa=E+\sigma Pc\approx E$, and $Pc=E\ (1-\overline{x}/d\cdot\cos\theta)$, respectively [4,7], where, *E* is the particle energy, *d* is the cathode-grid distance (2.7 cm), θ is the emission angle, σ is the grid inefficiency (5.9%), and $\overline{x}$ is the distance from the cathode to the center of gravity of the ionization trace. Three signals from the central cathode and two anodes are gathered concurrently by using a three parameter data acquisition system. Besides, α-particles are selected by adjusting the gas pressure [4]. By the way, DDX data can be obtained with a very high efficiency.

The present GIC has novel features to apply to the fast neutron induced reactions, i.e., a high stopping power, a low background production rate and a sample changing mechanism [4], and enabled systematic measurements of (n,xα) DDXs of Fe, ^{nat}Ni, ^{58}Ni, Cu and ^{50}Cr in the neutron energy range from "threshold" to 14 MeV [5,6,8] (Fig.4) using monoenergy neutron beams. Details of the spectrometer and the experimental method are described in Ref.4-6.

Figures 3 and 4 show examples of angle-integrated α-spectra and (n,xα) cross section data, respectively, obtained by GIC. For these measurements, metallic foils around 3 μm thick were used. The very high efficiency of GIC allowed experiments with much thinner samples (ex. down to 0.4 μm) and source neutrons with a low energy spread (≤ 120 keV) [7,8]. Such experiments enabled to resolve α-particles to each residual state (Fig.5), and provided excitation functions for each α_0, α_1, $\alpha_{i\geq 2}$ which will be useful to asses the validity of OMP through the comparison with calculations [8].

At present, however, GIC is difficult to apply to breakup reactions and neutrons higher than ~20 MeV because of limited stooping power of the counting gas.

2.2 Wide range ΔE-E telescope

A wide range α-spectrometer was newly developed at LANL [9]. Combined with a wide range spallation neutron source at LAMPF/WNR, it provides new systematic (n,xα) DDX data up to 30 MeV or higher from a "threshold" at a few MeV. Figure 6 illustrates a schematic view of the spectrometer and the experimental arrangement. Four telescopes are employed to obtain the data at four angles concurrently.

The spectrometer is a ΔE-E counter telescope consisting of a low pressure proportional ΔE counter and a Si E detector, 500 μm thick and 450 mm^2 wide. The proportional counter has a thin entrance window of Mylar, ~ 1.5 μm thick, and operated at a pressure of 1~3 kPa of Ar or Xe + 10% CO_2. This configuration enables to detect α-particles down to a few MeV. Thus, almost all the α-particles emitted in (n,xα) reactions are detected even for light elements like carbon. Experiments have been done for several elements from light to medium weight nuclei [9-11].

Figures 7 and 8 show, respectively, the α-emission spectra from carbon *vs* the neutron energy and the angular distributions of α-particles of ^{59}Co in comparison with the calculation using GNASH. The spectrometer is expected to be applicable up to 50 MeV or higher. At present, measurements are done only for α-particles.

A similar charged particle spectrometer is under development at Tohoku University to study (n,xα) reactions at ten's MeV region. The spectrometer will detect not only α-particles but also hydrogen isotopes by making the particle identification with a combination of the ΔE-E method and the pulse shape analysis method [12].

A multiple-counter telescope at Geel (Fig.9) was also extended to permit simultaneous measurements of α-particles and protons [13]. It provided DDX data for (n,xα) and (n,xp) reactions of structural elements in 5 to 14 MeV region.

2.3 New measurements by helium-accumulation and activation methods

A helium counting system was improved and applied to new measurements. As shown in Table 1, the (n,xα) cross sections have been obtained by the method for iron and nickel isotopes at 10 MeV using the H(t,n) neutron source [14], and Al, Si around 14 MeV [15].

New (n,xα) cross section data have been obtained by the activation technique in the neutron energy range between 8 and 14 MeV (Debrecen/Jeulich [16], JAERI [17]), above 15 MeV (JAERI, Tohoku Univ.[18]), and for reactions with small cross sections around 14 MeV (JAERI, Debrecen). As listed in Table 1, data have been obtained for various nuclei from light to heavy elements. Besides, the $^{16}O(n,\alpha_1\gamma)$ reaction cross section was measured by counting γ-rays. This technique will be useful also for other reactions.

3. Data status of (n,xα) cross section

Owing to the technical development described above, the experimental data base has been improved markedly during the recent years. In Table 1, recent experimental results are presented. Figure 10 shows the $^{56}Fe(n,x\alpha)$ cross sections. Recent experimental data by direct α-detection at LANL (Haight 94), Tohoku (Baba) and by helium-accumulation (Haight & Vonach) are in good agreement. Based on these experimental data, H.Vonach has made a new evaluation using the least-squares code GLUCS, and concluded that the cross sections have been determined within ±5 % [16]. Similarly, fair agreement is seen for ^{58}Ni and Ni data among LANL (preliminary), Tohoku and Geel measurements although the Obninsk data [7] are smaller. A new evaluation will be done for Ni. For Cr isotopes, however, new data are available only for ^{50}Cr (fig.4), and the data for the major isotope ^{52}Cr is still an open question because of difficulty in sample preparation. In the third RCM, therefore, experiments on ^{52}Cr were strongly recommended.

In the theoretical field, the effects of OMP and the level density parameter and formula were studied numerically [20], and new calculations were performed up to 50 MeV [21]. The survey calculation revealed that the shape of (n,xα) excitation functions depend mainly on the level density and the magnitude on OMP, and calculated cross sections may differ up to factor two according to a level density formula. Figure 11 shows calculation by Yamamuro using the SINCROS code system [21]. The calculation will be compared with the experimental data at LANL and others.

4. Future work

As noted above, the data base of neutron induced α-production cross sections has improved greatly during the recent years, and seems to be adequate for Fe and Ni. Nevertheless, some works are still ongoing and new works are expected with an extended scope.

In the summary of the third RCM, the followings were recommended.

(1) measurement for ^{52}Cr, ^{nat}Cr,
(2) extension of measurements to lighter elements, C, N, O, Si etc, and
(3) to higher energies up to GeV (for space technology, accelerator application),
(4) organization of Advisory Group Meeting (AGM) around 1997 Nuclear Data conference for discussion and summary of ongoing works.

References:

1)H.Vonach, S.Chiba, A.Pashchenko: *Proc.Int.Conf. on Nuclear Data for Sci.Technol.*, (Gatlinburg, 1994) p.925

2)V.A. Konshin and O.V.Konshin: *Proc.Int.Conf. on Nuclear Data for Sci.Technol.*, (Jeulich, 1992) p.877

3)A.Pashchenko (Ed.): INDC(NDS)-273 (IAEA 1993), INDC(NDS)-323 (IAEA 1995)

4)N.Ito et al.: *Nucl.Instrum.Methods* A337 474 (1994)
5)M.Baba et al.: *Ref.*1, p.941
6)M.Baba et al.: *J.Nucl.Sci.Technol.*, 31(7) 745 (1994), 3rd RCM
7)A.Goverdovski et al.: *Ref.*1, p.117
8)T.Sanami et al.: this proceedings
9)R.Haight et al.: 3rd RCM* and *Ref.*1, p.154, p.311
10)S.M.Sterbenz et al.: *Ref.*1, p.314
11)F.Goeckkner et al.: *Ref.*1, p.318
12)Y.Nauchi et al.: this proceedings
13)C.Tsabaris, E.Wattecamps, G.Rollin: 3rd RCM* and *Ref.*1, p.282
14)R.Haight et al.: *Ref.*1, p.275
15)Y.Takao et al.: 3rd RCM and *Ref.*1, p.929
16)G.Csikai et al.: 3rd RCM*
17)S.Chiba et al.: 2nd & 3rd RCM*
18)S.Iwasaki et al.: 3rd RCM*
19)H.Vonach: 2nd RCM*, and *Ref.1*
20)C.Y.Fu et al: 2nd & 3rd RCM*
21)N.Yamamuro: 3rd RCM* and private communication

* IAEA 3rd Research Coordination Meeting

Table 1 Recent experimental data on (n,xα) cross sections

1)Direct α measurements	
· ^{59}Co, ^{58}Ni, ^{60}Ni DDXs	@ <30 MeV; LANL
· ^{58}Ni, ^{nat}Ni high-resolution DDXs	@ 4.5-11.5 MeV; Tohoku Univ., IPPE
· ^{58}Ni	@ 5-14 MeV; Geel
2)He-accumulation measurements	
· ^{56}Fe, Fe, ^{58}Ni, ^{60}Ni, Ni	@ En=10 MeV; LANL
· Al, ^{nat}Si;	@ En~14 MeV; Kyushu Univ.,
3)Activation measurements	
· ^{45}Sc, ^{63}Cu, ^{65}Cu, ^{208}Pb	@~14 MeV; Debrecen
· ^{90}Zr, ^{51}V, ^{89}Y	@ 6.8-13.8 MeV; Debrecen
· ^{59}Co, ^{93}Nb	@ 12.0-20 MeV; Tohoku Univ.,
· ^{17}O, ^{18}O, ^{19}F, ^{23}Na, ^{35}Cl, ^{37}Cl, ^{55}Mn, ^{89}Y	@ 13.4-14.9 MeV; JAERI

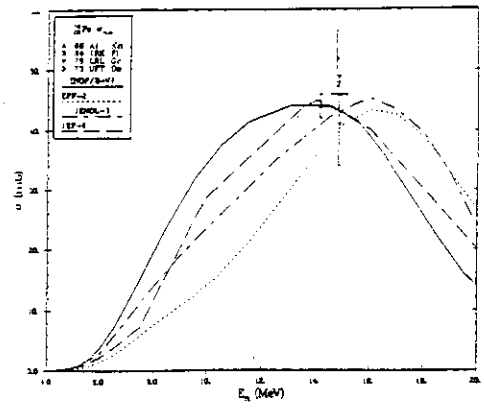

Fig.1: Evaluated data for $^{56}Fe(n,x\alpha)$ [1].

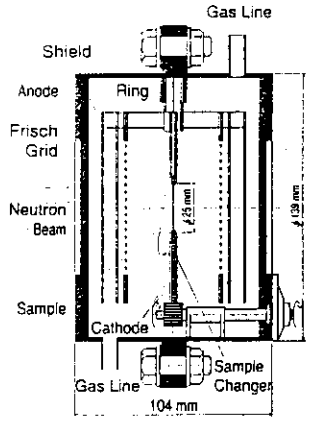

Fig.2: Schematic view of GIC [4]

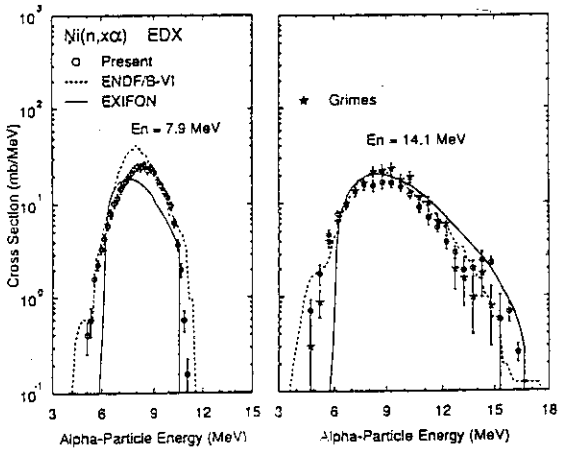

Fig.3: Emission spectra of Ni(n,xα) [5,6]

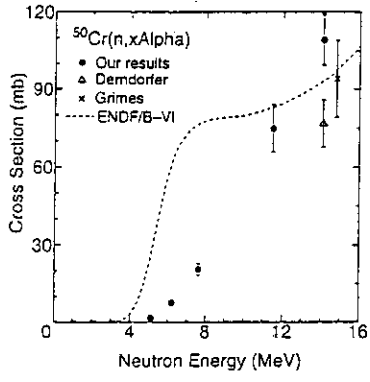

Fig.4: $^{50}Cr(n,x\alpha)$ cross section [5]

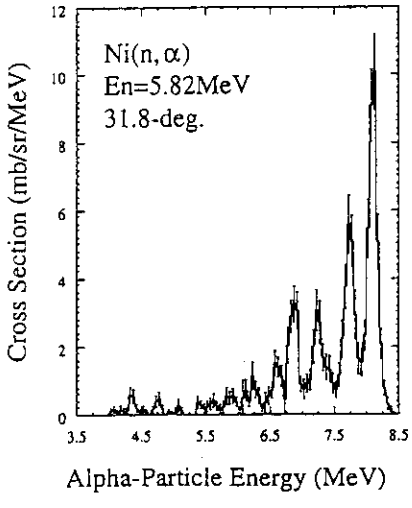

Fig.5: DDX of Ni(n,α) [8]

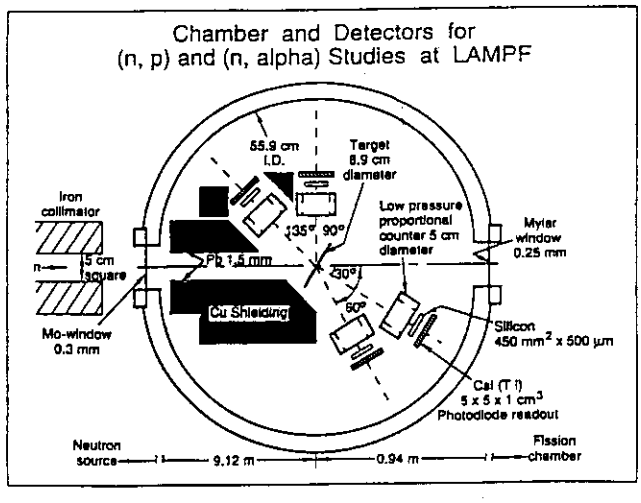

Fig.6: Experimental setup of LANL multi-telescope [9]

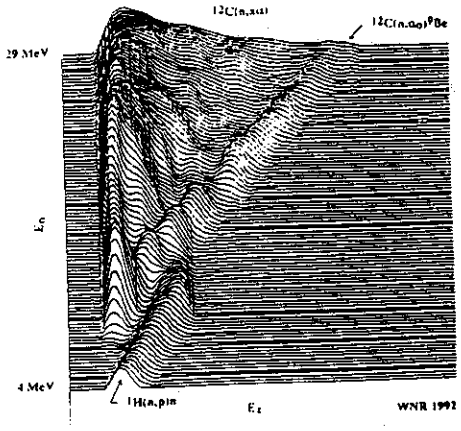

Fig.7: α-spectra *vs* incident energy for carbon [9]

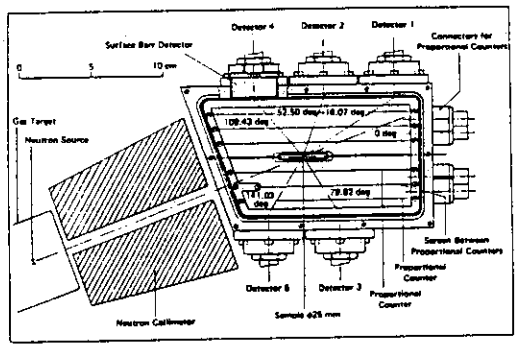

Fig.9: Multiple counter-telescope at Geel [11]

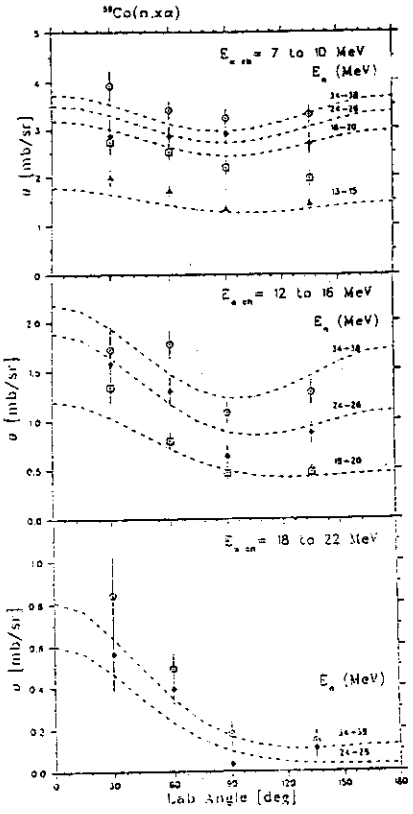

Fig.8: Angular distributions of $^{59}Co(n,x\alpha)$ [9]

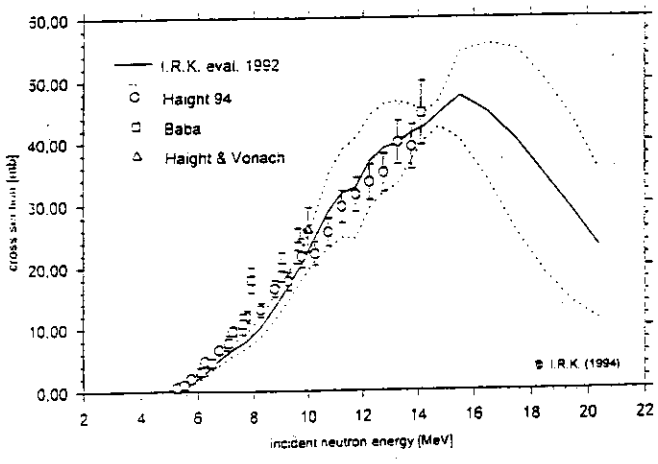

Fig.10: $^{56}Fe(n,x\alpha)$ cross section [19]

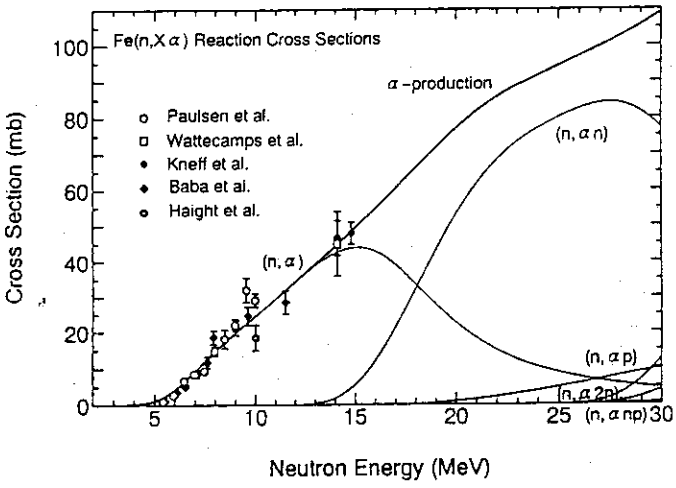

Fig.11: $^{56}Fe(n,x\alpha)$ cross section calculated by Yamamuro [21]

2.4.8 The First Data of Double Differential Cross-section of $^{12}C(p,p')$ at 300MeV with a Stacked NaI(Tl) Spectrometer

Hiroki MUROHKA[1], Hiroki YOSHIDA, Osamu IWAMOTO, Yusuke UOZUMI,
Akihiro NOHTOMI, Takeji SAKAE, Masaru MATOBA
Takashi MAKI+, Norihiko KOORI++
Dep. of Nuclear Engineering, Kyushu University, Fukuoka 812, Japan.
+School of Nursing and Technology, University of Occupational
and Environmental Health, Kitakyushu 807, Japan.
++Faculty of Integrated Arts and Sciences, the University
of Tokushima, Tokushima 770, Japan.

A stacked NaI(Tl) spectrometer is developed to study the pre-equilibrium process in intermediate energy. Detector tests were performed using 300 and 350MeV proton beams from the ring cyclotron at the Research Center for Nuclear Physics(RCNP), Osaka university. The ΔE-E technique is applied to identify particles and nuclear reactions in the detector materials. The tail in peak spectrum is suppressed clearly and the peak efficiency is reasonably estimated with a monochromatic energy particle.

The first and preliminary data of double differential cross section of $^{12}C(p,p')$ at 300MeV are obtained.

I. INTRODUCTION

In recent years, wide continuous spectra of charged particle reactions for intermediate energy are investigated to understand the feature of the reaction mechanism from low to high energy transition region. Systematic studies of (p,p'x) reactions are carried out below 200MeV, and there are a few data and some calculations of (p,nx) reaction at GeV energy region[1]-[3].

It is desired to measure continuous spectra of charged particle reactions from pre-equilibrium process in intermediate energy region. A wide energy acceptance spectrometer is required to realize this measurement. The stacked NaI(Tl) spectrometer is developed for this aim. In the present work, the results of the performance test and the first data of double differential cross section of $^{12}C(p,p')$ at 300MeV are reported.

II. EXPERIMENTAL DETAILS

A schematic diagram of the the stacked spectrometer is shown in Fig.1. It consists of two thin silicon detectors, 4 rectangular NaI(Tl) scintillators (2"×2"×2"), and a cylindrical NaI(Tl) scintillator (ϕ8cm×18cm). All detectors were set in line. The overall material thickness of 38cm is enough to stop protons up to about 400MeV. Two thin silicon detectors of 150μm and 300μm thick were placed in front of the NaI(Tl) crystals and each of silicon detectors has a effective area of 300mm^2.

[1] murooka@mars.nucl.kyushu-u.ac.jp

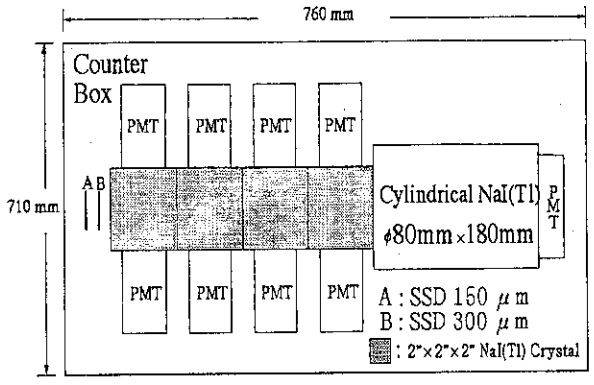

Fig.1 A schematic diagram of the stacked NaI(Tl) spectrometer is shown.

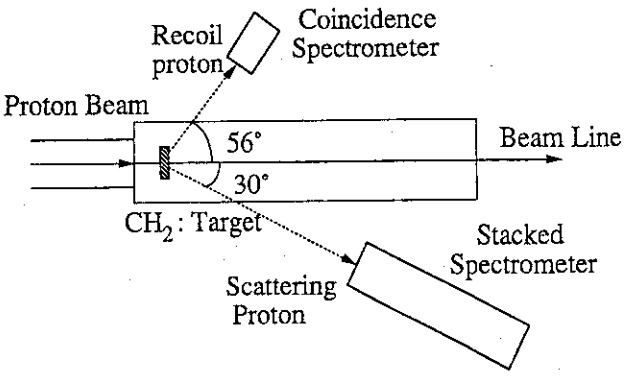

Fig.2 A typical arrangement is shown.

Each rectangular NaI(Tl) crystal is framed in 1mm thick aluminum vessel. It has two optical windows(top and bottom) which are packaged with pyrex film of 4mm thick. Two photo-multipliers(PMT: Hamamatsu R329-02) are attached to these optical windows. All optical contacts are kept with optical grease(OKEN 6262A). Between adjacent NaI(Tl) crystals, there exists a dead layer which consists of 100μm thick aluminum isolation foil and 6mm air gap. The last cylindrical NaI(Tl) crystal has an optical contact with photo-multipliers(PMT: Hamamatsu R1307) at the end of the crystal. The detector tests were performed using 300MeV and 350MeV[4] proton beams from the ring cyclotron at RCNP. A 1.2mm thick polyethylene(CH_2) was used as a target.

The stacked NaI(Tl) spectrometer was set in the way that its axis was directed along lines from 30° to 70° with angular step 10° and its front face was set at distance with about 80cm from the target. Typical arrangement of this spectrometer is shown in Fig.2.

As the performance test of the spectrometer, pp scattering events were measured. In this test, a coincidence spectrometer which consists of two thin silicon detectors of 150μm and 300μm thick and a rectangular NaI(Tl) scintillator with a PMT was arranged. Thus, quasi-monochromatic proton events could be detected. Coincidence signals between two silicon detectors and first NaI(Tl) scintillator in the stacked spectrometer were used as a gate signal for data acquisition system. The shaping time of each amplifier was set to 1μsec.

Energies of measured protons from pp elastic scattering were 215MeV, 115MeV, 64MeV, 22MeV at 300MeV incident energy and 250MeV, 160MeV at 350MeV incident energy.

For $^{12}C(p,p'x)$ measurements, coincidence signal from the coincidence spectrometer was removed.

III. EXPERIMENTAL RESULTS AND DISCUSSION

The energy calibration was performed using maximum energy loss for protons in each rectangular NaI(Tl) crystal from $^{12}C(p,p'x)$ reaction which corresponds to 122MeV and also the full energy peak of pp scattering protons for each angle.

To check the performance of this spectrometer, pp scattering protons were measured. Every events can be identified as events of full energy loss or of nuclear reactions using the ΔE-E technique[5]-[6]. Parameter E is the full energy of the particle and ΔE is the energy loss in the first scintillators.

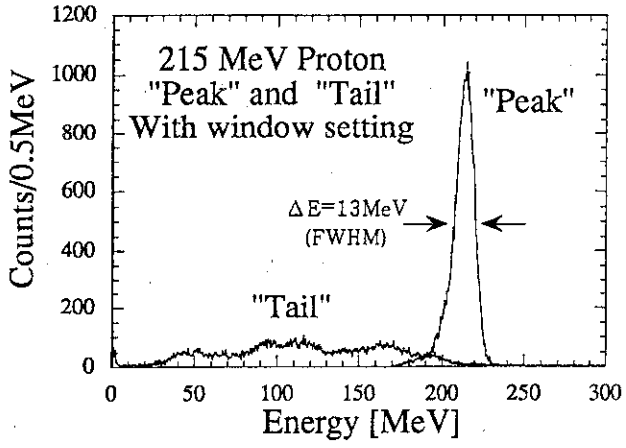

Fig.3 A typical spectrum at 215MeV protons from pp scattering is shown.

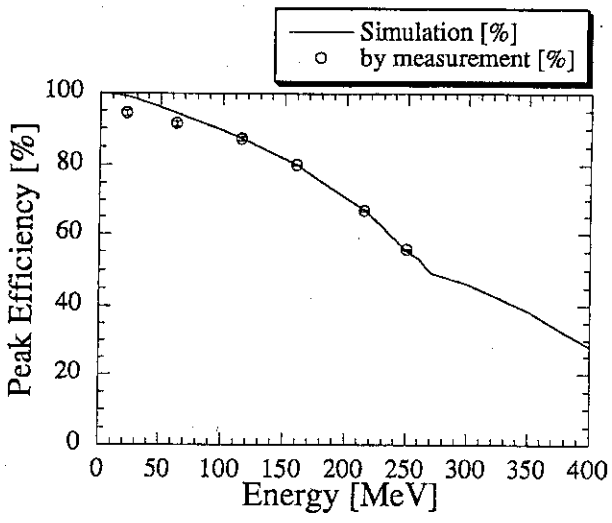

Fig.4 The peak efficiency at 22, 64, 115, 160, 215, 250MeV. The ±3 window setting for the particle identification spectrum is applied. Each error is within 0.7%.

The particle identification parameter 'P' [7]−[8] is defined as,

$$P = [E^b - (E - \Delta E)^b]/n \tag{1}$$

Here the parameter b is almost constant and is set to a value of 1.73 for proton. The parameter n is the number of the n-th scintillator as ΔE detectors.

Since the peak in a particle identification spectrum corresponds to protons of full energy, the Gaussian shape fitting can be applied. The window setting was set by a Gaussian shape fitting to the particle identification spectrum.

A typical spectrum is shown in Fig.3 together with two spectra of "peak" and "tail". The "best" spectrum is obtained in near $\pm\sigma 3$ window setting. In this result, the peak efficiency is estimated reasonably using these results. The peak efficiency was 67% at 215MeV proton in $\pm\sigma 3$ window setting, and energy resolution was about 6%.

By using above procedure, elastically scattered protons are clearly distinguished the events from nuclear reactions, and tail events in energy spectrum are completely suppressed.

Figure 4 represents the peak efficiency obtained in previous experiments. Points shows experimental results, and a line shows a result of a MonteCarlo simulation[9]−[10]. The results of MonteCarlo simulation are almost same as the experimental results.

To get ^{12}C(p,p') events, ^{12}C(p,p'x) events were measured. By using above particle identification technique, proton events were clearly selected. This ^{12}C(p,p') spectrum was degraded with pp-scattering events. To remove the pp scattering events, previous pp scattering results were applied. Subtract pp scattering events from ^{12}C(p,p') events which degraded with pp scattering events adjusting beam integration values. Using above procedures, events from ^{12}C(p,p') are clearly obtained. Obtained spectra from ^{12}C(p,p') is corrected with the peak efficiency. Applying these procedure, the first and preliminary data of double differential cross-section ^{12}C(p,p') are obtained at θ_L=30°, θ_L=40° and θ_L=50°.

The analysis for this double differential cross section is discussed with Kalbach's systematic study. The result of its calculation is shown in Fig.5. The point shows the results of ^{12}C(p,p') measurements, the its calculation results is shown in dashed lines. Because of a connection problem between each crystal, the spectrum of ^{12}C(p,p') is distorted around connection points of adjacent crystals or lost in high energy region.

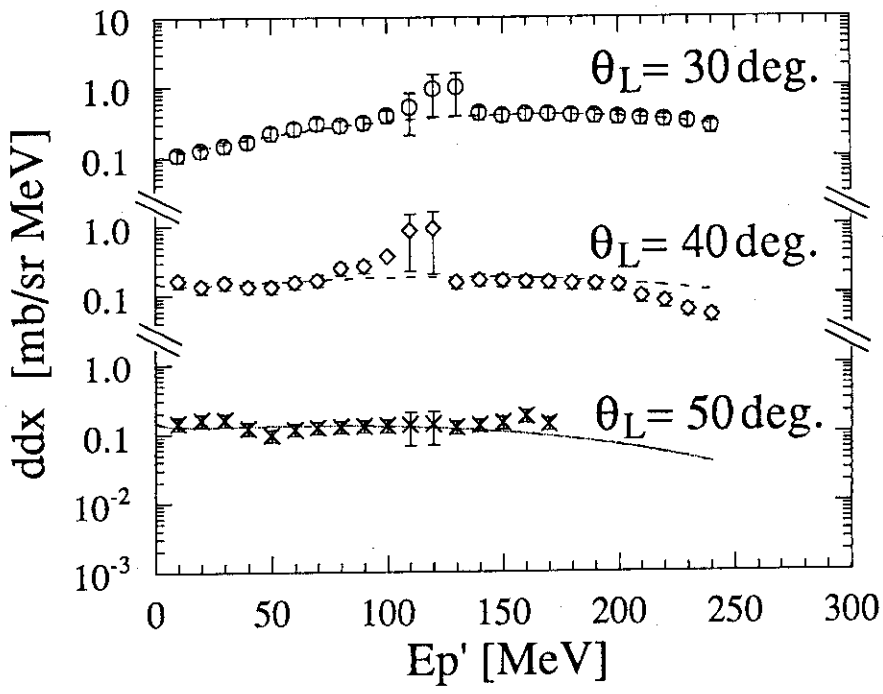

Figure 5: The double differential cross-section of ^{12}C(p,p') at θ_L = 30°,40° and 50° at 300MeV proton beam are shown.The point shows the results of measurements, the results of Kalbach's systematic calculation is shown in dashed lines.

IV. CONCLUSION

A stacked NaI(Tl) spectrometer for intermediate energy is developed to detect charged particles up to about 400MeV. By using the ΔE-E technique, it is easy to suppress tail events which come from nuclear reactions in the detector materials. In this results, a beautiful peak spectrum is obtained and the peak efficiency was reasonably estimated.

The experimental results of peak efficiency are almost same as the results of MonteCarlo simulation. The energy resolution of the stacked NaI(Tl) spectrometer is about 6%.

By using this technique and results of pp scattering measurement, ^{12}C(p,p') events which are corrected with peak efficiency are obtained,

In previous detector tests with intermediate energy protons, it is confirmed that the stacked spectrometer is quite useful to register intermediate energy charged particle, and the first and preliminary double differential cross-section data are obtained at θ_L = 30°, 40° and 50°.

V. ACKNOWLEDGEMENT

We are grateful to the staff of Research Center for Nuclear Physics(RCNP), Osaka University, for support of the experiments at the cyclotron facility. This work was performed at the RCNP under programs E44 and E75.

REFERENCES

[1] S.V.Förtsch,A.A.Cowley,J.V.Pilcher,D.M.Whittal,J.J.Jawrie,J.C.Van Staden,E.Friedl, Nuclear Physics A485,pp258,(1988)

[2] H.Feshbach, A.Kerman, S.Koonin,Ann. Phy. 125, pp429, (1980)

[3] W.A.Richer, A.A.Cowley, G.C.Hillhouse,J.A.Stander, J.W.Koen, S.W.Steyn, R.Lindsay, R.E.Julies, J.J.Lawrie, J.V.Pilcher, Phy. Rev. C49, pp1001, (1994)

[4] Y.Uozumi, M.Yamashita, H.Matsumoto, B.Sutomo, O.Iwamoto, A.Nohtomi, T.Sakae, M.Matoba, T.Maki, N.Koori, RCNP ANNUAL REPORT 1993, pp157

[5] M.Makino, R.Eisberg, D.Ingham and C.Waddell, Nucl. Inst. and Meth.80pp299, (1970)

[6] R.Eisberg, M.Makino, R.Cole, C.N.Waddell, M.Baker, J.J.Jarmer, D.M.Lee, P. Thompson, Nucl. Inst. and Meth. 146,pp487-495,(1977)

[7] C.A.Goulding, J.G.Rogers Nucl. Inst. and Meth. 153, pp511, (1978)

[8] J.M.Cameron,P.Kitching,R.H.Mccamis,C.A.Miller,G.A.Moss,J.G.Rogers,G.Roy,A.W. Stetz,C.A.Goulding,W.T.H. van Ores, Nucl. Inst. and Meth. 143,pp399, (1977)

[9] M.Yamashita, Y.Uozumi, H.Matsumoto, B.Sutomo, O.Iwamoto, A.Nohtomi, T.Sakae, M.Matoba, T.Maki, N.Koor, Prceedings of the Fifth Workshop on Topics in Nuclear Radiation Detection, pp167, (1994)

[10] H.Murohka, H.Yoshida, O.Iwamoto, A.Nohtomi, Y.Uozumi, T.Sakae, M.Matoba, T.Maki,N.Koori, KEK Prceedings of the 9th Workshop on Radiation Detectors and Their Uses pp169, (1995)

3. Papers Presented at Poster Session

3.1 Measurement of Fission Cross Section with Pure Am-241 Sample using Lead Slowing-Down Spectrometer

Katsuhei Kobayashi[1], Mitsuharu Miyoshi[2], Shuji Yamamoto[1], Yoshiaki Fujita[1], Itsuro Kimura[2], Ikuo Kanno[2], Satoshi Kanazawa[2] and Nobuo Shinohara[3]

1 Research Reactor Institute, Kyoto University
Kumatori-cho, Sennan-gun, Osaka 590-04, Japan
2 Department of Nuclear Engineering, Kyoto University
Yoshidahonmachi, Sakyo-ku, Kyoto 606-01, Japan
3 Isotope Products Laboratory, Japan Atomic Energy Research Institute
Tokai-mura, Naka-gun, Ibaraki 319-11, Japan

By making use of back-to-back type double fission chambers and a lead slowing-down spectrometer coupled to an electron linear accelerator, the fission cross section of ^{241}Am was measured relative to that of ^{235}U in the energy region from 0.1 eV to 10 keV. The measured result has been compared with (1) the evaluated nuclear data files, JENDL-3.2 and ENDF/B-VI and with (2) the existing experimental data by Dabbs et al., whose evaluated and measured data were broadened by the energy resolution function of the spectrometer. Slight discrepancies have been found between the evaluated data and the present measurement at energies of the dip and bump cross section regions. The JENDL-3.2 data are underestimated between 22 and 140 eV by 1.2 to 2.3 times, while the ENDF/B-VI and the Dabbs data are in general agreement with the measurement.

1. Introduction

Americium-241 is one of the minor actinides which are abundantly produced in light water reactors. The nuclear data for ^{241}Am are of interest in reactor design and for the system design of spent fuel reprocessing and waste disposal. The fission cross section of ^{241}Am is also of great importance for transmutation of the burdensome actinides[1,2].

Numerous measurements of the fission cross section of ^{241}Am have been made previously and often confronted with the difficulty by the extremely large alpha-particle activity due to its short half-life of 432 years as alpha-decay. In addition, the fission cross section of ^{241}Am is relatively low (0.02 to 0.5 b) over the neutron energy range between 100 eV and 300 keV. Several groups have measured the fission cross section below about 100 keV[3-9]. However, marked discrepancy can be seen between the data there, although the data measured at MeV energies show good agreement with each other[10]. Two newly evaluated data files of JENDL-3.2[11] and ENDF/ B-VI[12], which may mainly refer to the experimental data by Dabbs et al.[9], are in disagreement with the earlier data by Bowman et al.[4], Seeger et al.[6] and Gayther et al.[8] in the energy region above about 30 eV.

In the present measurement, the fission cross section for the ^{241}Am(n,f) reaction is measured

relative to that for ^{235}U by making use of back-to-back type double fission chambers and a lead slowing-down spectrometer coupled to 46 MeV electron linear accelerator (linac) of Research Reactor Institute, Kyoto University (KURRI). The experimental technique is the same as that of the fission cross section measurement of ^{237}Np[13]. The measured result is compared with the evaluated data in JENDL-3.2 and ENDF/B-VI, and with the existing experimental data.

2. Experimental Methods

2.1. Lead Slowing-down Spectrometer

The lead slowing-down spectrometer was recently installed coupling to the 46 MeV electron linear accelerator (linac) at Research Reactor Institute, Kyoto University (KURRI). The Kyoto University Lead Slowing-down Spectrometer (KULS) is composed of 1600 pieces of lead blocks (each size : 10x20x20 cm^3, and purity : 99.9 %) and these are piled up to make a cube of 1.5x1.5x1.5 m^3 (about 40 tons) without any structural materials[14], as seen in Fig. 1. At the center of the KULS, we have set an air-cooled photoneutron target of Ta to generate pulsed fast neutrons. Thermocouples were attached on the surface of the target case to monitor the temperature. The linac was operated to keep the temperature less than 300 °C. The KULS has eight experimental/irradiation holes (10x10 cm^2, 55 or 45 cm in depth), and one of the holes is covered by bismuth layers of 10 to 15 cm in thickness to shield high energy gamma-rays (6 to 7 MeV) produced by the Pb(n,γ) reaction in the spectrometer.

Characteristic behavior of neutrons in the KULS was studied by calculations with the continuous energy Monte Carlo code MCNP[15] and by experiments with resonance filter method[13, 14]. It was found that the slowing-down constant K in the relation of energy and slowing-down time $E=K/t^2$ was determined to be 190 ± 2 and 156 ± 2 (keV μs^2) for the bismuth and the lead experimental holes. The energy resolution was around 40 % for both experimental holes at energies from a few eV to about 500 eV and was larger in the lower and the higher energy regions. More detailed characteristics of the KULS are given elsewhere[13, 14].

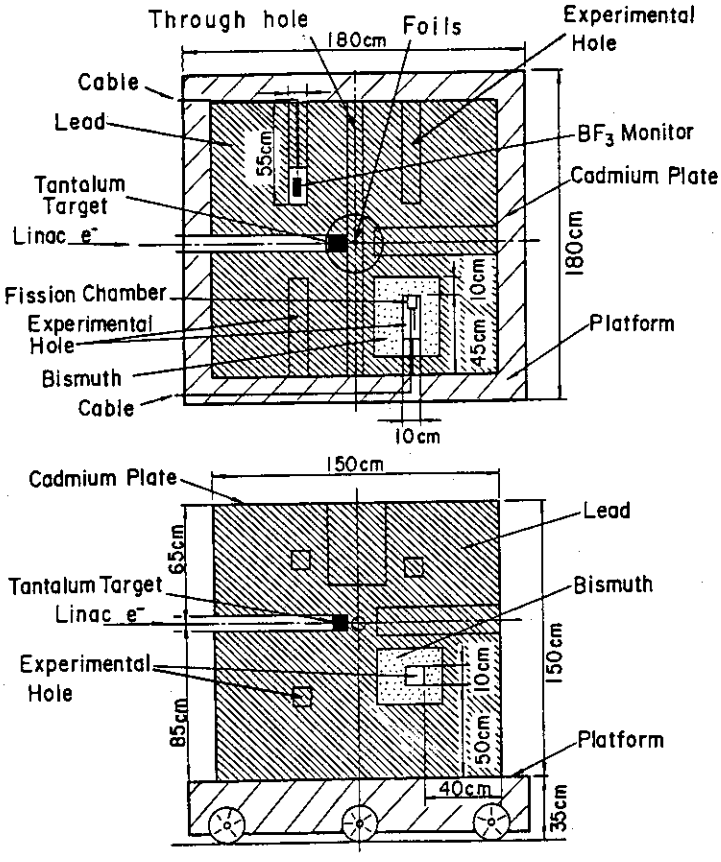

Fig. 1 Cross-sectional view of Kyoto University Lead Spectrometer, KULS.

2.2. ^{241}Am and ^{235}U Samples

Americium solution obtained from IAEA was purified at Isotope Products Laboratory, Japan Atomic

Energy Research Institute by anion-exchange method using nitric acid-methyl alcohol mixed media[16], in order to remove uranium, neptunium, plutonium and curium from the americium sample. The purified americium solution and isopropyl alcohol were mixed thoroughly and electrolyzed on a stainless steel disk (28 mm in diameter and 0.2 mm in thickness) for preparing an americium deposit (radioactive area of 20 mm in diameter)[17]. After electrodeposition, the sample was sintered with a gas burner to fix the americium layer on the disk by making americium oxide.

Alpha-ray from the deposit was measured with a silicon surface barrier detector. Impurities of ^{237}Np, $^{238-240}$Pu, ^{243}Am and ^{242}Cm on the americium deposit were not observed in the measured alpha-ray spectrum. Therefore, the isotopic composition of ^{241}Am for the deposit was estimated to be greater than 99.9 %. The number of the ^{241}Am atoms was determined by analyzing the alpha-rays of 5.322 to 5.544 MeV. The 59.5 keV gamma-ray from ^{241}Am was measured with a HPGe detector and the number of ^{241}Am was also determined by analyzing the gamma-ray spectrum obtained. The results measured by both detectors are in good agreement within the uncertainty of 5 %. The number of ^{241}Am atoms is determined to be $(1.72 \pm 0.02)\times10^{16}$, where the error was estimated by taking into account (i) statistics of the activity measurements, (ii) geometrical detection efficiencies, and (iii) uncertainties of the decay data used.

Highly enriched uranium oxide (99.91 % of ^{235}U) got from ORNL was chemically treated as almost same technique as the americium sample. The uranium deposit on the stainless steel disk was prepared at KURRI by the electrodeposition method. This ^{235}U sample was used to monitor the neutron flux in this study as the well-known reference cross section of the ^{235}U(n,f) reaction. Alpha-ray and gamma-ray spectrometries were carried out to determine the number of the uranium atom as well as the americium sample. From the analyses of the alpha-rays with 4.152 to 4.597 MeV from ^{235}U, the number of ^{235}U atoms was determined to be $(3.28 \pm 0.04)\times10^{16}$. The γ-ray measurement by 185.7 keV of ^{235}U showed good agreement within 1.5 % with the α-ray measurement.

2.3. Fission Chambers

The fission chambers employed for the present measurement are composed of two parallel plate type ionization chambers as shown in Fig. 2. The back sides of a sample deposit (^{241}Am) and a reference one (^{235}U) are faced each other, and it is called back-to-back type. The chambers were made of Al and filled with a mixed gas (97% Ar and 3% N_2) at 1 atm.

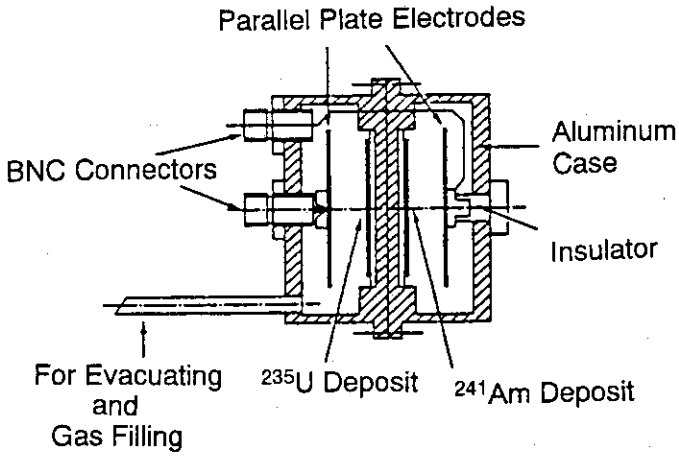

Fig. 2 Cross-sectional view of back-to-back type fission chambers.

2.4. Data Taking and Fission Rate Measurement

The back-to-back type fission

chambers were put in the Bi-covered hole of the KULS. Since we used quite thin ^{241}Am(2.2 μg/cm^2) and ^{235}U(4.1 μg/cm^2) deposits, fission pulses were clearly discriminated from background pulses caused by α-rays, and led to the respective time analyzer, as before[13]. The start signal for timing was taken from the linac electron burst. The channel number and the time width of each time analyzer were 4096 and 62.5 or 500 ns, respectively. The linac was operated with pulse width of 10−22 ns, repetition rate of 200 Hz, electron peak current of about 1 A, and accelerating energy of about 30 MeV. After about a hundred hours' experiment, the ^{241}Am and the ^{235}U deposited plates were exchanged each other to eliminate the systematic uncertainties in the cross section measurement.

The fission cross section of ^{241}Am is obtained by

$$\sigma_{Am}(E) = \frac{C_{Am}}{C_U}\frac{N_U}{N_{Am}}\sigma_U(E)$$

where

C_{Am} : fission counts of ^{241}Am,
C_U : fission counts of ^{235}U,
N_{Am} : number of ^{241}Am atoms in the sample deposit,
N_U : number of ^{235}U atoms in the reference deposit,
$\sigma_U(E)$: energy dependent fission cross section of ^{235}U.

We cited the numerical values of $\sigma_U(E)$ from ENDF/B−VI[12].

3. Results and Discussion

The present result is shown in Fig. 3 and is compared with the evaluated cross sections in JENDL−3.2[11] and ENDF/B−VI[12], which are broadened by the energy resolution function of the KULS. The experimental uncertainties are considered to be mainly due to (1) the statistical error in fission counts, (2) assignment of fission counts, (3) number of atoms for the ^{241}Am and the ^{235}U deposits, and (4) the reference fission cross section for the ^{235}U(n,f) reaction. Total amount of the experimental uncertainties is 4.6 to 5.6 %.

In Fig. 3, good agreement can be seen in general between the present measurement and the evaluated data in ENDF/B−VI and JENDL−3.2, and the both evaluated data show good agreement with each other. However, a little discrepancy can be seen between the evaluated data and the measurement at energies of the dip and the bump cross section regions. The difference is about 30 % in the energy region of 2 to 4 eV. Between 22 and 140 eV, the JENDL−3.2 data are underestimated by 1.2 to 2.3 times, while the ENDF/B−VI data are in good agreement with the present measurement.

The existing experimental data have also been broadened by the energy resolution function of the KULS, and compared with the present data in Fig. 4. The experimental data by Dabbs et al., whose result might be mainly cited in the evaluation for the ENDF/B−VI file, are in general agreement with the present data. The cross sections measured by Gayther et al. are higher above 55 eV by 50 to 100 % than the present measurement. The data by Bowman et al., Gerasimov et al. and Derrien et al. are close to the present cross section below several tens of eV, although Bowman et al. gave two times higher data above 200 eV. Leonard et al. gave higher values between 2 and 5 eV. Seeger et al. measured the cross section with a nuclear explosion technique

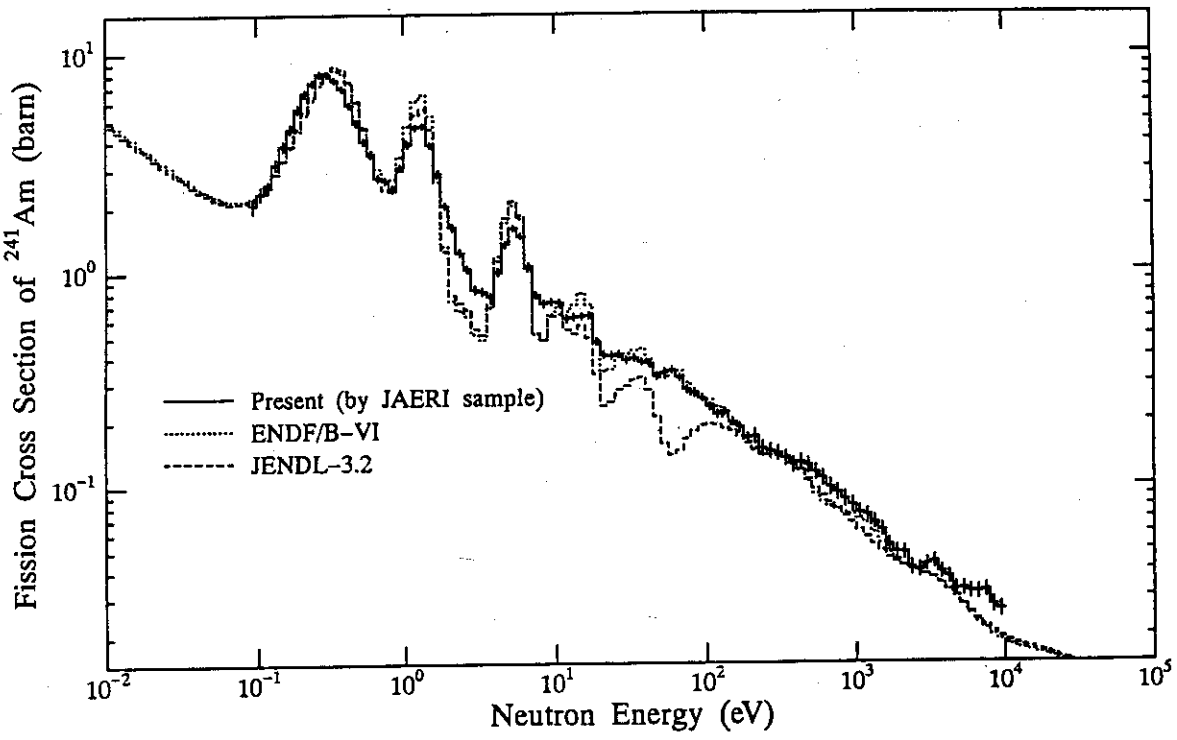

Fig. 3 Comparison of the evaluated fission cross section of ^{241}Am with the present measurement.

and obtained much higher values than the present data above 20 eV.

References

1. D. Lancaster, "Actinide Burning in a Standard Pressurized Water Reactor", Proc. of the Int'l Conf. and Technol. Exposition on Future Nucl. Systems: Global '93", Sept. 12−17, 1993, p.609, ANS, La Grange Park, Illinois, 1993.
2. J. Tommasi, et al., "Long−Lived Waste Transmutation in Reactor", ibid., p.1252, ANS, La Grange Park, Illinois, 1993.
3. B. R. Leonard Jr., et al., Bull. of the Am. Phys. Soc., 4, 31 (1959).
4. C. D. Bowman, et al., Phys. Rev., 137, B326 (1965).
5. V. F. Gerasimov, Yaderno−Fizicheskie Issledovaniya, 2, 16 (1966).
6. P. A. Seeger, et al., Nucl. Phys., A96, 605 (1967).
7. H. Derrien, et al., Proc. of the Int'l Conf. on Nuclear Cross Sections Technology, Washington D.C., 2, 637 (1975).
8. D. B. Gayther and B. W. Thomas, "Measurement of the Neutron Capture and Fission Cross−Sections of ^{241}Am, " Proc. of the 4th All−Union Conf. on Neutron Phys.", Kiev, Part 3, p.3 (1977).
9. J. W. T. Dabbs, et al., Nucl. Sci. Eng., 83 , 22 (1983).
10. V. McLane, et al., "Neutron Cross Sections", Vol.2, Neutron Cross Section Curves, Academic Press, Inc., London, 1988.

11. T. Nakagawa, "Evaluation of Nuclear Data for Americium Isotopes", JAERI-M, 89-008 (1989).
12. R. F. Rose (Ed.), "ENDF/B Summary Documentation", BNL-NCS-17541, 4th Ed. (ENDF/B-VI) 1991.
13. A. Yamanaka, et al., J. Nucl. Sci. Technol., 36, 863 (1993).
14. K. Kobayashi, et al., "Characteristic Behavior of Neutrons in the Lead Slowing-down Spectrometer Coupled to Electron Linac", JAERI-M 93-046, p.360, JAERI, 1993.
15. "MCNP - A General Monte Carlo Code for Neutron and Photon Transport, Version 3A", LA-7396-M, Rev.2, Los Alamos National Laboratory (1986).
16. S. Usuda and N. Kohno, Separation Science and Technology, 23, 1119 (1988).
17. N. Shinohara and N. Kohno, Appl. Radiat. Isot., 40, 41 (1989).

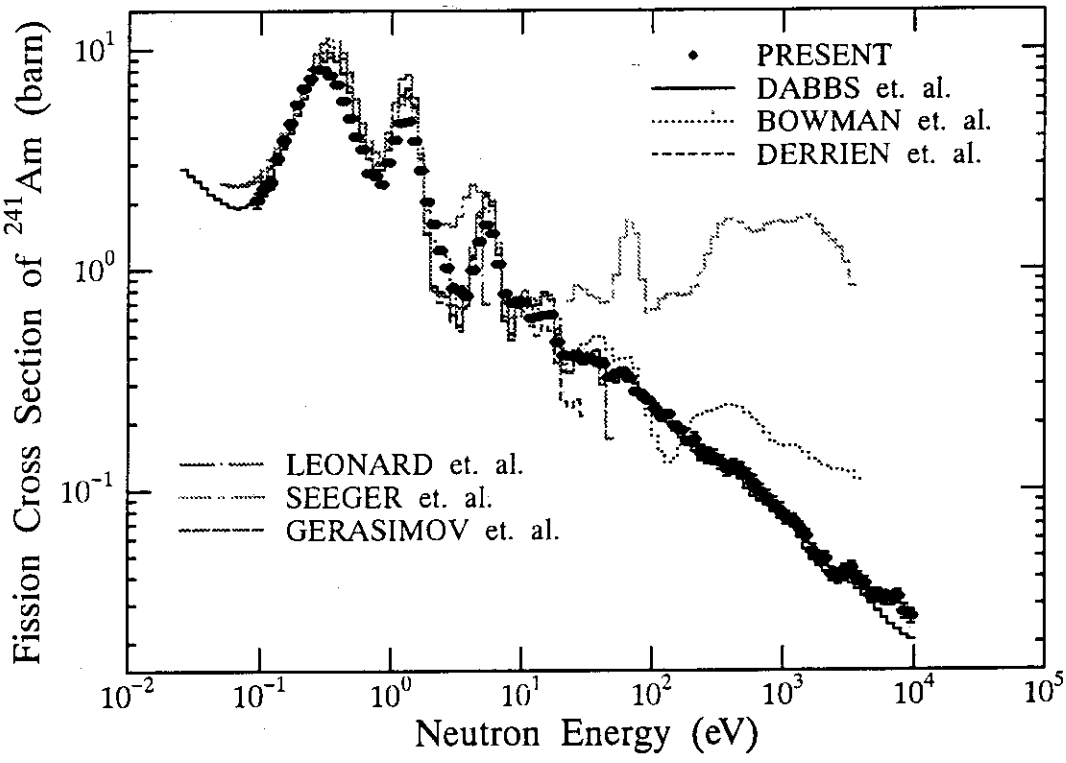

Fig. 4 Comparison of the existing experimental data with the present measurement.

3.2 Measurements of keV-Neutron Capture γ Rays of Fission Products(II)

Masayuki IGASHIRA
Research Laboratory for Nuclear Reactors, Tokyo Institute of Technology
2-12-1 O-okayama, Meguro-ku, Tokyo 152, Japan

γ rays from the keV-neutron capture reactions by ^{140}Ce, ^{141}Pr, and ^{147,148,149,150}Sm have been measured in a neutron energy region of 10 to 550 keV, using a large anti-Compton NaI(Tl) γ-ray spectrometer and the ^{7}Li(p,n)^{7}Be pulsed neutron source with a 3-MV Pelletron accelerator. The preliminary results for the capture cross sections and γ-ray spectra of those nuclei are presented and discussed.

1. Introduction

The keV-neutron capture cross sections of fission products(FPs) are indispensable for studies on innovative nuclear energy systems, and those of some FPs also for studies on the s-process nucleosynthesis in stars. Moreover, keV-neutron capture γ-ray spectra are necessary for studies on neutron capture reaction mechanism, and those of largely deformed nuclei would provide important information on nuclear excitation modes such as the M1 scissors mode[1]. However, those data, especially spectrum data, are quite inadequate both in quality and in quantity. Therefore, we are measuring keV-neutron capture γ rays of important FPs to obtain those nuclear data. For the past one year, we finished the measurements for ^{140}Ce, ^{141}Pr, and ^{147,150}Sm in a lower neutron energy region of 10 to 80 keV, and those for ^{148,149}Sm at a high energy of 550 keV. Preliminary results are presented and compared with previous results in literature.

2. Experimental Procedure

Both the lower-energy and 550-keV measurements were performed with the 3-MV Pelletron accelerator of the Research Laboratory for Nuclear Reactors at the Tokyo Institute of Technology. A typical experimental arrangement is shown in Fig. 1.

Pulsed keV neutrons were produced from the ^{7}Li(p,n)^{7}Be reaction by bombarding a Li-evaporated copper disk with the 1.5-ns bunched proton beam from the Pelletron accelerator. The average proton beam current was 5 to 7 μA at a 2-MHz pulse repetition rate. The incident neutron spectrum on a capture sample was measured by means of a time-of-flight(TOF) method without the sample, employing a ^{6}Li-glass scintillation detector. The angle between the detector axis and the proton beam direction was adjusted for each sample so that the average incident neutron spectrum could be observed.

Capture samples were disks with a diameter of 2 cm (Sm isotope samples) or 5.5 cm (^{140}Ce and ^{141}Pr samples) and a thickness of 0.3 to 0.5 cm. The sample was located 11.8 cm(the lower-energy measurements) or 19.8 cm(the 550-keV measurements) away from the neutron source at an angle of 0° with respect to the proton beam direction. Highly enriched oxide powder was used for each of the ^{140}Ce and ^{147,148,149,150}Sm samples, and natural oxide powder for the ^{141}Pr sample. Each powder sample was contained in a case made of graphite. Standard Au samples, disks with a diameter of 2 or 5.5 cm and a

thickness of 0.2 or 0.17 cm, were used to determine the absolute number of neutrons incident on each capture sample.

Capture γ rays were detected with a large anti-Compton NaI(Tl) spectrometer[2], employing a TOF method. The main detector of spectrometer is a 15.2-cm diameter by 20.3-cm NaI(Tl) detector, and is centered in a 33.0-cm outer diameter by 35.6-cm NaI(Tl) hollow Compton-suppression detector. The spectrometer was set in a heavy shield consisting of borated paraffin, borated polyethylene, cadmium, and potassium free lead. A ^{6}LiH shield that absorbed effectively the neutrons scattered by the sample was added in the collimetor of the spectrometer shield. The distance between the sample and the spectrometer was 86 cm. Capture γ rays were observed at an angle of 125° with respect to the proton-beam direction. Capture events detected by the spectrometer were stored in a workstation as two-dimensional data on TOF and pulse height(PH).

The measurement with each sample and the measurements with and without the standard Au sample were made cyclically to average out changes in experimental conditions such as the incident neutron spectrum. The three measurements were connected by the neutron counts of the ^{6}Li-glass scintillation detector.

3. Data Processing

The data processing method has been described in detail elsewhere[3,4] and so is summarized briefly in the present paper.

Typical incident neutron spectra for the lower-energy and 550-keV measurements are shown in Figs. 2(a) and 2(b), respectively. Those spectra were extracted from the TOF spectra observed with the ^{6}Li-glass scintillation detector and from the relative neutron detection efficiency of the detector. As seen from Figs. 2(a) and 2(b), white neutrons were used for the lower-energy measurements, and mono-energetic neutrons for the 550-keV measurements.

Figs. 3(a) and 3(b) show typical TOF spectra observed with the γ-ray spectrometer in the lower-energy and 550-keV measurements, respectively. The sharp and intense peaks at 940 channel in Fig. 3(a) and at 820 channel in Fig. 3(b) are due to γ rays from the ^{7}Li(p,γ)^{8}Be reaction. The broad peak around 750 channel in Fig. 3(a) and the sharp peak at 765 channel in Fig. 3(b) are due to keV-neutron capture γ rays from the ^{147}Sm and ^{149}Sm samples, respectively. The time spread of keV-neutron capture γ rays in Fig. 3(a) is caused by the whiteness of neutron energy.

Digital windows (DWs) were set in the TOF spectrum to obtain foreground and background PH spectra. The net capture γ-ray PH spectrum was extracted by subtracting the background PH spectrum from the foreground one.

A PH weighting technique[5] was applied to the net PH spectra to obtain the capture yields. The capture yields of Au and the standard capture cross section of Au[6] were used to determine the absolute number of neutrons incident on each sample.

Corrections were made for the self-shielding and multiple-scattering of neutrons in the sample, for the absorption of capture γ rays in the sample, and for the dependence of γ-ray detection efficiency on the position in the sample. The oxide powder samples are hygroscopic, and the exact characterization of the samples is a severe problem for accurate cross section measurements. However, we have not yet performed the characterization. Therefore, the correction for the water in the sample is not made.

4. Results and Discussion

Preliminary cross section values of ^{140}Ce, ^{141}Pr, and ^{147,148,149,150}Sm are shown in

Figs. 4-9, respectively. The present values of ^{140}Ce are larger than all the previous measurements[7-9] except for the measurement by Siddappa et al.[10], and so are about 50 % larger than the evaluated values of JENDL-3.2[11]. The present results of ^{141}Pr agree with those of Taylor et al.[12] within their experimental errors, but are systematically about 10 % larger than their values and the evaluations of JENDL-3.2. Other experimental values[13-17] are also compared with the present ones. The present results of ^{147,150}Sm are in good agreement with the recent measurements by Wisshak et al.[18]. There are no experimental data to be compared with the present results of ^{148,149}Sm at 550 keV, and so the present results are shown together with our previous results[19] and other measurements[18,20,21] in a lower energy region and compared with the evaluations of JENDL-3.2. The present result of ^{148}Sm is in excellent agreement with the evaluation, but that of ^{149}Sm is about 40 % larger than the evaluation.

The capture γ-ray PH spectra of ^{140}Ce and ^{141}Pr are shown in Fig. 10. The same bump is observed around 1.5 MeV in the spectrum of ^{141}Pr as in our early work[3], but such a bump is not clearly observed in the spectrum of ^{140}Ce because fine structures hide it. The γ-ray PH spectra of ^{148,149}Sm are shown in Fig. 11, and the same bump is observed around 2.5 MeV in both spectra as in the lower-energy measurements[19]. The spectra of ^{147,150}Sm are shown in Fig. 12, and the bump is observed around 3 MeV in the spectrum of ^{150}Sm and around 2 MeV in that of ^{147}Sm. The energy position of the bump is consistent with the systematics obtained from our early work[3]. The bump was attributed only to a resonance structure of the E1 γ-ray strength function in the work, but the origin of the bump should be investigated also from different aspects such as the excitation of nuclear M1 scissors mode.

References

[1] N. Lo Iudice and F. Palumbo, Phys. Rev. Lett. **41** (1978) 1532.
[2] M. Igashira, K. Tanaka and K. Masuda, Proc. the 8th Int. Symp. on Capture Gamma-Ray Spectroscopy and Related Topics, Fribourg, Switzerland, 1993, edited by J. Kern (World Scientific, Singapore, 1994) p.992.
[3] M. Igashira, H. Kitazawa, M. Shimizu, H. Komano and N. Yamamuro, Nucl. Phys. **A457** (1986) 301.
[4] S. Raman, M. Igashira, Y. Dozono, H. Kitazawa, M. Mizumoto and J. E. Lynn, Phys. Rev. **C41** (1990) 458.
[5] R. L. Macklin and J.H. Gibons, Phys. Rev. **159** (1967) 1007.
[6] ENDF/B-VI data file for ^{197}Au (MAT=7925), evaluated by P. G. Young (1984).
[7] R. P. Anand, M. L. Jhingan, D. Bhattacharya and E. Kondaiah, Nuovo Cimento, **50A** (1979) 247.
[8] A. R. de L. Musgrove, B. J. Allen and R. L. Macklin, Aust. J. Phys. **32** (1979) 213.
[9] H. Beer and F. Kappeler, Phys. Rev. **C21** (1980) 534.
[10] K. Siddappa, M. Sriramachandra Murty and J. Rama Rao, Nuovo Cimento, **18A** (1973) 48.
[11] M. Kawai, S. Chiba, H. Matsunobu, T. Nakagawa, Y. Nakajima, T. Sugi, T. Watanabe and A. Zukeran, Proc. Int. Conf. on Nuclear Data for Science and Technology, Gatlinburg, USA, 1994, edited by J. K. Dickens (American Nuclear Society, La Grange Park, 1994) p.727
[12] R. B. Taylor, B. J. Allen, A. R. de Musgrove and R. L. Macklin, Aust. J. Phys. **32** (1979) 551.
[13] R. Boot, W. P. Ball and M. H. MacGregor, Phys. Rev. **112** (1958) 226.
[14] J. H. Gibbons, R. L. Macklin, P. D. Miller and J. H. Neiler, Phys. Rev. **122** (1961) 182.
[15] R. L. Macklin, J. H. Gibbons and T. Inada, Phys. Rev. **129** (1963) 2695.
[16] V. A. Konks, Yu. P. Popov and F. L. Shapiro, Soviet Physics JETP, **19** (1964) 59.
[17] A. K. Chaubey and M. L. Sehgal, Phys. Rev. **152** (1966) 1055.
[18] K. Wisshak, K. Guber, F. Voss, F. Kappeler and G. Reffo, Phys. Rev. **C48** (1993) 1401.
[19] M. Igashira, Proc. the 1994 Symp. on Nuclear Data, 1994, Tokai, Japan, edite d by M. Kawai and T. Fukahori, JAERI-Conf **95-008** (1995) 129.
[20] M. Mizumoto, Nucl. Phys. **A357** (1981) 90.
[21] R. L. Macklin, J. H. Gibbons and T. Inada, Nature, **197** (1963) 369.

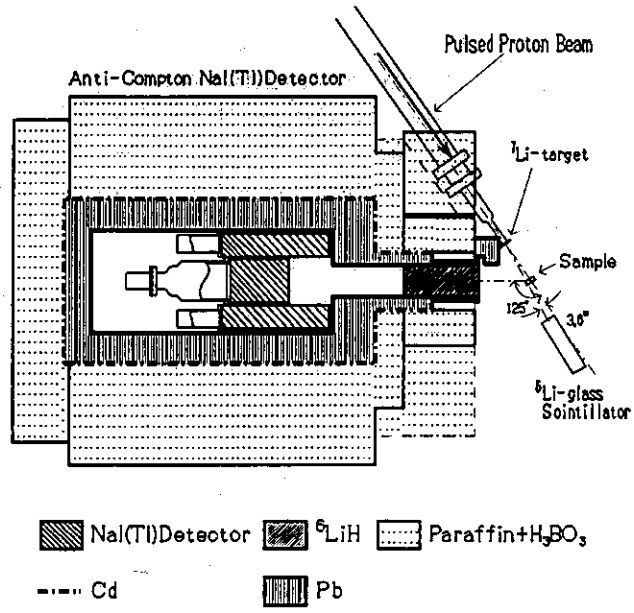

Fig. 1. Typical experimental arrangement.

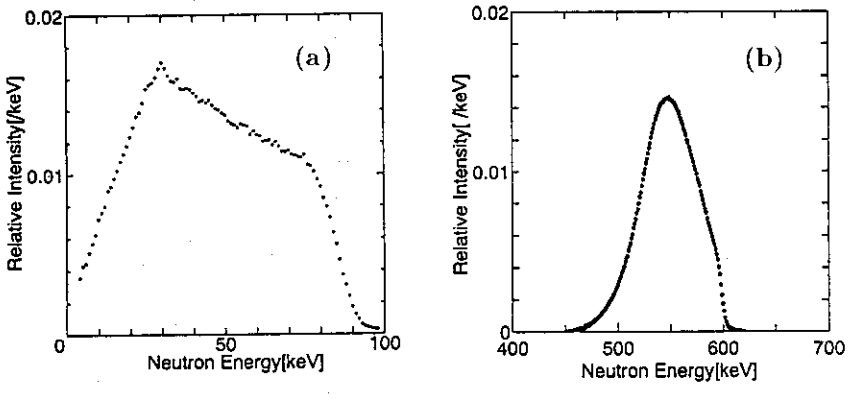

Fig. 2. Incident neutron spectra in the (a) lower-energy and (b) 550-keV measurements.

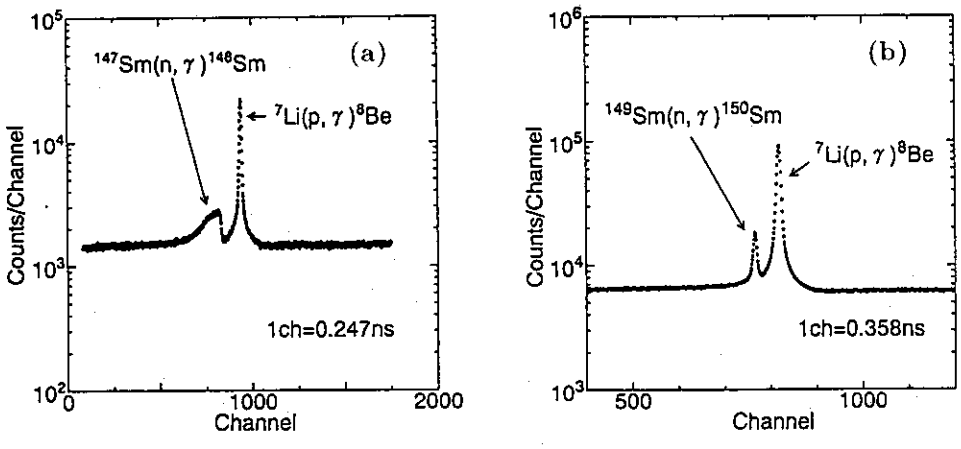

Fig. 3. TOF spectra observed by the γ-ray spectrometer in the (a) lower-energy and (b) 550-keV measurements.

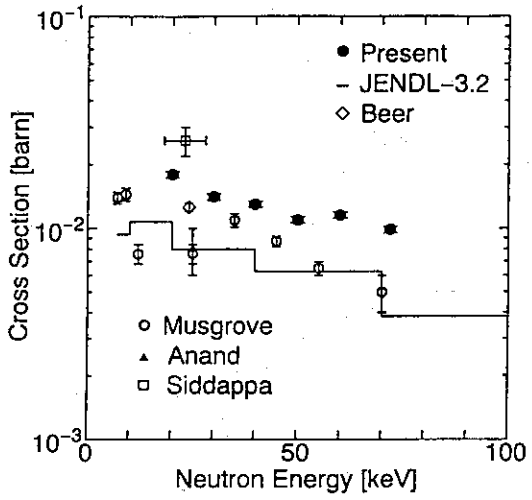

Fig. 4. Capture cross sections of ^{140}Ce.

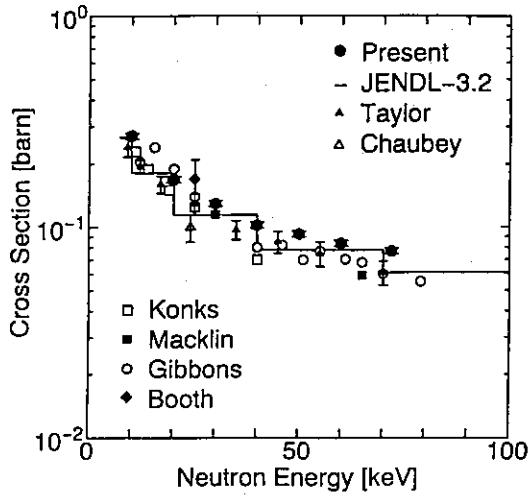

Fig. 5. Capture cross sections of ^{141}Pr.

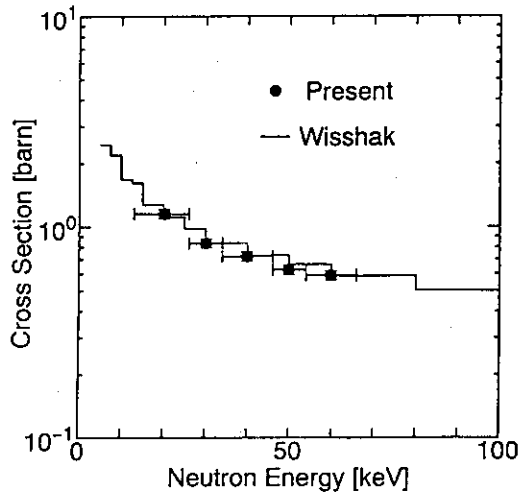

Fig. 6. Capture cross sections of ^{147}Sm.

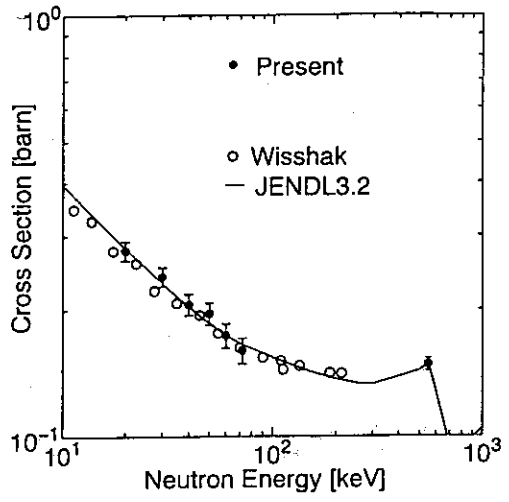

Fig. 7. Capture cross sections of ^{148}Sm.

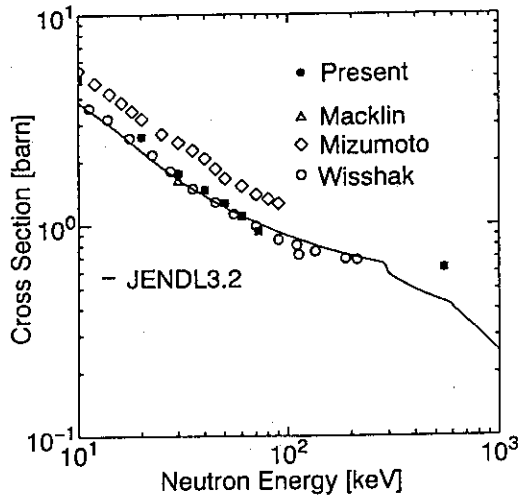

Fig. 8. Capture cross sections of ^{149}Sm.

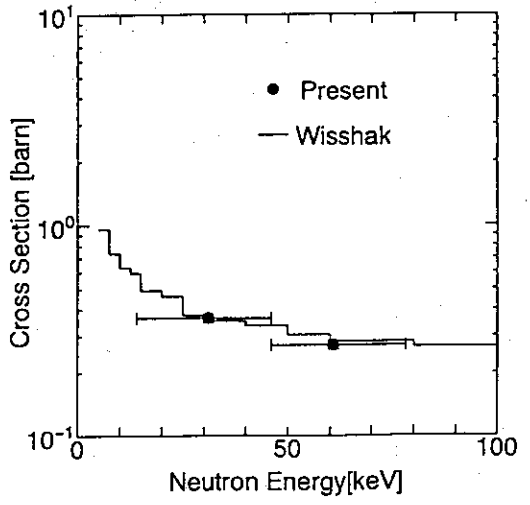

Fig. 9. Capture cross sections of ^{150}Sm.

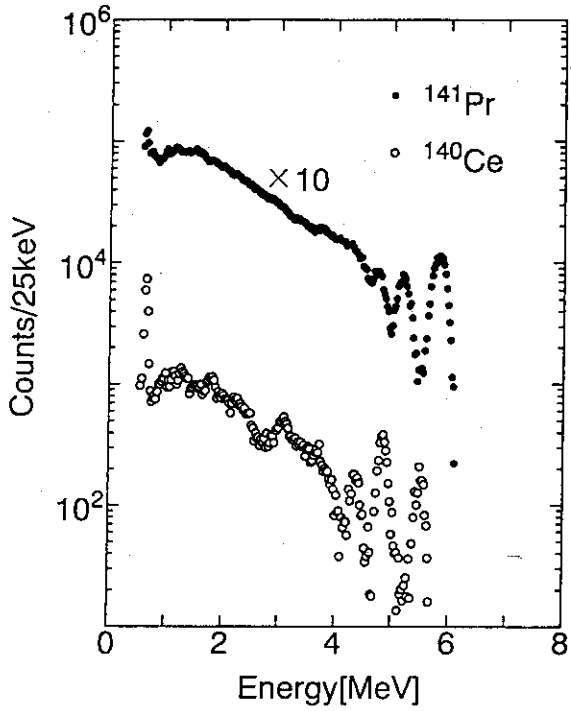

Fig. 10. Capture γ-ray PH spectra of ^{140}Ce and ^{141}Pr.The average incident neutron energy is 30 keV.

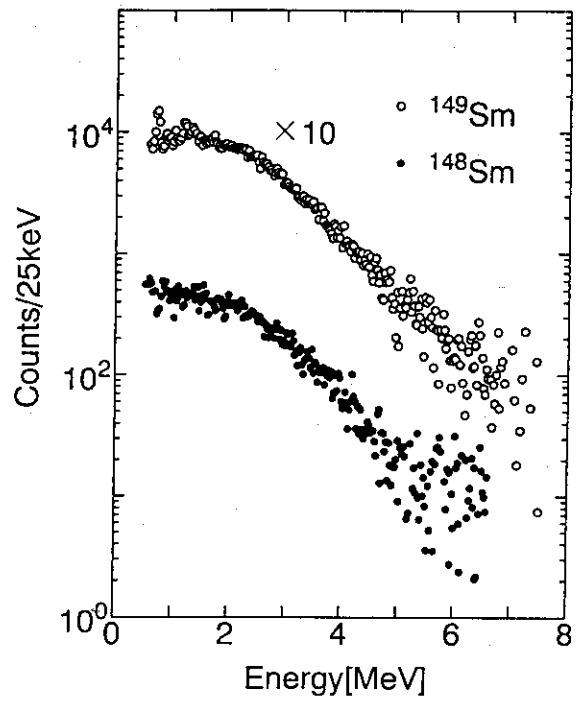

Fig. 11. Capture γ-ray PH spectra of ^{148}Sm and ^{149}Sm.The incident neutron energy is 550 keV.

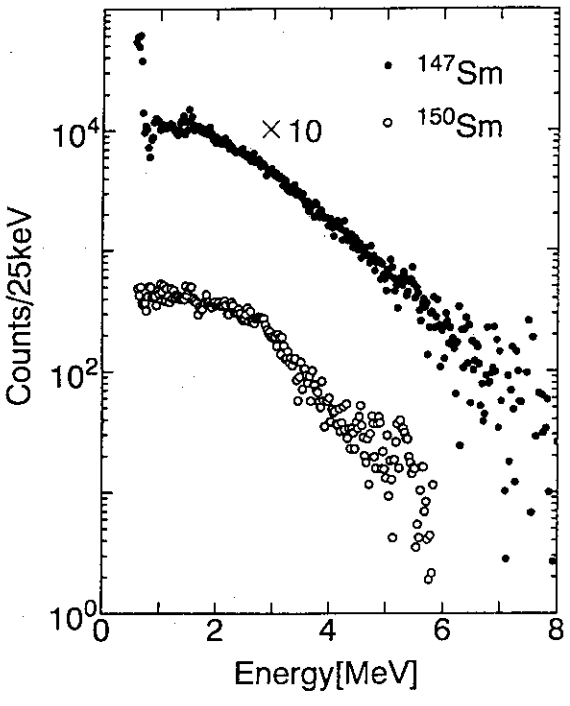

Fig. 12. Capture γ-ray PH spectra of ^{147}Sm and ^{150}Sm.The average incident neutron energy is 30 keV.

3.3 Verification of Dosimetry Cross Sections above 10 MeV based on Measurement of Activation Reaction Rates in Fission Neutron Field

Naoteru Odano, Toshimasa Miura
Tokai Branch, Ship Research Institute
Tokai-mura, Naka-gun, Ibaraki-ken 319-11, Japan
e-mail: odano@srimot.go.jp

and

Akio Yamaji
Office of Nuclear Ship Research and Development
Japan Atomic Energy Research Institute
Tokai-mura, Naka-gun, Ibaraki-ken 319-11, Japan

To validate the dosimetry cross sections in fast neutron energy range, activation reaction rates were measured for 5 types of dosimetry cross sections which have sensitivity in the energy rage above 10 MeV utilizing JRR-4 reactor of JAERI. The measured reaction rates were compared with the calculations reaction rates by a continuous energy monte carlo code MVP. The calculated reaction rates were based on two dosimetry files, JENDL Dosimetry File and IRDF-90.2.

1. Introduction

The Japan Atomic Energy Research Institute is conducting a design study of advanced marine reactor (MRX)[1]. The MRX is an integral type PWR with a water-filled containment vessel, in-vessel type control rod drive mechanisms and an emergency decay heat removal system using natural convection. One of important issues in the shielding design of the MRX is to estimate the dose rate in vicinity of the main steam line and the coolant line due to high energy γ rays from the secondary coolant in the steam generator which is located closed to the reactor core. Neutron transport calculation above 10 MeV plays an important role in such a dose estimation. In the shielding experiment to validate the shielding design, the activation method is one of established procedures to estimate the neutron attenuation in the shielding materials. For accurate analysis of the experiment, highly accurate dosimetry cross sections are required. In this study, dosimetry cross sections which is able to use in the energy region above 10 MeV and in the fission neutron filed were tested by comparing the measured reaction rates and calculated ones. The experiment is described in section 2 and the calculation of reaction rates is presented in section 3. In section 4, discussion regarding validity of the dosimetry cross sections in JENDL Dosimetry File[2] and IRDF-90.2[3] is described.

2. Measurement of Activation Reaction Rates

The JRR-4 reactor of JAERI, which is a light-water-moderated swimming pool type reactor whose nominal power is 3.5 MW, was used in the present study. The horizontal and vertical cross sections of the reactor is shown in Fig. 1. Reaction rates were measured in the pneumatic tube irradiation facility and aluminum pipe installed in water pool outside of the reactor core tank. Reaction rates were measured for 5 types of reactions listed in table 1. There exists limited number of reactions which can be used for fast neutron dosimetry above 10 MeV in fission neutron filed while there are many reactions for fusion neutron

dosimetry applications. Size of the irradiated samples and other characteristics is also listed in the table 1. The reactions have high sensitivities in fast neutrons above 10 MeV except for the $^{27}Al(n,\alpha)^{24}Na$ reaction which were considered as standard dosimetry reaction. Irradiation time was 1 to 2 minutes in pneumatic tube and 1 to 2 hours in Al pipe. The samples were irradiated when the power of the reactor was 3.5 MW. After the irradiation, induced γ rays were detected by high purity Ge detector. The detector efficiency was determined by experiment using standard γ ray sources. Distance from the detector surface to the sample was set to 20 cm to eliminate the sum-coincidence effect. As a correction factor, γ ray attenuations in sample itself was taken into account by one dimensional approximation. Correction for perturbation of neutron flux during the irradiation was neglected. Measured reaction rates are shown in table 2. The uncertainties of the reaction rates were mainly attributed to the uncertainty in determination of detector efficiency which were considered to be 5%.

3. Calculation of Activation Reaction Rates

To validate the dosimetry cross sections, calculated reaction rates and measured ones were compared. The vectorized continuous energy Monte Carlo code MVP[4], running on vector and parallel supercomputer VPP500 of JAERI, was used for the calculation of the reaction rates. The nuclear data library used in the code was prepared from JENDL-3.2. Three dimensional geometry was modeled in the MVP calculation as shown in Fig.1. The track length estimator was used to estimate the neutron flux in pneumatic pipe and Al pipe. Larger detector regions than those of actual irradiated sample were taken for efficient scoring of track length. Gradation of the neutron flux was considered to be very small because the detector region were filled with air or nitrogen gas. The weight window sampling method was employed as variance reduction technique. Neutrons with energy above 3 MeV was generated uniformly in reactor core region as input neutron source. The neutron energy distribution of the source was taken from that of ^{235}U in JENDL-3.2[5].

Calculated neutron spectra in pneumatic tube and Al pipe are shown in Fig. 2. The 90% response ranges of the dosimetry reactions for ^{235}U fission neutron spectrum are also shown in the figure. For the result of pneumatic tube, the neutron flux smoothly decrease as increase the neutron energy while several structures can be found in spectrum in Al pipe. The fractional standard deviation in each energy bin is less than 0.05 for both of the calculations.

4. Discussion

Comparison between measured reaction rates and calculated ones was shown in table 3. Because the uncertainties of calculated reaction rates is small (0.3 to 3 %), uncertainties of the C/E values are close to the ones of measured reaction rates. Calculated reaction rates were agreed with experimental data within 10 to 20 % except for the $^{127}I(n,2n)^{126}I$ reaction calculated by JENDL Dosimetry File whose discrepancy were 32% in the pneumatic pipe and 31% in Al pipe. The discrepancy can be improved if the cross section in IRDF-90.2 is used. Apparent difference between cross sections in the JENDL Dosimetry File and the IRDF-90.2 can be seen in Fig.3 which shows the differential data in both the files and experimental data[6-19] retrieved from the EXFOR[20]. Reason of the overestimation of reaction rate by JENDL Dosimetry File is attributed to the large cross section values from threshold energy to 16 MeV. Re-evaluation of the JENDL Dosimetry File is recommended to use this reaction in fast neutron dosimetry in fission neutron filed.

5. Conclusion

Activation reaction rates were measured for reactions which have sensitivities in the energy range above 10 MeV. The measured reaction rates were compared with calculated ones deduced from monte carlo calculation by MVP code. Calculated data were agreed with experimental data within 10 to 20 % except for the $^{127}I(n,2n)^{126}I$ reaction from JENDL Dosimetry File. From the comparison of measured data and

calculated ones, $^{93}Nb(n,2n)^{92m}Nb$, $^{90}Zr(n,2n)^{89}Zr$ and $^{58}Ni(n,2n)^{57}Ni$ reaction cross sections in JENDL Dosimetry File and IRDF-90.2 are accurate enough for the neutron dosimetry for shielding experiment we concern. Revision of the $^{127}I(n,2n)^{126}I$ reaction cross section in JENDL Dosimetry File is required so that the reaction is useful for fast neutron dosimetry above 10 MeV in fission neutron filed.

6. Acknowledgements

This work has been carried out under cooperative research program between Ship Research Institute and Japan Atomic Energy Research Institute. The authors express their sincere thanks to staff members of Division of Research Reactor of JAERI for their assistance in irradiation of the samples in the pneumatic tube irradiation facility and utilization of a high purity Ge detector at hot laboratory of the JRR-4.

7. References

[1] Office of Nuclear Ship Research and Development: "Conceptual Design of the Advanced Marine Reactor MRX", JAERI-M 91-004 (1991).
[2] Nakazawa M., *et al.*: "JENDL Dosimetry File", JAERI 1325 (1991).
[3] Kocherov N.P. and McLaughlin P.K.: "The International Reactor Dosimetry File (IRDF-90)", IAEA-NDS-141 (1990).
[4] Mori T. and Nakagawa M.: "MVP/GMVP: General Purpose Monte Carlo Codes for Neutron and Photon Transport Calculations based on Continuous Energy and Multigroup Methods", JAERI-Data/Code 94-007 (1995).
[5] Nakagawa T., *et al.*: "Japanese Evaluated Nuclear Data Library Version-3 Revision-2: JENDL-3.2", J. Nucl. Sci. and Techn., 32, 1259 (1995).
[6] Araminowicz J., *et al.*: INR-1464, 14 (1973).
[7] Barrall R.C., *et al.*: Nucl. Phys., A138, 387 (1969).
[8] Barrall R.C., *et al.*: AFWL-TR-68-134 (1969).
[9] Bormann M., *et al.*: Zeit. Phys., 166, 477 (1962).
[10] Havlik E.: Acta Physica Austriaca, 34, 209 (1971).
[11] Lu W.D., *et al.*: Pys. Rev., C1, 350 (1970).
[12] Lu Han-Lin, *et al.*: INDC(CRP)-16 (1989).
[13] Lu Han-Lin, *et al.*: Chinese J. Sci. and Techn. of At. En., 9, 113 (1975).
[14] Martin H.C., *et al.*: Phys. Rev., 89, 1302 (1953).
[15] Maslov G.N., *et al.*: Yadernye Konstanty, 9, 50 (1972).
[16] Paul E.B., *et al.*: Can. J. Phys., 31, 267 (1953).
[17] Pepelink R., *et al.*: Proc. Int. Conf. on Nuclear Data for Basic and Applied Science, Santa Fe, pp.211, (1985).
[18] Qaim S.M., *et al.*: J. Inorg. Nucl. Chem., 30, 2577 (1968).
[19] Santry D.C.: Proc. Int. Conf. on Nuclear Cross Sections for Technology, Knoxvill, pp.433, (1979).
[20] EXFOR, experimental data base available from OECD NEA Data Bank.

Table 1. Characteristics of reactions used for measurement of activation reaction rates. (*90% response for the ^{235}U fission spectrum. **^{235}U fission spectrum averaged cross section.)

Reaction	Threshold energy (MeV)	Response* (MeV)	Cross Section (mb)**	Half Life	γ-ray Energy(keV), branching ratio	Size of the Detector (mm)
$^{27}Al(n,\alpha)^{24}Na$	3.2	6.4 - 12.0	7.20×10^{-1}	14.959h	1368.63(99.99)	10×10×0.5t
$^{93}Nb(n,2n)^{92m}Nb$	8.9	9.4 - 15.0	4.80×10^{-1}	10.15d	934.53(100.0)	5φ3t
$^{127}I(n,2n)^{126}I$	9.2	9.7 - 15.0	1.05	13.02d	666.33(33.1)	10φ5t
$^{90}Zr(n,2n)^{89}Zr$	12.1	13.0 - 19.0	1.03×10^{-1}	3.268d	909.15(99.01)	5φ3t
$^{58}Ni(n,2n)^{57}Ni$	12.4	12.5 - 19.2	3.04×10^{-3}	35.9h	1377.59(80.0)	10φ5t

Table 2. Measured reaction rates in the pneumatic tube (upper column) and in the Al pipe (lower column) with the uncertainties (shown in parenthesis).

Reaction	Measured Reaction Rate ($sec^{-1}\cdot watt^{-1}$)
$^{27}Al(n,\alpha)^{24}Na$	1.17×10^{-21} (5.0%)
	1.47×10^{-21} (5.2%)
$^{93}Nb(n,2n)^{92m}Nb$	7.31×10^{-22} (5.4%)
	1.05×10^{-23} (5.3%)
$^{127}I(n,2n)^{126}I$	2.11×10^{-21} (5.3%)
	2.98×10^{-23} (5.5%)
$^{90}Zr(n,2n)^{89}Zr$	1.80×10^{-22} (6.1%)
	3.19×10^{-24} (6.1%)
$^{58}Ni(n,2n)^{57}Ni$	—
	1.11×10^{-25} (13%)

Table 3. The C/E values of reaction rates calculated from JENDL Dosimetry File and IRDF-90.2. Figures in upper column show the C/E values for the pneumatic tube while the those in lower column show the C/E values for the Al pipe.

Reaction	JENDL Dosimetry File	IRDF-90.2
$^{27}Al(n,\alpha)^{24}Na$	0.977	1.02
	1.12	1.17
$^{93}Nb(n,2n)^{92m}Nb$	1.14	1.06
	1.11	1.03
$^{127}I(n,2n)^{126}I$	1.32	0.966
	1.31	0.986
$^{90}Zr(n,2)^{89}Zr$	0.944	0.903
	0.821	0.790
$^{58}Ni(n,2n)^{57}Ni$	-	-
	0.862	0.900

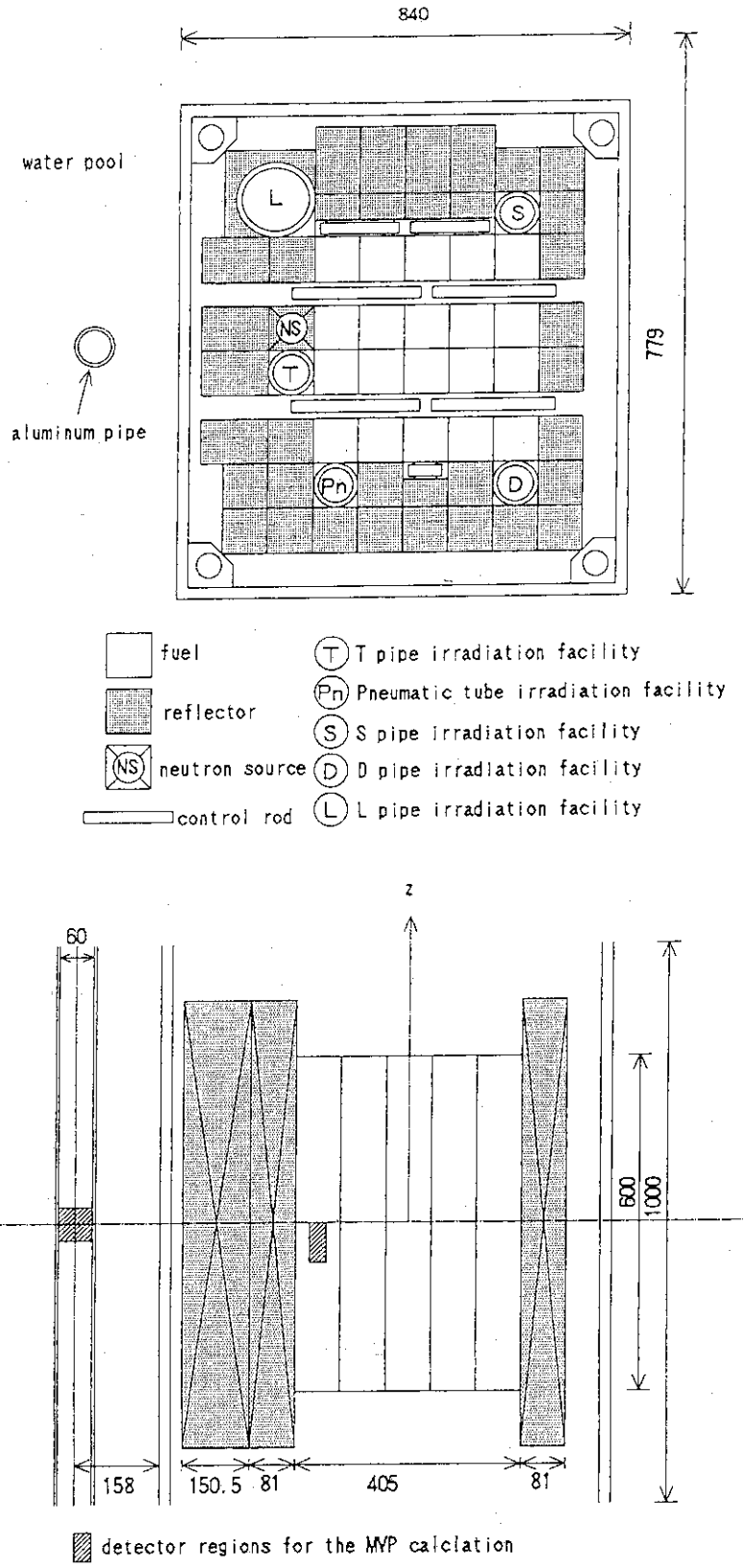

Fig. 1. Cross sectional view of the JRR-4 reactor core (unit in mm). Upper figure shows horizontal cross section and lower one shows vertical cross section.

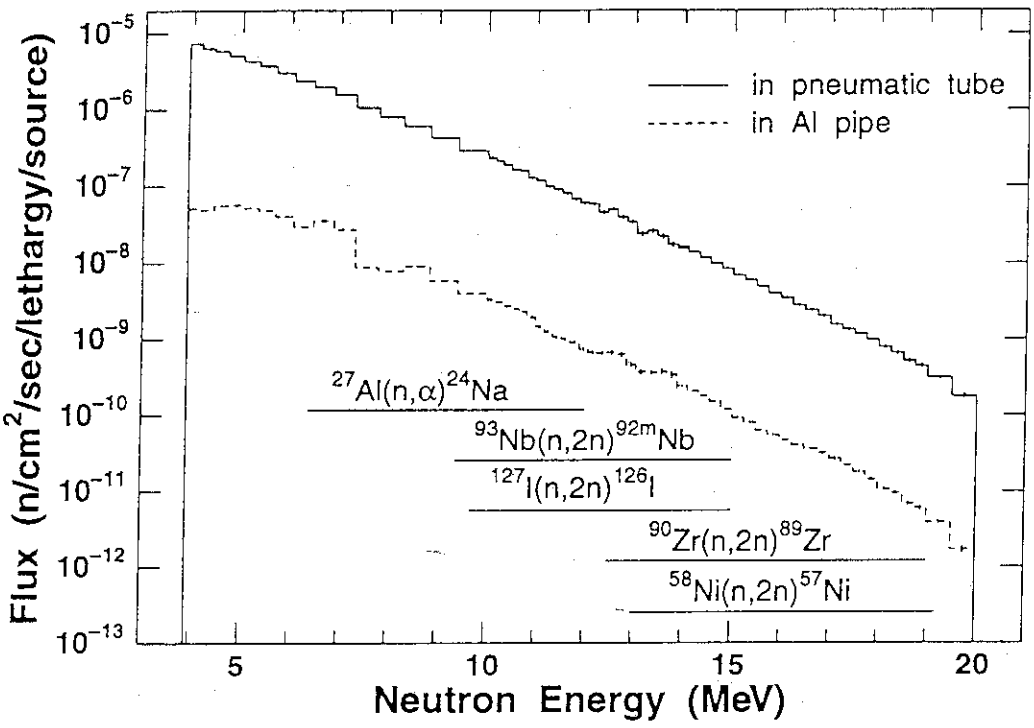

Fig. 2. Calculated neutron spectra in the pneumatic tube and Al pipe using the MVP code. Solid line shows the result for pneumatic tube while dashed line indicates the result for Al pipe. The 90% response ranges for dosimetry cross sections are also shown in the figure.

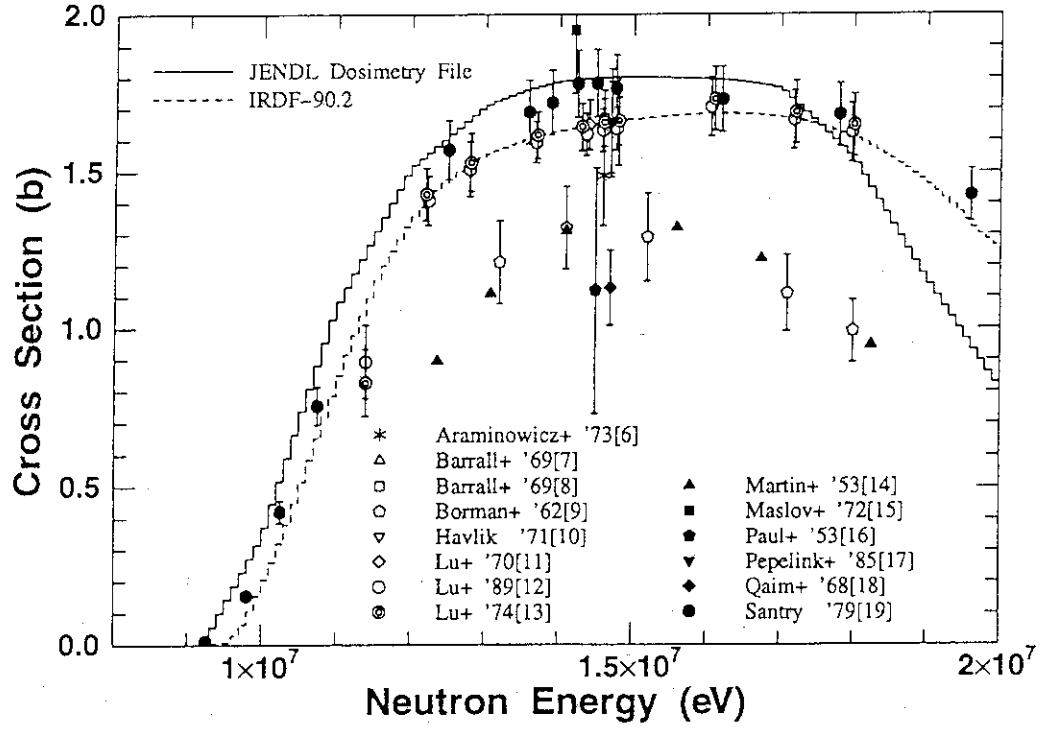

Fig. 3. Comparison of $^{127}I(n,2n)^{126}I$ reaction cross sections in the JENDL Dosimetry File and the IRDF-90.2 with experimental data from EXFOR, experimental data base available from OECD NEA Data Bank.

3.4 Benchmark Calculation of JMTRC core using JENDL-3

Yoshiharu NAGAO, Satoshi SHIMAKAWA, Yoshihiro KOMORI, Norikazu OOKA
Oarai Research Establishment
Japan Atomic Energy Research Institute
Oarai-machi Higashi Ibaraki-gun Ibaraki-ken 311-13
E-mail : nagao@jmtr.oarai.jaeri.go.jp

Applicability of MCNP/JENDL3.2 to the JMTR (Japan Materials Testing Reactor, 50MW) core calculation with plate type fuels has been studied. The JMTRC core, which is the critical facility of the JMTR, was selected for benchmark problem of the JMTR. Benchmark calculations(critical state, excess reactivity and shutdown margin), sensitivity analysis and comparison of JENDL3.1 and JENDL3.2 were performed. For results of these calculations, it was confirmed that MCNP/JENDL3.2 is applicable to the JMTR core calculation and the calculated k_{eff} with JENDL3.2 was higher than that with JENDL3.1.

1. Introduction

In the neutron irradiation tests of nuclear fuels and materials, the precision of the calculated neutron spectrum at the irradiation material position should be improved. Since distribution of thermal neutron is particularly complex due to effect of irradiation capsule materials, the calculation model should be described exactly. The improvement of calculation precision is however difficult by diffusion or transport calculation because of their limitation on model description. Monte Carlo code, which can represent complicated models exactly, is necessary to solve the problem. Although applicability of MCNP to shielding calculation and simple core calculation has been confirmed, it has not been verified that MCNP can be also used to complicated core calculation with the plate type fuel such as the JMTR. Therefore applicability of MCNP to the core calculation with the plate type fuel was studied.

2. Calculation model

The JMTRC core(Fig.1) consists of twenty-two standard fuel elements, five control elements made of borated stainless steel with fuel followers, beryllium reflectors and aluminum reflectors. The effective core height is 750 mm. The standard fuel element(Fig.2) consists of nineteen fuel plates. The fuel plate consists of fuel meat of uranium-aluminum dispersion alloy

and cladding of aluminum alloy. MCNP4A[1] was used for calculation and the cross section library (FSXLIBJ3R2) was the continuous energy cross section library[2] for MCNP compiled JENDL3.2. The JMTRC whole core calculation model was described in detail. For example, the grid plate region below fuel region was effected for critical calculation. The critical calculation was carried out with 10,000 histories (1000 particles per batch, 100 batch).

3. Benchmark problem

The critical core, excess reactivity and shutdown margin was calculated for the JMTRC benchmark problem[3]. The measured excess reactivity was obtained by fuel addition method. The shutdown margin was measured by the pulsed neutron technique. Calculated results are shown in Table 1 with measured one. The k_{eff} values in critical state and excess reactivity were overestimated compared with measured results by 0.5% and 0.9% respectively. Shutdown margin was underestimated by 3.4%, however the calculated k_{eff} value was estimated one of deep sub-criticality, therefore calculated shutdown margin was predicted relatively.

For the critical state model, calculated k_{eff} with 100,000 histories was compared with 1,000,000 histories one due to confirmation of reasonable result of 100,000 histories calculation in the JMTRC full core model. Calculated results are shown in Table 2. The calculated k_{eff} of 1,000,000 histories were agreed with of 100,000 histories within a standard deviation(1 σ). Therefore, k_{eff} calculation of 100,000 histories was enough to the estimation of k_{eff} in the JMTRC core.

4. Sensitivity analysis

For effect of control rod position, two critical core models were calculated(Fig.3). Calculated results ware shown in Table 3. 'Critical state A' is in normal operation model (center control rod are full insertion) and 'Critical state B' (center control rod are full up) is in special one. In both critical state, control rod A and B are full up, and control rods C and D are used for critical search. For the reactivity effect, shadowing effect of control rod C and D was treated well.

The JMTRC core was surrounded by beryllium reflector and effect of S(α , β) (thermal scattering treatment is a complete representation of thermal neutron scattering by molecules and crystalline solids) is important to calculation of this core. Calculations of the effect were performed with critical state, excess reactivity and shutdown margin models. Results are shown in Table 4. As result, the effect was negligible in critical calculation in the JMTRC, since importance of beryllium reflector region is smaller than of fuel region.

Comparison of k_{eff} calculations in the JMTRC core with JENDL3.1 and with JENDL3.2 shows Table 5. The k_{eff} with JENDL3.1 is approx. 0.8% lower than those with JENDL3.2. For this reason, ^{235}U capture cross section in JENDL3.2 was 10% reduced in

comparison with JENDL3.1.

For dependence of fuel loading in the JMTRC core, the k_{eff} in critical states was calculated for each step of the fuel addition from the minimum critical core to the final core. Calculated results are shown in Fig.4. Significant dependence of fuel loading was not observed.

5.Summary

It was confirmed to applicability of MCNP/JENDL3 to the JMTRC core calculation. For sensitivity analysis, shadowing effect of control rods was well treated. S(α , β) effect of Beryllium metal was negligible in the JMTRC core. The calculated k_{eff} in the JMTRC core with JENDL3.2 was higher than JENDL3.1. With calculated k_{eff} in the JMTRC critical core of difference in fuel loading by fuel addition, significant dependence was not observed.

Reference

1. Briesmeister J.F. (Ed.):"MCNP - A General Monte Carlo N-Particle transport Code, Version 4A," LA-12625(1993).
2. Kazuaki Kosano, et al.:"FSXLIB-J3R2: A Continuous Energy Cross Section Library for MCNP Based on JENDL-3.2," JAERI-Data/Code 94-020(1994)
3. S. Shimakawa, et al,:"Critical Experiments of JMTRC MEU Cores (II), " Proceedings of an International Meeting, RERTR(1985)

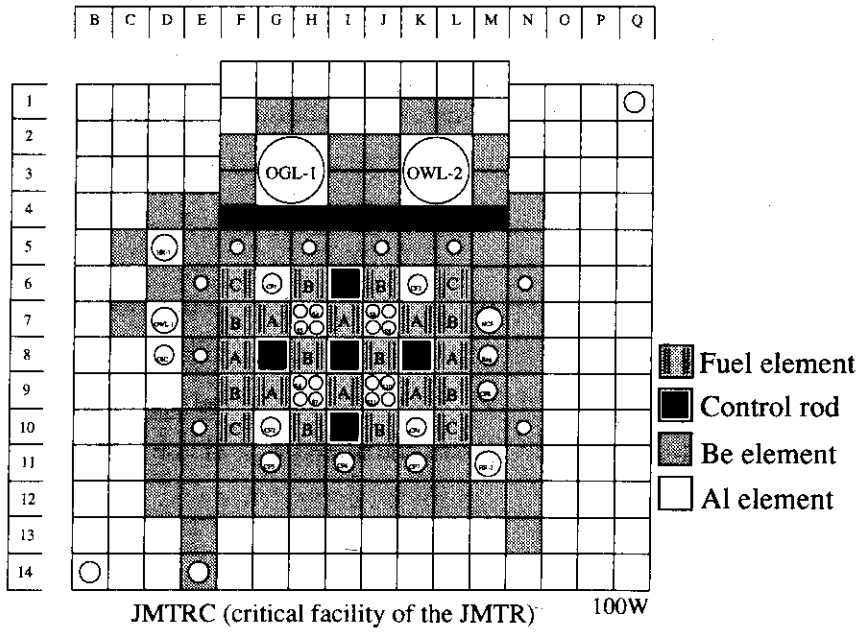

Fig.1 JMTRC core configuration

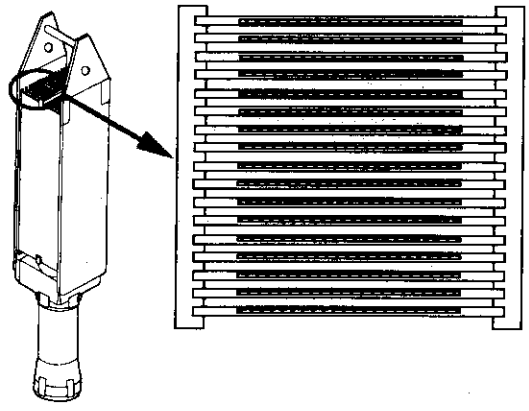

Fig.2 Fuel element of the JMTRC

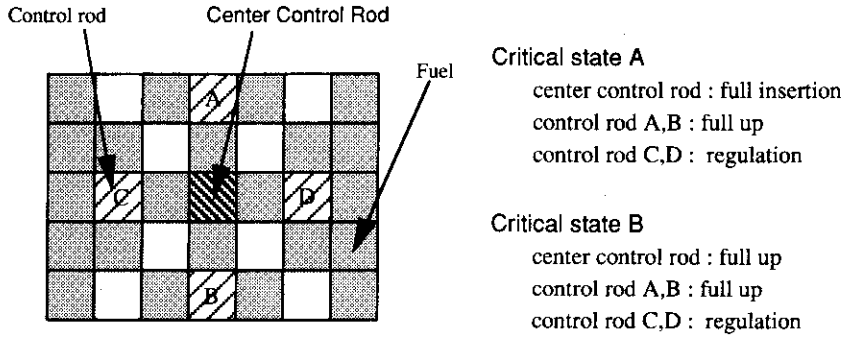

Fig.3 Effect of control rod positions

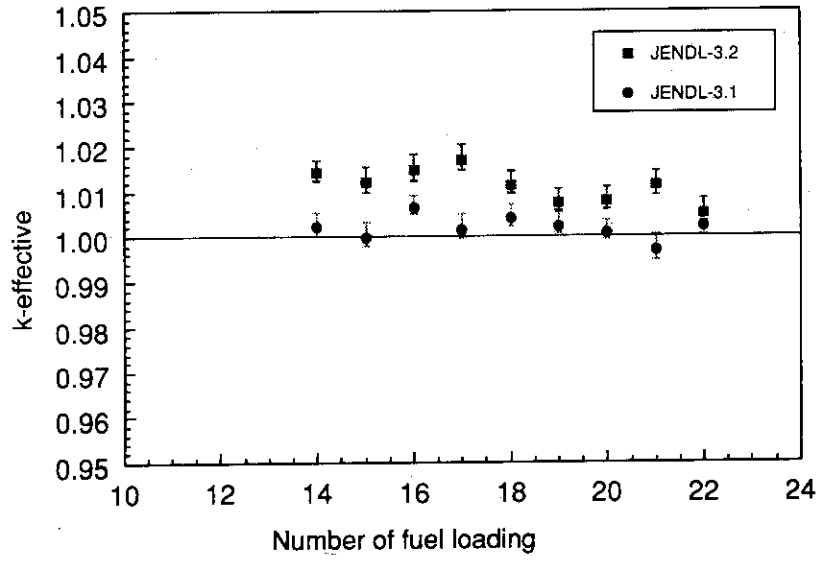

Fig.4 Effect of fuel loading

Table 1 JMTRC benchmark calculation results

	Calculation(C)		Measurement(M)	C/M
	k-effective	deviation(1 σ)		
Critical state	1.00544	0.00253	1.000	1.005
Excess Reactivity	1.13586	0.00226	1.126	1.009
Shutdown margin	0.84760	0.00253	0.877	0.966

Table 2 Comparison of calculated k_{eff} for difference in neutron histories

	k-effective	deviation(1 σ)
100,000 histories	1.00544	0.00253
1,000,000 histories	1.00733	0.00081

Table 3 Effect of control rod positions

	k-effective	deviation(1 σ)
Critical state A (center lod : full insertion)	1.00544	0.00253
Critical state B (center rod : full up)	1.00574	0.00265

Table 4 S(α , β) effect of Beryllium metal

	effect	no effect	ratio(effect/no effect)
Critical state	1.00544	0.99775	1.001
Excess Reactivity	1.13586	1.12638	1.000
Shutdown margin	0.84760	0.84396	0.999

Table 5 Comparison of the k_{eff} with JENDL3.1 and JENDL 3.2

	JENDL3.1	JENDL3.2	ratio(J3.1/J3.2)
Critical state	1.00544	0.99775	0.992
Excess Reactivity	1.13586	1.12638	0.992
Shutdown margin	0.84760	0.84396	0.996

3.5 Benchmark Tests of FP Nuclear Data in JENDL-3.2 and Consideration of Resonance Self-Shielding Effects for Neutron Strong Absorber Nuclei

JNDC FPND Working Group

T. Watanabe[1], M. Kawai[2], T. Nakagawa[3], Y. Nakajima[3], T. Sugi[4], S. Chiba[3], A. Zukeran[5], H. Matsunobu[6], H. Takano[3], H. Akie[3]

1) Kawasaki Heavy Industries, Ltd., Koto-ku, Tokyo, Japan

2) Toshiba Corporation, Kawasaki-ku, Kawasaki-shi, Japan

3) Japan Atomic Energy Research Institute, Tokai-mura, Naka-gun, Ibaraki-ken, Japan

4) Education Society for Wide Fields, Minato-ku, Tokyo, Japan

5) Hitachi Ltd., Hitachi-shi, Ibaraki-ken, Japan

6) Sumitomo Atomic Energy Industries, Ltd., Sumida-ku, Tokyo, Japan

Abstract Benchmark tests of the fission product nuclear data compiled in JENDL-3.2 have been carried out for the STEK reactivity worth data, CFRMF activation data and EBR-II sample irradiation data. From these tests, the following evidences were derived; 1) An average discrepancy of the calculated values from the measured ones for FP nuclei is less then 10 %, while systematic underestimation is seen for strong absorbers with A>130. 2) Discrepancies of the capture reactivity worth ratios for weak absorber are within 20%. 3) An average C/E-value of three lumped FP samples is 0.99. In order to clarify the underestimation of the item 1), investigations were made but any satisfactory explanation could not be obtained even with the best estimation using reliable measured data and advanced calculational method of reactor physics.

I. Introduction

The fission product nuclear data of JENDL-3.2[1] were revised for the 63 nuclei from JENDL-3.1[2] considering new experimental data, adopting the advanced evaluation methods and reflecting the experiences of the integral tests made for JENDL-3.1[3]. To evaluate the applicability of the new library JENDL-3.2, the present benchmark tests have been carried out using STEK reactivity worth data[4], CFRMF activation data[5] and EBR-II sample irradiation data[6]. In this work, the results of the tests are reviewed and the inconsistencies between the calculated and measured values of integral tests are investigated putting emphasis on resonance self-shielding effects.

II. Method

The method adopted in the present benchmark tests is the same as the previous tests[3] of FP nuclear data in the JENDL-3.1 library, i.e., the 70-group constants for JFS3-J3 library were prepared with the nuclear data processing code TIMS-PGG[7]. The 70-group normal and adjoint fluxes of the sample test zone were obtained with the cubic spline interpolation method from the fluxes reported in Refs. 4,5 and 8. As for the STEK experiments, the normal and adjoint fluxes were adjusted so as to reproduce the reactivity worth[8]. The flux depression in the sample region was estimated with a collision probability method.

In the present benchmark tests, total 67 FP nuclei, consisting of 57 FPs and 3 lumped FPs[9] in the STEk for reactivity worth data, 27 FPs of CFRMF as activation data and 9 FPs of EBR-II sample irradiation data, were tested.

The STEK experimental data are given as the reactivity worth ratios to the pseudo sample denoted by suffix 0 as shown by,

$$\frac{\rho}{\rho_0} = \frac{\sum_i \phi_i \left(\sum_k \sigma_{cik} N_k \right) \phi_i^* + \sum_{ij} \phi_i \left(\sum_k \sigma_{sk}(i \to j) N_k \right) \left(\phi_j^* - \phi_i^* \right)}{\sum_i \sigma_{fi}^{235} N_{235} \phi_i \sum_j X_j^{252} \phi_j} \qquad (1)$$

where N_k means atomic number densities of isotope k in the measured sample of unit weight or ^{235}U. The indexes i, j stand for energy group number index and l, k stand for nuclide index. The other variables have ordinary meanings of reactor physics.

For CFRMF and EBR-II, the average capture cross sections σ_c are obtained by the flux weight average as defined by

$$\sigma_c = \frac{\sum_i \phi_i \sigma_{ci}}{\sum_i \phi_i} \qquad (2)$$

The effective cross sections were obtained by table look-up of Bondarenko type cross section and the admixture background cross section σ_0 was defined by Eq.(3).

$$\sigma_{0k} = \sum_{l \neq k} \frac{\sigma_{tl} N_l}{N_k} + \frac{1}{\ell d N_k} \qquad (3)$$

III. Results and Discussion

1. Overall trends

In Fig. 1, the C/E-values averaged over all samples and spectra; denoted by <C/E>, are shown to verify overall improvement from JENDL-3.1 to JENDL-3.2 libraries. The deviations from C/E=1.0 are slightly smaller in the JENDL-3.2 than in the JENDL-3.1.

In order to clarify the capture contribution of weak absorbers, the average C/E-values of capture reactivity worth in STEK and the other average C/E-values of the CFRMF and EBR-II experiments are shown in Fig. 2. The C/E-values of capture components for the STEK experiments<C/E>$_{C,STEK}$ are derived from the following semi-empirical formula;

<C/E>$_{C,STEK}$ =(Calculated reactivity worth ratio)/

[(measured total reactivity worth ratio)-(calculated scattering worth ratio)] (4)

From the above studies, the following trends could be drawn.

1) In comparison with JENDL-3.1, the C/E-values of JENDL-3.2 are slightly improved and the resultant average discrepancy is reduced to 10 % as maximum. 2) For weak absorbers, the discrepancies of the capture reaction rates are within 20 % except few FP nuclei. As shown in Fig. 3 for the weak absorbers, the net reactivity worth are resulted as the cancellation between capture and scattering component, and thus their discrepancies tend to be enhanced. Therefore, rigid justification of such a material can not be discussed only from cross section data since the results are strongly affected by the calculational method of reactor physics. 3) While, the C/E-values for strong absorbers with mass number greater than 130 show systematical underestimation by amount of 0.85. 4) The lumped FPs give good C/E-values of 0.99.

2. Validation of Calculational Method

In order to investigate the reasons of the systematic underestimation of capture reaction rates mentioned above, cross section data in JENDL-3.2 were compared with the measured cross sections. The evaluated cross section data are consistent with the experimental data as shown in Fig. 4 for ^{133}Cs as a typical example. Therefore, the following approaches were performed to examine the calculation method for benchmark tests.

1) Validation of the adjusted fluxes.

As described in section **II**, the normal and adjoint fluxes of STEK cores were adjusted on the basis of the ECN's Bondarenko type cross section set[8]. Such a method can scarcely estimate the fine structure of fluxes and resonance self-shielding effect especially in the sample region. Therefore, as an alternative advanced method; the continuous Monte Carlo code MVP[10] and the 70 group diffusion calculation code CITATION[11] together with the cell calculation code SLAROM[12], were adopted in the present work. In both methods, the same geometry and atomic density[13] were used to keep consistency. The fluxes are shown in Fig. 5 for the STEK-4000 core with the softest spectrum. As shown in the figure, the reference fluxes explained in the section II agree well with the fluxes calculated present methods and the effect of flux replacement with the one based on the present method on the <C/E>s values is smaller than as expected.

2) Reactivity Worth Denominator Governed by Main Fuel Materials.

The effective cross section of ^{235}U and the spontaneous fission spectrum of ^{252}Cf used as the denominator were reevaluated by using the data of JENDL-3.2. However, the systematical underestimation of reactivity worth could not be improved.

3) Resonance Self-shielding Effects and Flux Depression.

In order to validate the effective cross section and the flux depression in the sample zone, cell calculation for the STEK-4000 and -500 cores was carried out with MVP in considering the inner core and the oscillator containing ^{133}Cs or ^{103}Rh samples. The calculated effective macroscopic cross section and the flux depression were compared with those of the reference methods explained in the section II. In Fig.6 large differences of the macroscopic cross sections could be seen at large resonances in the low energy region, which imply the crudeness of the Bondarenko procedure of resonance self-shielding effect. On the other hand, the effects of the difference of flux depression plotted in Fig.7 on <C/E>s were small, although there is still rather large fractional standard deviation in the MVP calculation. The further detailed cell calculation with the SRAC

code[14] was executed. The cell model was almost the same as the MVP calculation except that the SRAC calculation was a one dimensional cell model. The SRAC calculation uses ultra fine lethargy intervals between 961.12eV and the thermal cutoff energy of 2.38eV. The calculated flux depression and macroscopic cross sections in the 70-group structure were compared with those of the reference methods for 10 nuclide of ^{95}Mo, ^{99}Tc, ^{103}Rh, ^{109}Ag, ^{133}Cs, ^{143}Nd, ^{147}Sm, ^{149}Sm, ^{153}Eu and ^{159}Tb. The ratios of the calculated values with SRAC to the reference ones show the same trend as the ratios of MVP calculation to the reference case as shown in Fig.6 and 7. However ratio values for macro cross sections of the SRAC calculation were rather small. The similar trends were seen to all other nuclei with large resonances at low energies. The effect of these differences on the <C/E>s was less than 5%. Therefore, these insufficiency of the calculational model evaluating resonance self-shielding effect could not explain the all of the systematic underestimation of <C/E> in the atomic mass range above 130. In the Table 1, the inconsistent nuclide among high priority FP nuclei whose discrepancies are larger than 15% between the calculated and measured values are shown.

IV. Conclusion

In conclusion, FP nuclear data in JENDL-3.2 are applicable for FBR use. However, the systematical underestimation of reactivity worth for the heavy nuclei could not be explained even with the best estimation using reliable nuclear data and the advanced calculational methods. New integral experiments providing more detailed information for analysis are requested to the nuclei listed in Table 1 and supplemental integral tests by using the new experimental data are needed to the nuclei such as ^{134}Cs, ^{155}Eu which have neither measured cross section data nor integral experiments in the present.

References:

(1) M.Kawai et al., 1995 Gatlinburg Vol.2 p727(1995)
(2) M.Kawai et al., J.Nucl.Sci Tech.29,195(1992)
(3) T.Watanabe et al., NEA/NSC/DOC(92)9,p411(1992)
(4) J.J.Veenema and A.J.Jansen,ECN-10(1976)
(5) Y.D.Harker et al., NEANDC(E)-209"L" p.5(1980)
(6) R.A.Anderl,EGG-PHYS-5182(1081)
(7) H.Takano et al., JAERI-M 82-072(1982)
(8) J.W. Dekker et al., ECN-35(1978)
(9) R.J.Heibloer et al., ECN-11(1976)
(10) T.More. and M.Nakagawa, JAERI-data /Code 94-007(1994)
(11) T.B.Fowler et al., ORNL-TM-6054(1960)
(12) M.Nakagawa and K.Tsuchihashi,JAERI-1294(1984)
(13) H.T.Klippel and J.Smit,RCN-209(1974)
(14) K.Tsuchihashi et al., JAERI-1302(1986)

Table 1 <C/E> Values of Inconsistent Nuclei among High Priority FP's
Discrepancy Larger Than 15% Between Differential and/or Integral Experiments of STEK CFRMF and EBR-II

Nuclide	STEK	CFRMF/EBR-II	Nuclide	STEK	CFRMF/EBR-II
^{93}Zr	0.42±0.44 o	-	^{139}La	0.70±0.03 o	1.00±0.05
^{96}Zr	0.66±0.05 o	-	^{142}Ce	0.66±0.05 o	0.76±0.06
^{98}Mo	0.78±0.06	1.16±0.13	^{143}Nd	0.90±0.01 o	0.85±0.08 E
^{100}Mo	0.45±0.06	1.00±0.09	^{145}Nd	0.84±0.03 o	0.81±0.08 E
^{99}Tc	0.80±0.02	1.16±0.17	^{148}Nd	0.79±0.06 o	0.98±0.14
^{106}Pd	1.17±0.09	-	^{147}Pm	0.88±0.05 o	1.08±0.14
^{109}Ag	0.66±0.05	0.74±0.07	^{149}Sm	0.88±0.06 o	0.83±0.08 E
^{127}I	0.86±0.01 p	1.09±0.11	^{152}Sm	0.85±0.03 o	1.01±0.06
^{129}I	1.06±0.06 p	1.15±0.08	^{154}Sm	0.81±0.09 o	-
^{133}Cs	0.86±0.01 c	0.91±0.06	^{154}Eu	-	0.87±0.11 E

N.B. o;Oxide sample p;PbI2 sample c;CsCl sample E;EBR-II

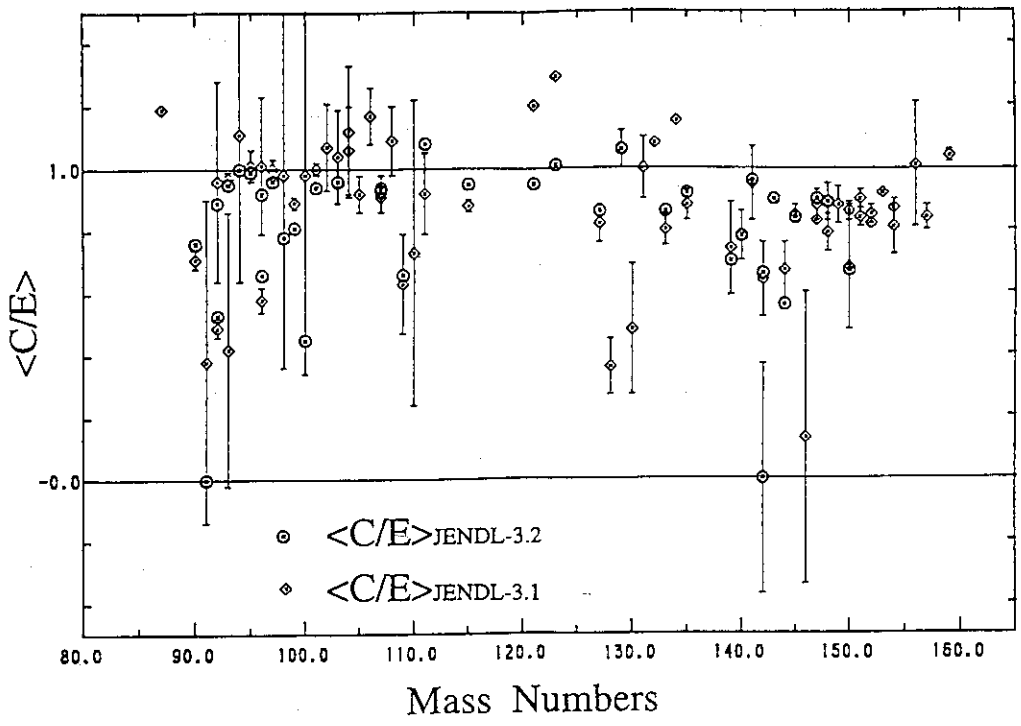

Fig. 1 Comparison of <C/E> Between JENDL-3.2 and JENDL-3.1

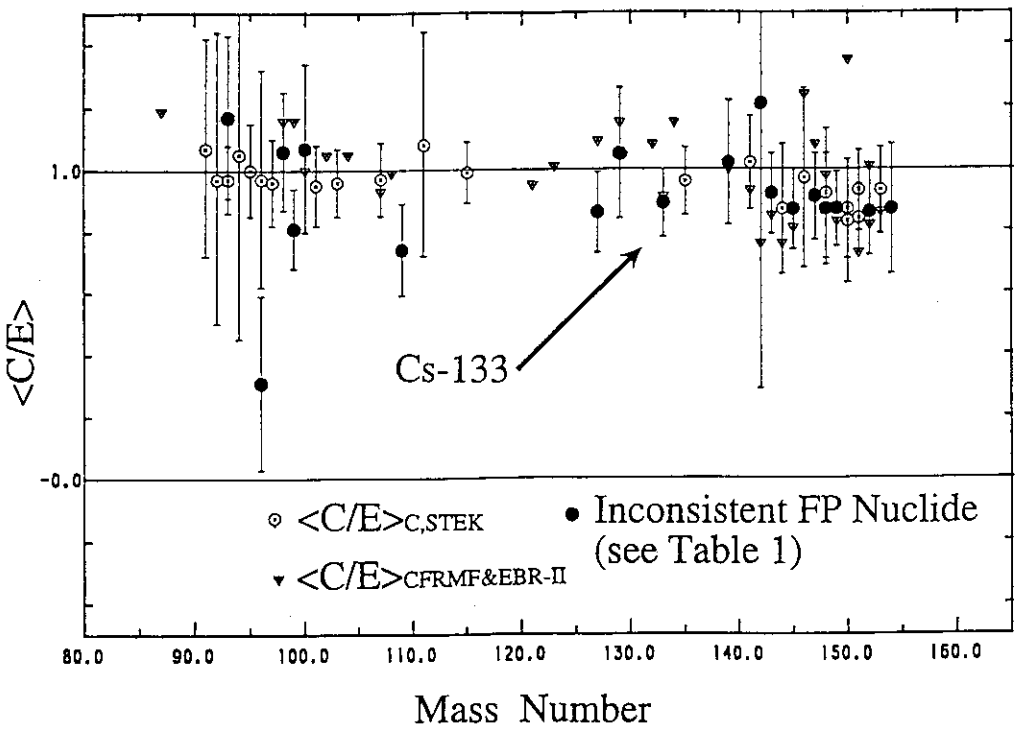

Fig. 2 Comparison of <C/E>C,STEK and <C/E>CFRMF&EBR-II

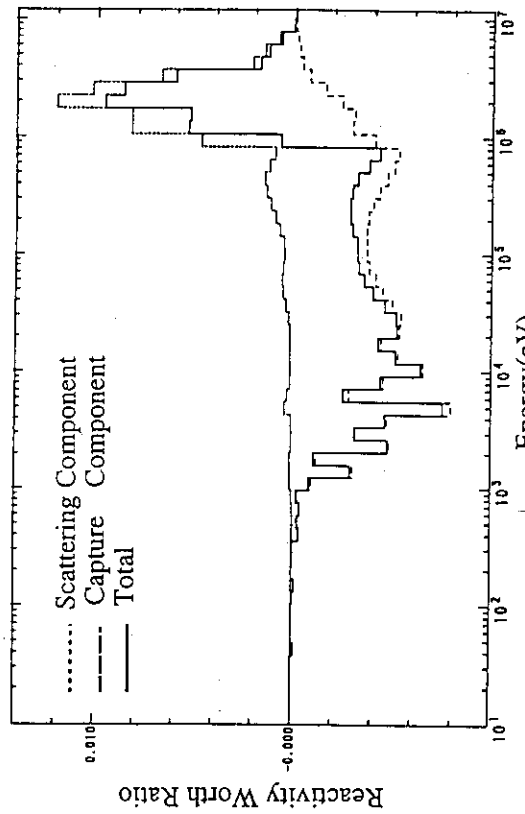

Fig. 3 Capture and Scattering Component of Reactivity Worth Ratio of Mo-94 in STEK-500 Experiment

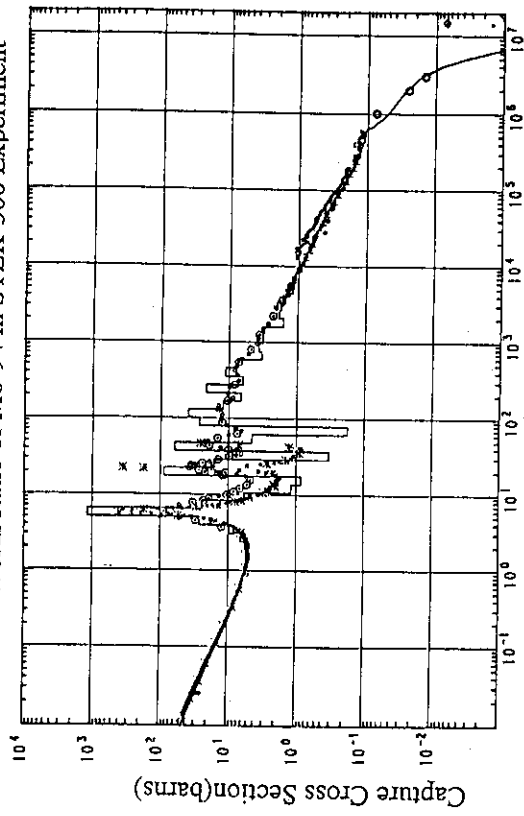

Fig. 4 Comparison of Cs-133 Capture Cross section Between JENDL-3.2 and Measured Data

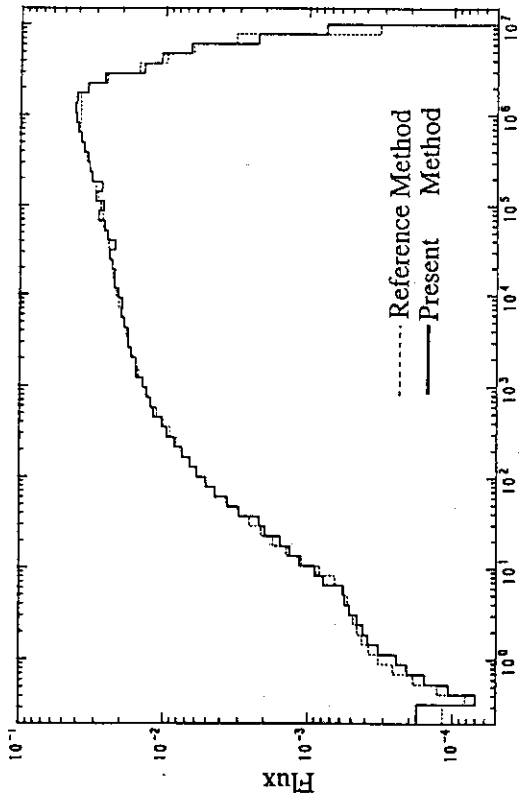

Fig. 5 Comparison of Flux at the Test Zone of STEK-4000 Between Calculated with Reference and Present Method

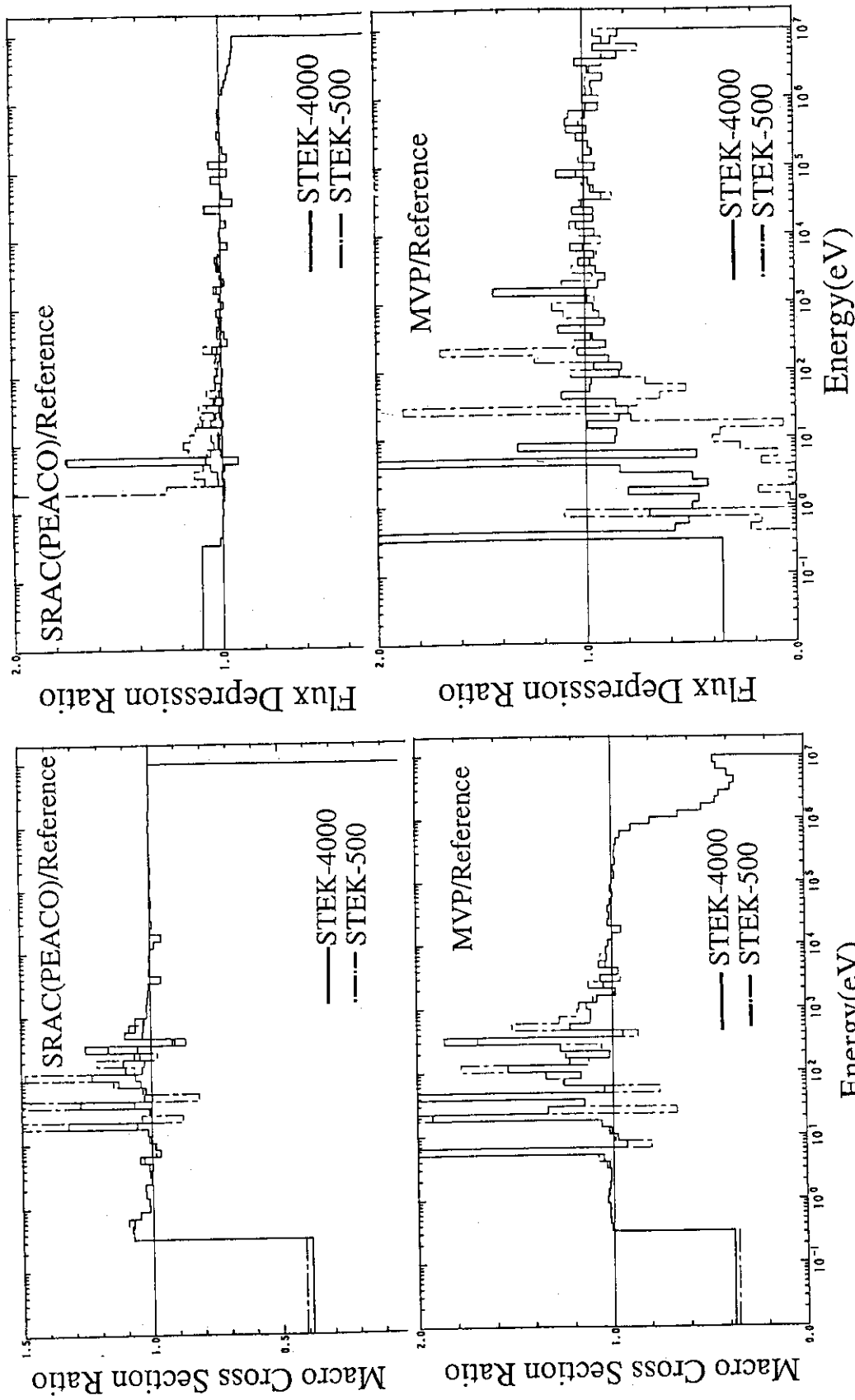

Fig. 7 Comparison of Flux Depression in Cs-133 Sample

Fig. 6 Comparison of Macro Cross Seciton of Cs-133 Sample

3.6 Measurements of Double-differential Neutron Emission Cross Sections for 18 and 11.5 MeV Neutrons

Daisuke Soda[1], Shigeo Matsuyama[2], Ibaraki Masanobu, Mamoru Baba,
Shin Iwasaki and Naohiro Hirakawa
Department of Nuclear Engineering, Tohoku University,
Aramaki-Aza-Aoba, Aoba-ku, Sendai, 980-77, Japan
E-mail [1]soda@rpl.nucle.tohoku.ac.jp
[2]shige@rpl.nucle.tohoku.ac.jp

Double-differential neutron emission cross sections (DDXs) of Fe and Si for 18 MeV neutrons and of Nb and Bi for 11.5 MeV neutrons have been measured at the Tohoku University 4.5 MV Dynamitron facility. In this study, the energy resolution was much improved than in previous studies by applying a long liquid scintillation detector (LLSD). Concerning the 11.5 MeV measurements, secondary neutron energy range was extended by adopting the double-TOF (D-TOF) method.

1. Introduction

Double-differential neutron emission cross sections (DDXs) for fast neutrons are very important for the neutronics design of fusion reactors, shielding design for high energy accelerator facilities and so on. DDXs for 18 and 11.5 MeV neutrons have been measured using neutrons from the $T(d,n)^4He$ and the $^{15}N(d,n)^{16}O$ reactions, respectively. To compensate the low intensity of these sources, we adopted a long liquid scintillation detector (LLSD) whose detection efficiency is three times as large as that of the detector used previously [1, 2]. Therefore, the energy resolution was much improved by taking a longer flight path than in previous measurements without loosing a counting rate. The neutrons from the $^{15}N(d,n)^{16}O$ reaction are not monoenergetic because of the neutrons from several excited states of residual ^{16}O, therefore the spectrum measured by the conventional single-TOF (S-TOF) method is distorted by background neutrons in the secondary neutron energy region lower than $\sim$6 MeV. Then, we adopted the double-TOF (D-TOF) method [3] that was similar to that employed at China Institute of Atomic Energy (CIAE) [4] and eliminated the effects of background neutrons in the TOF spectrum. As a result, we could extend the secondary neutron energy range down to $\sim$1 MeV.

2. Experiments and Data Reduction

Experiments were carried out using the Tohoku University Dynamitron time-of-flight spectrometer. The S-TOF method was employed for the 18 MeV measurements and the high energy part of 11.5 MeV measurements. For the 1.5 MeV measurements, we employed the

D-TOF method to get the neutron emission spectra for En'< 6 MeV. The source neutrons of 18 and 11.5 MeV were produced by bombarding tritium-loaded titanium (Ti-T) and $^{15}N_2$ gas targets, respectively, with a pulsed deuteron beam provided by a 4.5 MV Dynamitron accelerator.

The S-TOF experimental method was almost the same as that in previous studies [5] except for the neutron detector and the flight path length. By applying LLSD, the flight path could be extended to ～6 m (previously ～4 m). Figure 1 shows the schematic view of LLSD. It is a 80 cm long rectangular shaped NE213 scintillator coupled with two photomultipliers at both ends of the scintillator cell. In this study, we used LLSD as a single large detector and compensated the low intensity of neutron sources. Figure 2 shows the experimental set up of the S-TOF method. Scattering samples were cylinders of elemental iron (3 cm ϕ x 5 cm) and silicon (4 cm ϕ x 4 cm) in the 18 MeV measurements, and niobium and bismuth (3 cm ϕ x 5 cm) in the 11.5 MeV measurements. These samples were suspended vertically at a distance of 12 cm from the neutron targets. LLSD was housed in a massive shield placed on a turning table and the neutron emission spectra were measured at several angles between 20° and 150°. Special data acquisition and reduction systems were employed to make a efficient use of LLSD [2]. Absolute cross sections were determined by referring the elastic scattering cross section of the H(n,n) reaction.

The D-TOF method adopted a longer target-sample distance (～3 m) and shorter sample-detector distance (～85 cm) than in the S-TOF method. Figure 3 shows the experimental set up of the D-TOF method. The neutron target was shielded with iron, water, and concrete to reduce sample independent backgrounds. Secondary neutrons were detected by a 14 cm ϕ x 10 cm NE213 scintillation detector which was shielded with lead and paraffin. Measurements were dane at 90°. Figure 4 shows a typical D-TOF spectrum of Bi. It shows that the secondary neutrons by 11.5 MeV neutrons are separated well enough from those by background neutrons. Absolute cross sections were determined by normalizing the D-TOF data to the S-TOF data considering the resolution function.

The TOF spectra were converted into the energy spectra considering the effects of sample independent backgrounds and the detection efficiency. The energy spectra were corrected for the effects of finite sample-size by Monte-Carlo calculations.

3. Results

Figure 5 and 6 show typical DDXs of Fe and Si for 18 MeV neutrons in comparison with those derived from the evaluated nuclear data of JENDL-3.2 and ENDF/B-VI. While the neutrons of the first excited state of Fe-56 (E_x= 0.86 MeV) are hidden under the ground state peak, those of Si-28 (E_x= 1.78 MeV) are resolved sufficiently well from those of the ground state. Energy resolution in this measurement is estimated to be about 1 MeV at 18 MeV.

Figure 7 and 8 show the DDX of Nb and Bi for 11 MeV neutrons at 90° in comparison with those derived from the evaluated nuclear data. The data for En' > 6 MeV were derived from the S-TOF data and the data for En'< 6 MeV from the D-TOF data. By combining the S-TOF and D-TOF method, we can get almost entire DDX data for 11.5 MeV neutrons. Our results generally agree with the data from JENDL-3.2 at 90°, but differ largely from the evaluated data at other angles. (Figure 9 and 10)

References

[1] S.Matsuyama et al., JAERI-M 94-019 (1994) P.210
[2] S.Matsuyama et al., Nucl. Instr and Meth. A, to be published
[3] S.Matsuyama et al., JAERI-conf 95-008 (1995) p.157
[4] Q.Bujia et al.,Proc. Int. Conf. on Nucl. Data for Sci. and Technol., Julich 1991 p.436
[5] M.Baba et al., J. Nucl. Sci. Technol., 31(8), 757(1994)

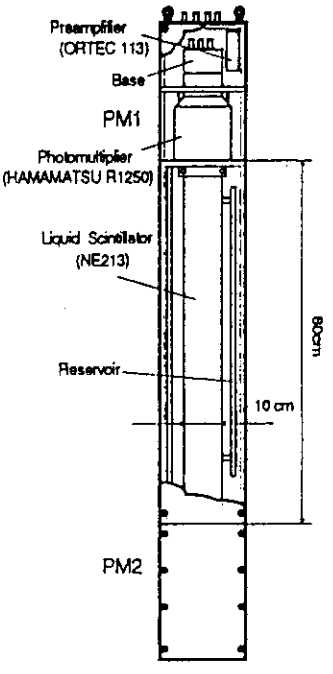

Fig.1 Schematic view of the LLSD

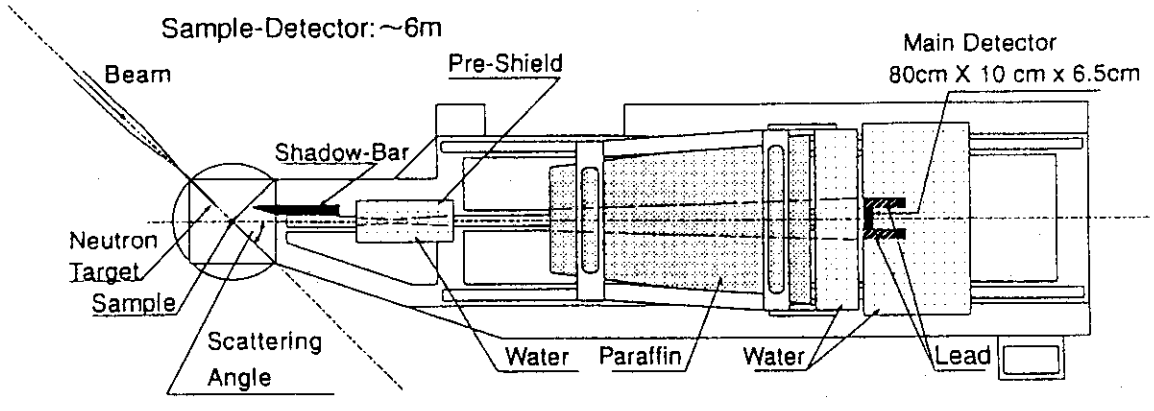

Fig.2 Experimental geometry of S-TOF method

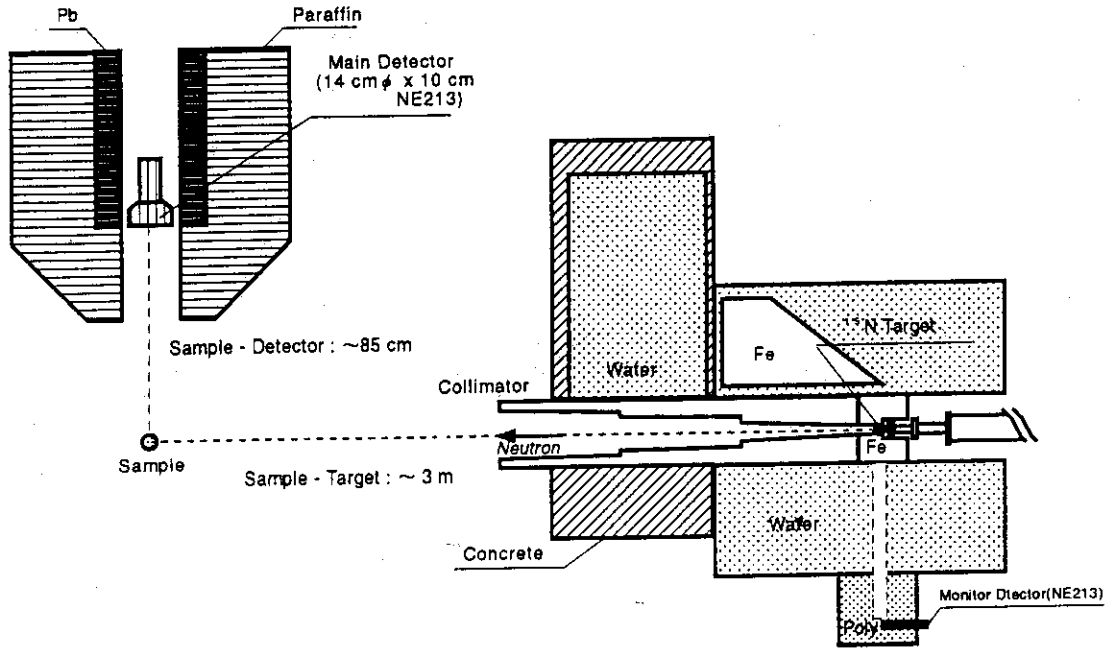

Fig.3 Experimental geometry of D-TOF method

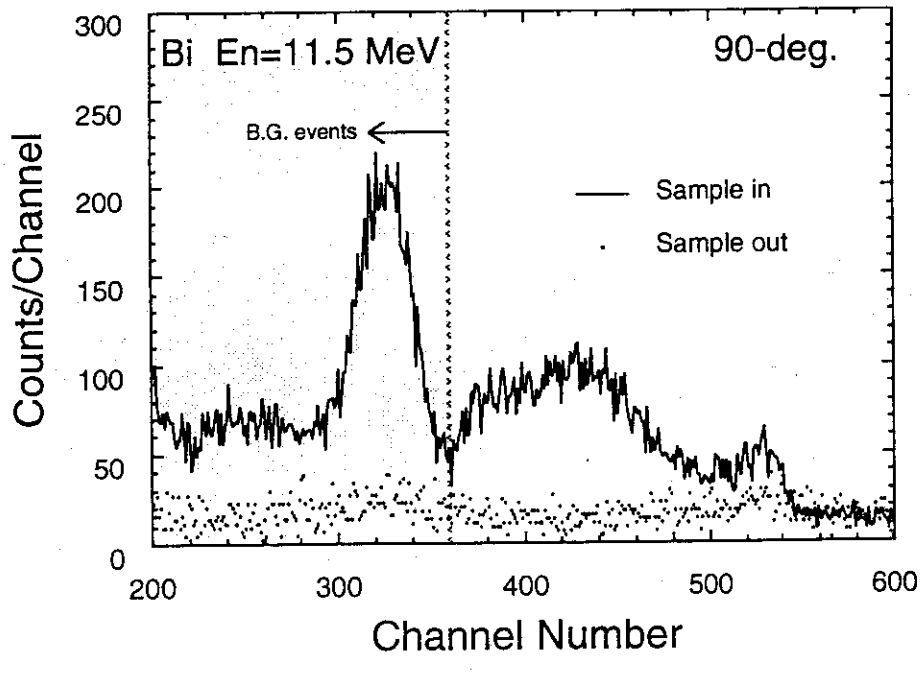

Fig.4 D-TOF spectrum of Bi at 90°

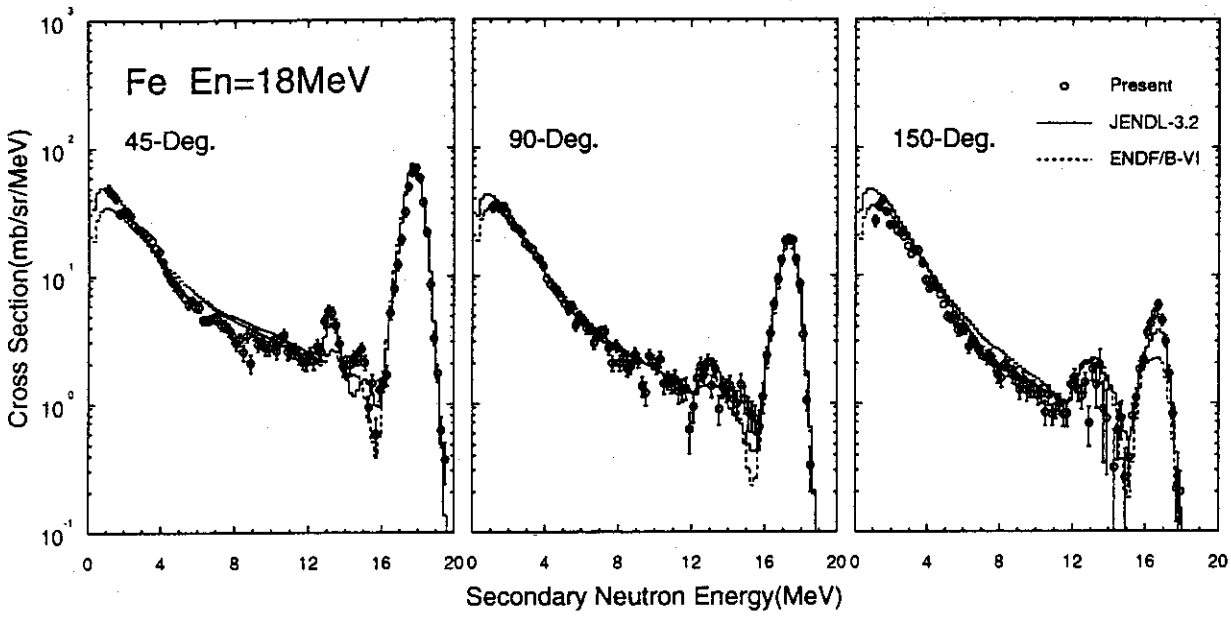

Fig.5 Double-differential neutron emission cross sections of Fe for 18 MeV neutrons

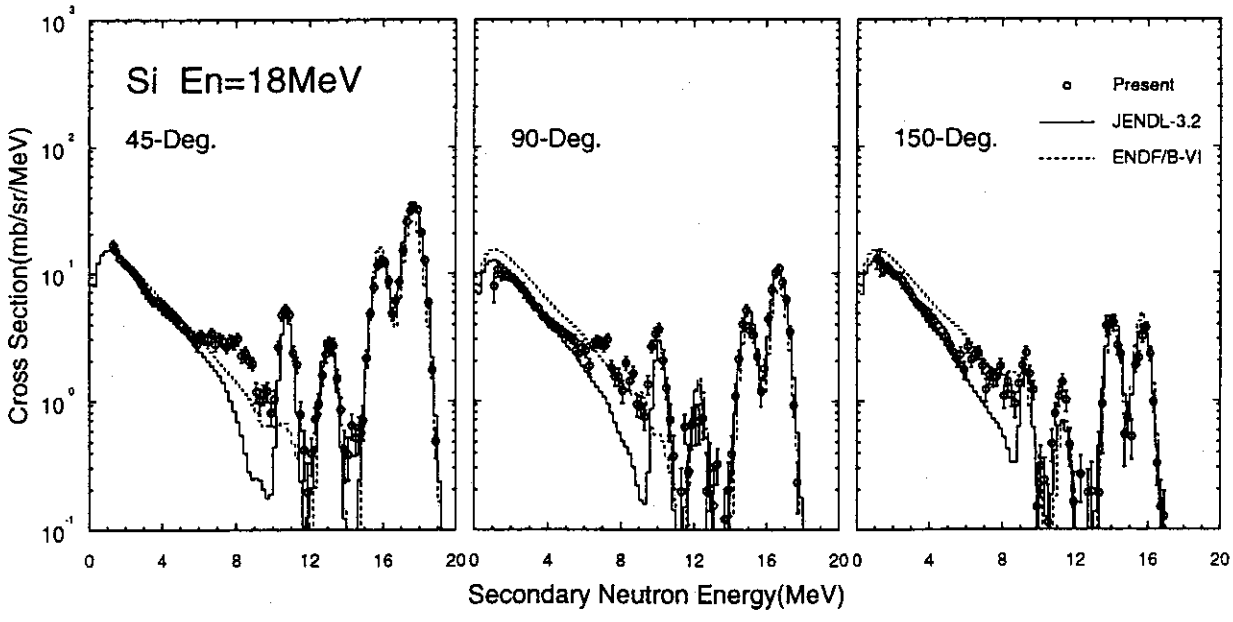

Fig.6 Double-differential neutron emission cross sections of Si for 18 MeV neutrons

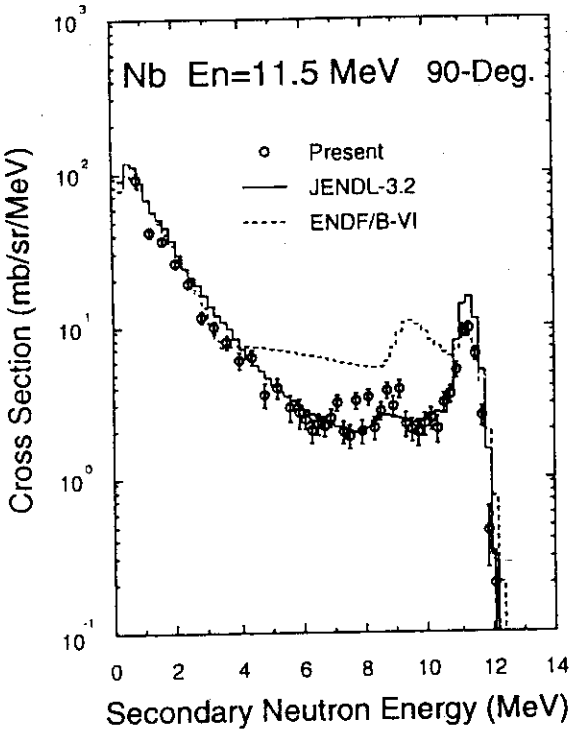

Fig.7 Double-differential neutron emission cross section of Nb at 90° for 11.5 MeV neutrons

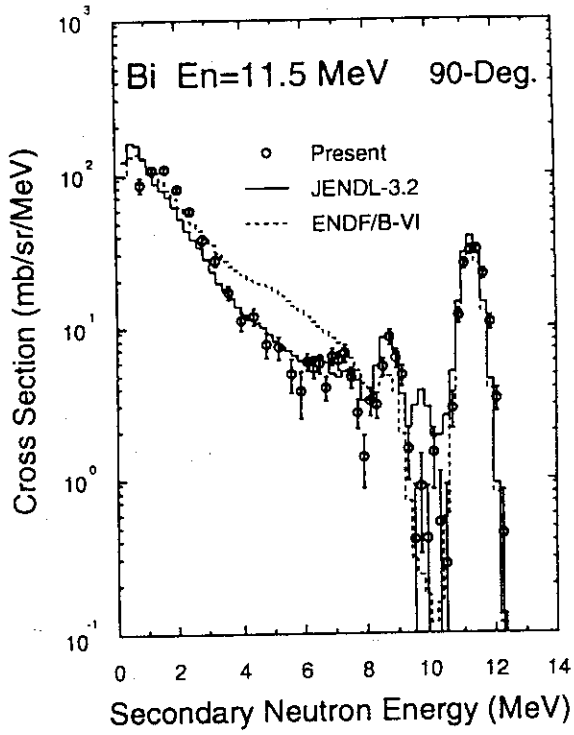

Fig.8 Double-differential neutron emission cross section of Bi at 90° for 11.5 MeV neutrons

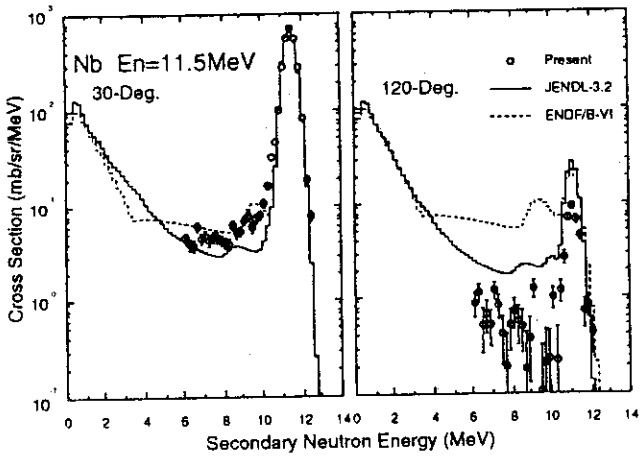

Fig.9 Double-differential neutron emission cross sections of Nb for 11.5 MeV neutrons

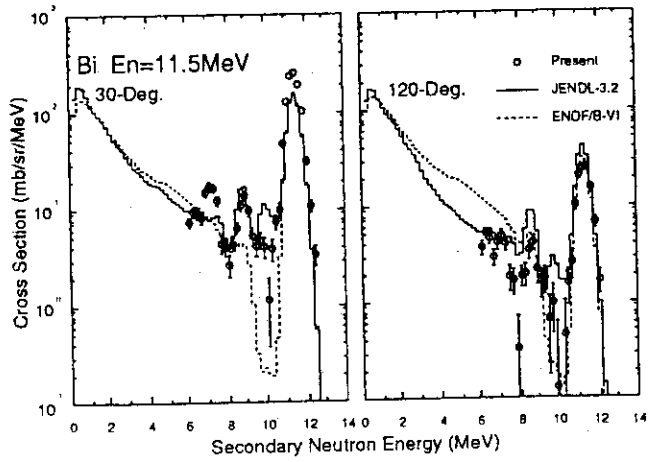

Fig.10 Double-differential neutron emission cross sections of Bi for 11.5 MeV neutrons

3.7 Development of Wide Range Charged Particle Spectrometer for Ten's MeV Neutron

*Yasushi NAUCHI[1], Mamoru BABA[1], Shigeo MATSUYAMA[1], Naohiro HIRAKAWA[1] and Susumu TANAKA[2]

1. Department of Nuclear Engineering, Tohoku University

Aramaki-Aza-Aoba, Aoba-Ku, Sendai, 980-77 Japan

**e-mail: nauchi@rpl.nucle.tohoku.ac.jp*

2. Takasaki Establishment, Japan Atomic Energy Research Institute, Takasaki 370-12

Abstract

A new wide range charged particle spectrometer system is developed to extend the measurement of double-differential hydrogen & helium isotopes production cross sections for ten's MeV neutrons. It consists of three telescopes mounted on a vacuum chamber. Each of the telescopes consists of a BaF_2 energy detector and a thin ΔE gas detector. Combining pulse shape discrimination (PSD) capability of BaF_2 with ΔE-E method, we will achieve particle identification (PI) over a wide range of charged particle energy.

1. Introduction

Double-differential cross sections (DDX) data of charged particle emission reactions for intermediate energy neutrons are required for estimation of radiation effects and biological effects over an almost entire range of the secondary energy. However, DDXs data beyond 20 MeV are scarce because of experimental difficulties and neutron source shortage. As for proton emission reactions, some DDXs data have been reported. However, these spectra did not include low energy part[3]. Measurements of α particles have been started only recently[4] using spectrometer specialized only for α particles.

For the study of ten's MeV neutron induced reactions, a $^7Li(p,n)$ neutron source in 20～90 MeV range (fig. 1) has been developed at TIARA (Takasaki Ion Accelerator for advanced Radiation Application). Using the source, we had measured (n,p), (n,d) DDXs of carbon with a SSD-NaI telescope operated in air[1]. However, α particles and low energy hydrogen isotopes are difficult to measure because of large energy losses. Besides, high backgrounds from air and low count rates occur many difficulties in the measurement of low energy particles and α particles.

For this reason, we have started the development of a new charged particle spectrometer for simultaneous measurement of hydrogen and helium isotopes production cross sections at TIARA over

the whole emission energy, i.e., 90 MeV protons down to a few MeV α particles. The reduction of backgrounds and the increase of the counting efficiency are also intended.

2. Basic Design

To identify α particles using the ΔE-E method, we employ a thin ΔE detectors of low pressure gas counter in a vacuum environment. However, in the ΔE detector, high energy protons loose too low energy to particle identification (PI). To provide the PI capability for high energy hydrogen isotopes, we use BaF_2 scintillators as energy detectors. The BaF_2 enables PI by pulse shape discrimination (PSD). This is because the light output of BaF_2 has two decay components (fast; 600 ps, slow; 620 ns), and the intensity ratio of these is different to each particle. PI by PSD will be done using gate integration method (fig. 2)[5]. By combining the ΔE-E with the BaF_2 PSD, we will achieve PI for the whole emission energy region.

Not only PSD capability, BaF_2 has several advantages. Its chemical stability eliminates the need of an entrance window, and enables the measurements of low energy α particles. Besides, a good timing resolution < 700 ps of BaF_2 enables to select events induced by the peak energy neutrons of the $^7Li(p,n)$ source, and its high stopping power reduces the edge effect for higher energy particles. Taking ΔE-E coincidence in the vacuum environment, backgrounds will be reduced down to an acceptable level.

To increase counting efficiency without deteriorating angular resolutions, we have planned to employ three telescopes at once. The geometrical parameters of the detectors were choosen using Monte Carlo simulation codes developed to study the relation among count rates, energy resolutions, and angular resolutions. A multi-telescopes chamber designed presently is shown in fig. 3 and calculated angular resolutions are shown in fig. 4.

3. Prototype telescope and test

As a component of the final multi telescopes, a prototype ΔE-E telescope has been fabricated. The schematic view of the telescope is shown in fig. 5. It consists of a BaF_2 scintillator, a thin gas detector, and a small vacuum chamber. The BaF_2 scintillator is 40 mm ϕ, 22 mm thick to stop 85 MeV protons, coupled to a fast PM tube . The ΔE detector is a 45 mm ϕ and 20 mm thickness of gas proportional counter. The gas detector window is 3.5 μm mylar and the anode wire is 0.1 mm ϕ W. With this set-up, 5 MeV α particles at the sample can reach the BaF_2 through the gas detector containing 1 atm of Ar. Some test experiments had been done.

The energy resolution of the BaF_2 was 8.7 % for 663 keV γ of ^{137}Cs, and the timing resolution was less than 700 ps for ^{60}Co cascade γ. PSD capability was tested using 22 MeV neutrons at Tohoku University Cyclotron Radio Isotope Center. Recoil protons from a sheet of 1.5 mm thickness of polyethylene which was put in front of BaF_2 entered into the scintillator together with direct neutrons

and γ rays. Photon and proton events were separated using the gate integration method (fast gate: 50 ns, total gate: 500ns) (fig.6). However, the energies of deuterons and α particles were too low to detect for this neutron energy. Further test will be done for composite of particle field.

Then, the gas detector has large scale (about 1600 mm^2), and thin (20 mm) detector (fig. 7). Its pulse height character was tested using a collimated ^{241}Am α source. Fig. 8 shows an α particle spectrum detected in the center of the counter with 1 atm of Ar and 5% CO_2. The energy resolution of the α spectrum is about 10 %. However, there was a position dependency in pulse height and timing feature. Now, we are modifying it to eliminate them.

As for the data acquisition circuit, we select a CAMAC system considering many data channels required for the operation of the multi telescope system. Gate integration is done using QDC LeCroy 2249A.

4. Summary

We have designed a wide range particle identification scheme combining the ΔE-E method and the pulse shaping discrimination technique, and geometrical set up using simulations. Then, we fabricated a prototype telescope, and studied the basic character of it. We will improve the telescope capability, and apply to the DDX measurement at TIARA.

The present work was undertaken as a part of special project research between universities and Japan atomic energy research institute.

Reference

1) M.Baba et al.,: *Proc. Int. Conf. on Nucl. Data for Sci. Technol.* (1994 Gatlinburg) p. 90

2) T.Kiyosumi et al.,: *JAERI-Conf 95-008* p. 193

3) A.Michaudon et al.,: *LA-UR-94-1320-First Edition* p. 50

4) R.C.Haight et al.,: *Proc. Int. Conf. on Nucl. Data for Sci. Technol.* (1994 Gatlinburg) p. 311

5) G.Lanzano et.al.,: *Nucl. Inst. Methods.* **A312**, 515 (1992)

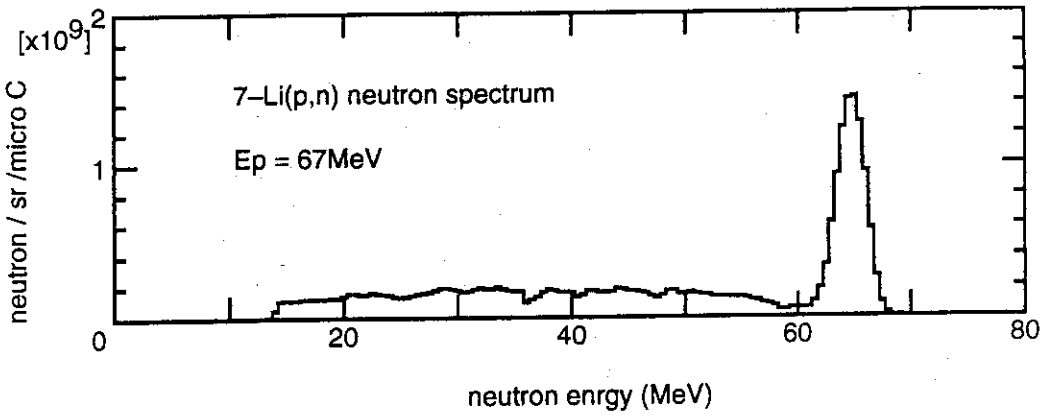

fig. 1: ^{7}Li(p,n) neutron spectra

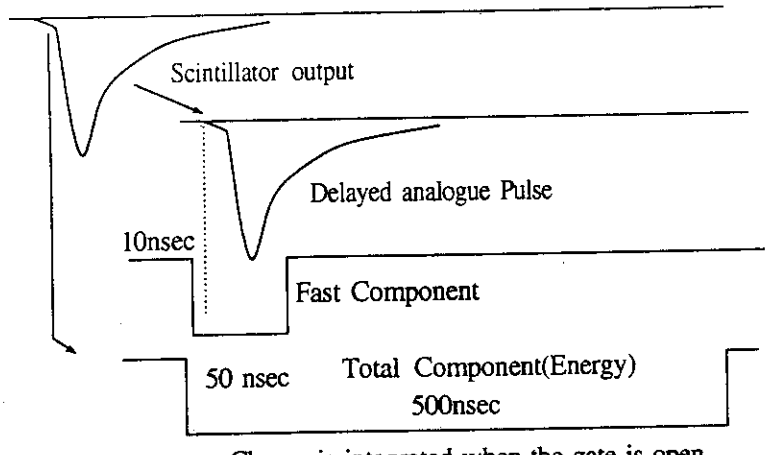

fig. 2: The gate integration method

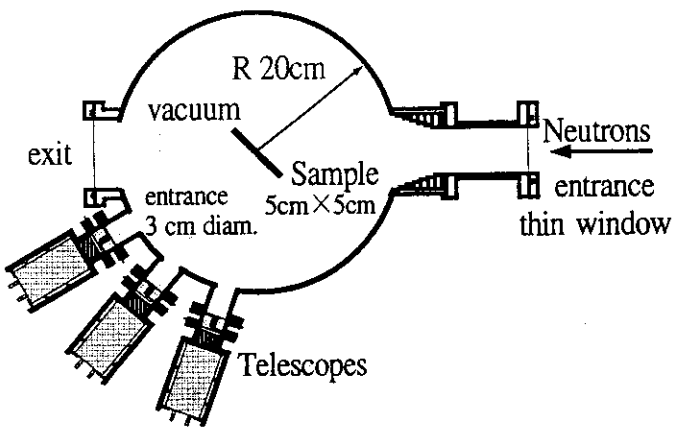

fig. 3: prototype multi telescopes chamber

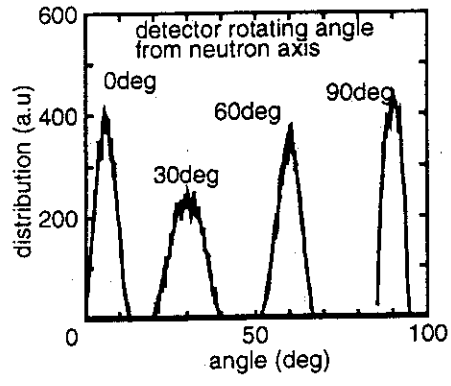

fig. 4: angular resolutions

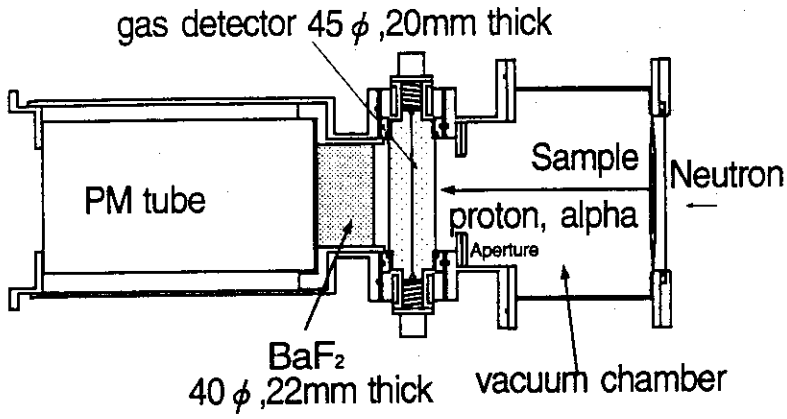

fig. 5: a prototype telescope

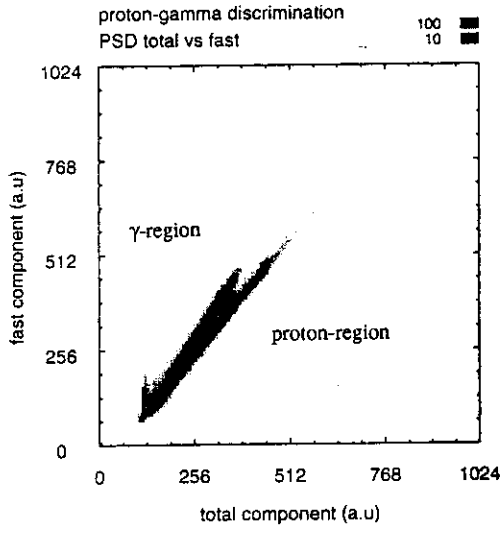

fig. 6: p-γ separation

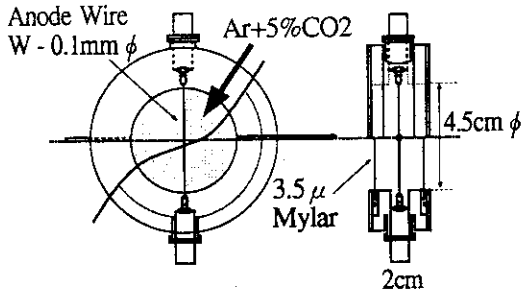

fig. 7: gas counter view

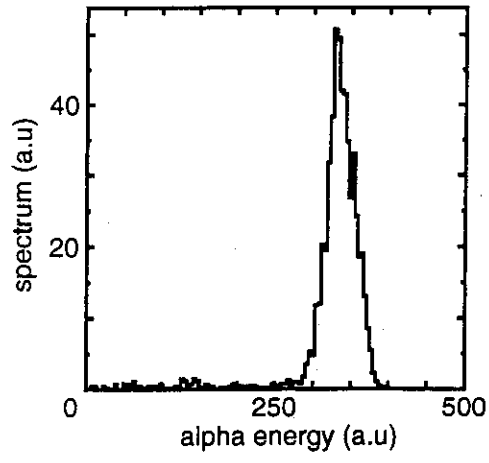

fig. 8: response of gas counter to α particle

3.8 Measurement of (n,2n) Cross-sections for Cu, Zn, Ag, and Sn between 12 and 20 MeV with activation technique

S. Iwasaki, S. Matsuyama, D. Soda, Y. Nauchi, H. Fukuda, M. Kitamura and N. Odano*

Department of Nuclear Engineering, Tohoku University
Aramaki-Aza-Aoba, Aobaku, Sendai 980, Japan
Fax.81-22-217-7907, E-mail: iwa@mine1.nucle.tohoku.ac.jp
*Tokai-branch, Ship Research Institute, 319-11 Tokai, Ibaragi, Japan

ABSTRACT

(n,2n) activation cross-sections for copper, zinc, silver and tin have been measured in the neutron energies from 12 to 20 MeV in order to validate the recent evaluated cross section file: JENDL Activation file and Dosimetry File. The experiment was carried out as the series of the neutron cross-section measurements at Dynamitron Accelerator Laboratory at Tohoku University. Absolute values of each cross section were determined using the activation rates of two niobium foils, the sample foils being inserted in between; the reference reaction was $^{93}Nb(n,2n)^{92m}Nb$ of which cross-section data was taken from the 1991 NEANDC/INDC standard files. The measured cross-sections are the following important dosimetry or activation reactions: (n,2n) on ^{65}Cu; (n,2n) on ^{66}Zn; (n,2n) on ^{107}Ag; and (n,2n) on ^{118}Sn.

1. INTRODUCTION

Precise cross sections above 12 MeV are still sparse except for the special energy of 14 MeV. These are important for the high energy dosimetry, and estimation of damage rates and/or activation level of structural materials tested or used in the proposed high energy accelerator-based neutron fields.[1] Such cross sections also provide indispensable information to establish the nuclear model for high energy cross sections.[2] In this study, (n,2n) activation cross sections for copper, zinc, silver and tin have been measured between 12 and 20 MeV.

2. EXPERIMENTAL

Source neutrons were produced via the T(d,n)4He reaction by bombarding a 2.9-MeV deuteron beam from the Dynamitron accelerator at Tohoku University. Eight packages of high or ultra-high purity (99.9-99.99%) metal foils were set around the neutron source at 5 cm from the target in the angular range from 0 to 140 deg. covering the incident neutron energies from 20 down to 12 MeV. Experimental arrangement and technique were almost the same as the previous experiments.[3,4,5] Neutron flux at each foil was determined from the activation rates of two niobium foils which sandwiched each sample foil in between; the reference cross section for the $^{93}Nb(n,2n)^{92m}Nb$ reaction was taken from the 1991 NEANDC/INDC standard file.[6] Sizes of the samples were all the same as 0.5tx10x20mm^3, while that of the niobium samples was 0.2tx10x20mm^3. Table 1 shows the related nuclear data for the expected activities of the samples.

3. RESULTS

The measured four (n,2n) cross sections data are compared with the previous experimental data and cross section files: JENDL Activation File[6] and JENDL Dosimetry File[7] in Fig.1 through 4. Filled circles show present results with the errors within the circles.

3.1. $^{65}Cu(n,2n)^{64}Cu$ cross section

There have been many sets of old experimental data, while very few old experimental data sets show a discrepant trend with major data sets. JENDL3.2 (=JENDL DOSIMETRY FILE) curve follows the main trend of the cross sections.Fig. 1-(a) and (b) show typical examles of the data base. The present result shown in the last figure (b) supports the cross section curve of JENDL3.2. The FNS data by Ikeda, et al., '89[8] around 14 MeV also support.

3.2. $^{65}Zn(n,2n)^{64}Zn$ cross section

There are less number of experimental data sets than the case of $^{65}Cu(n,2n)^{64}Cu$. Only one data set by Bormann, et al. shows discrepant with other data as shown in Fig. 2-(a). The recently measured data by Konno, et al. '93[9] at FNS gave most reliable data around 14 MeV. The present measurement data are consistent with those FNS data and major data trend. JENDL Activation File (=JENDL3.2 for this reaction) which is going to be released near future (see, Nakajima[6]) shows a curve giving a bit higher cross sections in the full energy range evaluated.

3.3. $^{107}Ag(n,2n)^{106m}Ag$ cross section

There are two group: higher group and lower group mainly below 14 MeV, while the discrepancy between the experimental data set is not so large. The recent FNS data by Konno, et al. does not support the curve by JENDL Activation File. The present data are consistent with those by Reyves, et al. at 14 MeV, and Bayhurst, et al. in the entire energy range. The present data also supports the JENDL Activation File except for the higher energy part from 18 to 20 MeV.

3.4. $^{118}Sn(n,2n)^{117}Sn$ cross section

Very few previously measured experimental data sets are found for this reaction. The present data are consistent with the JENDL Activation File, while this evaluation shows a little higher cross section around 14 MeV than Ikeda, et al. The odd behaviour of the present data above18 MeV should be re-examined.

4. SUMMARY

Excitation functions of four (n,2n) reactions on ^{65}Cu, ^{66}Zn, ^{107}Ag and ^{118}Sn were measured in the energy range from 12 to 20 MeV at Dynamitron Facility of Tohoku University, and briefly reported. As far as the measured reactions concerned, JENDL Dosimetry and JENDL Activation File showed almost consistent with the present data, and are acceptable for the aimed applications of the files.

Acknowledgements

Experimental details and final numerical data for all observed cross sections are in preparation, and will be presented elsewhere. This work was financially supported by JAERI in FY1994. The authors are grateful to Messrs. R.Sakamoto, and M. Fujisawa of the Dynamitron Facility.

REFERENCES

1. M. Sugimoto, K. Noda, Y. Kato, H. Ohno and T. Kondo: JAERI-M 92-027 p.58, (1992).
2. S. Iwasaki and N.Odano, Proceedings of the International Conference on Nuclear Data for Science and Technology, Gatlinburg, Tenn., USA, May 9-13, 1994.
3. M. Sakuma , S. Iwasaki, H. Shimada, N. Odano, K. Suda, J.R. Dumais and K. Sugiyama: JAERI-M 92-027, p.278 (1992).

4. S. Iwasaki, M. Sakuma, K. Sugiyama and N. Odano: JAERI-M 93-046, p.257, JAERI (1993).
5. S. Iwasaki, S. Matsuyama, T. Ohkubo, H. Fukuda, M. Sakuma, M. Kitamura and N. Odano: JAERI-Conf 95-008, p.165, JAERI (1995).
6. H.Vonach: *Nuclear Standards for Nuclear Measurements*', NEANDC-311"U", INDC(SEC)-101, NEA/OECD, p. 80, (1992).
7. Y. Nakajima: presented in this conference.
8. M. Nakazawa, et al.: "*JENDL Dosimetry File*", JAERI 1325 (1991).
9. Ikeda, et al.: JAERI 1313 (1988).
10. Konno, et al.: JAERI 1325 (1993).

Table 1 related nuclear data for the expected activities of the samples.

reaction*	half-life	decay mode	main gamma-rays (keV)	emission probabili-ty (%)	abun-dance (%)
$^{65}Cu(n,2n)^{64}Cu$	12.701(2)h	EC+, $\beta+$	1345.88 511(Annih.)	0.472(18) 35.8	30.83(2)
$^{66}Zn(n,2n)^{65}Zn$	243.9(1)d	EC(98.3%), $\beta+$	1115.5	50.70(13)	27.9(2)
$^{107}Ag(n,2n)^{106m}Ag$	8.5d	EC	450 many	28.4	51.839(5)
$^{116}Cd(n,2n)^{115m}Cd$	44.8d	$\beta-$	933.6	100	7.5
$^{118}Sn(n,2n)^{117m}Sn$	14.0d	IT	158.6	85.5	24.3(8)

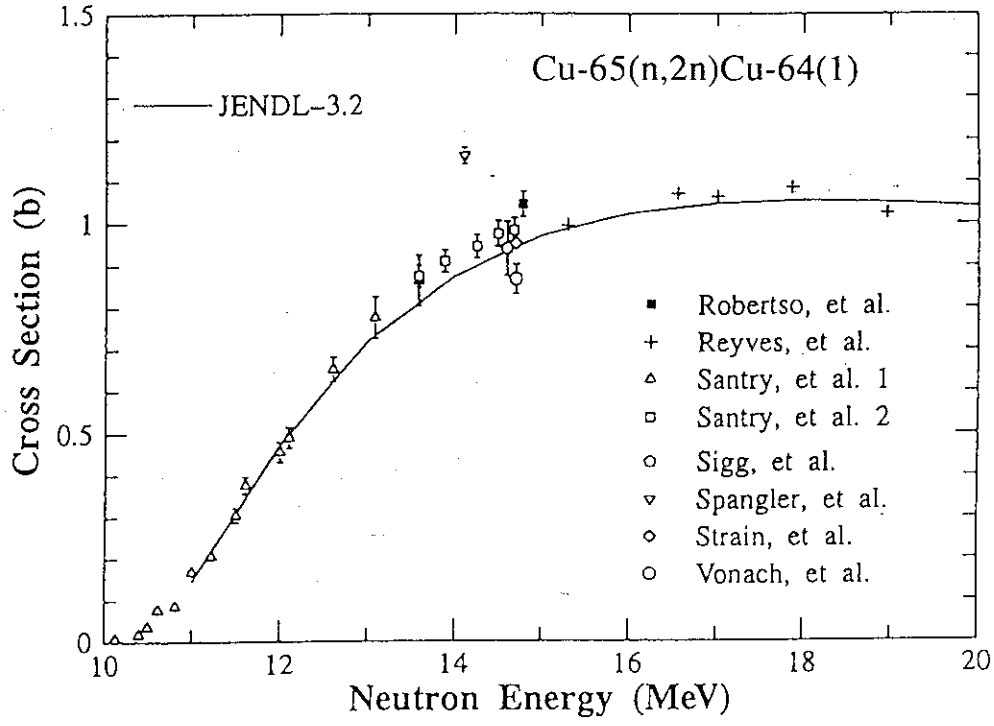

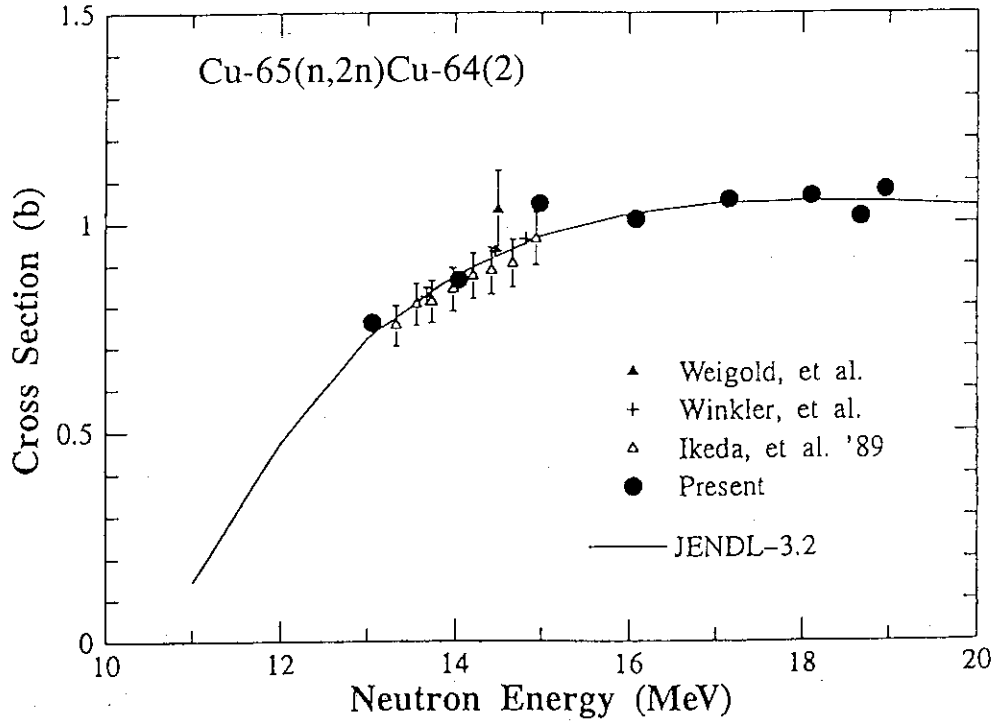

Fig.1-(a) (upper), -(b) (lower). Example of the previous experimental data with the curve of JENDL3.2 for ^{65}Cu(n,2n) reaction. The present data and Ikeda, et al.(ref. 9) data are also compared in (b).

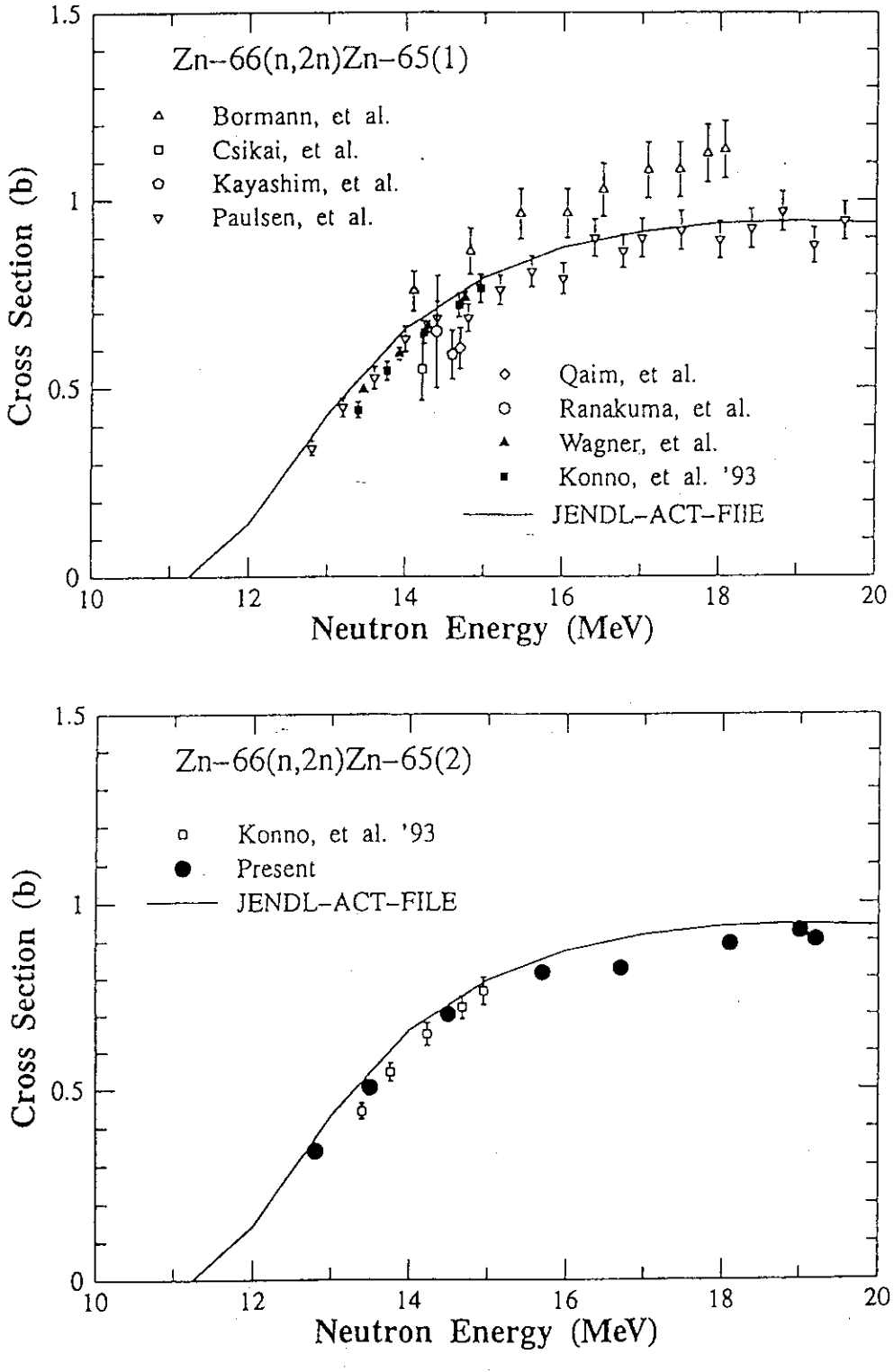

Fig.2-(a) (upper), -(b) (lower). Previous experimental data with the curve of JENDL ACTIVATION FILE for ^{66}Zn(n,2n) reaction.The present data and Konno, et al.(ref. 10) data are also shown in (b).

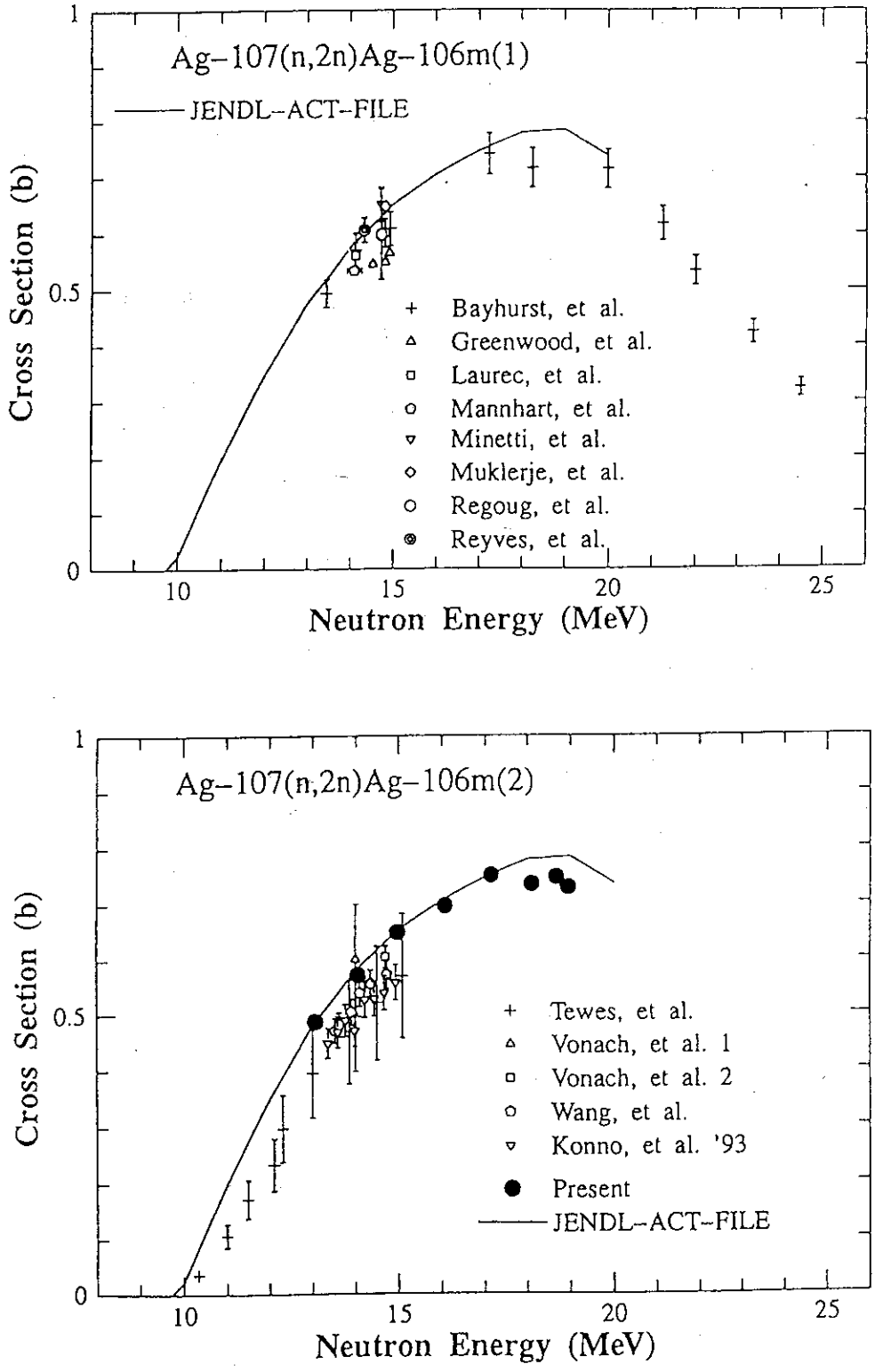

Fig.3-(a) (upper), -(b) (lower). Previous experimental data with the curve of JENDL ACTIVATION FILE for $^{107}Ag(n,2n)^{106m}Ag$ reaction. The present data and Konno, et al.(ref. 10) data are also shown in (b).

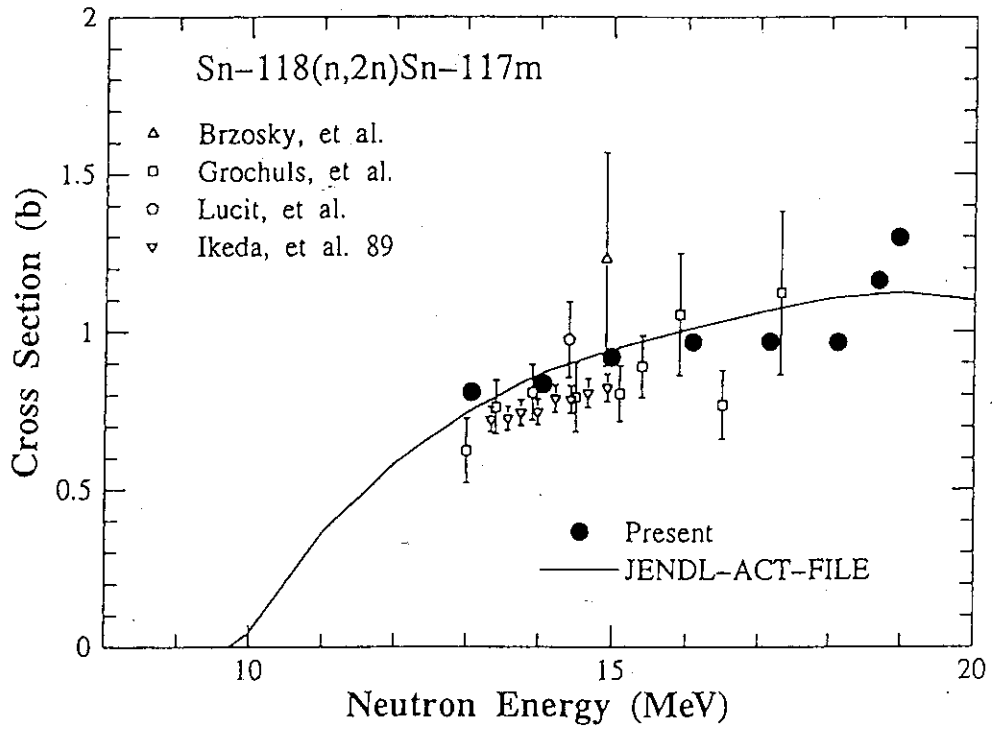

Fig.4. Previous experimental data with the curve of JENDL ACTIVATION FILE for $^{118}Sn(n,2n)^{117}Sn$ reaction. The present data and Ikeda, et al.(ref.9) data are also shown in (b).

3.9 Helium Production Cross Section Measurement by Helium Atoms Measurement System

Yoshiyuki TAKAO, Yukinori KANDA, Masako MIWA, Hiroshi ETOH,
Katuhiro YAMAGUCHI, Tamotu YONEMOTO, and Kouji NAGAE
Department of Energy Conversion Engineering,
Kyushu University, Kasuga, Fukuoka 816, Japan

Proton-induced helium production cross sections for nickel at proton energies up to 16MeV have been measured with a helium accumulation method. A sample is a nickel sheet (chemical purity 99.98%, sizes $12\times9\times0.119mm^3$) sandwiched between two gold foils (chemical purity 99.99%, size $12\times9\times0.051mm^3$) which are collectors for the emitted α-particles from the nickel surfaces. Nine nickel samples were irradiated by protons ranging from 8.8 to 17.5MeV at Kyushu University Tandem Accelerator Laboratory. The number of helium atoms produced and accumulated in the nickel foil and two gold collectors was measured using the helium atoms measurement system.

1. Introduction

In a nuclear data field, information on nuclear reactions relating to charged particles such as a proton and an α-particle are recently required. Nuclear reactions regarding the particles have become important in nuclear applications, for examples, to a fusion reactor development, to a medical treatment, and to astrophysics. The demanded data are on both charged-particle-induced reactions and charged-particle-emitted reactions.

In this work, the helium production cross sections of nickel by proton induced reactions have been measured by a helium accumulation method. Nickel is one of the elements contained in stainless steels. As stainless steels have been used in many kinds of productive facilities, the knowledge of their properties is abundant. Therefore, stainless steels are used for the structural materials of apparatuses such as an accelerator. It is important to measure the He production cross section of nickel for protons.

2. Experimental

2.1 Sample preparation

A sample is a Ni plate (chemical purity 99.98%, sizes $12\times9\times0.119mm^3$) sandwiched between two gold foils (chemical purity 99.99%, size $12\times9\times0.051mm^3$). Nine Ni samples were prepared for proton irradiation. Ni plates and Au foils were cleaned in an acetone bath ultrasonically for 20 minutes. The Ni plates were then annealed at 1273K for an hour in a vacuum of less than 7×10^{-4} Pa to remove He contained in the sample as given. Au foils were also processed at 1073K. These Au foils were collectors for the emitted α-particles from the Ni surfaces due to the kinetic energy of the (p,xα) reactions. The principle of this compensation for emitted α-particles and a schematic diagram of a sample are shown in Fig.1. We measure the produced He atoms in both of a Ni plate and two Au foils. Au foils are thick

enough to collect all emitted α-particles because the thickness of Au foils is larger than the projected range of α–particles in Au [1].

2.2 Irradiation of protons

The samples were irradiated by protons up to 17.5MeV at Kyushu University Tandem Accelerator Laboratory. Each sample was set in a sample holder with Faraday cup, which was put on a sample table so as to coincide a perpendicular to the sample and one of proton beam. A sample holder and the sample table are shown in Fig.2. The sample table was set on a turning table in a vacuum chamber. Figure 3 shows a schematic diagram of a vacuum chamber with a diameter of 100cm and a depth of 50cm. The turning table can move around the center of the vacuum chamber and allows to change samples easily. The sample table was cooled by liquid nitrogen which prevents the release of produced helium atoms due to the sample temperature rising by proton irradiation. The temperature of the samples was monitored by thermocouples and was below 223K during sample irradiation. Liquid nitrogen was supplied to the liquid nitrogen reservoir automatically when the temperature of the reservoir was more than 80K.

The number of protons was measured by using a current integrator and the samples were irradiated by protons of 150μC approximately. The current of a proton beam was less than 0.1μA to keep the sample temperature low enough.

2.3 Measurement of the number of helium atoms

The number of helium atoms produced by proton irradiation in the samples were measured by the Helium Atoms Measurement System (HAMS). Figure 4 shows the block diagram of HAMS. This apparatus is evacuated by turbo-molecular pumps in a vacuum of less than $1x10^{-6}$ Pa. A irradiated sample is set on a Mo evaporating boat in a furnace. The furnace is a resistance furnace; a sample is heated by the Mo evaporating boat electrically to more than a melting point of the sample. The released gases containing helium from the sample were purified by the trap of Ti-getter pump. The sample gas was then admitted into a quadrupole mass spectrometer (QMS). QMS is controlled by a personal computer, which stores the data of the measured result of the gas analysis.

The measuring efficiency of the released helium gas of HAMS is calibrated by a series of measurements of standard helium gases. The gases are known amount of helium gases and are produced by a standard He supply. The standard He supply has five vessels whose absolute volumes were previously measured, two absolute pressure gauges and a thermometer.

The procedure of preparing the standard He gas is as follows. The V2 is filled up to near the amount of He required to obtain the desired standard He monitoring with the absolute pressure gauge and the ambient temperature is measured, and then the He is expanded into V3. The He in V3 is diluted until a desired amount of He is obtained by repeating the expansion of He between V3 and V4 and alternate evacuation of them. The He prepared in V3 is finally expanded to V5 and processed in the same manner as the sample gas measurement.

3. Results and discussion

Figure 5 shows the results of this work. There are five isotopes in natural Ni. The threshold energies of Ni(p,α) range from 0.0 to 1.36 MeV and those of other reactions are

larger than 6.3MeV. The experimental excitation function is superposition of Ni(p,xα) cross sections. The proton energy at each sample was estimated from the energy loss data for the materials[2]. The thickness of the samples was not small enough to neglect the degradation of the proton energy; the range of proton energy in each sample is also indicated by a horizontal line in Fig. 5. The dots are plotted at the center of the horizontal lines.

The sources of errors are categorized into three groups: the proton energy, the measurement of incident protons to a sample, the measurement of He produced in a sample.

The uncertainty of the proton energy is estimated to be 1% referring to Ref. 2, which is used to compute the energy degradation in samples. The other uncertainties are the error from fluctuation of the incident proton energy controlled by an analyzing magnet is less than 1% and the contribution from the uncertainty of the sample thickness is 1%.

The uncertainty of measuring the number of incident protons to a sample is estimated to be ±2.2% from the uncertainty of ±1% for the incident proton charge measured by a current integrator and the uncertainty of ±2% caused by the secondary electrons escaping from the Faraday cup and incoming from the surrounding devices such as a slit of the beam line.

The uncertainties for measuring the number of He in individual samples are estimated to be more than 4.6%. Major uncertainties in the experiment are 3% for the calibration of HAMS depending on the uncertainty in the preparation of the standard He. The others are 1.5% in the fluctuation of the mass spectrometer, and more than 2% in the fluctuation of background measurements. The uncertainty resulted from the number of He produced in the Au catchers is more than 1%.

References

[1] Ziegler, J.F. : "Helium Stopping Powers and Ranges in all Elemental Matter", (1977), Pergamon Press, New York.

[2] Andersen, H.H., Ziegler, J.F. : "Hydrogen Stopping Powers and Ranges in all Elements", (1977), Pergamon Press, New York.

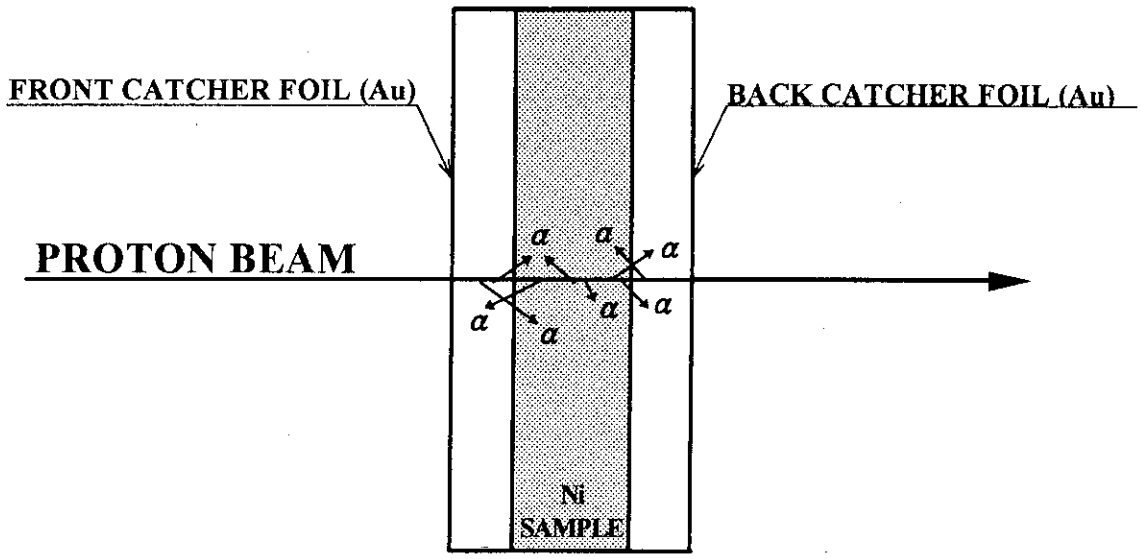

Fig. 1 A Ni sample consists of a nickel foil sandwiched between two gold foils. The α-particles emitted form the Ni foil are trapped in Au foils.

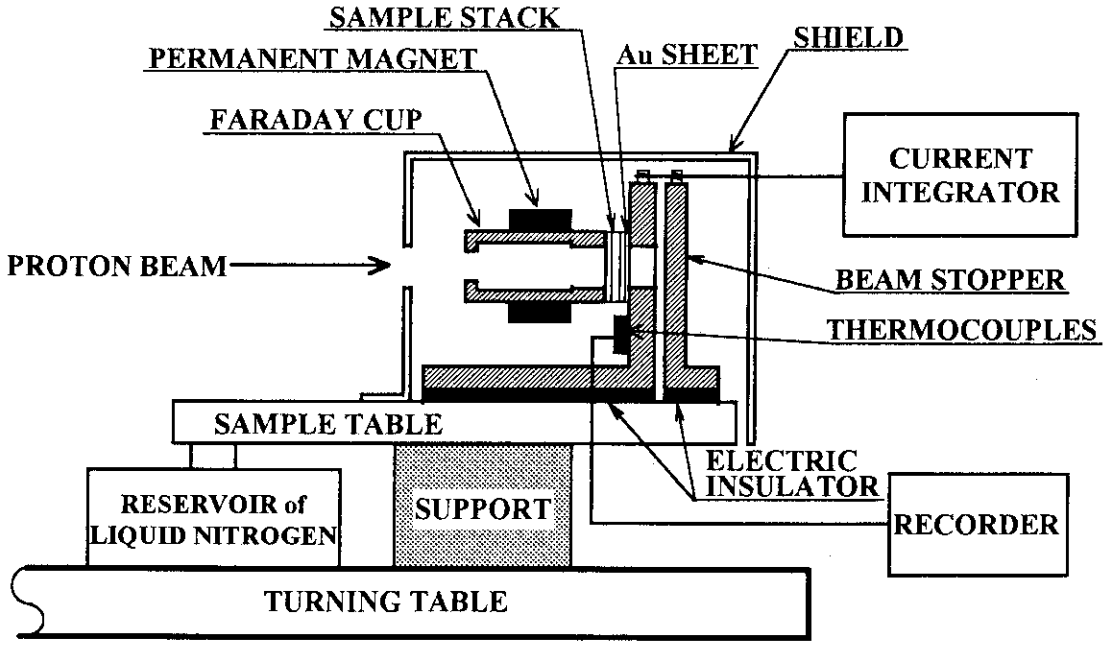

Fig. 2 Schematic diagram of the sample holder and the sample table.

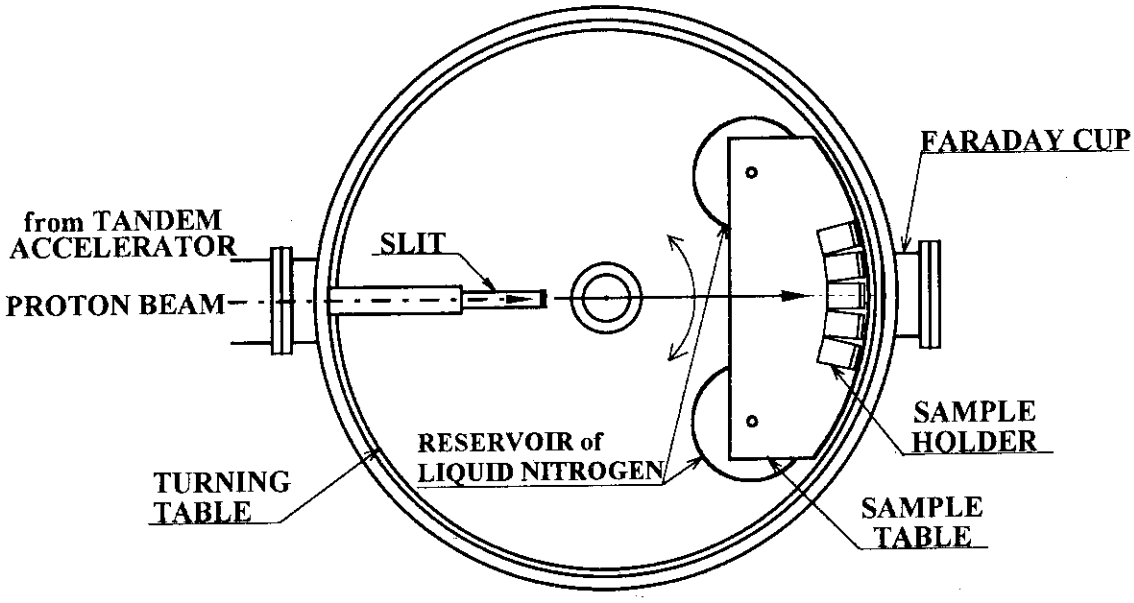

Fig.3 The schematic diagram of the vacuum chamber.

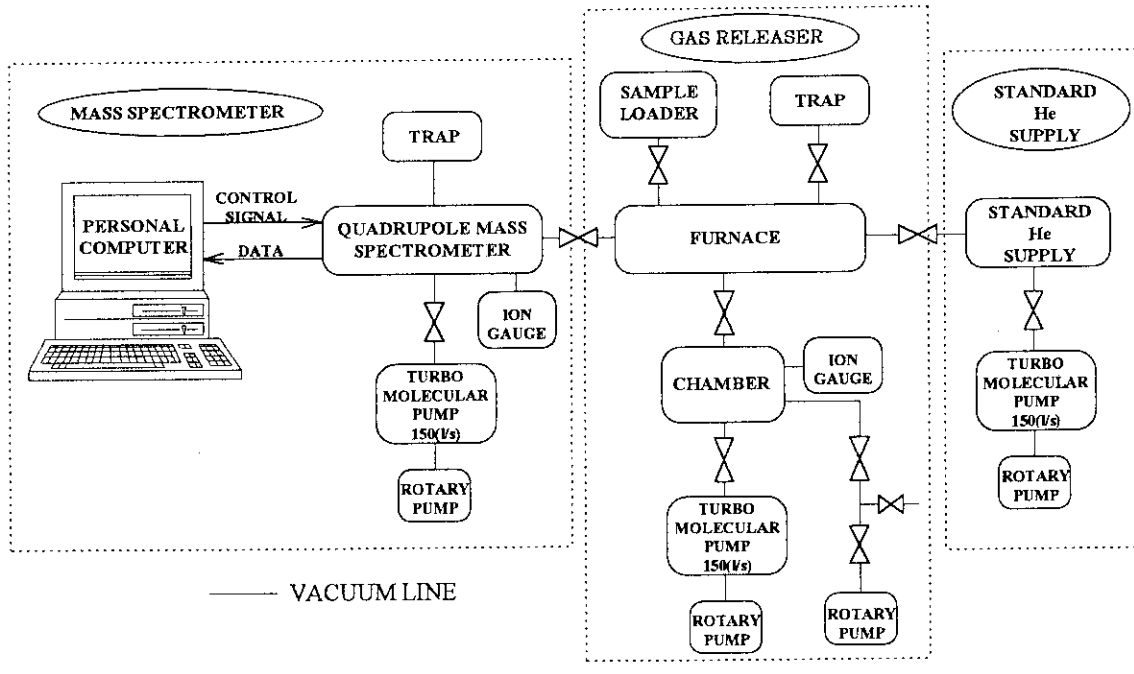

Fig.4 Block diagram of the Helium Atoms Measurement System (HAMS).

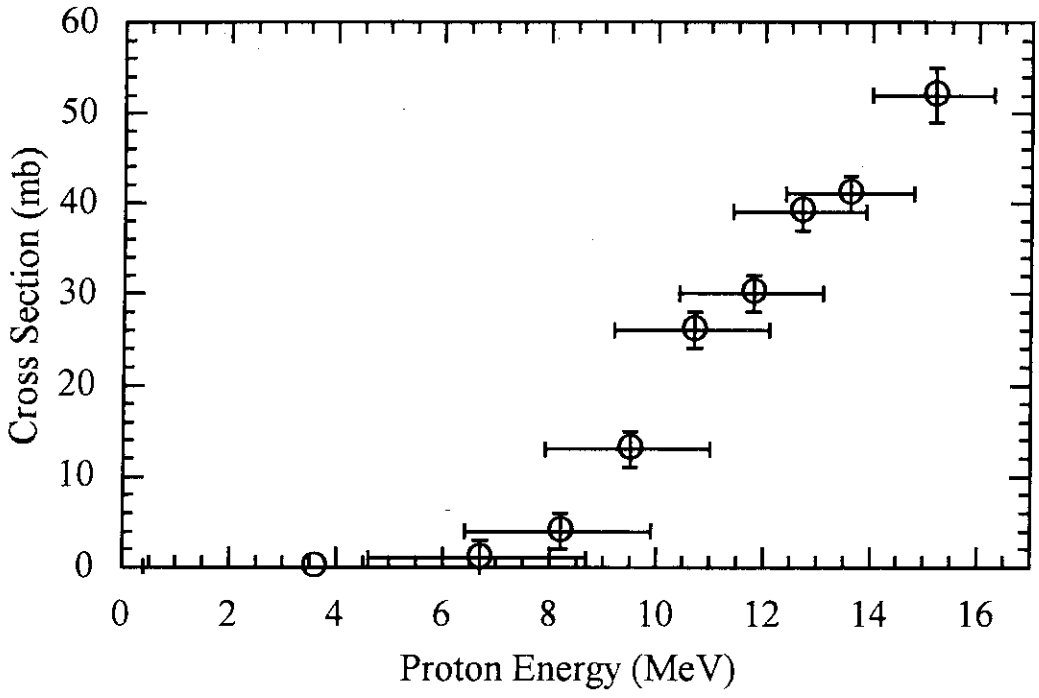

Fig. 5 Ni(p,xα) cross sections measured by the helium accumulation method.

3.10 Measurement of Formation Cross Sections Producing Short-lived Nuclei by 14 MeV Neutrons - Pr,Ba,Ce,Sm,W,Sn,Hf -

S.Murahira , Y. Satoh , N.Honda *, A.Takahashi**, T. Iida**
M.Shibata*, H.Yamamoto* and K. Kawade*

Department of Nuclear Engineering, Nagoya University
Furo-cho, Chikusa-ku, Nagoya, 464-01, Japan
*Department of Energy Engineering and Science, Nagoya University
Furo-cho, Chikusa-ku, Nagoya, 464-01, Japan
**Department of Nuclear Engineering, Osaka University
Yamadaoka, Suita-shi, Osaka, 565, Japan

e-mail : a40590a@nucc.cc.nagoya-u.ac.jp

Abstract

Thirteen neutron activation cross sections for (n,2n), (n,p), (n,np) and (n, α) reactions producing short-lived nuclei with half-lives between 56 s and 24 min were measured in the energy range from 13.4 MeV to 14.9 MeV for Pr,Ba,Ce,Sm,W,Sn and Hf. The cross sections of ^{179}Hf (n,np)^{178m}Lu and ^{180}Hf (n,p)^{180}Lu were measured for the first time.

1. Introduction

Neutron activation cross section data around 14 MeV have become important from the view point of fusion reactor technology, especially for calculations on radiation damage, nuclear transmutation, induced activity and so on. A lot of experimental data have been reported and great efforts have been given to compilations and evaluation.

However, there are still no available data for the reactions leading to short-lived nuclei with half-lives between a few seconds and 20 minutes in a reasonable accuracy although they are important, because of difficulty in measuring short-lived nuclei.

Activation cross sections of short-lived nuclei ($T_{1/2}$= 56 s-24 min) by 14 MeV neutrons at the Intense 14 MeV Neutron Source Facility (OKTAVIAN) of Osaka University in a qualified experimental condition by activation method we measured[1),2),3),4)].

2. Experiments and Results

Experiments were carried out at OKTAVIAN. A pneumatic sample transport system was used for the irradiation of samples. The angles of the irradiation position to the d^+ beam were 0° , 55° , 75° , 105° , 125° and 155° , which covered the neutron energies ranging from 14.9 to 13.4 MeV. The distance between the T-target and the irradiation position was 15 cm.

When high neutron flux was required, an additional tube set at 0° and at 1.5 cm was set. The induced activities were measured by 12% and 16% HPGe detectors at an equivalent distance at 5 cm. The neutron flux at the irradiation position was measured by using substandard $^{27}Al(n,p)^{27}Mg$ ($T_{1/2}$=9.462 min) reaction, whose cross sections were determined by referring to the $^{27}Al(n,\alpha)^{24}Na$ reaction (ENDF/B-V). The samples were sandwiched between two aluminum foils of 10 mm × 10 mm × 0.2 mm thick. The effective energy of incident neutron at the irradiation position was determined by the ratio of the $^{90}Zr(n,2n)^{89}Zr$ and $^{93}Nb(n,2n)^{92m}Nb$ cross sections (Zr/Nb method[5]). The errors in the neutron energy were estimated to be about 90 keV. Mass separated isotopes and samples of natural abundance were used. Powder samples were wrapped in powder papers with size of 10 mm × 10 mm and about 1 mm thick.

In Table 1, measured reactions and associated data[6] of the half-lives ($T_{1/2}$), the γ-ray energy (E_γ) and the γ-ray emission probability (I_γ) are listed together with the Q-value.

Corrections were made for time fluctuation of neutron flux, contribution of low energy neutrons below 10 MeV thickness of samples, self absorption of γ-ray, sum-peak effect of γ-ray and contribution of interfering nuclei. The details of the correction are described elsewhere[1),2),3),4)].

The total errors (δ_t) were described by combining the experimental errors (δ_e) and the errors of nuclear data (δ_r) in quadratic : $\delta_t^2 = \delta_e^2 + \delta_r^2$. Estimated major sources of the error are listed in Table 2. Accuracy of the obtained cross sections were around 4.1% in case of good statistics.

Numerical data table of cross sections are given in Table 3 and some of the results are shown in Fig. 1 and Fig. 2. The cross sections of $^{179}Hf(n,np)^{178m}Lu$ and $^{180}Hf(n,p)^{180}Lu$ were measured for the first time.

3. Conclusion

Neutron activation cross sections were measured for 13 reactions producing short-lived nuclei in the neutron energy from 13.4 to 14.9 MeV for Pr,Ba,Ce,Sm,W,Sn and Hf. The cross sections of $^{179}Hf(n,np)^{178m}Lu$ and $^{180}Hf(n,p)^{180}Lu$ were measured for the first time. The evaluated values of JENDL-3.2 and ENDF/B-VI showed reasonably agreement with the present results.

References

1) T. Katoh et al.: JAERI-M 89-083 (1989) (in Japanese).
2) K. Kawade et al.: JAERI-M 90-171 (1990).
3) K. Kawade et al.: JAERI-M 92-020 (1992).
4) Y. Kasugai et al.: JAERI-M 93-124 (1993).
5) V.E. Lewis et al.: Nucl. Instr. Meth. 174, 141 (1980).
6) E. Browne et al.: "Table of Radioactive Isotopes", John Wiley & Sons, New York (1986).

Table 1 Measured reactions and decay parameters [a]

Reaction	$T_{1/2}$	E_γ (keV)	I_γ (%)	Q(MeV)
^{118}Sn(n,p)$^{118m1+m2}$In	4.40(5)min,8.5(3)s	683.38	55(5)	-3.42
^{132}Ba(n,2n)^{131m}Ba	15.65(10) min.	108.12	55(2)	-9.99
^{138}Ba(n,2n)^{137m}Ba	14.6(2)min.	661.660	90.1(1)	-9.27
^{138}Ba(n, α)^{135m}Xc	2.552(1) min.	754.21	92.5(3)	-9.94
^{140}Ce(n,2n)^{139m}Ce	56.54(13) s[c]	526.563	81.2(10)	3.35
^{140}Ce(n, α)^{137m}Ba	2.552(1) min.	661.660	90.1(1)	4.63
^{141}Pr(n,2n)^{140}Pr	3.39(1)min.	1596.54	0.50(4)	-8.936
^{144}Sm(n,2n)^{143m}Sm	1.10(3) min.	754.01	90.0(1)	-10.52
^{144}Sm(n,2n)^{143g}Sm	8.83(2) min.	1056.48	1.75(18)	-11.27
^{178}Hf(n,p)^{178m}Lu	23.1(4)min.	426.352	97.4(19)	-1.47
^{179}Hf(n,np)^{178m}Lu [b]	23.1(4)min.	426.352	97.4(19)	-7.73 [c]
^{180}Hf(n,p)^{180}Lu	5.7(1)min.	407.95(5)	50(2)	-2.52
^{186}W(n,p)^{186}Ta	10.390(20) min [d]	198.05	59(10)	-3.11
^{27}Al(n, α)^{24}Na[e]	14.959(4) h	1368.6	99.994(3)	-3.13
^{27}Al(n,p)^{27}Mg[f]	9.462(11) min.	843.8	72.0(4)	-1.83

[a] Taken from ref 6.

[b] (n,np) means [(n,d)+(n,n'p)+(n,pn)]

[c] Q(n,n'p) is given here. Q(n, d)=Q(n,n'p)+2.225MeV.

[d] Measured in our previous work.

[e] Standard reaction (ENDF/B-V) used in this work.

[f] Secondary standard reaction used for short-lived nuclei.

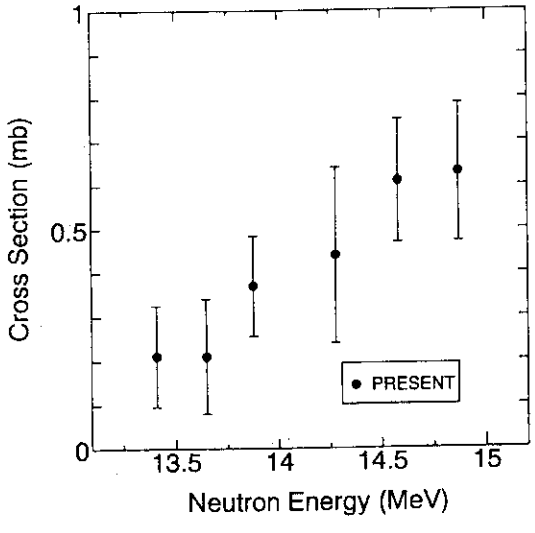

Fig 1. The cross section of ^{178}Hf(n,p)^{178m}Lu

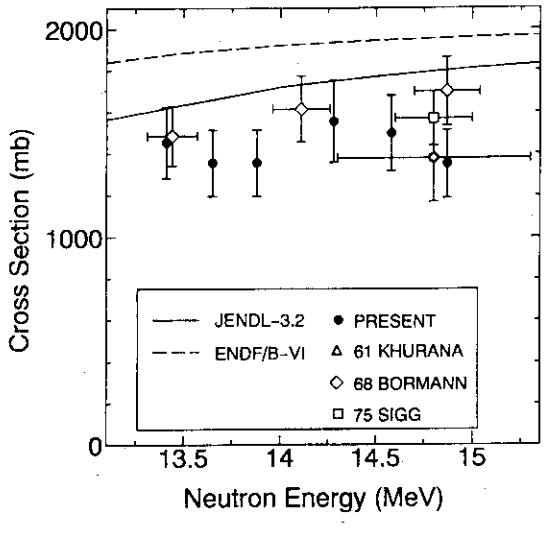

Fig 2. The cross section of ^{141}Pr(n,2n)^{140}Pr

Table 2. Principal sources of uncertainty in the measured cross sections

Experimental error (δ_e)

Source of error	Uncertainty (%)
Counting statistics	0.5-61.8
Sample mass including purity	0.1
Neutron flux fluctuation	<0.4 (20% of correction)
Gamma-peak area evaluation	0.5
Detector efficiency	1.5 (E_γ >300 keV)
	3 (E_γ =300-80 keV)
	5 (E_γ <80 keV)
Efficiency calibration at 0.5 and 5 cm	2.0
Correction for	
true coincidence sum	0-2.0
random coincidence sum	<0.4
sample thickness	0-0.5 (20% of correction)
self-absorption of γ -rays	0-1.0 (20% of correction)
low energy neutrons	0-1.2 (50% of correction)
Secondary reference cross section for $^{27}Al(n,p)^{27}Mg$ reaction	0.3-1.0 (only statistics)

Error of nuclear data (δ_r)

Source of error	Uncertainty (%)
Reference cross section of $^{27}Al(n, \alpha)^{24}Na$ (ENDF/B-V)	3.0
Absolute γ -ray intensity	0.1-17
Half-life	0.04-2.73

Table 3 Activation cross sections of short-lived nuclei

$^{118}Sn(n,p)^{118m1+m2}In$

En(MeV)	σ (mb)	δ_e(%)	δ_r(%)	δ_t(%)
14.87	9.75	8.6	9.7	13.0
14.58	11.1	8.0	9.7	12.6
14.28	8.22	11.6	9.7	12.4
13.88	6.67	9.7	9.7	13.8
13.65	6.95	10.5	9.7	14.3
13.40	4.65	12.5	9.7	15.8

$^{132}Ba(n,2n)^{131m}Ba$

En(MeV)	σ (mb)	δ_e(%)	δ_r(%)	δ_t(%)
14.87	880	6.8	3.9	7.8
14.58	813	6.0	3.9	7.1
14.28	792	6.9	3.9	7.9
13.88	761	4.9	3.9	6.3
13.65	698	7.3	3.9	7.3
13.40	709	5.1	3.9	6.3

$^{138}Ba(n,2n)^{137m}Ba$

En(MeV)	σ (mb)	δ_e(%)	δ_r(%)	δ_t(%)
14.87	983	3.2	3.0	4.4
14.58	975	3.2	3.0	4.4
14.28	963	3.9	3.0	4.8
13.88	967	3.2	3.0	4.4
13.65	945	3.1	3.0	4.3
13.40	877	2.8	3.0	4.1

$^{138}Ba(n,\alpha)^{135m}Xe$

En(MeV)	σ (mb)	δ_e(%)	δ_r(%)	δ_t(%)
14.87	0.79	33.6	3.3	33.8
14.58	0.85	37.0	3.3	37.1
14.28	0.80	46.2	3.3	46.3
13.88	0.78	34.3	3.3	34.5
13.65	0.74	36.8	3.3	36.9
13.40	0.73	48.9	3.3	49.0

$^{140}Ce(n,2n)^{139m}Ce$

En(MeV)	σ (mb)	δ_e(%)	δ_r(%)	δ_t(%)
14.87	983	3.1	3.0	4.3
14.58	966	3.0	3.0	4.3
14.28	958	3.2	3.0	4.3
13.88	948	3.0	3.0	4.3
13.65	899	3.0	3.0	4.3
13.40	865	2.9	3.0	4.3

$^{140}Ce(n,\alpha)^{137m}Ba$

En(MeV)	σ (mb)	δ_e(%)	δ_r(%)	δ_t(%)
14.87	3.02	25.8	3.0	26.0
14.58	3.01	28.1	3.0	29.5
14.28	2.64	37.5	3.0	37.6
13.88	2.83	26.5	3.0	26.7
13.65	2.51	31.8	3.0	31.9
13.40	1.99	29.6	3.0	29.8

$^{141}Pr(n,2n)^{140}Pr$

En(MeV)	σ (mb)	δ_e(%)	δ_r(%)	δ_t(%)
14.87	1352	8.4	8.7	12.1
14.58	1498	8.3	8.7	12.0
14.28	1554	9.2	8.7	12.7
13.88	1356	8.0	8.7	11.8
13.65	1356	7.9	8.7	11.7
13.40	1454	7.9	8.7	11.7

$^{144}Sm(n,2n)^{143m}Sm$

En(MeV)	σ (mb)	δ_e(%)	δ_r(%)	δ_t(%)
14.87	587	4.2	4.0	5.8
14.58	574	3.2	4.0	5.2
14.28	495	3.3	4.0	5.2
13.88	462	2.5	4.0	5.0
13.65	419	3.3	4.0	5.2
13.40	357	2.7	4.0	5.0

$^{144}Sm(n,2n)^{143g}Sm$

En(MeV)	σ (mb)	δ_e(%)	δ_r(%)	δ_t(%)
14.87	1088	11.3	10.4	15.4
14.58	946	9.6	10.4	14.1
14.28	839	11.2	10.4	15.3
13.88	944	4.2	10.4	11.3
13.65	737	10.8	10.4	15.0
13.40	662	10.5	10.4	11.7

$^{178}Hf(n,p)^{178m}Lu$

En(MeV)	σ (mb)	δ_e(%)	δ_r(%)	δ_t(%)
14.87	0.63	24.8	4.2	25.1
14.58	0.61	22.8	4.2	23.2
14.28	0.44	45.2	4.2	45.4
13.88	0.37	30.4	4.2	30.7
13.65	0.21	61.8	4.2	62.0
13.40	0.21	54.5	4.2	54.6

$^{179}Hf(n,np)^{178m}Lu$

En(MeV)	σ (mb)	δ_e(%)	δ_r(%)	δ_t(%)
14.87	1.02	35.6	4.53	35.9
14.58	0.77	50.7	4.53	50.9
14.28	0.63	54.0	4.53	54.2
13.88	0.84	31.6	4.53	31.9
13.65	0.51	50.4	4.53	50.6
13.40	0.61	39.0	4.53	39.3

$^{180}Hf(n,p)^{180}Lu$

En(MeV)	σ (mb)	δ_e(%)	δ_r(%)	δ_t(%)
14.87	2.49	17.9	5.5	18.7
14.58	1.65	28.3	5.5	28.9
14.28	1.19	41.3	5.5	41.7
13.88	1.08	24.5	5.5	25.1
13.65	1.07	30.8	5.5	31.3
13.40	0.76	35.4	5.5	35.8

$^{186}W(n,p)^{186}Ta$

En(MeV)	σ (mb)	δ_e(%)	δ_r(%)	δ_t(%)
14.87	2.30	11.4	17.3	20.7
14.58	1.84	14.4	17.3	22.5
14.28	1.78	24.6	17.3	30.1
13.88	1.31	16.7	17.3	24.0
13.65	1.20	23.7	17.3	29.3
13.40	0.59	15.0	17.3	22.9

3.11

Measurement of Beta-decay Half-lives of Short-lived Nuclei with Spectrum Multi-Scaler(SMS)

T.Hirose, T.Shibuya, S.Murahira, *H. Yamamoto,
**T. Iida, **A. Takahashi and *K. Kawade
Department of Nuclear Engineering, Nagoya University
Furo-cho, Chikusa-ku, Nagoya, 464-01, Japan
*Department of Energy Engineering and Science, Nagoya University
Furo-cho, Chikusa-ku, Nagoya, 464-01, Japan
**Department of Nuclear Engineering, Osaka University
Yamadaoka, Suita-shi, Osaka, 565, Japan

e-mail:a40590a@nucc.cc.nagoya-u.ac.jp

Abstract

The half-lives of short-lived nuclei produced by 14 MeV or thermal neutron bombardments were measured with a Ge detector, a Spectrum Multi-Scaler (Laboratory Equipment Corporation SMS-48) and a High-Rate Spectroscopy Amplifier(EG&G ORTEC Model 973) in the multi-scaling mode. The corrections for pile-up and dead-time losses were performed by applying source and pulser methods. The half-lives of ^{91m}Mo, ^{97m}Nb, ^{138}Cs, ^{139}Ba, ^{174}Tm and ^{203m}Pb were determined with accuracy of 0.22 $\sim$ 0.6 % and the accuracy has been much improved.

1 Introduction

The half-life of β-decay is one of the most fundamental constants on radioactive isotopes. In the activation cross section measurements, the uncertainty brings a strong effect to the results. Most of the values previously published were obtained with GM counters, ionization chambers, proportional counters and scintillation counters. In order to improve the precision and reliability of the half-lives of short-lived nuclei ($T_{1/2}$ = 6 s $\sim$ 83 min), the Ge detector was used, and to measure the half-lives of short-lived nuclei in the range of seconds, the Spectrum Multi-Scaler(SMS) was used for the present work.

2 Experiment

The γ-rays were measured with ORTEC 22 % Ge detector in the spectrum multi-scaling mode. Decay was followed for about 10 times the half-life at equal intervals

of 1/3 of half-life. We measured the half-lives in the range of seconds with Spectrum Multi-Scaler(SMS) to reduce the data transfer time, as shown in Fig.1. A long-lived γ source and a constant-pulser were simultaneously measured together with the short-lived activity for the correction of the pile-up and the dead time losses (source method, pulser method). Sources of ^{91m}Mo, ^{97m}Nb, ^{138}Cs, ^{174}Tm and ^{203m}Pb were produced by 14 MeV neutron bombardment at OKTAVIAN of Osaka University. Source of ^{139}Ba was produced by thermal neutron irradiation at TRIGA-II reactor of Rikkyo University(100 kW).

3 Results

A decay curve of ^{203m}Pb is shown in Fig.2. The results are summarized in Table 1 together with production reactions, γ-rays, reference sources, number of measurement, measured and previous values [1]. In Fig.3, the result is compared with previous works. The present result has shown good agreement with previous works, and the accuracy has been much improved. In Fig.4, relative deviations of previous values from the present ones are shown. It is clearly seen that previous values [2], [3] shorter than about 10 min deviate systematically and those become larger as the half-lives become shorter. The cause might result from insufficient correction for pile-up and dead time losses. It is likely to start measurements at too high counting rates in order to get good statistics. If the corrections at high counting rates are not enough, the decay curve will show a longer half-life compared with the true value.

4 Summary

The half-lives of short-lived nuclei were determined with accuracy of $0.22 \sim 0.6$ %. With the Spectrum Multi-Scaler(SMS), the half-lives of short-lived nuclei in the range of seconds could be measured. Previous values shorter than about 10 min deviate systematically and those deviations become larger as the half-lives become shorter.

References

[1] E. Browne et al., *Table of Radioactive Isotopes*, (1986) John Wiley & Sons, New York

[2] C. M. Lederer and V. S. Shirley, *Table of Isotopes 7th Ed.*, (1978) John Wiley & Sons, New York

[3] Nuclear Data Sheets

[4] K.Kawade et al., JAERI-M 90-171 (1990)

Table 1 Results of half-life measurement

Nuclide	Production Reaction	E_γ (keV)	Ref. Source[a] (E_γ in keV)	Number of Measurement	Half-life Present	Reference[b]
^{91m}Mo	^{92}Mo(n, 2n)	652.98	^{57}Co(122.1)	1	62.5(4) s	65.2(8) s
^{97m}Nb	^{97}Mo(n, p)	743.32	^{57}Co(122.1)	5	58.44(27) s	58.7(18) s[c]
^{138}Cs	^{138}Ba(n, p)	462.8 1435.8	^{57}Co(122.1) ^{60}Co(1332.5)	6	32.11(8) m	32.2(1) m
^{139}Ba	^{138}Ba(n, γ)	165.85	^{241}Am(87.3)	2	82.75(18) m	84.6(42) m
^{174}Tm	^{174}Yb(n, p)	366.6	^{57}Co(122.1)	10	5.33(2) m	5.4(1) m
^{203m}Pb	^{204}Pb(n, 2n)	820.32 825.24	^{137}Cs(661.7)	2	6.303(26) s	6.3(2) s

a) These sources were used for corrections of dead time and pile-up losses.

b) Taken from ref. 1.

c) The reported value in ref. 4, 52.7(18) s, was misprinted. The right, refer to this table.

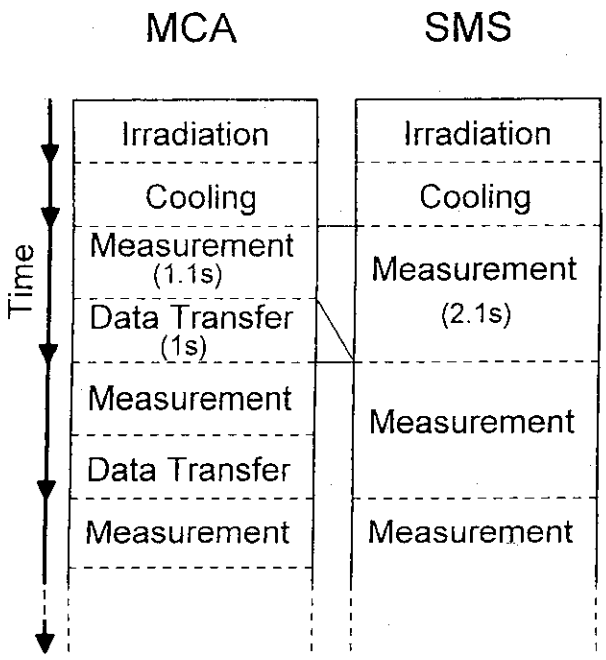

Fig.1 Spectrum multi-scaling mode. (e.g. ^{203m}Pb)

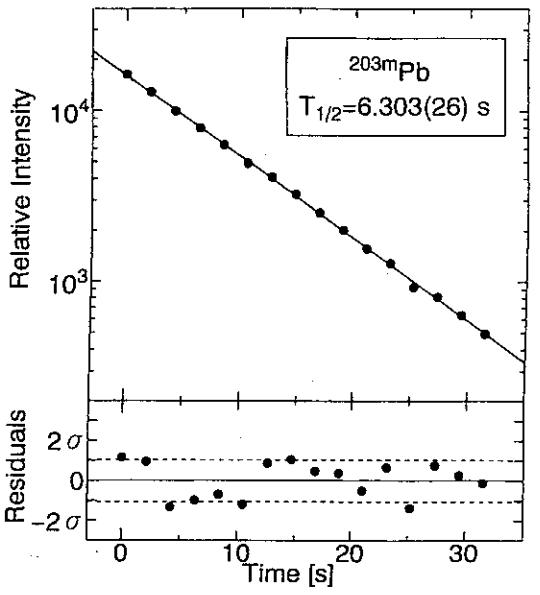

Fig.2 Decay curve of ^{203m}Pb and residuals from a least squares fitting analysis.

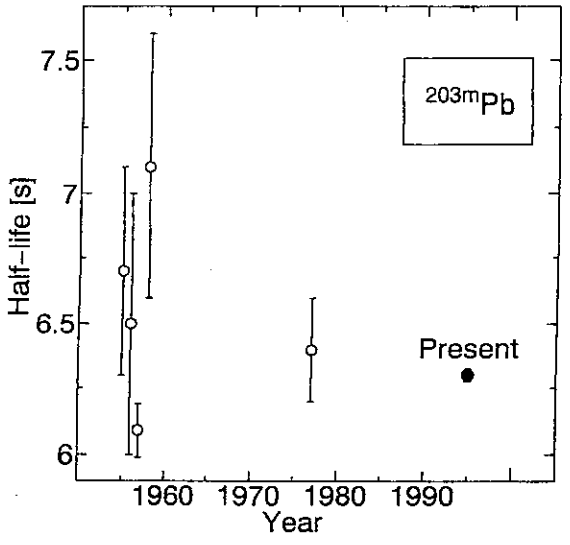

Fig.3 Comparison with previous works taken from ref.3.

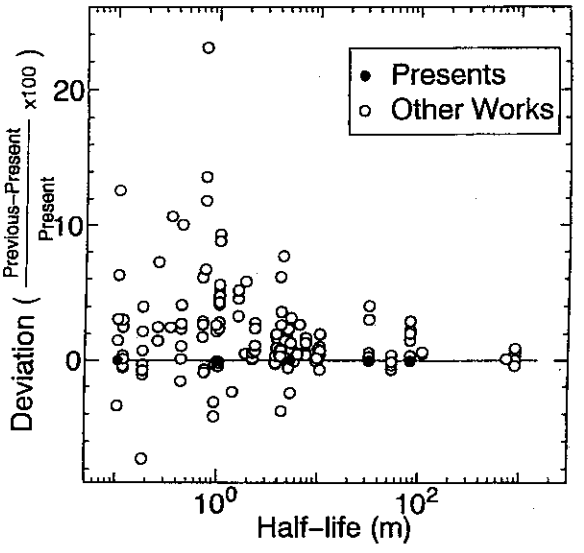

Fig.4 Deviation of previous half-life values from the present.

3.12 Calibration for Absolute Detection Efficiency of γ-ray Detector in High Energy Region with ^{56}Co

Atsushi Yoshida, Hiroshi Miyahara and Chizuo Mori
Nagoya University, Department of Nuclear Engineering
Furo-cho, Chikusa-ku, Nagoya 464-01

To precisely determine the γ-ray detection efficiencies in the energy region more than 1500 keV, we selected ^{56}Co which emits many γ-rays with precisely determined-emission probabilities in the energy region. The disintegration rates of ^{56}Co sources were determined by means of the 4πβ-γ coincidence method. The γ-ray detection efficiencies in the energy region more than 1000 keV were calibrated with accuracy better than 1% using ^{24}Na, ^{60}Co, ^{152}Eu and ^{56}Co.

1. Introduction

When a γ-ray detector is used in spectrometry it is necessary to precisely determine the γ-ray detection efficiencies. Standard sources used for calibration are desired to have long half-lives and precise γ-ray emission probabilities. Furthermore, it must be easy to obtain a source with a known disintegration rate. However, in the energy region of more than 1500 keV, the nuclides that fill these requirements are few, and it is therefore difficult to precisely calibrate the γ-ray detection efficiency. We then selected ^{56}Co which emits multi-γ rays with precisely determined-emission probabilities in the energy region, and tried to prepare the standard source and precisely measure the disintegration rate. Figure 1 shows the decay scheme for ^{56}Co with the

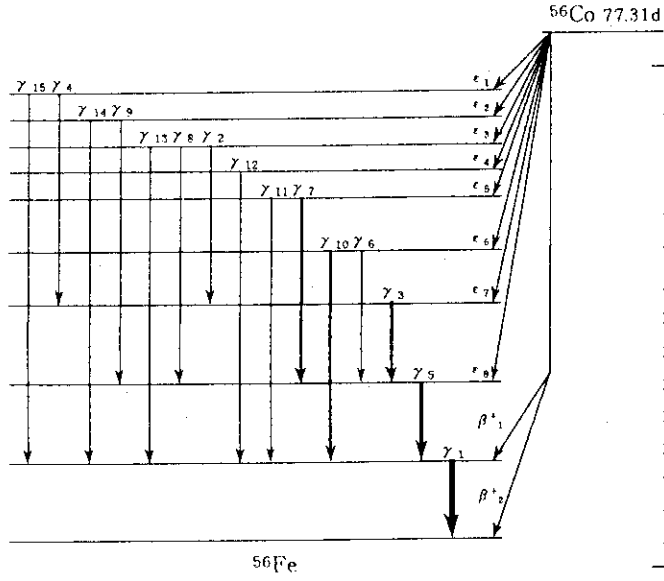

	γ-ray energy [keV]	γ-ray emission probability
γ 1	846.8	0.99951 (7)
γ 2	977.4	0.01435 (10)
γ 3	1037.8	0.1409 (6)
γ 4	1175.1	0.0227 (2)
γ 5	1238.3	0.670 (7)
γ 6	1360.2	0.0426 (2)
γ 7	1771.4	0.1549 (5)
γ 8	2015.2	0.0303 (4)
γ 9	2034.8	0.0778 (12)
γ 10	2598.5	0.1695 (6)
γ 11	3009.6	0.0106 (5)
γ 12	3202.0	0.0318 (8)
γ 13	3253.4	0.0764 (20)
γ 14	3273.0	0.018 (1)
γ 15	3451.2	0.0093 (3)

Fig. 1 A decay scheme for ^{56}Co.

evaluated γ-ray emission probabilities [1]. An example of γ-ray spectrum measured by an HPGe detector is shown in Fig. 2. The γ-rays with more than 1% of emission probabilities in the energy region lower than 3300 keV and with about 0.5% of emission probabilities at the energy near 3500 keV were seen in the figure.

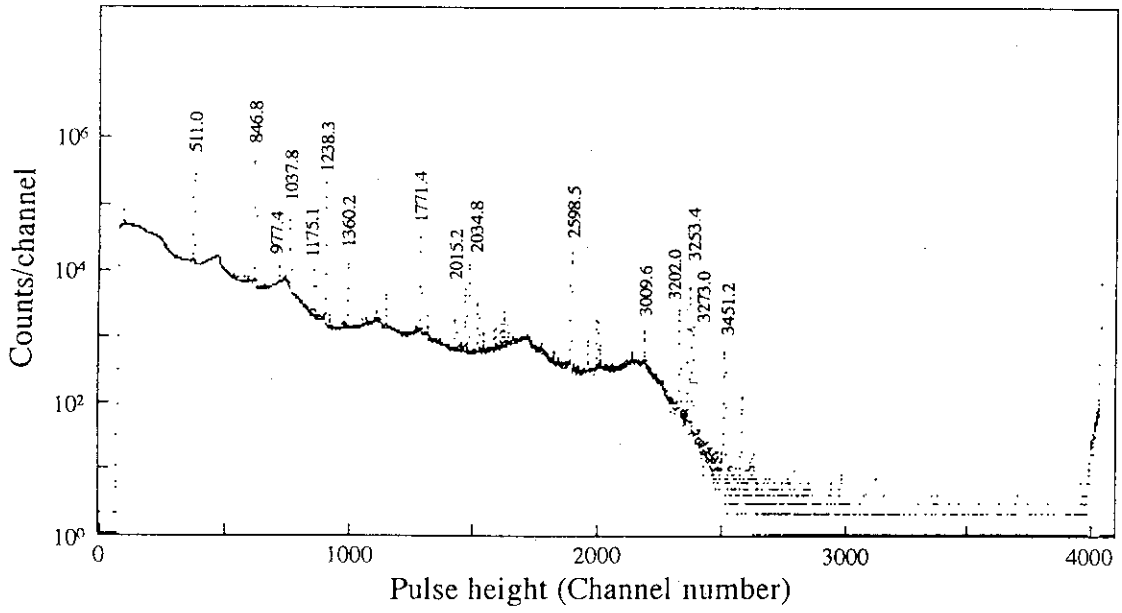

Fig. 2 A γ-ray spectrum of ^{56}Co.

2. Source preparation

As ^{56}Co solution of high radioactive concentration is not available, the ^{56}Co sources were prepared by proton-irradiation of natural Fe foils. In 1993 a ^{56}Co source was prepared by the ^{56}Fe (p, n) ^{56}Co reaction using a fixed-energy cyclotron of 22 MeV. However ^{52}Mn, ^{55}Fe and ^{57}Co which were made by ^{56}Fe (p, αn), ^{56}Fe (p, pn) and ^{57}Fe (p, n) reactions, respectively, seriously affected the disintegration-rate measurements. Considering the excitation functions, it is better that an Fe foil is irradiated by protons with lower energy. The produced nuclides and the cross sections are listed in Table 1. In 1994 natural Fe foils with a thickness of 10 μm (purity: 99.85%) were irradiated with protons of 13 and 14 MeV using the cyclotron at the Institute for Nuclear Study, the University of Tokyo. ^{52}Mn was not produced, but ^{55}Fe and ^{57}Co affected

Table 1 The produced nuclides and the cross section for each proton energy.

Nuclide	Reaction	Cross section			
		13 MeV	14 MeV	15 MeV	22 MeV
^{56}Co	^{56}Fe (p, n)	4000 mb	3500 mb	3000 mb	550 mb
^{55}Fe	^{56}Fe (p, pn)	170 mb	150 mb	120 mb	480 mb
^{52}Mn	^{56}Fe (p, αn)				3.5 mb
^{57}Co	^{57}Fe (p, n)	80 mb	70 mb	55 mb	33 mb

disintegration-rate measurements. A calculation based on the excitation functions [2] shows that ^{55}Fe is less in 13 MeV proton irradiation, and that ^{57}Co is less in 14 MeV proton irradiation. A difference depended on the amounts of these impurities is scarcely recognized in β-ray and γ-ray spectra. Furthermore, in 1995 natural Fe foils with a thickness of 10 μm and 50 μm (purity: 99.95%) were irradiated with protons of 15 MeV. The irradiated 10 μm foil was cut into appropriate size, and sandwiched with two metallized VYNS films. The 50 μm foil irradiated was dissolved in HCl solution, and ^{55}Fe was removed by ion exchange method. The solution was dropped and dried on metallized VYNS film.

3. Measurement of disintegration rate

All measurements were made with a 4πβ pressurized proportional counter (4πβ(ppc)), a high purity germanium (γ(HPGe)) detector and coincidence apparatus with a live-timed bi-dimensional data acquisition system [3]. Figure 3 shows a block diagram of measuring apparatus. To determine the disintegration rates of the sources, the coincidence efficiency functions were obtained by computer discrimination [4] using the β and γ spectra and the β spectrum coincident with γ pulses. Figure 4 shows an example of coincidence efficiency function derived by a two-dimensional calculation for the gate sets of the 511 and 847 keV γ-rays for a 10 μm foil source irradiated with protons of 15 MeV. This function shows an abrupt increase of the apparent disintegration rate in high β-efficiency region because of existence of ^{55}Fe. Extrapolation was carried out using a linear function fitted to the limited data, and the disintegration rate was determined.

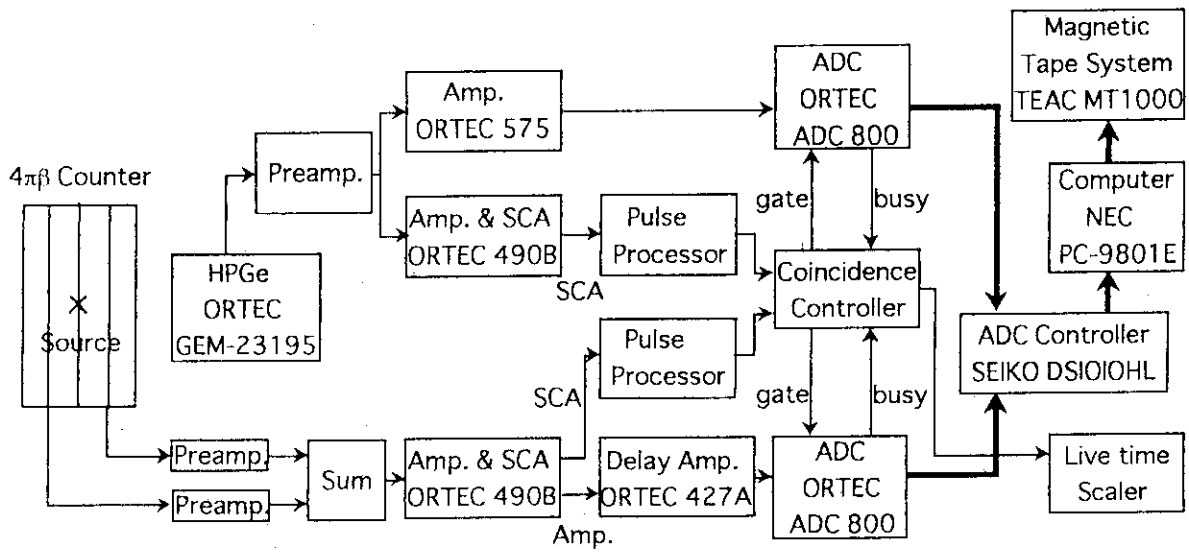

Fig. 3 A block diagram of the electronics for the live-timed bi-dimmensional data acquistion system composed of the 4πβ (ppc) and the HPGe detector.

Figure 5 shows an example of coincidence efficiency function of the ion exchange source derived by a two-dimensional calculation for the gate sets of the 511 and 847 keV γ-rays. This function shows no clear increase of the apparent disintegration rate like the foil source. Therefore extrapolation was carried out using a linear function fitted to the data in wide region to determine the disintegration rate. Furthermore, simple calculation method using single γ-gate can be applied for the ion exchange source because of no existence of ^{55}Fe. A number of measurements were carried out for each source and the disintegration rates corrected for the decay agreed with each other in all measurements. The disintegration rates for foil and ion exchange sources can be determined with uncertainty better than 0.5%.

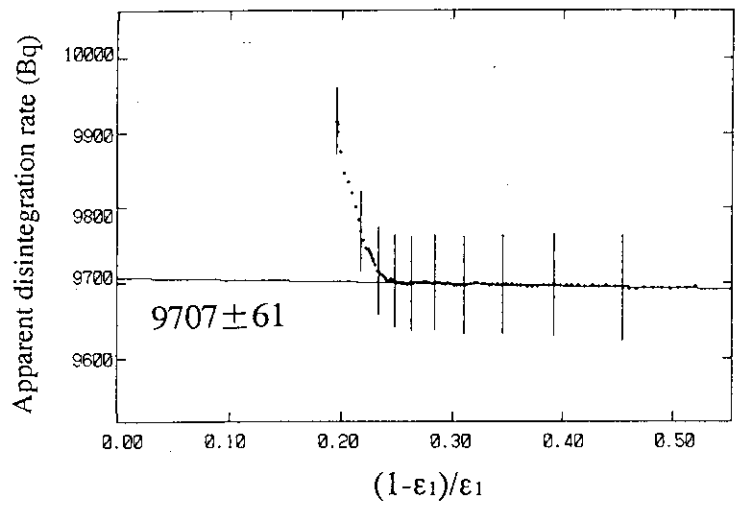

Fig. 4 An example of coincidence efficiency function of 10 μm foil source derived by a two-dimensional calculation for the gate sets of the 511 and 847 keV γ-rays.

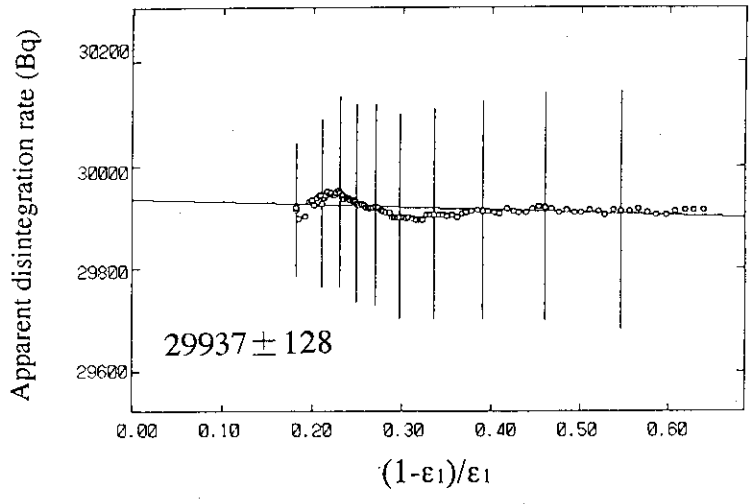

Fig. 5 An example of coincidence efficiency function of ion exchange source derived by a two-dimensional calculation for the gate sets of the 511 and 847 keV γ-rays.

4. Calibration for γ-ray detection efficiency and its utilization

The γ-ray detection efficiency was calibrated using ^{24}Na, ^{56}Co, ^{60}Co and ^{152}Eu sources as standard. The evaluated values [5] of γ-ray energy and γ-ray emission probability for ^{24}Na, ^{60}Co and ^{152}Eu are listed in Table 2. To correct for cascade summing effect, total γ-ray detection efficiency curve was determined from the measurement of ^{57}Co and ^{60}Co sources. The γ-ray

detection efficiency function was determined by fitting to the fourth-order polynomial function of both logarithmic scales of energy and γ-ray detection efficiency by using a covariance matrix. Figure 6 shows the γ-ray detection efficiency curve and deviations of measured values from the function. The γ-ray detection efficiencies were determined with accuracy of about 1% in the energy region lower than 3400 keV.

The precise calibration for the γ-ray detection efficiency suggests the possibility of absolute measurement of the precise γ-ray emission probability. The absolute γ-ray emission probabilities for ^{88}Rb which includes the β-transition to the ground state of ^{88}Sr were measured as an example of the utilization. The measurements were carried out five times, and the four or five sources of ^{88}Rb were prepared in each measurement. The emission probabilities for three strong γ-rays were measured. Table 3 shows the present results of the emission probabilities of the 898, 1836 and 2678 keV γ-rays and the evaluated values [6]. The present results comparatively agree with the evaluated values, and the uncertainties are improved. The emission probabilities for 898, 1836 keV γ-rays of ^{88}Rb were determined

Table 2 Evaluated values of γ-rays for standard sources.

Nuclide	γ-ray energy [keV]	γ-ray emission probability
^{24}Na	1368.6	0.999936 (15)
	2754.0	0.99855 (5)
^{60}Co	1173.2	0.99857 (22)
	1332.5	0.99983 (6)
^{152}Eu	778.9	0.1297 (6)
	867.4	0.04214 (25)
	964.1	0.1463 (6)
	1086.4	0.1013 (5)
	1112.1	0.1354 (6)
	1408.0	0.2085 (9)

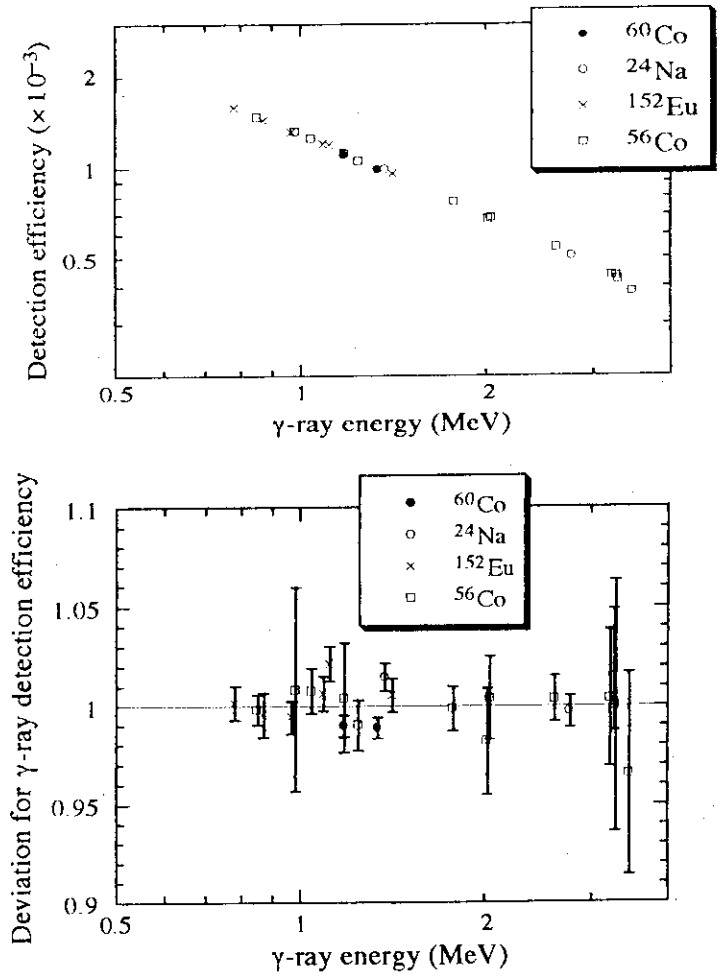

Fig. 6 An example of γ-ray detection efficiency curve and the deviations of measured values from the function.

Table 3 The measured results of the emission probabilities for the 898, 1836 and 2678 keV γ-rays of ^{88}Rb and the evaluated values.

γ-ray energy [keV]	γ-ray emission probability	
	Present result	Evaluated value [6]
898.0	0.1493 (9)	0.141 (3)
1836.0	0.2292 (15)	0.214 (4)
2677.9	0.0210 (3)	0.0196 (4)

with the uncertainty better than 1%.

5. Conclusion

The ^{56}Co sources were prepared by irradiation of natural Fe foils with protons of 13, 14, 15 and 22 MeV using two cyclotrons. However, the sources contain the impurities of ^{52}Mn, ^{55}Fe, ^{57}Co in 22 MeV irradiation, and ^{55}Fe and ^{57}Co in 13, 14 and 15 MeV irradiation. These impurities affected disintegration-rate measurements, and the coincidence efficiency function derived by a two-dimensional calculation showed an abrupt increase of the apparent disintegration rate in high β-efficiency region. Extrapolation using a linear function fitted to the limited data showed determination of the correct disintegration rate. To remove the most affective impurity ^{55}Fe, ion exchange method was applied and the coincidence efficiency function derived by a two-dimensional calculation showed no clear increase. Then, the extrapolation was carried out using a linear function over wider region. Furthermore, more common and simple computer discrimination method was possible and the disintegration rate was easily determined. The introduction of ^{56}Co source as standard made it possible to determine of the γ-ray detection efficiency with accuracy better than 1% in the energy region between 1500 and 3400 keV.

References

[1] F.Lagoutine, N. Coursol and J. Legrand; Table de radio nucleides (CEA-LMRI, 1980)

[2] H. Chopper, "Landolt-Börnstein" **13** (Springer, Berlin, 1991) 14.

[3] H. Miyahara et al., Appl. Radiat. Isot. **40** (1989) 343.

[4] D. Smith and L. E. H. Stuart, Metrologia **11** (1975) 67.

[5] IAEA; X-ray and γ-ray standards for detector calibration, IAEA-TECDOC-619 (IAEA, Vienna,1991).

[6] E. Browne and R. Firestone; Table of Radioactive Isotopes (1986).

3.13 Application of the Slowing Down Time Method for Neutron Spectrum Measurement in the Energy Region of eV in Various Neutron Field

Fujio MAEKAWA and Yukio OYAMA
Fusion Neutronics Laboratory
Japan Atomic Energy Research Institute
Tokai-mura, Naka-gun, Ibaraki-ken 319-11
e-mail: fujio@fnshp.tokai.jaeri.go.jp

The Slowing Down Time (SDT) method was adopted for several fusion benchmark experiments, and neutron spectra below 10 keV were successfully measured in Be, Fe, Cu, SS316 and SS316/water assemblies with experimental errors of around 10 %. It was found that the SDT method had a wide applicability and many advantages in comparison with other techniques for neutron spectrum measurement in the energy region below 10 keV. As a result, the techniques of in-situ neutron spectrum measurement in the whole energy were established for D-T fusion environment at FNS with combination of the SDT method and the existing proton-recoil methods for higher energies.

1. Introduction

A neutron spectrum is one of the most fundamental quantity in wide applications in the area of atomic energy such as fission, fusion reactors and accelerator facilities. No accurate nor extensively applicable method, however, has been established so far for neutron spectrum measurement between 1 eV and 1 keV. We proposed to utilize the principle of the Slowing Down Time (SDT) method for a new technique for neutron spectrum measurement in the energy range below 10 keV [2]. A principle of the SDT method which utilized the phenomenon of slowing down of pulsed neutrons in a bulk medium was proposed by Bergman et al [1]. The principle has been applied for so-called "Lead Slowing Down Spectrometers." In this study, measurements of neutron spectra below 10 keV in various bulk media were conducted with the SDT method for fusion benchmark experiments at the Fusion Neutronics Source (FNS) facility in JAERI. Applicability and features of the SDT method was investigated through the measurement.

2. Experiment

Neutron spectra were measured inside of five bulk media, i.e., beryllium, iron, copper, type 316 stainless steel (SS316) and SS316/water layered assemblies by the SDT method. Details of the measurements are described elsewhere [2-5]. Brief explanation for a typical measurement of copper is given here.

A copper assembly of 630 mm in diameter and 608 mm in thickness was placed in front of the D-T neutron source of FNS. A BF3 gas proportional counter was inserted in the copper assembly. Pulsed D-T neutrons of 1 μs in pulse width and 200 μs in pulse interval were injected to the assembly, and a time-spectrum of $^{10}B(n,\alpha)^{7}Li$ reaction was recorded. Energy-calibration, which was to determine a relation between slowing down time and neutron energy, was performed with both the resonance

filter technique and the capture gamma technique at 6 energy points between 4.91 eV and 580 keV. The energy-calibration curve was calculated by a Monte Carlo transport calculation with MCNP-4A [6], and the curve was fitted so as to be consistent with the experimentally obtained relations between slowing down time and neutron energy, as shown in Fig. 1. The measured time-spectrum of $^{10}B(n,\alpha)^{7}Li$ reaction was converted to an energy-spectrum with using the energy-calibration curve, and then a neutron energy-spectrum was derived taking account of the detector sensitivity, the neutron yield, the cross section of $^{10}B(n,\alpha)^{7}Li$ reaction and some corrections.

3. Results

Figure 2 shows neutron spectra in the copper assembly measured by using three techniques. In this work, spectra between 0.3 eV and 10 keV were obtained by the SDT method with experimental uncertainties around 10 %. In the previous experiment [7], spectra above 1 MeV were obtained with an NE213 liquid scintillation counter, and those between 3 keV and 1 MeV were measured with proton recoil gas proportional counters (PRCs), in combination with the unfolding technique. The SDT method supplements the lower energy part of the spectra in considerably wide energy ranges more than 4 orders of magnitude. There is an overlapping energy region between 3 and 10 keV for the SDT method and PRCs, and agreement of both the spectra are good. This fact implies that the validity of the both methods. In the spectra measured by the SDT method, depressions of the neutron flux due to the large resonance of neutron capture reaction at 230 and 580 eV are recognized at corresponding energies.

Neutron spectra in the SS316/water assembly measured with the three techniques are shown in Fig. 3. In general, adoption of the SDT method in light atomic mass media is more difficult than that in the media of medium or heavy atomic mass because of experimental difficulty in the energy calibration determination. The measurement in the SS316/water assembly was one of the most difficult cases for application of the SDT method since the assembly contained the lightest atoms, hydrogen. Nevertheless, the spectra below 10 keV were obtained by the SDT method as shown in Fig. 3, although experimental uncertainties, typically 10 - 30 %, were somewhat large. In addition, total thermal fluxes in the SS316/water assembly were obtained by extending the SDT method as presented in Fig. 3.

Energy resolution of a spectrum measured by the SDT method primarily depends on the atomic mass number of the medium in which the spectrum is measured [2]. A better energy resolution can be attained in heavier atomic mass media. Figure 4 shows an energy resolution function in copper assembly estimated by an MCNP calculation. The energy resolution is around 50-60 % in FWHM below 1 keV. Energy resolution for iron and SS316 assemblies is nearly the same as those for copper because of the similar atomic mass. The beryllium and SS316/water assemblies consist of light atomic mass atoms, and estimated energy resolution for them were about 130 and 240 %, respectively.

For all the assemblies, i.e., beryllium, iron, copper, SS316 and SS316/water, spectra could be successfully measured by adopting the SDT method. These measurements demonstrated that neutron spectra below 10 keV could be measured by the SDT method for various media including light mass media such as SS316/water and beryllium. As a result, as shown in Figs. 2 and 3, the techniques of the whole energy measurement of in-situ neutron spectrum were established for D-T fusion environment at FNS with combination of the SDT method and the existing proton-recoil methods for higher energies.

4. Features of the SDT method

Table 1 summarizes comparisons of the SDT method with other techniques for neutron spectrum measurement in the energy region of eV, i.e., the Time-Of-Flight method, the Multi-Foil Activation method and the Multi-Sphere Bonner Counter method.

To adopt the SDT method, the following conditions are required;

(1) a suitable pulsed neutron source,
(2) measuring positions inside a bulk assembly, and
(3) feasibility of energy calibration.

It was found from the present measurements that the SDT method has many advantages in comparison with the other three methods in terms of the following points;

(1) high accuracy (uncertainty around 10 % for most cases),
(2) high sensitivity to save measuring time,
(3) reasonable energy- and spatial-resolution,
(4) in-situ measurement to enable background free measurement, and
(5) reliable spectrum with explicit error assignment and without spectrum oscillation due to unfolding process.

5. Concluding Remarks

The SDT method was established as a new technique for neutron spectrum measurement below 10 keV. Through the adoption of the SDT method for several fusion benchmark experiments, the following facts were found.

(1) The SDT method was very effective for medium atomic mass media such as iron, copper and SS316, and even for light atomic mass media such as beryllium and SS316/water.
(2) The SDT method had many advantages for neutron spectrum measurement in the energy range below 10 keV comparing with the existing method, i.e., the Time-Of-Flight method, the Multi-Foil Activation method and the Multi-Sphere Bonner Counter method.

As a result, the techniques of the whole energy measurement of in-situ neutron spectrum were established for D-T fusion environment at FNS with combination of the SDT method and the existing proton-recoil methods for higher energies.

Acknowledgments

The authors gratefully acknowledge the operating staff of FNS for their efforts to make particular neutron pulses for the experiments. They also wish to express their gratitude to Drs. H. Maekawa and Y. Ikeda for their great support to the work.

References

[1] Bergman A. A., et al.: Proc. 1st Int. Conf. Peaceful Uses Atomic Energy 4 (1955) 135.
[2] Maekawa F. and Oyama Y.: "Measurement of Low Energy Neutron Spectrum below 10 keV with the Slowing Down Time Method," submitted to Nucl. Instrum. Meth. Section A (1995).
[3] Maekawa F. and Oyama Y.: "Measurement of Neutron Energy Spectrum below 10 keV in an Iron Shield Bombarded by D-T Neutrons and Benchmark Test of Evaluated Nuclear Data from 14 MeV Down to 1 eV," submitted to Nucl. Sci. Eng. (1995).
[4] Konno C., et al.: JAERI-Research 94-043 (1994).
[5] Konno C., et al.: JAERI-Research 95-017 (1995).
[6] Briesmeister J. F., Ed., "MCNP - A General Monte Carlo N-Particle Transport Code, Version 4A," LA-12625-M, Los Alamos National Laboratory (1993).
[7] Konno C., et al.: Fusion Eng. Des. 28 pp. 745-752 (1995).

Table 1 Comparisons of the four methods of neutron spectrum measurement in the energy region around eV. Bold letters indicate advantages.

	Slowing Down Time	Time of Flight	Multi-Foil Activation	Multi-Sphere Bonner Counter
Position of measurement	inside a bulk assembly	outside an assembly with long flight path	**any position**	in a large open space
Pulsed neutron	necessary	necessary	not necessary	not necessary
Sensitivity	**high**	low	low	**high**
Accuracy	**high (~10%)**	**high**	low	low
Exp. error	**clear**	**clear**	not clear	not clear
Energy resolution	**high or moderate** (50-200%)	**high** mean-emission-time flight-time	low difficult to determine	low difficult to determine
Spatial resolution	**high**	low	**high**	low
Initial guess	**not necessary**	**not necessary**	necessary	necessary

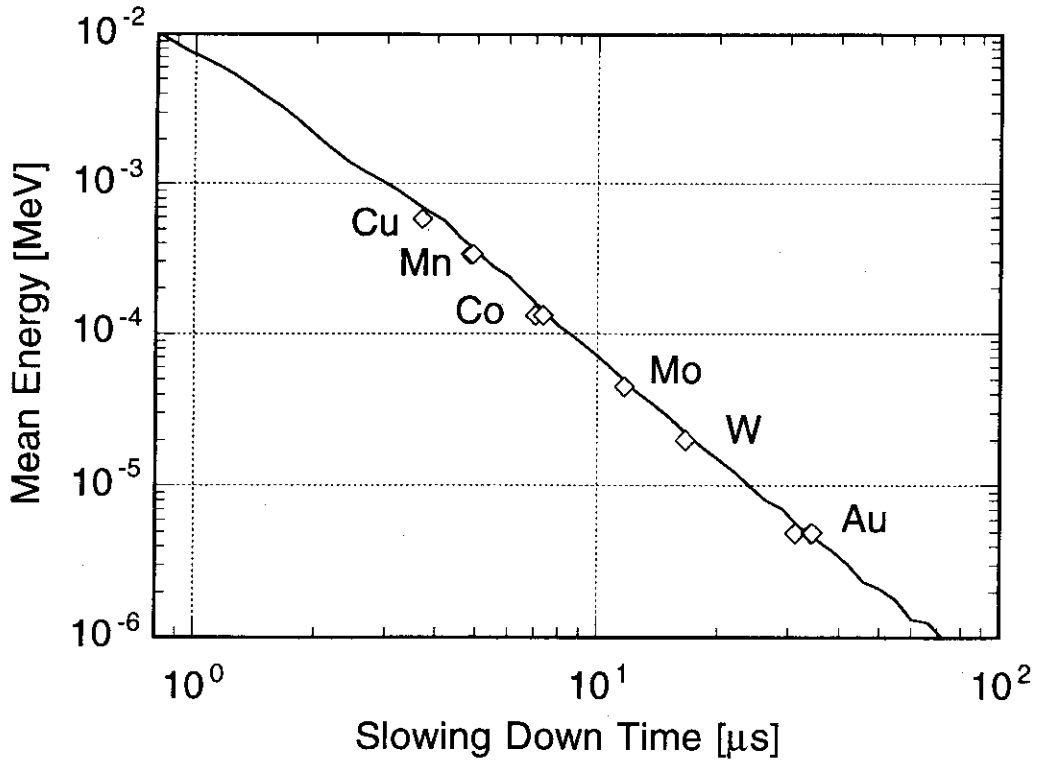

Fig. 1 Relation between slowing down time and mean neutron energy experimentally determined (open diamonds) and energy calibration curves obtained by the MCNP calculation.

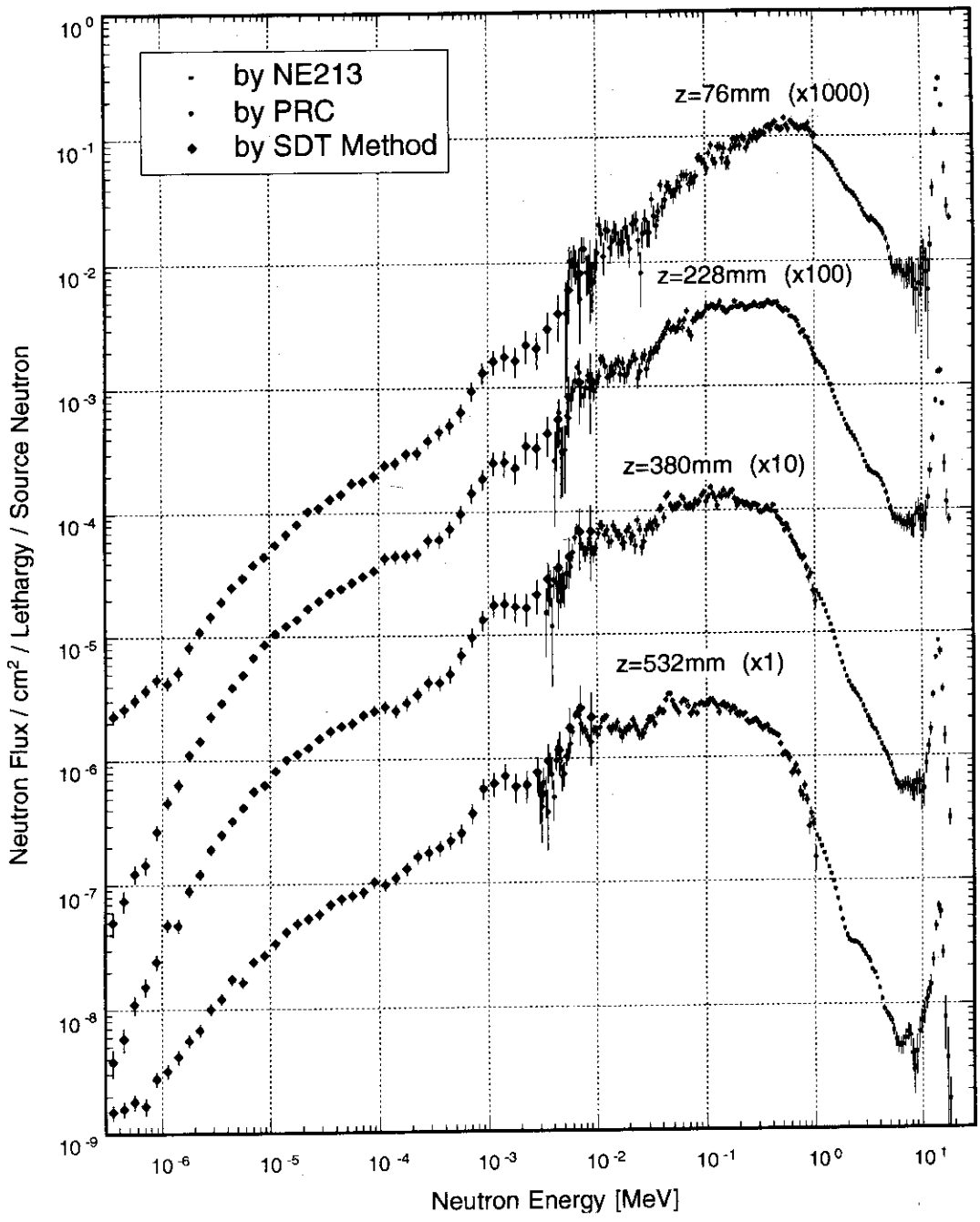

Fig. 2 Neutron spectra measured at four positions in the copper assembly. The spectra below 10^{-2} MeV are obtained by the SDT method in this work. Those between 3 x 10^{-2} MeV - 1 MeV and above 1 MeV are previously measured [7] by proton recoil gas proportional counters and an NE213 liquid organic scintillation spectrometer.

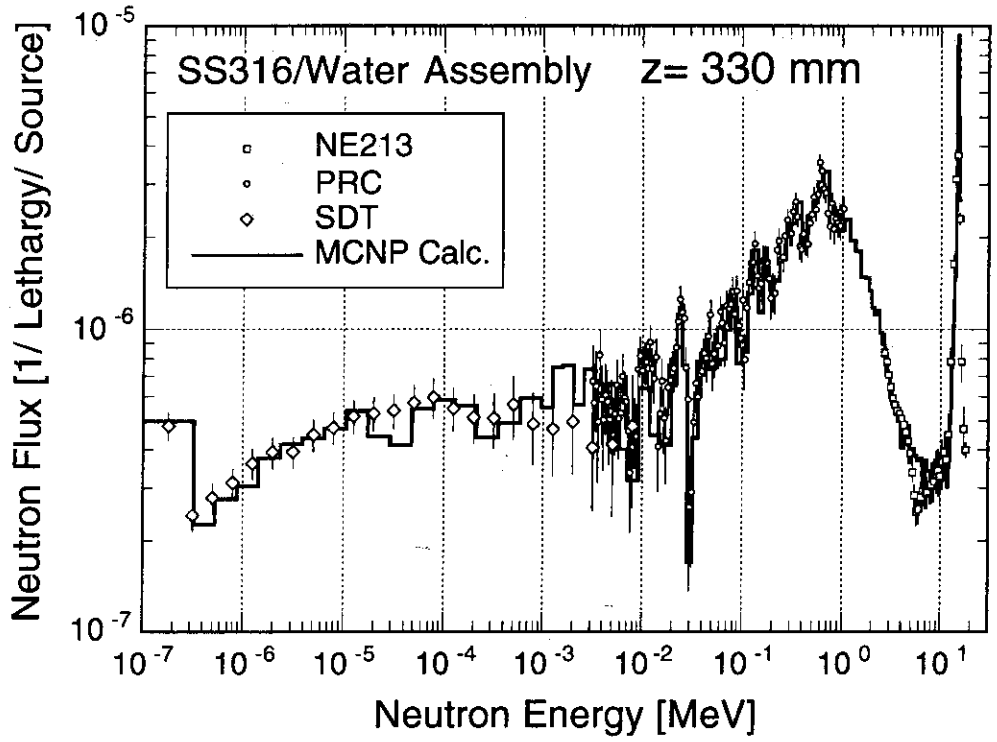

Fig. 3 Neutron spectra measured at the 330 mm depth in the SS316/water assembly in comparison with the MCNP calculation. The spectra below 10^{-2} MeV are obtained by the SDT method in this work. Those between 3 x 10^{-2} MeV - 1 MeV and above 1 MeV are previously measured [5] by proton recoil gas proportional counters and an NE213 liquid organic scintillation spectrometer.

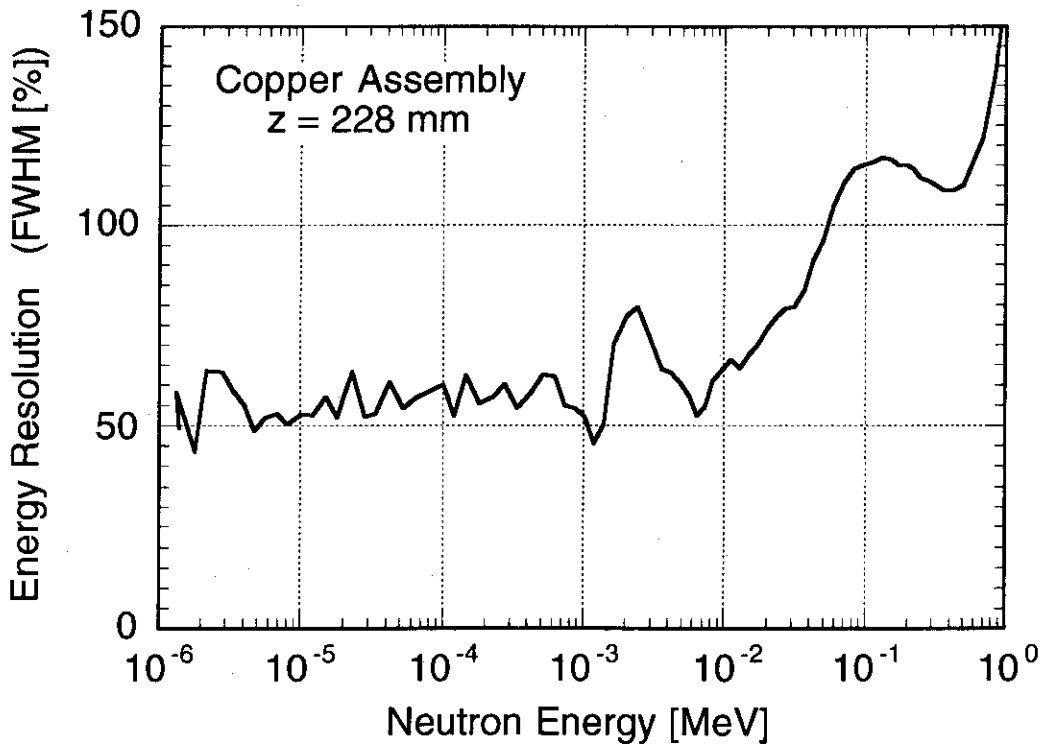

Fig. 4 Energy resolution of the measured neutron spectrum by the SDT method at the 228 mm position in the copper assembly estimated by the MCNP calculation. Small fluctuation of the curve is due to statistical uncertainty of the Monte Carlo calculation.

3.14 The Evaluation of Multigroup and Pointwise Cross Section Libraries for Monte Carlo Calculation of 14 MeV Neutron Streaming Through Fusion Reactor Penetration.

Alexei JIRKIN
Department
of Quantum Engineering and Systems Science,
Faculty of Engineering, University of Tokyo
7-3-1 Hongo, Bunkyo-ku,Tokyo 113, Japan
e-mail: jirkin@sophie.gen.u-tokyo.ac.jp

The verification of available nuclear data for Monte Carlo calculations of radiation streaming through fusion reactor penetrations has been carried out on the base of comparison calculational and experimental neutron and gamma-ray energy spectra resulting from the streaming of 14 MeV neutrons through a 0.30- m-diam duct (length-to-diameter ratio = 2.83). The neutron calculated spectra were obtained using two Monte Carlo codes: MORSE-CG with DLC-23 (CASK), EURLIB-IV multigroup cross sections and MCNP-4.2 with continuos point cross sections from ENDF/B-IV, ENDL-85 nuclear data files. Gamma-ray energy spectra were also calculated using the MCNP code.

1 Introduction

The effects of radiation streaming on the design of fusion reactors have prompted the need for verifying the radiation transport methods and nuclear data being used in the analysis of these types of problems. In previous papers [1, 2] the utility of the Monte Carlo method for fusion reactor shielding calculations was demonstrated on the base of comparison of calculated and measured energy spectra.

In this paper the verification of the DLC-23 (CASK), EURLIB-IV multigroup cross section libraries using the MORSE-CG code and point cross sections from ENDF/B-IV, ENDL-85 using the MCNP-4.2 code was performed.

2 Details of the calculations

The experimental facility and its calculational model in cylindrical geometry are described in [1, 2, 3] and shown in Fig.1 and 2.

The 14 MeV neutrons are produced in the D-T fusion reaction is given by

$$D + T \rightarrow n + {}^{4}_{2}He + 17.36MeV. \quad (1)$$

4 detector locations were chosen for analysis. They were placed at the points with the r-z geometry coordinates of z=151 cm and r=0,19,39,59 cm.

The comparison of calculated and measured spectra were made for neutrons with energies above 850 keV and for gamma-rays with energies above 750 keV.

The calculated neutron and gamma-ray flux per unit energy was smoothed with energy dependent Gaussian response function having a width determined from

$$(R_n = (300 + 800/E_n)^{\frac{1}{2}}, \quad (2)$$

$$(R_\gamma = (300 + 800/E_\gamma)^{\frac{1}{2}}, \quad (3)$$

where R_n is the full-width a half-maximum (in percent) of the NE-213 detector resolution to neutrons of energy E_n and R_γ is the analogous value to gamma-rays of energy E_γ.

3 Discussion of results

The comparison of calculated and measured spectra are presented in Fig.3 through 5.

The neutron spectra calculated using MORSE-CG with DLC-23 (CASK) and EURLIB-IV are in satisfactory agreement with measured data within 10 to 50% depending on the detector location and neutron energy. The disagreement in results may be explained by uncertainties of neutron multigroup cross sections, untaking into account the neutrons reflected from the reactor room walls and statistical uncertainty that was within to 35%.

The measured neutron spectra and calculated spectra using MCNP-4.2 with ENDF/B-IV and ENDL-85 cross sections agree well within 5 to 30% at neutron energies lower 10 MeV. At energies above 10 MeV the disagreement was within to 50%. The statistical uncertainty was within 5 to 30%.

The gamma-ray spectra calculated using MCNP-4.2 with ENDL-85 nuclear data were in favorable agreement with measured results within 5 to 50%. The analogous spectra calculated using ENDF/B-IV cross sections are in large disagreement at off-axis detectors sometimes by a factor of 8, because of the lack of the gamma-ray generation cross sections for some reactions at ENDF/B-IV. The statistical uncertainty of calculated spectra was within 5 to 30%.

4 Conclusion

The neutron spectra calculated using multigroup and point cross sections disagree with measured data within to 50% at energies above 10 MeV. The gamma-ray spectra calculated using ENDL-85 disagree within to 50%. The analogous spectra obtained using ENDF/B-IV disagree sometimes by a factor of 8.

References

[1] R.T.Santoro, R.G.Alsmiller, Jr.,J.M.Barnes et.al.: "Streaming 14-MeV Neutrons Through an Iron Duct - Compaison of Measured Neutron and Gamma-Ray Energy

Spectra with Results Calculated Using the Monte Carlo MCNP Code", Nucl. Sci. and Engin., **84**, 260-270 (1983).

[2] R.T.Santoro, R.G.Alsmiller, Jr.,J.M.Barnes et.al.:"Calculated Neutron and Gamma-Ray Energy Spectra from 14-MeV Neutrons Streaming Through an Iron Duct: Comparison with Experiment",Nucl. Sci. and Engin., **80**, 586-602 (1982).

[3] Cross Section Working Group Benchmark Specifications, National Nuclear Data Center Brookhaven National Laboratory, BNL 19302,II, Supplement, September 1986, ENDF-202 Informal report.

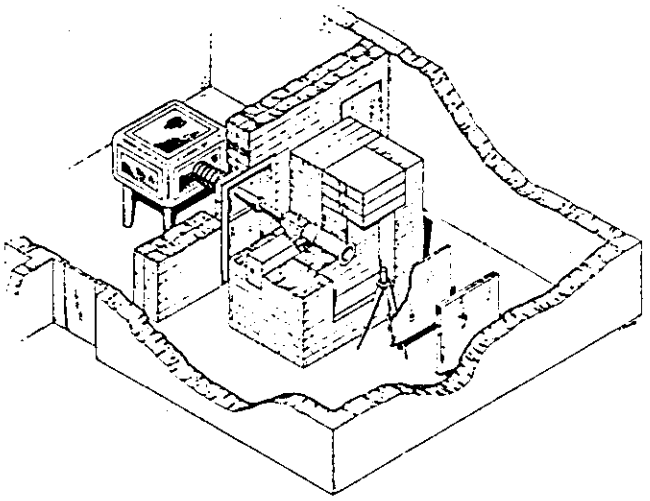

Fig.1 The view of experimental facility.

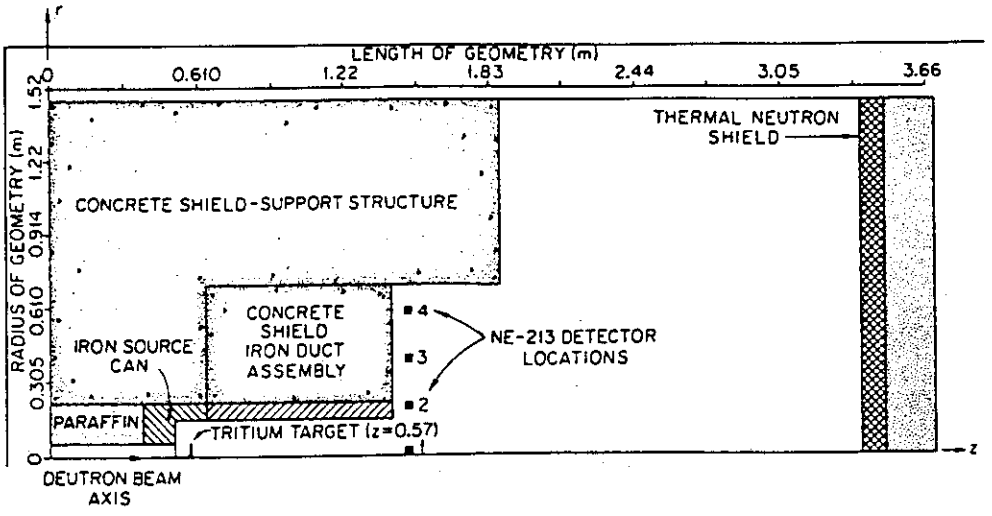

Fig.2 The two-dimentional calculational model.

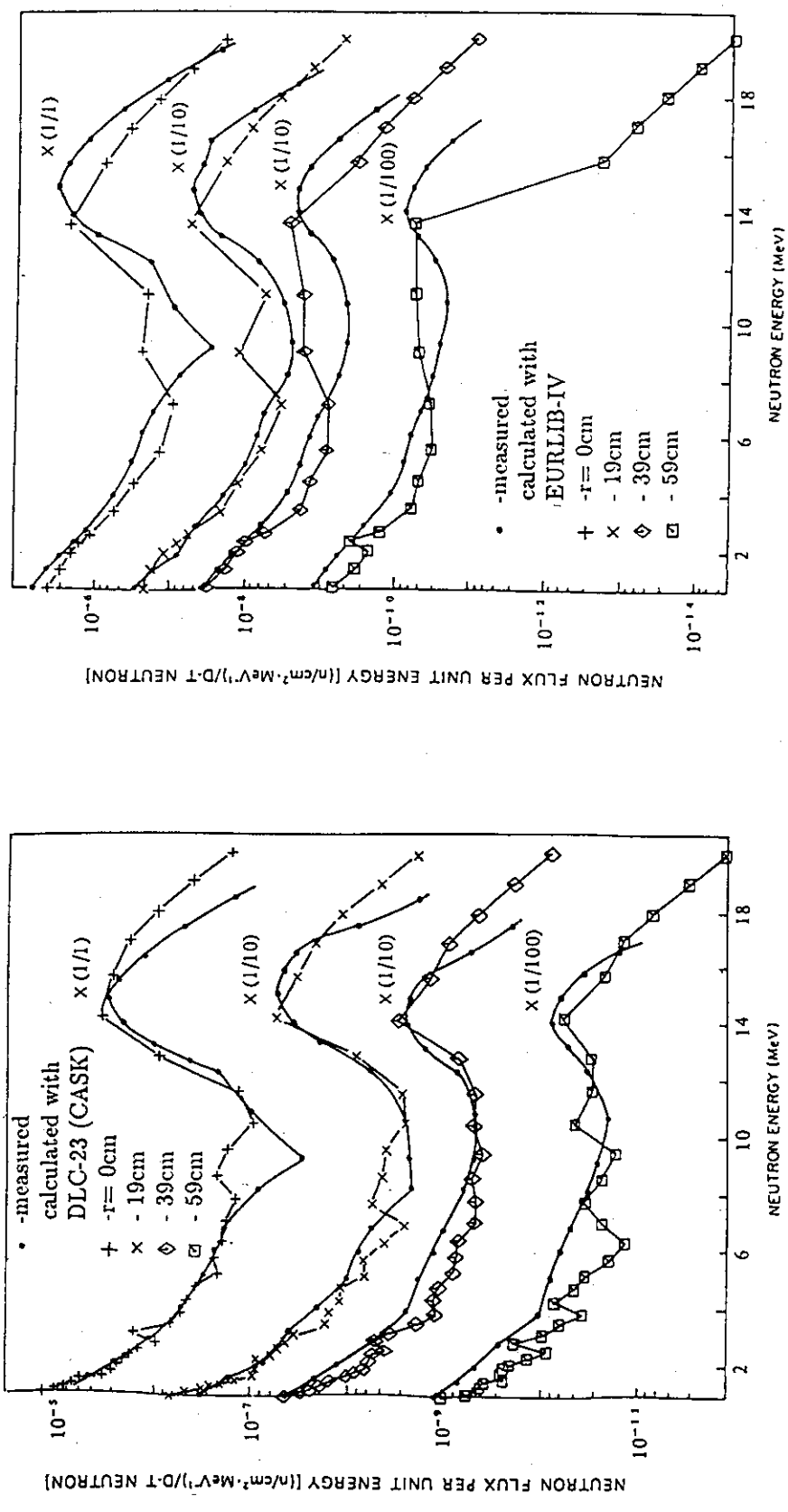

Fig.3 The measured neutron energy spectra and spectra calculated using MORSE-CG with the multigroup cross-section libraries.

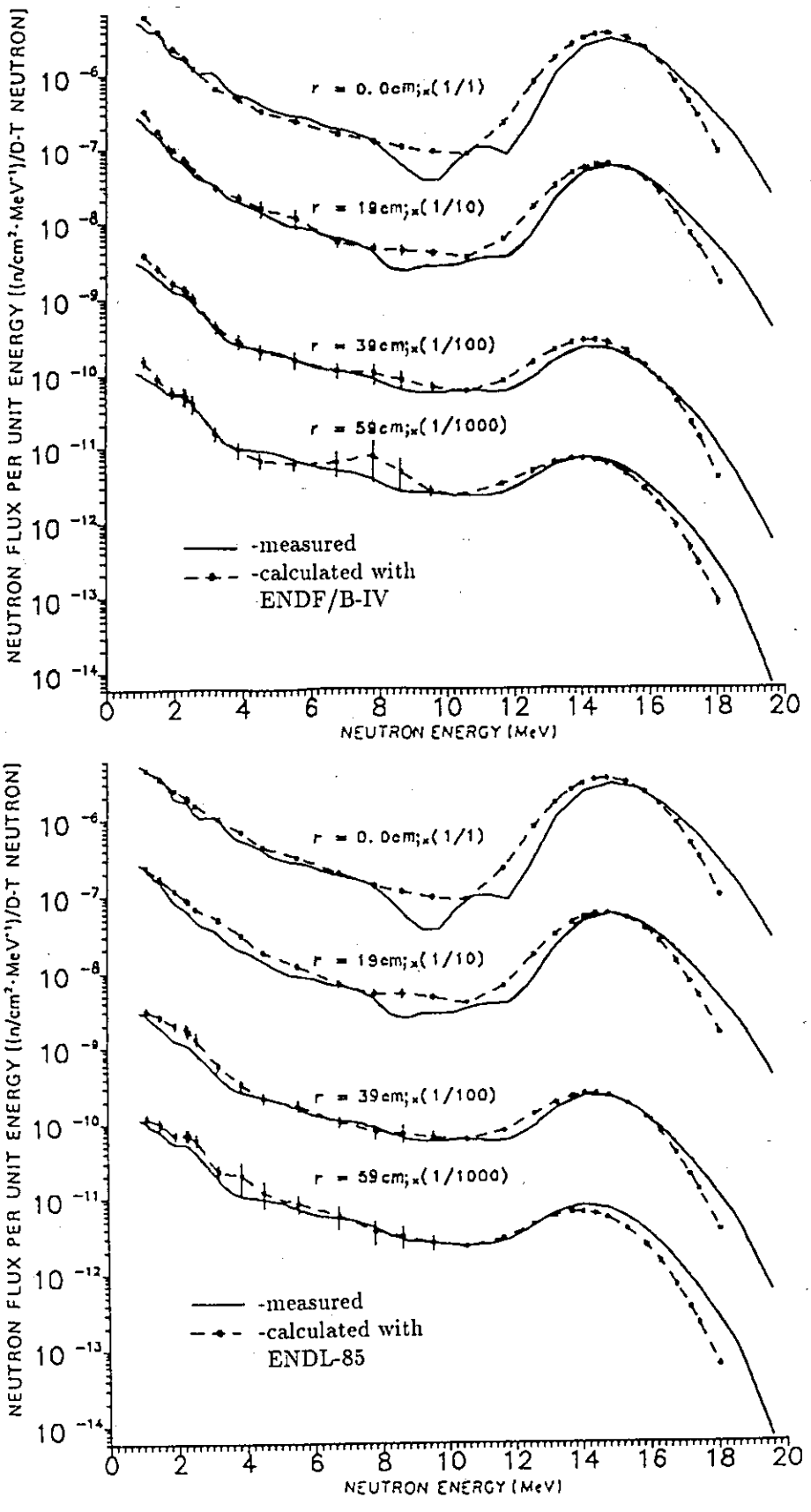

Fig.4 The measured neutron energy spectra and spectra calculated using MCNP-4.2 with the continuos point cross sections.

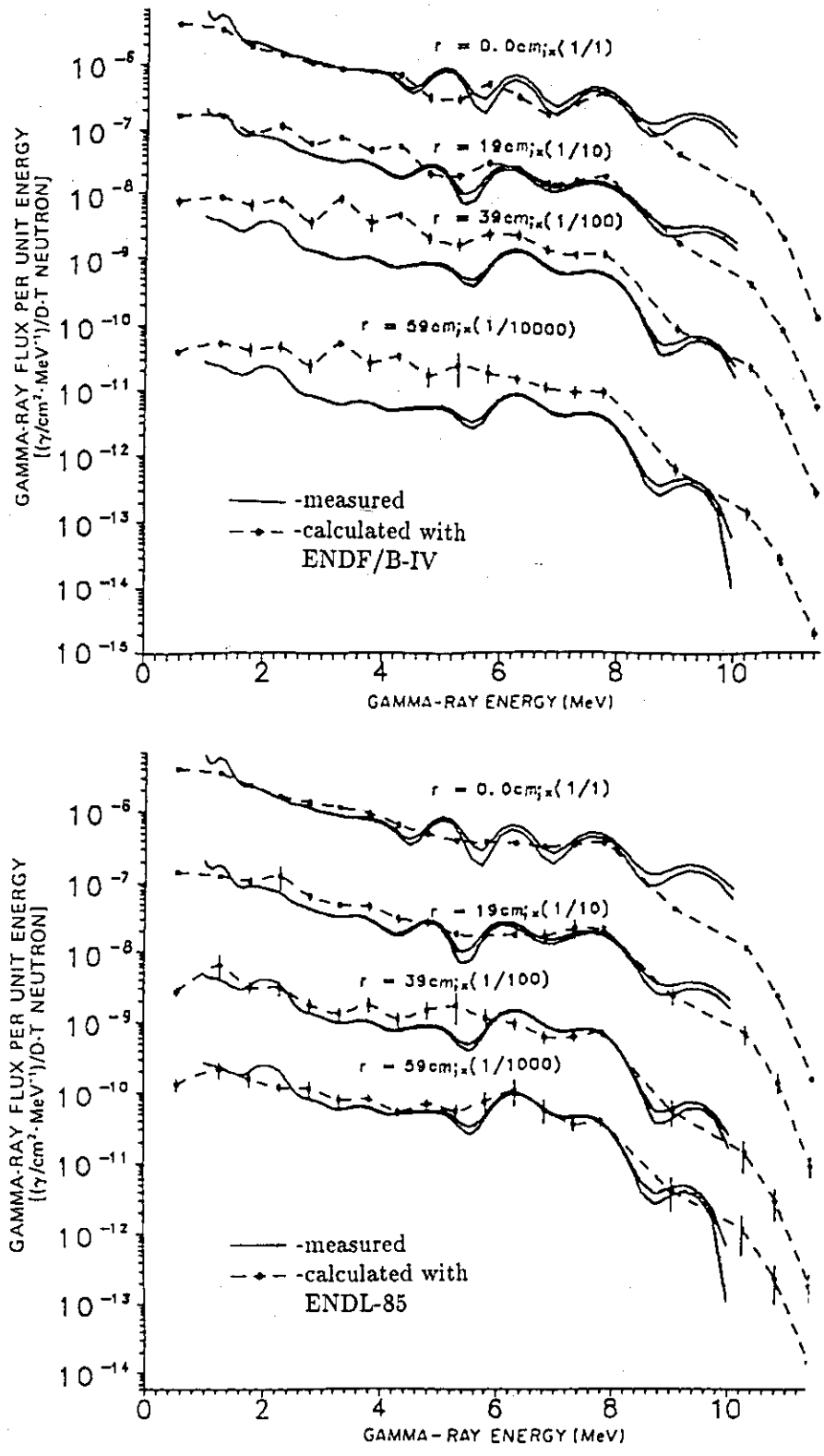

Fig.5 The measured gamma-ray energy spectra and spectra calculated using MCNP-4.2 with the continuos point cross sections.

3. 15 Investigation of Shielding Design Margin Evaluation in Fusion Reactors

Koichi Maki, Katsumi Hayashi*, Chikara Konno**, Hiroshi Maekawa**, Fujio Maekawa**
Hitachi Research Laboratory, Hitachi Ltd. *Hitachi Engineering Co., Ltd.
**Japan Atomic Energy Research Institute

Abstract

The shielding design margins in nuclear properties, which are nuclear heating rate, insulator dose, copper dpa and fast neutron fluence in winding pack of superconductive magnets, are considered given by uncertainties in the calculated nuclear properties and correction factors for gap streaming, void and inhomogeneity effects on the properties. The uncertainties are categorized into those caused by ambiguities in nuclear data and numerical methods in transport codes, number of spatial meshes, order of Legendre expansion for scattering, division number of angular space and number of energy groups. The uncertainties caused by these categories were estimated by analysis in SS+H_2O bulk shield experiment and numerical calculations with transport codes. The correction factors were estimated by numerical calculation with two dimensional transport code. On the basis of the uncertainties and the correction factors, we can evaluate the shielding design margins to be 1.7, 1.59, 1.56 and 1.54 for nuclear heating rate, insulator dose, copper dpa and fast neutron fluence in winding pack of superconductive magnets in ITER, respectively.

1. Introduction

In radiation shielding design for fusion reactors, two kinds of shieldings are exist. One is to protect facilities themselves from radiation and the other is to do human bodies against radiation exposure. Determining the necessary and sufficient thicknesses of the shieldings for the protections is one of the most important role in shielding design. Especially in fusion reactors, the shielding design for protecting facilities themselves from radiation must be held a important position in reactor design differently from fission reactors and accelerators, in which biological shielding is main shielding design. Particularly shielding design for superconductive magnets (SCM) from radiation is held a main part of position together with structural design in fusion reactor design.

Fortunately now we established calculational methods, that is, we have various code systems and many nuclear constant sets. We need not perform experiments every occasion to determine the thicknesses of shieldings, since we can calculate the thicknesses by using them. However, uncertainties occur in calculated values by incompleteness of the calculational codes, modeling and ambiguities in nuclear data, etc.

From these considerations, the principal purposes of the present paper are to estimate the uncertainties in calculated nuclear properties in SCM with radiation shielding, correction factors in typical shielding design, and to evaluate the shielding design margins for a typical experimental fusion reactor of ITER (International Thermonuclear Experimental Reactor)[1], as shown in Fig.1, on the basis of the shielding design margin evaluation method[2].

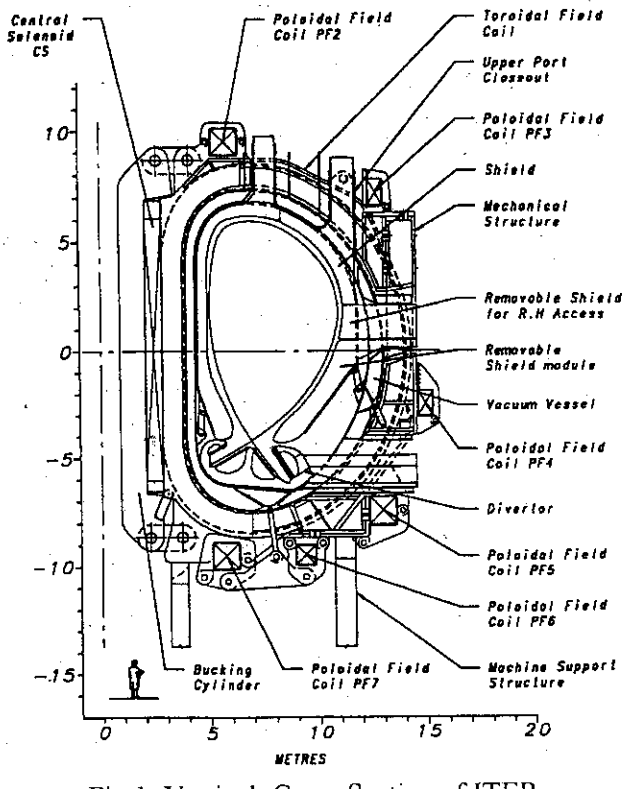

Fig.1 Vertical Cross Section of ITER

2. Evaluation Method

2.1 definition of shielding design margin

Shielding design is to determine shield thicknesses so that a shielding design value a^d_i of nuclear property i must become less than the design limit of $\hat{a}_i$. That is, $a^d_i \leq \hat{a}_i$. The value a^d_i is calculated with multiplying a_i by shielding design margin m_i, which includes uncertainties in calculated nuclear properties for shielding design and correction factors. Shield thickness is therefore determined so as to satisfy the following relation,

$$a_i \leq \hat{a}_i \ / m_i \ . \tag{1}$$

The margin m_i is given by uncertainties ε_i in the calculated nuclear properties and the correction factors f_{ik} of correction item k, such as gap streaming, as,

$$m_i = \prod_k f_{ik} \cdot (1 + \varepsilon_i) \tag{2}$$

2.2 uncertainty evaluation

We suppose that the two dimensional transport code DOT3.5[3] is used as a basic shielding design code. Then uncertainties in calculated nuclear properties of SCM is formulated as,

$$\varepsilon_i = \{(\varepsilon_i^{(Nucl+method)})^2 + (\varepsilon_i^{Mesh})^2 + (\varepsilon_i^{NPl})^2 + (\varepsilon_i^{Sn})^2 + (\varepsilon_i^{Ng})^2\}^{1/2} , \tag{3}$$

where, $\varepsilon_i^{(Nucl+method)}$, ε_i^{Mesh}, ε_i^{NPl}, ε_i^{Sn} and ε_i^{Ng} are respectively the uncertainties caused by ambiguities in nuclear data and numerical method in transport codes, number of spatial meshes, order of Legendre expansion for scattering anisotropy, division number of angular space and number of energy groups. The subscript i indicates a kind of the nuclear property in SCM, that is nuclear heating rate, insulator dose, copper displacement per atom and fast neutron fluence in winding pack.

The uncertainties of $\varepsilon_i^{(Nucl+method)}$ can be estimated from analysis of bulk shielding experiments. Gamma-ray heating rates were observed by C. Konno[4], etal and those data were analyzed by F. Maekawa[5], etal. The values of C/E were estimated in the experimental analysis as shown in Fig.2. From this figure we can obtain the value 20% of ε_{heat} =|1-C/E| as the uncertainties in calculated nuclear properties of SCM at the point of 75cm from bulk shield surface corresponding to position of plasma side winding pack in SCM. When uncertainties in gamma-ray heating rates is known, we can take sufficiently them for uncertainties in total nuclear heating rates since gamma-ray heating rate is occupied more than 95% in nuclear heating rate in SCM. The uncertainties in nuclear properties derived from C/E include uncertainties caused by numerical calculation in experimental analysis. They are the uncertainties resulting from number of spatial meshes, order of Legendre expansion, division number of angular space and number of energy groups. The uncertainties in nuclear data and numerical method can be estimated by removing the uncertainties caused by experimental analysis from the uncertainties in nuclear properties derived from C/E.

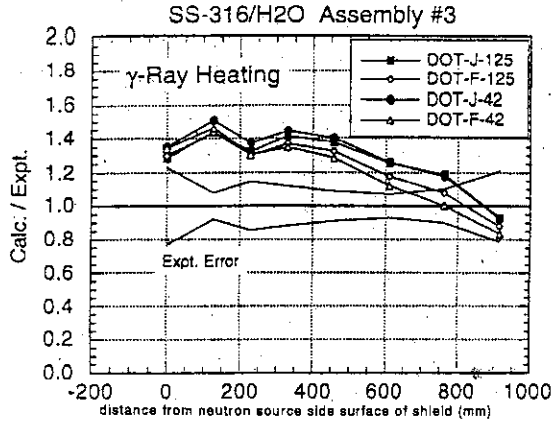

Fig.2 C/E of gamma-ray nuclear heating rates in SS/water shielding estimated by DOT3.5 code with different group constant sets

(J-125,J-42:without self shielding effect F-125,F-42:with self-shielding effect)

Uncertainty given by the experiment is only that in nuclear heating rate. The uncertainties in the nuclear properties in SCM concerning insulator dose, copper displacement per atom (dpa) and fast

neutron fluence in winding pack are approximately regarded as that in nuclear heating rate of 20%, since the nuclear properties in SCM relating to nuclear heating rate, that is, insulator dose is a transformed value from nuclear heating rate in insulator, and copper dpa and fast neutron fluence are determined with above medium energy neutrons contributing to nuclear heating rate.

Uncertainties in the values in experimental analysis include uncertainties caused by calculation in the analysis, that is, those caused by number of spatial meshes, order of Legendre expansion, division number of angular space and number of energy groups. Considering these uncertainties in calculated values used in experimental analysis, $\varepsilon_i^{(Nucl+method)}$ for each i is obtained as in Table 1.

On the other hand, the uncertainties of ε_i^{Mesh}, ε_i^{NPl}, ε_i^{Sn} and ε_i^{Ng} can be predicted with numerical analyses performed by one and two dimensional transport codes, respectively ANISN[6] and DOT3.5[3]. The nuclear properties of nuclear heating rate, insulator dose, copper displacement per atom and fast neutron fluence in winding pack are normalized with those values in mesh width→0 as shown in Figs.3(a), 3(b), 3(c) and 3(d), respectively. The values in mesh width→0 were predicted from extrapolated one based on calculated values in three cases of the mesh widths of 5cm, 7cm and 10cm. In the same manner, the nuclear properties normalized with those values in Legendre expansion order for scattering angular distribution Pl →∞ can be obtained as shown in Figs.4(a), 4(d), 4(c) and 4(d), respectively. The nuclear properties normalized with those values in angular division numbers of Sn → ∞ can be estimated as shown in Figs. 5(a), 5(d), 5(c) and 5(d), respectively. The nuclear properties of nuclear heating rate, insulator dose and fast neutron fluence normalized with predicted values in energy group number of Ng →∞ can be obtained as shown in Figs. 6(a), 6(b) and 6(c), respectively.

In shielding design for ITER, we adopt the mesh width of 7cm, the order of Legendre expansion P5, division number in angular space of S16, and energy group number of neutron 42groups and gamma-ray 21 groups for neutron and gamma-ray transport calculation with two dimensional RZ torus model. Considering these conditions in the reference shielding design for SCM in ITER, the uncertainties of ε_i^{Mesh}, ε_i^{NPl}, ε_i^{Sn} and ε_i^{Ng} can be estimated from these figures based on eq.(3) as shown in Table 1.

Table 1. Categorized uncertainties (%) for nuclear properties of superconductive magnets in shielding design margin case of 80%SS + 20%water shield.

	Nuclear heating rate	Insulator dose	Copper dpa	Fast neutron fluence
$\varepsilon^{nucl+Method}$	23	23	23	21
ε^{Mesh}	1	3	14	12
ε^{NPl}	0	0	0	1
ε^{Sn}	0	0	0	0
ε^{Ng}	3	5	3	0
total	23	24	27	24

2.3 correction factor evaluation

The correction factors of f_{ik} having considerable influences upon nuclear properties of nuclear heating rate, insulator dose, copper displacement per atom and fast neutron fluence in winding pack of SCM with radiation shielding are those due to gap streaming, void effect and inhomogeneity effect in a blanket. The typical gap exists between blanket modules and its width is considered 2cm and its depth 50cm. This gap enhances the nuclear properties of SCM by several ten per cent. The correction factor due to the gap is estimated as shown in Table 2. The typical voids in shield is for supporting

Table 2. Estimated correction factors for nuclear properties of superconductive magnets in shielding design margin in the case of 80%SS + 20%water shield.

	Nuclear heating rate	Insulator dose	Copper dpa	Fast neutron fluence
gap streaming*	1.31	1.20	1.18	---
void effect**	1.02	---	---	---
anisotropy	1.06	1.05	1.02	1.03

* Gap of 2cm in width and 50cm in depth
** One void of 7cm in diameter and 5cm in length

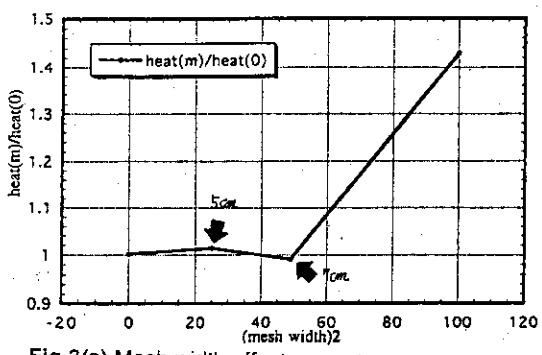

Fig.3(a) Mesh width effect on nuclear heating rate in winding pack of superconductive magnet with 80%SS+20%H2O shield in ITER.

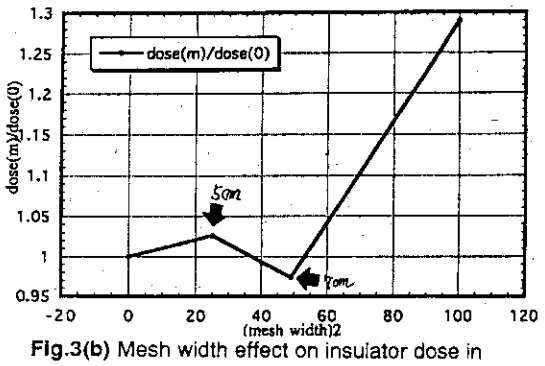

Fig.3(b) Mesh width effect on insulator dose in winding pack of superconductive magnet with 80%SS+20%H2O shield in ITER.

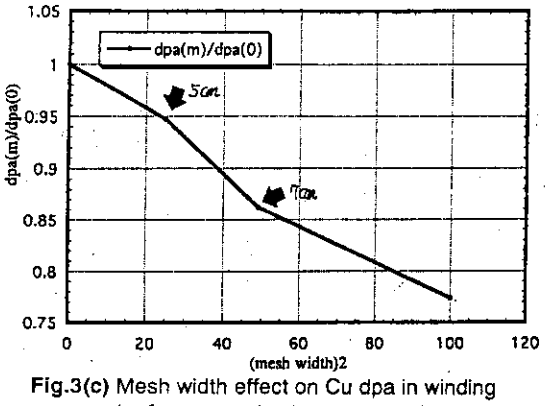

Fig.3(c) Mesh width effect on Cu dpa in winding pack of superconductive magnet with 80%SS + 20%H2O shield in ITER.

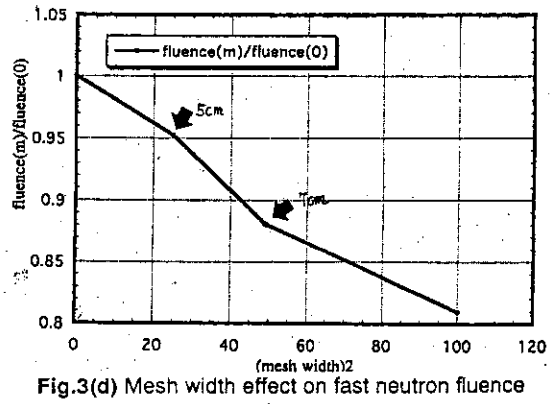

Fig.3(d) Mesh width effect on fast neutron fluence in winding pack of superconductive magnet with 80%SS+20%H2O shield in ITER.

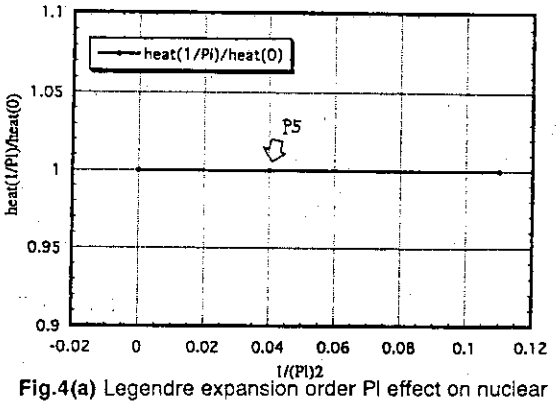

Fig.4(a) Legendre expansion order PI effect on nuclear heating rate in winding pack of superconductive magnet with 80%SS+20%H2O shield in ITER.

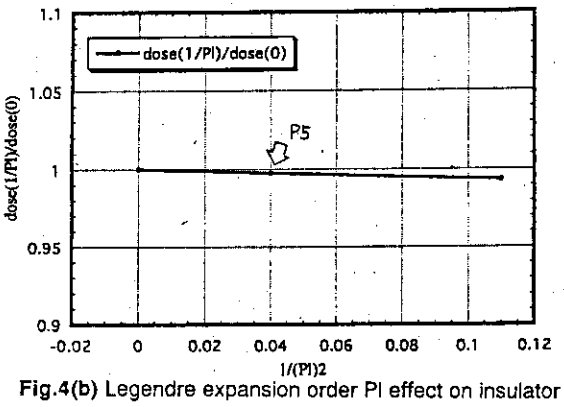

Fig.4(b) Legendre expansion order PI effect on insulator dose in winding pack of superconductive magnet with 80%SS+20%H2O shield in ITER.

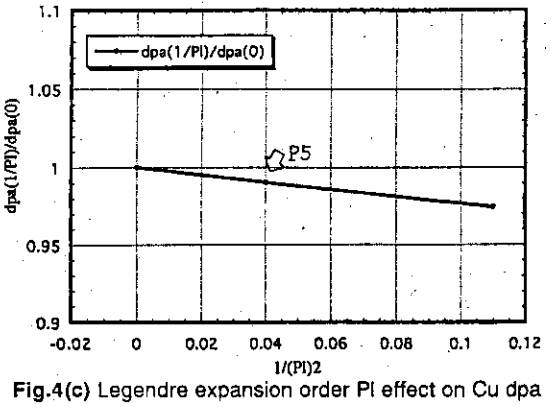

Fig.4(c) Legendre expansion order PI effect on Cu dpa in winding pack of superconductive magnet with 80%SS + 20%H2O shield in ITER.

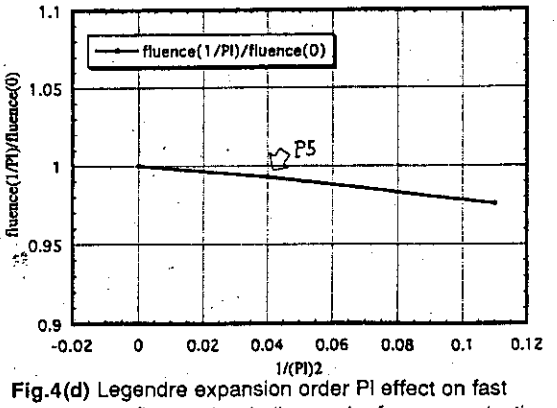

Fig.4(d) Legendre expansion order PI effect on fast neutron fluence in winding pack of superconductive magnet with 80%SS+20%H2O shield in ITER.

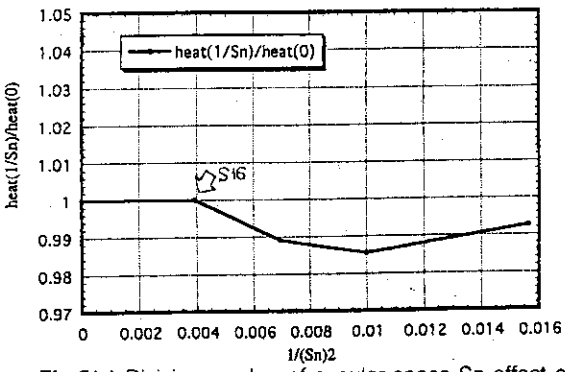

Fig.5(a) Division number of angular space Sn effect on nuclear heating rate in winding pack of superconductive magnet with 80%SS+20%H2O shield in ITER.

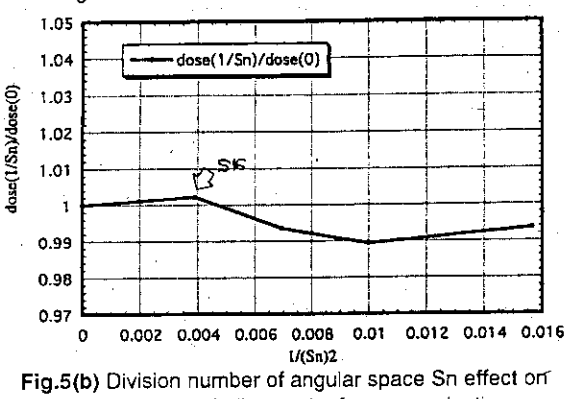

Fig.5(b) Division number of angular space Sn effect on insulator dose in winding pack of superconductive magnet with 80%SS+20%H2O shield in ITER.

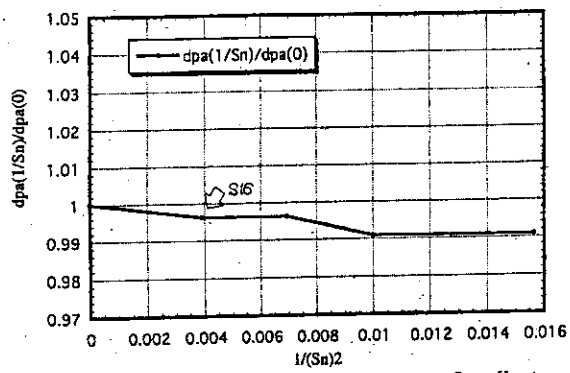

Fig.5(c) Division number of angular space Sn effect on Cu dpa in winding pack of superconductive magnet with 80%SS + 20%H2O shield in ITER.

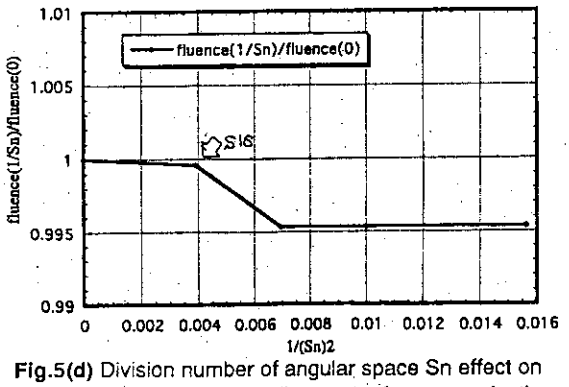

Fig.5(d) Division number of angular space Sn effect on fast neutron fluence in winding pack of superconductive magnet with 80%SS+20%H2O shield in ITER.

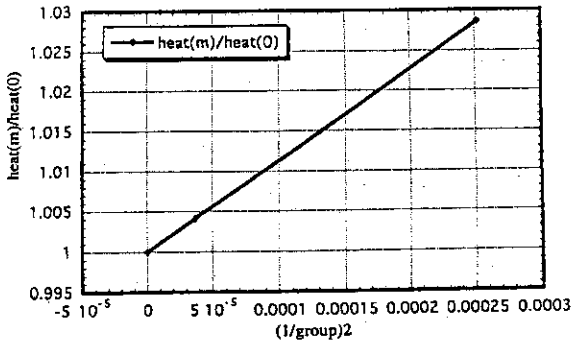

Fig.6(a) Number of energy group effect on nuclear heating rate in winding pack of superconductive magnet with 80%SS+20%H2O shield in ITER.

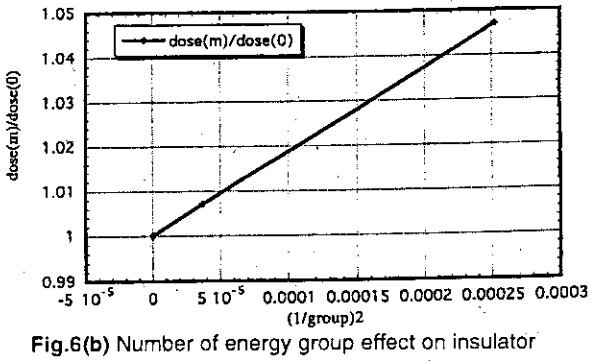

Fig.6(b) Number of energy group effect on insulator dose in winding pack of superconductive magnet with 80%SS+20%H2O shield in ITER.

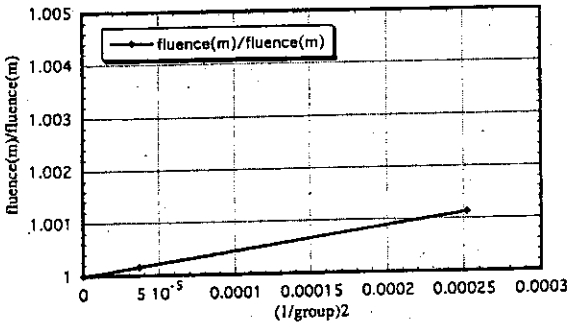

Fig.6(c) Number of energy group effect on fast neutron fluence in winding pack of superconductive magnet with 80%SS+20%H2O shield in ITER.

blanket modules, and its diameter and length are respectively 7cm and 5cm. The void increases the nuclear properties in SCM by a few per cent. The correction factor due to the void is calculated as shown in Table2. Considering inhomogeneity in the blanket enhances calculated nuclear properties in SCM with homogeneity shielding medium. The correction factor due to the inhomogeneity is predicted as shown in Table 2.

2.4 shielding design margin evaluation

The value of $\varepsilon_i^{(Nucl+method)}$ was obtained 23% as shown before in Table 1. The uncertainties of ε_i^{Mesh} were 1%, 3%, 14% and 12% for the nuclear properties of the nuclear heating rate, the insulator dose, the copper displacement per atom and the fast neutron fluence in winding pack of SCM, respectively, in the case of applying mesh width of 7cm so as to decreasing rate less than one-half in neutron fluxes. The uncertainties of ε_i^{NPI} and ε_i^{Sn} were 0 - 1 % for the nuclear properties and ε_i^{Ng} were 3%, 5%, 3% and 0% for the nuclear heating rate, the insulator dose, the copper displacement per atom and the fast neutron fluence, respectively, in computing by adopting neutron 42 groups and gamma-ray 21 groups. The correction factors of the gap streaming, the void effect and the inhomogeneity effect were respectively 1.3, 1.02 and 1.06 as shown previously in Table 2. Using these data, shielding design margins of the nuclear heating rate, the insulator dose, the copper dpa and the fast neutron fluence can be evaluated as 1.7, 1.59, 2.56 and 1.54, respectively, based on eq.(2).

3. Summary

The calculated nuclear property uncertainties caused by ambiguity categories of nuclear data and numerical method in transport codes, number of spatial meshes, order of Legendre expansion, division number of angular space and number of energy groups were estimated by experimental analysis of SS+H_2O bulk shielding experiment and numerical calculations. The investiganted nuclear properties are nuclear heating rate, insulator dose, copper dpa and fast neutron fluence in winding pack of superconductive magnets in ITER. The uncertainties caused by ambiguities in nuclear data and numerical method in transport codes were 23%, which are largest among these categories. The considerable correction factors due to gap streaming, void effect and inhomogeneity effect in a blanket were evaluated by numerical calculation. On the basis of these uncertainties and correction factors, we can obtain the shielding design margins of 1.7, 1.59, 1.56 and 1.54 for nuclear heating rate, insulator dose, copper dpa and fast neutron fluence in winding pack of superconductive magnets in ITER, respectively.

References

[1] ITER Technical Advisory Committee, "Executive Summary Project Management Plan for International Thermonuclear Experimental Reactor," The 4th Meeting of the Technical Advisory Committee, Garching Joint Work Site, (Nov. 1994).

[2] K. Maki, et al., C39 in Fall Meeting of the Atomic Energy Society of Japan.

[3] W. A. Rhoades and F. R. Mynatt, "The DOT-III Two Dimensional Discrete Ordinates Transport Code," ORNL-TN-4280, Oak Ridge National Laboratory (1973).

[4] C. Konno, et al., "Bulk Shielding Experiment on a Large SS316/Water Assembly Bombarded by D-T Neutrons Volume I: Experiment," Japan Atomic Energy Research Institute, JAERI-Research 95-017.

[5] F. Maekawa ,et al., "Bulk Shielding Experiment on a Large SS316/Water Assembly Bombarded by D-T Neutrons Volume II: Analysis," Japan Atomic Energy Research Institute, JAERI-Research 95-018.

[6] W. W. Engle, "A User's Manual for ANISN, A One Dimensional Discrete Ordinate Transport Code with Anisotropic Scattering," K1693, Union Carbide Corporation, Computing Technology Center (1967).

3.16 Process of PKA File for FENDL from JENDL Fusion File with Effective single Particle Emission Approximation

T. Fukahori, S. Chiba
Nuclear Data Center, JAERI, Tokai-mura, Naka-gun, Ibaraki-ken, 319-11 Japan
fukahori@cracker.tokai.jaeri.go.jp, chiba@cracker.tokai.jaeri.go.jp
and
M. Kawai
Nuclear Engineering Laboratory, Toshiba Co., 4-1 Ukishima-cho, Kawasaki-ku,Kawasaki, 210 Japan
kaw@rcg.nel.rdc.toshiba.co.jp

The code ESPERANT using an effective single particle emission approximation (ESPEA) was developed for nucleus except light mass elements as a processing method the of JENDL PKA/KERMA File from an evaluated nuclear data file. The code SCINFUL/DDX is used for light mass nuclides. As a trial task of ESPERANT usage, PKA file for the FENDL project in the energy range below 20 MeV was processed from the JENDL Fusion File. The processed PKA file was compared with results of Monte-Carlo calculation by MCEXCITON and calculated results from ENDF/B-IV. The results of three methods gave similar trends. It was concluded that the processing method with ESPEA was applicable to produce PKA File.

1. Introduction

In the Japanese Nuclear Data Committee, the PKA/KERMA file containing primary knock-on atom (PKA) spectra, KERMA factors and displacement per atom (DPA) cross sections in the energy range between 10^{-5} eV and 50 MeV is prepared from the evaluated nuclear data file, for radiation damage calculations used to such as the International Fusion Material Irradiation Facility (IFMIF)[1] which is an FMIT-type accelerator facility using Li(d,n) neutron source for irradiation tests of fusion reactor materials. **Table 1** shows physical quantities included in PKA/KERMA File as well as MF number defined in the ENDF-6 format. The processing code system, ESPERANT, was developed to calculate quantities of PKA, KERMA and DPA from evaluated nuclear data for medium and heavy elements by using an effective single particle emission approximation (ESPEA). For light elements, the PKA spectra are evaluated by the SCINFUL/DDX[2] and EXIFON[3] codes, simultaneously with other neutron cross sections. Finally, the PKA/KERMA file will contain the data for 78 isotope of 29 elements in the energy region up to 50 MeV.

As a trial task of ESPERANT, a file of PKA spectra for 69 nuclides from ^{19}F to ^{209}Bi in the energy region up to 20 MeV has been generated for fusion application from the JENDL Fusion File[4], in order to supply the PKA data to the FENDL-2 project[5]. The considered reactions to process were elastic (MT=2) and discrete inelastic (MT=51-90) scattering, continuum neutron emission reaction (MT=201) and charged particle emission reactions (MT=203-207). Damage energy spectra were also processed. The PKA spectra file was compared with the results of Monte Carlo calculation using MCEXCITON[6] and of Doran's processing[7] ENDF/B-IV[8], as data check and benchmark test. It was concluded that processed result of present work had an good accuracy for PKA spectra. In this report, the processing method, ESPEA, is explained and the results of comparison are discussed.

2. Effective Single Particle Emission Approximation (ESPEA)

It is often impossible to calculate PKA spectra exactly for reactions emitting two or more particles from evaluated nuclear data file which usually has no separated spectrum of each reaction step and channel. For these cases, the effective single particle emission approximation (ESPEA) has been developed to calculate spectra. In ESPEA, it is assumed that the particles are emitted from sequential reactions, which can not emit the particles simultaneously, and only the first emitted particle contributes to determination of energy and angular distributions of PKA. In this section, basic notations are indicated that superscripts of C and L mean center-of mass system

(CMS) and laboratory system (LAB), subscripts of p, t, 1 and 2 show incident particle, target nucleus, outgoing particle and residual nucleus, and symbols of E, m and θ are energy, mass and emitted angle ($\mu = \cos\theta$).

Double-differential cross section (DDX) of emitted particle in CMS, $DDX_1{}^C(E_p{}^L, E_1{}^C, \mu_1{}^C)$, is assumed to be given in evaluated nuclear data files. PKA spectrum in CMS, $DDX_2{}^C(E_P{}^L, E_2{}^C, \mu_2{}^C)$, is directly calculated by using energy and momentum conservation lows. That for particle emission reaction is written

$$DDX_2^C(E_p^L, E_2^C, \mu_2^C) = \frac{m_2}{m_1} DDX_1^c(E_p^L, E_1^C, \mu_1^C) ,$$
$$E_2^C = \frac{m_1}{m_2} E_1^C , \quad \mu_2^C = -\mu_1^C$$

and that for γ-ray emission reaction is

$$DDX_2^C(E_p^L, E_2^C, \mu_2^C) = \frac{m_2 c^2}{E_\gamma} DDX_\gamma(E_p^L, E_\gamma, \mu_\gamma) ,$$
$$E_2^C = \frac{E_\gamma^2}{2m_2c^2} , \quad \mu_2^C = -\mu_\gamma$$

where c is light speed. Since particle production cross sections (MT=201, 203-207 in ENDF-6 format, similar as following) are compiled by summing up individual production cross sections, which are given as a product of reaction cross section and particle multiplicities, exceeds the total reaction cross section, some re-normalization is necessary to treat as single particle emission. A normalization factor, R, for ESPEA is given as following.

$$R = \frac{\sigma_R}{\sum_x \int_{\varepsilon_x^{(min)}} d\varepsilon_x \int d\mu_x \sigma_x(E_p^L, \varepsilon_x, \mu_x)}$$

where σ_R and σ_x indicate cross sections of total reaction and each particle emission channel, and $\varepsilon_x{}^{(min)}$ is lower limit of energy for spectrum considered, which means the first emitted particles are distributed in higher energy region in the emitted spectra. It is assumed that no PKA is created by light particles emitted below this energy. The lower energy limit, $\varepsilon_x{}^{(min)}$, is determined to be satisfied the following equation of average energy for light particle emitted from the reaction x.

$$\int_{\varepsilon_x^{(min)}} \varepsilon_x f_x(\varepsilon_x) \, d\varepsilon_x = \left(\frac{m_t}{m_p+m_t} E_p^L + Q_x\right) / \left[1 + \left(\frac{m_{1x}}{m_{2x}}\right)^2\right]$$

$$\int_0^\infty f_x(\varepsilon_x) \, d\varepsilon_x = 1$$

where Q_x is Q-value of reaction x, and f_x the normalized $DDX_1{}^C$ of reaction x.

DDX of PKA in LAB, $DDX_2(E_P{}^L, E_2{}^L, \mu_2{}^L)$, is obtained after conversion from CMS to LAB, then the damage energy spectra, σ_D, can be given by

$$\sigma_D(E_p^L, E_2^L, \mu_2^L) = E_D(E_2^L) \cdot DDX_2(E_p^L, E_2^L, \mu_2^L)$$

where E_D is given by Lindhard-Robinson model[9] as following.

$$E_D(E_2^L) = \frac{E_2^L}{1+k\cdot g(\varepsilon)}, \quad E_2^L \ [eV],$$
$$k = 0.13372\, Z^{2/3} / A^{1/2},$$
$$g(\varepsilon) = 3.48008\, \varepsilon^{1/6} + 0.40244\, \varepsilon^{3/4} + \varepsilon,$$
$$\varepsilon = E_2^L / 86.931\, Z^{7/3}$$

3. PKA File for FENDL

The PKA File for FENDL-2 Project has been processed to supply the PKA data as a trial task of ESPERANT, generating from the JENDL Fusion File below 20 MeV. Nuclides included in JENDL Fusion File (69 isotopes) is processed and they are summarized in **Table 2**. Considered reactions are elastic (MT=2) and discrete inelastic scattering (MT=51-90), continuum neutron emission reaction (MT=201), and charged particle emission reactions (MT=203-207). Damage energy spectra has been also processed. In **Table 3** the energy meshes in PKA File for FENDL-2 Project is given. The processing accuracy was 5.0 %, including uncertainties of CMS-LAB conversion, averaging, PKA energy calculation, and so on.

The results of PKA spectra processed by ESPERANT from JENDL Fusion File were compared with those calculated with MCEXCITON and given by Doran. Since the PKA spectrum strongly depends on emitted light particle spectrum, the particle spectra in PKA file and calculated by MCEXCITON were also compared. For example, the particle and PKA spectra for ^{27}Al and ^{56}Fe at incident neutron energies of 10 and 20 MeV are shown in **Figs. 1-8**. The light particle spectra for neutron, proton and α-particle in **Figs. 1,3,5 and 7** indicate that both ESPERANT and MCEXCITON results are generally consistent with each other, although the nuclear model parameters used for the JENDL Fusion File evaluation are not entirely the same as those of the MCEXCITON calculation. The PKA spectra processed by ESPERANT are in good agreement with those calculated by MCEXCITON with considering the large secondary particle energy meshes (**Figs. 2,4,6 and 8**). In **Fig. 2**, the PKA spectra given by Doran at incident energies of 9 and 11 MeV is also indicated. Doran processed the PKA spectra from ENDF/B-IV with assuming evaluation spectra for charged particles, since ENDF/B-IV does not have charged particle spectrum. However, his processing gives similar result to present result. From above discussion, it is concluded that the approximation used in ESPERANT can well process PKA spectrum data from the evaluated nuclear data file.

4. SUMMARY

The present status of the JENDL PKA/KERMA File was reviewed, especially for FENDL usage (En < 20 MeV). The processing method, ESPEA, was explained and the results of comparison were discussed. It was confirmed by comparing with the results of Monte-Carlo code, MCEXCITON, calculation and of Doran's processing by using ENDF/B-IV, as data check and benchmark test that ESPEA was well worked for processing PKA spectra from the evaluated file.

Acknowledgements

The authors wish to thank the members of PKA Spectrum WG in Japanese Nuclear Data Committee for their fruitful discussion about the ESPEA and the ESPERANT code development. The authors would also like to give acknowledgements to Mr. Kazuaki Kosako for his helping to improvement of the ESPERANT code.

References

[1] Noda K.; "International Fusion Material Irradiation Facility (IFMIF) Program," *Proc. 1994 Symposium on Nuclear Data, Tokai, Ibaraki, Nov. 17-18, 1994, JAERI-Conf 95-008*, p.112 (1995).

[2] Kashimoto H., Watanabe Y., Koyama Y., Shinohara H. and Chiba S.; "Study of the ^{12}C Breakup Process and Carbon Kerma Factor," *Proc. 1992 Symposium on Nuclear Data, Tokai, Ibaraki, Nov. 26-27,*

1992, JAERI-M 93-046, p.287 (1993).

[3] Kalka H.; "Statistical Multistep Reaction Model for Nuclear Data", *Proc. Int. Conf. on Nuclear Data for Science and Technology, Julich, May 13-17, 1991*, p.897 (Springer-Verlag, Berlin, Heidelberg, 1992).

[4] Baosheng Y., Chiba S. and Fukahori T.; *J. Nucl. Sci. Technol.*, **29**, 677 (1992).

[5] e.g. for FENDL-1: Ganesan S. and McLaughlin P.K.; "FENDL/E: Evaluated Nuclear Data Library of Neutron Nuclear Interaction Cross-Sections and Photon Production Cross-Sections and Photon-Atom Interaction Cross-Sections for Fusion Applications," *IAEA-NDS-128 Rev.1* (1995).

[6] Kishida N. and Kadotani H.; "On the Validity of the Intranuclear-Cascade and Evaporation Model for High Energy Proton Induced Reactions," *Proc. Int. Conf. on Nuclear Data for Science and Technology, Mito, May 30 - June 3, 1988*, p.1209 (Saikon Publishing, Tokyo, 1988).

[7] Doran D.G. and Graves N.J.; "Displacement Cross Sections and PKA Spectra: Table and Applications," HEDL-TME 7670 (1976).

[8] (Ed.) Garber D.; "ENDF/B Summary Documentation," *BNL-17541*, 2nd Edition (1975).

[9] Lindhard J., et al.; *Kgl. Danke Vidensk Selsk. mat-fis. Medd.*, **33**, Np.10 (1963) and Robinson N.T.; *Proc. BNES Conf. on Nuclear Fission Reactors, Culham 1969*, p.346 (BNES, London, 1969).

Table 1 Physical Quantities Included in the PKA/KERMA File (En=10^{-5} eV - 50 MeV)

MF	quantities
3	Cross sections and KERMA factor
4	Angular distributions for discrete levels
6	Double-differential light particles and PKA cross sections
63	DPA cross sections
66	Damage energy spectra

Table 2 Nuclides Included in PKA File for FENDL-2 Project (En=10^{-5} eV - 20 MeV)

69 isotopes included in JENDL Fusion File is processed.
^{19}F, ^{27}Al, ^{28,29,30}Si, ^{40,42,43,44,46,48}Ca, ^{46,47,48,49,50}Ti, ^{51}V, ^{50,52,53,54}Cr,
^{55}Mn, ^{54,56,57,58}Fe, ^{59}Co, ^{58,60,61,62,64}Ni, ^{63,65}Cu, ^{75}As, ^{90,91,92,94,96}Zr,
^{93}Nb, ^{92,94,95,96,97,98,100}Mo, ^{121,123}Sb, ^{182,183,184,186}W,
^{112,114,115,116,117,118,119,120,122,124}Sn, ^{204,206,207,208}Pb, ^{209}Bi

Table 3 The Energy Meshes in PKA File for FENDL-2 Project

- Incident Energy Mesh [eV]: 37

1.00E-5,2.53E-2,5.00E-1,1.00E+0,2.00E+0,5.00E+0,1.00E+1,2.00E+1,5.00E+1,1.00E+2,2.00E+2,5.00E+2,
1.00E+3,2.00E+3,5.00E+3,1.00E+4,2.00E+4,5.00E+4,1.00E+5,2.00E+5,5.00E+5,1.00E+6,2.00E+6,
3.00E+6,4.00E+6,5.00E+6,6.00E+6,7.00E+6,8.00E+6,9.00E+6,1.00E+7,1.20E+7,1.40E+7,1.50E+7,
1.60E+7,1.80E+7,2.00E+7

- Outgoing Energy Mesh [eV]: 53

1.00E-5,2.53E-2,5.00E-1,1.00E+0,2.00E+0,5.00E+0,1.00E+1,2.00E+1,3.00E+1,4.00E+1,5.00E+1,
6.00E+1,7.00E+1,8.00E+1,9.00E+1,1.00E+2,2.00E+2,3.00E+2,4.00E+2,5.00E+2,6.00E+2,7.00E+2,
8.00E+2,9.00E+2,1.00E+3,2.00E+3,3.00E+3,5.00E+3,1.00E+4,2.00E+4,5.00E+4,1.00E+5,2.00E+5,5.00E+5,
1.00E+6,2.00E+6,3.00E+6,4.00E+6,5.00E+6,6.00E+6,7.00E+6,8.00E+6,9.00E+6,1.00E+7,1.10E+7,
1.20E+7,1.30E+7,1.40E+7,1.50E+7,1.60E+7,1.70E+7,1.80E+7,1.90E+7,2.00E+7

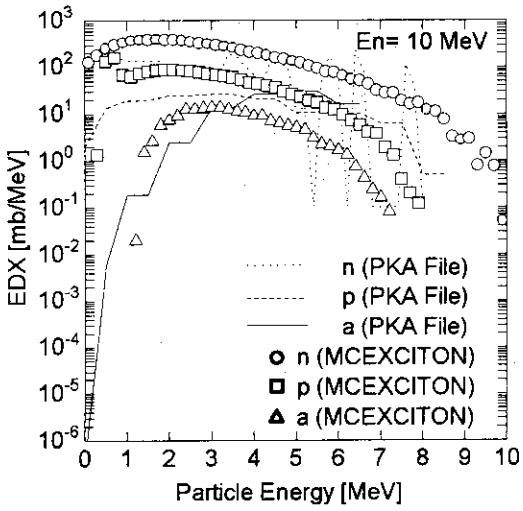

Fig. 1 Particle Spectra of PKA File and MCEXCITON for ^{27}Al at En=10 MeV

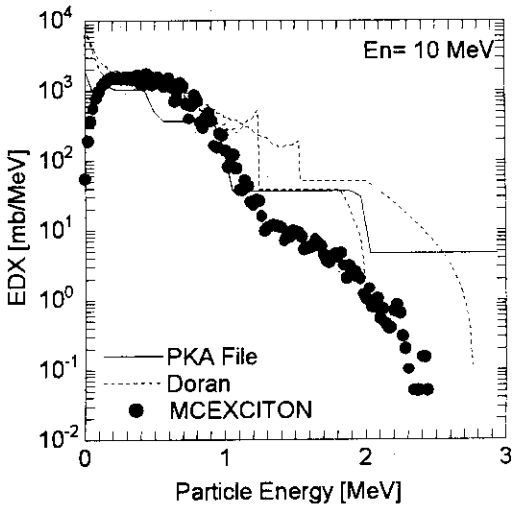

Fig. 2 PKA Spectrum for PKA File and MCEXCITON Compared with Doran's Calculation for ^{27}Al at En=10 MeV

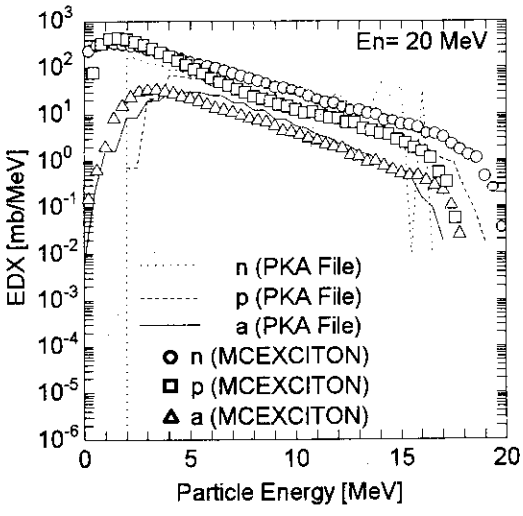

Fig. 3 Particle Spectra for PKA File and MCEXCITON for ^{27}Al at En=20 MeV

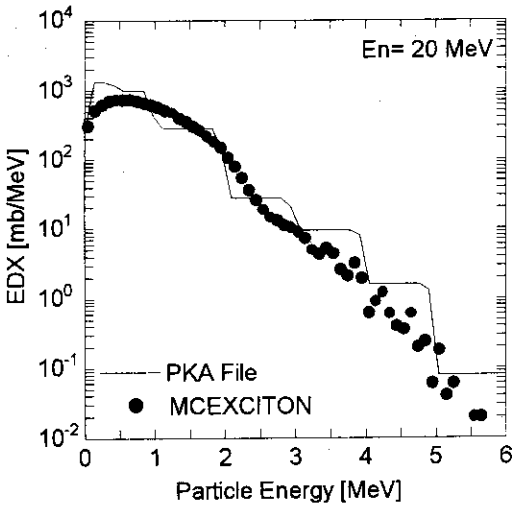

Fig. 4 PKA Spectrum for PKA File and MCEXCITON for ^{27}Al at En=20 MeV

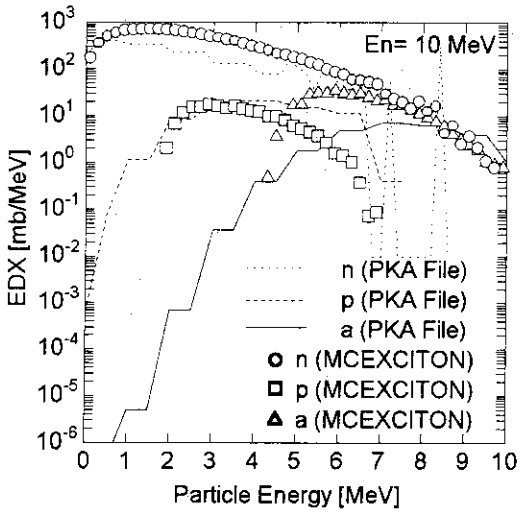

Fig. 5 Particle Spectra for PKA File and MCEXCITON for ^{56}Fe at En=10 MeV

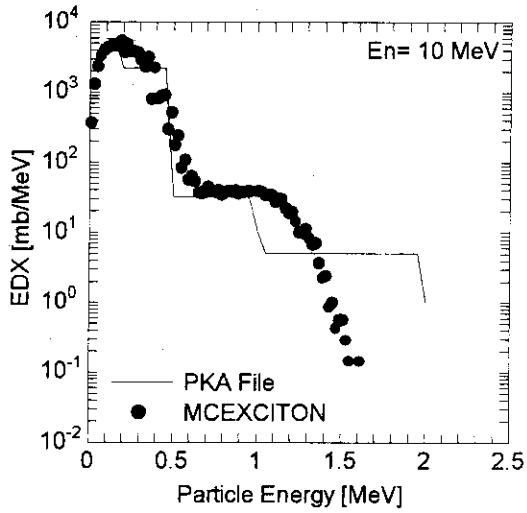

Fig. 6 PKA Spectrum for PKA File and MCEXCITON for ^{56}Fe at En=10 MeV

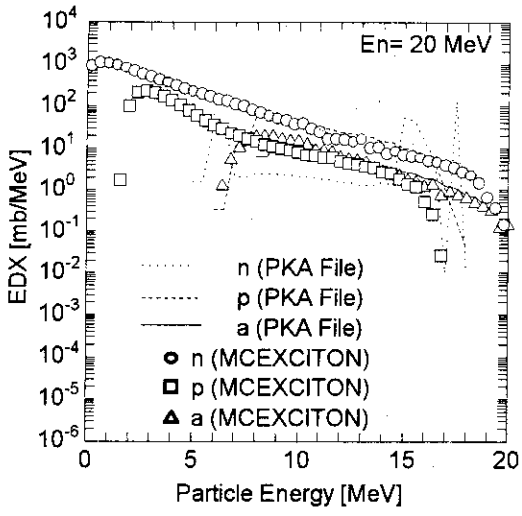

Fig. 7 Particle Spectra for PKA File and MCEXCITON for ^{56}Fe at En=20 MeV

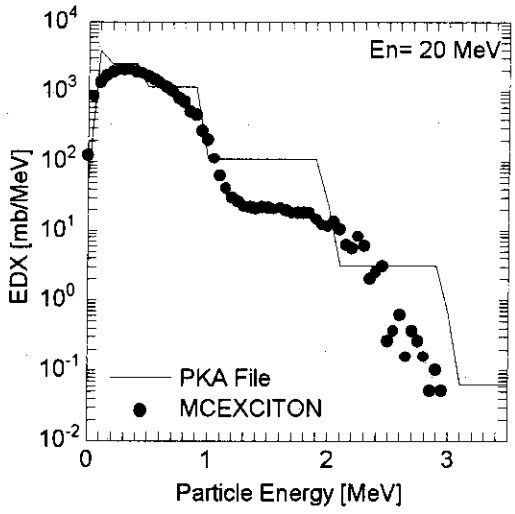

Fig. 8 PKA Spectrum for PKA File and MCEXCITON for ^{56}Fe at En=20 MeV

3.17 Damage Energy Cross Sections of Charged Particles from Light Nuclides Irradiated with High Energy Neutrons

T. Aruga, S. Chiba, M. Harada*, H. Kashimoto*,
Y. Watanabe* and M. Kawai**

Tokai Research Establishment, JAERI
Tokai-mura, Naka-gun, Ibaraki-ken 319-11
*Department of Energy Conversion Engineering,
Kyushu University, Kasuga, Fukuoka 816
**Toshiba Corporation, Ukishima-cho, Kawasaki-ku, Kawasaki 210

The energies deposited as damage energy in carbon are evaluated for each charged particles emitted from carbon irradiated with 20 and 50 MeV neutrons, using energy spectra of charged particles calculated based on a Monte Carlo technique using a code SCINFUL. The method developed is applicable to the damage energy estimation for breakup reactions of light nuclides irradiated with highly energetic neutrons.

1. Introduction

Elements of light nuclide such as carbon, beryllium, lithium and so on are considered to be major constituents of materials to be used in a future fusion reactor. Lack of efficient neutron sources for irradiation testing of fusion reactor materials forced recently again people to reconsider D+Li FMIT[1] type neutron source, this time, called IFMIF or International Fusion Material Irradiation Facility[2].However, D+Li neutron source is known to provide much broader energy spectrum of neutrons above ~15 MeV, and some 50% of the total neutron flux is shown to be distributed above this energy, so called a high energy tail. Displacement damages of the light nuclide materials due to these high energy neutrons can not be accurately evaluated by a conventional method as realized in well known codes such as DISCS[3], SPECTER[4] or NJOY[5], because of disregarding the internal bombarding effects of charged particles emitted from the breakup nuclear reactions for the light nuclides irradiated with highly energetic neutrons.

In this study the energies deposited as damage energy are evaluated for the each emitted particles as a function of energy, with carbon ^{12}C being taken as an example.

2. Calculational procedures

Energy spectra of charged particles emitted from ^{12}C at the incident neutrons of energies with 20 and 50 MeV have been calculated based on a Monte Carlo technique using a code SCINFUL[6] revised for this purpose by Watanabe et al.[7]. Two energies of 20 and 50 MeV are selected for the present preliminary study aiming at elucidating the significance of internal bombarding effects due to emitted charged particles on the displacement damage.

Kinds of charged particles predicted to be emitted are summarized in Table 1 and examples of emitted charged particle energy spectra are shown in Fig.1(a)-

(d), for ^{12}C irradiated with neutrons of 20 and 50 MeV, respectively.

Using these energy spectra, the damage energy cross sections $\sigma_{DAM}(E_n)$ for 20 and 50 MeV neutron irradiation to carbon are calculated in the following way:

$$\sigma_{DAM}(En)=\sum_{i\in all}\sigma^{i}_{DAM}(En)=\sum_{i\in all}\int_{E_{min}}^{E_{max}}\frac{d\sigma^{i}(E_n,E_p)}{dE_p}D^{i}(E_p)dE_p \quad .....(1),$$

where $d\sigma^{i}(E_n,E_p)/dE_p$ is an energy spectra of i-type charged particle emitted from carbon at the incident neutron energy of E_n, which are shown in Fig. 1 in mb/MeV, $D^{i}(E_p)$ is a damage energy of the i-type charged particle emitted with an energy of E_p. $D^{i}(E_p)$ can be calculated approximately,

$$D^{i}(Ep)=\int_{Ed}^{Tmax(Ep)}dT\int_{0}^{Ep}dE'_p\left(-\frac{dE'_p}{dx}\right)^{-1}T\eta(T)\frac{d\sigma(E'_p,T)}{dT} \quad .....(2),$$

where T is the energy transferred to the knocked-on carbon atom from the charged particle with an energy of E_p' which is emitted and starts moving with an energy of E_p(of i-type; in the right hand of eq.(2) the suffix i is dropped), $\eta(T)$ is the damage efficiency giving the fraction of nuclear energy loss to the total (nuclear + electronic) energy loss for the carbon atom knocked-on with T by moving charged particle and is given by LSS theory[8,9] as $(1+kg(\varepsilon(T))^{-1}$, $d\sigma(E_p',T)/dT$ is the nuclear collision cross section for charged particle of E_p' producing carbon knocked-on atom of T, an integration of $(dE_p'/dx)^{-1}$ over charged particle energy accounts for the distribution of charged particle energy over its range starting out with energy E_p, and finally E_d is the displacement threshold energy. In the approximate eq.(2), the effect of straggling of charged particle during the slowing down is not taken into account. For the purpose of accurately evaluating the energy dissipated by the emitted charged particles moving in the material and by the recoiled atoms through the nuclear collision, a code E-DEP-1-ext[10] was applied to the present study. The code has been extended from a E-DEP-1 code[11], well-known to the calculation of damage energy depth profile of ion-irradiated samples.

In the code the damage energy is calculated as, with suffix of i-type being dropped,

$$D(E_p)=\int_{0}^{\infty}S_D(x)dx \quad .....(3),$$

$$S_D(x)=\int_{x}^{\infty}S_I(E_p[x'-x])f(x')dx \quad .....(4),$$

where $S_I(x)=S_I[E_p(x'-x)]$ is the damage energy as an implicit function of particle's residual range $x'-x$, where x is the projected range along the particle's starting direction, and the range distribution is assumed to be the Gaussian $f(x')$

around the average projected range **R** with the straggling ΔR. $S_l[E_p(x'-x)]$ and $f(x')$ are given as

$$S_l(E_p)=\int_{E_d}^{T_{max}} \frac{T}{(1+kg(\varepsilon(T)))} \frac{d\sigma(E_p,T)}{dT} dT \quad .....(5),$$

$$f(x)=\frac{1}{\Delta R\sqrt{2\pi}} exp(-\frac{(x-R)^2}{2(\Delta R)^2}) \quad .....(6).$$

3. Results and discussion

The damage energies,$D(E_p)$,deposited in carbon by several emitted charged particles, as calculated by the eq. (3), are shown in Fig.2 as a function of emitted particle energy up to 40 MeV, for p to ^{8}Li and for ^{9}Be to ^{12}C, in (a) and (b) of the figure, respectively. It is seen from the figure that the damage energy of the most light particle, p, for the emitted energy of 10 MeV, for example, is only 3×10^{-3}MeV or 0.03% of the emission energy. For heavier particle, for example, ^{12}B emitted with 0.1MeV, on the other hand, the corresponding damage energy amounts to 15% of the emitted energy: that is, 0.015 MeV is dissipated in nuclear collisions with carbon atoms during the slowing down, which can create the lattice defects through displacements of atoms from the lattice sites. The difference of energies between the emitted and the damage energy is dissipated in exciting and ionizing electrons, which will be finally transformed into heat in conducting materials, but will also create the lattice defects in insulating materials such as oxides.

Using $D^i(E_p)$ obtained above, and eq.(1), with $d\sigma^i(E_n,E_p)/dE_p$ several of which are shown above in Fig.1, the damage energy cross sections for 20- and 50-MeV neutron irradiation were evaluated for carbon and the results are summarized in Table 2. The total damage energy cross sections for 20 and 50 MeV neutrons are 30.5 and 21.5 MeV.mb, respectively, which are including the contributions from not only the emitted charged particles but also PKAs(primary knock-on atoms) produced by elastic and inelastic scattering. The averaged damage energy cross section for 13.7-14.9 MeV neutron group were calculated to be 35 MeV.mb, as calculated using a code previously developed[12] and usingJENDL3 (called JENDL3-T1,then). It is noted that with increasing the neutron energy up to 50 MeV from 14 MeV, the damage energy cross section tends to decrease, which is a marked contrast with a kerma factor or kinetic energy release in matter for carbon. The kerma for carbon continues to increase with enutron energies of these ranges.[13]. This difference will be attributable to the fact that, although both the number of kinds of the emitted particles and the emission energies increase for 50 MeV neutrons compared with those for 20 MeV neutrons, the charged particle emission reaction cross sections themselves $d\sigma^i(E_n,E_p)/dE_p$ decrease considerably. The decrease in the cross sections can be well compensated for the kerma factor due to the increase in the emitted particle energies. However, the increase in the emitted particle energies,especially for lighter particles such as p, d, t and α ,do not contribute to the increase of the damage energy, but are dissipated in electronic energy losses.

The damage energy cross sections due to the emitted charged particles only do not differ so much between 20 and 50 MeV neutron irradiations,namely 8.6 and 8.9

MeV.mb, respectively. The fractions to the total damage energy cross section for 50 MeV neutrons however is larger to be 41 % than that of 29 % for 20 MeV neutrons. The fraction for 13.7-14.9 MeV neutron group based on the calculational results cited above is 4.3%, which is only due to PKAs produced by α particle emissions. The fraction due to α particles is negligibly small to be 1×10^{-3} % of the total damage energy.

4. Summary

The damage energies have been calculated taking into a full account for the contribution from emitted charged particles slowing down in one-element material irradiated with highly energetic neutrons, taking carbon as an example. The damage energy due to charged particles occupies 29 % of the total damage energy for carbon at the incident neutron energy of 20 MeV and the fraction increases to 41 % for the neutron energy of 50 MeV. These higher fractions compared with that due to 14 MeV neutron irradiation suggests that energy spectra of atoms recoiled by these charged particles will have a larger fraction of lower energy part, and the damage produced by these recoiled atoms will result in simpler defects or more freely migrating defects.

References

[1] Opperman,E.K. : "Fusion Materials Irradiation Test Facility-Experimental Capabilities and Test Matrix", HEDL-TME 81-45(1982).

[2] Journal of Fusion Energy Vol. 8, Nos. 3/4 (1989). Papers contented therein.

[3] Odette,G.D. and Doiron, D. R.: J. Nucl. Technol., **29**, 346 (1976).

[4] Greenwood, L. R. and Smither, R. K.: "SPECTER,Neutron Damage Calculations for Materials Irradiations", ANL/FPP/TM-197 (1985).

[5] MacFarlane, R. E., Muir, D. W. and Borcourt, R. M. :"The NJOY Nuclear Data Processing System, Vol II, LA-9303-M (1982).

[6] Dickens, J. K.:"SCINFUL, A Monte Carlo Based Computer Program to Determine a Scintillator Full Energy Response to Neutron Detection for En Between 0.1 and 80 MeV: Program Development and Comparisons of Program Predictions with Experimental Data", ORNL-6462,-6463 (1988).

[7] Kashimoto, H., Koyama, Y., Shinohara, H., Watanabe, Y. and Chiba, S.:"Study of the ^{12}C Breakup Process and Carbon Kerma Factor", JAERI-M 93-046, p. 287 (1993).

[8] Lindhard, J., Nielsen, V., Scharff, M. and Thomsen, P. V.:"Integral Equations Governing Radiation Effects",Kg. Dan. Mat. Fys. Medd. Dan. Vid. Selsk. Vol 33, No 10 (1963).

[9] Robinson, M. T.:"The Energy Dependence of Neutron Irradiation Damage in Solids",Proc. B.N.E.S. Nuclear Fusion Reactor Conf. at Culham Laboratory, Sept.,1969, p.364.

[10] Aruga, T., Nakata, K. and Takamura, S.: Nucl. Instr. and Meth. **B33**, 748 (1988).

[11] Manning, I. and Mueller, G. P.: Comp. Phys. Commun., **7**, 85 (1974).

[12] Aruga, T. and Shiraishi, K.:"Comparisons of Neutron Radiation Damage Parameters Obtained Using JENDL-3T and ENDF/B-IV Libraries", JAERI-M 89-026,p.342(1989).

[13] Harada, M. et al., these proceedings.

Table 1

Charged Particles Predicted to Be Emitted from Nuclear Reactions Occuring in Carbon, 12C, with incident neutrons

20 MeV	n + 12C :	50MeV
p		p , ^{9}Be
d		d , ^{10}Be
α		t , ^{11}Be
^{7}Li		^{3}He , ^{10}B
^{9}Be		α , ^{11}B
^{11}B		^{6}Li , ^{12}B
^{12}B		^{7}Li , ^{12}C
^{12}C		^{8}Li ,
(n)		(n)
Total 8 kinds + (n)		Total 15 kinds+(n)

Table 2 Summary of Results

	20 MeV	50MeV
Total damage energy (MeV · mb): $\sigma_{DAM}(En)=\sum_{i\in all}\sigma^{i}_{DAM}(En)=\sum_{i\in all}\int_{E_{min}}^{E_{max}}\frac{d\sigma^{i}(E_n,E_p)}{dE_p}D^{i}(E_p)dE_p$	30.5	21.5
Damage energy due to chaged particles (except for contribution from ^{12}C PKA produced by (n,n), (n,n')) (MeV · mb):	8.6	8.9
The fraction to the total (%):	29	41

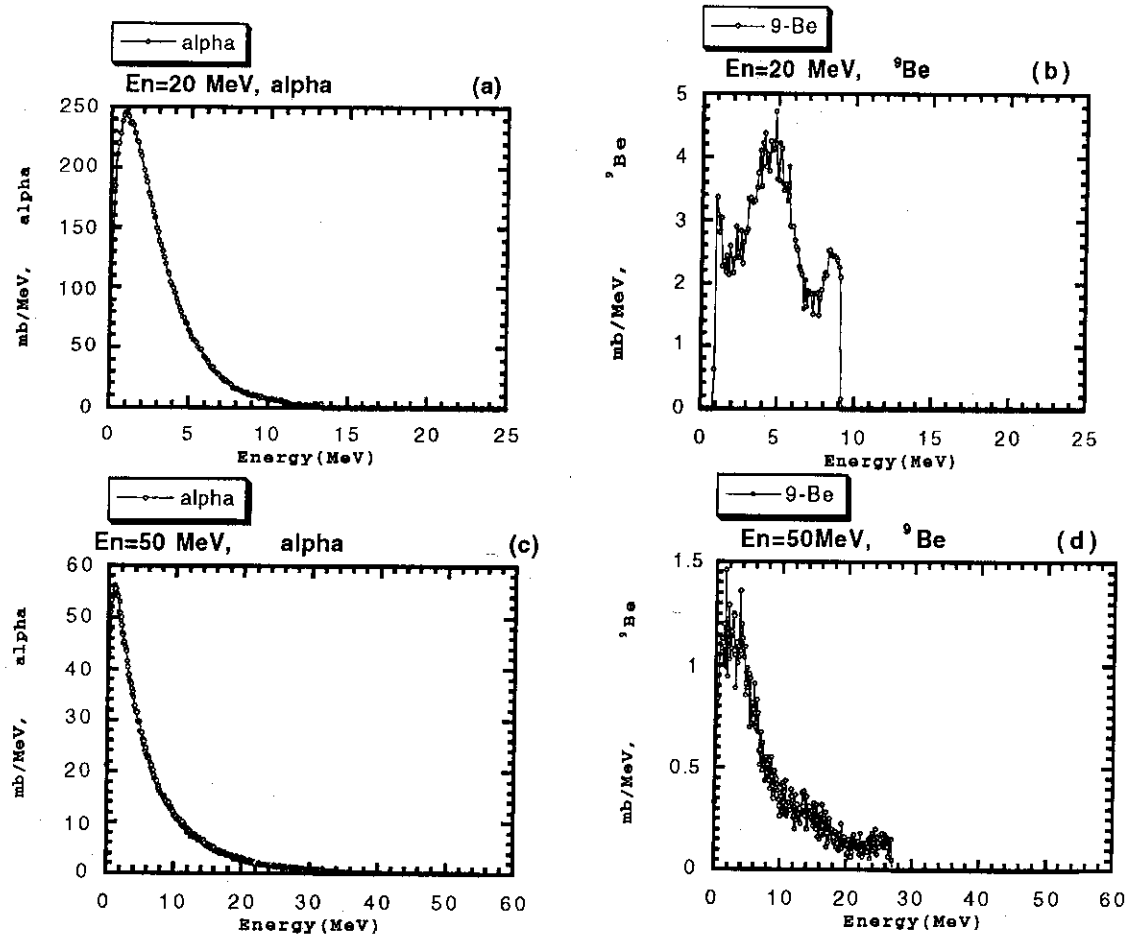

Fig. 1 Examples of $d\sigma^{i}(E_n,E_p)/dE_p$ calculated by revised SCINFUL code for ^{12}C irradiated with neutrons of 20 MeV(a,b) and 50 MeV(c, d).

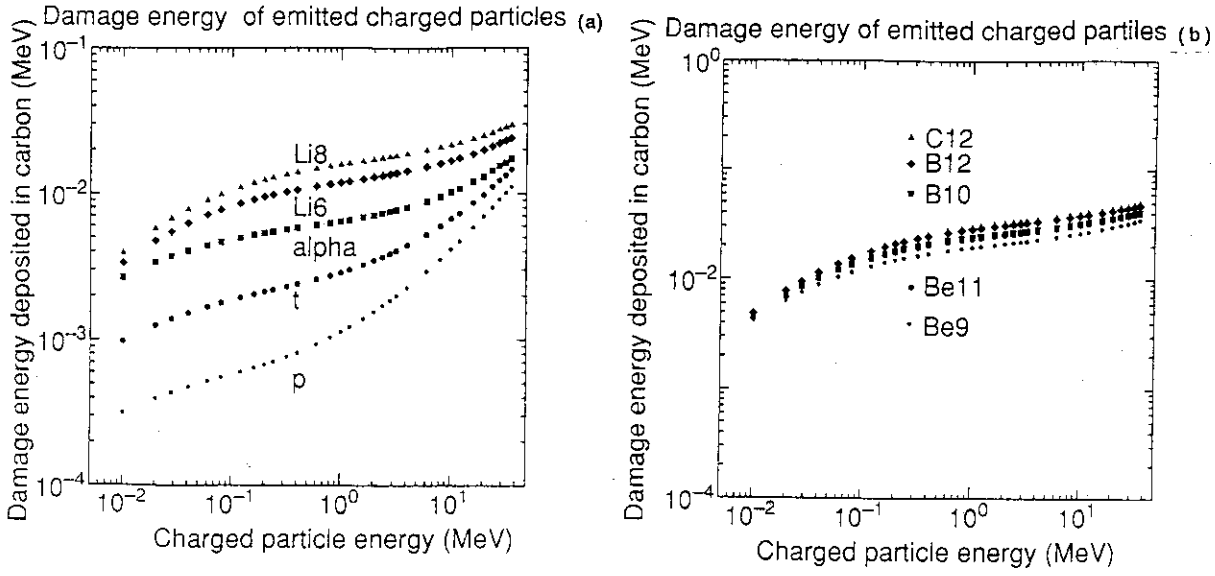

Fig. 2 Damage energies calculated by E-DEP-1.ext as a function of emitted charged particle energy in carbon: (a) p to ^{8}Li and (b) ^{9}Be to ^{12}C.

3. 18 Measurements of Neutron Spectra from Stopping-Length Targets Bombarded with Light Ions

Shin-ichiro MEIGO[1], Hiroshi TAKADA, Hiroshi NAKASHIMA,Toshinobu SASA,
Susumu TANAKA*, Kazuo SHIN** and Shinji ONO**
Tokai Establishment, Japan Atomic Energy Research Institute, Tokai-mura 319-11
*Takasaki Establishment, Japan Atomic Energy Research Institute, Takasaki 370-12
**Department of Nuclear Engineering, Kyoto University, Sakyo-ku, Kyoto 606-01
[1]Email: meigo@linac.tokai.jaeri.go.jp

Using a Time-of-Flight technique, we have measured neutron spectra from stopping-length targets of C, Fe, Zr and Au bombarded with 68-MeV protons and 100-MeV α-particles. The measured spectra were used to validate the results calculated by the cascade model NMTC/JAERI plus MCNP-4A and the Quantum Molecular Dynamics (QMD) plus Statistical Decay Model (SDM). It was found that the results of the cascade model calculation reproduced the experimental data quite well when several modifications were applied. The results of QMD plus SDM codes reasonably agreed with the experimental data.

1. Introduction

Applications of high energy light ion accelerators are rapidly growing in many fields such as the accelerator-based actinide transmutation system, the intensive neutron source based on the spallation reaction and a the cancer therapy. In the shielding and neutronics design of these facilities, detailed knowledge is crucially important on the neutron spectra produced by primary beam and their subsequent transport in bulk media. Historically, the cascade model such as NMTC/JAERI[1] has been employed as a tool to calculate the neutron spectra in such design studies. On the other hand, a code system based on the Quantum Molecular Dynamics (QMD) plus Statistical Decay Model (SDM) has been developed in JAERI[2] recently and were applied successfully to analyze the (p,xn) and (p,xp') reactions at intermediate energies [3,4]. These computational methods have been generally used to calculate the nuclear reactions in the energy region above approximately 100 MeV and, in the case of NMTC/JAERI, the subsequent transport of nucleons and mesons in bulk materials. However, validity of these models for lower energy region is not verified well. Furthermore, the QMD plus SDM approach has never been tested in a calculation for bulk media.

The purpose of this work is to measure the neutron spectra produced from stopping-length C, Fe, Zr and Au targets bombarded with 68-MeV protons of 100-MeV α-particles and validate the predictions by NMTC/JAERI and QMD models for such low-energy region. This paper describes the experimental procedure, data reduction method, computation methods and results of the comparison of measured and calculated values in the following sections.

2. Experimental Procedure

The experimental arrangement is shown in Fig. 1. The measurements were carried out at the HB-1 beam course at the AVF-cyclotron in the TIARA facility of JAERI. By a chopper and buncher of the accelerator, incident ions were pulsed to a width of 2.5 ns in FWHM. A carbon and gold target were irradiated by 68-MeV protons and a carbon, iron, zirconium and gold target were irradiated by 100-MeV alpha particles. The sizes of the targets are listed in table 1. Each target was thicker than the range of incident particles, but self-absorption of produced neutrons was negligibly small. The number of injected particles was counted with a digital current integrator (ORTEC 439) connected to the target that was surrounded by a -500V suppressor grid to repel secondary electrons. Neutrons were measured by the TOF method with an organic scintillator (BC501A) of 12.7 cm in diameter and 12.7 cm in length at emission angles of 0°, 15°, 30°, 45°, 60°, 90° and 120°. The flight path was 5.0 m for the measurements between 0° and 45°, and 2.5 m for those between 60° and 120°.

The BC501A scintillator was optically coupled to a photo-multiplier tube (HAMAMATU R4144). Three signals, pulse height, pulse shape and TOF were accumulated by a three-parameter data acquisition system (CANBERRA GENIE system). The pulse height was calibrated by the standard sources of ^{137}Cs ($E\gamma$ = 0.66 MeV), ^{60}Co ($E\gamma$ = 1.17 ,1.33 MeV) and Am-Be ($E\gamma$ = 4.43 MeV). In order to discriminate between neutron

and gamma-rays pulses, a pulse shape discriminator (CANBERRA 2160) having a dynamic-range over 500:1 was employed.

The contribution of the background neutrons caused by the room-scattering was measured at every angle placing a rectangular iron block with the size of 20 × 20 × 40 cm^3 between the target and detector. By subtracting the contribution of background neutrons from the foreground spectra measured without iron block, we obtained the net neutron spectrum produced from the target.

3. Data Reduction

The neutron TOF spectra were obtained by an off-line discrimination between the neutron and gamma pulses. By the following equation, the neutron energy spectrum was transformed from TOF spectrum,

$$\frac{d^2n}{dEd\Omega} = \frac{dn}{dt} \bullet \frac{dt}{dE} \bullet (Np\ \varepsilon\ \Delta\Omega)^{-1} \quad (1),$$

where, *dn/dt* is the neutron TOF spectrum, *Np* the number of incident particles, ε detection efficiency and ΔΩ the solid angle sustained by the detector to the center of the target.

The detector bias was set at half height of ^{137}Cs Compton edge (0.497 MeVee). This bias enabled us to obtain the neutron spectra above 2.6 MeV. The detection efficiency for this bias was calculated with SCINFUL[5] which included modified deuteron light output[6] and the angular distribution of H(n,n) reaction cross-section[7].

4. Calculation

In this study, the neutron spectrum was calculated by the two code systems; NMTC/JAERI plus MCNP-4A, and QMD plus SDM.

4.1 NMTC/JAERI plus MCNP-4A code system

NMTC/JAERI[1] calculated the nuclear reactions and the particle transport above 20 MeV. MCNP-4A[8] calculated the neutron transport below 20 MeV using a continuous energy cross section library FSXLIB-J3R2[9] processed from the nuclear data file JENDL-3.2[10]. In the NMTC/JAERI calculation, the following modifications have been carried out;

(1) In the transport calculation part, the systematics of Pearlstein[11] was implemented to estimate the total, elastic and non-elastic nucleon-nucleus cross sections.
(2) In the statistical decay calculation of nuclear reaction, the level density parameter derived by Baba[12] was also employed.
(3) In the nuclear reaction calculation part, the in-medium effects were taken into account by using ISOBAR code. The in-medium nucleon-nucleon cross sections (NNCS) were employed instead of the free ones. The in-medium NNCS was parametrized similarly to those of Cugnon[13]. The process of the reflection and the refraction was taken into account.
(4) Q values of the reaction (p,n) and (n,n) were taken into account.

Because NMTC/JAERI can not deal with injected particles heavier than proton or neutron, NMTC/JAERI plus MCNP-4A code system was employed only for the calculation of the neutron spectra from the target bombarded with protons

4.2 QMD plus SDM code system

The neutron spectra were calculated based on the neutron production double differential cross sections (DDXs) that were obtained by the Quantum Mechanics Dynamics (QMD) theory[2] plus the statistical decay model (SDM)[2]. The neutron spectrum from the dynamical process was calculated by the QMD and the contribution from the statistical process was obtained by the SDM. The switching time from QMD to SDM was decided 5×10^{-22} s (150 fm/c). The maximum impact parameter was decided to $1.4\times(A_i^{1/3}+A_t^{1/3})$ (fm), where A_i and A_t is mass number of the incident and target nucleus, respectively. The calculated energies for the incident protons are 10, 20, 30, 40, 50, 60 and 68 MeV and for the α particles are 10, 20, 40, 60, 80, 100 MeV.

The final neutron spectrum that has to be compared with the experimental data was calculated from the following equation using the DDXs as calculated by the QMD plus SDM,

$$\frac{d^2N}{d\Omega dE_n} = \int_0^{E_\alpha} n \frac{d\sigma}{d\Omega dE_n} \left|\frac{dE}{dx}\right|^{-1} \exp\left(-\int_E^{E_\alpha} \Sigma_{non}(E') \left|\frac{dE'}{dx}\right|^{-1} dE'\right) dE \quad (2),$$

where $d^2N/d\Omega/dE_n$ is double differential neutron yields, n an atomic density of the target material (/cm^3), $d\sigma/d\Omega/dE_n$ (mb/sr/MeV) the neutron production DDX, E_α the incident energy of particle, dE/dx (MeV/cm) stopping power[14] and $\Sigma_{non}(E')$ the non-elastic cross section for incident particle with energy E'. The exponential term of the equation (2) shows the attenuation of the incident particles by the nuclear reaction in the target. The non-elastic cross section of the incident particles was calculated by the optical model using the code ECIS-79[15]. In the present calculation, the elastic scattering of the incident particles was ignored. Because the target is enough thinner than the minimum of the mean free path of the neutron, the effect of the neutron reaction with the target nucleus was ignored.

In table 2, the observed energy resolution and the uncertainty of neutron yield are summarized. In the neutron energies region below 50 MeV, the resolution and the uncertainty of the experimental data were smaller than 8% and 10 %, respectively. These values were much smaller than the ones obtained by the unfolding technique.

5. Results

The measured neutron spectra from C and Au targets irradiated by 67-MeV protons are compared in Figs 2 and 3, respectively, with the predictions of NMTC/JAERI plus MCNP-4A(solid histograms) and QMD plus SDM (dashed histograms) models.

Figure 2 shows that both the calculations reproduce the measured data fairy well. At the forward angles, the NMTC/JAERI plus MCNP-4A calculation is lower than the data, while the intermediate angles, the measured data lie in between the QMD plus SDM and NMTC/JAERI plus MCNP-4A results. For p+Au data, the NMTC/JAERI plus MCNP-4A calculation gives agreement definitely better than that of the QMD plus SDM calculation, the latter being too large compared with the measured data as shown in Fig. 3. The reason of having such overestimation in the neutron yield with the QMD plus SDM calculation is not yet clear. In Ref. [4] the double-differential (p,xp') and (p,xn) reactions of ^{27}Al were investigated with the QMD approach at 90 MeV: the calculated results agreed with the measured values very well. Nevertheless, applicability of the QMD approach may have to be investigated further in the energy region below 100 MeV.

Figures 4 and 5 exhibit the 100 MeV α+C and Au targets, respectively. The measured data and results calculated by the QMD plus SDM approach were shown, because the NMTC/JAERI cannot calculate the cross sections for such composite-particle incident reactions as explained previously. Given the very low incident energy (25 MeV/u), agreement of the measured and calculated results are rather good.

6. Summary

We have measured neutron spectra from stopping-length targets bombarded with 68-MeV protons and 100-MeV alpha particles. By using the time-of-flight technique, we obtained more precise spectra than ones obtained by the unfolding technique. The minimum energy of the measured neutron spectrum was 2.6 MeV.

It has been found through the comparison between the experimental and the calculated results of the target irradiated by protons that the calculated results of improved NMTC/JAERI plus MCNP-4A code system are superior than the QMD plus SDM one for heavy targets. For the incident energy region less than 100 MeV/u, it would suggest that a further improvement of the QMD theory is necessary.

References

[1] Y. Nakahara and T. Tsutui, JAERI-M 82-198 (1982), (in Japanese).
[2] K. Niita, et al., Phys. Rev., C 52, 2620 (1995).
[3] M. B. Chadwick et al., *ibid.*, C 52, 2000 (1995).
[4] S.Chiba, et al., Phys. Rev. C, in press.
[5] J. K. Dickens, ORNL-6462, Oak Ridge National Laboratory (1988).
[6] S. Meigo, et al., private communication.
[7] R. A. Arndt, et al., Phys. Rev., D 35, 128 (1987).
[8] J. F. Briesmeister, (Ed.), LA-12625 (1993).
[9] K. Kosako, F. Maekawa, Y. Oyama, Y. Uno and H. Maekawa, JAERI-Data/Code 94-020 (1994).
[10] K. Shibata, et al., JAERI-1319 (1990).
[11] S. Pearlstein, Astrophys. J., 346, 1049 (1989).
[12] H. Baba, Nucl. Phys., A159, 625 (1970).
[13] J. Cugnon, T. Mizutani and J. Vandermeulen, Nucl. Phys., A352, (1981).
[14] J. F. Janny, Atom. Data and Nucl. Data Tabl., 27, 147 (1982).

[15] J. Ravnal., Notes on ECIS79, unpublished.
[16] R. A. Cecil, et al., Phys. Rev., C 21, 2471, (1980).

Table 1. Size of the target and incident particle employed in the preset experiment.

Target	Incident Particle	Target Size (mm)
C	p	φ30 x 31
	α	φ30 x 3.2
Fe	α	φ20 x 1.3
Zr	α	φ30 x 1.8
Au	p	φ30 x 6
	α	φ30 x 2

Table 2. Uncertainties and energy resolution of the present experiment.

Neutron Energy (MeV)	Uncertainties (%)				Energy Resolution (%)
	Statistical Error	Detection Efficiency	Incident Proton	Neutron Yield	
4	0.3 ~ 1.7	3		4.3~4.6	1.5 ~ 2.3
5	0.4 ~ 1.3	3		4.3~4.6	1.7 ~ 2.8
10	0.5 ~ 1.3	3		4.3~4.4	2.2 ~ 3.8
15	0.6 ~ 1.4	3		4.3~4.5	2.6 ~ 4.7
20	0.5 ~ 1.5	10	3.0	10.5~10.6	2.9 ~ 5.4
30	0.5 ~ 1.6	10		10.5~10.6	3.5 ~ 6.6
50	1.3 ~ 20.0	10		10.5~22.6	4.5 ~ 8.5
67	7.4 ~ 33.8	10		12.8~35.3	5.3*

* For angle ≦ 45°

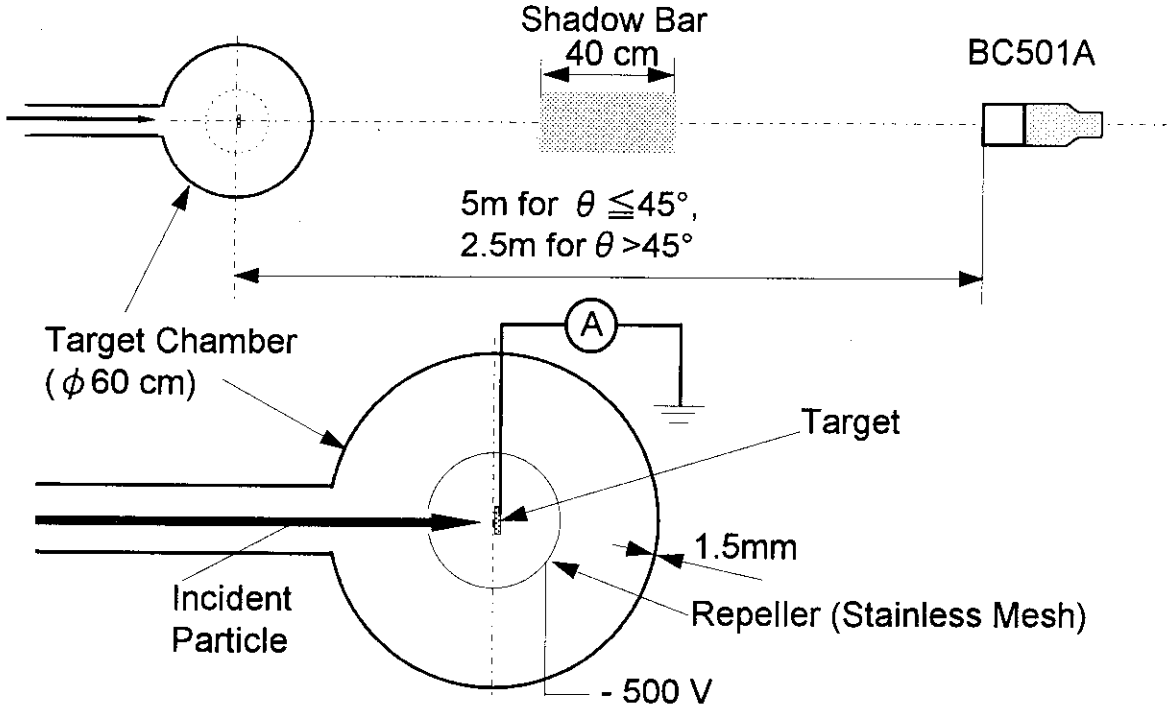

Fig. 1 Schematic view of the experimental setup (above; view of target and detector. below; view of target chamber) .

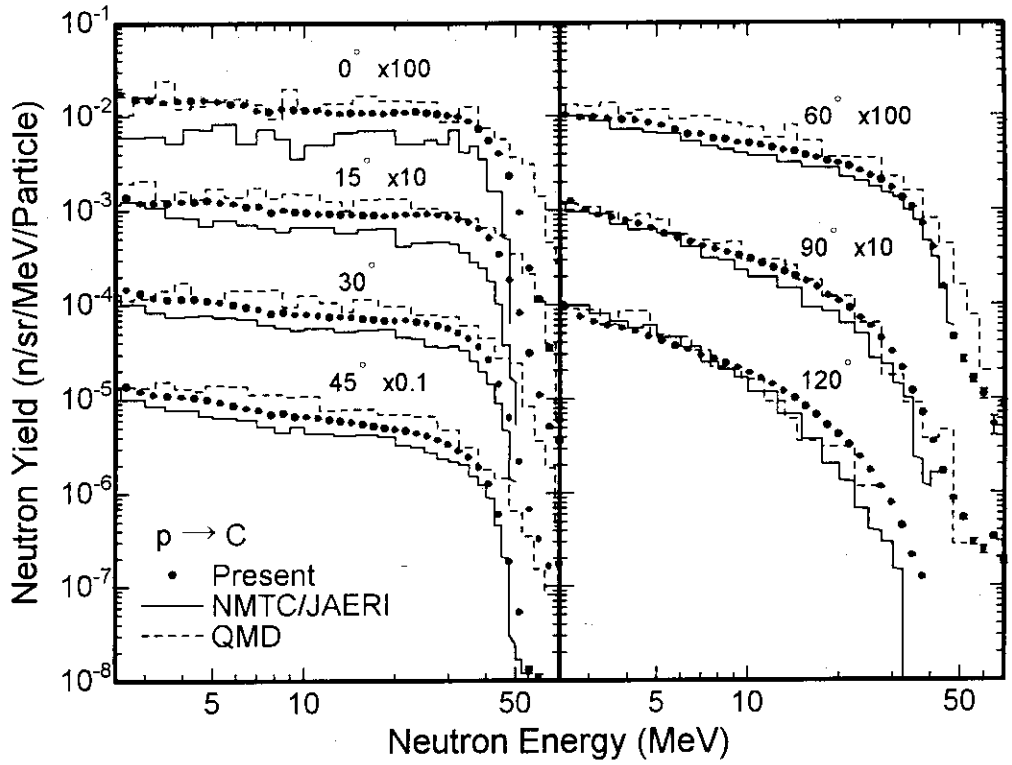

Fig. 2 Neutron energy spectra for 68 MeV proton incidence on stopping-length C target. The solid and the dashed lines stand for the results of calculation with NMTC/JAERI+MCNP-4A and QMD+SDM, respectively.

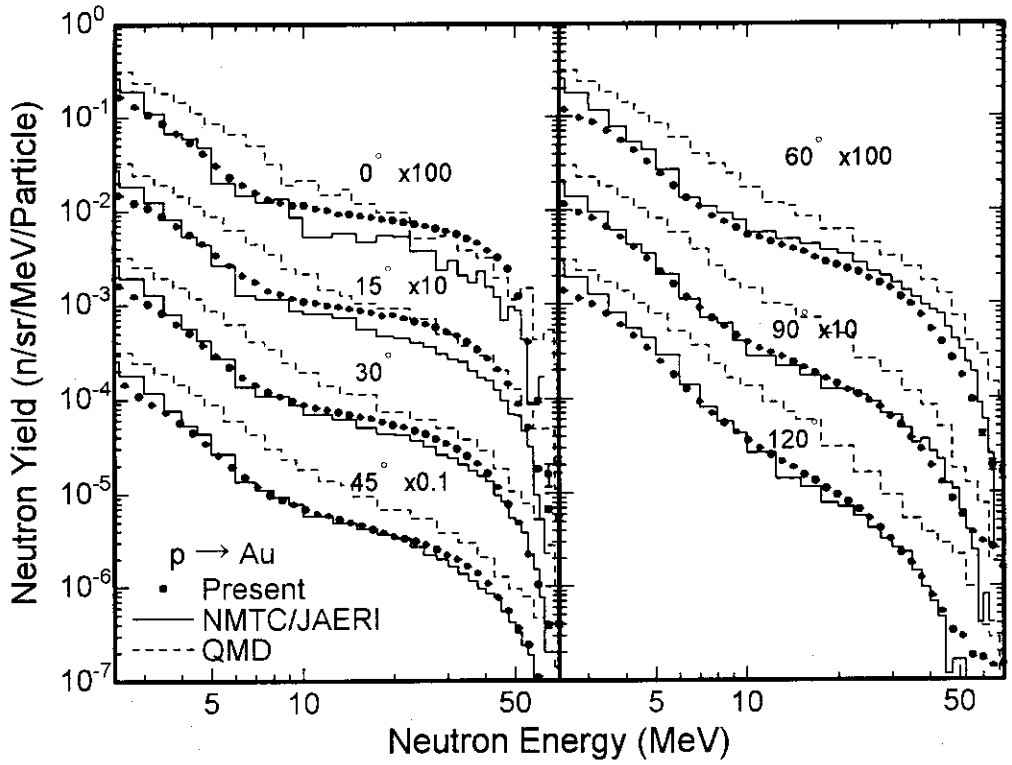

Fig. 3 Neutron energy spectra for 68 MeV proton incidence on stopping-length Au target. The solid and the dashed lines stand for the results of calculation with NMTC/JAERI+MCNP-4A and QMD+SDM, respectively.

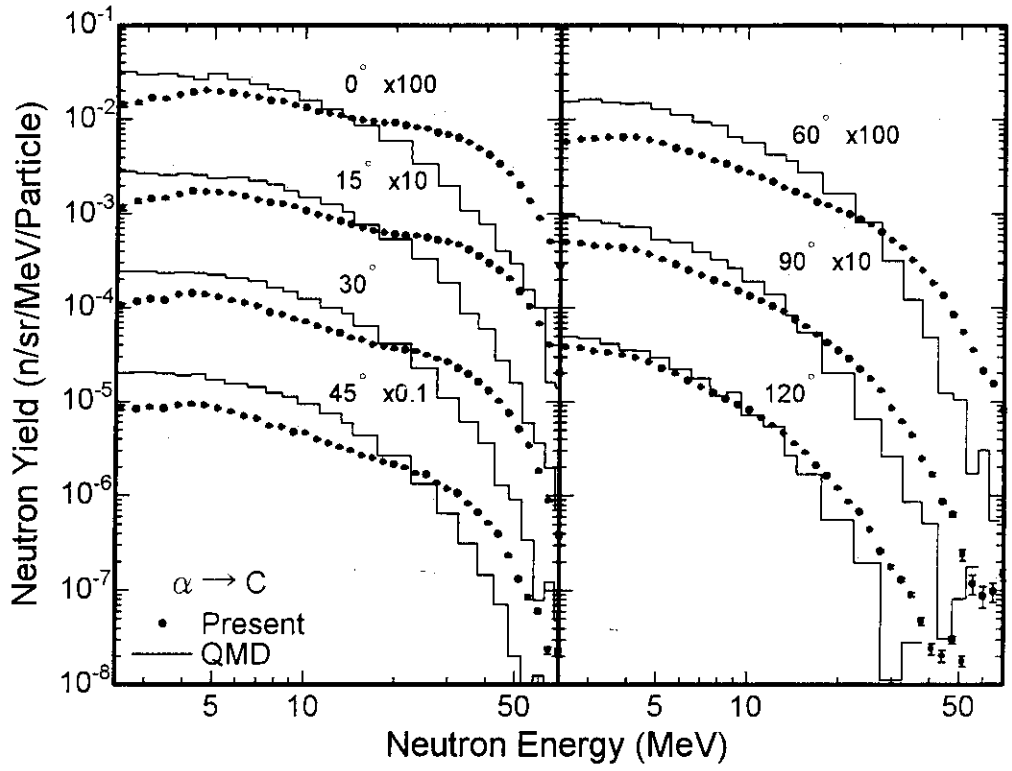

Fig. 4 Neutron energy spectra for 100 MeV alpha particle incidence on stopping-length C target. The solid lines stand for the results of calculation with QMD+SDM.

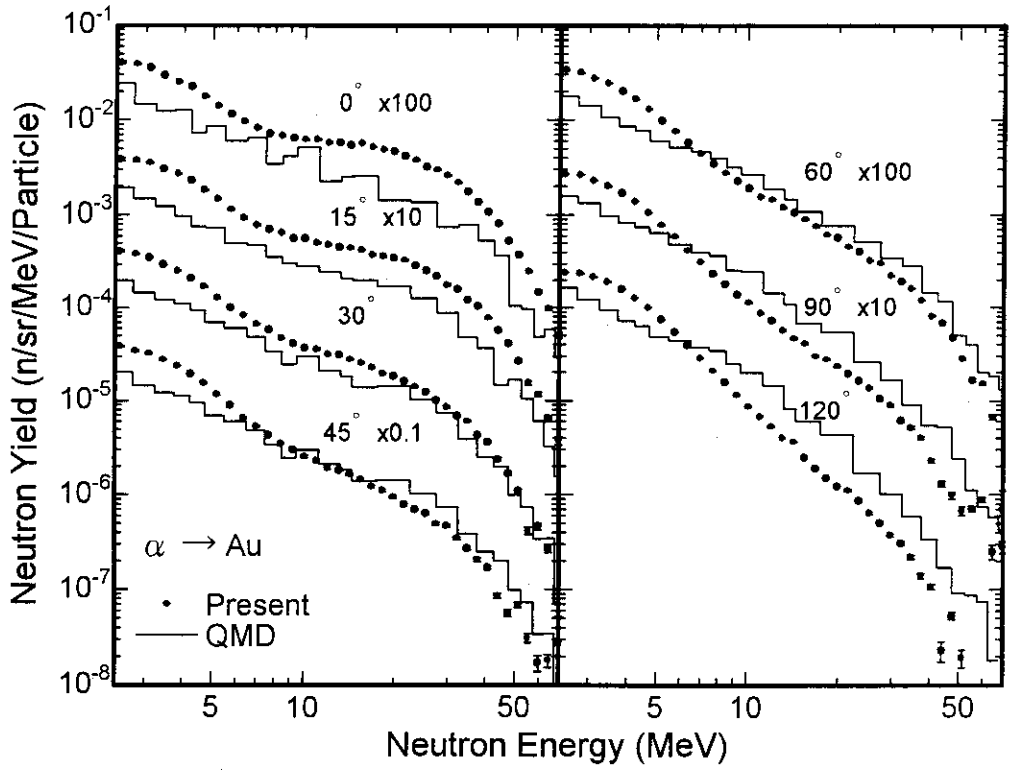

Fig. 5 Neutron energy spectra for 100 MeV alpha particle incidence on stopping-length Au target. The solid lines stand for the results of calculation with QMD+SDM.

3.19 Evaluation of Neutron Production Rate in Electron Accelerator Facility

Yoshiaki Shigetome[1], Hideo Harada[1], Tsutomu Noguchi[2] and Tetsuo Yamazaki[2]

[1]Power Reactor and Nuclear Fuel Development Corporation, Tokai Works
4-33 Muramatsu, Tokai-mura, Nakagun, Ibaraki-Ken 319-11
E-mail : tomesan@tokai.pnc.go.jp
[2]Electrotechnical Laboratory
1-1-4 Umezono, Tsukuba-shi, Ibaraki-Ken 305

Abstract

In the electron accelerator facility, photoneutrons caused by bremsstrahlung photons come into problem. In this work, a method of calculating the neutron flux in high energy electron accelerator facility is presented. To deduce the neutron flux, three calculation codes EGS4, ALICE-F and MCNP3.a were employed.

1. Introduction

Measurement of photonuclear reaction cross section with a high resolution and high energy photon spectrometer (HHS)[1] is being planned in the electron storage ring TERAS[2] at Electrotechnical Laboratory. The HHS consists of large volume Ge detectors and BGO detectors. Energy resolution degradation of the Ge detector induced by photoneutrons comes into a problem in planning the measurement. Main purpose in this work is to establish the method of calculating the neutron flux at the experimental hall in high energy electron accelerator facility to estimate how long Ge detectors keep their resolution in the hall. To deduce the neutron flux, three calculation codes EGS4[3], ALICE-F[4] and MCNP3.a[5] were employed.

2. Object of the Calculation

The experimental hall is schematically shown in Fig. 1. The HHS is set in a 5 cm thick Pb shield box in the hall. The hall is surrounded by concrete walls and its entrance is covered with a 15 cm thick Pb shield door. The process of the photoneutron production in the hall is as follows. Accelerated 300 MeV electrons (0.6 μA) bombard the 2 cm thick Fe wall. Bremsstrahlung photons are produced and they hit on the Pb shield door. Photoneutrons are mainly generated in this door.

3. Calculation Method

The photon flux $\phi_\gamma(r,z,E)$ and the rate of photonuclear reaction $R(r,z,E_\gamma)$ in the hall as shown in Fig.1 was calculated by electron-photon transport code EGS4 which was modified to include photonuclear reaction. Figure 2 shows the photonuclear cross section of natural lead used in this simulation which was given by reference [6]. Neutron energy spectrum $S_{E_\gamma}(E_n)$ and neutron

multiplicity $\nu(E_\gamma)$ were given for each photon energy using nuclear statistical code, ALICE-F which was modified to treat photonuclear reaction[4]. The photoneutron production rate $P(r,z)$ was calculated by

$$P(r,z) = \int_{E_\gamma} \nu(E_\gamma) R(r,z,E_\gamma) dE_\gamma . \qquad (1)$$

The averaged photoneutron spectrum $S(E_n)$ was calculated by

$$S(E_n) = \frac{\int\int\int_{E_\gamma} S_{E_\gamma}(E_n)\nu(E_\gamma)R(r,z,E_\gamma)drdzdE_\gamma}{\int\int\int_{E_\gamma} \nu(E_\gamma)R(r,z,E_\gamma)drdzdE_\gamma} . \qquad (2)$$

Monte Calro code simulating neutron and photon transport MCNP 3.a was employed in order to evaluate the neutron flux at the experimental hall. Figure 3 shows the flow chart of the calculation.

4. Results

Figure 4 shows the z-dependence of the photonuclear reaction rate and the neutron production rate. From this result, the thickness of the door is enough to shield the photons.

The total photoneutron production rate in the shield door is 2.4×10^{11} (1/sec). The result of photoneutron spectrum $S(E_n)$ is shown in Fig. 5. The spectrum was found to be well fitted by the Maxwell fission spectrum. The result is

$$S(E_n) = \sqrt{E_n} \exp(-E_n/0.69). \qquad (3)$$

Figure 6 shows the neutron spectrum in the experimental hall and in the Pb shield box. The results of the averaged neutron fluxes are 6.0×10^6 (1/cm²•s) in the hall and 5.9×10^6 (1/cm²•s) in the shield box.

5. Conclusion

The method of calculating the neutron flux at the experimental hall in high energy electron accelerator facility was presented using three calculation codes EGS4, ALICE-F and MCNP3.a.

The neutron flux at the experimental hall was obtained to be the order of 10^6 (1/cm²•s). The threshold fluence where Ge detectors show energy resolution degradation is the order of 10^9 (1/cm²) dose via fast neutron. To use Ge detectors in such high neutron flux environment, it is necessary to investigate the design of the neutron shield using this method.

References

[1] H.Harada and Y.Shigetome, J. Nucl. Sci. Tech., 32,1189 (1995).
[2] T. Tomimasu, et al., IEEE Trans. Nucl. Sci. NS-30, 3133 (1983).
[3] W. R. Nelson, et al., SLAC-Report-265 (1985).
[4] T.Fukahori, private communication (1992).
[5] J. F. Briesmeister, LA-7936-M (1986).
[6] S.S.Dietrich and B.L.Berman, UCRL-94820 (1986).

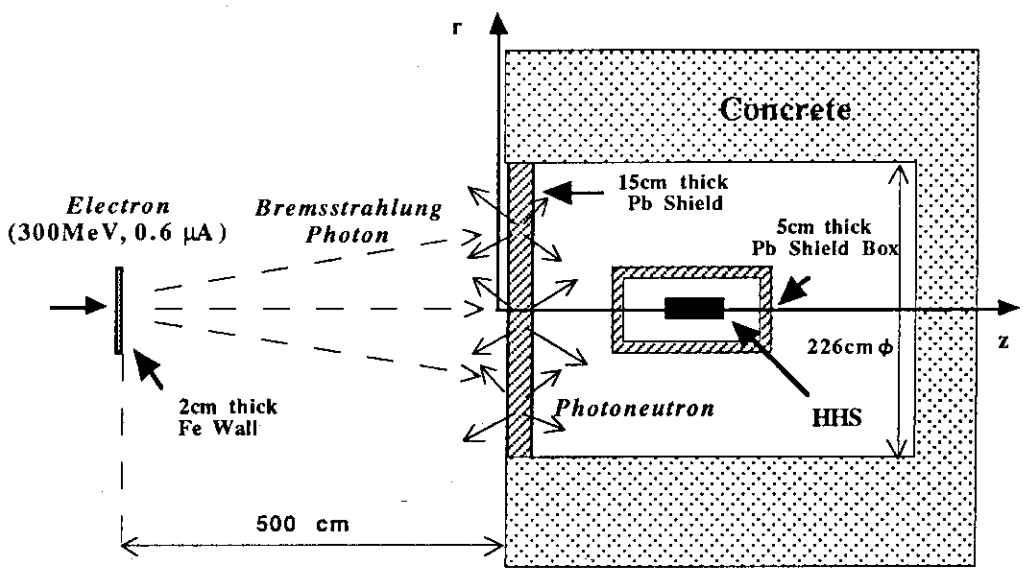

Fig. 1 Geometry of the Experimental Hall

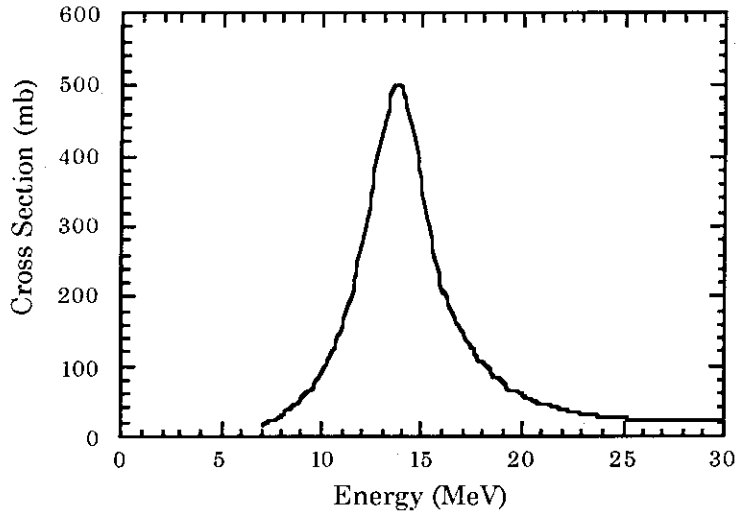

Fig. 2 Photonuclear Cross section of ^{nat}Pb

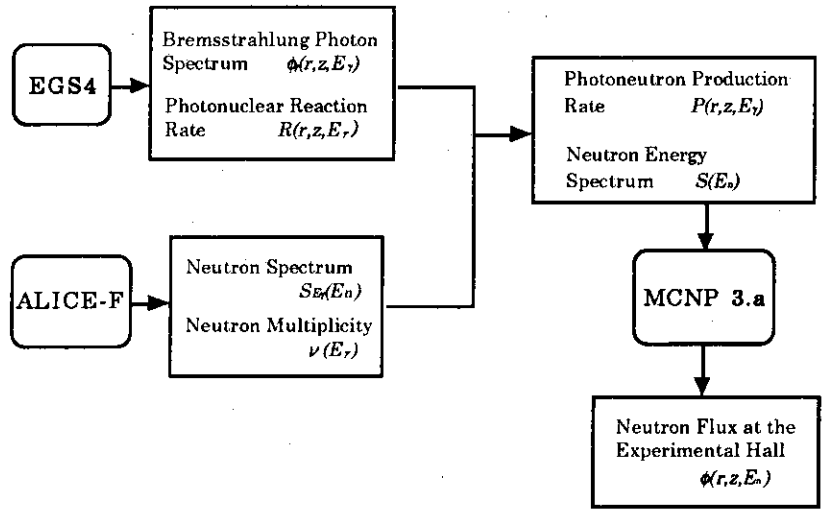

Fig. 3 Flow Chart of the Calculation

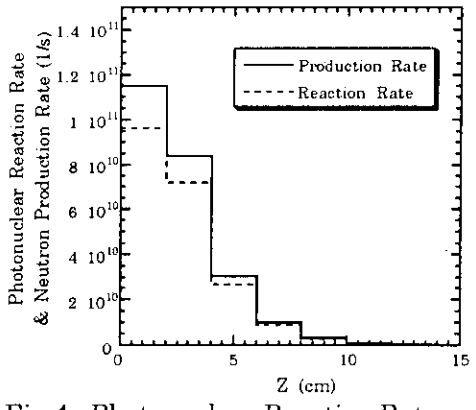

Fig.4 Photonuclear Reaction Rate and Neutron Production Rate

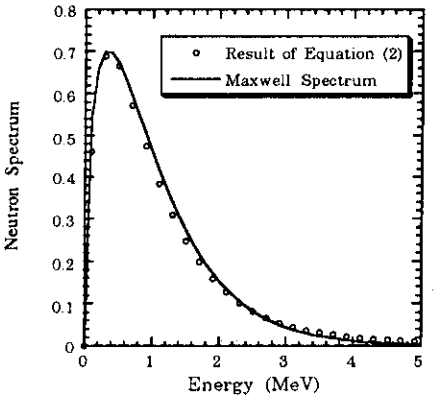

Fig. 5 Photoneutron Spectrum

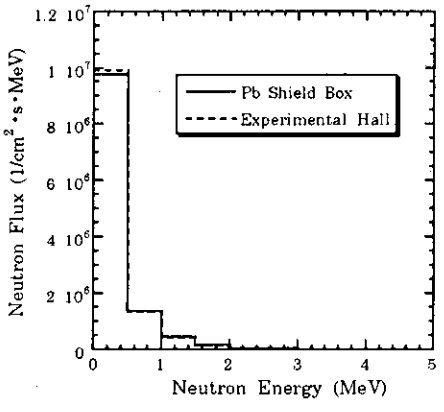

Fig.6 Neutron Spectrum in the Experimental Hall

3.20 High energy resolution measurement method of photonuclear reaction

Hideo Harada, Yoshiaki Sigetome and Yukio Wada

Nuclear Fuel Technology Development Division,
Power Reactor and Nuclear Fuel Development Corp.
Tokai-mura, Ibaraki-ken, 319-11
E-mail: harada@tokai.pnc.go.jp

Abstract

High resolution measurement method was proposed to observe fine structure of photonuclear reaction in giant resonance region. A high resolution spectrometer was designed to measure high energy photons transmitted from a target. The Monte Carlo simulation showed that the energy resolution of the photonuclear cross section measurement was improved to 0.1%.

1. Introduction

Fine structure of photonuclear reaction cross section in giant resonance (GR) region can provide important information about the excitation mechanism of photonuclear giant resonance and also for the study of the nuclear transmutation process using monochromatic photons(1). Especially, the intrinsic width of the fine peak in the GR is important because it determines the peak value of the cross section. However, very little is known about the width at present. To obtain the intrinsic peak width, we propose high resolution measurement method.

Figure 1 shows the conceptual setup of the experiment. The incident white photon should cover the energy range of interest. The transmitted photons from a thick target is measured by the high resolution and high energy photon spectrometer (**HHS**) composed of large volume hybrid Ge detectors surrounded by a BGO anticoincidence spectrometer. The energy resolution of the experiment in the GR region should be improved to 10-20 keV because the Ge detector has an energy resolution of about 0.1 %(2) for high energy photons.

2. Simulation and Results

2.1 Spectrometer design

Figure 2 schematically shows the cross section of the HHS. To obtain the large photopeak efficiency for high energy photons, two large N-type Ge detectors (relative efficiency of each crystal was 90% at 1.33MeV) were arranged like twins along a beam axis. To improve their peak/background response, the twins was surrounded by thick BGO crystals that were used as an anti-coincidence spectrometer.

Figure 3 shows the response function of the HHS for a parallel photon beam of 15 MeV. This was the result simulated by a Monte Carlo electron-gamma-shower code EGS4[3]. The results show responses for the next three cases: (1) the single Ge detector, (2) the twin Ge detector, and (3) the twins with the BGO anticoincidence spectrometer, that is, the HHS. The photopeak counts in the three spectra were normalized to be the same number, and the spectra were broaden with the energy resolution ($\Delta E_\gamma/E_\gamma$) of the Ge detector of 10^{-3}. The improvement in the peak/background ratio is very important for the measurement of dip peaks in the transmitted continuum spectrum. The HHS could improve this peak/background ratio to be extremely large value. The ratio obtained by the HHS was 3.8, which was more than one order larger compared to that of other Ge-BGO spectrometers[4] designed for the detection of relatively low energy photons.

2.2 Simulated transmission spectra

To simulate the experiment of the photonuclear cross section measurement with the HHS, the flux distribution of the transmitted photons from the thick water target was calculated as an example. The details of the simulation was described in ref.(5). The size of the target was 5 cm in diameter and 60 cm in length. The modified simulation code EGS4[6] was used to include the photonuclear cross section of ^{16}O as a part of photon material interaction. The two narrow photon absorption cross-section peaks of ^{16}O were artificially included in the code to simulate narrow dip peaks in the transmission spectrum. The artificial cross section of the Breit-Wigner shape is shown in **Fig. 4a**. The incident photon flux was assumed to be white with an energy range of 14.8 to 15.1 MeV; this kind of quasi-monochromatic photon flux could be supplied using laser Compton scattering device[7]. **Figure 4b** shows an incident white photon flux and transmitted photon flux distribution. Two dip peaks could be clearly seen in the transmitted photon flux distribution.

Figure 4c shows the transmission spectra observed by the single Ge detector (lower spectrum) and the HHS (upper spectrum). These were obtained by folding the transmitted flux distribution (Fig. 4b) using the response function of each detector in Fig. 3. The peaks were not clear in the spectrum observed by the single

Ge detector because of its low peak/background ratio. On the other hand, the dip peaks were clearly shown in the spectrum observed by the HHS. The FWHM of the dip observed at 14.9 MeV is about 20 keV. Therefore, the width of fine peaks in GR region could be measured with the energy resolution of 10^{-3} by observing transmitted photons using the HHS.

3. Conclusions

Fine structure of the photonuclear reaction in GR energy region was shown to be observable using the specially designed high resolution and high energy photon spectrometer, HHS, composed of hybrid type Ge detectors and a thick BGO anti-coincidence spectrometer. The Monte Carlo simulation showed that the HHS could measure high energy photons as a full energy photopeak with extremely high energy resolution and high peak/background ratio. By taking advantage of these features of the HHS, the dip peak produced by the photonuclear reaction in the transmitted white photon spectrum could be observable with an energy resolution of 10-20 keV.

References

(1) Satoh, I.: Private communication, (1993).
(2) Cecel, F.E., Wilkinson III, F.J., Ristinen, R.A., and Rieppo, R.: Nucl. Instr. Meth., **A234**, 479 (1985).
(3) Nelson, W.R., Hirayama, H., and Rogers, D.W.O.: SLAC-265 (1985).
(4) de Voigt, M.J.A., Bacelar, J.C., Micek, S.L., Schotanus, P., et al.: Nucl. Instr. Meth. **A356**, 362 (1995).
(5) Harada, H. and Shigetome, Y.: J. Nucl. Sci. and Technol., **32**, 1189 (1995).
(6) Kase, T., Konashi, K., and Kishimoto, Y.: PNC report (in Japanese) TN8410 92-350 (1992) p.70-72.
(7) Ohgaki, H., et al.: Nucl. Instr. Meth. **A353**, 384 (1994).

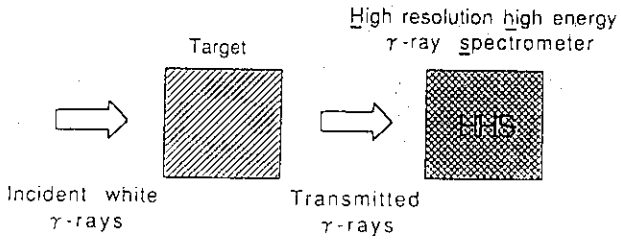

Fig.1 Schimatic setup of the high resolution experiments of photo nuclear cross section using the HHS

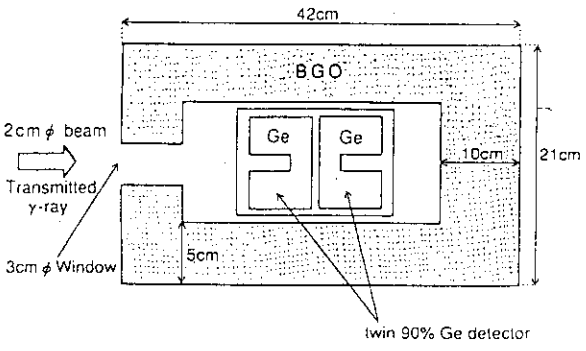

Fig.2 Cross section of the HHS

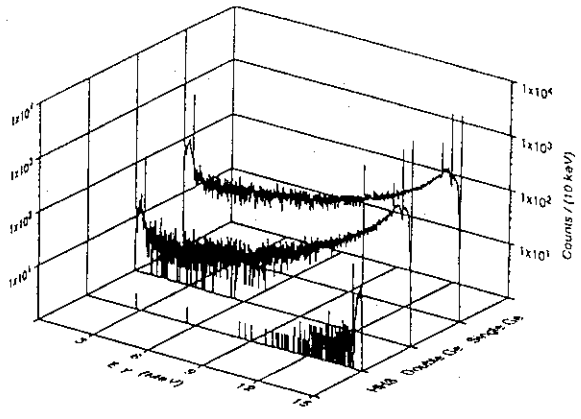

Fig.3 Responce functions of three type spectrometer for 15 MeV photon

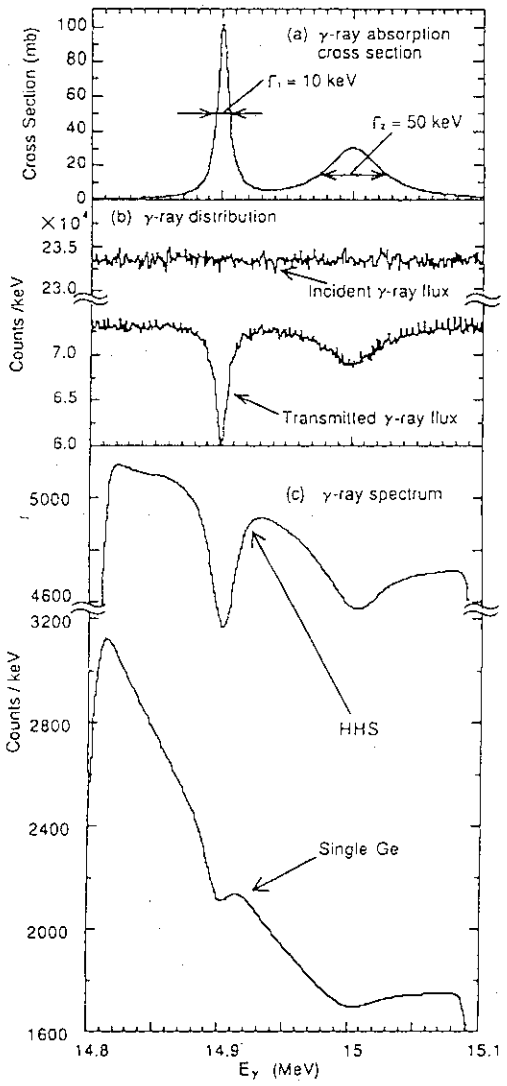

Fig.4 (a) Assumed photonuclear cross section curve, (b) Incident white photon flux (upper) and transmitted photon flux (lower) distribution, and (c) Transmission photon spectrum observed by single Ge detector (lower) and the HHS (upper)

3.21 Measurement of Double-Differential Neutron-Induced α-particle Emission Cross-Sections of ^{58}Ni and ^{nat}Ni

Toshiya SANAMI*), Mamoru BABA**), Shigeo MATSUYAMA, Toshihiko KAWANO#),
Takehide KIYOSUMI[1], Yasushi NAUCHI, Keiichiro SAITO and Naohiro HIRAKAWA
Department of Nuclear Engineering
Tohoku University
Aoba, Aramaki, Sendai 980-77, Japan
*)*E-mail : toshi@rpl.nucle.tohoku.ac.jp*
**)*E-mail : baba@fermi.nucle.tohoku.ac.jp*
#)Department of Energy Conversion Engineering
Kyushu University
Kasuga-Kouen 6-1, Kasuga-si, Fukuoka 816

Double differential (n,α) cross sections of ^{58}Ni and ^{nat}Ni were measured by using a high efficiency gridded ionization chamber. An energy resolution around 200 keV was accomplished using a thin sample (≈ 280 μg/cm^2) and a neutron source with low energy spread (≤ 150 keV). The cross sections and the angular distributions corresponding to the ground and low-lying excited states of the residual nucleus, ^{55}Fe, were obtained. Furthermore, the ^{60}Ni(n,α) cross sections were also deduced by combining the (n,α) cross sections of ^{58}Ni and ^{nat}Ni. These results are compared with other recent experiments and an optical-statistical model calculation.

1. Introduction

Neutron-induced charged particle emission cross sections are important for the evaluation of radiation damage and nuclear heating in fusion and fast reactors. Especially, double-differential (n,α) cross sections (DDXs) are indispensable to deduce the spectrum of primary knock-on atoms. We developed a gridded ionization chamber (GIC) which is very effective for charged particle emission reaction studies, and measured DDXs of structural elements: Fe, Ni, ^{50}Cr, Cu for 4.0 ~ 14.1 MeV neutrons **[1-3]**. Recently, Goverdovski et al. reported the ^{58}Ni(n,α) cross section with improved energy resolution using a thin sample **[4]**. Their data are different from our results in energy dependence and magnitude. The Ni(n,α) cross section is expected as the standard for (n,α) cross section measurement of structural elements, because of its large cross section. We measured DDXs of ^{58}Ni and ^{nat}Ni for 4.5~6.5 MeV neutrons with improved energy resolution. We obtained the cross sections of discrete levels which will be convenient for the evaluation validity of the optical potential parameters for reaction cross section calculation in this energy region, because the total (n,α) cross section was

---

1 Present address ; Japan Research Co.Ltd.

decided without the effect of level density parameters.

2. Experiment

An experimental setup is shown in Figure 1 and is almost the same as in previous studies [1-3]. Neutrons were produced at a D_2-gas target via the D(d,n) reaction using the Tohoku University 4.5 MV Dynamitron accelerator. The ^{58}Ni, ^{nat}Ni sample and a Au or Ta foil which is used for background measurement were set on the central cathode of GIC and bombard by the 4.5~6.5 MeV neutrons. Owing to good energy resolution of GIC (< 1.5 %), a thin sample (≃ 280 μg/cm^2) and a low energy spread in neutron source (≤ 150 keV), an overall energy resolution around 200 keV was achieved. α particles emitted from each sample were detected with a nearly 4π geometry. The counting gas was a Kr + 3~5 % CH_4 mixture with the pressure optimally adjusted to the emitted α-particle energy [1]. Because of the high efficiency of GIC, an enough counting statistics was obtained within several hours measurement with a ~4μA beam current. Figure 2 shows two-dimensional spectra for ^{58}Ni(n,α) and background measurement at En=6.21 MeV. A satisfactory signal-to-background ratio is achieved. The anode channel corresponds to a particle energy and the cathode one to angular distribution for each particle energy according to the following equations;

$$Pa = E + \sigma \cdot Pc \quad , \qquad Pc = E(1 - (\bar{x}/d)\cos\theta) \quad ,$$

where E is the α-particle energy, d is the cathode-grid distance (2.5 cm), θ is the emission angle, σ is the grid inefficiency (5.9 %), and $\bar{x}$ is the distance from the cathode to the center-of-gravity of ionization trace. The straight and curved lines in the figure represent particle emissions of 90° and 0° angles, respectively. Owing to a good energy resolution, a few stripes corresponding to α particles for the ground and excited states of the residual nuclei, ^{55}Fe, are observed clearly. DDXs were deduced from the α-particle yields for each angular mesh determined by the above two equations. The neutron flux was determined using a single proton recoil telescope (PRT) consisting of a 20 μm thick polyethylene radiator and a silicon surface barrier detector in a vacuum chamber. For normalization between sample-in and -out runs, and, GIC and PRT measurements, we employed two NE213 scintillation detectors as the neutron monitors in the direction of 0° and 90°.

3. Results and Discussion

Figure 3 indicates typical results of DDXs at 32° and 148° for En=5.21 and 6.21 MeV. The separation between α-particles to ground (α_0) and low-lying states ($\alpha_{1,2,3..}$) of ^{55}Fe are good enough, while it gets worse for higher states at background angle. Angular differential cross sections (ADX) for (n,α_0), (n,α_1), (n,$\alpha_{2,3..}$) are deduced form DDXs. Figure 4 shows ADXs for En=5.21 and 6.21 MeV. In the figure, the lines show the second order Legendre polynomials fit. All ADXs are almost 90° symmetric in CM-system. The magnitude of (n,α_0), (n,α_1) are almost the same in two energies and, therefore, the (n,$\alpha_{2,3..}$) component mainly contribute to the increase of the total (n,α) cross section with neutron energy which is shown in Figure 7.

Figure 5 represents the experimental results for ^{58}Ni(n,α_0), (n,α_1), (n,$\alpha_{2,3..}$) cross sections in comparison with those by Goverdovski et al. [4] and H.F.Calculation. "H.F.Cal" indicates the results of optical statistical model calculation based on the Hauser-Feshbach formula. The calculation employs

the following parameters: (1) Neutron optical potential (OMP) by A.B.Smith et al. [5], (2) proton and alpha OMP by Perey and Lemos, respectively, (3) level density parameters by Gilbert-Cameron, (4) nuclear structure data from Nuclear data seats and Table of isotopes. The present points for (n,α_0), (n,α_1) include the results by ^{nat}Ni as well as ^{58}Ni. The results by ^{nat}Ni were converted to the ^{58}Ni cross sections considering the number of ^{58}Ni and ^{nat}Ni atoms, because there is no contribution of ^{60}Ni. Our results of the ^{58}Ni(n,α_0) are in fair agreement with H.F.Cal., but are about twice as large as the data of Goverdovski et al.. The difference in (n,α_0) causes the disagreement in total (n,α) cross section results in Figure 7 and Ref. 4. The agreement between H.F.Cal. and the present data will imply appropriateness of OMP adapted. To calculate higher energy cross sections, the level density parameter of residual nuclei becomes important, because the $(n,\alpha_{2,3..})$ component mainly contribute to the increase of the total (n,α) cross section the higher neutron energy,

Figure 6 shows the present results of ^{nat}Ni(n,α) cross section together with other data [1,2,3,6,7], the evaluated data (JENDL-3R2 and ENDF/B-IV) and calculations (H.F.Cal and EXIFON [8]). Results by the thin sample (Present) are in agreement within error with our previous values (Baba) by a thick sample. However, the results by the thin sample tend to differ from those by the thick one above 6 MeV region. This should be checked more. The ^{60}Ni(n,α) cross section obtained by combining the ^{58}Ni(n,α) and ^{nat}Ni(n,α) results are shown in Figure 8.

4. Summary

We have measured the double differential cross sections of ^{58}Ni(n,α) and ^{nat}Ni(n,α) in En=4.5~6.5 MeV region using GIC with a thin sample and neutron source with low energy spread. Great improvement was achieved in energy resolution of DDXs. Owing to good peak separation, the ^{58}Ni(n,α_0), (n,α_1), $(n,\alpha_{2,3..})$ cross section were obtained.

The present work was partly supported by Japan Atomic Energy Research Institute (JAERI). The authors wish to thank Messrs. R.Sakamoto and M.Fujisawa for their help in the experiments using the Tohoku University Dynamitron accelerator.

Reference

1. N.Ito et al., Nucl.Instr.Methods **A337**, 474(1994)
2. M.Baba et al., J.Nucl.Sci.Technol., 31[7] 745 (1994)
3. M.Baba et al., Proc.Int.Conf. on Nucl.Data for Sci.Technol., (1994 Gatlinburg), p.941
4. A.A.Goverdovski et al., Proc.Int.Conf.Nucl.Data for Sci.Technol., (1994, Gatlinburg), p177
5. A.B.Smith, ANL/ADM-120
6. A.Paulsen, H.Liskin, F.Arnotte and R.Widera, Nucl. Sci. Eng., 78, 377 (1981)
7. C.Tsabaris et al., Proc.Int.Conf.Nucl.Data for Sci.Technol., (1994, Gatlinburg), p282
8. H.Kalka, Z.Phys., A231, 298 (1992) and private communication

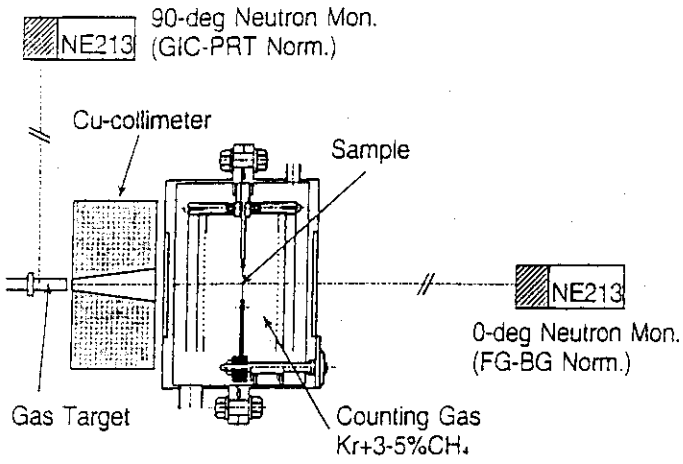

Fig.1. Experimental setup

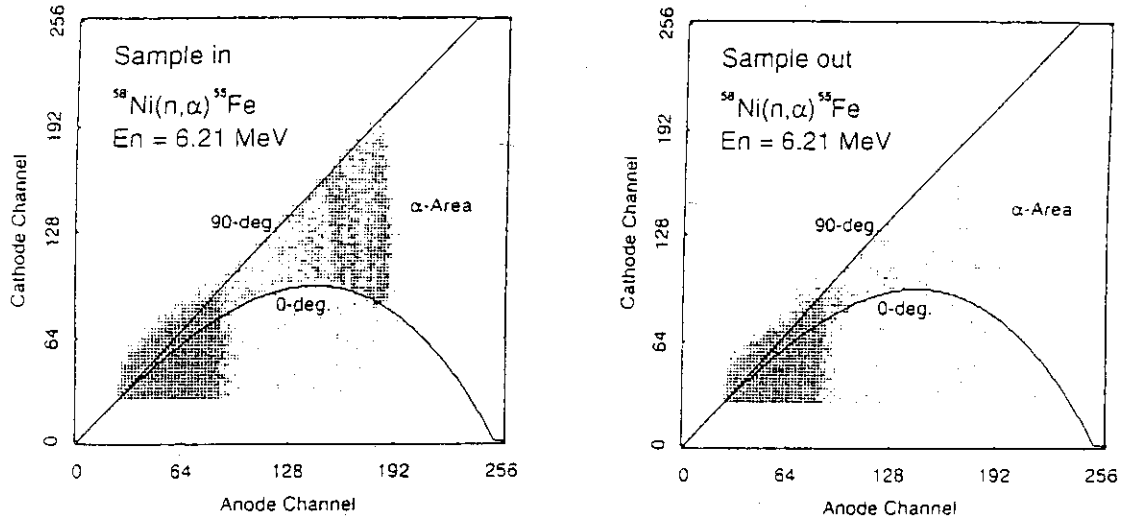

Fig.2. Two-dimensional spectrum of ^{58}Ni(n,α)

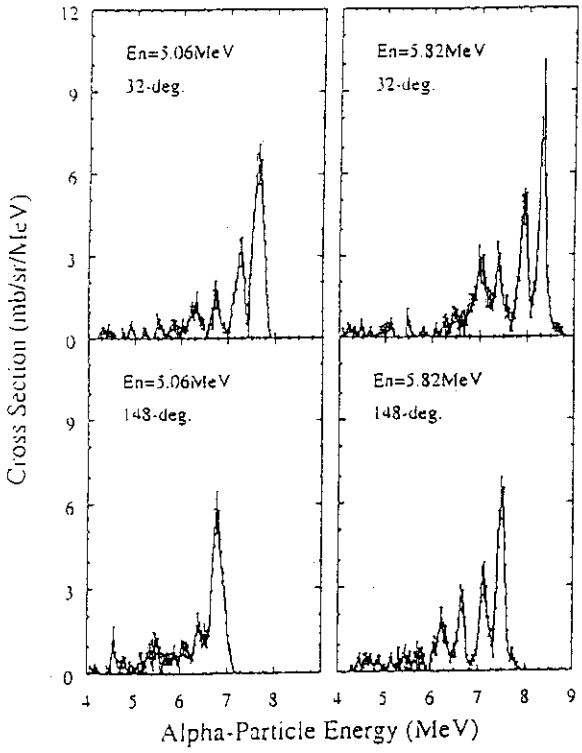

Fig.3. DDX of ^{58}Ni(n,α)

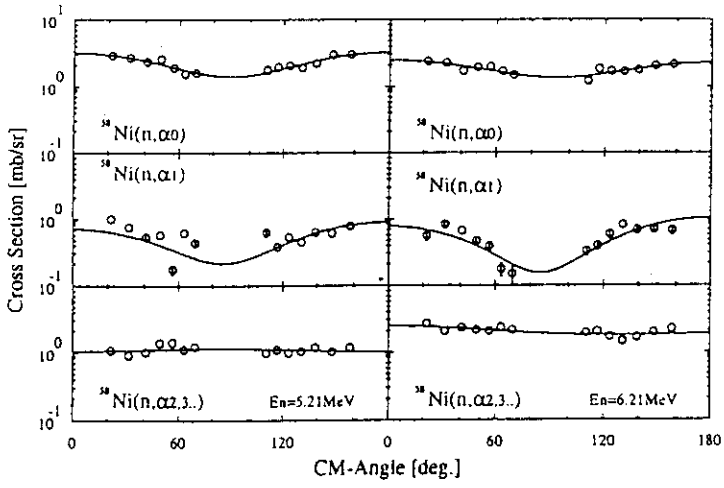

Fig.4. ADX of ^{58}Ni(n,α_0), (n,α_1), (n,$\alpha_{2,3..}$)

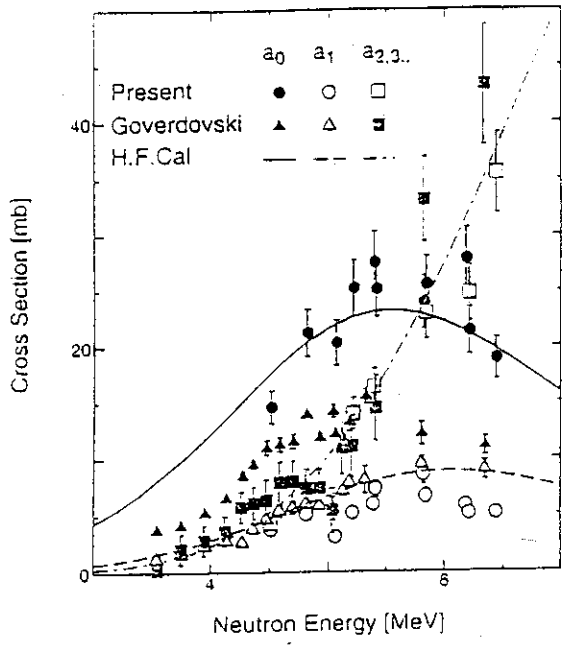

Fig.5. ^{58}Ni(n,α_0), (n,α_1), (n,$\alpha_{2,3..}$) cross section
Goverdovski[4]

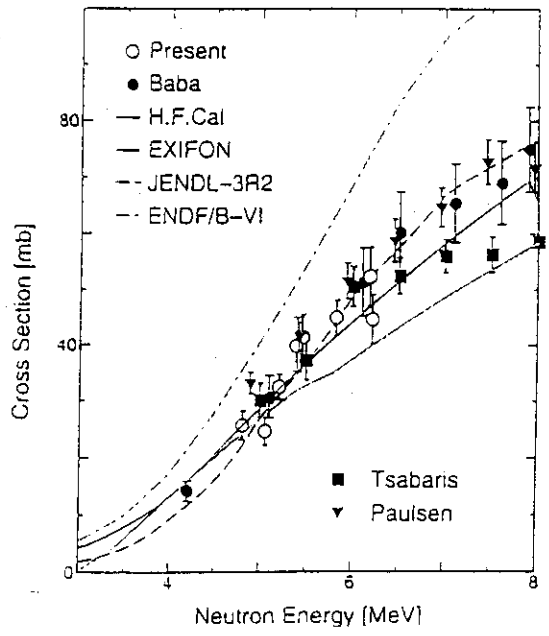

Fig.6. ^{nat}Ni(n,α) cross section
Baba[2,3], Tsabaris[7], Paulsen[6], EXIFON[8]

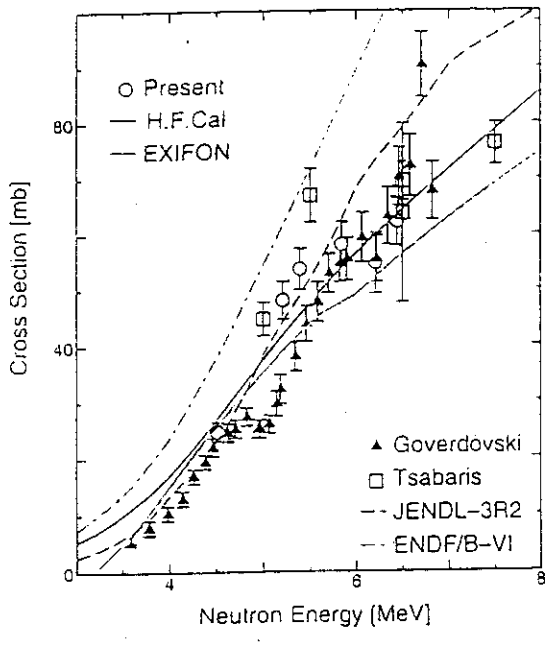

Fig.7. ^{58}Ni(n,α) cross section
Goverdovski[4], Tsabaris[7], EXIFON[8]

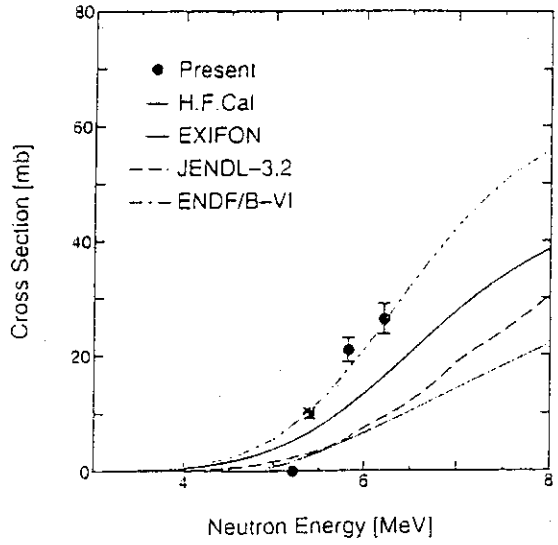

Fig.8. ^{60}Ni(n,α) cross section
EXIFON[8]

3.22 Measurement of Neutron Spallation Cross Sections

E.Kim,T.Nakamura,A.Konno(CYRIC,Tohoku Univ.),M.Imamura,N.Nakao
T.Shibata(INS,Univ.of Tokyo),Y.Uwamino,N.Nakanishi(Institute of Physical and Chemical Research),Su.Tanaka,H.Nakashiman, Sh.Tanaka,(JAERI)

Neutron spallation cross sections of $^{12}C(n,2n)^{11}C$ and $^{209}Bi(n,xn)^{210-x}Bi$ were measured in the quasi-monoenergetic p-Li neutron fileds in the energy range of 20MeV to 210MeV which have been established at four AVF cyclotron facilities of 1)INS of Univ. of Tokyo, 2)TIARA of JAERI, 3)CYRIC of Tohoku Univ., and 4)RIKEN.

Our experimental data were compared with other experimental data and the ENDF/B-VI high energy file data.

1. Introduction

At present, a demand for neutron reaction data is world-wide increasing from the viewpoints of intense neutron source of material study, induced radioactivity and shielding design of high energy accelerators. Nevertheless, neutron reaction data in the energy range above 20MeV are very poor and no evaluated data file exists at present mainly due to very limited number of facilities having quasi-monoenergetic neutron fields. In this study, we measured the neutron spallation cross sections of ^{12}C, ^{27}Al, ^{59}Co and ^{209}Bi which has been and will be used for high energy neutron spectrometry, by using quasi-monoenergetic p-Li reutrons in the energy range of 20MeV to 210MeV.

2.Experiment

The experiments were performed at four cyclotron facilities of 1)Institute for Nuclear Study (INS),University of Tokyo for 20 to 40 MeV, 2)Cyclotron and Radioisotope Center (CYRIC),Tohoku University for 20 to 40 MeV, 3)Takasaki Research Establishment, Japan Atomic Energy Reserch Institute (TIARA) for 40 to 90MeV and 4)Institute of Physical and Chemical Research (RIKEN) for 80 to 210MeV.

The ^{7}Li-targets of 2 to 10mm thickness were bombared by proton beams of 20 to 210MeV energies which were extracted from these cyclotrons. The neutrons produced in the forward direction from the target were transported through the collimater for sample irradiation and the proton beams passed through the target were swept out by the magnet to the beam dump at CYRIC,TIARA and RIKEN. The cross section measurements between 20 and 40MeV were performed at INS, because the neutron fluence of the CYRIC neutron field was too low for sample irradiation. The samples were placed only 10cm away from the Li-target in the forward direction at INS,and the neutron spectra were measured at CYRIC where the same target configuration was prepared, because the INS neutron field has not enough space for neutron spectrometry with the TOF method. In the CYRIC, TIARA and RIKEN experiments, the neutron spectra were measured with the TOF method using a organic liquid scintillator. The absolute neutron fluence of the monoenergy peak was determined with the PRT (Proton Recoil counter Telescope) at TIARA, and with the Li activation method to detect the ^{7}Be activity from the $^{7}Li(p,n)^{7}Be$ reaction at CYRIC and RIKEN. Figs.1 and 2 show the neutron spectra for 43,58,68 and 88MeV proton incidence at TIARA and for 90, 100, 110,and 120 MeV proton incidence at RIKEN, respectively .

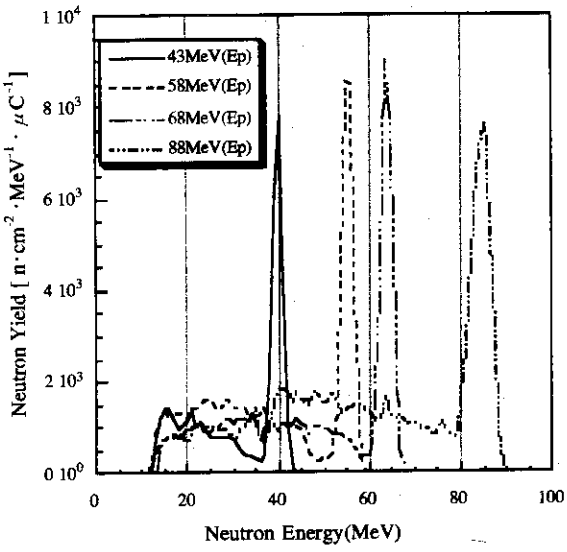

Fig 1. Neutron spectra of 43,58,68 and 88MeV p-Li reactions at TIARA

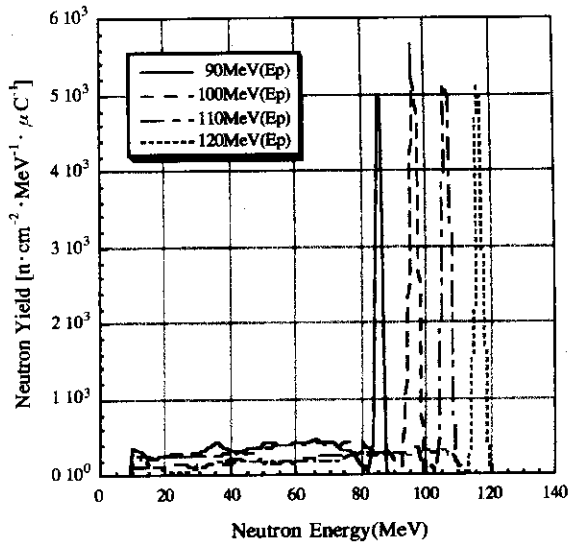

Fig 2. Neutron spectra of 90,100,110, and 120MeV p-Li reactions at RIKEN

The irradiation samples are ^{12}C, ^{27}Al, ^{29}Cu, ^{59}Co and ^{209}Bi . Tables 1, 2 and 3 show the physical data of irradiation samples in INS,TIARA and RIKEN experiments.

Table1. Physical data of irradiation samples at INS

Sample	Diameter	Thickness	Weight	Purity
^{12}C	20mm	2.2mm	1.57g	98.81%
^{27}Al	30mm	2.0mm	3.80g	100.00%
^{209}Bi	15mm	0.6mm	0.65g	99.99%

Table 2. Physical data of irradiation samples at TIARA

Sample	Diameter	Thickness	Weight	Purity
^{12}C	33mm	1mm	1.83g	98.81%
^{27}Al	29mm	2mm	3.64g	100.00%
^{59}Co	33mm	2mm	20.1g	99.9%
^{209}Bi	29mm	2mm	6.90g	99.99%

Table 3. Physical data of irradiation samples at RIKEN

Sample	Diameter	Thickness	Weight	Purity
^{12}C	80mm	10.0mm	104g	98.81%
^{27}Al	80mm	10.0mm	149g	100.00%
^{209}Bi	80mm	10.8mm	530g	99.99%

The samples were irradiated 10cm, 400cm, and 837cm behind the Li target at INS,TIARA and RIKEN, respectively. Irradiation time consisted of short irradiation time (1

to 2 hours under 120MeV, 30min above 120MeV) and long irradiation time (about 20 hours) by considering the half life of produced nuclei. During sample irradiation, proton beam currents were monitered with the digital current integrator and scaler. The gamma rays emitted from irradiated samples were measured with a high purity Ge detector by coupling with the 4096 multi-channel analyzer. The carbon samples were put into an aluminum case to absorb the positron energy from ^{11}C nuclei produced by the $^{12}C(n,2n)^{11}C$ reaction, since the annihilation gamma rays of 511keV were measured with the Ge detector.

The peak efficency of the Ge detector was obtained from the mixed standard source and the self absorption of samples was calculated with the PEAK code (1) and the EGS4 code(2).

3.Analysis

The reaction rates of identified radioisotopes were obtained by analyzing gamma-ray spectra after corrected for the peak efficiency, sum-coincidence and self-absorption effects, also for the beam current fluctuation during sample irradiation.

The reaction rate corrected for the beam current fluctuation becomes

$$R=\frac{\lambda \cdot C}{N \cdot \varepsilon \cdot \gamma \cdot e^{-\lambda T_c} \cdot (1-e^{-\lambda T_m}) \cdot \sum_i \{Q_i \cdot e^{-\lambda (n-i)\Delta t}\}} \qquad (1)$$

where is decay constant, C is counts of gamma-ray peak area , N is atomic number of the target , ˆ is peak efficiency, ` is branching ratio of gamma rays, T_m is counting time , T_c is cooling time and Q_i is beam current for irradiation time interval Δt.

As the neutron energy spectra used in this activation cross section measurement have a monoenergetic peak and the lower energy continuum as seen Figs.1 and 2, the reaction rate is divided into two components as follows,

$$R=N\int_{E_{th}}^{E_{min}} \sigma(E)\cdot\phi(E)dE+N\int_{E_{min}}^{E_{max}} \sigma(E)\cdot\phi(E)dE \qquad (2)$$

where N is the number of target nucleus, –(E) the spallation cross section, (E) the neutron fluence, E_{th} the threshold energy, E_{min} the minimum energy of the neutron peak and E_{max} the maximum energy of the neutron peak. The first term corresponds to the contribution from the lower energy neutrons, and the second term from monoenergetic peak neutrons. R is written as

$$R=\int_{E_{th}}^{E_{min}} \sigma(E)\cdot\phi(E)dE+\sigma(E_{peak})\cdot\Phi(E_{peak}) \qquad (3)$$

where $-(E_{peak})$ is the average cross section at the monoenergetic peak E_{peak} ,and

$$\Phi(E_{peak})=\int_{E_{min}}^{E_{max}} \phi(E)dE \qquad (4)$$

is the peak neutron fluence which is given by PRT or Li activation method.

Finally, from Eq. (3) the cross section at E_{peak} can be estimated by

$$\sigma(E_{peak})=\frac{R-\int_{E_{th}}^{E_{min}}\sigma(E)\cdot\phi(E)dE}{\Phi(E_{peak})} \qquad (5)$$

If the threshold energy E_{th} is higher than E_{min}, the second term of the numerator of Eq.(5) is zero, otherwise, this term can be estimated by successive subtraction method using the neutron flux (E) having lower peak energy. The -(E) values in lower energy region were estimated from the evaluated data file, ENDF/B-VI[3], experimental data compiled by McLane et al.[4] and our experimental data obtained in lower energy region.

The errors of cross section data were obtained from the error propagation law by combining the error of activation rate (2～10%), peak neutron fluence (5～15%), contribution from the reference cross section used to estimate the low energy neutron activation (4～48%).

4.Results and Discussions

At present,we obtained the cross section values of $^{209}Bi(n,4n)^{206}Bi$ to $^{209}Bi(n,10n)^{200}Bi$, and $^{12}C(n,2n)^{11}C$ reactions. As examples, Figs.3,4,5 and 6 give the obtained cross section data. The cross section data of $^{209}Bi(n,xn)^{210-x}Bi$ reactions were compared with the ENDF/B-VI high energy file data calculated with the ALICE code[5]. Our experimental results are the first experimental data and are generally in good agreement with them except for $^{209}Bi(n,9n)^{201}Bi$. A big discrepancy, about a factor of 4, between our experiment and ENDF/B-VI may come from the uncertainty of the decay scheme of ^{201}Bi,where we assumed the 100% branching ratio of 628keV gamma rays from the first excited state to the ground state. If this ratio is 25%, then our data well agree with the ENDF/B-VI. Our cross section data of $^{12}C(n,2n)^{11}C$ shown in Fig.6 are lower in the peak region around 40MeV than the ENDF/VI high energy file data, but much higher than the ENDF/VI data above 60MeV. Our results below 40MeV show good agreement with the Brill's data[6]. Our first experimental data above 40MeV show almost a constant value of 20mb, which reveals that the ENDF/VI data of $^{12}C(n,2n)^{11}C$ reaction may be inaccurate.

References

[1]T.Nakamura and T.Suzuki, Monte Carlo Calculation of Peak Efficiencies of Ge(Li) and Pure Ge Detector to Voluminal Sources and Comparison with Environmental Radioactivity Measure ment. Nucl.Instr.and Meth. 205,211(1983)
[2]W.R.Nelson, H.Hirayama,and D.W.O.Rogers, SLAC-265 (Standard University,Stanford 1985)
[3]National Nuclear Data Center, Brookhaven National Laboratoty, " Evaluated Nuclear Data File" . ENDF/B-VI(1990)
[4] V.McLane, C.L.Dunford and P.F.Rose," Neutron Cross Section" , Vol.2, Neutron Cross Section Curves, Academic Press.,New York(1988)
[5]M.Blann, CODE ALICE/89, private communication(1989)
[6]O.D.Brill, N.A.Vlasov, S.P.Kalinin and L.S.Sokolov, Cross Section of the (n,2n)Reaction in C12, N14, O16and F19 in the Energy Interval 10-37MeV, DOK 136, Inst.Atom Energy I.V., Kurchatova, Moscow,55(1961)
[7]B.Anders, P.Herges and W.Scobel, Excitation Functions of Nuclear Reactions Producing C-11, Z.Für Physik A 301, 353 (1981)

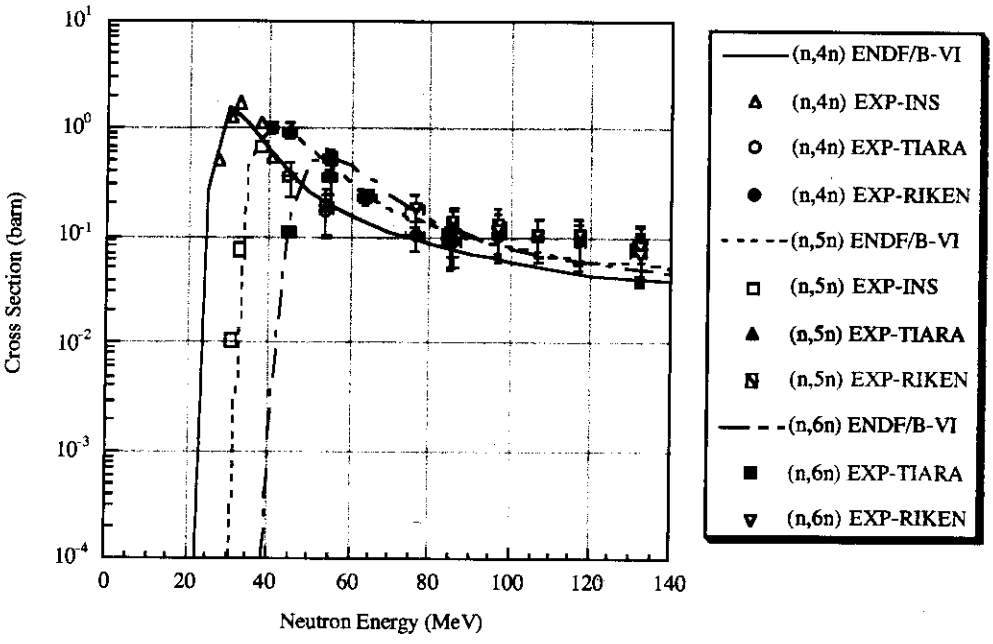

Fig.3 $^{209}Bi(n,4n)^{206}Bi$, $^{209}Bi(n,5n)^{205}Bi$, $^{209}Bi(n,6n)^{204}Bi$ reaction cross sections

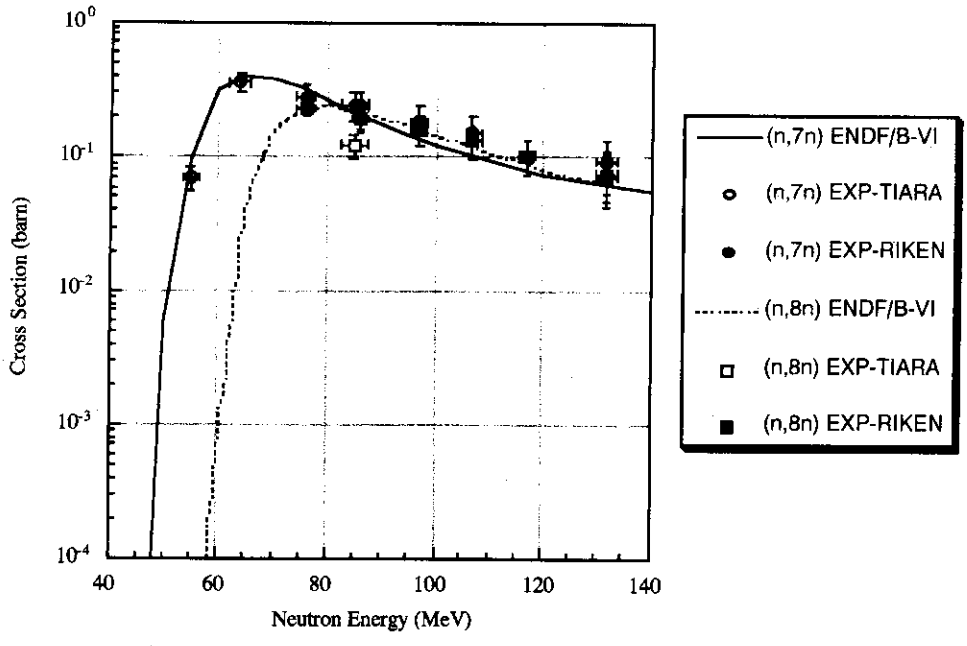

Fig.4 $^{209}Bi(n,7n)^{206}Bi$, $^{209}Bi(n,8n)^{205}Bi$ reaction cross sections

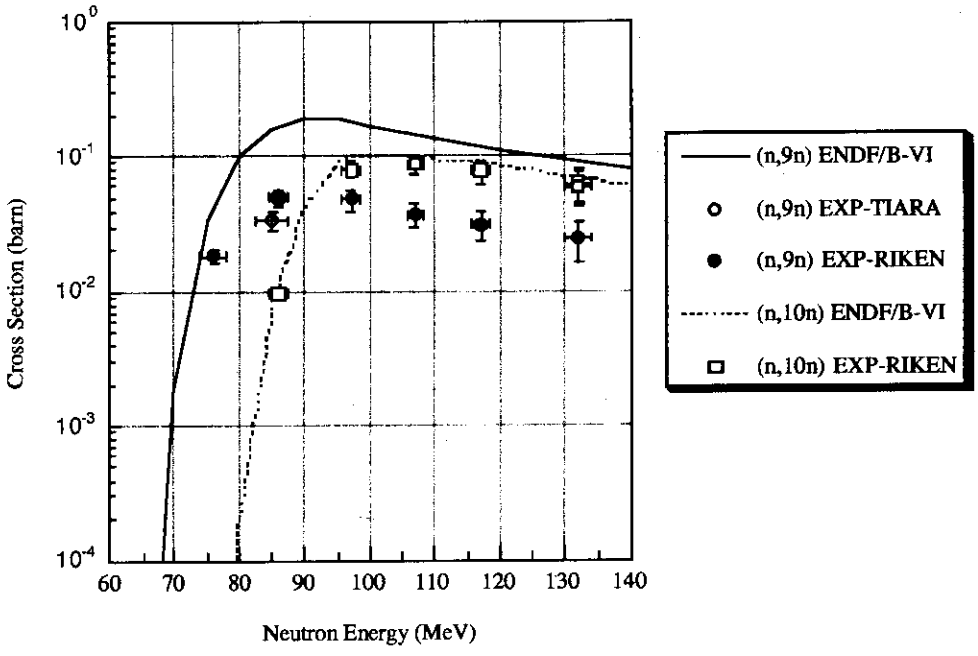

Fig.5 $^{209}Bi(n,9n)^{206}Bi$, $^{209}Bi(n,10n)^{205}Bi$ reaction cross sections

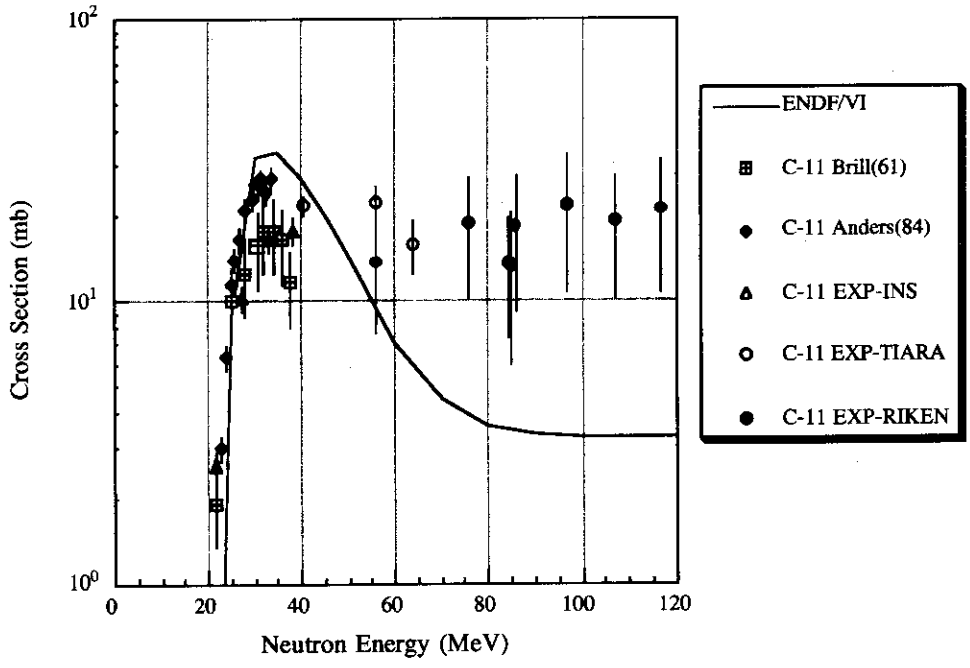

Fig.6 $^{12}C(n,2n)^{11}C$ reaction cross section

3. 23 Gamma-Ray Emission Cross Section From Proton-Incident Spallation Reaction

Kiminori IGA[*1], Kenji ISHIBASHI[*1], Nobuhiro SHIGYO[*1], Tatsushi NAKAMOTO[*1],
Keisuke MAEHATA[*1], Naruhiro MATSUFUJI[*2], Shin-ichirou MEIGO[*3],
Hiroshi TAKADA[*3], Satoshi CHIBA[*3], Masaharu NUMAJIRI[*4],
Takashi NAKAMURA[*5], Yukinobu WATANABE[*6]

*1 Department of Nuclear Engineering, Kyushu University, Hakozaki, Higashi-ku, Fukuoka-shi 812-81.
*2 National Institute of Radiological Sciences, Anakawa, inage-ku, Chiba-shi 263.
*3 Japan Atomic Energy Research Institute, Tokai-mura, Ibaraki-ken 319-11.
*4 National Laboratory for High Energy Physics, Oho, Tsukuba-shi, 305.
*5 Cyclotron Radioisotope Center, Tohoku University, Aramaki, Aoba-ku, Sendai-shi 980-77.
*6 Energy Conversion Engineering, Kyushu University, Kasuga-koen, Kasuga-shi 816.
e-mail: iga@kune2a.nucl.kyushu-u.ac.jp

Gamma-ray emission double differential cross sections from proton-incident spallation reaction have been measured at incident energies of 0.8, 1.5 and 3.0 GeV with Al, Fe, In and Pb targets. The experimental results have been compared with calculate values of HETC-KFA2. The measured cross sections disagree with the calculated results in the gamma ray energies above 10 MeV.

1.Introduction

Gamma-ray spectra from spallation reaction may show information about the target nucleus at excited state. However, the systematic experimental data have not been taken for the spallation reaction so far. Simulation codes such as HETC-KFA2[(1)] consider the gamma-ray emission with a simplified assumption, but their prediction adequacies have never been tested in detail for the spallation reaction. In this study we obtained the gamma-ray emission double differential cross sections by incident protons of a GeV range. The results were compared with HETC-KFA2.

2.Experiment

The experiment was carried out at the $\pi 2$ line of the 12 GeV proton synchrotron at National Laboratory for High Energy Physics. The experimental arrangement is illustrated in Fig. 1. Incident proton energies were 0.8, 1.5 and 3.0 GeV, and targets were Al, Fe, In and Pb. The detectors were placed in the directions of 15, 30, 60, 90, 120 and 150° . Since the primary purpose of this experiment was to measure neutrons by the TOF method, both gamma rays and neutrons were detected by $\Phi 5''$

×5" and Φ2"×2" liquid scintillator NE213. The Φ2"×2" scintillator data, however, were not analyzed, because they produced unclear spectra for gamma rays of interest. The discrimination between gamma ray and neutron was accomplished by the two-gate integration method[2]. The example of ADC spectrum of gamma rays is shown in Fig. 2.

3.Analyses

The energies of ADC channels were corrected by gamma rays from checking sources of ^{137}Cs, ^{60}Co and Am-Be gamma rays up to 4.4 MeV. Above 4.4 MeV, we converted neutron energy that was measured by TOF method, into gamma-ray energy in terms of empirical expression by Cecil et al. [3]

$$E_e = 0.83E_p - 2.82[1.0 - \exp(-0.25E_p^{0.93})] \quad (1)$$

where the electron energy E_e and the recoil proton energy E_p in detector are presented in units of MeV. The calibration result for ADC channel is plotted in Fig. 3.

The response functions of NE213 were calculated by EGS4 code[4]. The calculated response function for ^{60}Co gamma ray is presented in Fig. 4 together with measured one. Because of the poor energy resolution of NE213 the response function shows the sum of 1.173 MeV and 1.333 MeV gamma rays. The disagreement at lower energies was caused by background events. The response functions above 60 MeV are shown in Fig. 5. When incident gamma ray energies were higher than 60 MeV, the response functions of the scintillator are almost the same due to the use of small size NE213 containing low atomic number elements of C and H. This situation made it impossible to analyze gamma-ray spectra below 60 MeV.

Gamma-ray emission cross sections were obtained by unfolding ADC spectra by FERDo-U code[5]. The spectra contained a small amount of gamma rays that were created in scintillator by neutron: the peak at 4.4 MeV that made by $^{12}C(n,n')^{12}C^*$ reaction was eliminated by eye measure. Gamma-ray attenuation in targets was corrected by the simulation calculation with EGS4 code.

Experimental double differential cross sections are shown in Figs. 6, 7, 8 and 9 with the results of HETC-KFA2. The error bars indicate statistical ones and they are expressed only upper part for ease of looking. Since HETC-KFA2 calculates gamma-ray emission from the evaporation process, the results are isotropic and the same shape at different angles. The experimental results were in mostly good agreement with the results of HETC-KFA2 below 10 MeV, whereas the measured data are considerably larger than the calculation beyond this energy. Above 10 MeV, gamma rays may be emitted by such process as nuclear bremsstrahlung, preequilibrium processes, dipole resonance and high-spin state nucleus.

4.Conclusion

Gamma-ray emission double differential cross sections were obtained below 60 MeV. We compared the experimental results with the calculation results of HETC-KFA2. The experimental results are in good agreement with the calculation values only in the energy range of the evaporation process.

Acknowledgements

We gratefully acknowledge Prof. H. Hirayama and Dr. Y. Namito for use of EGS4, and Prof. S. Ban for use of FERDo-U.

References

(1) Cloth, P., et al. : KFA-IRE-E AN/12/88 (1988)

(2) Zucker, M. S., et al. : Nucl. Instrum. Methods, A299, 281 (1990)

(3) Cecil, R. A., et al. : Nucl. Instrum. Methods, 161, 439 (1979)

(4) Nelson, W. R., et al. : SLAC-Report-265 (1985)

(5) Burrus, W. R. : ORNL-3743 (1965)

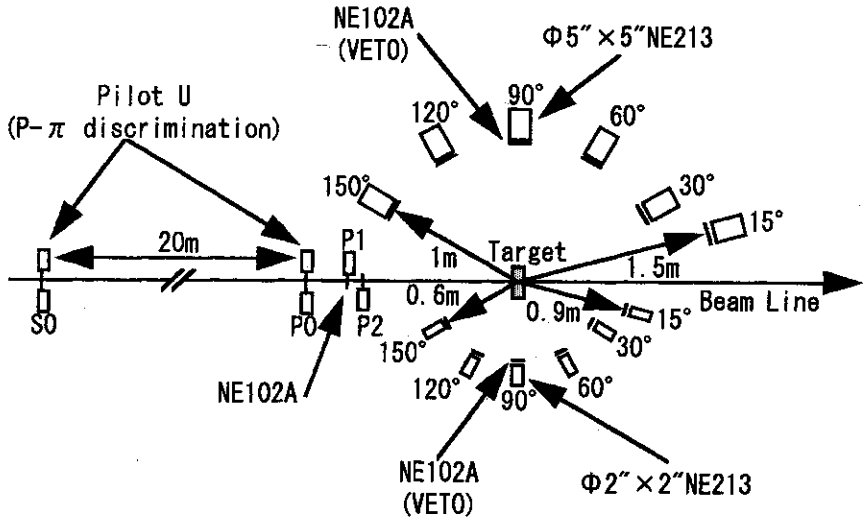

Fig. 1 Illustration of experimental arrangement

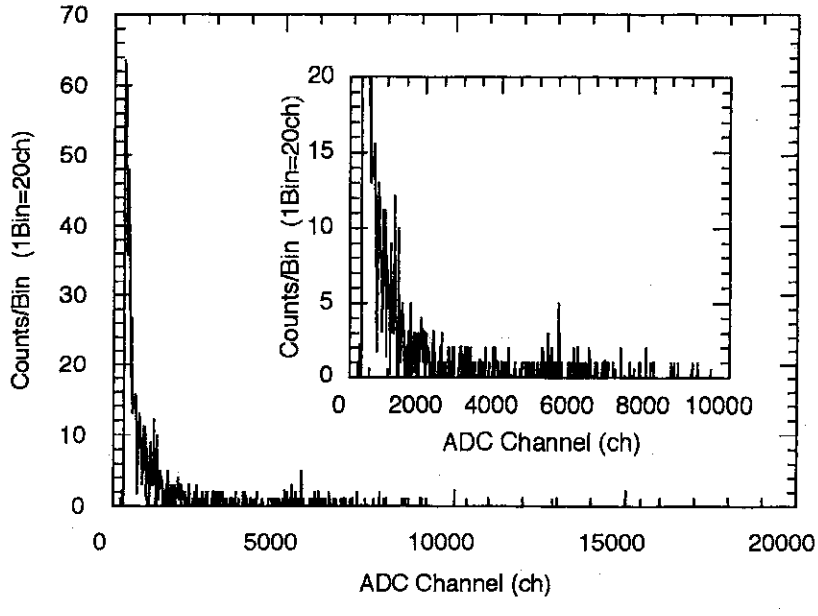

Fig. 2 ADC spectrum at 15deg by 0.8 GeV proton incident on Pb.

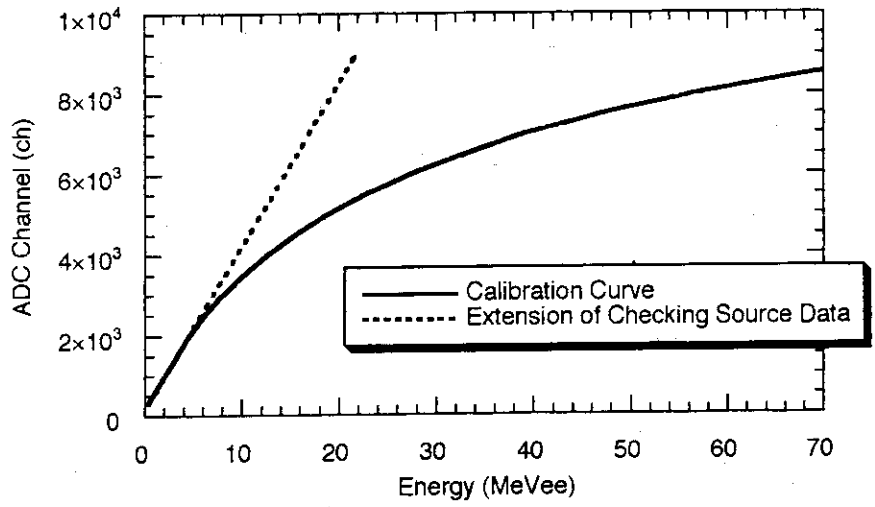

Fig. 3 Energy calibration for ADC channel for the detector.

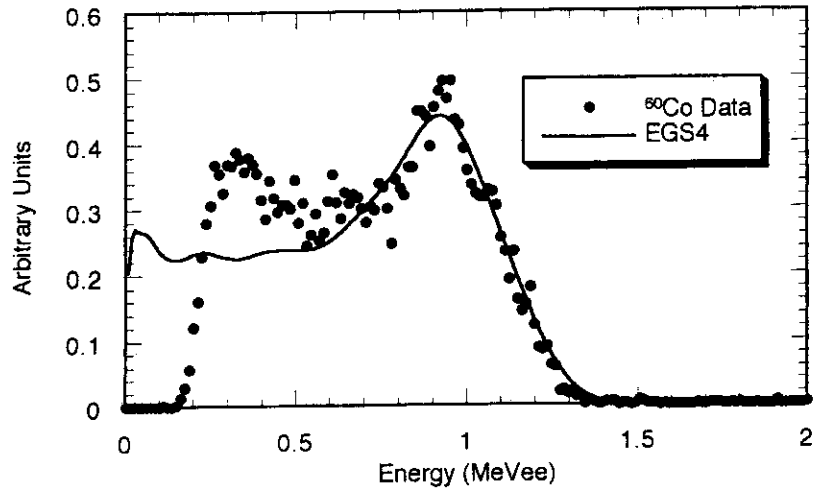

Fig. 4 Response functions from ^{60}Co gamma-ray source. The result as calculated was modified to take an actual energy resolution into consideration.

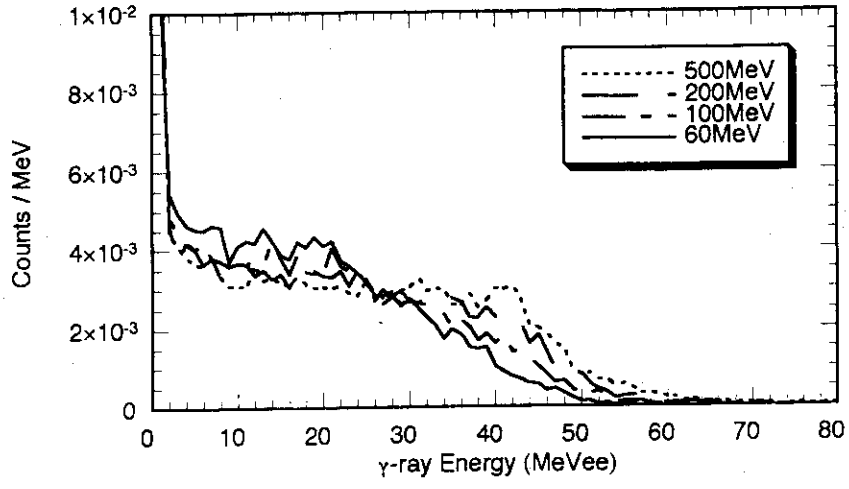

Fig. 5 Response functions for gamma rays with energies above 60 MeV.

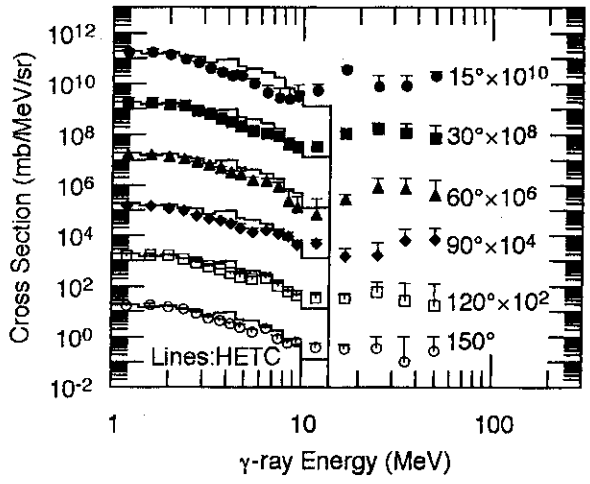

Fig. 6 (a) Gamma-ray spectra for 0.8GeV-proton incidence on Al.

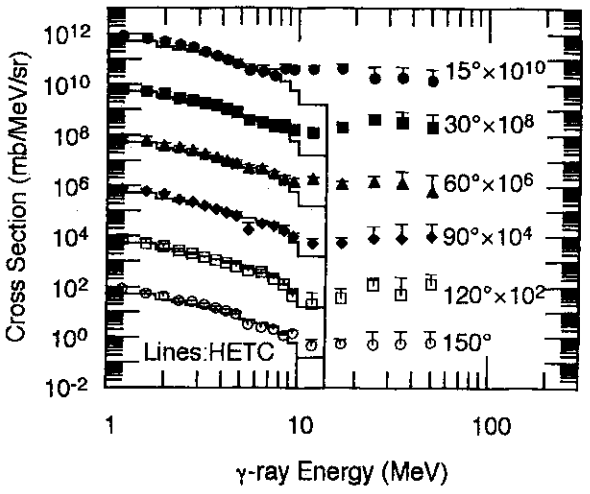

Fig. 7 (a) Gamma-ray spectra for 0.8GeV-proton incidence on Fe.

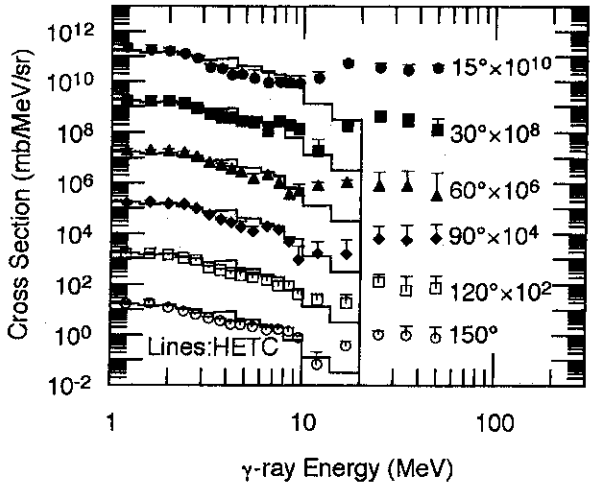

Fig. 6 (b) Gamma-ray spectra for 1.5GeV-proton incidence on Al.

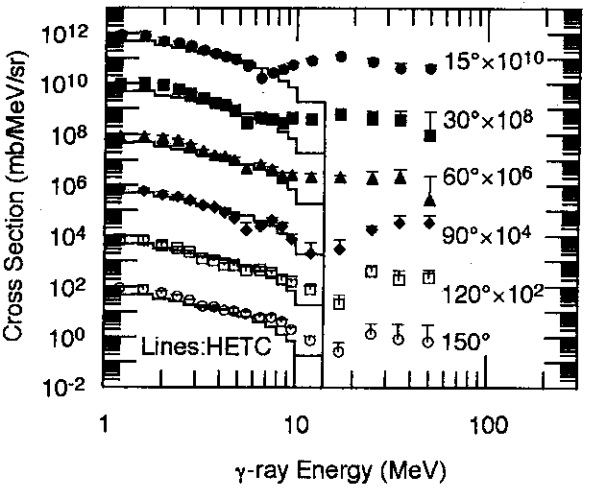

Fig. 7 (b) Gamma-ray spectra for 1.5GeV-proton incidence on Fe.

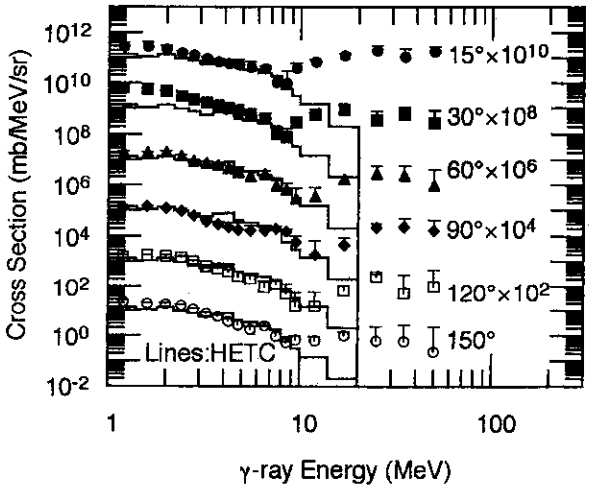

Fig. 6 (c) Gamma-ray spectra for 3.0GeV-proton incidence on Al.

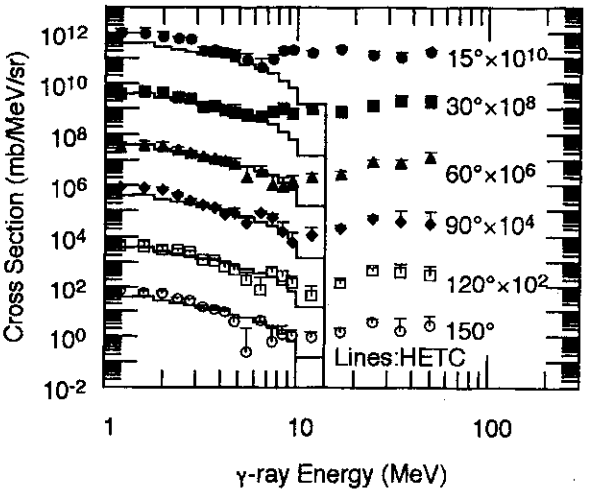

Fig. 7 (c) Gamma-ray spectra for 3.0GeV-proton incidence on Fe.

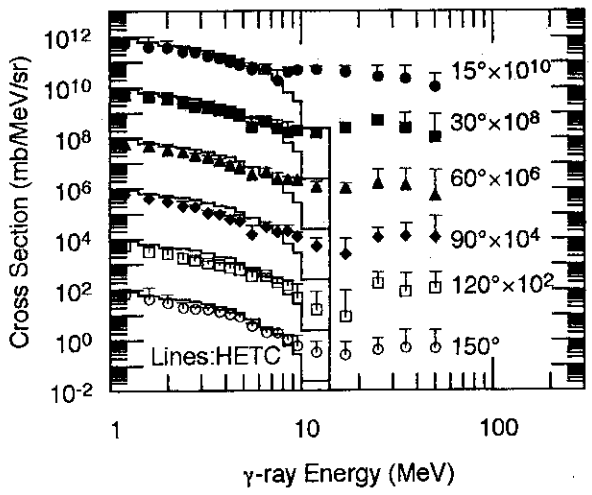

Fig. 8 (a) Gamma-ray spectra for 0.8GeV-proton incidence on In.

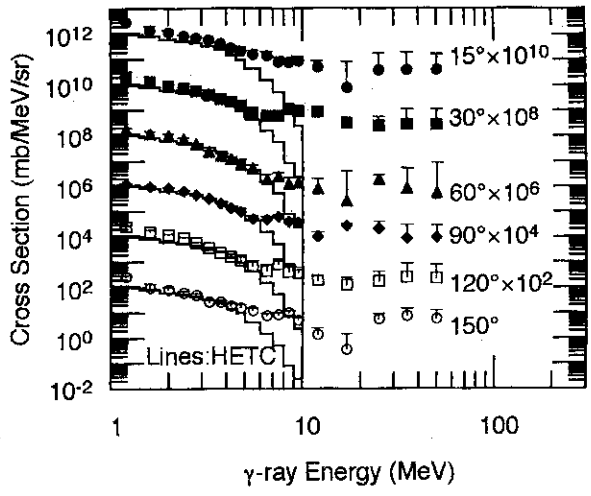

Fig. 9 (a) Gamma-ray spectra for 0.8GeV-proton incidence on Pb.

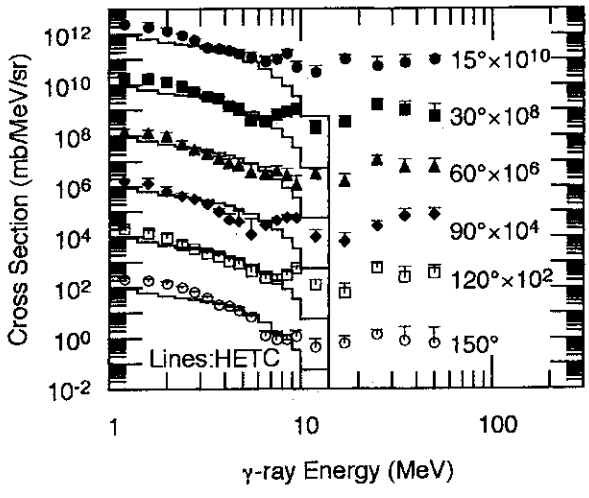

Fig. 8 (b) Gamma-ray spectra for 1.5GeV-proton incidence on In.

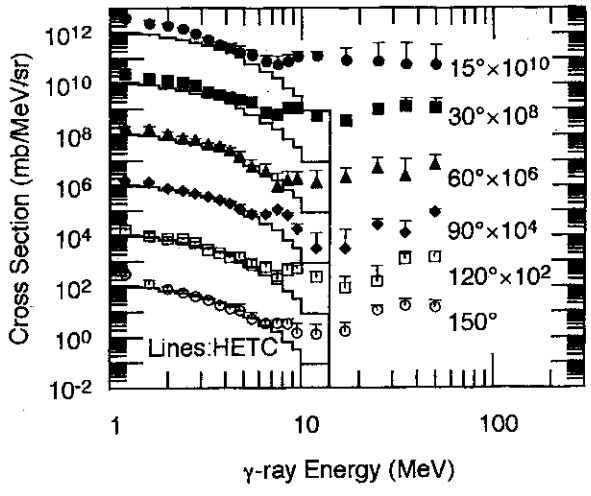

Fig. 9 (b) Gamma-ray spectra for 1.5GeV-proton incidence on Pb.

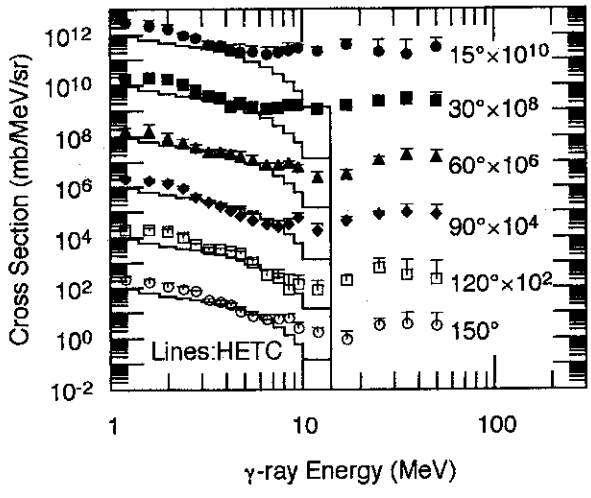

Fig. 8 (c) Gamma-ray spectra for 3.0GeV-proton incidence on In.

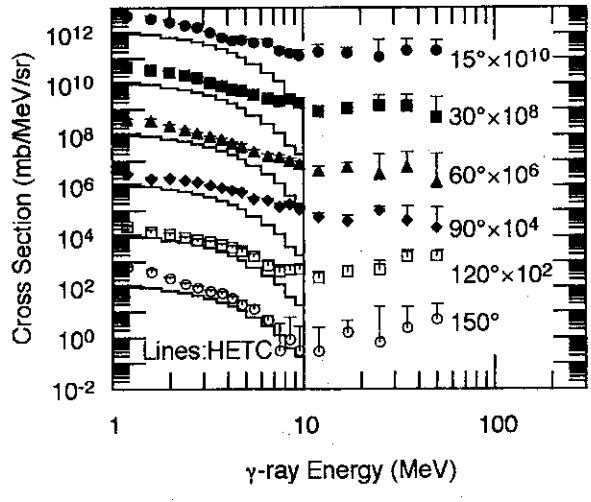

Fig. 9 (c) Gamma-ray spectra for 3.0GeV-proton incidence on Pb.

3.24 Measurement of Nuclear Reaction Cross Sections of Therapeutic Heavy Charged Particles

Akifumi Fukumura, Takeshi Hiraoka, Takehiro Tomitani,
Tatsuaki Kanai, Takeshi Murakami, Shinichi Minohara,
Naruhiro Matsufuji, Hiromi Tomura, Yasuyuki Futami,
Toshiyuki Kohno* and Takashi Nakamura**

National Institute of Radiological Sciences
4-9-1, Anagawa, Inage-ku, Chiba-shi, 263
e-mail: fukumura@nirs.go.jp
(*Tokyo Inst. Tech., **Tohoku Univ.)

We have measured the attenuation of 290 MeV/u carbon beam and 400 MeV/u neon beam due to projectile fragmentation in the target material such as water, polyethylene, PMMA, graphite, aluminum or copper. Using the obtained attenuation data, we also determined the total charge-changing cross section for both beams. The obtained cross section data are in good agreement with both other experiments and the semi-empirical calculation.

1. Introduction

The clinical trial for heavy-ion therapy commences at HIMAC facility in NIRS. Accelerated heavy ions exhibit a flat depth-dose distribution as far as the vicinity of their range, where there is a marked increase in dose, called the Bragg peak. To superimpose this sharp peak over the whole tumor volume, the peak is spread out by the ridge filter and the maximum range is shifted roughly by the range shifter and finely by the three-dimensional bolus, as shown in Fig. 1.

However projectile fragmentation along the beam path in those devices causes an attenuation of the primary particles and may disturb the depth-dose distribution which is essential in the treatment planning.

We have therefore measured the attenuation of carbon and neon beams due to projectile fragmentation as a function of thickness of several target materials. Using the obtained attenuation data, we also determined the total charge-changing cross sections.

2. Material and Method

We measured the attenuation of 290 MeV/u carbon beam and 400 MeV/u neon beam impinging on a target such as water, polyethylene, polymethyl-methacrylate (PMMA), graphite, aluminum or copper. As shown in Fig. 2, we placed the target between two plate-type plastic scintillators along the beam axis. The upstream scintillator was used to count N_0, the number of incoming primary particles. The other was used as a ΔE detector which generated a pulse in accordance with the energy deposited by the particle passing through the detector. Fig. 3 shows an example of the measured ΔE-spectra. One can find many peaks of secondary fragment in the right semi-logarithmic graph. Integrating the peak of primary particle in the spectra, we evaluated N, the number of primaries that survived after passing through the target. Dividing N by N_0 for each target thickness, we obtained the nuclear attenuation of primary beam as a function of target thickness.

3. Results and Discussion

Fig. 4 shows the measured attenuation of carbon and neon beams in copper, aluminum and graphite as a function of target thickness. It also shows the calculation based on the semi-

empirical formulation given by L. Sihver et al [1]. They are in good agreement. One can find different attenuation for each target.

Fig. 5 also shows the attenuations in water, PMMA and polyethylene, which are used as tissue equivalent material, the range shifter and the bolus respectively at HIMAC. The horizontal axis is graduated in water equivalent thickness, which was determined through the range measurement and is the unit used in the treatment planning. In the left graph in Fig. 5 it is found that the attenuations of carbon beam in PMMA and polyethylene agree well with that in water. This means that one can regard PMMA and polyethylene as water equivalent material also in terms of nuclear attenuation of the carbon beam. We therefore find that it is appropriate to select PMMA and polyethylene as stuff of the range shifter and the bolus respectively in the carbon beam therapy. On the other hand, the right graph shows the agreement between them is not so good in case of neon beam compared with carbon beam. One should take this result into consideration when selecting materials of range shifter and bolus for neon beam.

We have also determined the total charge-changing cross sections, $\sigma_{\Delta Z}$, of the carbon and neon beams for the six different target materials from the slope of the measured attenuation using the following relation;

$$\sigma_{\Delta Z}(\text{barn}) = 10^{24} \times \lambda \times A_t / N_A ,$$

where λ, A_t and N_A are the slope in $(g/cm^2)^{-1}$, molecular weight of target material and Avogadro number, respectively. Fig. 6 -11 show that these cross sections in six different target materials were in good agreement with both other experiments [2, 3, 4, 5] and the semi-empirical calculation on the whole.

4. Summary

We have measured the attenuation of 290 MeV/u carbon beam and 400 MeV/u neon beam impinging on a target such as water, polyethylene, PMMA, graphite, aluminum or copper. We find that for the carbon beam it is appropriate to select PMMA and polyethylene as stuff of the range shifter and the bolus respectively also in terms of nuclear attenuation. We also determined the total charge-changing cross section for such beams. The obtained cross section data are in good agreement with both other experiments and the semi-empirical calculation on the whole.

Acknowledgments

This work was performed under Research Project with Heavy Ions at NIRS-HIMAC.

References

[1] L. Sihver, D. Schardt and T. Kanai, to be published.
[2] W. Schimmerling, T. S. Subraminian, W. J. McDonald, S. N. Kaplan, A. Sadoff and G. Gabor, Nucl. Instr. and Meth. 205, 531 (1983)
[3] J. Llacer, J. B. Schmidt and C. A. Tobias, Med. Phys. 17, 158 (1990)
[4] W. R. Webber, J. C. Kish and D. A. Schrier, Phys. Rev. C41, 520 (1990)
[5] I. Schall, Ph. D thesis, Technische Hochschule Darmstadt (1994)

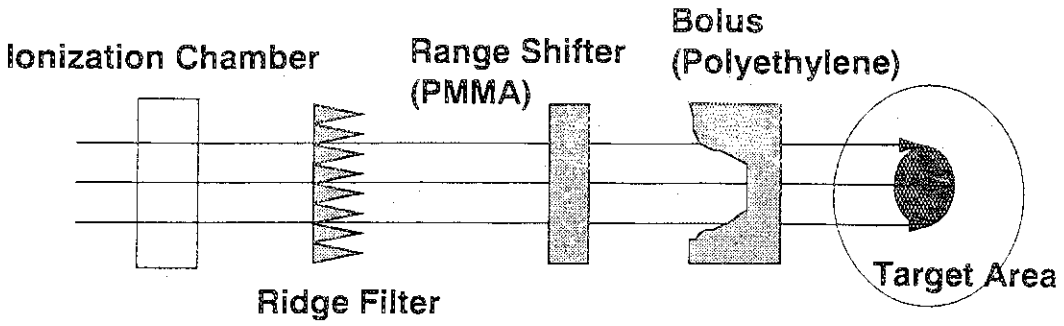

Fig. 1: Schematic Layout of HIMAC Irradiation Facility

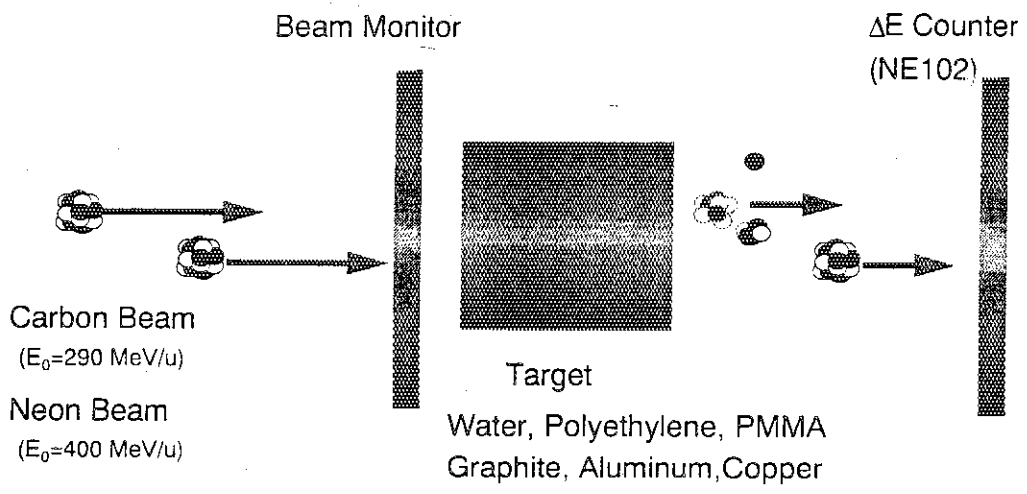

Fig. 2: Experimental Arrangement

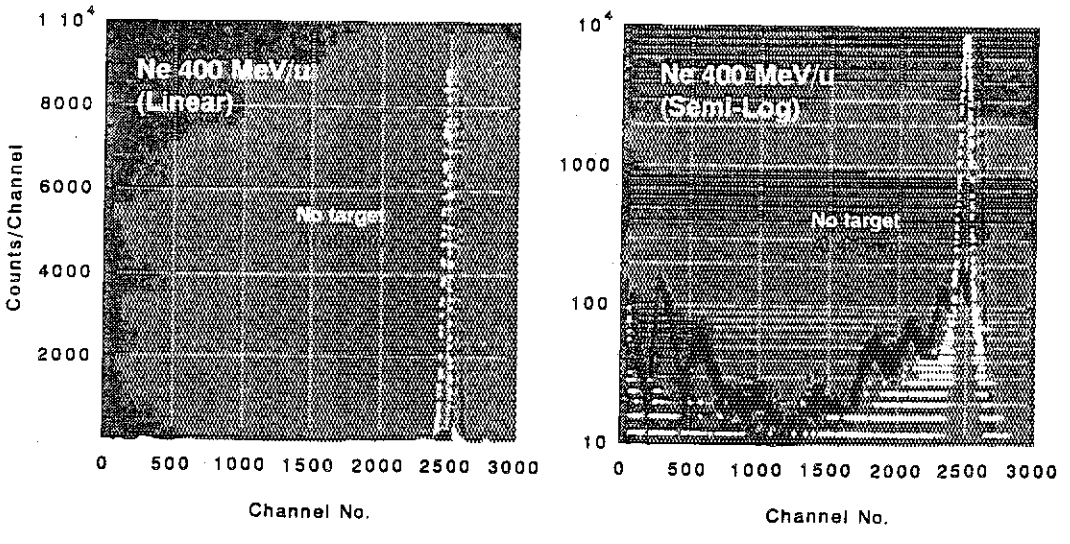

Fig. 3: Pulse Height Spectrum Obtained by ΔE Detector

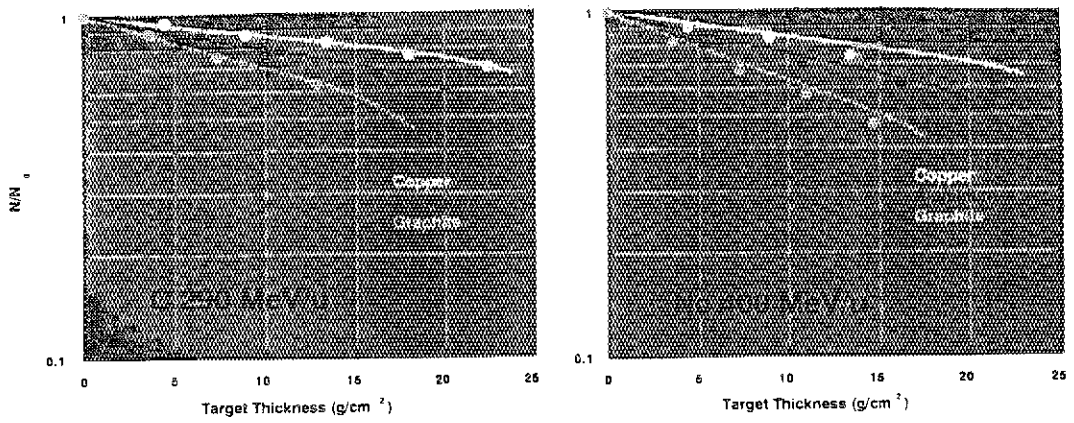

[●This study .....Calculation (L. Sihver et al.)]

Fig. 4: Attenuation of Primary Beam in Copper, Aliminum and Graphite

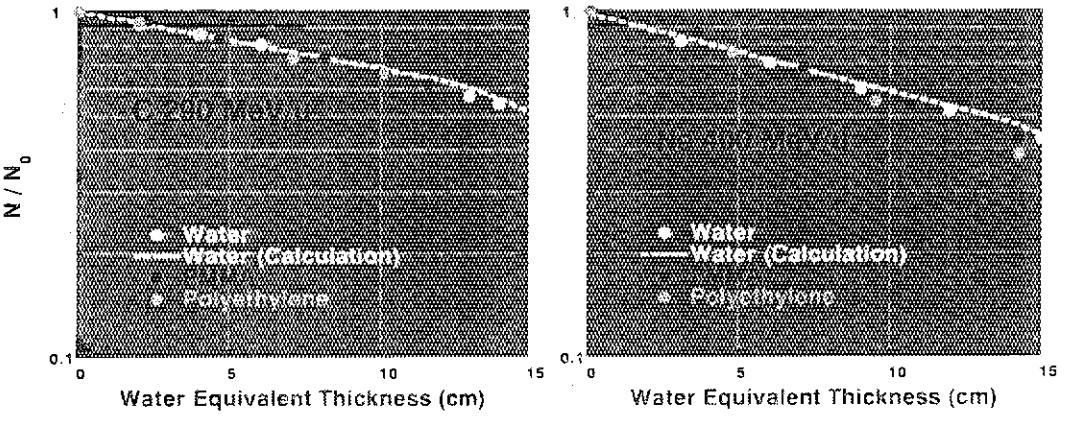

[●This study .....Calculation (L. Sihver et al.)]

Fig. 5: Attenuation of Primary Beam in Water, PMMA and Polyethylene

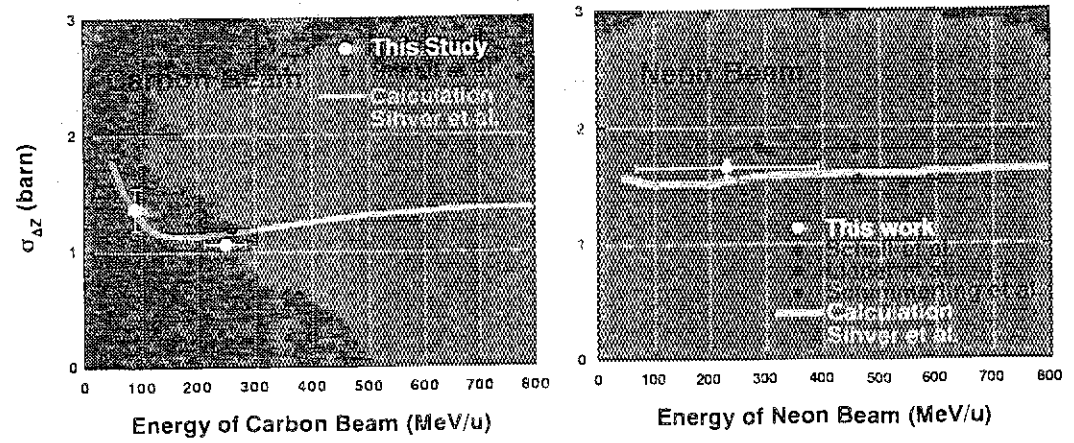

Fig. 6: Total Charge-Changing Cross Section in Water

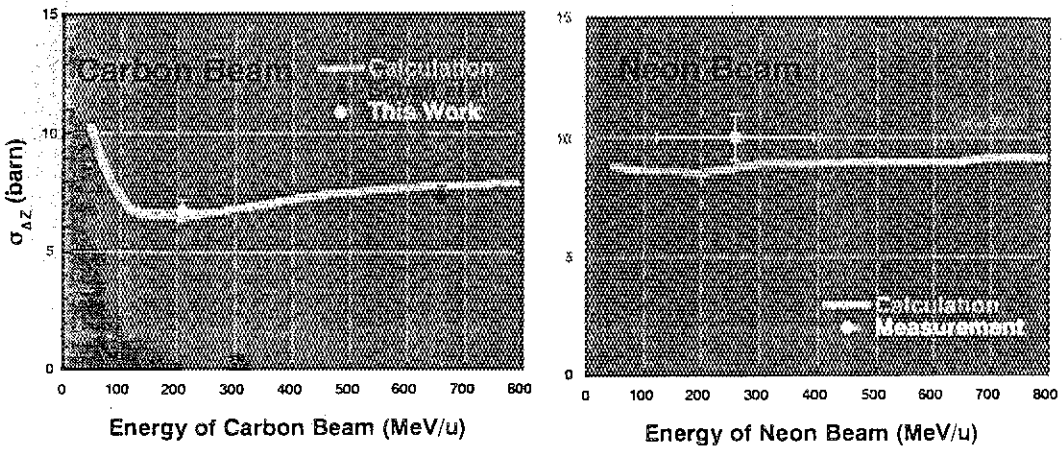

Fig. 7: Total Charge-Changing Cross Section in PMMA

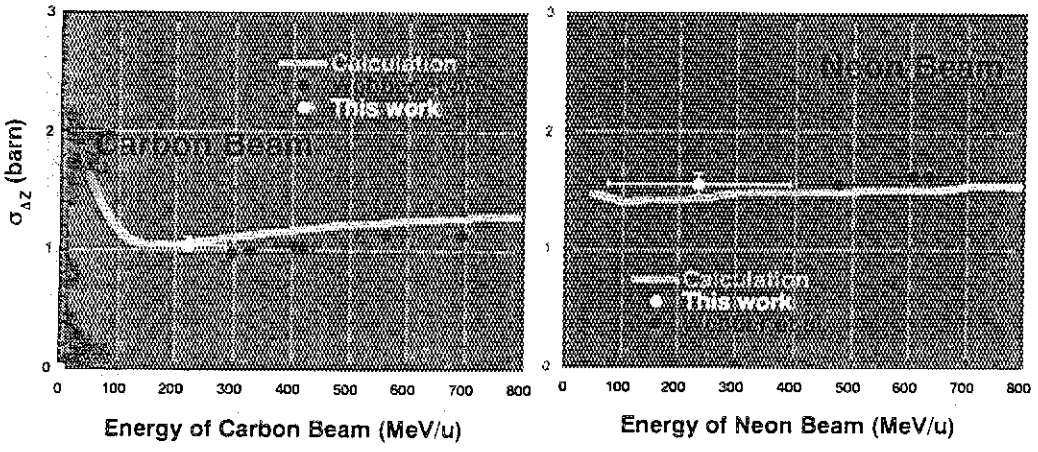

Fig. 8: Total Charge-Changing Cross Section in Polyethylene

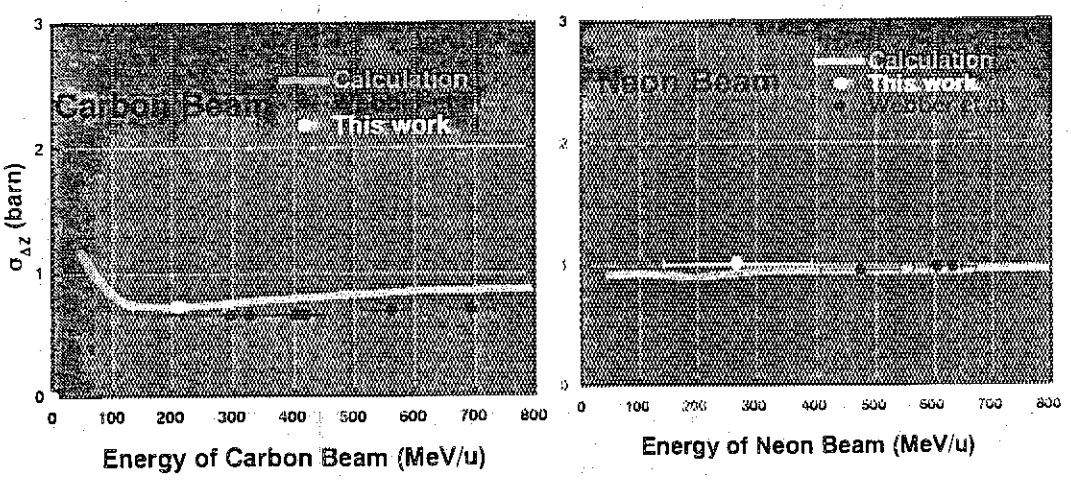

Fig. 9: Total Charge-Changing Cross Section in Graphite

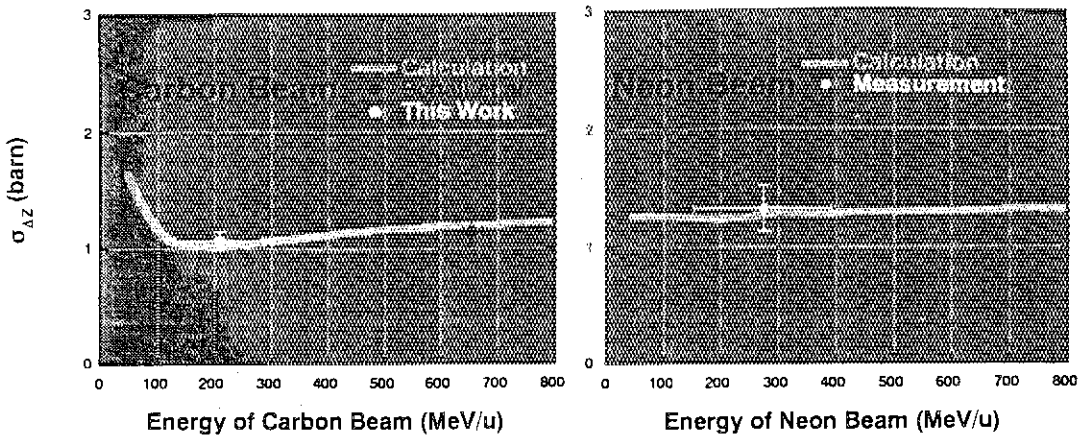

Fig. 10: Total Charge-Changing Cross Section in Aluminum

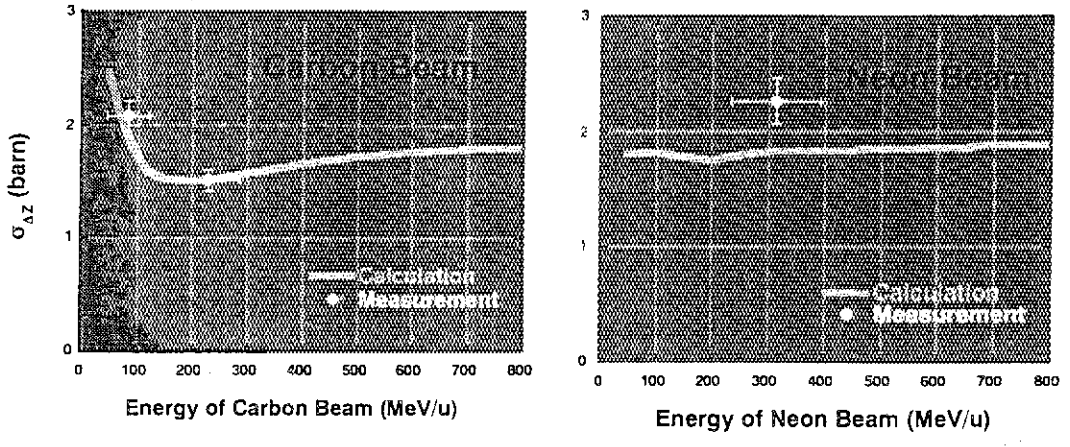

Fig. 11: Total Charge-Changing Cross Section in Copper

3.25 Evaluation of the Dependencies Without Systematic Errors

Nikolay EFIMKIN
Centre for Photonuclear Experiments Data
Institute of Nuclear Physics
Moscow State University

Joint evaluation of energy-dependent cross-sections measured in different experiments is analysed with assumption that systematic errors in energy and cross-section scales have been already removed. At this stage of evaluation the "accumulation of the information" from different experiments must occur. The improvement of energy resolution and/or statistical uncertainty is intuitively expected. The individual apparatus functions from different experiments and the correlations between data points cause the situations when is not evident that the data accuracy is improved. Simple numerical experiment shows that under certain conditions the errors of joint evaluation are larger than the errors of individual evaluation for the same energy resolution. The procedure of the error minimisation developed removes the contradiction with the common knowledge.

1. Introduction

The process of joint cross-section evaluation can be divided by two major stages [1,2]:

1) minimisation of systematic uncertainties of energy and cross-section scales determination, e.g. errors in calibration and normalization;

2) simultaneous evaluation of scales-corrected experimental data sets from various experiments.

The individual apparatus functions and statistical uncertainties are taken into account to improve the energy resolution and statistical accuracy during the second stage.

The process of the energy resolution improvement is well understood[3]. The experimental data (finite dimensional vector ξ) and the cross-section energy dependence (continuous function f) are connected by the expression

$$\xi = \mathbf{A}f + \nu$$

where $\mathbf{A}$ is linear integral operator describing the experimental apparatus function. ν is a statistical uncertainty with covariance matrix Σ.

In order to obtain vector fe with higher energy resolution than that of ξ it is necessary to find operator R, so that

$$fe = \mathbf{R}\xi = \mathbf{U}f + \mathbf{R}\nu$$

Where operator $\mathbf{U}$ provides higher energy resolution than $\mathbf{A}$ does.

To make it possible without any additional information about the cross-section f, the operator **U** must be[4]:

$$\mathbf{U}=\mathbf{U}_0\mathbf{A}^{-}\mathbf{A}.$$

This **U** is the closest possible operator to the operator $\mathbf{U}_0$.

In order to find the highest possible energy resolution the evaluator has to order some high resolution operator $\mathbf{U}_0$, e.g. having Gaussian line-shape. If the **U** corresponding to $\mathbf{U}_0$ has inappropriate shape, e.g. it has oscillations, or **U** is too far from Gaussian $\mathbf{U}_0$, it is necessary to increase the width of the Gaussian. The attempts must be repeated while the shape of **U** does not satisfy the evaluator. As a rule, the operator **U**, having appropriate line-shape still has better resolution than experimental apparatus function **A**.

The highest extractable resolution depends on the shape of experimental apparatus function and the energy step of experimental data. The quasimonochromatic and bremsstrahlung photonuclear experiments were investigated. It is shown that the highest extractable resolution equals to 1.5 and 1 experimental energy step for these kinds of experiments correspondingly.

Therefore: the more data are included into the evaluation, the higher resolution may me achieved. However the resolution improvement up to the highest achievable value makes sense only if statistical errors are small enough or if the joint data evaluation is targeted only on the resolution improvement.

Typically the energy resolution improvement causes dramatic growth of statistical uncertainty. By this reason it was important to investigate, how the statistical accuracy grows for some fixed resolution with adding new data.

2. Numerical Experiment

The model cross-section was taken to have a 10 keV width Gaussian peak, located at 11.11 MeV. Both bremsstrahlung and quasimonochromatic yields were simulated with energy step 50 keV . The line-width of quasimonochromatic apparatus function was 330 keV. The highest extractable resolution for simultaneous evaluation in this case has been found to be 40 keV due to the effective experimental energy step. The yields were recalculated to the resolution 150 keV. The statistical error of the cross-section maximum was 1.4 a.u. for both results. The cross section error was naturally expected to be about 1 a.u. for the joint evaluation. The result for joint evaluation was 2 in reality.

Afterwards the results of separate evaluation were simply averaged. The error turned out to be 1 as expected. This was the reason of careful investigation of the apparatus functions **U** resulted in each case. The apparatus functions $\mathbf{U}_1$ for bremsstrahlung case, $\mathbf{U}_2$ for quasimonochromatic case, $(\mathbf{U}_1+\mathbf{U}_2)/2$ - average between $\mathbf{U}_1$ and $\mathbf{U}_2$ and $\mathbf{U}_j$ for joint evaluation were very close to each other and could not be distinguished by eye. Meanwhile they were different.

3. Explanation

Each of operators U_1, U_2, $(U_1+U_2)/2$ and U_j are closest to U_0, which is Gaussian with the width 150 keV. However they belong to different subspaces. The subspace which U_j of joint evaluation belongs to has larger dimension, than all the rest. Therefore it can be obtained to be closer to U_0. The requirement to be closest to U_0 does not have to match the requirement of the minimisation of the statistical error of the cross-section.

4. Data presentation

We choose U_0 to be Gaussian. Gaussian does not have asymmetries, tails etc., which make data interpretation more complicated. Other line-shapes, such as rectangular, are also often used. We can pose a problem as a minimisation of the statistical error making small deviations from Gaussian line-shape possible.

The procedure employing conjugated gradient method and penalty functions controlling the width and the proximity to Gaussian inside the thin gap around it has been developed. As a result we succeeded to make statistical error 0.9 a.u., that is 10% less than the error after averaging. At the same time the resulting apparatus function U was not separable by eye from Gaussian (Fig.1).

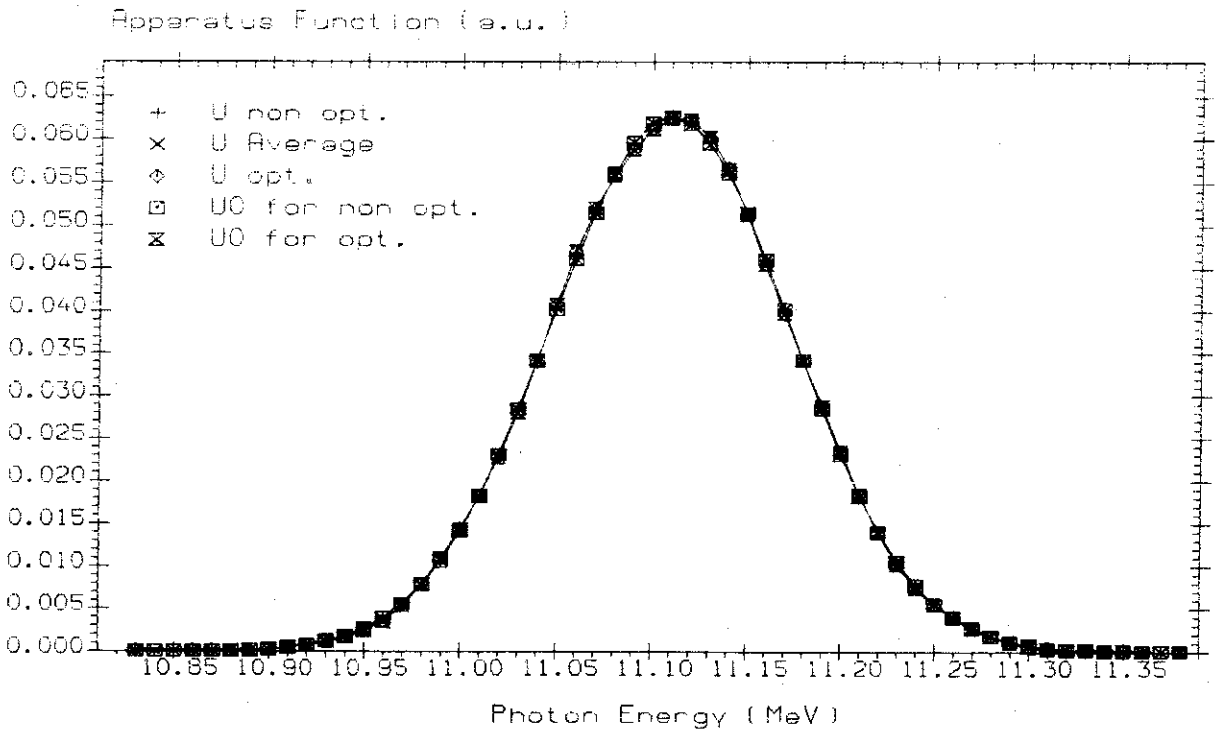

Fig.1. Apparatus functions of evaluated data.
U for non optimised joint evaluation;
U Average from separate evaluations of Bremsstrahlung and Quasimonochromatic data sets;
U for optimised joint evaluation;
U0 for non optimised joint evaluation (Gaussian);
U0 for optimised joint evaluation (slightly different from Gaussian).

The total errors, calculated as

$$\mathbf{tr(R\Sigma R^*)}$$

were essentially reduced after optimisation.

The results of evaluation are shown at Figs.2-5. The curve "Model" is the model cross-section folded with the Gaussian apparatus function with the energy resolution 150 keV. The points with the error bars are:
the evaluation results of Bremsstrahlung and Quasimonochromatic data sets separately (Fig.2);
joint evaluation without optimisation (Fig.3);
evaluation by averaging separate Bremsstrahlung and Quasimonochromatic results (Fig.4);
joint evaluation with optimised apparatus function U_0 (Fig.5).

5. Conclusion

The statistical accuracy of the evaluated data strongly depends on the quality of the apparatus function with which the evaluation result is obtained. The hunt for the proximity of apparatus function to the Gaussian line-shape may result in too large statistical errors of the cross-section. If small deviations from the Gaussian line-shape are allowed the statistical error can be essentially reduced.

Acknowledgements

Author is grateful to Drs. V.V.Varlamov, B.S.Ishkhanov, Yu.P.Pytiev M.E.Stepanov of the Moscow State University for help and attention to this work.

Author thanks Drs. Ya. Kikuchi, T.Fukahori, S.Chiba of the Japan Atomic Energy Research Institute for invitation and help in participation in the 95 NDS.

References

[1] Varlamov V.V., Efimkin N.G., Ishkhanov B.S.: "Simultaneous Analysis of Discrepant Photonuclear Data", Proc. Int. Conf. on Nuclear Data for Science and Technology, May 9-13, 1984, Gatlinburg, USA, p.662 (1994, American Nuclear Society)

[2] Efimkin N.G., Varlamov V.V.: "Photonuclear Data File Development Strategy", Proc. Int. Conf. on Nuclear Data for Science and Technology, May 9-13, 1984, Gatlinburg, USA, p.702 (1994, American Nuclear Society)

[3] Efimkin N.G., Rodionov D.A., Stepanov M.E: "Comparative Analysis of Mathematical Tools for Spectrometer resolution Improvement", Proc. Int. Conf. on Nuclear Data for Science and Technology, May 9-13, 1984, Gatlinburg, USA, p.662 (1994, American Nuclear Society)

[4] Efimkin N.G., Ishkhanov B.S., Pytiev Yu.P.: "Method of Reduction in the Problem of Resolution Improvement of Photonuclear Experiments", Vestnik Moskovskogo Universiteta. Fizika. Astronomia. v32, p.48 (1991).

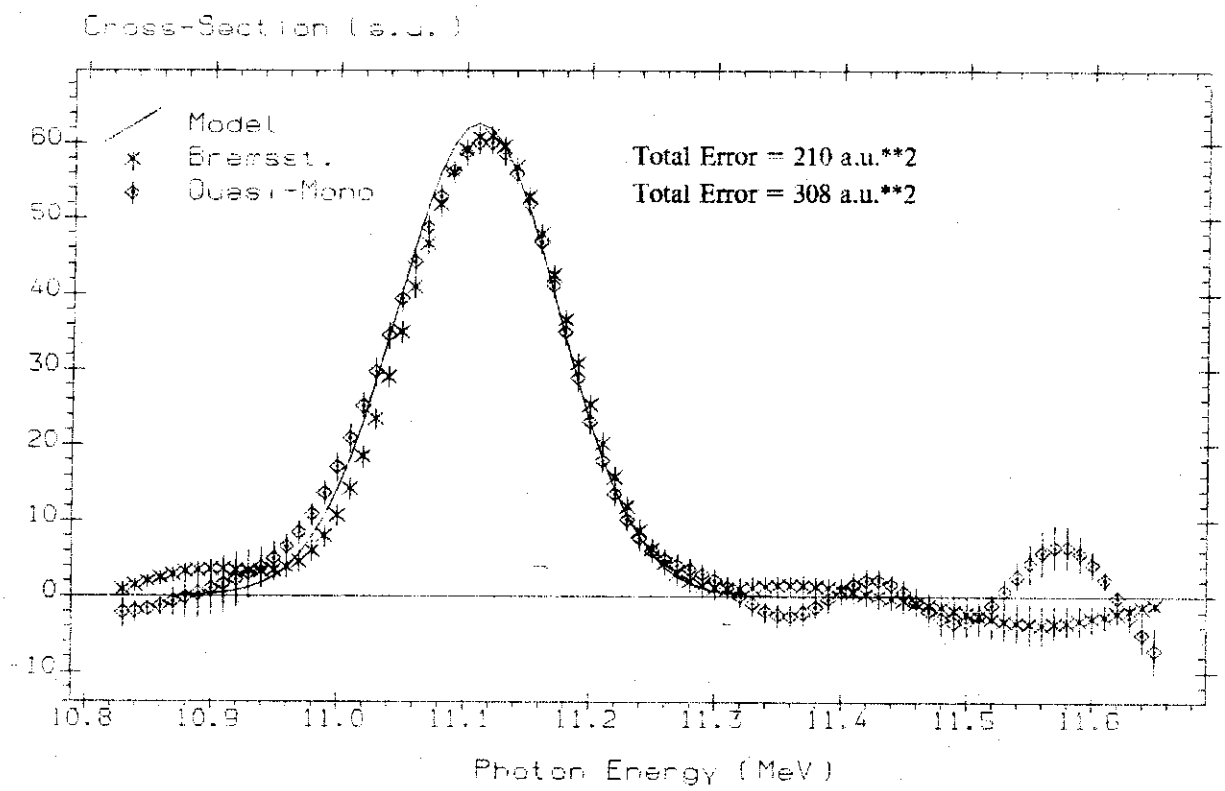

Fig.2. Separate evaluation of Bremsstrahlung and Quasimonochromatic data sets.

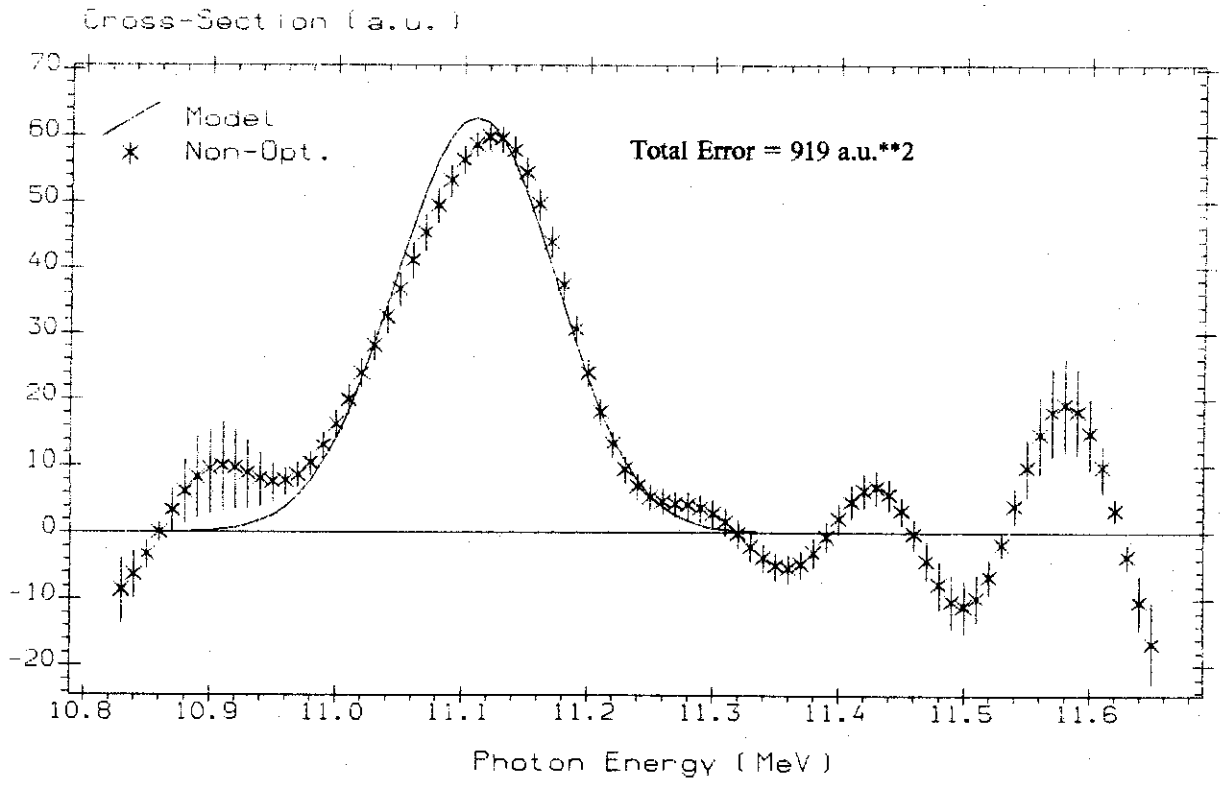

Fig.3. Joint evaluation. The data are recalculated to the apparatus function closest to Gaussian.

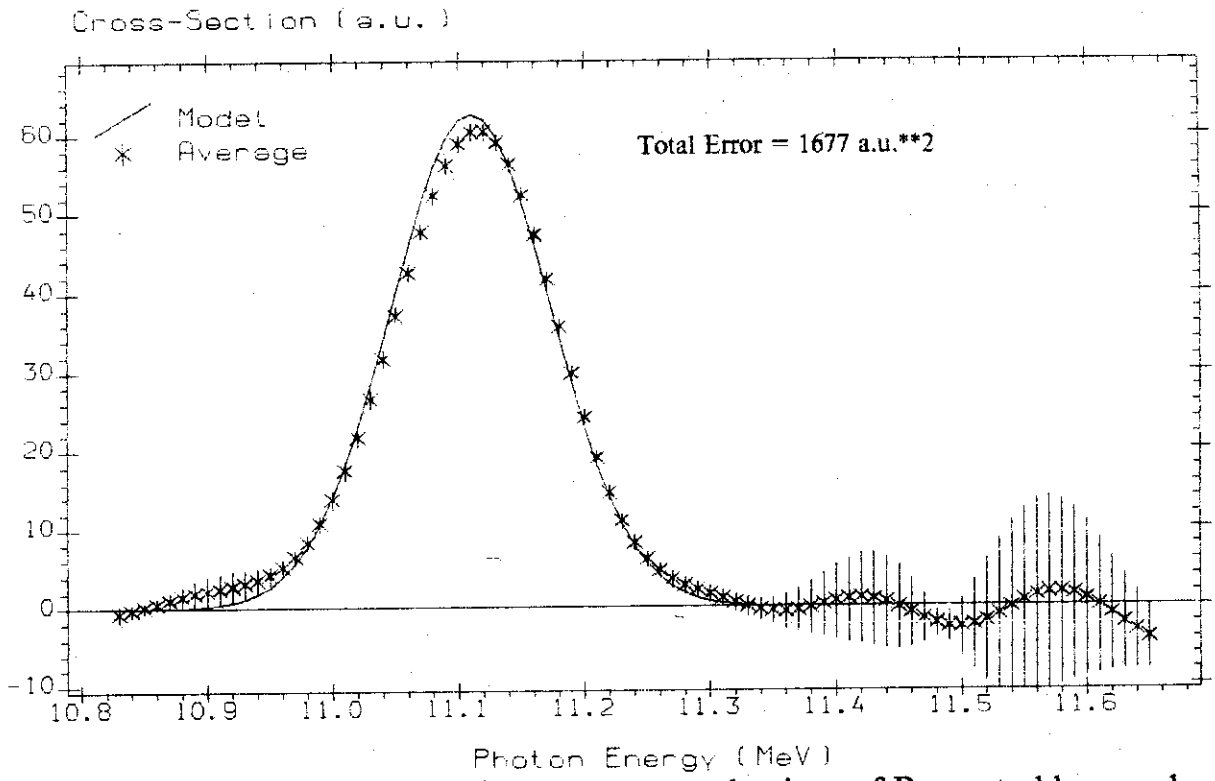

Fig.4. Joint evaluation. Average from separate evaluations of Bremsstrahlung and Quasimonochromatic data sets.

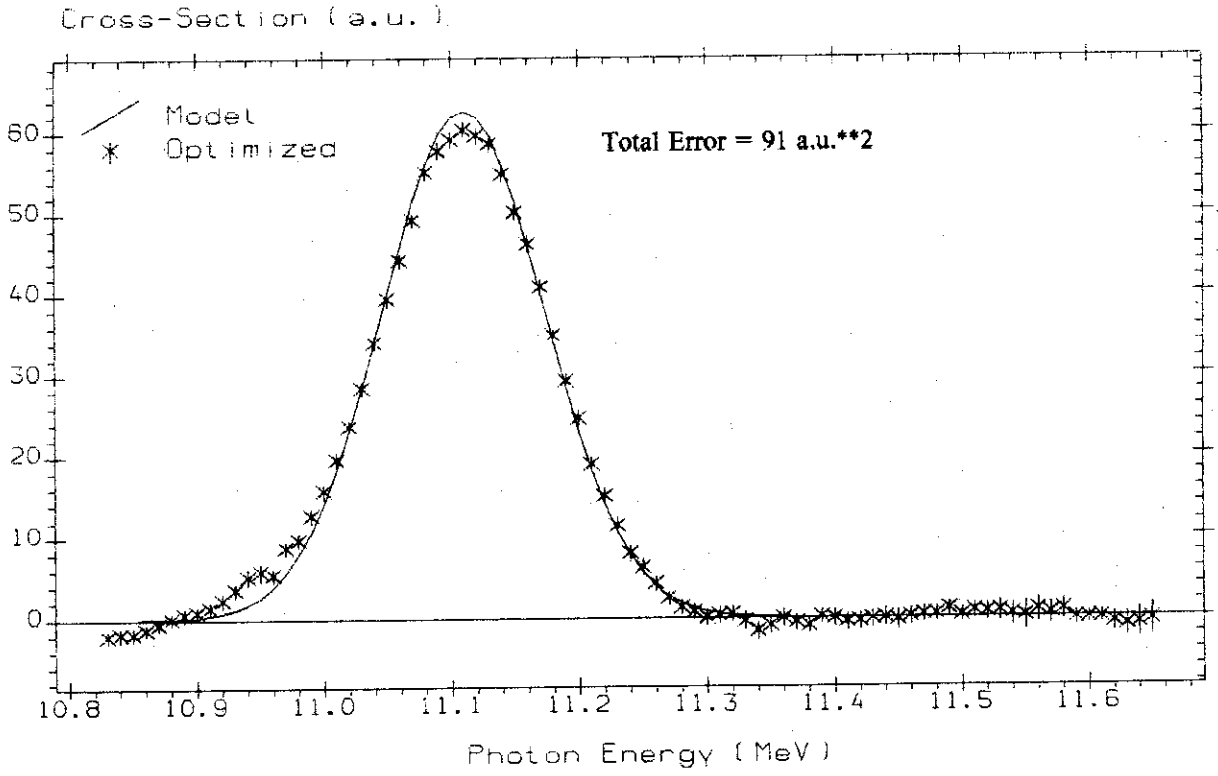

Fig.5. Joint evaluation. The data are recalculated to the apparatus function which is allowed to be slightly different from the Gaussian.

3. 26 Nuclear data evaluation for ^{12}C in the energy region more than 20 MeV and kerma factor calculation

M. Harada[1], Y. Watanabe[2] and S. Chiba*[3]
Department of Energy Conversion Engineering, Kyushu University, Kasuga, Fukuoka 816
**Japan Atomic Energy Research Institute, Tokai-mura, Naka-gun, Ibaragi 319-11*

We have developed a practical code system to calculate double differential cross sections of all emitted particles and kerma factors for the n+^{12}C reaction in the energy region from 20 to 80 MeV, and compared the results calculated using the code system with experimental data. As a result, it has been found that the code system is applicable to nuclear data evaluation of ^{12}C in JENDL high energy file.

1. Introduction

Intermediate energy nuclear data for ^{12}C are requested with high priority in several applied fields, such as accelerator-based transmutation and radiation therapy using fast neutron or proton beam[1]. In particular, double differential cross sections (DDXs) of all emitted particles are required to calculate the transport of secondary particles generated from reactions with ^{12}C and the energy deposit of incident neutron in matter. Some progress has recently been made in the measurement of DDXs[2,3] for neutron-induced reactions, but there is still not sufficient compared with the data for energies below 20 MeV. Moreover, the theoretical model calculation for light nuclei has not been so well-established as for medium-heavy nuclei because many-body breakup processes, such as simultaneous 3α decay process, are involved in the n+^{12}C reaction. Therefore, it is necessary to establish a reliable model for nucleon-induced reactions on ^{12}C from the viewpoint of the evaluation of intermediate energy nuclear data.

The aim of the present work is to develop a practical code system to calculate DDXs of all emitted particles (n, p, d, t, ^3He, α, and heavier reaction products) and neutron kerma factors in the energy region from 20 and 80 MeV. The major part of the code consists of a Monte Carlo simulator of the n+^{12}C reactions based on the SCINFUL code[4] which is used for neutron efficiency calculations for organic scintillators. Using this computational method, we can take into account many-body breakup processes such as the (n,n')3α process in a simple way and the energy conservation in the kerma factor calculation correctly even for the reaction process including simultaneous many-body breakup emission. The first version of the code system was reported and its applicability to nuclear data evaluation was demonstrated[5]. Afterwards, we have re-evaluated the major cross sections (total cross section, total reaction cross section, and elastic cross section)[6,7], and have improved the code system to reproduce consistently well the experimental data for DDXs and kerma factors.

In Sec. 2, the code system is outlined and some improvements on the input data and modification of the code are described. In Sec. 3, we present some of the calculated DDXs as well as calculated kerma factors and compare them with experimental data. Finally, we summarize the present work and mention the future prospect in Sec. 4.

[1]Email address : *harada@ence.kyushu-u.ac.jp*
[2]Email address : *watanabe@ence.kyushu-u.ac.jp*
[3]Email address: *chiba@cracker.tokai.jaeri.go.jp*

2. The code system

2.1 Outline of the code system

The n+^{12}C reaction processes can be classified by combination of nine primary reaction processes and the following sequential or simultaneous decay processes as shown in Fig. 1. As the primary reaction, elastic scattering, inelastic scattering to the first 2^+ state, (n,n')3α, (n,p), (n,d), (n,t), (n,α), (n,^{3}He), and (n,2n) are included in the present calculation. Consequently, total 35 processes of the n+^{12}C reaction are taken into consideration as in the SCINFUL code[4].

A schematic flow chart of our code system is shown in Fig. 2. The code system is divided into two major parts. The first part (i) simulates the n+^{12}C reaction using a Monte Carlo method based on the SCINFUL code. In the simulation, the cross section for each primary reaction, the angular distribution for each emitted particle in the primary reaction and branching ratios of the following decay processes are needed as the input data. Using a Monte Carlo approach with these data and the two-body or three-body kinematics, the energy and angle of all emitted particles are calculated event by event and are stored as output information. Then, the simulation result is used as an input data for the next parts (ii) which calculate DDXs, energy differential cross sections, production cross sections and kerma factors.

2.2 Modification and improvement

Several problems were found in the cross section data of ^{12}C used in the original SCINFUL code[3]. The data of the original SCINFUL are compared with the experimental data of total, elastic and reaction cross section in Fig. 3. The original SCINFUL data of total and reaction cross section underestimate the experimental data in the whole energy region. In addition, the maximum order of the Legendre coefficients for elastic and inelastic(2^+) angular distribution is limited to the sixth order in the original SCINFUL. Because of this limitation, the original SCINFUL code cannot reproduce well the forward-peaked experimental data as the incident energy increases. Therefore, we have replaced elastic scattering, inelastic(2^+) scattering cross sections, those angular distributions and total reaction cross section by our newly evaluated values [6,7] which are represented by the solid line in Fig. 3.

In addition, we have modified the first version of the code[5] so that the three-body simultaneous breakup (3BSB) process[8] (n+^{12}C -> n+ α + ^{8}Be) can be considered. This modification leads to improvement of the energy spectra of neutron and α particle emitted with intermediate outgoing energies. Kalbach systematics[9] is also applied to reproduce the forward-peaked angular distributions of light mass particles emitted from the primary reactions. Note that the angular distributions of all particles emitted in the following secondary stage are assumed to be isotropic.

3. Results and discussion

Calculated energy spectra of the (n,n') reaction at 40 MeV are compared with experimental (p,p') data in Fig. 4. The dotted line represents the result with the input data used in the original SCINFUL code. Remarkable underestimation seen at intermediate outgoing energies is obviously improved by the present calculation. This is due to the inclusion of the 3BSB process mentioned above.

Figure 5 shows comparisons of calculated DDXs of (n,xα) at 39.7 MeV, (n,xp) and (n,xd) reactions at 42.5 MeV with the experimental data as a typical sample. The calculated DDXs for the (n,xα) reaction are in good agreement with the experimental data. Whereas the calculated DDXs of the (n,xp) and (n,xd) reaction underestimate the experimental data in the high outgoing energy region. The similar results are obtained for other incident energies.

Figure 6 shows a comparison of the calculated total kerma factors with the experimental data. The dotted line (a) represents the result with the first version of our code[5] in which the original SCINFUL is used for all input data. The dash-dotted line (b) is the result of the calculation in which only total reaction cross section and elastic scattering cross section are replaced by our newly evaluated data and other input quantities and reaction

processes considered are same as those used in the original SCINFUL. The solid line (c) is the result with the present improved version. Both results of (a) and (c) are in agreement with the experimental data to similar extent. On the other hand, the calculation (b) shows overestimation at energies less than 70 MeV. The overestimation is mainly because the average kinetic energy of the recoil nucleus ^{12}C is overpredicted by use of incorrect elastic angular distribution and the 3BSB process is not included in the original SCINFUL. Although the result of (a) sounds good, the total reaction cross section used in the calculation are about 20% smaller than the experimental data as shown in Fig. 3 and the energy spectrum of emitted neutrons shows underestimation in the intermediate outgoing energy region as shown in Fig. 4. From these considerations, therefore, we find that the improvement made in the present work is essential to obtain a consistent description of both DDXs and kerma factors.

The calculated partial kerma factors of emitted particles are shown in Fig. 7. For low incident energies, the contribution of α particles from the (n,n')3α reaction is the largest and amounts to about 60 % at 30 MeV. As the incident energy increases, it decreases gradually and the contributions from protons and deuterons become important and amount to about 60 % of the total kerma factor at 80 MeV.

4. Summary

We have developed an improved version of the code system to calculate both DDXs of all emitted particle and kerma factors for the n+^{12}C reaction in the incident energy region from 20 to 80 MeV. The DDXs calculated with the improved version were in better agreement with the experimental data than the result of the previous version, especially for neutron emission. Also the calculated kerma factors was found to reproduce the experimental data well within the error. The calculated DDXs for all emitted particles and heavy recoiled nuclei are scheduled to be stored in JENDL high energy file. The task is now in progress. This code system is also applicable to proton-induced reactions. In the future, we plan to start proton nuclear data evaluation of ^{12}C for energies up to 200 MeV using this code system.

Acknowledgment

The authors wish to thank Dr. I. Slypen for providing the numerical data of their latest experiments of (n,p), (n,d), (n,t), and (n,α) reactions on ^{12}C.

References

[1] A. J. Koning, "Requirements for an evaluated nuclear data file for accelerator-based transmutation", ECN-C-93-04 (1993).
[2] I. Slypen et al., Nucl. Instr. & Method, **A 337**, 431 (1994); I. Slypen et al., Phys. Med. Biol., **40**, 73 (1995).
[3] M. Baba et al., Proc. Int. Conf. on Nuclear Data for Science and Technology, Gatlinburg, Tennessee, USA, May 9-13, 1994, Ed. J. K. Dickens (1994), p.90.
[4] J. K. Dickens, ORNL-6402, Oak Ridge National Laboratory (1988).
[5] Y. Watanabe et al., Proc. Int. Conf. on Nuclear Data for Science and Technology, Gatlinburg, Tennessee, USA, May 9-13, 1994, Ed. J. K. Dickens (1994), p.574.
[6] S. Chiba et al., Proc. of the 1993 Nuclear Data Symp., JAERI-M 94-019 (1994), p.300.
[7] S. Chiba and M. Harada, submitted to J. Nucl. Sci. and Tech.(1995).
[8] B. Antolkovic and Z. Dolenec, Nucl. Phys. **A237**, 235 (1977); B. Antolkovic, Proc. Int. Conf. on Nuclear Data for Science and Technology, Jülich, Germany, May 13-17, 1991, Ed. S. M. Qaim (Springer-Verlag, 1992), p.594.
[9] C. Kalbach, Phys. Rev. C **37**, 2350 (1988).

(1) n + ^{12}C -> n + ^{12}C (elastic)
(2) n + ^{12}C -> n' + ^{12}C (2^{+})
(3) n + ^{12}C -> α + ^{9}Be
(4) n + ^{12}C -> n' + 3α
(Sequential decay, 3BSB)
(5) n + ^{12}C -> p + ^{12}B
p + α + ^{8}Li
p + n + ^{11}B
p + n + α + ^{7}Li
p + 2n + ^{10}B
p + 2n + α + ^{6}Li
p + 2n + d + 2α
p + n + t + 2α
2p + ^{11}Be
2p + n + ^{10}Be
2p + 2n + ^{9}Be
(6) n + ^{12}C -> d + ^{11}B
d + α + ^{7}Li
d + n + ^{10}B
d + n + p + ^{9}Be
d + n + α + ^{6}Li
2d + n + 2α
(7) n + ^{12}C -> 2n + ^{11}C
2n + p + ^{10}B
(8) n + ^{12}C -> t + ^{10}B
t + p + ^{9}Be
t + d + 2α
t + α + ^{6}Li
t + p + n + 2α
t + p + d + ^{7}Li
(9) n + ^{12}C -> ^{3}He + ^{10}Be
^{3}He + n + ^{9}Be
^{3}He + 2n + 2α
^{3}He + n + p + ^{8}Li
^{3}He + 2n + p + ^{7}Li
^{3}He + 2n + p + t + α

Fig. 1: All reaction processes of n+^{12}C

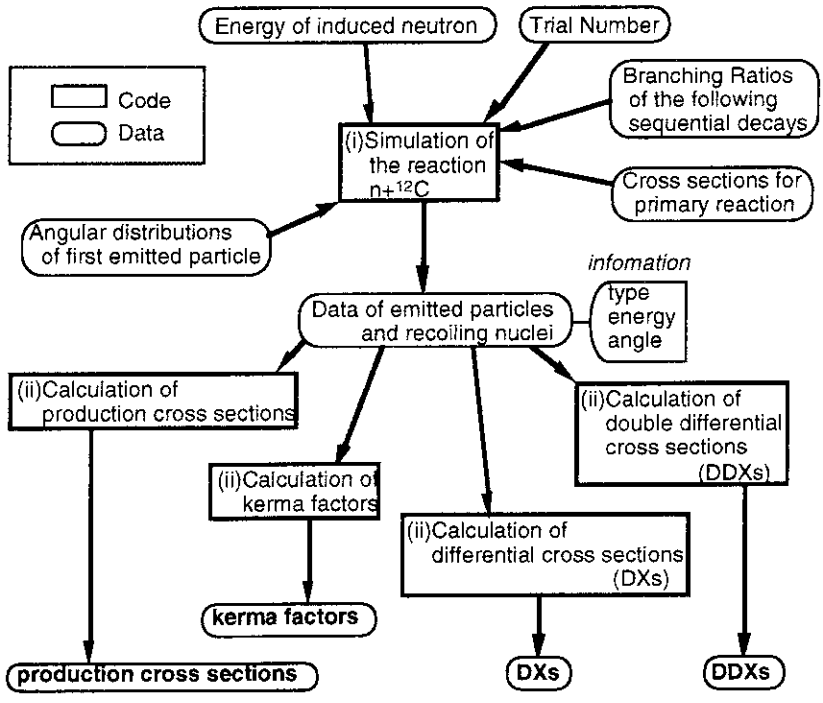

Fig. 2 : Schematic flow chart of the present code system

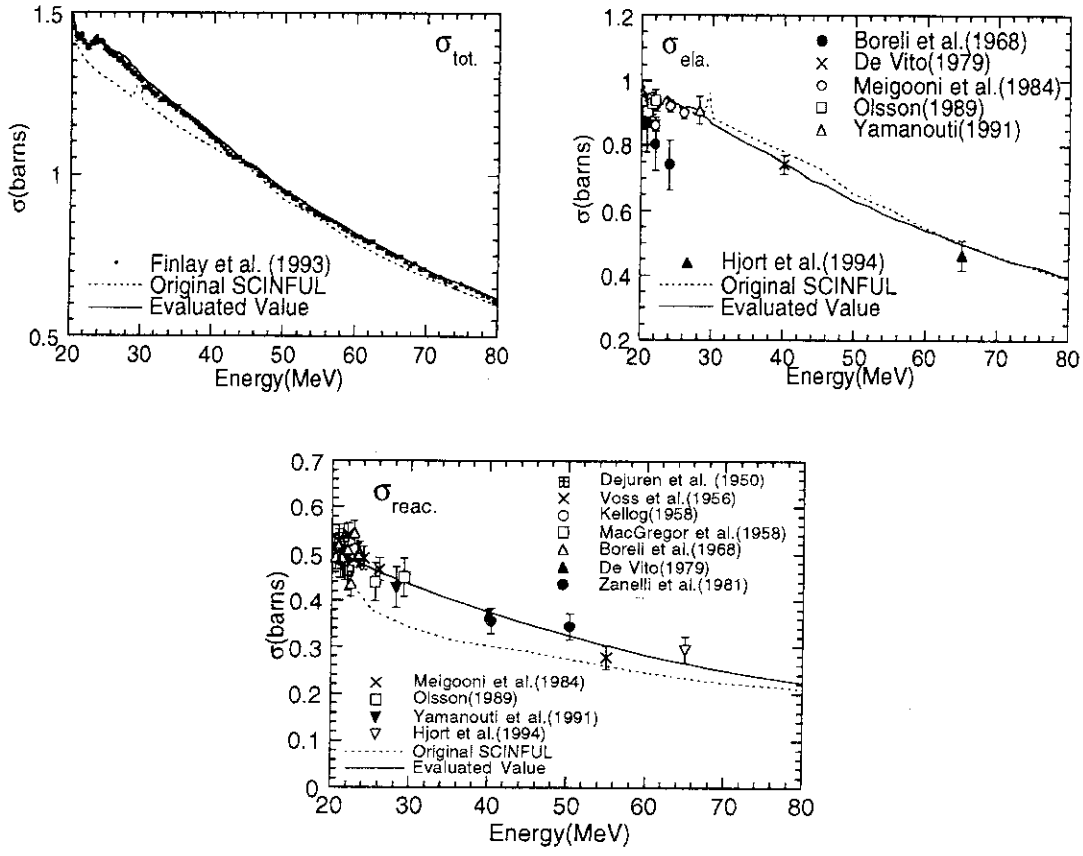

Fig. 3 : Total, elastic and reaction cross section

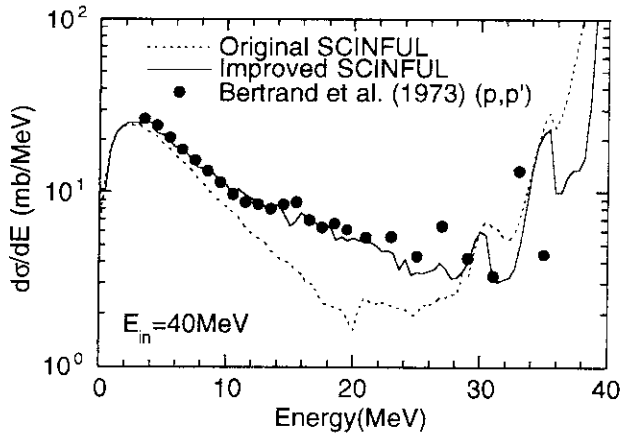

Fig. 4 : Calculated energy differential (n,n') cross sections and experimental (p,p') data

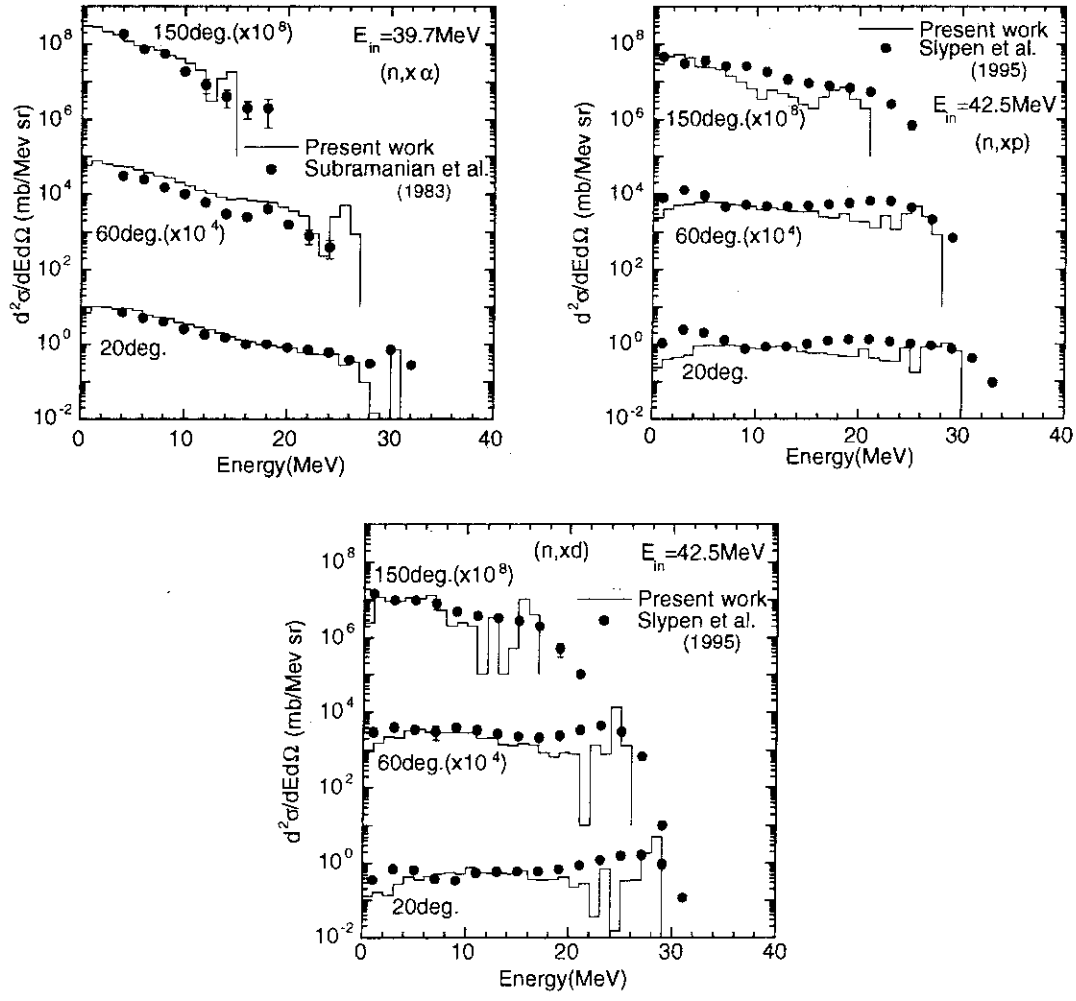

Fig. 5 : Comparison of calculated DDXs of (n,xα), (n,xp) and (n,xd) reaction with experimental data

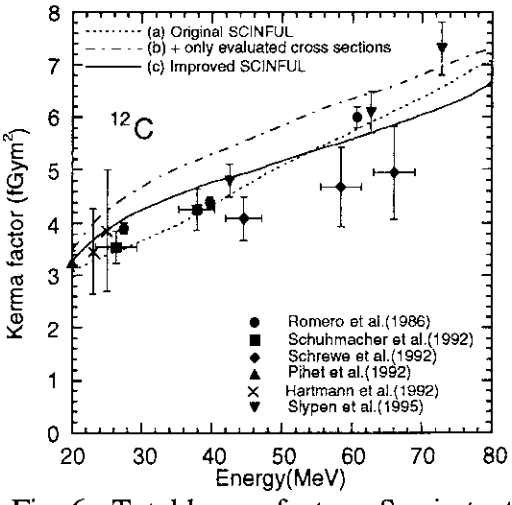

Fig. 6 : Total kerma factors. See in text for explanation of each line.

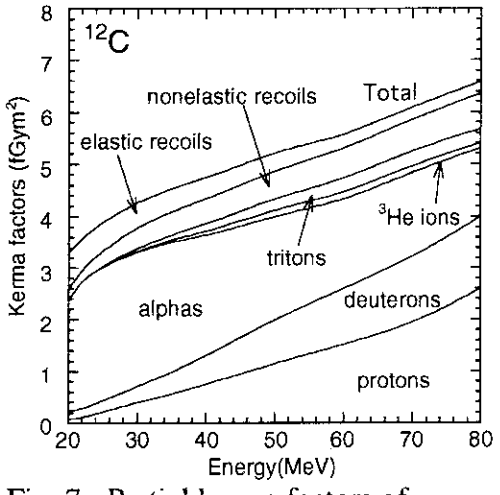

Fig. 7 : Partial kerma factors of emitted particles

3. 27 Semi-Classical Distorted Wave Model Analysis of (p,p'x) and (p,nx) Reactions at Intermediate Energies

Y. Watanabe[1], H. Shinohara[2], M. Higashi, and M. Kawai*

Department of Energy Conversion Engineering, Kyushu University
Kasuga, Fukuoka 816
**Department of Physics, Kyushu University, Fukuoka 812*

Present status of Semi-Classical Distorted Wave (SCDW) model to describe multistep direct (p,p'x) and (p,nx) processes for intermediate energies is reported with particular attention to the effect of in-medium nucleon-nucleon scattering cross sections on the SCDW calculation.

1. Introduction

In nucleon-induced reactions for energies of more than tens of MeV, multistep direct (MSD) processes to continuum becomes dominant and the energy spectra with smoothly forward-peaked angular distributions are observed in intermediate outgoing energy region. Analyses of the MSD processes have recently been made using quantum-mechanical statistical models (FKK[1], TUL[2] and NWY[3]) and microscopic simulation methods (QMD[4] and AMD[5]). As an alternative approach, we have proposed a Semi-Classical Distorted Wave (SCDW) model[6] which is based on DWBA series expansion of T-matrix as in the quantum-mechanical statistical models. Under some semiclassical approximation and assumptions, the double differential MSD cross section can be expressed in a simple closed-form which allows us a straightforward intuitive interpretation like the intra-nuclear cascade(INC) model.

So far, we have applied the SCDW model to analyze the 1- and 2-step processes in (p,p'x) and (p,nx) reactions for incident energies up to 200 MeV and compared with other MSD models[7,8]. In these analyses, we have used in-medium NN cross sections given by Li-Machleidt[9] to describe nucleon-nucleon scattering inside the nucleus and found that in-medium effect on nucleon-nucleon scattering plays an essential role to reproduce experimental data satisfactorily. In the present work, we calculate in-medium NN cross sections using the g-matrix calculated in the non-relativistic Brueckner-Hartree-Fock(BHF) approach[10] with a realistic N-N force in order to make comparisons with those by Li-Machleidt[9] and the others. Through the comparison, the effect of in-medium NN cross sections on the SCDW model calculation is discussed.

2. Semi-Classical Distorted Wave Model

2.1 Outline of the SCDW model

The SCDW model is based on DWBA series expansion of the T-matrix and its energy average in a given energy bin of the exit channel. In this model, the following assumptions and approximations are used; the assumption of the local density Fermi gas model for nuclear states, a local semi-classical approximation to the distorted waves, and Eikonal approximation to the intermediate state Green functions. Thus, the cross section of each step of MSD

[1]Email address : watanabe@ence.kyushu-u.ac.jp
[2]Present address: Hitachi Works, Hitachi, Ltd., Hitachi, Ibaraki 317

processes can be expressed in a simple closed form in terms of (a) the distorting potentials, (b) the nucleon-nucleon scattering cross sections in the nuclear medium (the in-medium NN cross sections), and (c) the nucleon density distribution as follows:

$$\left(\frac{\partial^2\sigma}{\partial\varepsilon_f\partial\Omega_f}\right)^{(1step)} = \left(\frac{A}{A+1}\right)^2 \int d\mathbf{r}_1 \frac{k_i(\mathbf{r}_1)/k_i}{k_f(\mathbf{r}_1)/k_f} \left|\chi_f^{(-)}(\mathbf{r}_1)\right|^2 \left[\left(\frac{\partial^2\sigma}{\partial\varepsilon_f\partial\Omega_f}\right)_{\mathbf{r}_1} \rho(\mathbf{r}_1)\right] \left|\chi_i^{(+)}(\mathbf{r}_1)\right|^2, \tag{2.1}$$

$$\begin{aligned}\left(\frac{\partial^2\sigma}{\partial\varepsilon_f\partial\Omega_f}\right)^{(2step)} = \left(\frac{A}{A+1}\right)^4 \int d\varepsilon_m \int d\mathbf{r}_1 \int d\mathbf{r}_2 \frac{k_i(\mathbf{r}_1)/k_i}{k_f(\mathbf{r}_2)/k_f} \left|\chi_f^{(-)}(\mathbf{r}_2)\right|^2 \left[\left(\frac{\partial^2\sigma}{\partial\varepsilon_f\partial\Omega_f}\right)_{\mathbf{r}_2} \rho(\mathbf{r}_2)\right]_v \\ \times \frac{\exp[-2\gamma_m|\mathbf{r}_2-\mathbf{r}_1|]}{|\mathbf{r}_2-\mathbf{r}_1|^2} \left[\left(\frac{\partial^2\sigma}{\partial\varepsilon_m\partial\Omega_m}\right)_{\mathbf{r}_1} \rho(\mathbf{r}_1)\right] \left|\chi_i^{(+)}(\mathbf{r}_1)\right|^2\end{aligned} \tag{2.2}$$

Note that explanation of each notation in eqs. (2.1) and (2.2) is given in Ref. [6].

The physical quantities (a) to (c) are given either empirically or theoretically. Therefore, no free adjustable parameter is involved. For (a), the global nucleon optical potentials of Refs. [11] and [12] are used. The non-locality of the distorting potentials is considered by means of the well-known Perey factor[13]. Note that the Perey factor is unity for bound state wave functions in the Fermi gas model because of normalization. The range of non-locality is taken to be 0.85 fm. For (b), we use N-N scattering cross sections in the nuclear medium mentioned in the preceding subsection and also those in the free space for comparison. For (c), we use the density distribution of Woods-Saxson shape whose parameters are taken from Ref. [14].

2.2 In-medium NN cross sections

In-medium NN cross sections are calculated in the Born approximation using the g-matrix based on the BHF approach instead of the t-matrix describing the free NN scattering. In the present work, the g-matrix calculated by Kohno [15] is used to obtain the in-medium NN cross sections. His calculation is based on the non-relativistic BHF approach with the Paris potential[16] as a realistic NN force. Pauli-blocking for intermediate states and the effect of the nucleon mean field are taken into account in the g-matrix calculation. The resultant in-medium NN cross sections are energy- and density-dependent. For comparison, we also use the NN cross section parameterized by Cugnon[17] which is independent of density and used in QMD calculations[4]. Note that angular distributions of two-nucleon scattering in the nuclear medium are assumed to be isotropic in c.m. system.

3. Results and discussion

3.1 Results of SCDW calculation

We show typical results of the previous calculations with the in-medium NN cross sections by Li-Machleidt in Figs.1 and 2. Figure 1 show the angular distribution of ^{58}Ni(p,p'x) at 120 MeV for the different outgoing proton energies $E_{p'}$. Agreement with the experimental data[18] is satisfactory. Agreement in the absolute magnitude of the cross sections is significant since the model has no adjustable parameter. The peak in the 1-step cross sections at high $E_{p'}$ roughly corresponds to the quasi-elastic scattering. It is seen that the 2-step cross section is larger than the 1-step one at large and very small angles where the 1-step process is inhibited by the kinematics. The 2-step process gradually takes over the 1-step process as $E_{p'}$ gets lower. Similar results were obtained for ^{58}Ni(p,p'x) at other incident energies.

The SCDW model is applicable to (p,xn) reactions as well. We show the angular distribution of the ^{90}Zr(p,xn) reaction at 120 MeV in Fig. 2. The calculation is in reasonably good agreement with the experimental data[19], except at very large angles for the case of

E_n=40 MeV. The reason for the discrepancy is not clear at present. It may be due to higher order processes of more than 3-step.

3.2 Comparison of in-medium NN cross sections

Three kinds of in-medium NN cross sections are compared for p-p and p-n scattering in Fig.3 (a) and (b): the in-medium NN cross sections with the g-matrix by Kohno (referred to as "Kohno"), those given by Li-Machleidt ("L-M") and those parameterized by Cugnon et al.("Cugnon"). For comparison, the free NN cross section parameterized by Metropolis et al.[20] is also plotted by the solid lines in Fig.3.

Both in-medium cross sections of Kohon and L-M are density-dependent. The values for the nuclear density ρ = 0.18 fm^{-1} at the center of nucleus are shown in Fig.3. The in-medium NN cross sections of Kohno are smaller than the free ones for both p-p and p-n scattering at energies below 120 MeV and become close to the latter at the higher energies. The in-medium p-p cross sections of Cugnon are similar to those of Kohon except at energies below 50 MeV. For the p-n cross section, the result of Cugnon is much smaller than that of Kohno in the whole energy region. On the other hand, the in-medium NN cross sections of L-M, which were used in the SCDW calculations in Figs.1 and 2, are smaller than the free NN cross sections for both p-p and p-n scattering in the whole energy region. Note that the in-medium NN cross sections of Kohno and L-M become almost equal to the free ones at ρ = 0. The difference between them seems to lie in the BHF calculations: the former is based on the non-relativistic approach and the latter the relativistic one. However, the reason is not clear at present and is under investigation from the viewpoints of the effective mass.

3.3 Effect of in-medium NN cross section on SCDW calculation

We have performed SCDW calculations using different in-medium NN cross sections and compared them with those using the free NN cross sections. The result for ^{58}Ni(p,p') at E_p = 120 MeV and $E_{p'}$ = 60 MeV is shown in Fig.4. It can be seen that the 2-step cross sections are more sensitive to a choice of in-medium NN cross sections than the 1-step cross sections. This may be because two NN collisions occurs in the 2-step process as represented in eq. (2.2) and the collisions are likely to take place in the region inside the nucleus rather than near the surface. The result with in-medium NN cross sections of Kohno is almost same as that with the free NN cross sections. The reason is that the density-dependence becomes weak at high energies above 120 MeV and the in-medium NN cross sections of Kohno are very close to the free ones as shown in Fig.3. On the other hand, Both SCDW results of L-M and Cugnon are similar except at backward angles.

As can been seen in Figs. 1 and 2, the SCDW prediction with in-medium NN cross sections of L-M is in satisfactory agreement with the experimental data. Therefore, one can imagine that use of in-medium NN cross sections of Kohon results in much overprediction. From comparisons in Figs. 3 and 4, we have found that strongly density-dependent in-medium NN cross sections are preferable to reproduce the experimental (p,p'x) data well. In a microscopic description of inelastic (p,p') scattering[21], the transition potential is derived with the g-matrix including a rearrangement term given by $\rho(\partial g/\partial\rho)$ where ρ is the nuclear density. We have taken into account the rearrangement term in the calculation of in-medium NN cross sections of Kohno. The preliminary result shows that the rearrangement effect is appreciable at energies lower than about 50 MeV but is very weak at energies above 100 MeV. Consequently, the results shown in Fig.4 would be little changed even if one consider the rearrangement term in the calculation of the g-matrix for inelastic proton scattering.

4. Conclusion

We have studied the effect of in-medium NN cross sections on the MSD processes of (p,p'x) and (p,nx) reactions in the framework of the SCDW model. Three different in-medium NN cross sections for p-p and p-n scattering were compared with the free ones in the incident energy region up to 200 MeV. Although all of them are smaller than the free NN cross sections at low energies, there appear some differences among them with respect to the

absolute values and the density-dependence. It was found that the 2-step SCDW cross sections are more sensitive to in-medium NN cross sections, especially at low outgoing energies, than the 1-step ones. From these considerations, we have found that in-medium cross sections with such strong density-dependence as Li-Machleidt's ones[9] are preferable to obtain good agreement with the experimental (p,p'x) and (p,nx) data. Further study of SCDW model, such as extension to 3-step process, will be required to draw more clear conclusion on the medium effect on N-N collisions inside the nucleus.

Acknowledgments

We wish to thank Prof. M. Kohno for providing a code to calculate the g-matrix and valuable discussions about our work. This work was supported in part by the Grant-in-Aids No. 07640416 of the Japanese Ministry of Education, Science and Culture. The financial aid of RCNP, Osaka University, for the computation is gratefully acknowledged.

References

[1] H. Feshbach, A.K. Kerman and S. Koonin,, Ann. of Phys. **125**, 429 (1980).
[2] T. Tamura, T. Udagawa and H. Lenske, Phys. Rev. C **26**, 379 (1982).
[3] H. Nishioka, H.A. Weidenmüller and S. Yoshida, Ann. of Phys. **183**, 166 (1988).
[4] Koji Niita et al., Phys. Rev. C **52**, 2620 (1995).
[5] E.I. Tanaka et al., Phys. Rev. C **52**, 316 (1995).
[6] Y. Luo and M. Kawai, Phys. Rev. C **43**, 2367 (1991); M. Kawai and H.A. Weidenmüller, Phys. Rev. C **45**, 1856 (1992); Y. Watanabe and M. Kawai, Nucl. Phys. **A560**, 43 (1993).
[7] Y. Watanabe, H. Shinohra and M. Kawai, *Proceedings of the Second Specialists' Meeting on High Energy Nuclear Data*, January 26-27, 1995, JAERI, Tokai, Japan, JAERI-conf 95-016, (1995) pp. 1.; Y. Watanabe, JAERI-Conf 96-012 (1995), pp. (in Japanese)
[8] Y. Watanabe, H. Shinohra and M. Kawai, acta physica slovaca **45**, 693 (1995).
[9] G.Q. Li and R. Machleidt, Phys. Rev. C **48**, 1702 (1993); Phys. Rev. C **49**, 566 (1994).
[10] K. Brueckner, R.J. Eden and N.C. Francis et al, Phys. Rev. 100, 891 (1955).
[11] R.L. Walter and P.P. Guss: *Proc. of Int. Conf. on Nuclear Data for Basis and Applied Science*, Santa Fe, New Mexico, 1985, ed. P.G. Young, (Gordon and Breach, New Yor, 1986) p.1075.
[12] P. Schwandt et al., Phys. Rev. C **26**, 55 (1982).
[13] F.G. Perey and B. Buck, Nucl. Phys. **32**, 353 (1962).
[14] J. W. Negele, Phys. Rev. C **1**, 1260 (1970).
[15] M. Kohno, private communication (1995).
[16] M. Lacombe et al., Phys. Rev. C **21**, 861 (1980).
[17] J. Cugnon et al., Nucl. Phys. **A352**, 505 (1981); J. Cugnon, Phys. Rev. C **22**, 1885 (1980).
[18] S.V.Förtsch et al., Phys. Rev. C **43**, 691 (1991).
[19] W. Scobel et al., Phys. Rev. C **41**, 2010 (1990).
[20] See, K. Kikuchi and M. Kawai, *Nuclear matter and nuclear reactions*, (North-Holland, Amsterdam, 1968), pp. 33.
[21] T. Cheon et al., Nucl. Phys. **A445**, 227 (1985).

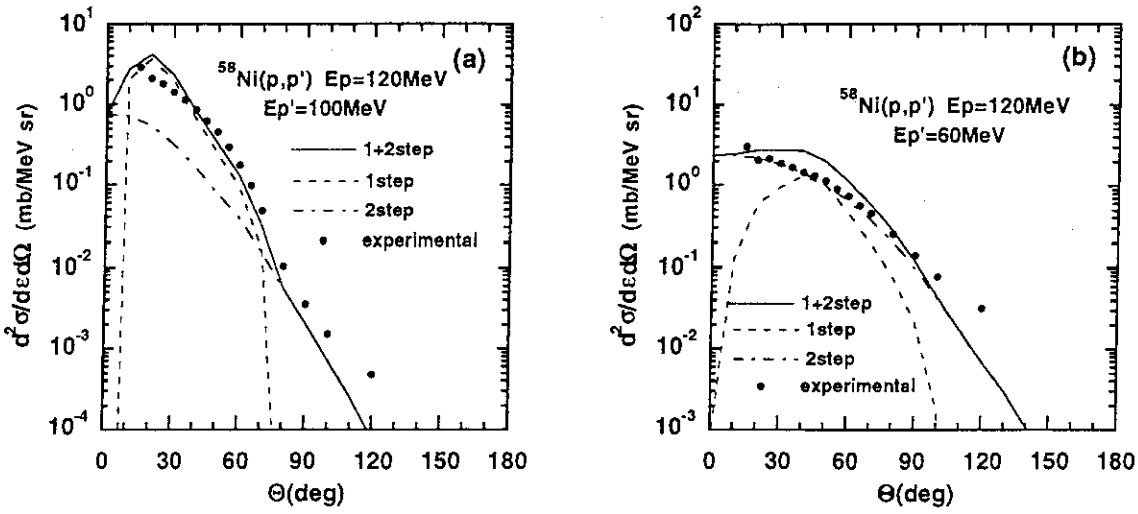

Fig.1 SCDW double differential cross section for ^{58}Ni(p,p') at E_p=120 MeV and $E_{p'}$=100 and 60 MeV. The dotted (dot-dashed) lines are 1(2)-step cross sections and the solid lines are the sum of them. The closed circles are the experimental data from Ref. [18].

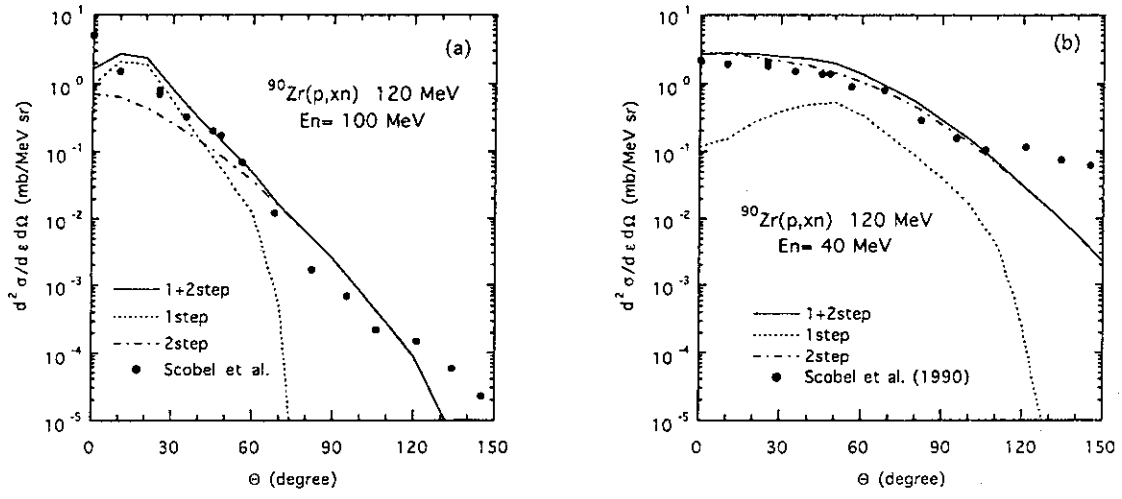

Fig.2 SCDW double differential cross section for ^{90}Zr(p,nx) at E_p=120 MeV and E_n=100 and 40 MeV. Notations are the same as in Fig.1. The experimental data are than from Ref. [19].

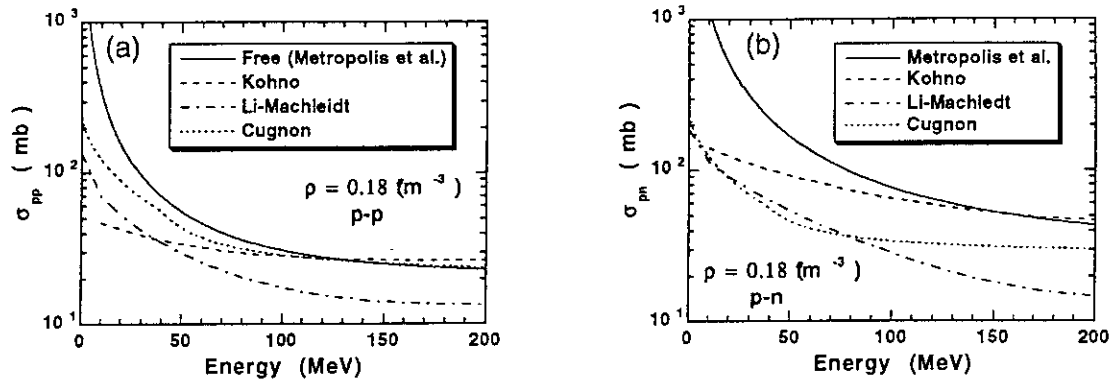

Fig.3 Comparison of in-medium NN cross sections at the nuclear density ρ=0.18 fm^{-1} for (a) p-p and (b) p-n scattering.

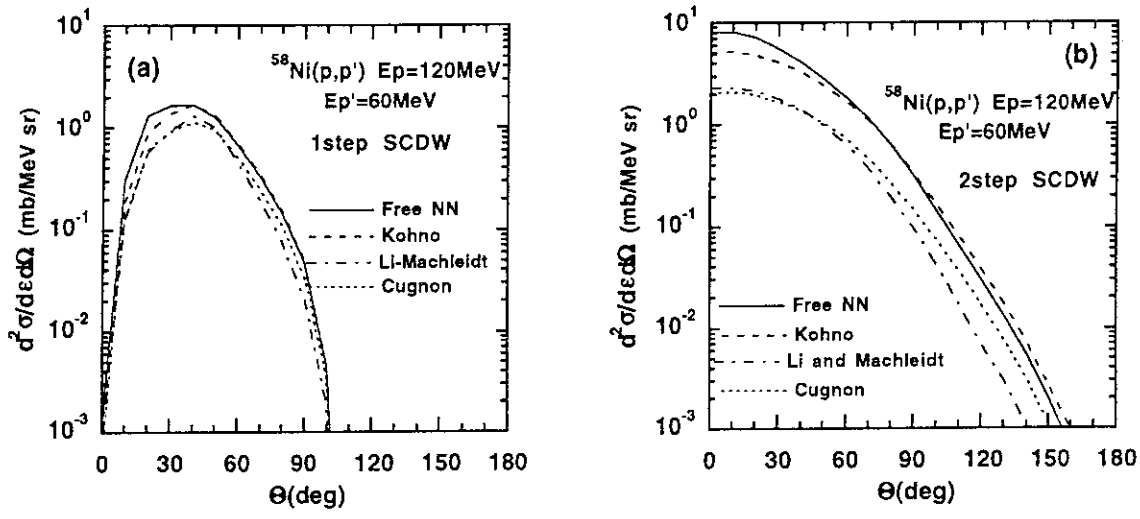

Fig.4 SCDW cross sections for ^{58}Ni(p,p') at E_p=120 MeV and $E_{p'}$=60 MeV with different in-medium NN cross sections. (a) 1-step process and (b) 2-step process.

3.28 Fragmentation Cross Sections by HETC

Nobuhiro SHIGYO, Tatsushi NAKAMOTO, and Kenji ISHIBASHI
Department of Nuclear Engineering, Kyushu University
Hakozaki, Higashi-ku, Fukuoka-shi 812-81.
e-mail: shigyo@kune2a.nucl.kyushu-u.ac.jp

High Energy Transport Code (HETC) based on the intranuclear cascade-evaporation is modified for calculating the fragmentation cross section. The nucleon-nucleon cross sections are used for computation in the intranuclear cascade process, and the values for the free-space collision are changed to the these for the in-medium collision. The fragmentation reaction is incorporated into the original code as a subroutine set by the use of the systematics of the reaction. The modified HETC reproduces experimental fragment yields to a reasonable degree.

1. Introduction

Reliable high-energy nuclear data have been required for application of the spallation reaction to the accelerator based transmutation[1], the high intensity neutron source[2], and so on. The fragmentation reaction is induced by incident nucleons of intermediate energies above several hundred MeV, and the cross sections are also necessary as the high-energy nuclear data. Since it is difficult to obtain the whole fragmentation data by experiments, calculation models need to be developed. At present, High Energy Transport Code (HETC)[3] is often used for the engineering purpose at intermediate energies. The code mainly considers the intranuclear cascade and evaporation processes. The code is incapable of representing the production yields of the fragments such as ^{7}Be or ^{22}Na, since HETC dose not take the fragmentation process into consideration. Then, we modify this code to calculate the intermediate-energy proton induced fragmentation cross sections.

2. In-medium correction

The free-space nucleon-nucleon (NN) cross sections are used in the intranuclear cascade process of HETC. However, Since the NN collisions occur inside the nucleus, it is necessary to take the in-medium NN cross section correction into consideration. The nucleon-nucleon (NN) cross section in the intranuclear cascade process of HETC is modified. The cross sections in medium are obtained by the simple and practical parametrizations[4, 5]. These parametrizations

are applicable to the energies up to 300 MeV. Above 300 MeV, the *NN* cross section in medium is postulated to increase linearly, and is equal to the free-space *NN* cross section at the energy of 500 MeV.

Figure 1 shows the ratio of the in-medium proton-neutron cross sections to the free-space ones for the various nuclear density, while Fig. 2 stands for that in the case of the proton-proton or neutron-neutron collisions. Because of the correction, the excitation energy of the nucleus after the intranuclear process decreases to some degree.

3. Incorporation of fragmentation into HETC

Before incorporation of the proton incident fragmentation process into HETC, the systematics on the mass yields and the kinetic energy spectra of the process have been constructed[6]. The former was obtained on the basis of a liquid-gas phase transition model[7], and was parametrized by the incident proton energy, the target and the fragment mass and the fragmentation nuclear temperature. For the latter, a formula was devised to have a simple expression considering the Coulomb barrier. The kinetic energy spectra were represented by the parameters of the fragmentation nuclear temperature, the fragment and the target nucleus and the incident proton energy. The nuclear temperature of the fragmentation was determined by the incident proton energy.

It is assumed that the fragmentation process occurs between the intranuclear cascade process and the evaporation one. The systematics are incorporated with some modification as a subroutine set into HETC[8].

The probability and the nuclear temperature of the fragmentation are decided by the state of the nucleus of the intranuclear cascade process instead of the incident proton energy. The probability of the fragmentation is evaluated by the excitation energy after the intranuclear cascade process. The nuclear temperature is first obtained without considering a degree of freedom of the fragmentation after that process, regardless of the incident proton energy. This temperature is given by the excitation energy and the mass of the nucleus after that process. Then the temperature considering the fragmentation is represented as a function of the temperature without consideration of the fragmentation. The usefulness of this method holds for different states of nucleus after the intranuclear cascade process.

4. Calculation results

The cross sections of the fragments are calculated by the fragmentation-incorporated HETC (HETC-FRG). Fig. 3 shows the mass yields of the fragments from Ag and Xe targets[9-11]. Fig. 4 represents the kinetic energy spectra of the fragments of Be, C, N, O from Xe target. In these figures, marks indicate the experimental data, and solid lines stand for the results of HETC-FRG. These figures show that the cross sections by HETC-FRG are in considerable

agreement with the experimental ones.

Figure 5 presents the charge yields from Au target for various incident proton energies. Figs. 6, 7 show the nuclide production yields from Fe target. The nuclide production yields from Zr target are represented in figs 8 - 10. In these figures marks again indicate the experimental data[12-14] and solid lines the cross sections by HETC-FRG. Fig. 6 show that this code reproduces the production yield of ^{7}Be within a factor of five above the incident proton energy of 600 MeV. The difference of the cross sections between the experimental values and the results by HETC-FRG are within a factor of two above 600 MeV in Fig. 8. These production cross sections are not reproduced by original HETC at all. In the case of the nuclide heavier than these light mass fragments, this code also represents the experimental data appropriately as shown by Fig. 7 ,9, and 10.

5. Summary

In order to calculate the cross section of the proton-induced fragmentation reaction, High Energy Transport Code (HETC) was modified. The nucleon-nucleon cross sections in the intranuclear cascade process were changed from free-space values to in-medium ones. The fragmentation reaction is incorporated into the code as a subroutine set on the basis of the systematics of the reaction. The modified HETC is appropriate to obtain the fragmentation cross sections for the wide target mass range at the incident proton energy above 600 MeV. Although the production yields of the light mass fragments like ^{7}Be which is not reproduced by original HETC at all, they are represented considerably by HETC-FRG.

Acknowledgments

The authors express their gratitude to Mr. H. Takada of Japan Atomic Energy Research Institute and Mr. N. Yoshizawa of Mitsubishi Research Institute for useful suggestion and discussion.

References

(1) BOWMAN, C.D., et al.: *Nucl. Instr. and Meth.*, **A320**, 336 (1992).

(2) CARPENTER, J.M., et al.: "*Proceedings of the twelfth Meeting of International Collaboration on Advanced Neutron Sources 24 - 28 May 1993*", *Rutherford Appleton Laboratory Report*, **94-025**, T-95 (1994).

(3) CHANDLER, K.C., and ARMSTRONG, T.W.: *ORNL*-4744 (1972).

(4) LI, G.Q., and MACHLEIDT, R.: *Phys. Rev.*, **C48**, 1702 (1993).

(5) LI, G.Q., and MACHLEIDT, R.: *Phys. Rev.*, **C49**, 566 (1994).

(6) SHIGYO, N., et al.: *J. Nucl. Sci. Technol.*, **32**, 1 (1995).

(7) PANAGIOTOU, A.D., et al.: *Phys. Rev.*, **C31**, 55 (1985).

(8) SHIGYO, N., et al.: *JAERI-Conf.*, **95-008**, 217 (1995).

(9) GREEN, R.E.L., et al.: *Phys. Rev.*, **C29**, 1806 (1984).

(10) ANDRONENKO, L.N., et al.: *Phys. Lett.*, **B174**, 18 (1986).

(11) PORILE, N.T., et al.: *Phys. Rev.*, **C39**, 1914 (1989).

(12) AVDEICHIKOV, V.V., et al.: *Sov. J. Nucl. Phys.*, **48**, 1043 (1988).

(13) MICHEL, R., et al.: *Nucl. Instr. and Meth.*, **B103**, 183 (1995).

(14) ILJINOV, A.S., et al.: "*Production of Radionucleids at Intermediate Energies*", Springer Verlag, Landolt-Bornstein, New Series, subvolumes I/13a (1991), I/13b (1992), I/13c (1993), I/14d (1994).

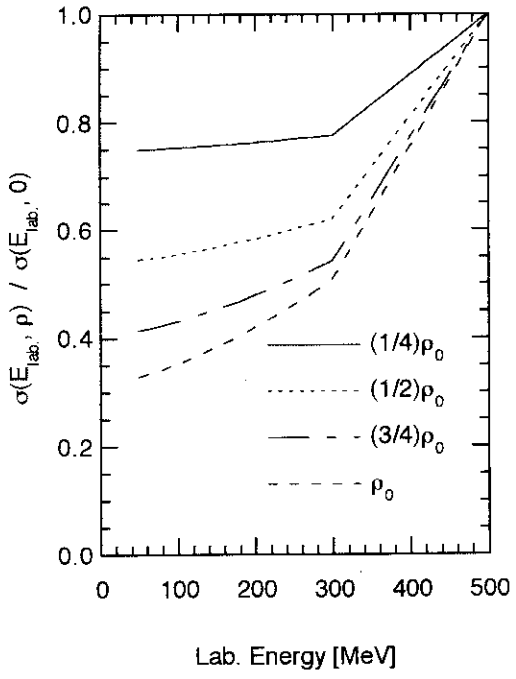

Fig. 1 Ratio of in-medium np total cross section to free-space cross sections.

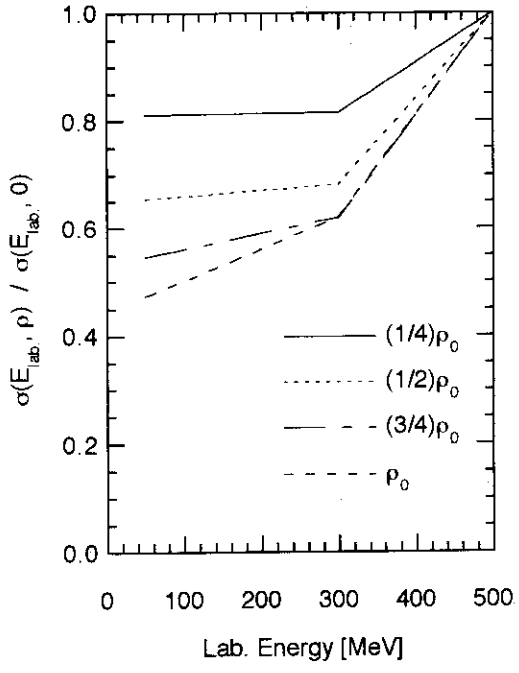

Fig. 2 Ratio of in-medium pp, nn total cross section to free cross sections.

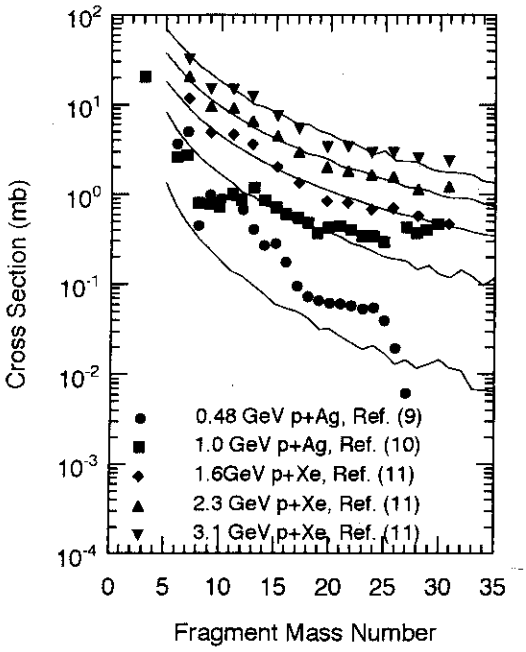

Fig. 3 Fragment mass yields. Marks show experimental values, and lines are results of HETC-FRG.

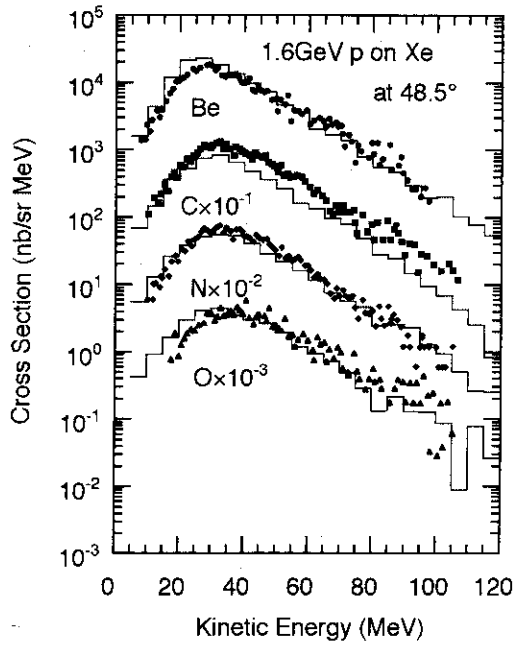

Fig. 4 Kinetic energy spectra of fragments from Xe. Marks show experimental values, and lines are results of HETC-FRG.

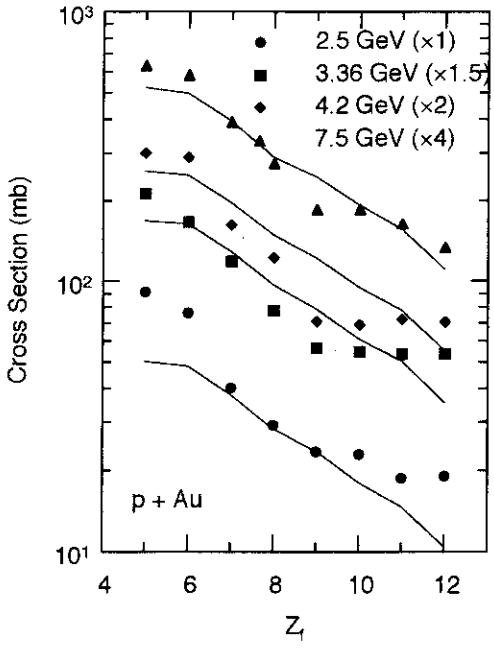

Fig. 5 Charge yields of fragments in the reaction p + Au for four values of proton energy. Marks show experimental values, and lines are results of HETC-FRG.

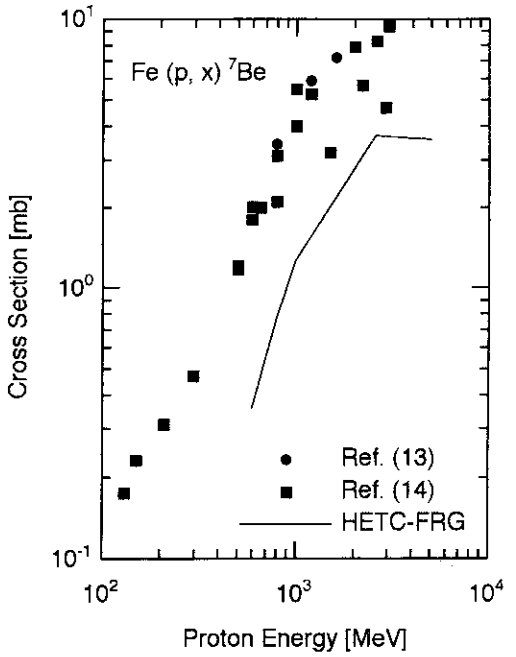

Fig. 6 Production of ^{7}Be from Fe compared with HETC-FRG.

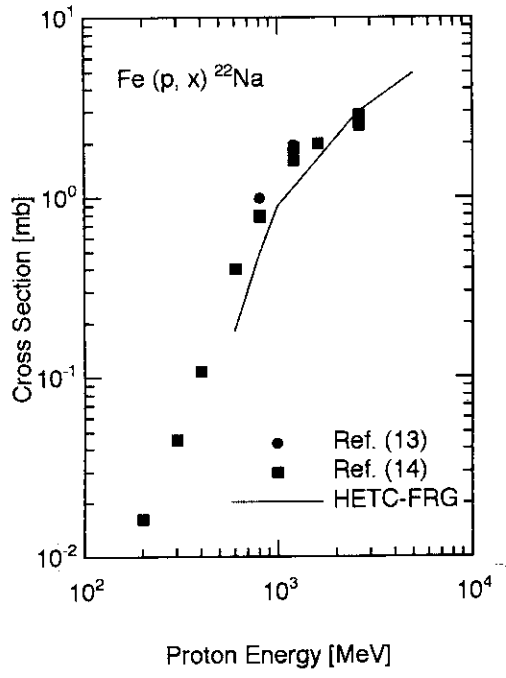

Fig. 7 Production of ^{22}Na from Fe compared with HETC-FRG.

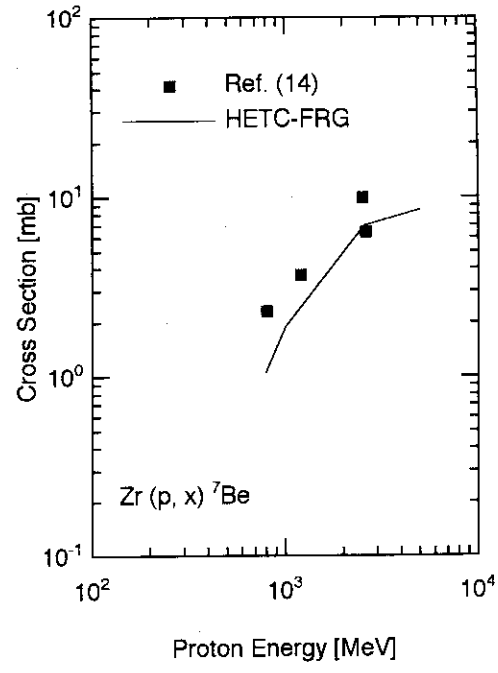

Fig. 8 Production of ^{7}Be from Zr compared with HETC-FRG.

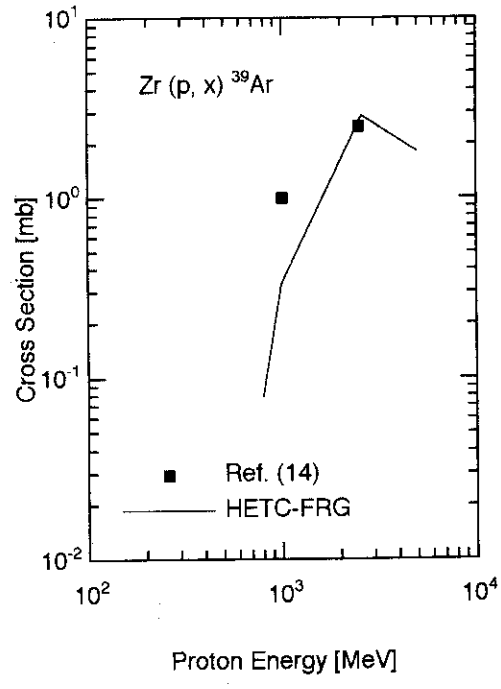

Fig. 9 Production of ^{39}Ar from Zr compared with HETC-FRG.

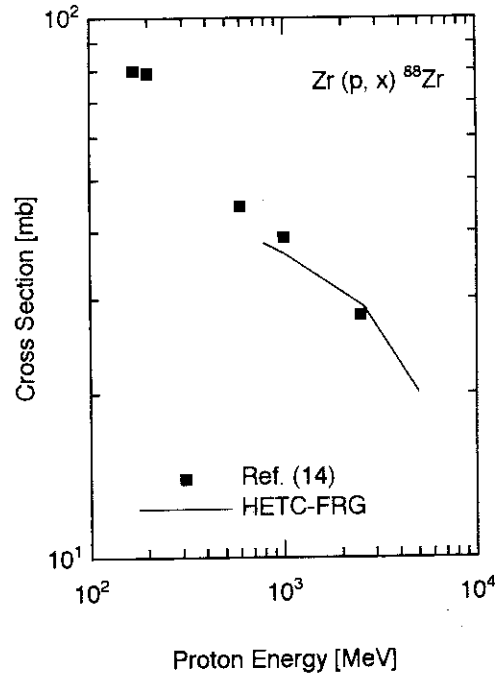

Fig. 10 Production of ^{88}Zr from Zr compared with HETC-FRG.

3. 29 Semi-Gross Theory of Nuclear β-decay II

Hidehiko NAKATA
Department of Physics and Applied Physics, Waseda University, 3-4-1 Okubo, Shinjuku-ku, Tokyo 169, Japan
e-mail:63l509@cfi.waseda.ac.jp

Takahiro TACHIBANA and Masami YAMADA
Advanced Research Center for Science and Engineering, Waseda University, 3-4-1 Okubo, Shinjuku-ku, Tokyo 169, Japan
e-mail:tachiban@cfi.waseda.ac.jp
myamada@cfi.waseda.ac.jp

The semi-gross theory of nuclear β-decay is a theory obtained from the conventional gross theory by inclusion of some shell effects. In this theory, the one-particle strength function of the Gamow-Teller (G-T) transition depends on the orbital and total angular momenta of the decaying nucleon to take into account the effect of the spin-flip in the G-T transition, which is estimated both from theoretical consideration and from inspection of experimental data. The β-decay strength function is calculated as an integral of the one-particle strength functions, and some results calculated with this function are given and discussed.

1. Introduction

The conventional gross theory of nuclear β-decay[1, 2] is a theory which treats the β-decay strengths to all the final nuclear levels as an averaged function based on sum rules of the β-decay strengths. The Q-value is one of the input data of the model, and the shell effects are included only through it. In this theory, it is assumed that the strength function $\left|M_{\Omega}(E, \varepsilon)\right|^2$ is given by an integral of one-particle strength function $D_{\Omega}(E, \varepsilon)$ as follows:

$$\left|M_{\Omega}(E)\right|^2=\int_{\varepsilon_{\min}}^{\varepsilon_{\max}} D_{\Omega}(E, \varepsilon)W(E, \varepsilon)\frac{\mathrm{d}n_1}{\mathrm{d}\varepsilon}\mathrm{d}\varepsilon. \qquad (1)$$

Here, Ω denotes the type of the β-decay operator (in the conventional gross theory, the allowed and first-forbidden transitions are taken into account), E represents the energy of the final nuclear state measured from the initial state, ε is the one-particle energy of the decaying nucleon (i.e., the kinetic energy of this nucleon plus the sum of the potential energies between this nucleon and the others), $\mathrm{d}n_1/\mathrm{d}\varepsilon$ represents the one-particle energy distribution of decaying nucleon, and, finally, $W(E, \varepsilon)$ is a weight function to take into account the Pauli exclusion principle.

In the semi-gross theory [3], we keep the above assumption, and modify the one-particle strength function $D_{\Omega}(E, \varepsilon)$ and the one-particle energy distribution $dn_i/d\varepsilon$ so as to include the shell effect of the parent nucleus. Since the shell effect of the daughter nucleus is not included, this model is called "semi-" gross theory. So far the semi-gross theory treats the Fermi and G-T transitions only.

2. One-particle states

The one-particle energy levels, each doubly degenerate, are derived from nuclear mass data by a method similar to the one of ref. [4]. Then, we assign a set (l, j) or a mixture of sets (l, j)'s to each level, where l and j are, respectively, the orbital and total angular momenta of a nucleon. These angler momentum sets, by which we roughly express configuration mixing, are obtained from single-particle shell model calculation with a Woods-Saxon-type potential. The occupation and vacancy probabilities of the paired nucleons (the U-V factors) of the BCS paring theory are also calculated from these one-particle energy levels, rather than treated as a constant value as in the conventional gross theory.

3. One-particle strength function for the G-T transition

In the Gamow-Teller transition, the spin-flip of the decaying nucleon can occur. In the case of no spin-flip, the nucleon with $j=l+1/2$ $\{j=l-1/2\}$ mainly decays to the states having $j'=l+1/2$ $\{j'=l-1/2\}$ around the isobaric analogue state (IAS). On the other hand, in the case of spin-flip, the nucleon with $j=l+1/2$ $\{j=l-1/2\}$ decays to the states having $j'=l-1/2$ $\{j'=l+1/2\}$, which have, on the average, somewhat higher {lower} excitation energies than IAS. In order to take into account this situation, we express the one-particle strength function as a superposition of two functions, one with a peak situated at the IAS and another with a peak above IAS (for $j=l+1/2$) or below IAS (for $j=l-1/2$). The relative weights of these two functions are determined so as to be consistent with the single-particle shell model.

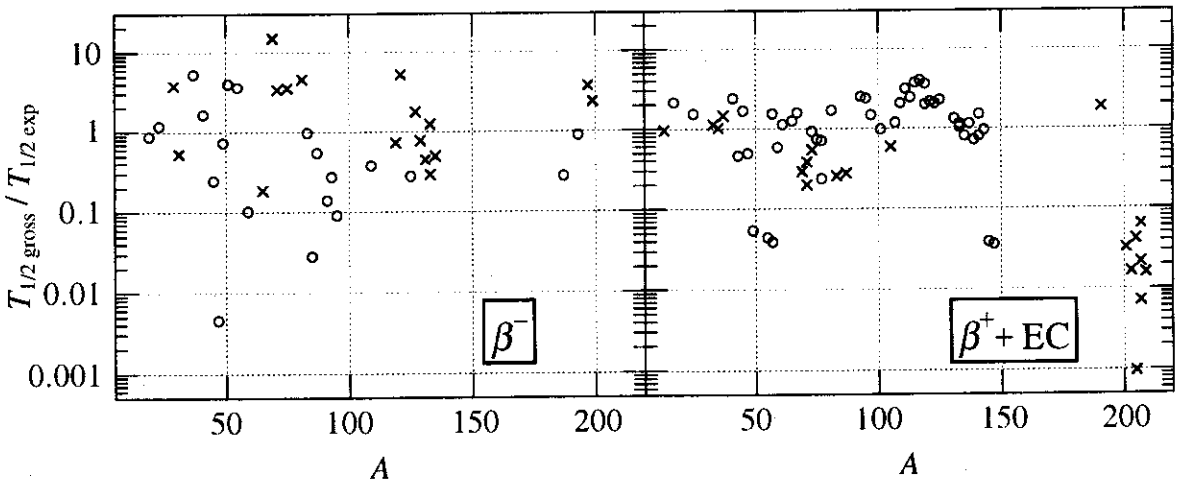

Fig. 1 Ratios between the calculated and experimental half-lives. The calculations are made by the conventional gross theory to see the shell effect of parent nuclei. Circles are for the nuclei with $j=l+1/2$, and crosses are for the nuclei with $j=l-1/2$.

We examine whether the spin-flip effect mentioned above is actually observed in the experimental data [5] or not. In Fig. 1, we show the ratios of the half-lives calculated by the conventional gross theory to the experimental half-lives. In this examination, we select the nuclei with odd (even) N and even (odd) Z for the β^--decay (β^+-decay or electron capture) with an additional condition that the ground-state spin-parity of each nucleus is equal to the spin-parity of the last odd-particle of the nucleus. When the experimental G-T transition to the ground state is highly forbidden, the "bottom raising" of the strength function [2] is introduced in the gross theory calculation. We choose the magnitude of the "bottom raising" in each nucleus by referring to the experimental data.

As seen in Fig. 1, the experimental half-lives of the nucleus with $j=l+1/2$ are relatively longer for the β^--decay (shorter for the β^+-decay or electron capture) compared with those of the nucleus with $j=l-1/2$ on the average. This trend is considered to be caused by the effect of spin-flip in the G-T transition. We estimate that this effect gives the strength about 2~3 times stronger or weaker than the averages in the β-decay windows.

In ref. [2], the one-particle strength function $D_\alpha(E, \varepsilon)$ is obtained from a function $F_{GT}(E)$ by correcting for the one-particle energy distribution and pairing gap. We incorporate the above-mentioned spin-flip effect in the shape of $F_{GT}(E)$. We also use the experimental information on the G-T giant resonance. We express $F_{GT}(E)$ as a superposition of $F_{GT}^{nfl}(E)$ having a peak situated at IAS and $F_{GT}^{fl}(E+\Delta)$ having a peak above IAS (or below IAS) as follows:

$$F_{GT}(E) = C^{nfl} F_{GT}^{nfl}(E) + C^{fl} F_{GT}^{fl}(E+\Delta). \tag{2}$$

Here C^{nfl} and C^{fl} are introduced to give a proper normalization and proper relative weights of the two terms; for the latters we take the values determined from the single-particle shell model. The functions F_{GT}^{nfl} and F_{GT}^{fl} are assumed to be composed of wide and narrow components (designated by superscripts w and n) as

$$F_{GT}^{nfl}(E) = 0.3\, g_1^{w}(E) + 0.7\, g_1^{n}(E),$$

$$F_{GT}^{fl}(E) = [0.3\, g_2^{w}(E) + 0.7\, g_2^{n}(E)]\eta(E) \tag{3}$$

with

$$g_i^{w}(E) = N_i^{w}\,\mathrm{sech}[\pi(E-\Delta_c)/2\sigma_i],$$

$$g_i^{n}(E) = N_i^{n}\,\mathrm{sech}[\pi(E-\Delta_c)/2\sigma_i]\frac{1}{(E-\Delta_c)^2+\Gamma_i^2} \qquad (i=1 \text{ or } 2) \tag{4}$$

and

$$\eta(E)=\begin{cases}\dfrac{1}{2}+\dfrac{\alpha(E-\Delta_c)}{(E-\Delta_c)^2+\alpha^2} & \text{for } j=l+\dfrac{1}{2}\,,\\[2ex] \dfrac{1}{2}-\dfrac{\alpha(E-\Delta_c)}{(E-\Delta_c)^2+\alpha^2} & \text{for } j=l-\dfrac{1}{2}\,.\end{cases} \tag{5}$$

Here, N_i^{w},N_i^{n} (i=1 or 2) are normalization factors, Δ_c is the Coulomb displacement energy, and the width parameters Γ_i (i=1 or 2) are assumed in the form

$$\Gamma_i=\sqrt{\Gamma_0^2+\left\{\mu_i(l+\tfrac{1}{2})/A^{1/3}\right\}^2}\,, \tag{6}$$

with Γ_0 and μ_i being adjustable parameters. The function $\eta(E)$, in cooperation with Δ, takes into account the effect of spin-flip. We take α as

$$\alpha=\frac{\hbar\omega}{2}\approx 20A^{-1/3}\ \mathrm{MeV}, \tag{7}$$

and determine Δ so that the distance between the peaks of $F_{\mathrm{GT}}^{\mathrm{nfl}}(E)$ and $F_{\mathrm{GT}}^{\mathrm{fl}}(E+\Delta)$ be equal to the experimental spin-orbit splitting.

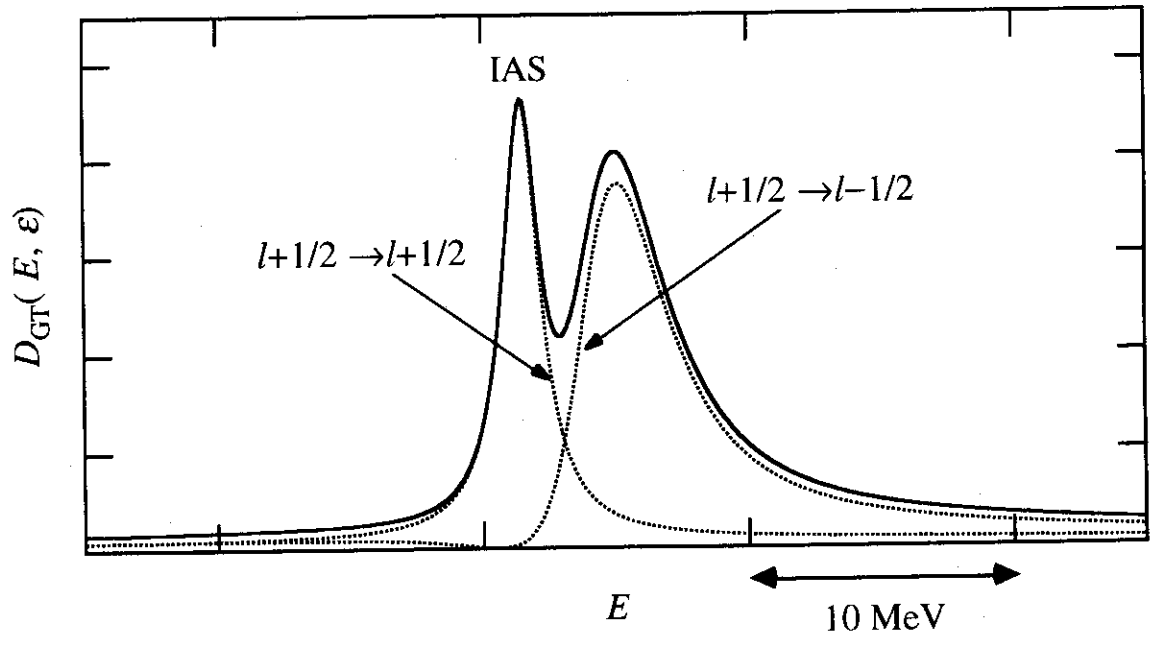

Fig. 2 Example of the one-particle strength function $D_{\mathrm{GT}}(E,\ \varepsilon)$ (solid line), which is a superposition of two functions (doted lines) corresponding to the transitions j=l+1/2 → j=l+1/2, and j=l+1/2 → j=l−1/2. Shown is the case of l=5 and A=190.

We take the adjustable parameters (in units of MeV) in eqs. (4) and (6) at this stage as follows:

$$\sigma_i = 50,\ \Gamma_0 = 1.9,\ \mu_1 = 0.45,\ \mu_2 = 4.5. \tag{8}$$

An example of the one-particle strength function $D_{GT}(E, \varepsilon)$ calculated by using the above $F_{GT}(E)$ are shown in Fig. 2.

4. Results and discussion

In Figs. 3 and 4, we show the G-T giant resonance peaks calculated by the semi-gross theory as well as those calculated by the conventional gross theory for ^{208}Pb(p, n)^{208}Bi and ^{90}Zr(p, n)^{90}Nb. Shown also are the experimental data [6, 7], in which there seems to be considerable ambiguity with respect to the subtraction of the background. The sums of these experimental strengths are only about 36% and 37% of their sum rule values for ^{208}Pb(p, n)^{208}Bi and ^{90}Zr(p, n)^{90}Nb, respectively. This fact and the fact that the calculated strengths distribute in a wider energy region suggest that the background was overestimated. If some background is added to the experimental strengths, the results of the semi-gross theory are in fairly good agreement with experimental data although the theoretical strengths have more structures. In the case of ^{90}Zr(p, n)^{90}Nb, the semi-gross theory gives a strength peak near IAS in addition to the giant-resonance peak, while in the experiment a peak is observed at a lower energy. The level density of the excited states in ^{90}Nb is not very high in

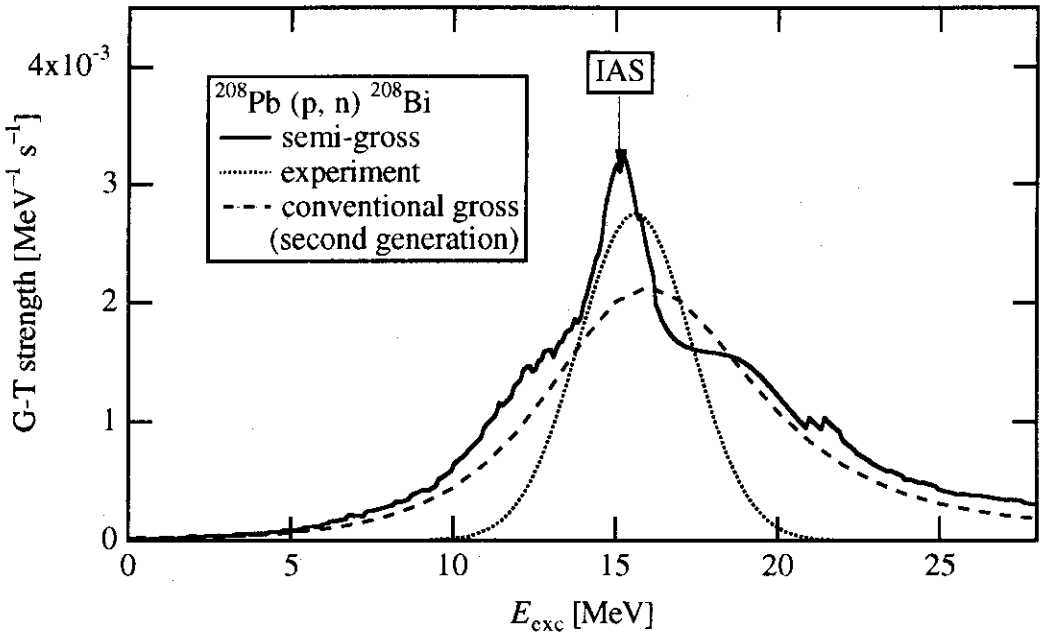

Fig. 3 The G-T strength function in the giant-resonance region for ^{208}Pb(p, n)^{208}Bi. The solid line is for the semi-gross theory and the dashed line for the gross theory. The experimental strength function [6] is shown by a dotted line.

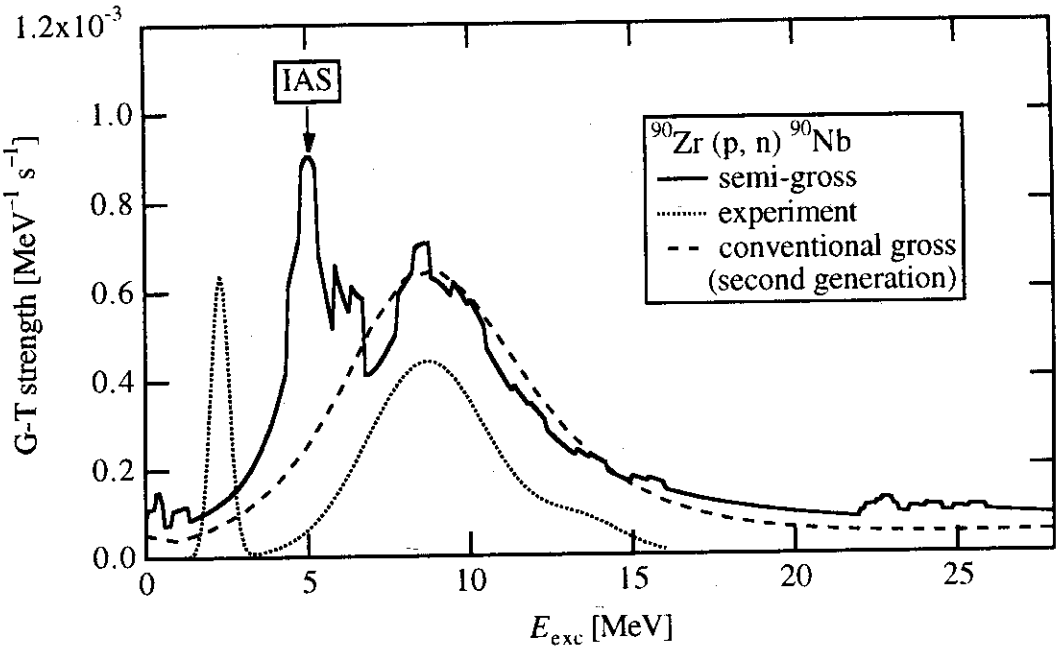

Fig. 4 The G-T strength function in the giant-resonance region for ^{90}Zr(p, n)^{90}Nb. The experimental data are from ref. [7]. See also the caption of Fig. 3.

the region of IAS. Thus it is likely that, in the real ^{90}Nb, there is no adequate levels for the final states of the G-T transition near IAS and the non-spin-flip strengths are shared to higher and lower excited states.

In this study, we have calculated only the G-T strengths in the giant-resonance region and determined the adjustable parameters. The β-decay half-lives will be the subject of the next study by the semi-gross theory. The tail part of the one-particle strength function in the β-decay window plays a crucial role in the calculation of the half-life. As shown in eq. (8), σ_i=50 which was used in the gross theory is also adopted in the present study, but some readjustment may be necessary for better reproduction of half-lives. Apart from this relatively minor adjustment, the present study has established the foundation of the semi-gross theory.

References

[1] Kondoh T., Tachibana T. and Yamada M.: Prog. Theor. Phys., 74, 708 (1985), and references therein
[2] Tachibana T, Yamada M. and Yoshida Y.: Prog. Theor. Phys. 84, 641 (1990)
[3] Tachibana T, Yamada M. and Nakata H.:JAERI-M 93-046 236 (1993)
[4] Kondoh T. and Yamada M.: Prog. Theor. Phys. Supplement No.60, 136 (1976)
[5] Evaluated Nuclear Structure Data File (ENSDF), 1994 August version, communicated through Nuclear Data Center Japan Atomic Energy Research Institute
[6] Horen D.J. et al.: Phys. Lett. 95B, 27 (1980)
[7] Bainum D.E. et al.: Phys. Rev. Lett. 44, 1751 (1980)

3. 30 Determination of Shell Energies — Nuclear Deformations and Fission Barriers —

Hiroyuki KOURA, Takahiro TACHIBANA*, Masahiro UNO** and Masami YAMADA*

Department of Physics and Applied Physics, Waseda University, 3-4-1 Okubo, Shinjuku-ku, Tokyo, JAPAN
*Advanced Research Center for Science and Engineering, Waseda University, 3-4-1 Okubo, Shinjuku-ku, Tokyo, JAPAN
**Ministry of Education, Science and Culture, 3-2-2 Kasumigaseki, Chiyoda-ku, Tokyo, JAPAN

e-mail address: H. Koura: *64l508@cfi.waseda.ac.jp*
T. Tachibana: *tachiban@cfi.waseda.ac.jp*
M. Uno: *unom@cfi.waseda.ac.jp*
M. Yamada: *myamada@cfi.waseda.ac.jp*

We have been studying a method of determining nuclear shell energies and incorporating them into a mass formula. The main feature of this method lies in estimating shell energies of deformed nuclei from spherical shell energies. We adopt three assumptions, from which the shell energy of a deformed nucleus is deduced to be a weighted sum of spherical shell energies of its neighboring nuclei. This shell energy should be called intrinsic shell energy since the average deformation energy also acts as an effective shell energy The ground-state shell energy of a deformed nucleus and its equilibrium shape can be obtained by minimizing the sum of these two energies with respect to variation of deformation parameters. In addition, we investigate the existence of fission isomers for heavy nuclei with use of the obtained shell energies.

§1. Introduction

The nuclear ground-state energy can be expressed as a sum of a smooth function of Z (proton number) and N (neutron number) and a deviation from it (see, for example, refs. [1-3]). The deviation energy, which we may call shell energy in a broad sense, is considered to be mainly due to the nuclear shell structure and deformation. For several years we have been developing a method of calculating the shell energy. In this study we newly devised a method of expressing the shell energy of a deformed nucleus as a linear combination of the shell energies of spherical nuclei. In this report, the shell energy of a deformed nucleus is mainly treated. In section 2 we comment on the spherical shell energies, in section 3 explain how to take into account the deformation effect on them, and finally give a concluding remark in section 4.

§2. Spherical shell energy

Our method of determining shell energies starts from an extreme single-particle shell model. An extended *spherical* Woods-Saxon potential of neutron (or proton) is assumed for each nuclide. We obtain the minimum of the total energy of n neutrons (or n protons) put in this potential. These minima plotted against n show some deviations from a smooth curve, and these deviations are the origin of the shell energies. In order to extract these deviations we subtract smooth energies whose main parts are the Thomas-Fermi energies. Then, a "crude" neutron (or proton) shell energy of a nucleus with Z and N is obtained as the deviation at n=N (or n=Z). Next, we refine these crude shell energies by taking into account the effect of pairing interactions; we take a weighted average of the crude shell energies of neighboring nuclei in which the weight is related to the occupation probability of the BCS theory. The effect of high-energy configuration mixing is simply treated by multiplying a reduction factor μ for the shell energies. The shell energies thus obtained are called "spherical shell energies" in the following. See ref. 4 for the detailed explanation.

§3. Deformation effects

The shell energy of a deformed nucleus is expressed as a sum of two parts: an intrinsic shell energy and an average deformation energy.

3. 1 *Intrinsic shell energy*

We state three important assumptions for our prescription to obtain the intrinsic shell energies of deformed nuclei.

Assumption [1]: The intrinsic shell energy comes only from the differences between the single-particle levels and their structureless positions as

$$E_{\mathrm{in}}(Z, N) = \mu \sum_{\nu} w_{\mathrm{p}\nu}(Z, N)\,(\varepsilon_{\mathrm{p}\nu} - \overline{\varepsilon_{\mathrm{p}\nu}}) + \mu \sum_{\nu} w_{\mathrm{n}\nu}(Z, N)\,(\varepsilon_{\mathrm{n}\nu} - \overline{\varepsilon_{\mathrm{n}\nu}})\ . \qquad (1)$$

Here, $\varepsilon_{j\nu}$ (ν =1,2,3...) are single particle energies in the spherical potential, $\overline{\varepsilon_{j\nu}}$ are their structureless positions, and $w_{j\nu}(Z, N)$ are occupation probabilities of the ν-th spherical single-particle states in the deformed nucleus (j = n or p).

In the case of a spherical nucleus eq. (1) changes into

$$E_0(Z, N) = \mu \sum_{\nu} w_{0\mathrm{p}\nu}(Z, N)\,(\varepsilon_{\mathrm{p}\nu} - \overline{\varepsilon_{\mathrm{p}\nu}}) + \mu \sum_{\nu} w_{0\mathrm{n}\nu}(Z, N)\,(\varepsilon_{\mathrm{n}\nu} - \overline{\varepsilon_{\mathrm{n}\nu}})\ , \qquad (2)$$

where the subscript "0" indicates the spherical nucleus.

Assumption [2]: Each occupation probability in a deformed nucleus can be expressed as a linear combination of the occupation probabilities in the spherical states as

$$w_{\mathrm{p}\nu}(Z, N) = \sum_{Z'} W_{\mathrm{p}}(Z'; Z, N)\, w_{0\mathrm{p}\nu}(Z', N)\ ,$$

$$w_{n\nu}(Z, N) = \sum_{N'} W_n(N'; Z, N)\, w_{0n\nu}(Z, N') , \tag{3}$$

where $w_{0j\nu}(Z', N)$ are occupation probabilities in the selected spherical states, and $W_p(Z'; Z, N)$ and $W_n(N'; Z, N)$ are their weights.

Assumption [3]: The directionally-averaged proton and neutron radial distributions are simple weighted sums of the radial density distributions of the single-particle states,

$$\rho_j(r; Z, N) = \sum_{\nu} w_{j\nu}(Z, N)\sigma_{j\nu}(r) , \tag{4}$$

where $\sigma_{j\nu}(r)$ are radial density distribution in ν-th single-particle states.

From these assumptions, we can deduce the following equations:

$$E_{in}(Z, N) = \sum_{N'} W_n(N'; Z, N)\, E_{0n}(Z, N') + \sum_{Z'} W_p(Z'; Z, N)\, E_{0p}(Z', N) , \tag{5}$$

$$\rho_p(r; Z, N) = \sum_{Z'} W_p(Z'; Z, N)\rho_{0p}(r) ,$$
$$\rho_n(r; Z, N) = \sum_{N'} W_n(N'; Z, N)\rho_{0n}(r) . \tag{6}$$

Equation (6) implies a possibility of determining the mixing weights $W_n(N'; Z, N)$ by comparing the directionally-averaged distributions in deformed nuclei with those in spherical nuclei. For example, in the case of uniform density with sharp-cut surface, the mixing weight $W_n(N'; Z, N)$ is obtained as

$$W_n(N'; Z, N) = -\frac{1}{4\pi}\frac{d\Omega_{occ}(r(N'))}{dN'} , \tag{7}$$

where $\Omega_{occ}(r(N'))$ is the occupied solid angle for the radial coodinate $r(N')$ (See Figs. 1 and 2). This shows that the mixing weight is related to the decrease of the occupied solid angle.

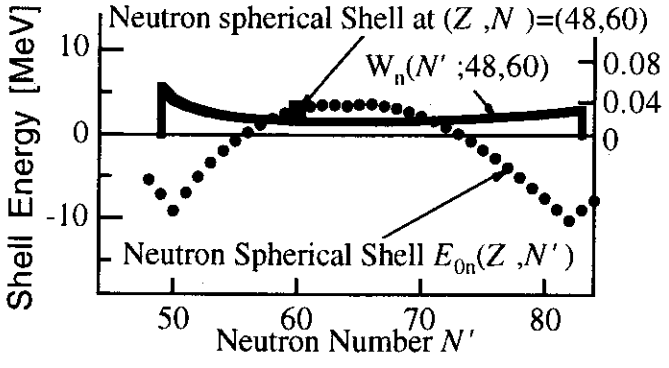

Fig. 1: Mixing weight $W_n(N'; Z, N)$ for the nucleus with $Z = 48$, $N = 60$ (right scale) and spherical shell energies $E_{0n}(Z, N')$ (left scale)

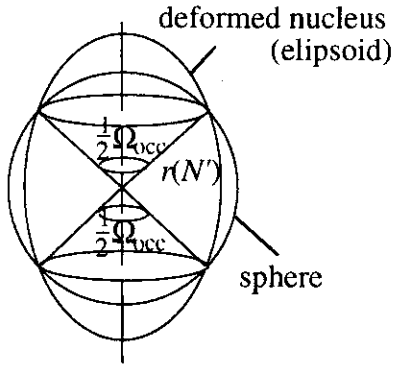

Fig. 2: Illustration of the occupied solid angle $\Omega_{occ}(r(N'))$ in the case of prolate deformation

3. 2 *Average deformation energy*

The average deformation energy can be estimated from the liquid-drip model or its slight modification. From the liquid-drop model,

$$\Delta E_{\mathrm{DFLD}} = \Delta E_{\mathrm{surf}} + \Delta E_{\mathrm{Coul}} , \tag{8}$$

where ΔE_{surf} and ΔE_{Coul} are the differences of the surface and Coulomb energies of a deformed nucleus from those of the spherical nucleus.

According to experimental data, the prolate shape is dominant in most deformed nuclei. We phenomenologically use an additional term to take into account this situation as

$$\Delta E_{\mathrm{prl}}(\alpha_2, A) = - C_{\mathrm{prl}}\, \alpha_2\, A^{1/3} , \tag{9}$$

where C_{prl} is a parameter and the A-dependence is chosen somewhat arbitrarily with a conjecture that the dependence should be a little weaker than that of the surface area.

The average deformation energy is expressed as

$$\overline{E_{\mathrm{def}}} = \Delta E_{\mathrm{DFLD}} + \Delta E_{\mathrm{prl}} . \tag{10}$$

3. 3 *Refined shell energy*

The sum of the intrinsic shell energy and the average deformation energy is the effective shell energy of a deformed state. If we are concerned with the ground state, we should search for the minimum of the effective shell energies of various deformed states, i.e.,

$$E_{\mathrm{sh}}(Z, N) = \min_{\mathrm{deformation}} \left[E_{\mathrm{in}}(Z, N) + \overline{E_{\mathrm{def}}} \right] . \tag{11}$$

We call $E_{\mathrm{sh}}(Z, N)$ the refined shell energy. So far we have made numerical calculations for Y_2 and Y_4 deformations with deformation parameters α_2 and α_4 as

$$r(\theta) = \frac{r_0}{\lambda} \left[1 + \alpha_2 P_2(\cos\theta) + \alpha_4 P_4(\cos\theta) \right] , \tag{12}$$

where

$$\lambda = \left[1 + \frac{3}{4\pi} \left(\frac{4\pi}{5} \alpha_2^2 + \frac{4\pi}{9} \alpha_4^2 \right) \right]^{1/3} ,$$

which is introduced to stand for the condition of the volume conservation.

The shell energy of a deformed nucleus and its equilibrium shape are thus obtained. In Fig. 3 the shell energies are shown and in Fig. 4 the deformation parameters α_2 are shown.

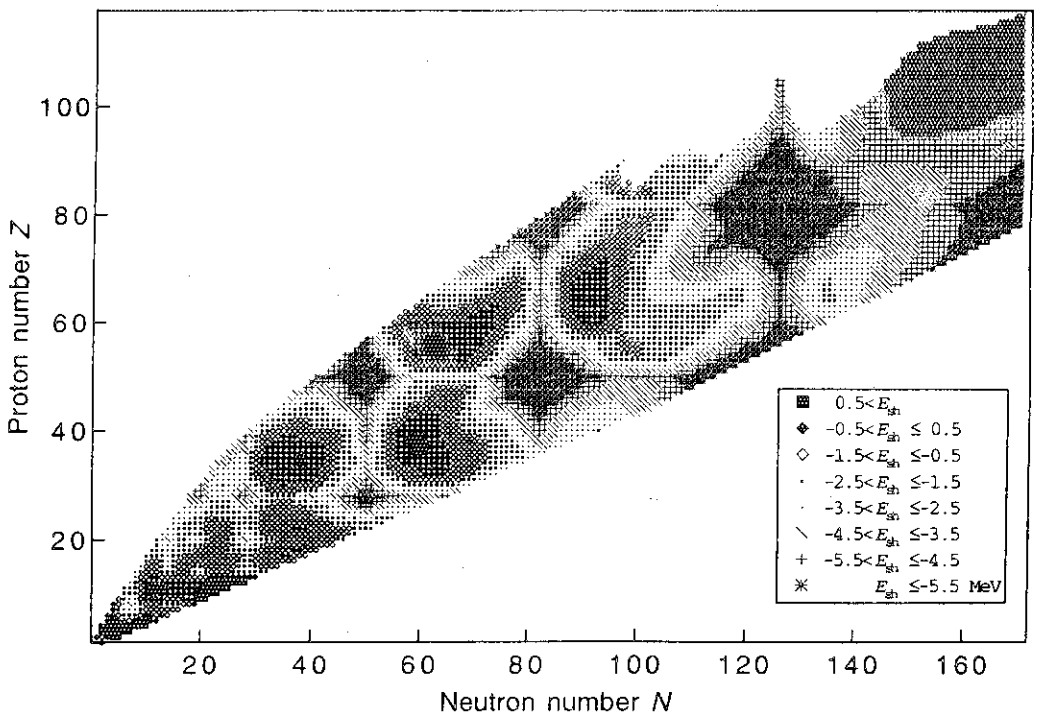

Fig. 3: Refined shell energy

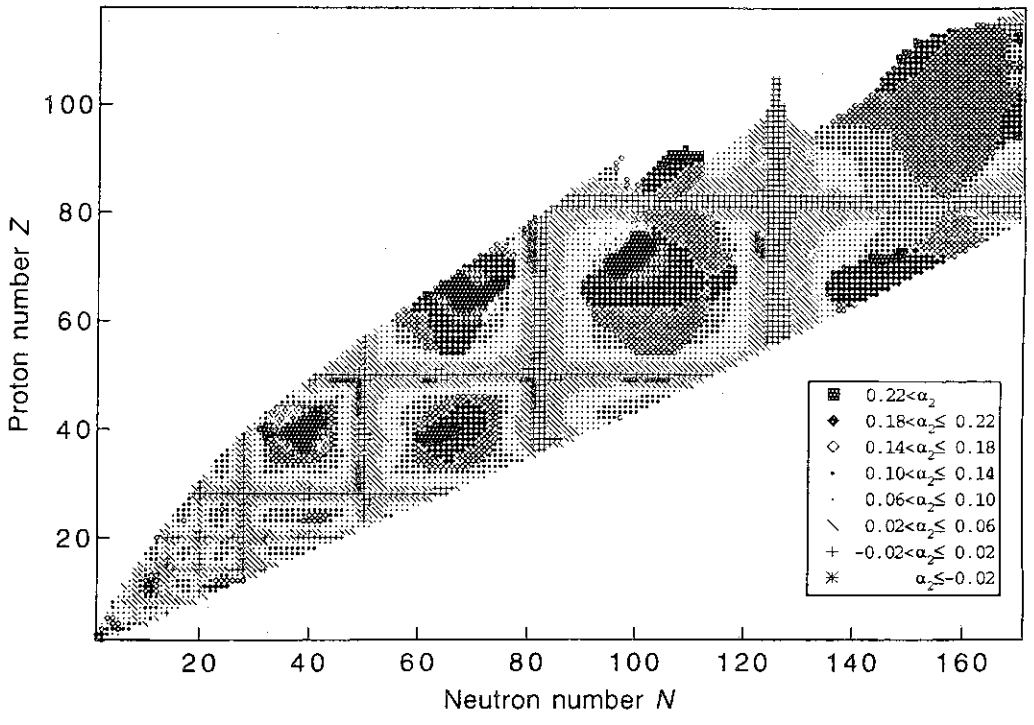

Fig. 4: Deformation parameter α_2

We can obtain the energy surface of a nucleus by mapping the effective shell energies against the deformation parameters α_2 and α_4. We, for example, show in Fig. 5 the energy surface of ^{260}106.

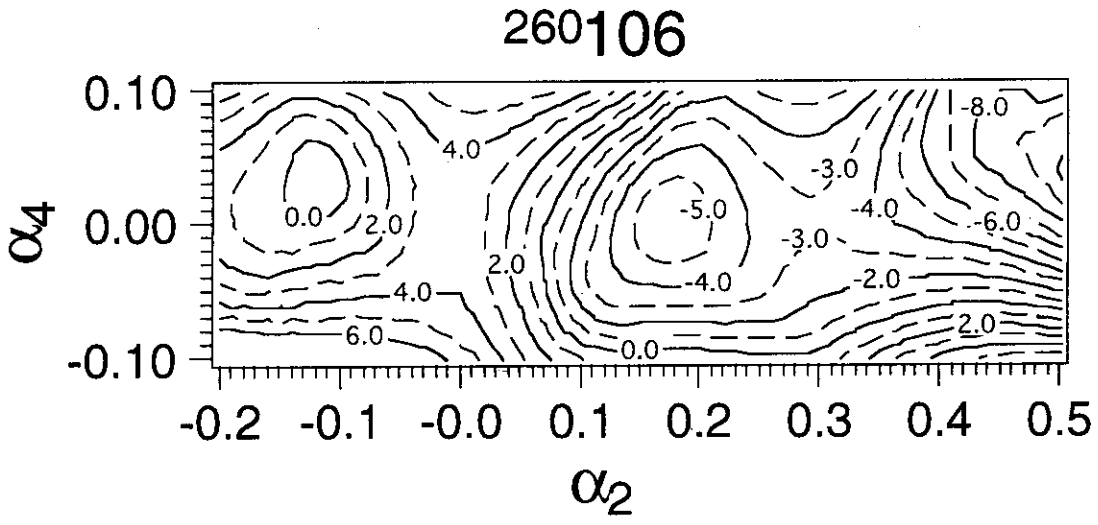

Fig. 5: Energy surface of ^{260}106 on the deformation parameter plane (α_2, α_4)

§4. Concluding remark

The results shown in Fig. 4 can be compared with results of ref [5] in which a deformed potential is used. The ground-state deformation of ^{260}106 calculated by our method is somewhat larger than that of ref [5], and our fission barrier is smaller.

Our previous mass formula[2] is expressed as a sum of three parts: the gross part $M^{\mathrm{TUYY}}_{\mathrm{gross}}(Z, N)$, the even-odd part $M^{\mathrm{TUYY}}_{\mathrm{even-odd}}(Z, N)$ and the shell part $M_{\mathrm{sh}}(Z, N)$. The refined shell energies $E_{\mathrm{sh}}(Z, N)$ in §3 can be adopted as $M_{\mathrm{sh}}(Z, N)$, which, at present, give the root mean square deviation of 854 keV from experimental masses. Further improvement is under way.

References

[1] M. Uno and M. Yamada, Prog. Theor. Phys., **65**, (1981), 1332
[2] T. Tachibana, M. Uno, M. Yamada and S. Yamada, Atomic Data and Nuclear Data Tables **39**, (1988), 251
[3] P. Möller and J. R. Nix, Atomic Data and Nuclear Data Tables **39**, (1988), 43
[4] H. Koura, T. Tachibana, M. Uno and M. Yamada, JAERI-Conf, 95-008, 250; M. UNO, T. Tachibana, M. Takano, H. Koura and M. Yamada, *Nuclei Far From Stability 6 / Atomic Masses and Fundamental Constants 9* (BernKastel-Kues, 1992), (IOP 132), 117
[5] R. Smolańczuk, H. V. Klapdor-Kleingrothaus and A. Sobiczewski, Acta Phys. Pol. **B24**, (1993), 457

3.31 A SIMPLE METHOD FOR EVALUATION OF UNCERTAINTIES IN FISSION PRODUCT DECAY HEAT SUMMATION CALCULATIONS

Hirokazu Ohta , Kazuhiro Oyamatsu and Kanji Tasaka*
Department of Energy Engineering and Science
Nagoya University
Furo-cho , Chikusa-ku , Nagoya , 464-01 JAPAN
e-mail address: g44092a@nucc.cc.nagoya-u.ac.jp

ABSTRACT

The present precision of nuclear data for the aggregate decay heat evaluation is analyzed quantitatively for 50 fissioning systems. In the practical calculation, a simple approximate method is proposed in order to avoid complication of the calculation and to point out easily the main causal nuclei of the uncertainties in decay heat calculations. As for the independent yield, the correlation among the values is taken into account. For this evaluation, nuclear data and their uncertainty data are taken from ENDF/B-VI nuclear data library.

1. INTRODUCTION

The precise knowledge of decay heat power from fission products is very important irrespective of the reactor systems as far as we utilize nuclear fission energies. The evaluation of the decay heat power is necessary, for example, in predicting the heat-up of nuclear fuel rods during a loss-of-coolant accident (LOCA) of a nuclear reactor, designing a heat removal system of a reactor or designing a spent fuel reprocessing plant.

The decay heat power has been measured since 1940's when a nuclear reactor was operated for the first time. Attempts to calculate the decay heat power theoretically began almost at the same time. Although the calculation may be preferred by virtue of its generality, in such earlier years the calculated results disagreed with the measured power at short cooling times because decay data for short-lived fission products were not available. Later, owing to accumulation of measured decay data and progress of computers together with refinement of estimation methods of nuclear data for nuclides without experimental data, the decay heat calculations for several fissioning systems come to give a good agreement with the measured values. However, this agreement does not guarantee the precision of the whole nuclear data or the prediction power for other fissioning systems. In the future, light water reactors (LWRs) will be operated using a higher burnup fuel. In the meantime new type reactors, such as reactors for transmutations of actinides and long-lived fission products, have proposed. Therefore, the more precise nuclear data are now required in order to calculate decay heat power more accurately not only for ^{235}U and ^{239}Pu but also for other minor actinides such as Am and Cm. Furthermore as the number of evaluated nuclear data increased, it seems a good time to assess maturity of the present nuclear data library. Since the uncertainties in decay heat calculations result from both uncertainties in each nuclear data and sensitivities of each parameter toward the total decay heat power, the evaluation of their uncertainties is useful for finding out problems in the present nuclear data clearly.

From these viewpoints, we evaluate the uncertainties in decay heat calculations and analyze the present precision of their nuclear data in the decay heat evaluation.

---

* Deceased, February, 14, 1995.

2. DECAY HEAT CALCULATION BY SUMMATION METHOD

The total decay heat power $P(t)$ at a cooling time t after fission is obtained by summing up each decay heat power generated from each fission product (summation method) :

$$P(t) = \sum_{i}^{All\ F.P.} \lambda_i N_i(t) E_i \quad , \tag{1}$$

where λ_i, E_i and N_i (t) are the decay constant of nuclide i, the average decay energy of nuclide i and the number of atoms of nuclide i at the cooling time t after fission, respectively. Both λ_i and E_i are constants which are characteristic nuclear data of the nuclide i. On the other hand, N_i (t) must be calculated at every cooling time by solving simultaneous linear differential equations for production and decay of fission product nuclides. Practically, we compute N_i (t) using FPGS90N-code[1] in Bateman's method. The decay heat power calculated with this code is referred to as 'exact decay heat power' in the following.

3. NUCLEAR DATA AND THEIR UNCERTAINTY DATA

The various basic nuclear data for about 1,000 nuclides must be compiled for the summation calculation. Since the uncertainties of each basic nuclear data cast over the decay heat calculation results, we analyze the uncertainties in decay heat calculations propagated from the uncertainties in various basic nuclear data (decay constants, fission yields and average decay energies). All nuclear data and their uncertainty data necessary for this evaluation are taken from ENDF/B-VI nuclear data library. There are fission yield data for 50 fissioning systems and decay data for 891 fission products in this library. In addition, uncertainty data for experimental data are available in this library. However for nuclides without experimental data, the uncertainty values in their estimated nuclear data are not available in this library. The uncertainty data for these nuclides are supplemented by the following theoretical estimation.

3.1 Supplement of uncertainty data of estimated average decay energy

In ENDF/B-VI, the gross theory of β decay is adopted to estimate average decay energies. The same theory is applied here to estimate their uncertainty values. In this theory, there is a free parameter Q_{00} in order to take into account the prohibition of too much transition to the ground state of the daughter nuclide. In practical calculations, this parameter is determined not theoretically but empirically. As it is known that almost all Q_{00} values (about 95% of all Q_{00}) lie between 0.0MeV and 2.5MeV [2], the difference between the average decay energies at these limits of Q_{00} is assumed to give $\pm 2\sigma$ variance of estimated average decay energy values. Then the uncertainties of average β and γ decay energies of nuclide i are given by

$$\delta E_i^{\nu} = \frac{1}{4}\left| E_i^{\nu}(Q_{00} = 2.5\mathrm{MeV}) - E_i^{\nu}(Q_{00} = 0.0\mathrm{MeV}) \right| \quad , \ (\nu = \beta \ or \ \gamma) \quad , \tag{2}$$

where $E_i^{\nu}(Q_{00}=2.5\mathrm{MeV})$ and $E_i^{\nu}(Q_{00}=0.0\mathrm{MeV})$ are the average β or γ decay energies of the nuclide i calculated with limiting Q_{00} values of 2.5MeV and 0.0MeV, respectively.

The uncertainties of total $(\beta+\gamma)$ decay energies were not specified in ENDF/B-VI, either. The uncertainties of the total decay energies δE_i^t are calculated neglecting the correlation between β and γ decay energies:

$$\delta E_i^t = \sqrt{\left(\delta E_i^{\beta}\right)^2 + \left(\delta E_i^{\gamma}\right)^2} \quad . \tag{3}$$

This assumption should lead to an overestimation because there must be very strong negative correlation between β and γ decay energies in reality. The above method for the supplement of the uncertainty data was originally proposed by Katakura and Iijima[3] while our evaluation leads to larger uncertainty values due to a modification.

3.2 Supplement of uncertainty data of decay constant

In any theories or systematics, it is not a surprise that the estimated values of decay constant, λ_i, are too short or too long by an order of magnitude. Therefore we assume that their uncertainty values are equal to themselves:

$$\delta\lambda_i = \lambda_i \quad . \tag{4}$$

4. APPROXIMATE SUMMATION METHOD FOR DECAY HEAT CALCULATION

Since exact summation calculations are very complex, the uncertainty evaluation based on this exact method requires more complicated calculations. Hence, the main causal nuclides of the evaluated uncertainties cannot be pointed out easily because of this complication. Therefore we propose an alternative simple approximate method to overcome this difficulty.

Let us consider a linear decay chain without any branch or link:

$$X_1 \rightarrow X_2 \rightarrow X_3 \rightarrow \cdots\cdots \rightarrow X_{i-2} \rightarrow X_{i-1} \rightarrow X_i \rightarrow \cdots\cdots \rightarrow X_n$$

In general, nuclides far in the upper stream of a decay chain decay so quickly that they give little effects to the production of nuclides in the lower stream. Therefore in the practical calculation, the number of atoms of nuclide i, N_i, is assumed to be determined only by the decays of itself i, its parent i-1, (*mother* of i) and her parent i-2, (*grandmother* of i).

Namely,

$$\frac{dN_{i-2}}{dt} = -\lambda_{i-2}N_{i-2} \qquad \left(N_{i-2}(0) = Y_{i-2}\right), \tag{5}$$

$$\frac{dN_{i-1}}{dt} = -\lambda_{i-1}N_{i-1} + \lambda_{i-2}N_{i-2} \qquad \left(N_{i-1}(0) = y_{i-1}\right), \tag{6}$$

$$\frac{dN_i}{dt} = -\lambda_i N_i + \lambda_{i-1}N_{i-1} \qquad \left(N_i(0) = y_i\right), \tag{7}$$

where $N_i(0)$, y_i and Y_{i-2} are the number of atoms of nuclide i at cooling time 0(s), independent fission yield of nuclide i and the cumulative fission yield of nuclide i-2, respectively. Note that the initial number of *grandmother* nuclide i-2 is taken to be its cumulative yield Y_{i-2} in order to conserve the total number of atoms.

In Fig. 1, the decay heat power calculated by this approximate method are compared with that by the exact method (FPGS90N). This approximation is excellent at cooling times less than 10^{10}(s). Throughout this paper, the abbreviations (T) and (F) stand for thermal and fast neutron induced fission, respectively. However the decay heat power calculated by the approximate method (especially for γ-decay heat power) deviates from the exact result at cooling times longer than 10^{10}(s). The reason for this deviation is a break down of the assumption for this approximation in the decay chain of mass number A=126. Therefore the uncertainty evaluations are performed at cooling times between 0 and 10^{10}(s) after a burst fission in this paper.

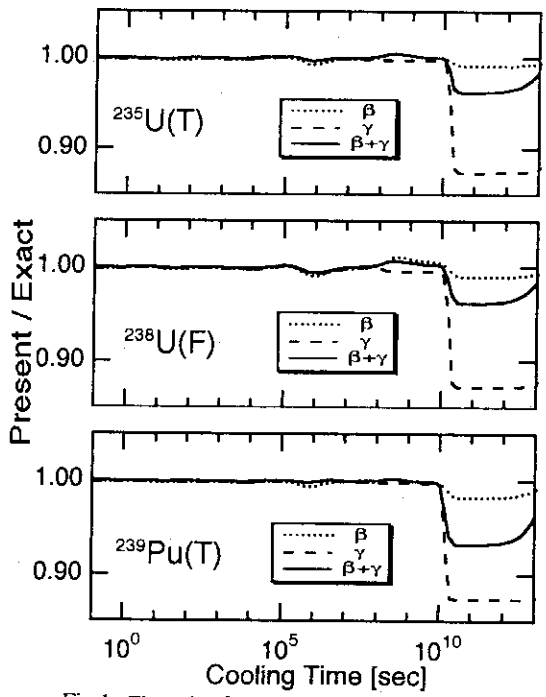

Fig.1 The ratio of the decay heat power calculated by our approximate method to that by the exact method (FPGS90N). Results for ^{235}U(T), ^{238}U(F) and ^{239}Pu(T) burst fissions are shown.

5. THE CALCULATION FOR DECAY HEAT UNCERTAINTIES

Uncertainties in decay heat summation calculations are evaluated with use of the law of error propagation.

$$\left(\delta P(t)\right)^2 = \sum_{i=1}^{all\,F,P} \left\{ \left(\frac{\partial P}{\partial E_i}\right)^2 \left(\delta E_i\right)^2 + \left(\frac{\partial P}{\partial \lambda_i}\right)^2 \left(\delta \lambda_i\right)^2 + \left(\frac{\partial P}{\partial y_i}\right)^2 \left(\delta y_i\right)^2 + \left(\frac{\partial P}{\partial Y_i}\right)^2 \left(\delta Y_i\right)^2 \right\} . \qquad (8)$$

Here, the symbol δ denotes the uncertainty of each parameter.

In addition, since approximate method is adopted in this study, the error due to this approximation, δP_i^a, is also taken into account:

$$\delta P_i^a = E_i \lambda_i (N_i^a - N_i^e) , \qquad (9)$$

where N_i^a and N_i^e are the number of atoms of nuclide i calculated by the approximate and exact methods, respectively. Then we rewrite Eq. (9) as

$$\left(\delta P(t)\right)^2 = \sum_{i=1}^{all\,F,P} \left\{ \left(\frac{\partial P}{\partial E_i}\right)^2 \left(\delta E_i\right)^2 + \left(\frac{\partial P}{\partial \lambda_i}\right)^2 \left(\delta \lambda_i\right)^2 + \left(\frac{\partial P}{\partial y_i}\right)^2 \left(\delta y_i\right)^2 + \left(\frac{\partial P}{\partial Y_i}\right)^2 \left(\delta Y_i\right)^2 \right\} + \sum_{i}^{all\,F,P} \left(\delta P_i^a\right)^2 . \quad (10)$$

6. THE STRONG CORRELATION AMONG INDEPENDENT YIELD VALUES

It is known that there is a very strong correlation among independent yield values. This correlation is due to the following constraints:

1. The sum of independent yields in a decay chain is equal to the mass chain yield.
2. The total sum of the mass chain yields is equal to 2.0.

In this paper, uncertainties in decay heat calculations are evaluated taking this correlation effect into account.[4,5] This strong correlation makes uncertainty values smaller irrespective of cooling time as shown in Figs. 2 and 3.

On the other hand, it is more advantageous to adopt the method without correlation effects in pointing out main causal nuclides of large uncertainties. Therefore we also perform the uncertainty calculation without correlation effects in order to specify these causal nuclides.

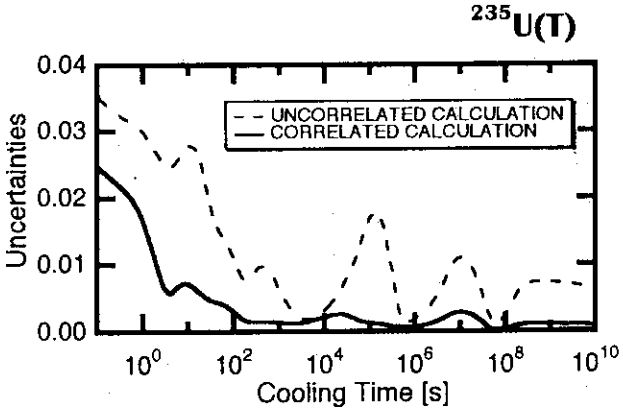

Fig. 2. Correlation effects for uncertainties in fission yields for ^{235}U thermal fission.

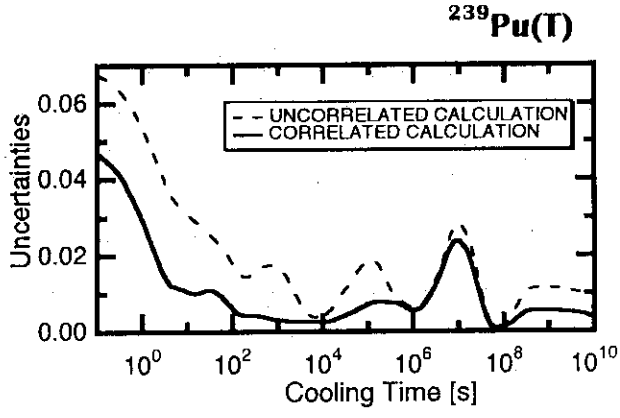

Fig. 3. Correlation effects for uncertainties in fission yields for ^{239}Pu thermal fission.

7. RESULTS

In this section, we discuss uncertainties in decay heat summation calculations with the correlation effects. Results for ^{235}U thermal fission and ^{241}Am fast fission are shown in Figs. 4 and 5, respectively. Generally the uncertainties due to decay constants, decay energies and independent yields are large at short cooling times while those due to cumulative yields are dominant at relatively long cooling times.

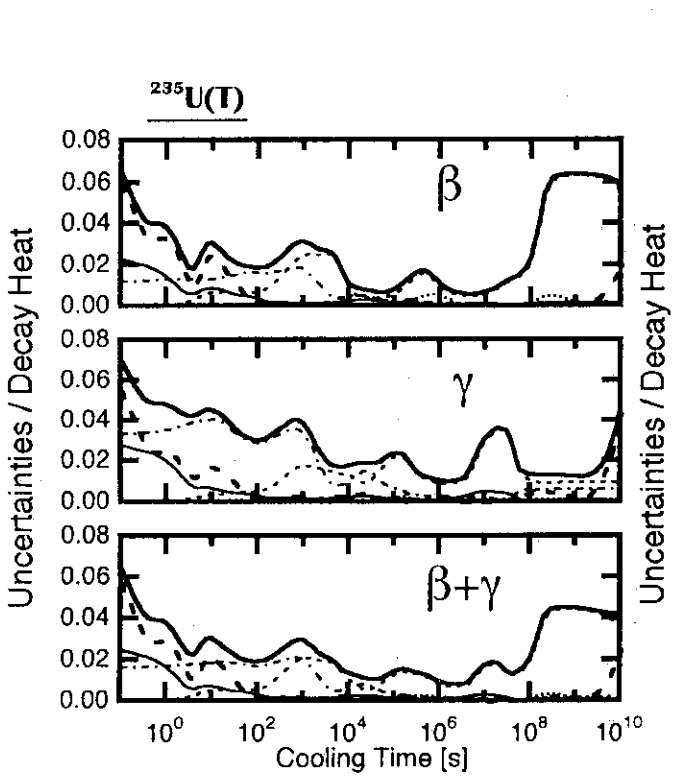

Fig.4. The uncertainties in decay heat calculations for ^{235}U thermal fission

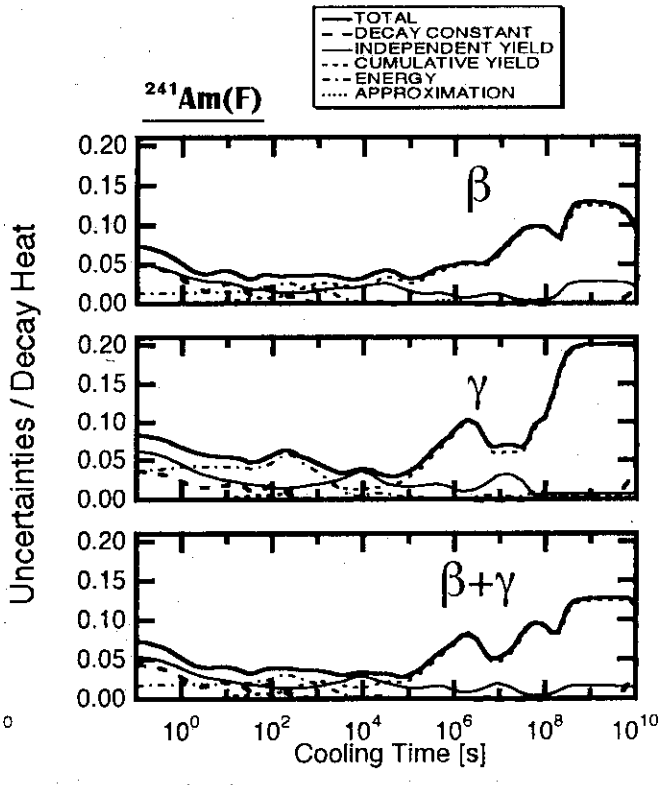

Fig.5. The uncertainties in decay heat calculations for ^{241}Am fast fission

Uncertainty values for several fissioning systems are listed in Table 1. We see clearly that the uncertainty values depend heavily on the fissioning systems. However, the cooling time dependence of the uncertainty value is similar irrespective of the fissioning systems. Namely, uncertainty values are relatively large at short cooling times and far long cooling times while they are inversely small in the range of cooling time about 10^4~10^8 (s) as shown in Figs. 4 and 5.

Furthermore we note that the uncertainties for minor actinides are larger by a factor of 3~5 than those for major actinides.

Table 1. The uncertainties in decay heat calculations for several fissioning systems [%]

Fissioning systems	β	γ	$\beta+\gamma$
^{235}U(T)	1~6	1~6	1~6
^{238}U(F)	1~5	2~5	2~4
^{239}Pu(T)	2~12	2~13	2~7
^{237}Np(F)	3~12	3~9	3~9
^{241}Am(F)	4~13	4~20	4~13
^{243}Am(F)	5~13	5~16	4~12
^{244}Cm(F)	4~13	5~20	5~13
^{246}Cm(F)	5~14	6~17	5~12
^{248}Cm(F)	5~15	6~15	5~12

As shown in Fig. 6 the present result is consistent with AESJ recommendation[6]. These results need not to be exactly equal because of different nuclear data are used in the two evaluations.

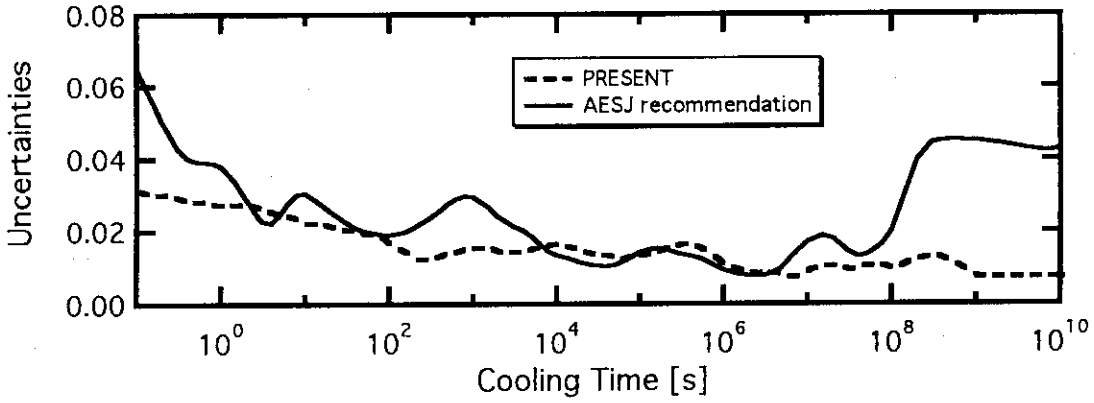

Fig. 6 Comparison between the present results and AESJ recommendations for ^{235}U thermal fission

8. CONCLUSION

We propose a simple approximate method to evaluate uncertainties in the decay heat summation calculations. The approximation is found to be excellent at cooling times between 0 and 10^{10}(s). With this method, we evaluate uncertainties in the decay heat calculations for 50 fissioning systems of which 46 are not available in AESJ recommendation. We find that cooling time dependence of the uncertainty is similar irrespective of the fissioning systems. The uncertainty is relatively small at 10^4~10^8(s) compared with those at the shorter or longer cooling times. We also find the uncertainties for minor actinides are larger, by a factor of 3~5, than those for major actinides. Typical examples of uncertainty values are about 1~6% for ^{235}U(T) and about 4~12% for ^{241}Am(F). Furthermore the main causal nuclides for the uncertainties in decay heat calculations are pointed out for ^{235}U(T) at each cooling time. The lists of these nuclides will be a great help in coming preparation of nuclear data. More detailed results including the lists of main causal nuclides will be published elsewhere in the near future.

[1] Ihara H. Katakura J. and Nakagawa T.: " A Computer Code for Calculation of Radioactive Nuclide Generation and Depletion, Decay Heat and γ Ray Spectrum -FPGS90-" JAERI-Data / Code 95-014 (1995).
[2] Yoshida T.: Nucl. Sci. and Eng., 63, 379-390 (1977).
[3] Katakura J. and Iijima S.: J. Nucl. Sci. Technol., 29[1], 11-23 (1992).
[4] Schmittroth F.: Nucl. Sci. and Eng., 59, 117-139 (1976).
[5] Spinrad B I.: Nucl. Sci. and Eng., 62, 35-44 (1977).
[6] Research Committee on Standardization of the Decay Heat Power in Nuclear Reactors, Atomic Energy Society of Japan.: " Houkainetsu no suisyouchi to sono shiyouhou." (in Japanese) (1990).

3.32 Direct radiative capture mechanisms and the structure of light nuclei

A. MENGONI
RIKEN, Radiation Laboratory, 2-1 Hirosawa, Wako, Saitama 351-02, Japan,
and ENEA, Applied Physics Section, v. Don Fiammelli 2, 40128 Bologna, Italy
e-mail: mengoni@rikvax.riken.go.jp

Abstract

The neutron capture cross section of ^{12}C and ^{16}O in the neutron energy region up to $\approx$ 1 MeV has been calculated in the framework of the direct radiative capture (DRC) model. The role played by incident p-wave and higher partial l-wave neutrons has been investigated in connection with the description of peculiar nuclear structure properties of light nuclei (neutron halo).

1 Introduction

Following the discovery of light drip-line nuclei with halo structure, it has been recently recognized [1, 2, 3] that the neutron capture mechanism may provide a useful and in some case a unique tool for analyzing the structure of wave function components outside the nuclear radius. Some aspect of the capture process has received particular attention because of the results of a set of new measurements of neutron reaction cross sections made available from the Tokyo Institute of Technology [4, 5]. These experimental works made it possible to check the validity of the direct radiative capture (DRC) model assumptions, in connection with the discovery of exotic nuclear structure properties in light, neutron-rich nuclei.

Because for some of the light nuclei the capture cross sections are relatively small (of the order of millibarns, in the keV neutron energy region), nuclear data evaluations for light isotopes have usually received low priorities. However, some neutron capture reaction processes in light nuclei are relevant also for applications in nuclear astrophysics, in particular for primordial and stellar nucleosynthesis. The knowledge of the neutron capture cross section are therefore necessary.

In trying to fill up these requirements, we have recently carried out a series of neutron capture cross section calculations in the energy region from thermal up to a few MeV, using the DRC model. Whenever appropriate, the contribution due to neutron resonances has been included. Here we will show only a sub-set of the results so far obtained, namely the cross section calculation for the ^{12}C(n,γ) and for the ^{16}O(n,γ) reaction processes.

2 (n,γ) cross section calculation

For incident neutron energies up to a few hundred of keV and in a situation in which the level density is low and isolated compound states are located at higher energy, the (n,γ) reaction mechanism may be dominated by a direct radiative capture (DRC) process. Then, the cross section is essentially determined by a radial overlap of the incoming (or channel) wave function with the residual nucleus capturing state wave function.

We have recently shown [3] that, when the capture cross section is dominated by incident s-wave neutrons, the matrix elements for E1 emission, $Q^{(1)}_{i\to f} = < \Psi_f|\hat{T}^{E1}|\Psi_i >$, are sensitive to the neutron-nucleus interaction. On the contrary, the cases in which the incident p-wave or higher l-wave components dominate the capture process, the matrix elements are *insensitive* to the neutron-nucleus interaction. In particular, for p-wave incident neutrons, all the information on the capture process is carried by the structure of the final capturing state wave function. For E1 transitions, the final state must have a strong single-particle l=0 configuration, the same condition required for having neutron halo structure. Thus, the DRC process of p-wave neutrons may provide information in the halo structure of the final state, whether this is the ground state or a nuclear excited state.

2.1 ^{12}C(n,γ)

The DRC model description and the parameters used for the calculation of $n + {}^{12}$C are given elsewhere[3]. Here we show the results of the capture leading to the four bound levels of ^{13}C. The four states are bound by 4.946 ($1/2^-$), 1.857 ($1/2^+$), 1.262 ($3/2^-$) and 1.093 ($5/2^+$) MeV (total angular momentum and parity are indicated between brackets). The results are shown in the Figures 1 to 4, respectively.

In comparison with the calculations provided in the reference [3], we have extended the incident neutron energy range up to 800 keV. A new experimental result at E_n = 550 keV has been made available recently [6] and the respective values are shown in the figures. These new experimental values agree well with the model predictions. In particular, from Figure 1 and 3 it is possible to notice the onset of d-wave capture. Overall, the DRC model calculations reproduce well the experimental results.

2.2 ^{16}O(n,γ)

The calculation for $n+{}^{16}$O has been done following the technique used in the carbon case. Here, the contribution of incident p-waves shows up in the capture leading to the ground and to the first excited state of ^{17}O. These two levels are bound by 4.145 ($5/2^+$) and 3.273 ($1/2^+$) MeV respectively. They both have strong single-particle character (a spectroscopic factor $\approx$ 1 can be assumed for both levels), making the DRC model assumptions particularly reliable in the present case.

The cross section for the transitions leading to the two negative-parity states, bound by 1.088 ($1/2^-$) and 0.303 ($5/2^-$) MeV, is essentially due to incident s-wave neutrons. This contribution can be derived from the ^{16}O thermal neutron capture, $\sigma_\gamma = 202 \pm 28$ μb. A $1/v$ approximation can be adopted to evaluate this contribution at higher energies. The contribution of the capture leading the two negative-parity levels is negligible compared to the contribution coming from incident p-wave neutrons.

The results of our calculation are shown in Figure 5. Here, we show the DRC calculation as the sum of the neutron capture cross section leading to the ground ($5/2^+$) and first excited state ($1/2^+$) of ^{17}O. The contribution due to incident s-wave neutrons is shown as a $1/v$ extension of the thermal neutron capture.

In the ^{16}O(n,γ) case, there is a resonance state at 434 keV. The neutron and gamma widths of this resonance are respectively $\Gamma_n = 45 \pm 5$ keV and $\Gamma_\gamma = 2.7 \pm 0.5$ eV. The single-level Bright-Wigner formalism has been applied to evaluate the contribution coming from this resonance state. No interference contribution was included in the present calculation.

The results of Figure 5 show good agreement with the experimental values of Igashira *et al.*[5].

3 Conclusion

Using a DRC model we have calculated $^{12}C(n,\gamma)$ and $^{16}O(n,\gamma)$ capture cross sections. A comparison with recent cross section measurements provided the necessary quantitative test of the model. The interplay of the DRC mechanism with the neutron halo structure in light nuclei has been shown.

Acknowledgments

This work has been partially supported by a Science and Technology Research Fellowship (JIS-TEC - 194102).

References

[1] T. Otsuka, M. Ishihara, N. Fukunishi, T. Nakamura and M. Yokoyama
"Neutron halo effect on direct neutron capture and photodisintegration"
Phys. Rev. C **49**, R2289 (1994).

[2] A. Mengoni, T. Otsuka, and M. Ishihara
"Halo structure of nuclear excited states and the neutron radiative capture process"
Proceedings of the Workshop on Experimental Perspectives with Radioactive Nuclear Beams, Padova, 14-17 November 1994. In press (1995).

[3] A. Mengoni, T. Otsuka, and M. Ishihara
"Direct radiative capture of p-wave neutrons"
Phys. Rev. C **52**, (1995) 2334.

[4] T. Ohsaki, Y. Nagai, M. Igashira, T. Shima, K. Takeda, S. Seino and T. Irie
"New measurement of the $^{12}C(n,\gamma)$ reaction cross section"
Ap. J. **422**, 912 (1994).

[5] M. Igashira, Y. Nagai, K. Matsuda, T. Ohsaki and H. Kitazawa
"Measurement of the $^{16}O(n,\gamma)$ reaction cross section at stellar energy and the critical role on nonresonant p-wave neutron capture"
Ap. J. **441**, (1995) L89.

[6] Y. Nagai and T. Shima
Private communication (1995).

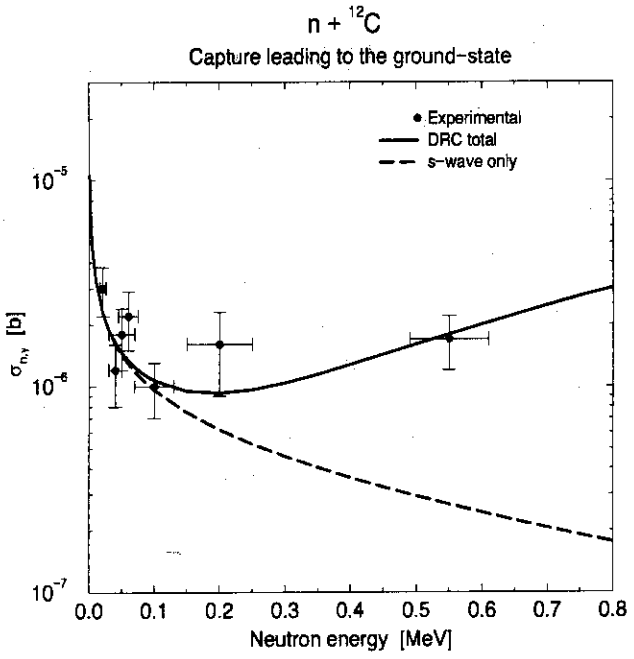

Figure 1: Neutron capture cross section of ^{12}C leading to the ground state of ^{13}C ($J^\pi = 1/2^-$). The experimental values are from [4, 6].

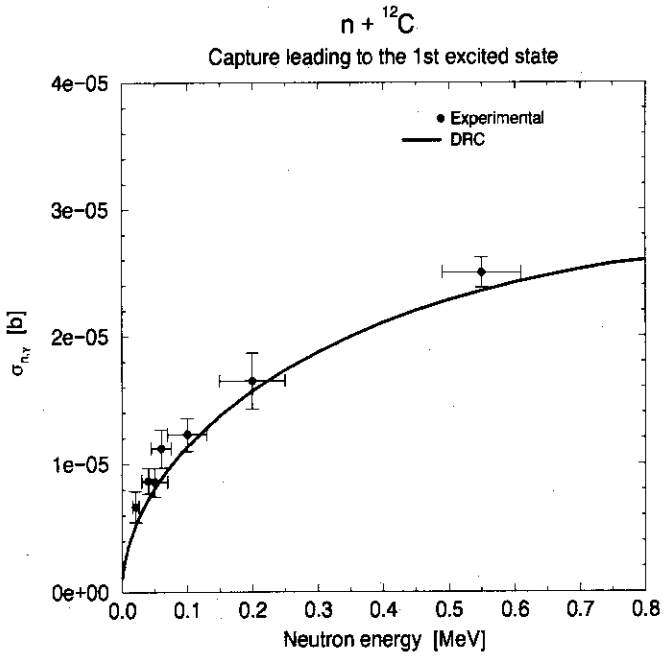

Figure 2: Neutron capture cross section of ^{12}C leading to the first excited state of ^{13}C ($J^\pi = 1/2^+$). The experimental values are from [4, 6].

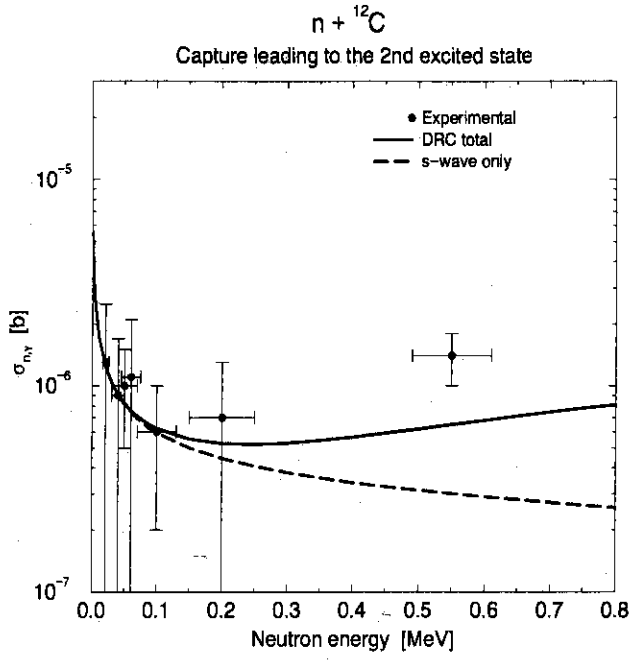

Figure 3: Neutron capture cross section of ^{12}C leading to the second excited state of ^{13}C ($J^\pi = 3/2^-$). The experimental values are from [4, 6].

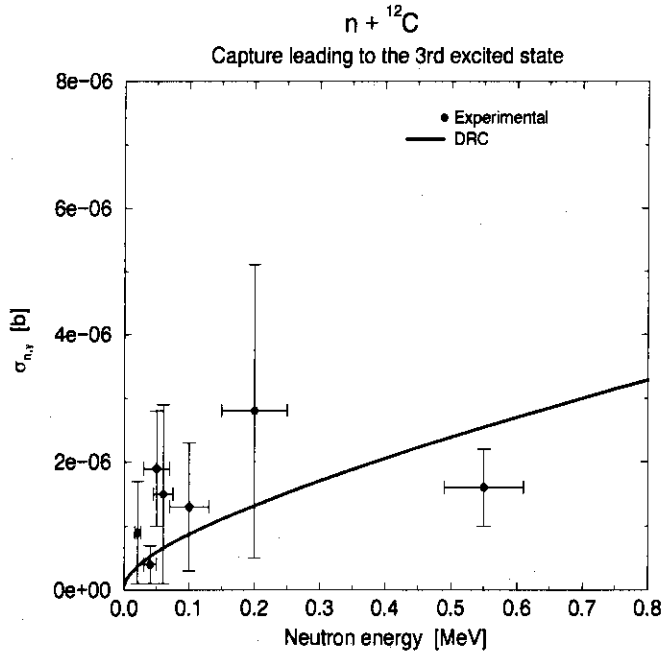

Figure 4: Neutron capture cross section of ^{12}C leading to the third excited state of ^{13}C ($J^\pi = 5/2^+$). The experimental values are from [4, 6].

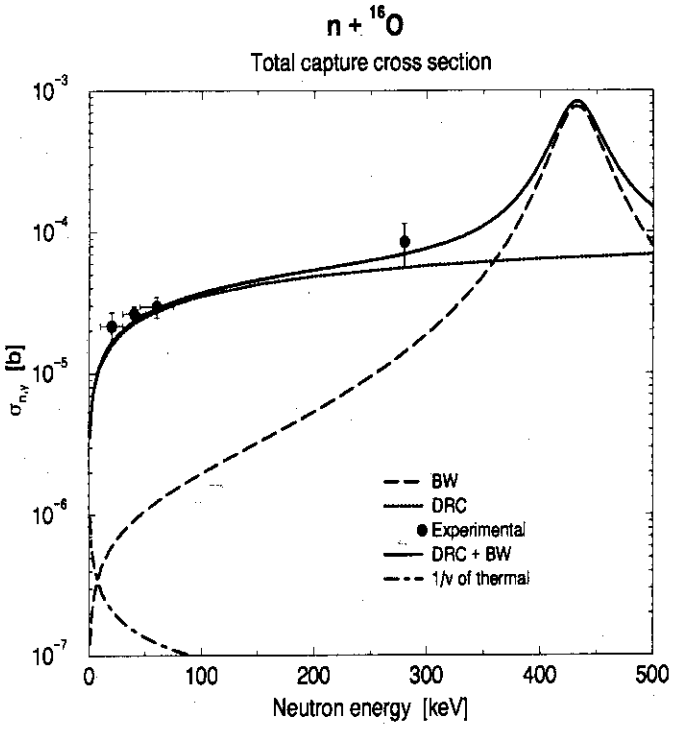

Figure 5: Neutron capture cross section of ^{16}O. The various contribution shown have been calculated as described in the text. The experimental values are from [5].

3. 33 Future Prospects of Superfine Structure of Neutron Resonance Levels

Kazumi IDENO
Advanced Science Research Center, JAERI
Tokai, Ibaraki 319-11

Neutron resonance spectra appear simply and regularly in the light of superfine structure (SFS). It is found that the relative shifts (i.e. the relative distances) between the SFSs for groups of nuclei have definite values and are closely interrelated to the symmetry properties of the compound systems if we treat neutron zero energy as a common reference point. An origin of the SFSs and its possible application to an evaluation of nuclear data are discussed.

Can we disentangle complex spectra of neutron resonance levels and discover any systematic laws in the distributions of level positions from one nucleus to another? An enterprise to answer this question will encounter a difficult situation which mainly originates from the predominance of chaotic motion in a compound nucleus[1]. Our long-term search for regularities in the level distributions, however, revealed the existence of characteristic level distances for intermediate and heavy nuclei[2]. This level structure has been named by I. M. Frank[3] as *superfine structure (SFS)* in the sense that it relates to many different nuclei with eV-scale interactions. The simplest type of characteristic level distances is an unit level distance with which level positions are determined in a way closely interrelated among different nuclei[4]. To detect the SFSs and study its mutual relationship, we need a new concept and a special technique of analysis, which are described in the following.

Detection of the SFSs and relative shifts

First, as a reference, we use the levels of the ^{123}Sb, ^{168}Er, ^{177}Hf and ^{179}Hf nuclei where the SFSs are typically observed[4]. For these nuclei, most of the observed level energies can be expressed by $E_i = n\varepsilon + \eta$, where n takes integers, ε is an unit level distance and η a shift to the lattice points $n\varepsilon$ starting from neutron zero energy. Table 1 shows the parameters for these nuclei. The upper energy ranges were limited by the experimental energy resolutions of the data[5].

Second, we treat the neutron zero energy as a common reference point, which is equal to a point of neutron separation energy. It is stressed that this reference point acts for correlated levels.

Third, we determine a relative shift $\Delta\eta$ (i.e. relative distance) between the SFSs of a sampled and a reference nucleus. For this purpose we use a (20+1)-point correlation function A_{20}[2,4]; its values at ε, 2ε, 3ε,... represent the dominance of the unit level distance ε. The variance of A_{20} can be approximated by the average value of A_{20}: var $A_{20} \approx \langle A_{20} \rangle$. This approximation holds good especially for the GOE[4]. A normalized function of A_{20} is denoted by a_{20}, which is equal to the probability of finding a level from each level separated at the distances of $m\varepsilon$ (m = 1, 2, ..., 20) within the window width ΔE. The relative shift $\Delta\eta$ between the SFSs of the two nuclei can be obtained in the following way. Adding a constant to all the observed level energies $\{E_i\}$ of a sampled nucleus, we superpose these shifted levels on the

Table 1 Unit level distances and shifts for reference nuclei*

Target Nucleus	Unit level distance ε (eV)	Shift η (eV)	Energy range (eV)
^{179}Hf	3.06	-0.5	<300
^{177}Hf**	4.37	0.8	<300
^{123}Sb	5.44	0.0	<1050
^{168}Er	17.6	-3.2	<5000

* The resolution was ΔE = 0.6 eV for the ^{179}Hf and ^{177}Hf levels, ΔE = 2 and 6 eV, respectively, for the ^{123}Sb and ^{168}Er levels.
** J = 3 levels

unshifted levels of a reference nucleus whose level energies are $\{E_j\}$. Then the level energies of the superposed ensemble are $\{E_i + \alpha\} + \{E_j\}$. If we calculate the correlation function A_{20} for the superposed ensemble as a function of relative shift, it will have the largest value at a relative shift $\Delta\eta$ between the SFSs of the two nuclei. Fig. 1 shows such an example for a case of the 4.37-eV unit level distance where the ^{177}Hf nucleus in Table 1 was taken as a reference and the ^{238}U nucleus as a sample. It is seen that the ^{238}U nucleus has a dominant component of the 4.37-eV level structure at a relative shift of -0.8 eV in reference to the ^{177}Hf levels. If the level structure of the ^{238}U nucleus has no relevance to that of the ^{177}Hf reference nucleus, the peak

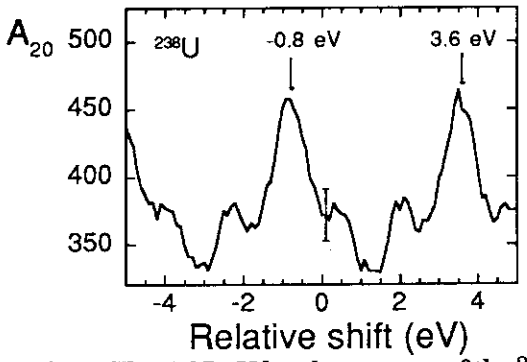

Fig. 1 The 4.37-eV level structure of the ^{238}U nucleus in reference to the J = 3 levels of the ^{177}Hf nucleus below 300 eV. The resolution was ΔE = 0.6 eV. Here the ^{238}U levels include all the observed s- and p-wave ones.

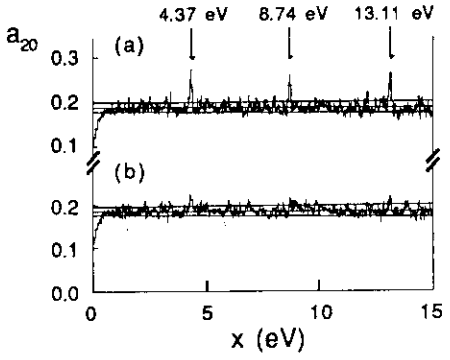

Fig. 2 Plots of a_{20} for the superposed levels of the ^{177}Hf and ^{238}U nuclei below 300 eV. The resolution was 0.6 eV. The J = 3 levels of the ^{177}Hf nucleus was taken as a reference and the s- and p-wave ^{238}U levels were added to the reference levels with the relative shifts of -0.8 eV (a) and 0 eV (b).

height of A_{20} at any relative shift would be within the level expected for uncorrelated levels. Fig. 2 shows plots of a_{20} for the superposed ensembles with the relative shifts of -0.8 and 0 eV. It is seen that a_{20} has large periodic peaks at $x = \varepsilon$ (4.37 eV), 2ε and 3ε with the relative shift of -0.8 eV while these peaks disappear with the relative shift of zero. The probability to have periodic peaks larger than the actually observed ones with a particular relative shift can be easily estimated by means of a simulation of random levels[4]. The probability is very small (<0.0001) for the case of the ^{238}U nucleus in Fig. 2. In the following, characteristic features of the relative shifts revealed in reference to the nuclei listed in Table 1 are described.

A. The 4.37-eV level structures

Fig. 3 shows the 4.37-eV level structures of the ^{232}Th, ^{234}U and ^{236}U nuclei in reference to the J = 3 levels of the ^{177}Hf nucleus. The relative shifts of the 4.37-eV level structures for all the nuclei in Figs. 1 and 3 have approximately the same value of -0.8 eV; this is the case also for the independent ensembles of s-wave and p-wave levels of the ^{232}Th and ^{238}U nuclei[4]. The probabilities of obtaining the observed correlations at the relative shift of -0.8 eV were 0.01 for these nuclei. As seen from Fig. 3, the ^{232}Th and ^{236}U nuclei have also a component of the 4.37-eV level structure at the relative shift of ~(1/2)ε. For odd rare-earth nuclei of ^{163}Dy, ^{173}Yb and ^{157}Gd, the 4.37-eV level structure appears at the relative shifts nearly equal to -(1/6)ε, (1/6)ε and (1/2)ε, respectively. Fig. 4 shows the 4.37-eV level structure for a superposed ensemble of the ^{157}Gd, ^{163}Dy and ^{173}Yb levels. As seen from Figs. 3 and 4, the relative shifts of these 4.37-eV SFSs take the discrete values of -(1/6)ε, (1/6)ε and (1/2)ε in steps of (1/3)ε. The ^{238}Pu and ^{239}Pu nuclei have the 4.37-eV level structure similar to one shown in Fig. 4, while the ^{240}Pu and ^{242}Pu nuclei have the level structures with the relatvie shifts of ~(1/2)ε and 0 respectively.

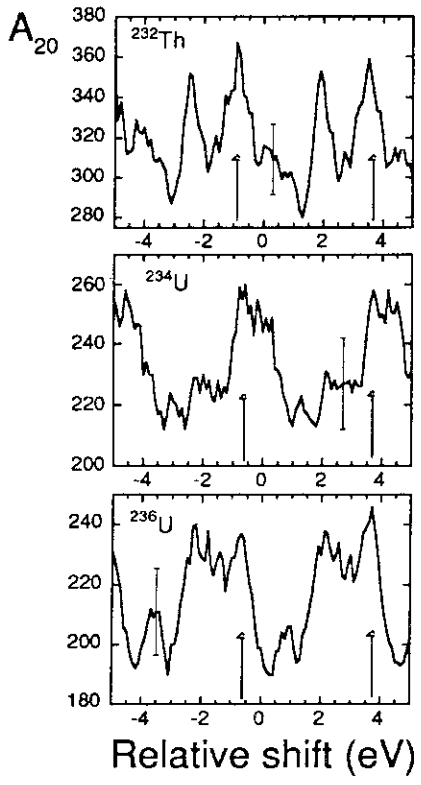

Fig. 3 The 4.37-eV level structures of the ^{232}Th, ^{234}U and ^{236}U nuclei in reference to the J = 3 levels of the ^{177}Hf nucleus below 300 eV. The resolution was ΔE = 0.6 eV. The ^{232}Th levels include s- and p-wave ones and the ^{234}U and ^{236}U levels only s-wave ones.

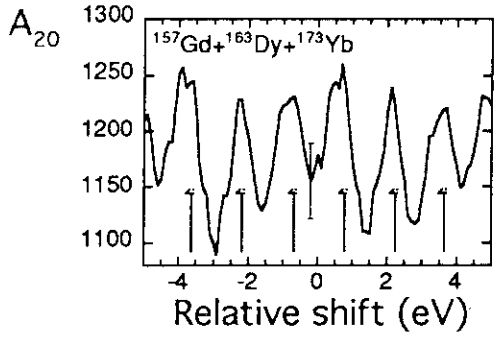

Fig. 4 T he 4.37-eV level structure for a superposed ensemble of the ^{157}Gd, ^{163}Dy and ^{173}Yb levels in reference to the J = 3 levels of the ^{177}Hf nucleus below 300 eV. The resolution was ΔE = 0.6 eV.

B. The 17.6-eV level structures

Fig. 5 shows a plot of mass number dependence of the relative shifts for the 17.6-eV level structures in even rare-earth nuclei with A = 144 ~ 166; here the ^{168}Er levels were taken as a reference. Except for the ^{160}Gd nucleus, the relative shifts in Fig. 5 have the values of either ~0 or ~(1/2)ε, where ε= 17.6 eV. The probabilities to have the observed 17.6-eV level structures for these nuclei are very small, if we assume these levels are uncorrelated with the ^{168}Er reference levels. For example, the probability is less than 0.0001 for the case of the ^{154}Sm nucleus. An observed preference to the particular values of relative shifts $\Delta\eta \approx 0$ and (1/2)ε in Fig. 5 suggests the existence of some physical constraints imposed on the level position distributions with respect to the common reference point. Table 2 shows a classification of the nuclei according to the discrete values of the relative shifts. The

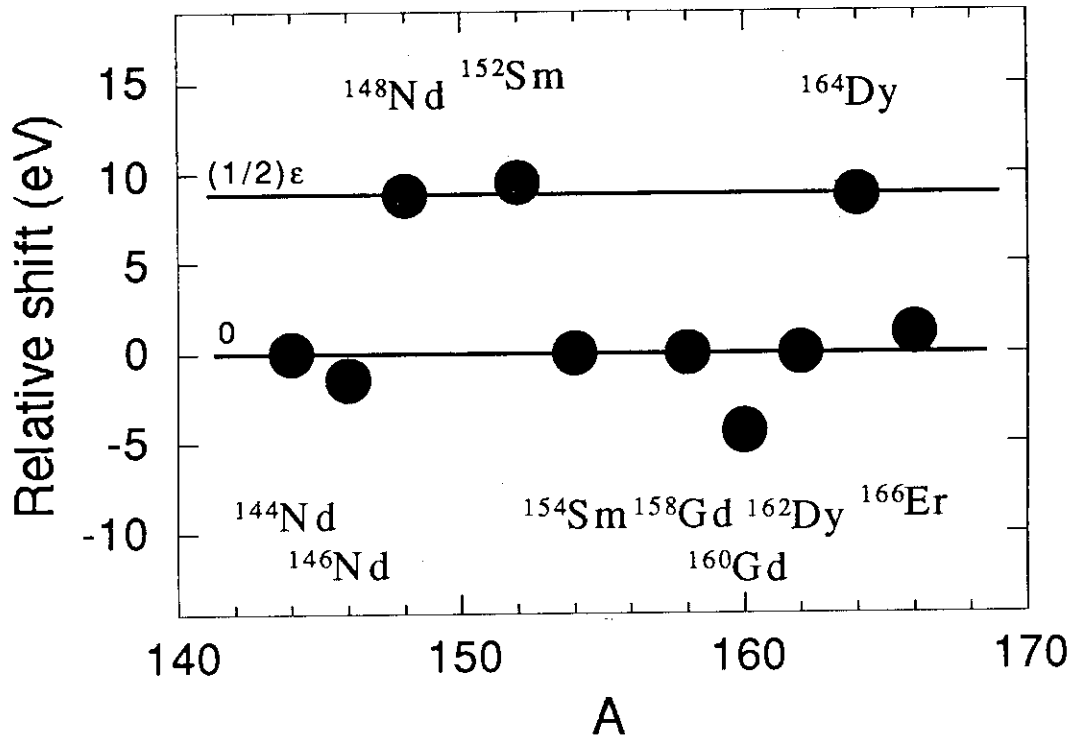

Fig. 5 Relative shifts of the 17.6-eV level structures for even rare-earth nuclei. The ^{168}Er levels below 5000 eV were taken as a reference. The resolution was ΔE = 6 eV.

listed nuclei comprise about 80% of the nuclei examined in the mass region of A = 144 ~ 170. In the analyses, we included all the observed levels, most of which were s-wave ones; exclusion of p-wave levels did not essentially change the relative shifts except for the case of the ^{152}Sm nucleus. As seen from Table 2, the relative shifts appear to be determined by the combination of proton and neutron numbers, i.e. isospin components. We can make one-to-one correspondence between the relative shifts and symmetry properties of the nuclei in the following way. For the eight nuclei of ^{146}Nd ~ ^{166}Er in Table 2, we can see that the change ΔT_z of isospin components by even or odd numbers are associated with the relative shifts of $\Delta\eta \approx 0$ or (1/2) ε, respectively, whereΔT_z is counted from a fixed nucleus, for example, from the ^{154}Sm nucleus. This experimental observation encourages us to think that symmetry properties such as isospin components play a major role in determining the relative shifts between the 17.6-eV SFSs. Here we assume that the isospin

Table 2 Relative shifts of the 17.6-eV level structures

Relative shift	$\Delta\eta \approx 0$	$\Delta\eta \approx (1/2)\varepsilon^*$
Target nuclei	^{144}Nd	
	^{146}Nd →	^{148}Nd
	^{154}Sm ←	^{152}Sm
	^{158}Gd	
	^{162}Dy →	^{164}Dy
	^{166}Er	

* ε is the 17.6-eV unit level distance for the ^{168}Er levels below 5000 eV.

components at the highly excited states of neutron resonances coincide with those of the ground states except for the ^{144}Nd nucleus. Since the relative shift of the ^{144}Nd nucleus is same as that of the ^{146}Nd nucleus, the isotopic component of the ^{144}Nd nucleus is expected to differ from that of the ^{146}Nd nucleus by even numbers at the high excitation; otherwise, some other quantum numbers should cancel the unbalance of the symmetry. A similar situation holds for a case of the ^{166}Er and ^{168}Er nuclei which have the same relative shift, although the difference between their isotopic components at the ground states is $\Delta T_z = 1$.

C. The 5.44-eV level structures

We can find a similar correspondence rule between the changes of the relative shifts and isotopic components for the 5.44-eV SFSs revealed in reference to the ^{123}Sb levels (Table 1). Fig. 6 shows plots of A_{20} for the pairs of nuclei ^{238}Pu - ^{240}Pu and ^{244}Cm - ^{246}Cm, where the 5.44-eV level structures have the relative shifts of $\{-(1/2)\varepsilon + 1.1\} = -1.5$ eV or 1.1 eV, that is, these relative shifts are in opposite phase with each other. As for the relative shifts for the ^{240}Pu and ^{244}Cm nuclei, they are in opposite phase with each other while $\Delta T_z = 0$ at the ground states; again, we interpret that at the high excitations there should be a mechanism which cancels the unbalance of the symmetries between the ^{240}Pu and ^{244}Cm nuclei.

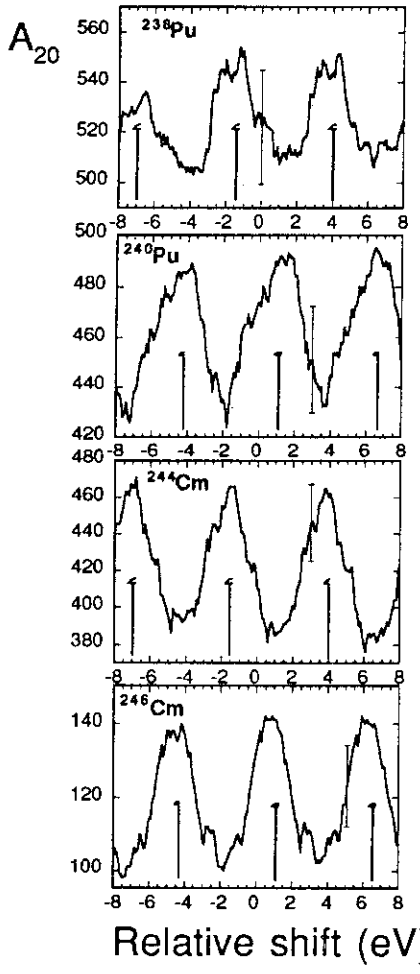

Fig. 6 The 5.44-eV level structures of the ^{238}Pu, ^{240}Pu, ^{244}Cm and ^{246}Cm nuclei in reference to the ^{123}Sb levels below 800 eV; for the ^{238}Pu nucleus, the energy region was below 500 eV. The resolution was $\Delta E = 2$ eV.

D. The 3.06-eV level structures

The 3.06-eV SFSs revealed by the ^{179}Hf reference nucleus in Table 1 are important in that they extensively demonstrate the relation between the relative shifts and the symmetry properties of the compound systems. For example, in the mass range of $A \approx 90$ to 120, the changes of the relative shifts by an amount of $\sim(1/2)\varepsilon$ can be associated with the changes in quantum numbers of spins and isospin components. The details will be described elsewhere[6].

Origin of the SFSs

We dealed with the SFSs composed of a few unit level distances whose appearances are characterized by the relative shifts. From present-day experimental limitations, the numbers of observed levels in individual nuclei are usually not so large. The level densities of heavy nuclei amount to the order of $\sim 10^6$/MeV, while the number of experimentally observed levels at our hands for one nucleus is several tens to several hundreds at most. These levels lie in the very thinnest region above the neutron separation energy of several MeV. However, neutron resonance levels are now used as an object for studying the violation of fundamental symmetry and

invariance[7]. Besides, slow neutron resonance data have an uniquely good energy resolution, which enables to study periodic motion in a nucleus with a long time scale from the uncertainty relation for energy and time[8]. Most of semiclassical studies of periodic motions are limited to rather simple orbits, i.e., with a short period of time, vice versa, with a large energy resolution[9]. At first glance, long-period motions in a compound nucleus seem too much complex to be attacked. However, the time-based understanding of the compound nucleus reaction will be facilitated by our finding of the simple patterns of the relative shifts and the existence of close interconnections between the relative shifts and symmetry properties of the compound systems.

The SFSs as a nuclear data evaluation

The appearance of the SFS is sensitive to the experimental data. A general tendency is that the SFSs become more consistent as the experimental energy resolution becomes better. As a result, the SFS analysis will serve as a data evaluation.

Future prospects of the SFS

We expect that the SFS will shed new light into the understanding of many-body nuclear interactions and the constraints of the symmetry properties of the compound systems imposed on the level distributions. We also expect that the SFS will find practical applications in a strong electromagnetic field induced with lasers.

References

[1] Porter C. E.: "Statistical Theories of Spectra: Fluctuations", (1965, Academic Press); Brody, T. A.: Rev. Mod. Phys., **53**, 385 (1981).
[2] Sukhoruchikin, S. I.: Sov. J. Nucl. Phys., **10** , 285 (1970); Ideno, K. and Ohkubo, M.: J. Phys. Soc. Jpn., **30** , 620 (1971); Ideno, K.: ibid., **37** , 581(1974).
[3] Frank, I. M., "Progress in the Study of Nuclear Structure with Neutrons", Proc. Int. Conf. on Nuclear Structure Study with Neutrons, 1972, Budapest, Hungary, p. 27 (1974, Plenum Press, London &New York).
[4] Ideno, K., Proc. Int. Conf. on Nuclear Data for Science and Technology, 1988, Mito, Japan, p. 783, (1988, Saikon, Tokyo,); Ideno, K., Contributions to the Int. Nuclear Physics Conference, Beijing, China, 1995, p. 6.3-19.
[5] Mughabghab, S. F. et al.: BNL-325, Neutron Cross Sections, 4th edi., Vol. 1, Part A and B (1981, 1984, Academic Press, N.Y.); Coceva, C. et al.: "Statistical Properties of Nuclei", p. 447 (1972, Plenum Press, N. Y.).
[6] Ideno, K.: To be published.
[7] Bowman, J. D. et al.: Annu. Rev. Nucl. Part. Sci., **43**, 829 (1993).
[8] Izumo, K.: Prog. Teor. Phys., **54**, 1378 (1975); ibid., **55**, 1827; Ohkubo, M.: To appear in Phys. Rev. B.
[9] Arita, K.: Phys. Lett., **B336**, 279 (1994).

3. 34

Nuclear level density formula with energy-dependent shell and pairing corrections

Hisashi Nakamura
Nuclear Engineering Division, Fuji Electric Co., Ltd
1-1 Tanabe-Shinden, Kawasaki 210, Japan

A new phenomelogical level density formula is based on the analytical expression of the single-particle state density. The main features of the proposed formula is the existence of not only the excitation-dependent shell correction energy but also the excitation-dependent pairing correction with the shell-pairing correlations (thus called SPC model), so far considered only by means of the microscopic Fermi-gas model, and no need of independent shell and pairing correction energy tables as often used for the previous formulas. At the ground states the shell and pairing corrections with the shell-pairing correlation terms are computed by using 6 constants for each shell, values of which are determined as to fit the empirical mass excess data. The analyses by using the obserbed s-wave neutron and proton resonance spacings of the mass range A= 41~67 show that the prediction of the SPC model and its parameters will be superior to those of the previous models of the traditional Fermi-gas. This improvement seems to be due to the prescriptions of the excitation-dependent correction energies both for the shell and for the pairing effects.

1. INTRODUCTION

At the present time [1] the most statistical theory calculations of nuclear reactions are carried out by using the semiempirical level density formula proposed by Gilbert and Cameron [2] in 1965 and by others, which are based essentially on the Fermi-gas (FG) model and seems to be enough to predict the level densities at the narrow range of excitations. This model relates the constant shell and pairing corrections on the level density to the ground state correction energies, E_S and E_P,respectively defined as the differences of the experimental mass and the liquid drop mass (gross terms). The foregoing shell and pairing corrections do not take the unique contents but depend on the different mass formulas,from which the shell and pairing corrections are available. Separation of those corrections on the level density parameters is not clear in literatures. The typical correction energies are those of Meyers and Swiatecki [3] for the shell energy E_S, and of Gilbert and Cameron [2] for the pairing energy E_P.

However, it has been in fact well established [4] that the extrapolation of this formula to a wide range of excitation energies is subject to large errors, and that washing out of shell and pairing effects should be considered. Among the semiempirical models which account for the energy-dependent shell correction of the nuclear level density, the model of Kataria, Ramamurthy and Kapoor (KRK model) [5] is considered as the typical one. On the other hand, the energy-dependent pairing corrections with the shell-pairing correlation seems to be correctly considered only by means of the microscopic Fermi-gas model [6], which has, however, still an inaccuracy due to the formalism in the superconducting phase [4].

The purpose of the present work is to make those contents of correction clear, and to obtain the

new systematics on parameters of the level density formula. In the current SPC model,an analytical expression similar to the previous KRK model is adopted for the single-particle state density, but introducing the shell-pairing correlation term, and so we call it 'SPC' model. The next sections are the descriptions of the proposed semiempirical level density formula in the present work.

2. THERMODYNAMICAL PROPERTIES OF PAIRED NUCLEON SYSTEM

A nuclear level density formula is derived from the Fourier expansion of single-particle state density, considering only a fundamental harmonic for the main-shell with the sub-shell associated to the pairing interaction:

$$g(\varepsilon) = \Sigma\, g_{0X}[1+f_X\cdot\cos\{\omega(\varepsilon-\varepsilon_X)\}]\cdot[1-\cos\{\omega_P(\varepsilon-\lambda)\}], \tag{1}$$

where ω = frequency related to the main-shell spacing, ω_P = frequency related to the pairing energy, ε_X = main-shell position, λ = Fermi level, g_{0X} = average single-particle state density (2-fold degenerate), and f_X = amplitude of main-shell, x = stand for proton(=p) or neutron(=n) shell.

In Eq.(1) the main-shell terms are just those of the KRK model [5], and when $f_X = 0$ the so-called quasi-particle state density under the pairing correlation becomes as

$$g(\varepsilon) = \Sigma\, g_{0X}[1-\cos\{\omega_P(\varepsilon-\lambda)\}], \tag{2}$$

which is the prescription of the SPC model for the pairing correlations. A better understanding of meanings of Eq.(2) can be obtained if the thermodynamical properties of quasi-particle system are analyzed by using the traditional method of statistical mechanics. The main quantities for that are the excitation energy Ex, the entropy S(Ex) and the moment of inertia I:

$$Ex = a_0 t^2 - E_P\{h_1(T_P)\, h_2(T_P)-1\} \tag{3}$$

where t = thermodynamic temperature, $T_P = \pi\omega_P t$, $h_1(T_P) = T_P\cdot\mathrm{cosech}(T_P)$, $h_2(T_P) = T_P\cdot\coth(T_P)$, a_0 = asymptotic level density parameter $\{=(\pi^2/3)\, g_0\}$, $g_0 \equiv (g_{0z}+g_{0n})$, E_P = pairing correction energy at the ground state $(= g_0/\omega_P^2)$.

$$S(Ex) = 2\, a_0 t - t^{-1} E_P h_1(T_P)\{h_2(T_P)-1\}, \tag{4}$$

$$I = I_0\,[1-(1/2)(\delta_P+\delta_n)\, h_1(T_P)], \tag{5}$$

where $I_0 = I_r$(for spherical nuclei), $I_r = 0.015A^{5/3}$(Fermi-gas moment of inertia), A = nuclear mass-number, δ = 1(even protons or neutrons),= 0(odd). In the above formulation of Eqs.(3)~(5) the small correction terms due to the energy dependence of Fermi level λ is ignored as the previous KRK model.

The main feature of the current prescription for pairing correlations can be seen on the basis of the simple version [7] of the superconductivity theory of BCS [8], where the following relations were used :

$$2\Delta_0/t_c = 3.50, \quad E_P = g_0\Delta_0^2 = 2\Delta_0. \tag{6}$$

In the above notation Δ_0 is the energy gap in the ground state, t_c is the critical temperature of the phase transition. Then, in FIG.1 the entropy of SPC model are compared with those of the FG model and the foregoing superconductor model for the example of nucleus ^{60}Ni [Z=28, N=32, A=60], with the parameter systematics from the relations in Eq.(3): $\omega_P^2 = g_0/Ep$, $g_0 = (3/\pi^2)a_0$, $a_0 = 0.137A$,

$$\omega_P = 0.144A^{1/2}, \quad E_P = 2.0\text{MeV}. \tag{7}$$

As seen in FIG.1 the entropy of SPC does not have the finite critical temperature of the phase transition, but shows a moderate energy-dependence at the vicinity of the phase transition point.

By using the full scope of the single-particle state density Eq.(1) with $f_X \neq 0$, the traditional statistical procedure leads to the following nuclear level density formula

$$\rho(Ex,J,\Pi) = \frac{1}{2}\Omega(J)\cdot R(Ex)\cdot K_{rot}(Ex) \tag{8}$$

where the factor 1/2 is assumed for equal probability of parity states Π and K_{rot} is the rotational enhancement factor [9], and each factor is well known respectively.

3. SYSTEMATICS OF PARAMETERS

The systematics for the shell and pairing corrections, E_S and E_P at the ground state are obtained by fitting the empirical mass excess data, assuming for Es as,

$$[E_S]_{exp} = \{C_s X(1-X) - C_1\cdot X - C_2\}\cdot FF, \tag{9}$$

where X = occupied fraction for each shell of proton or neutron, and magic numbers are assumed as [14, 28, 50, 82, 126, 184]. The factor FF = 1.0 (for spherical regions), $FF = \exp\{-C_3\cdot(X-X_{D1})(X_{D2}-X)\}$ (for deformed regions), (D1, D2) = 60<Z<77 or Z>90, 89<N<115 or N>131.

$$[E_P]_{exp} = C_P\delta[1 - F_P(E_S/C_S)] : \text{for proton or neutron shell} \tag{10}$$

where $[E_S]_{exp}$, $[E_P]_{exp}$, empirical shell and pairing energies for protons and neutrons espectively, adjusted by using those (constant-shell terms and the gross term) of Ref..10) as the first guess, and the empirical mass excess data of Ref..11).

Free parameters included in the present formula are,

C_S, C_i(i=1,3) : shell correction const.

C_P : pairing correction const., F_P : amplitude for shell-pairing correlation.

The result is shown in FIG.2, which is for the case of neutron shells.

Free parameters of the excited state are a_0, ω in Eqs.(3),(5). In the KRK model the dependences on the mass number A of a_0, ω were assumed as $a_0 = \alpha A$, $\omega = \omega_0 A^{1/3}$.

A set of values (α , ω_0) is determined for the level density formula to fit the s-wave neutron or the proton resonance spacings, which have been analyzed in the previous study [4]. The results are presented in Tables 1,there shown are also for FG and KRK models. The shell and pairing corrections are those of the present model for all models. A measure of the quality associated with systematics is taken as the root mean squares (rms) deviation defined for the parameter a_0 as $\chi^2 = \Sigma(a_{0i} - \alpha \cdot A_i)^2$: i for all nuclei. The values for α, ω_0 of KRK and SPC models, and α of FG model respectively are found by minimizing the quantity χ^2. The χ^2 value of the KRK model in Table 1 is somewhat larger than that of the previous work [4]. This result may be caused by the difference between the current E_S, E_P values and those of the previous one.

Constants of Systematics*	FG model	KRK model	SPC model
α (MeV^{-1})	0.138	0.123	0.125
ω_0(MeV^{-1})	--	0.220	0.180
χ^2	17.015	3.001	3.417

Table 1 The Systematics of Level Density Parameters

* $a_0 = \alpha \cdot A$,
$\omega = \omega_0 \cdot A^{1/3}$,
A : mass number

Since the systematics of the SPC model is quite well described by the relation $a_0 = \alpha A$, the predictions of the SPC model will be superior to those of the FG model. This systematic improvement in Table 1 is due to the excitation-dependent shell and pairing correlation terms in the level density formula.

Further studies of the systematics for the mass range of A > 70, specially for deformed nuclei,will be necessary to confirm the usefulness of the present SPC model over a wide range of nuclei.

References ;

[1] Proceedings of OECD Meeting on Nuclear Level Densities, ENEA, Bologna,Italy, Nov. 15-17, 1989, edited by G.Reffo, M.Herman and G.Maino. World Scientific.
[2] Gilbert. A. and Cameron A.W.G., Can.J.Phys.,43,1446 (1965).
[3] W. D. Meyers and W. S. Swiatecki, Ark. Fys.,36,343(1967).
[4] H. Vonach ,et al., Phys.Rev.C 38,2541(1988).
[5] S. K. Kataria., V. S. Ramamurthy and S. S. Kapoor, Phys.Rev.C18,549(1978).
[6] L. G. Moretto, Nucl.Phys. A182, 641(1972).
[7] M. Sano and S. Yamasaki, Prog.Theor.Phys. 23, 871(1963).
[8] J. Bardeen, L. N. Cooper and J. R. Schrieffer, Phys.Rev. 108, 1175(1957).
[9] Ignatyuk A.V.,Istekov K.K. and Smirenkin G.N.:Sov.J.Nucl.Phys.29, 50(1979).
[10] Ando Y.,Uno M. and Yamada M.: JAERI-M 83-025(1983).
[11] Audi G. and Wapstra A.H.: Nucl.Phys.A565. 1and 66 (1993).
[12] Moller P. and Nix J.R.: ibid.,39,213(1988).

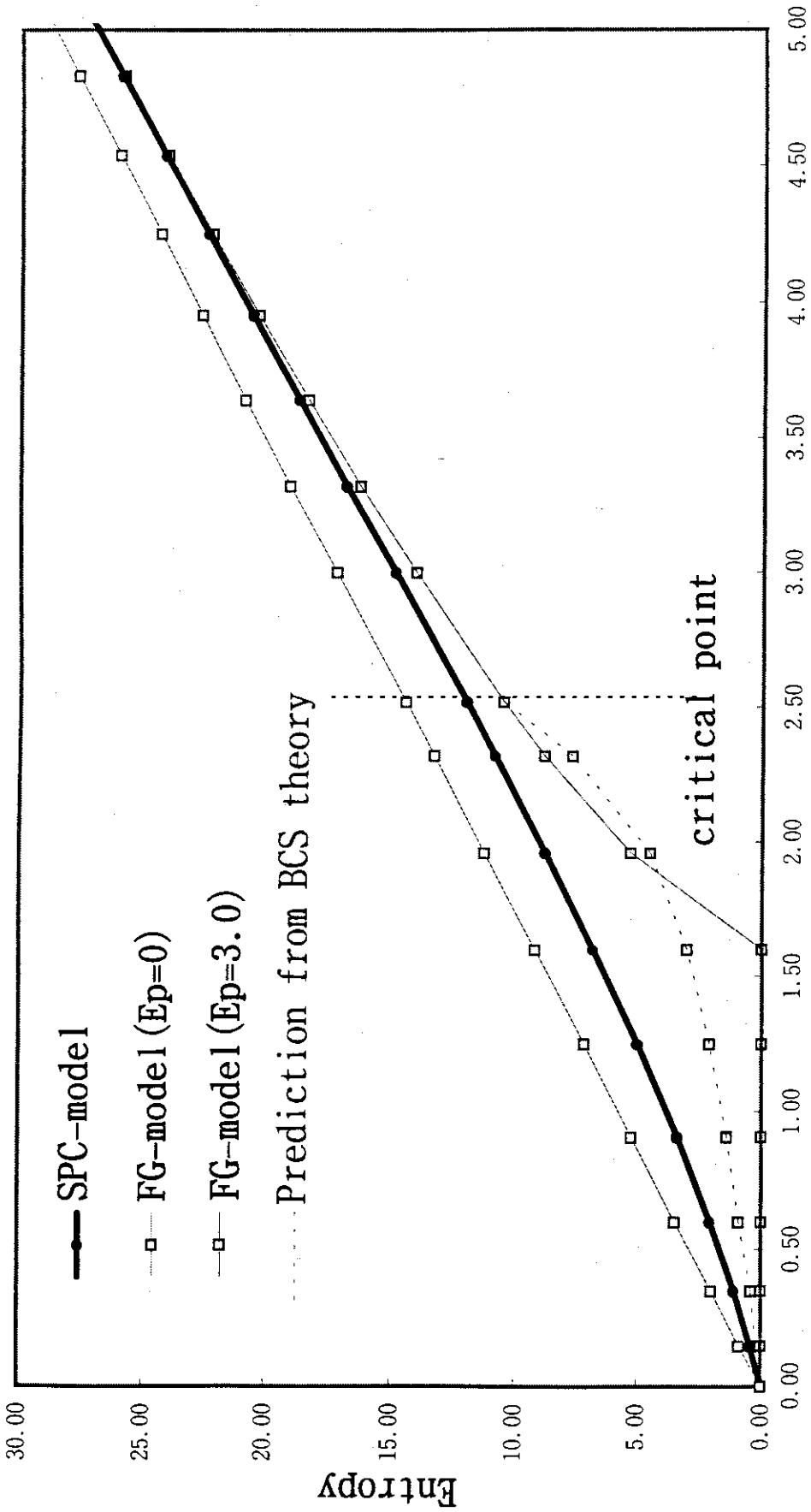

FIG.1 Entropy vs. the excitation energy

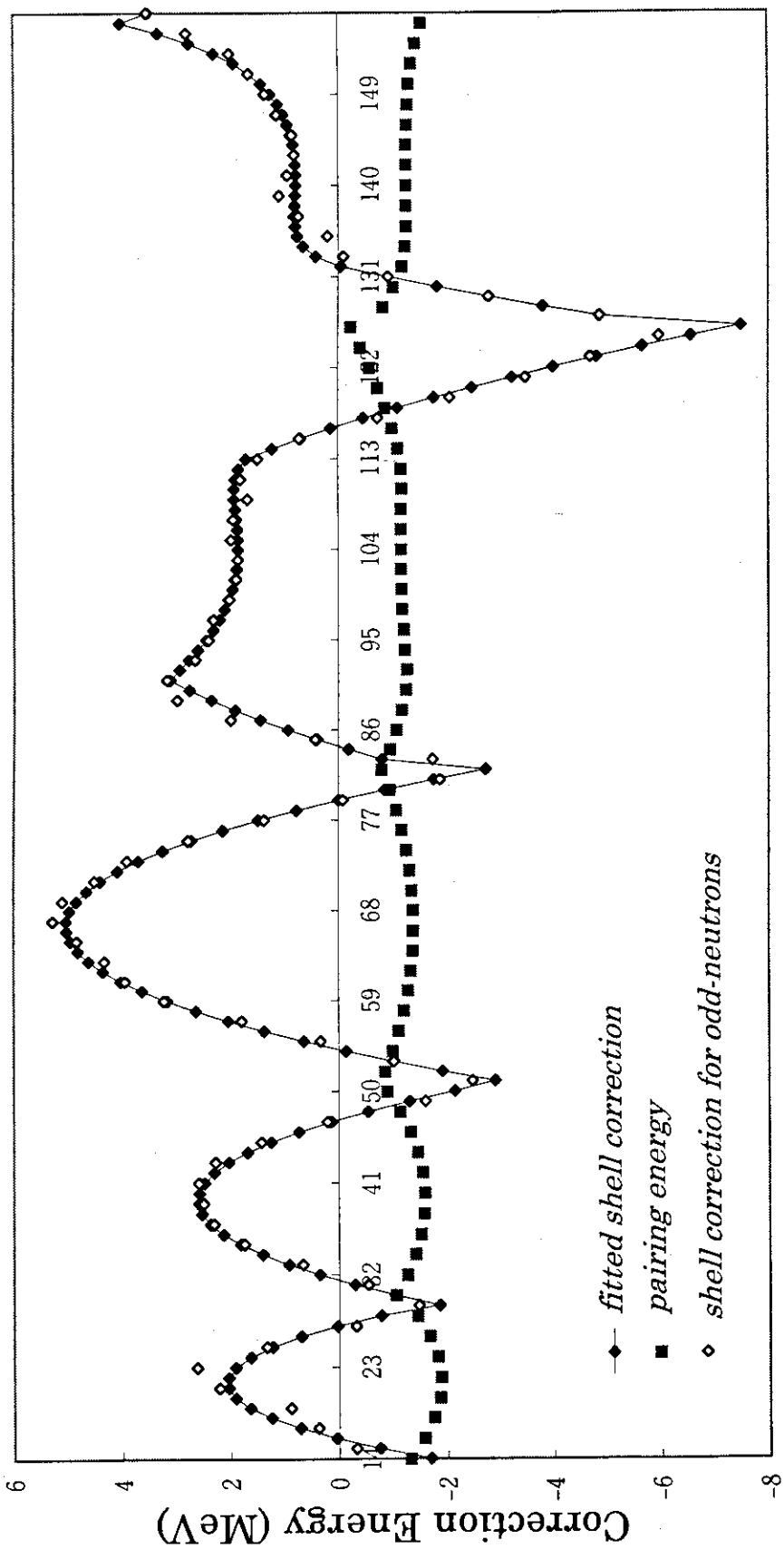

FIG.2 Neutron Shell and Pairing Corrections

3.35 Neutron Resonance Level Clusters and Localized Crystalline Structures

Makio OHKUBO
Dept. of Reactor Engineering, Japan Atomic Energy Research Institute

Abstract

Regular structures have been found in the s-wave neutron resonance spectra of ^{40}Ca+n and ^{206}Pb+n in the energy region up to 1.5 MeV. For both nuclei, similar branching patterns can be seen in the multiplets of level clusters.

1. Introduction

Statistical properties of observed neutron resonances are in rather good agreement with the predictions of the random matrix theory. Some of them are Wigner distribution(GOE) for the nearest neighbour level spacing distribution, $\triangle_3$ statistics for long range correlation and Porter-Thomas distribution for partial widths. For this reason, the neutron resonances are believed to be typical example of quantum chaos.

However, non-chaotic periodic level dispositions have been reported by several authors[1][2][3][4][5]. The regular structures, the other features in the neutron resonance spectra, provide a clue to study the mechanism of compound nuclear resonances. By the correlation analyses, we can classify the levels using small number of parameters. In this article, we present crystalline like regular structures in the s-wave neutron resonances of ^{40}Ca+n and ^{206}Pb+n in the region up to 1.5 MeV. In the spectra of both nuclei, similar branching patterns are found in the multiplets of level clusters.

2. Methods of analysis

For n observed neutron resonance levels in certain energy region, they are numbered from lower to higher energy, as E_i (i=1,2,..., n), where $E_j > E_i$ for j>i. The nearest level spacings S_{ii+1} are defined as $S_{ii+1} = E_{i+1} - E_i$ (i=1,2,..., n-1). We have studied the level spacings between arbitrary two levels S_{ij}, defined as $S_{ij} = E_j - E_i$ (j>i, i=1,2,..,n-1, j=2,3,..,n). The number of spacings S_{ij} is n(n-1)/2. For further analyses, we have utilize a correlation spectrum G{x/s}, which is sum spectrum around given spacing s. If the spacing s appear m times, g{x/s} peaks at x=0 and x=s due to m-time appearance of the spacing s. In the histogram of G{x/s}, we can find other peaks which correspond to spacings correlate with the spacing s.

By these methods, we have analyzed the level correlations of the observed neutron resonances of ^{40}Ca+n and ^{206}Pb+n. The resonance data are taken from the reference book, BNL-325 4th ed.. For clarity, the results on s-wave

resonances are presented here, because s-wave resonances have significantly large neutron widths, and missing levels are expected to be small.

3. Results

1) $^{40}Ca + n$

Thirty s-wave resonance levels are observed up to 1500 keV. Reduced neutron width Γ_n^0 of the resonance levels vs. incident neutron energy are shown in the upper part of Fig. 1. In the lower part of the Fig. 1, S_{ij} is shown, where peaks are seen at 232 keV, 418 keV and 650 keV, etc. We name the spacing "a" for 232 keV, and "b" for 186(=418-232) keV. It is found that the spacing a appears frequently neighboring b, and a and b compose chains. The chains of types a-b-a, (a+b)-a, and a-(a+b) are shown in lower part of Fig. 2. Several chains overlap in the same energy region, and the same levels are shared by different chains. Twentyfour levels out of 30 levels are members of these chains. The significant peaks at 232, 418 and 650 keV in S_{ij} correspond to a, a+b, and 2a+b. The ratios among these spacings are, a:a+b:2a+b = 5:9:14, within 1% accuracy.

Probability of appearance of these chains by chance is estimated assuming that the resonance levels despose without correlation. In Fig. 3, G{x/650} is shown where distribution of levels surrounding the 650 keV spacings (=2a+b) are summed up. The 650 keV spacings appear 10 times between pairs of levels within an error ±10 keV. In nine pairs out of ten, levels are found at the position 418 keV(=a+b) above the lower partners of the pairs within an error ΔE= 13.8 keV, as shown in Fig. 3. If the levels are positioned without correlation, the probability of appearance of such a peak at any point by chance is calculated to be 3.4×10^{-4}. This means that the frequent appearance of a-b-a is not by chance but by regularity, a part of regular structures of ^{40}Ca+n resonances developed in this energy region.

We call the structure a-b-a as branching pattern (BP), which composed of four levels. In the BP, it seems that the spacing a(=232keV) branches from both ends of spacing (a+b)(=418keV). Similary, a BP of next size is found, and the spacing (a+b)(=418keV) branches from both ends of the spacing (2a+b)(=650keV). These BP seem to compose a nest structure; small BP are folded in the next large BP. The sizes of these BP are found to be propotional to the square of integers; a:a+b:2a+b= 232:418:650 = $3^2:4^2:5^2$ with a unit spacing of 26 keV. So we call the structure a-b-a as BP of size-5. We can find BP of the next size, size-6, of which length is 923 keV. The BP of size-5 are nested in the BP of size-6, as shown in the botom of Fig. 2. Spacing ratios are; a:a+b:2a+b:2c+d=232:418:650:923 = 5:9:14:20 = $3^2:4^2:5^2:6^2$ within 1% accuracy.

2) $^{206}Pb + n$

Thirty five s-wave resonance levels are observed up to 1000 keV. Reduced neutron width Γ_n^0 vs. incident neutron energy are shown in the upper part, and S_{ij} in the lower part of the Fig. 4. Peaks are seen at 36, 127, 164, 234, 340, 363 keV etc. As in ^{40}Ca+n, we name the spacing "a" for 128 keV, and "b" for 106 keV. The chains of types a-b-a, (a+b)-a, and a-(a+b) are shown in lower part of Fig. 5. Twenty-five levels out of 35 levels are members of these chains. The ratios among these spacings are; a:a+b:2a+b=128: 234: 363 keV = 5:9:14. They are also $3^2 : 4^2 : 5^2$ within 1% accuracy, with a unit of U= 14.2 keV. They form a branching pattern of size-5. As in ^{40}Ca+n, BP of the next size(size-6: 525keV) are found, in which BP of size-5 are nested, as shown in the bottom of Fig. 5. Spacing ratios are; a:a+b:2a+b:2c+d=232:418:650:923 = 5:9:14:20 = $3^2:4^2:5^2:6^2$ within 1% accuracy.

4. Discussion

It is interesting that the similar branching patterns are found in ^{40}Ca+n and ^{206}Pb+n. The similarity in BP may be due to the similar situation in both nuclei; that a few neutrons in the low spin filled orbits are excited to the low spin higher unoccupied orbits across the energy gap of closed shell. The length of BP of size-5 is 650 keV for ^{40}Ca+n and 363 keV for ^{206}Pb+n, and the length ratio is 650/363 $=4^2/3^2=1.77$. This ratio is nearly equal to the inverse ratio of both nuclear radi. The BP seems to relate fractal nature in chaotic spectrum. Such BP structures may be special for these nuclei. Other types of branching patterns are found in other nuclei. The physical meaning of these branching patterns for each nucleus is an open problem, a part of which will be related to the recurrence properties of the compound nucleus[6].

We wish to thank Dr. M. Ishii for the discussions on branching patterns.

Referrences

[1] K. Ideno and M. Ohkubo: J. Phys. Soc. Japan 30, 620(1971),
K. Ideno:ibid 37, 581(1974)

[2] S. I. Sukhoruchkin: Sov. J. Nucl. Phys. 10, 285(1970),
S. I. Sukhoruchkin: Proc. Int. Conf. on Statistical Properties of Nuclei (Plenum Press, New York 1972) p 215

[3] C. Coceva, F. Corvi, P. Giacobbe and M. Stefanon: Proc. Int. Conf. on Statistical Properties of Nuclei(Plenum Press, New York 1972) p 447

[4] F. N. Belyaev and S. P. Borovlev: Yad. Fiz. 27, 289-292 (1978)

[5] G. Rohr: Proc. 8th Int. Symp. on Capture Gammaray Spectroscopy and Related Topics, Fribourg, Switzerland, Sept. 1993, Jean Kern ed. World Scientific Pub. Co. 1994, p626

[6] M. Ohkubo: to be published in Phys. Rev. C

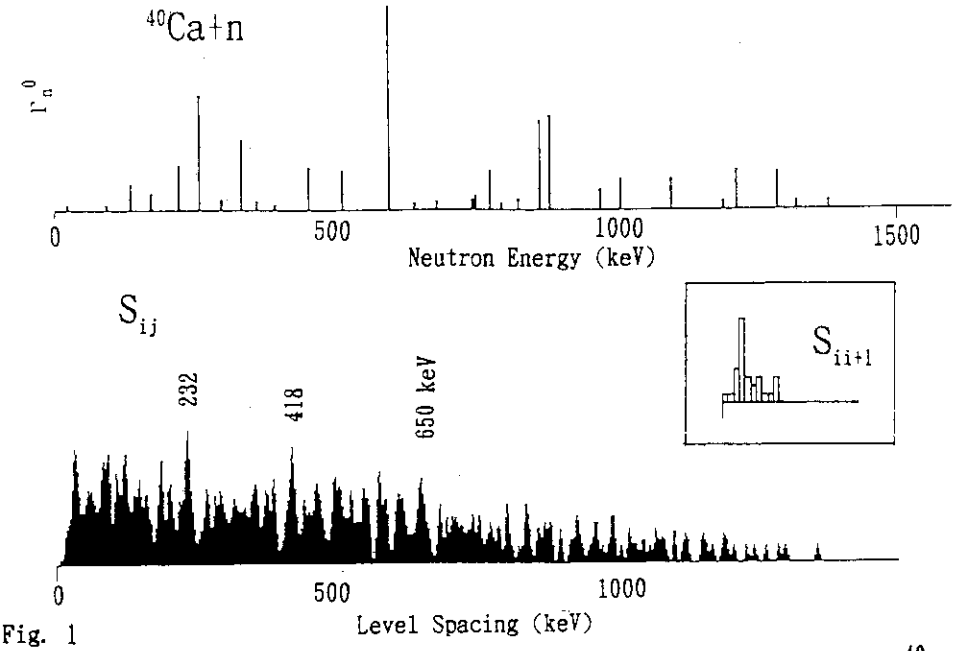

Fig. 1

Upper part: Reduced neutron widths of thirty s-wave resonances of ^{40}Ca+n up to 1500 keV. Lower part: Level spacing distribution between arbitray two levels. Insert : Nearest neighbor level spacing distribution in the same energy scale.

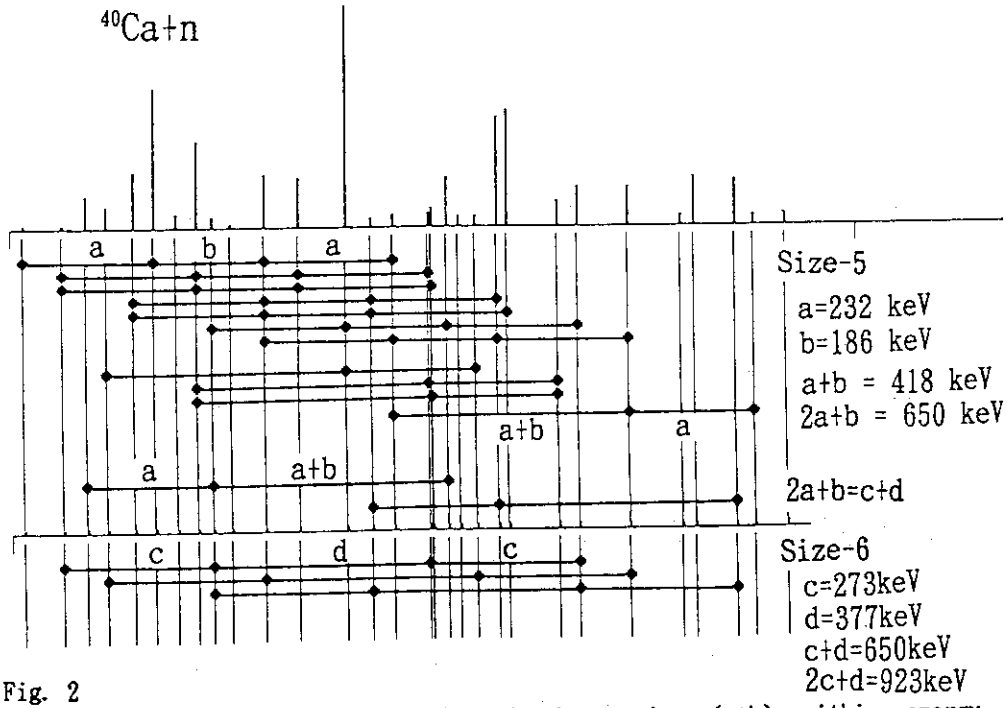

Fig. 2

Branching patterns of size-5 a-b-a, (a+b)-a, and a-(a+b) within energy error $\triangle E = \pm 15$ keV. In the bottom, branching patterns of size-6 are shown, where BP of size-5 are nested on both sides. The ratios among these spacings are a:a+b:2a+b:2c+d= 232:418:650:923= 5:9:14:20 = 3^2: 4^2: 5^2: 6^2 with ～1% accuracy.

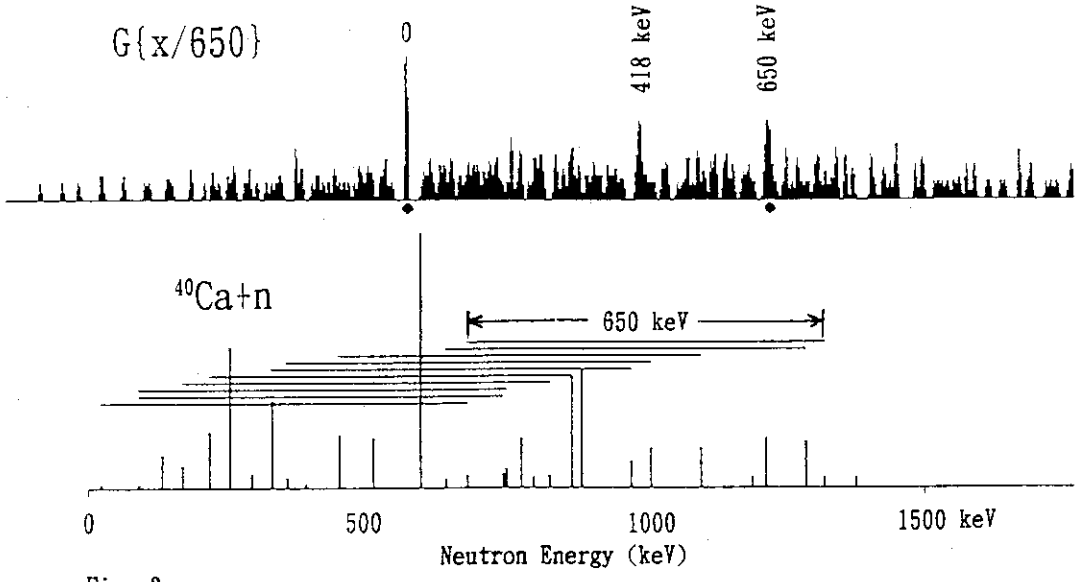

Fig. 3

Upper part : G{x/650}, sum up of the level dispositions aroud 650 keV spacings. It is shown that levels are almost always exist at 418 keV. Probabilty of appearance of this peak at any point by chance is calculated to be 3.4×10^{-4}. Lowere part : Level pairs of 650 keV spacing are shown as the holizontal bars.

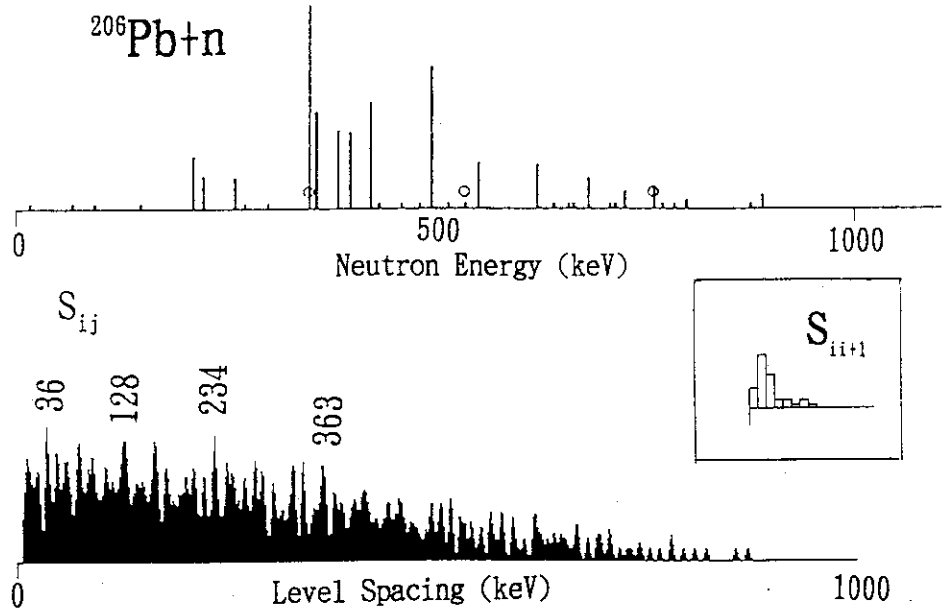

Fig. 4

Upper part: Reduced neutron widths of thirty-five s-wave resonances of ^{206}Pb+n up to 1000 keV. Lower part: Level spacing distribution between arbitray two levels. Insert : Nearest neighbor level spacing distribution.

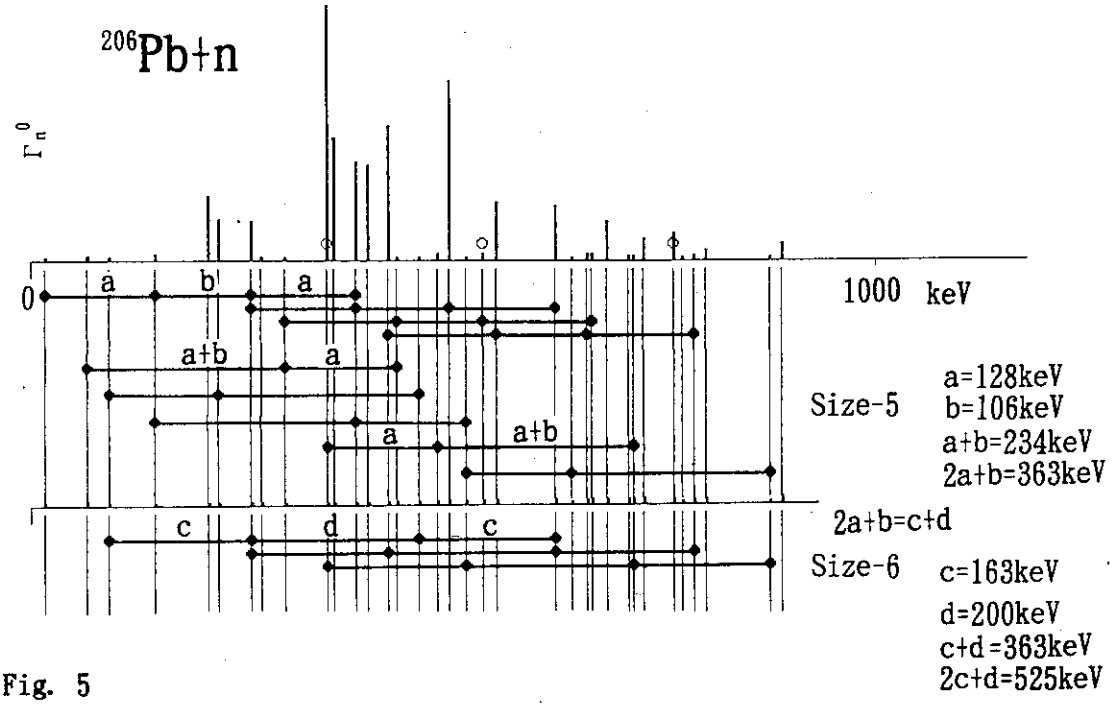

Fig. 5

Branching patterns of size-5 a-b-a, (a+b)-a, and a-(a+b) within energy error $\triangle E = \pm 5$ keV. In the bottom, branching patterns of size-6 are shown, where BP of size-5 are nested in both sides. The ratios among these spacings are a:a+b:2a+b:2c+d= 128:234:363:525= 5:9:14:20 = 3^2: 4^2: 5^2: 6^2 with ～1% accuracy.

3.36 IntelligentPad for Exchanging and Reusing Nuclear Reaction Data Information as Shared Resources

Masaki CHIBA(*)
Division of Electronics and Information Engineering, Hokkaido Univ.
Sapporo, 060 JAPAN
e-mail: chibam@huee.hokudai.ac.jp

As an application of the IntelligentPad system, the NRDF database system is re-designed and developed. In the system, every component of the user interface is represented by reactive media objects called Pad. The exploitation of the IntelligentPad architecture in developing the system enhances the usability and reusability of the tools developed. Several pads specially designed for the NRDF database system are shown together with the examples of how to use them.

1. Introduction

A newly designed system for the NRDF database is introduced. This system is developed using the IntelligentPad system for the distribution, exchange, and reuse of various intellectual resources including observed data and their descriptive information, and analysis tools in nuclear reaction experiments. All of the components in this new NRDF system such as nuclear reaction data, database search programs, graph drawing tools, and their operation environments are represented by composite pads in the IntelligentPad architecture. Therefor this system provides a user environment consisting of various reactive media objects; they look like paper sheets on the display screen, and work as GUI to the databases. The exploitation of these media objects enhances the usability and reusability of the tools developed.

2. NRDF needs IntelligentPad architecture

The NRDF (which stands for Nuclear Reaction Data File) system is a data compiling, storage and retrieval system for charged-particle nuclear reaction data[1]. The current system was implemented in 1975. Although several modifications and facilities have been added to the system, the major part of the system has been in service since then, running on a main frame computer. We need a new NRDF system based on new concepts and technologies in order to get benefit of recent hardware and software technology developments such as multimedia technologies, and object-oriented

(*)research fellow granted on the Foundation for In-Service Training and Welfare of the Private School Personel; His permanent affiliation is Department of Social Information, Sapporo-Gakuin Univ., Bunkyodai 11, Ebetsu 069,JAPAN. e-mail: chiba@sgudns.sgu.ac.jp

modeling and development technologies.

The IntelligentPad is a new object-oriented media system[2]. The IntelligentPad system was proposed and developed at Hokkaido University so as computers to work as meta-media that provide us with an overall integrated environment for our intellectual activities. This system provides a unified framework for the modeling, the presentation, the synthesis, and the management of multimedia documents, system-provided functions, and application programs. Every intellectual resource is represented as a pad. Pads can be pasted on another pad, and later can be peeled off their base pad.

So we have decided to expoit the IntelligentPad architecture in developing the new NRDF database system, and have developed several new functional pads for this specific application.

3. IntelligentPads for the NRDF system

we will show several pads specially designed and developed for the NRDF database system. We are using these pads to compose various interactive tools for the database access, the graphical visualization of the record distribution, the filtering of these records, and the viewing of their details.

3.1 Overall appearance of the system

An application of the IntelligentPad system appears on a RootPad that is actually an X-window. Fig.1 shows a display snapshot of the NRDF database system, which contains all the pads specially developed for this application.

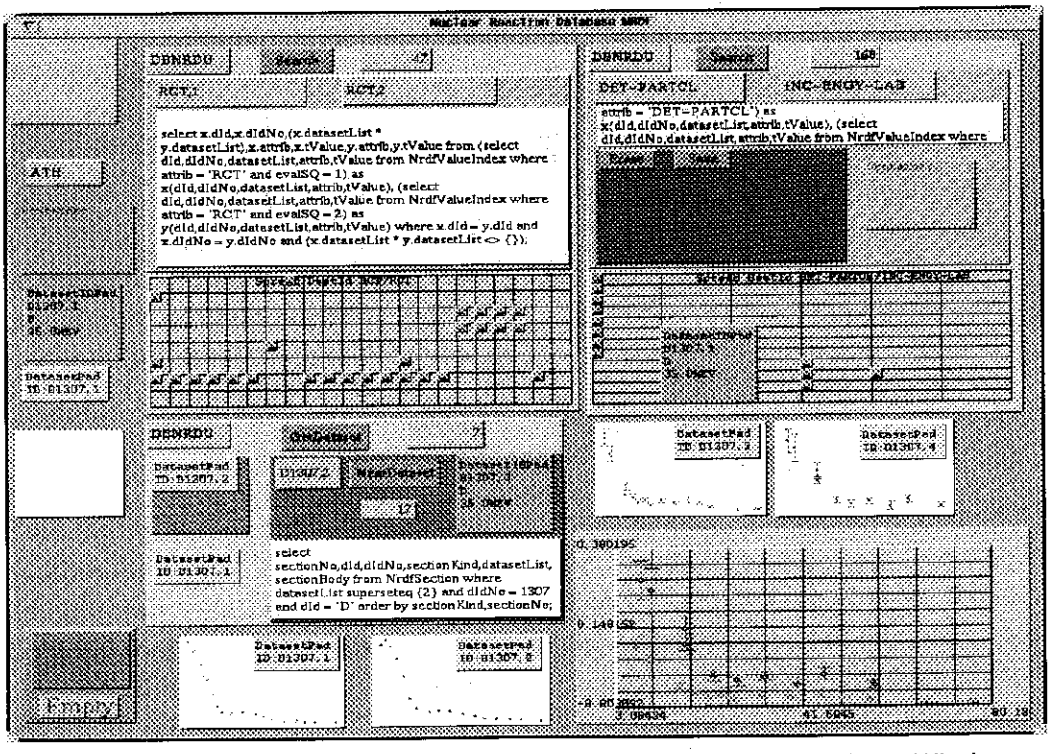

Fig.1 Overall appearance of the NRDF system on IntelligentPad in a Window

In the figure, pads are arranged in three columns. The left hand column are some component pads and tool pads used in this application. Among them are Input/OutputPad, ContainerPad that transports any number of pads from one pad to another, DatasetIdPad that represents each NRDF data entry, DatasetPad that holds a data table and its related information, GraphPad that graphically presents table data, and TrashPad that erases any pads.

In the middle and the right hand columns are the composite pads that perform some functions of this application. Among of them are arranged: two pads for indexed record search (the top of the two columns), one pad for section records (in the middle of middle column), four GraphPads with one DatasetPad, and one GraphBasePad with two GraphPads pasted on it (in the bottom of right hand column).

Now, we will explain each composite pad in the following sections.

3.2 Visualization of record distribution with respect to arbitrarily selected attributes and step-wise filtering of records

The pad in Fig.2 is a composite pad for the access of NRDF database and graphical visualization of record distribution. This pad is composed of one DatabaseProxyPad, five Input/OutputPads, one ButtonPad, one SqlQueryMakerPad and one RecordDistributionPad.

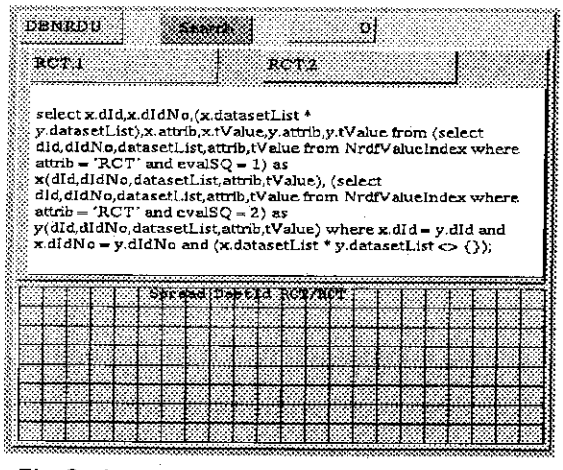

Fig.2 A composite pad for index record retrieval; Two attributes specified and the SQL select statement generated for these parameters are shown on I/O pads

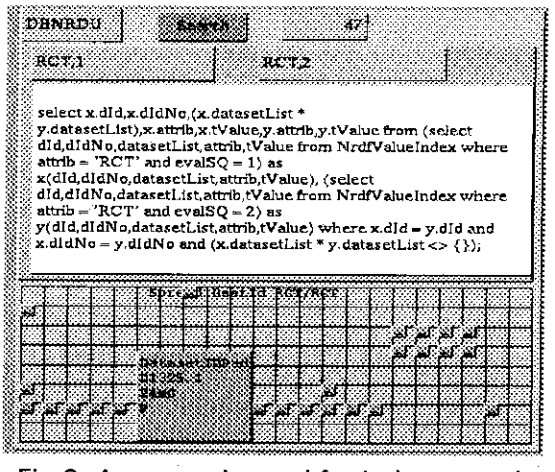

Fig.3 A composite pad for index record retrieval; DatasetIdPad for each record found

First, you can specify one or two attributes that describe information in the NRDF database. Among candidate attribute are RCT,1 and RCT,2; where RCT,1 and RCT,2 mean *target nucleus* and *projectile* respectively in the nuclear reaction formalism. Then the SQL query is made up with the attributes specified, which can be seen by an OutputPad connected to the query slot of the DatabaseProxyPad.

If you click SearchButtonPad, the NRDF database (named DBNRDU) is retrieved. When database search has finished, the number of retrieved items is displayed on the OutputPad as "47" for example, and the records found are graphically distributed as

pads (DatasetIDPad) on the RecordDistributionPad (Fig. 3). The RecordDistributionPad represents the target variety as its X-coordinate, and the incident particle variety as its Y-coordinate. In this case, you can see the *target nucleus* and the *incident particle* of the corresponding record when you select a DatasetIdPad (which is enlarged as shown Fig.3) on the RecordDistributionPad.

You can inspect the record distribution of the database with respect to different pairs of attributes. In the top of the right column of Fig.1, you can see another pad. This pad is just the same as the one mentioned above except the additional use of AndSetWorkMakerPad. Assuming that you want to inspect the record distribution with respect to *detected particles* and *incident energy values* for an arbitorarily selected subset of the previous database retrieval result. For an arbitrary selection of records, you can use the ContainerPad. This pad picks up the pads covered by this pad; you can just select the ContainerPad, move and resize it to cover the records you want to pick, then popup the menu to specify the get operation (Fig.4). After picking up records, you can move the ContainerPad to the AndSetWorkMakerPad (Fig.5 as after move), select the ContainerPad, and popup the menu to specify the release operation (Fig.6). The picked up DetasetIdPads are released from the ContainerPad and pasted on the AndSetWorkMakerPad. Now you can click the SaveButtonPad, then dataset identification records transported by DatasetIdPads are saved in the work file of the database.

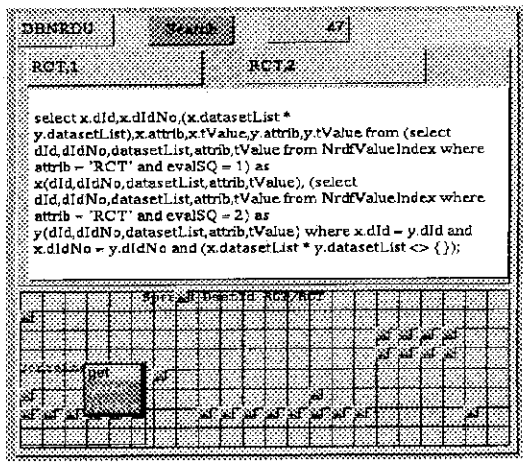

Fig.4 A ContainerPad getting some DatasetIdPads

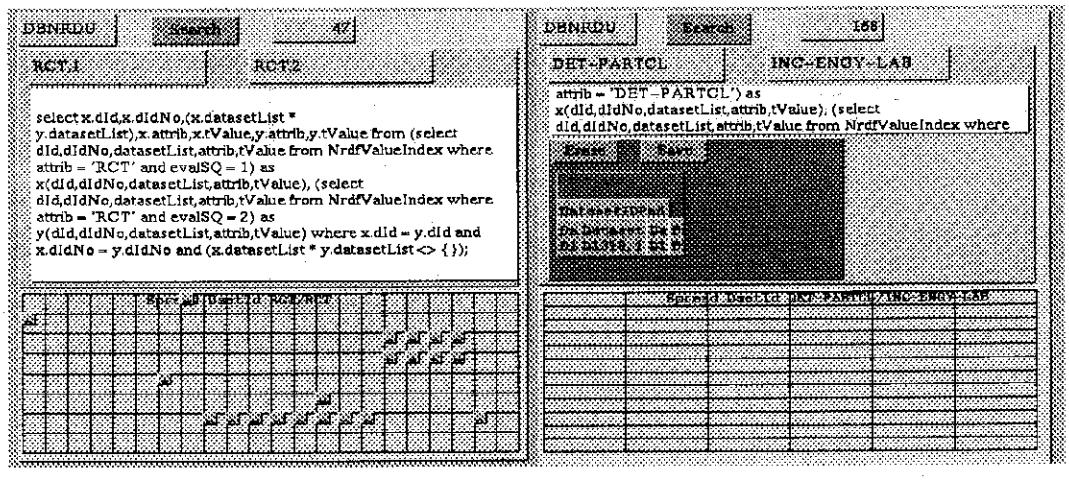

Fig.5 A ContainerPad used to transfer some DatasetIdPads from one context to another

Now you can perform search operation with respect to a new pair of attributes. When you click the SearchButtonPad on the DatabaseViewerPad, search operation begins and the retrieved records are distributed with respect to the new pair of

attributes, "DET-PARTCL" and "INC-ENGY-LAB" (Fig.7).

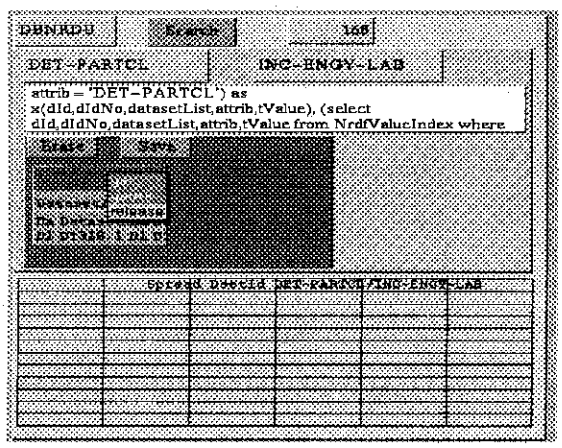

Fig.6 A composite pad releasingDatasetIdPads on an AndSetMakerPad

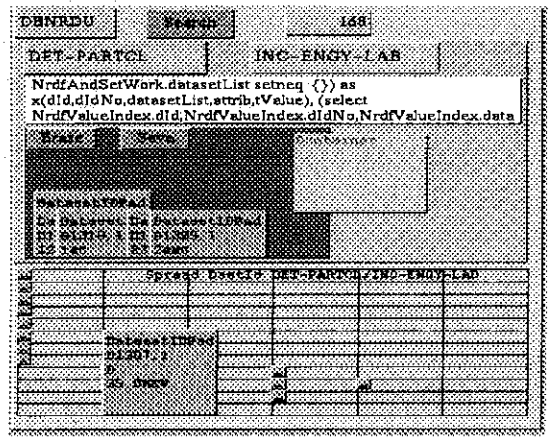

Fig.7 A composite pad for index record retrieval in another context

If you want to inspect the record distribution independently from the previous retrieval, you can use this composite pad or its copy without AndSetWorkMakerPad.

3.3 Getting full information of each dataset

You can make DatasetPads from a DatasetIdPad. To do so, you can use the composite pad shown in Fig.8. You may paste any DatasetIdPad on it; the first element in the set of dataset identification records is removed and displayed such as "D1307,1" (Fig. 8). This identification code of the record is also put into SQL select statement as a parameter. Now, if you click the GetDatasetButtonPad, the DatasetPad for the DatasetId will be created (Fig.9). You can click the NextDatasetButtonPad to create the DatasetPad for the next element in the set of dataset identification records.

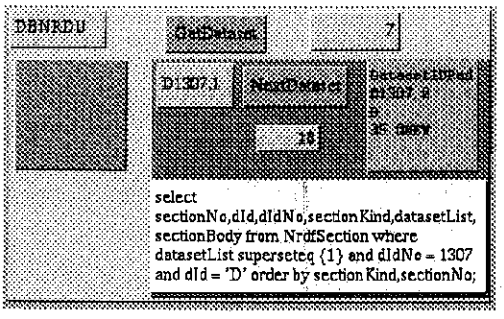

Fig.8 A composite pad for dataset assembling from section records; a DatasetIdPad is pasted on this pad

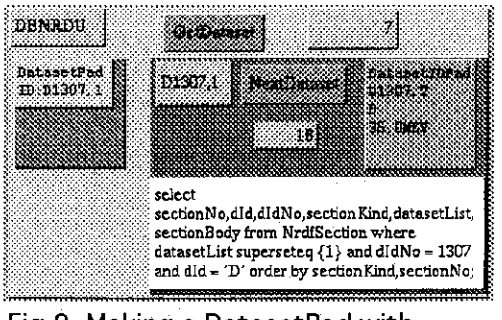

Fig.9 Making a DatasetPad with the DatasetIdPad pasted

3.4 Graphical representation of table data

If you obtain a DatasetPad, you can see any details of the dataset through appropriate viewer pads for different purposes. For Example, we provide two graphical viewing pads for datatables: GraphPad and GraphBasePad. The GraphPad shows a numerical data table as a data point graph with or without error bars. The GraphBasePad is used to compare several datatables visually. This pad makes the

background color of each GraphPad transparent. It also adjust the scale of coordinates of all the GraphPads pasted on itself. Fig.10 shows two GraphPads showing two datatables of Dataset D1301,3 and D1301,4 (above), and a GraphBasePad (below). On the GraphBasePad, these two GraphPads are overlayed.

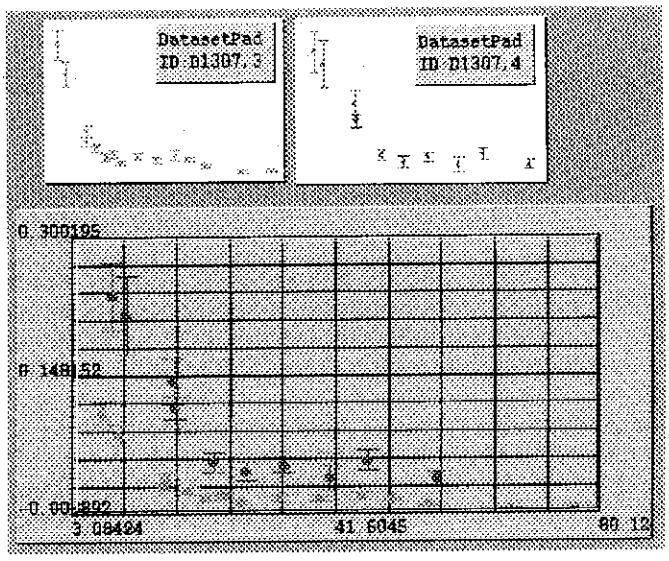

Fig.10 Two GraphPads and one GraphBasePad overlaying the two Graphpads

4. concluding remarks

we have shown several pads specially designed for the NRDF database, together with the examples of how to use them. A pad in the IntelligentPad system is a reusable media object. Once a new pad is developed, it can be registered in a common pool of pads as a shared resource: it can be reused in different contexts by different people in the community. It is noticeable that only about three months was taken to design and develop the pads for this system. The IntelligentPad system itself is now evolving as a meme media system, in which you can easily distribute any composite pads worldwide through the Internet and exchange them with other researchers. We could be convinced that the IntelligentPad architecture might be effective in developing application systems shared in some community as the NRDF system.

Acknowledgments

The author would like to thank Professor Y. Tanaka for his helpful discussion and suggestions, and M. Nakagawa and other members of the Laboratory for their assistance in developing the system. He also acknowledges K.Kato and A. Ohnishi for their comments on the design of pads.

References

[1] K. Kato:" Charged-Particle Nuclear Reaction Database NRDF", Genshikaku Kenkyu, Vol.39 No.5,(1995), pp63-73.

[2] Tanaka,Y:"A Synthetic Dynamic-Media System",Proc. of International Conference on Multimedia Information Systems, pp.299-310, Singapore (1991).

3. 37 Nuclear Data Information System for Nuclear Materials

Mitsutane FUJITA*, Tetsuji NODA* and Misako UTSUMI
National Research Institute for Metals
1-2-1, Sengen, Tsukuba, Ibaraki 305 Japan

The conceptual system for nuclear material design is considered and some trials on WWW server with functions of the easily accessible simulation of nuclear reactions are introduced. Moreover, as an example of the simulation on the system using nuclear data, transmutation calculation was made for candidate first wall materials such as 9Cr-2W steel, V-5Cr-5Ti and SiC in SUS316/Li_2O/H_2O(SUS), 9Cr-2W/Li_2O/H_2O(RAF), V alloy/Li/Be(V), and SiC/Li_2ZrO_3/He(SiC) blanket/shield systems based on ITER design model. Neutron spectrum varies with different blanket/shield compositions. The flux of low energy neutrons decreases in order of V<SiC<RAF<SUS blanket/shield systems. Fair amounts of W depletion in 9Cr-2W steel and the increase of Cr content in V- 5Cr-5Ti were predicted in SUS or RAF systems. Concentration change in W and Cr is estimated to be suppressed if Li coolant is used in place of water. Helium and hydrogen production are not strongly affected by the different blanket/shield compositions.

1. Introduction

Many phenomena cased by neutron irradiation under thermal, fast and fusion reactors can be little understood except through the examination. Easily accessible material information system is required for design of nuclear materials and analyses or simulations of the phenomenon. In order to construct such a system, a project, "Data-Free-Way", has been under way from April in 1990 under the cooperation of National Institute for Metals (NRIM), Japan Atomic Energy Research Institute (JAERI) and Power Reactor and Nuclear Fuel Development Corporation (PNC) [1,2]. In NRIM besides the cooperated construction of the distributed database for nuclear materials, a simulation system of nuclear transmutation and radioactivation has been created.

On the other way, the new system is created on the basis of the substantial concept and data used in IRAC [3]. IRAC was developed in 1984, however the use of it is limited to the inside of NRIM. Therefore, the system as was improved to be easily used mutually through the network. The system consists of a nuclide database with several tables storing the data on nuclear reaction and two simulation processes on transmutation and radioactivation integrated under user-friendly interface. In the near future, the system will be combined with "Data-Free-Way".

Transmutation resulting in change of composition, helium and hydrogen production, and induced activity under neutron irradiation is considered as one of severe problems for first wall materials of fusion reactors. The compositional change and gaseous products lead the degradation of materials and induced activity should be lowered from the viewpoint of reactor and environmental safety. Since the degree of transmutation depends on the neutron spectrum[3], designs of fusion reactor structures such as blanket and shield must be considered to understand the transmutation behaviors of materials. Recently, high burn-up of some metals such as Mo, Re, W, Ta, V are predicted under fusion neutron irradiation conditions[3,4].

In the present paper, the outline of the new simulation system for nuclear transmutation is introduced. Then, the necessary functions of the system are discussed. Moreover, in order to verify the simulation using the system, the transmutation behaviors of several candidate first wall materials such as 9Cr-2W steels, V-5Cr-5Ti and SiC have been examined for various types of blanket and shields based on ITER design structures[5] using the simulation calculations[6].

2. Conceptual Material Information System for Nuclear Materials Design

In the system for nuclear materials, it has to be considered that irradiation in various reactors produces radiation damage as a consequence of the formation of impurity nuclide by transmutation and the displacement of atoms from their equilibrium lattice positions by high energetic neutron or atom collision. Moreover, induced radioactivity by transmutation is an important problem from the viewpoints of the reduction of radiological hazards such as contact maintenance, waste management and environmental safety. The calculation code for the simulation and various databases required for the system is as follows.

Code: a. Neutron spectrum calculation, b. Transmutation and Induced activity calculations, c. Damage calculation.

Database: a. Facts Material Database, b. Nuclear Database, c. Reactor Operation Database, d. Reactor Design Database, e. Safety criteria Database.

We are unable to employ readily all of them because these many database are now under construction. Thus, in the present situation, the conceptual flow diagram of a information system for the alloy design and selection

of nuclear materials is shown in Fig.1. At the first, candidate materials are selected by using material database such as "Data-Free-Way"[1,2]. The properties of the materials under irradiation are checked by the three types of simulations and then the other properties will be evaluated.

In the data system, it is necessary for the functions for analysis of data retrieved from database and the simulation of various phenomenon in material field. An example of the simulation of transmutation on WWW server is shown in Fig. 2. In this system, the results of simulation of the compositional change are easily obtained by the operation of mouse-click.

3. Effect of neutron spectra on the transmutation of first wall materials

3.1 Reactor designs and neutron spectra

The neutron spectrum calculation was made using ANISN for ITER inboard structure design[5]. Fig. 3 shows the one dimensional model of mid-plane of the reactor used for calculation. The main structures are composed of carbon armor of 2cm, first wall of 1.5cm, blanket/shield of around 150cm, SUS 316 vacuum vessel, super-conducting magnet, and liquid helium vessel. In the present study, the compositions of first wall and blanket/shield materials were changed. In Fig.3, several combinations of blanket/shield materials are shown. ITER originally adopts the blanket(SUS blanket) made of stainless steel, Li_2O with condensed ^6Li, Be and water, and the shield materials made of stainless steel and water, respectively. In the RAF blanket, SUS316 was replaced by 9Cr-2W steel. V blanket was one of options for ITER where V-5Cr-5Ti was considered as the first wall and liquid lithium is used as breeder and coolant. The composition of SiC blanket was taken from ARIES-1 blanket model[7]. The blanket is composed of SiC, Li_2ZrO_3, Be and He gas.

In the shield, B_4C is added to SiC and He gas to improve the shielding efficiency. Nuclear data library with respectively 42 and 21 energy groups of neutron and gamma ray used was FUSION- 40[8] based on JENDL-3. The calculation was made with scattering order of P5 and angular quadrature order of S8.

3.2 Transmutation calculation

Transmutation calculation of materials was conducted based on the neutron spectra obtained ANISN using IRAC[4] code considering several step reactions if reactions have large cross sections. Nuclear data with 42 energy groups used for the transmutation calculation were CROSSLIB[9], JENDL-3 and FENDL/GA-1.1[10]. The neutron wall loading was assumed to be $1MW/m^2$.

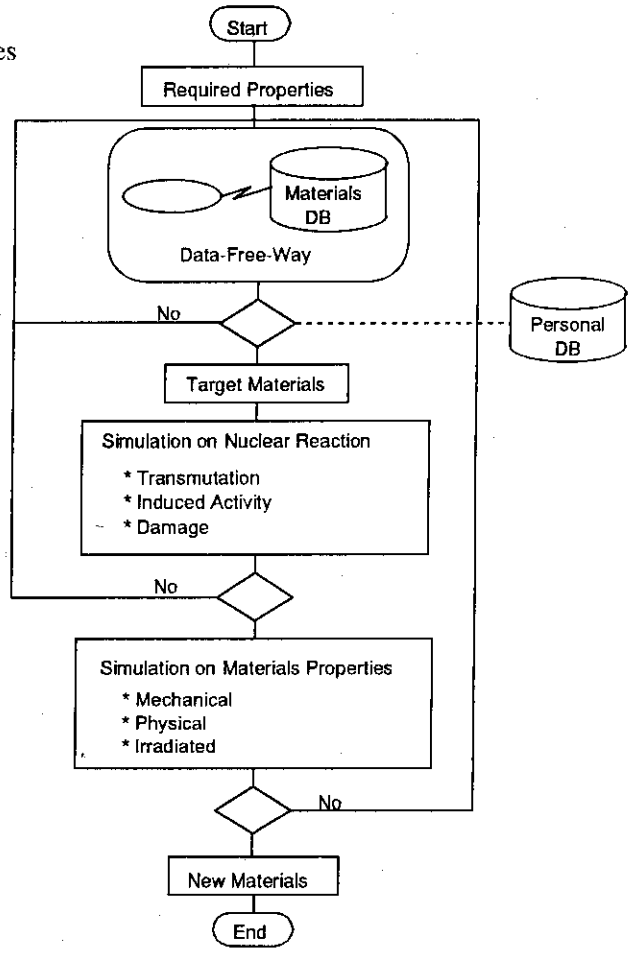

Fig. 1 Flow diagram on the concept of the ata system for nuclear material design and selection.

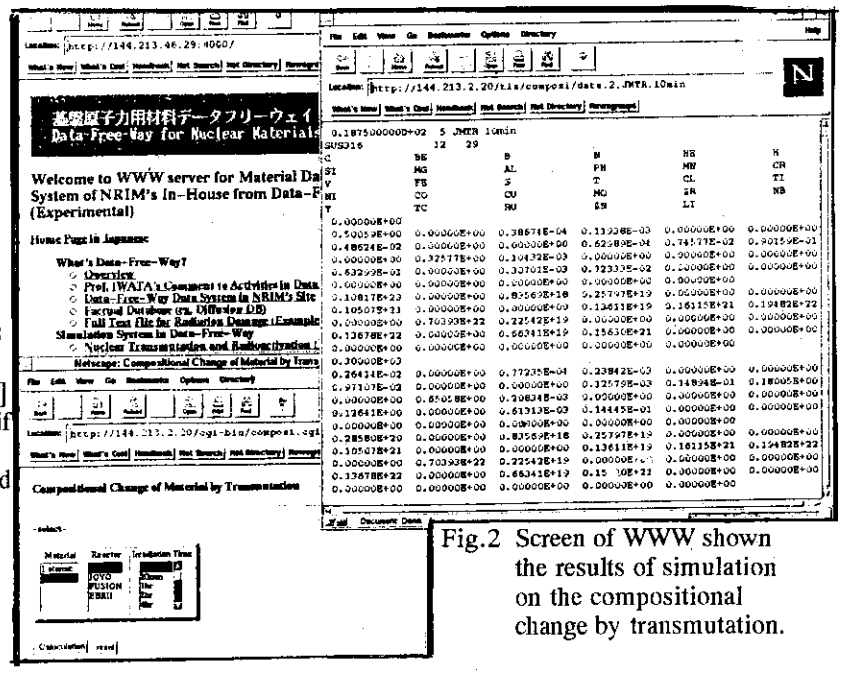

Fig.2 Screen of WWW shown the results of simulation on the compositional change by transmutation.

4 Results

Fig. 4 shows the typical neutron spectra at the first wall, the first shield and the vacuum wall for SUS blanket system. The flux of 14 MeV neutron remarkably decreases with the distance from plasma. The relations between 14 MeV neutron flux and the distance from the plasma center for various blanket systems are shown in Fig. 5

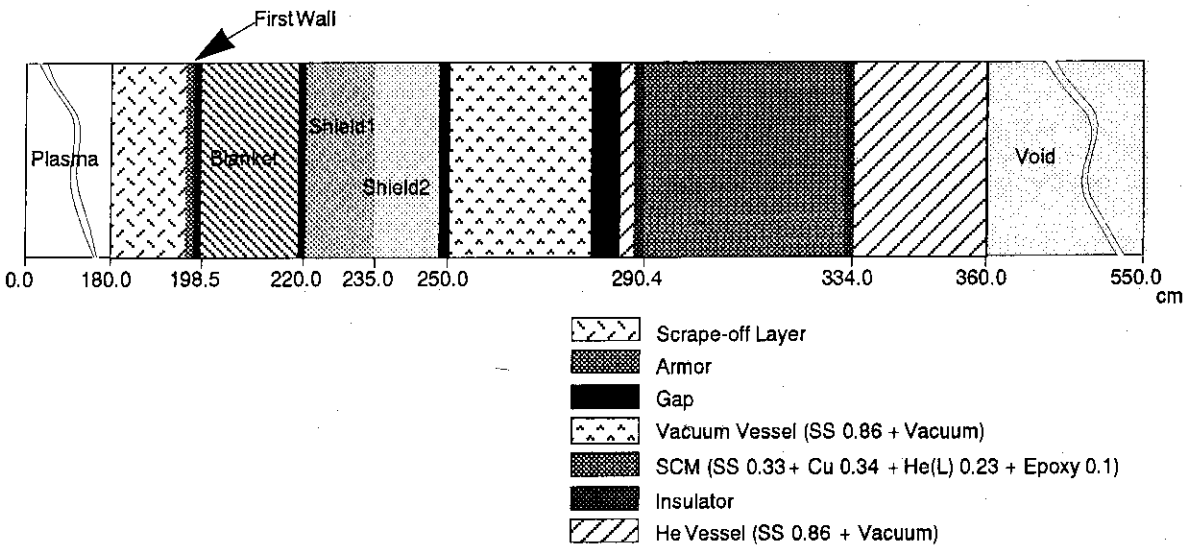

	Region	Thickness (cm)	Outer Radius (cm)	Composition
SUS	First Wall	1.5	198.5	SS 0.7+H 2O 0.3
	Blanket	19.5	218.0	SS 0.05 + Li 2 O 0.1575+ Be 0.4725+ H 2O 0.05 + He 0.1
	Shield1	15.0	235.0	SS 0.9 + H 2O 0.1
	Shield2	13.0	248.0	SS 0.95 + H 2 O 0.05
RAF	First Wall	1.5	198.5	9Cr2W 0.7+H 2O 0.3
	Blanket	19.5	218.0	9Cr2W 0.05 + Li 2 O 0.1575+ Be 0.4725 + H 2O 0.05 + He 0.1
	Shield1	15.0	235.0	9Cr2W 0.9 + H 2O 0.1
	Shield2	13.0	248.0	9Cr2W 0.9 + H 2O 0.1
V	First Wall	1.5	198.5	V Alloy (V5 Cr5 Ti)
	Blanket	19.5	218.0	Li + Be
	Shield1	15.0	235.0	V Alloy + Li
	Shield2	13.0	248.0	V Alloy+ Li
SiC	First Wall	1.5	198.5	SiC
	Blanket	19.5	218.0	SiC 0.25 + Li 2 ZrO3 0.14 + Be 0.56+ He 0.05
	Shield1	15.0	235.0	SiC 0.56 + B 4 C 0.24 + He 0.20
	Shield2	13.0	248.0	SiC 0.665 + B 4C 0.285 + He 0.05

Fig.3 One dimensional inboard model of a fusion wall reactor based on ITER design and aterial compositions of several first wall, blanket and shield models.

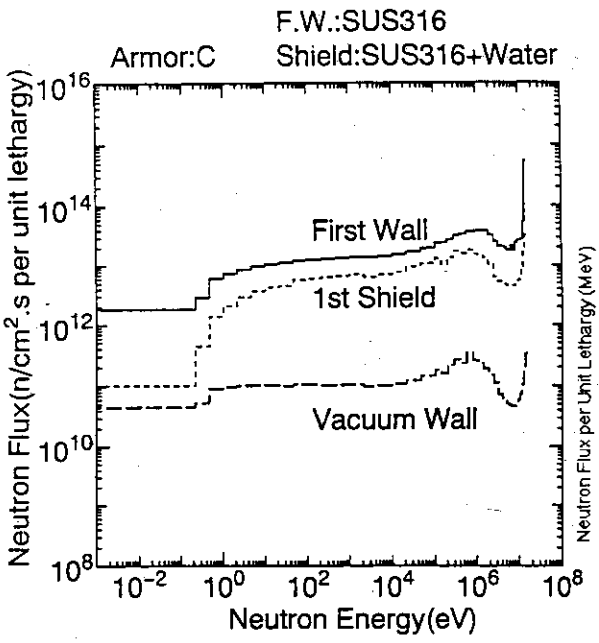

Fig.4 Neutron spectra at first wall, shield and vacuum position under 1 MW/m^2 wall loading.

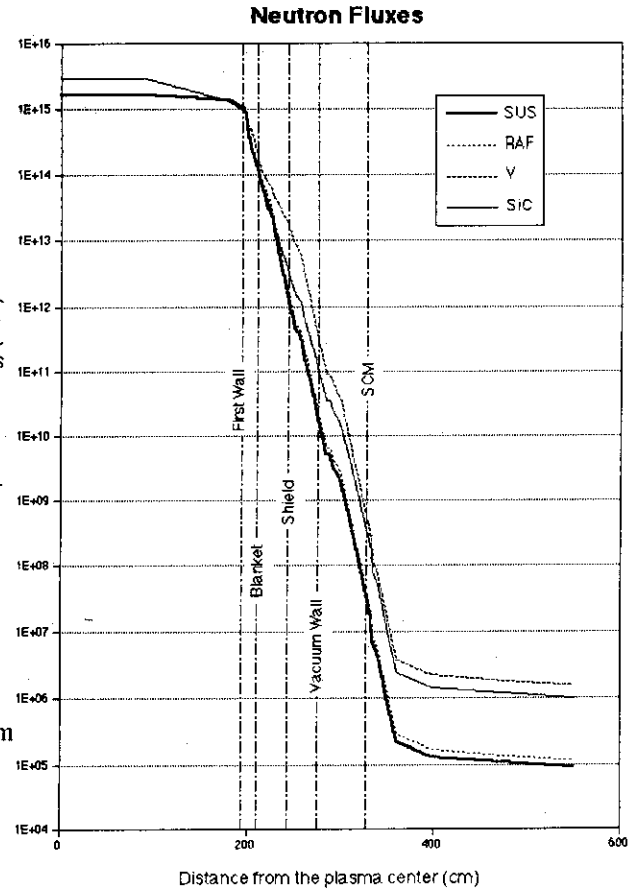

Fig.5 Neutron flux of 14 MeV as a function of the distance from the plasma center.

The flux almost linearly decreases with the distance from the armor. The decay slope is around one order magnitude per 15-17cm independently on the blanket/shield compositions.

Figure 6 shows the neutron spectra at the position of first wall for various blanket/shield compositions. There is a large difference in neutron flux at low energy region between blanket/shield materials. Especially, in the V blanket/shield system where liquid Li is used as a coolant, the sharp decrease of the neutron flux is observed with decreasing neutron energy.

Compositional changes of 9Cr-2W steel, V-5Cr-5Ti and SiC for the respective blanket/shield systems with neutron fluence are shown in Fig.7. The concentration of main constituents does not change remarkably for V-5Cr-5Ti and SiC except helium and hydrogen production. On the other hand, tungsten content in 9Cr-2W steels decreases with the neutron fluence. Next the effect of neutron spectrum on the compositional change of 9Cr-2W steel, V-5Cr-5Ti and SiC were examined for various blanket/shield systems by changing the first wall materials.

Table 1 and 2 show the concentration change of some elements in 9Cr-2W steel, V-5Cr-5Ti, and SiC for different blanket/shield systems after 10MW.y/m^2 irradiation. In 9Cr-2W steel, W is transmuted to Re and Os and reduces the concentration below half of an initial value in SUS and RAF systems, while the transmutation is suppressed in V blanket/shield system. Chromium, another main alloying element, is hardly affected in concentration by neutron spectrum, though it is slightly transmuted to Mn.

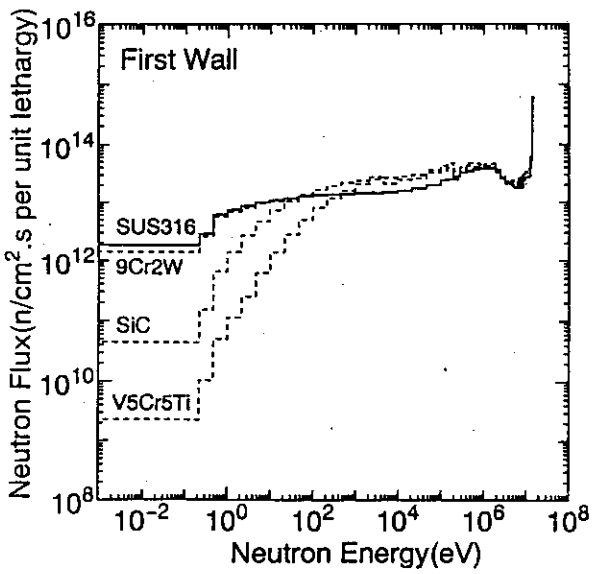

Fig.6 Comparison of neutron spectra at first wall for various blanket/shield compositions.

If V-5Cr-5Ti is used as a first wall in SUS or RAF blanket/shield system, Cr content increases by about 40% in contrast to V blanket/shield system where only several % of the increase is predicted. Titanium concentration is not affected by the neutron spectrum as seen in table 1.

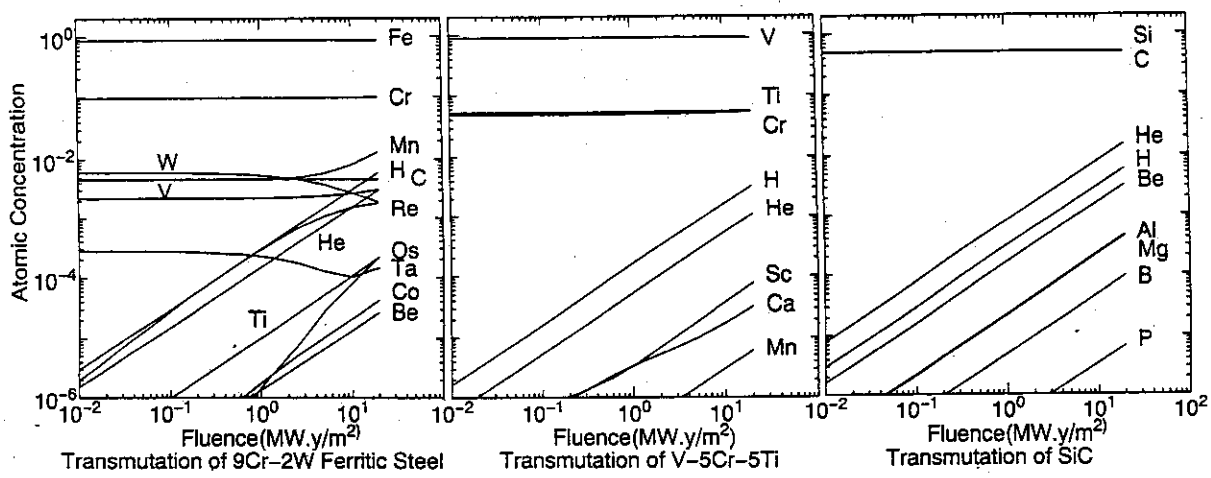

Fig.7 Compositional change of 9Cr-2W steel for RAF , V-5Cr-5Ti for V and SiC for SiC blanket/shield system as a function of neutron fluence.

Table.1 Concentration change of some elements for candidate first wall materials after 10MW.y/m^2 irradiation in various blanket/shield systems (at %)).

Material	Blanket / shield				
	Before	SUS	RAF	V	SiC
9Cr2W steel					
W	0.61	0.27	0.27	0.48	0.32
Re+Os	0	0.17	0.16	0.06	0.14
Cr	9.71	9.80	9.80	9.81	9.81
Mn	0.46	0.81	0.81	0.84	0.81
V5Cr5Ti					
Cr	4.89	6.77	6.47	5.13	5.35
Ti	5.31	5.36	5.36	5.40	5.39
SiC					
Si	50.0	49.6	49.6	49.5	49.5
C	50.0	49.2	49.2	49.1	49.2

Table.2 Helium and hydrogen production for candidate first wall materials after 10MW.y/m^2 irradiation in various blanket/shield systems (appm).

Material	Blanket / shield			
	SUS	RAF	V	SiC
9Cr2W steel				
He	1510	1510	1710	1630
H	3020	3020	3440	3300
V5Cr5Ti				
He	476	475	509	537
H	1420	1420	1620	1550
SiC				
He	7310	7310	8250	7800
H	2740	2740	5970	3130

Regarding SiC, compositional change except gaseous products is not obvious. However substantial He formation occurs in SiC for any blanket/shield systems. Helium of about 0.7-0.8 at % is produced after 10 MW.y/m^2 irradiation.

The results in table 2 indicates that the amounts of He and H are produced in V and SiC blanket/shield systems where fluxes with energies of 100 keV-1 MeV are rather higher than other systems.

5. Discussion

The concentration change of W in 9Cr-2W steel and Cr in V-5Cr- 5Ti due to the transmutation is affected by the neutron spectrum. Especially significant transmutation of W and V occurs when the neutron flux with low energy is considerably high in such case of SUS blanket/shield system.

As have pointed out in the previous works[1,2], stable isotopes of W have a large cross section for (n, γ) reaction in low energy region of neutrons. W is composed of 0.135% ^{180}W, 26.4% ^{182}W, 14.4% ^{183}W, 30.6% ^{184}W and 28.4% ^{186}W. Re and Os productions mainly occur through following paths:

$^{184}W(n,\gamma)^{185}W$ (75.1days)->$^{185}Re(n,\gamma)^{186}Re$ (90.64h)->^{186}Os (1)
$^{184}W(n,\gamma)^{185}W$->$^{185}Re(n,\gamma)^{186}Re(n,\gamma)^{187}Re(n,\gamma)^{188}Re$(16.98h)->$^{186}Os$ (2)
$^{186}W(n,\gamma)^{187}W$ (23.9h)->$^{187}Re(n,\gamma)^{188}Re$->$^{188}Os$ (3)

Most Os is produced through reaction of (3). Neutron capture is also significant for the transmutation of vanadium. Chromium is formed according to the following reaction:

$^{51}V(n,\gamma)^{52}V$(3.75min)->^{52}Cr (4)

As have seen in table 2, W depletion and Cr accumulation caused by the transmutation are much affected by the neutron spectrum. Especially neutron fluxes with energies below around 100eV determine the degree of concentration change of these elements. Returning to the neutron spectra of various blanket/shield compositions, it is necessary to examine the factors controlling spectrum changes. In the present study, V blanket/shield system showed the lowest flux at low energies of neutrons. In order to clarify the compositional dependence of the spectrum, V-5Cr-5Ti, structural material of V blanket/shield system, was replaced by 9Cr-2W steel and the neutron spectrum was calculated.

Figure 8 shows the comparison of neutron spectra for RAF blanket/shield systems with different coolant and breeder. It is clear that H_2O softens the neutron spectrum resulting the production of more neutrons with low energies than Li. The neutron spectra in this figure suggest that W depletion in 9Cr-2W steel is minimized if Li coolant is used.

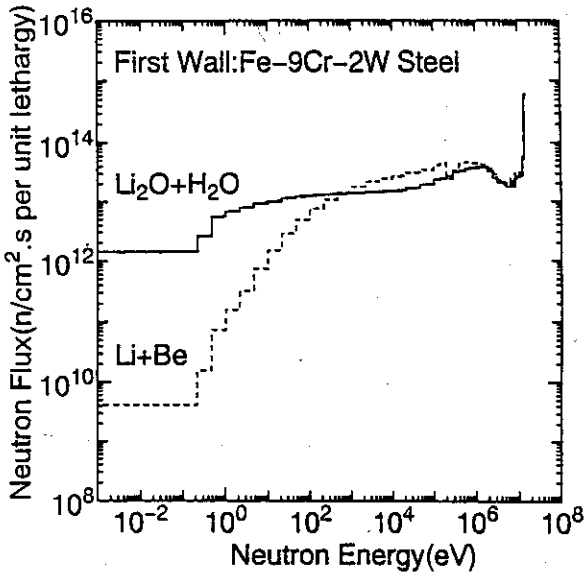

Fig.8 Neutron spectra at the first wall of 9Cr-2W/Li_2O H_2O nd 9Cr-2W/Li/Be blanket/shield systems.

Considering the real first wall/blanket/shield system, the combination of V alloy/Li_2O/H_2O is not necessary realistic because vanadium is not stable in water. Therefore Cr accumulation in V alloys will not be significant so far as V alloy/Li/Be system is considered.

6. Conclusion

Concept of data system for nuclear material design was considered. It is necessary that the system consists of a nuclide database storing the data on nuclear reaction and two calculating processes for the simulation of transmutation and radio activation.

The transmutation of 9Cr-2W steel, V-5Cr-5Ti and SiC for SUS316/Li_2O/H_2O(SUS), 9Cr-2W/Li_2O/H_2O(RAF), V-5Cr-5Ti/Li/Be(V), and SiC/Li_2ZrO_3/He(SIC) blanket/shield systems were examined by using the simulation calculation code. Conclusions are as follows:

1. Neutron spectrum depends on the composition of blanket/shield materials.
2. The flux of neutrons with energies lower than around 100 eV decreases in order of V<SiC<RAF<SUS blanket/shield system.
3. Fair amounts of W depletion in 9Cr-2W steel and Cr accumulation in V-5Cr-5Ti were predicted for H_2O coolant system.
4. Transmutation of W and V is suppressed if Li coolant is used.
5 .Helium and hydrogen production are not strongly affected by the different blanket/shield systems.

References

[1] H.Nakajima, N.Yokoyama, F.Ueno, S.Kano, M.Fujita, Y.Kurihara and S.Iwata, J. Nucl. Mat,. 212-215(1994)117.
[2] F.Ueno, S.Kano, M.Fujita, Y.Kurihara, H.Nakajima, N.Yokoyama and S.Iwata, J. Nucl. Sci. Tech., 31(1994)1314.
[3] L.R.Greenwood and F.A.Garner, Nucl. Mat., 212-215(1994)634.
[4] C.B.A.Forty, G.J.Butterworth, J.-Ch.Sublet, ibid., 212- 215(1994)640.
[5] K.Maki,H.Takatsu,T.Kuroda,Y.Seki,M.Kajiura,N.Tachikawa, R.Saito, H.Kawasaki, JAERI-M 91-017(1991).
[6] T.Noda, H.Araki, F.Abe, and M.Okada,Trans NRIM,30(1988)185.
[7] S.Sharafat, C.P.C.Wong and E.E.Reis, Fusion Technol.,19(1991)901.
[8] K.Maki, K.Kosako,Y.Seki, and H.Kawasaki,JAERI-M 91-072(1991).
[9] Y.Seki, H.Iida and H.Kawasaki, JAERI-1280,(1982).
[10] A.Pashchenko and P.Maclauglin, FENDL/GA-1.1, IAEA-NDS-148 Rev.1(1993).

3.38 An User-Interface for Retrieval of Nuclear Data

Misako UTSUMI, Mitsutane FUJITA and Tetsuji NODA
National Research Institute for Metals
1-2-1 Sengen, Tsukuba-City, Ibaraki, JAPAN, 305

A database storing the data on nuclear reaction was built to calculate for simulating transmutation behavious of materials. In order to retrieve and maintain the database, the user interface for the data retrieval was developed where special knowledge on handling of the database or the machine structure is not required for end-user. It is indicated that using the database, the possibility of He formation and radioactivity in a material can be easily retrieved though the evaluation is qualitatively.

1. Introduction

In the data system for nuclear material design and selection used in various reactors, huge material databases and several kinds of tools for data analysis or simulation code of the phenomena under irradiation are required. The challenge of a computer-based simulation system for the transmutation, radio activation, decay-heat and biological hazard potential of materials is done, since the simulation of the phenomenon under neutron irradiation is important in view of alloy design and selection of materials used in various reactors. A database storing the data on nuclear reaction needs to calculate of the simulation. In the database for nuclear reaction, the data of nuclear reaction for material design is stored and we can understand qualitatively the behavior of nuclear reaction such as the transmutation or decay. The database is required for the friend user-interface for the retrieval of necessary data.

In the paper, features and functions of the developed system are described and especially, examples of the easy accessible search of material properties are introduced.

2. Outline of the nuclide database for nuclear materials

2.1 Data collection

Various data, which are required for simulation on nuclear reaction, have been collected from reports as follows.

1) Nuclear data such as neutron cross-section are collected from JAERI's CRROSLIB, ENDF/B-6, JENDL-3 and FENDL 1.1. The number of element stored in the database is 54 at present, however, this will increase to be 89 in near future.
2) The data on element and isotope are collected from (a) "Table of Radioactive Isotopes" E. Browne and R. B. Firestone, 1986, LBLU of C, John Wiley & Sons, (b) "Chart of the Nuclides" compiled by Y. Yoshizaw and T. Horiguchi and M. Yamada, 1980, JNDC and NDC in JAERI.

2.2 Database system

In the nuclide database, the data of nuclear reaction for material design is stored and we can understand qualitatively the behavior of nuclear reaction such as the transmutation or decay. The database is managed by 4th Dimension where RDBMS (relational database management system) is supported on the PC (Macintosh). The RDBMS and PC were selected to be able to build the friend user-interface for the retrieval of necessary data.

2.3 Data structure

The database consists of five main tables and three supplemental tables, as shown Fig. 1. Main tables are element, isotope, spontaneous decay, transmutation and cross section table. The element table has the data such as element name, atomic weight and etc. These data are input values obtained from ordinary periodic table. The data in the isotope table consist of the natural abundance ratio, half-life data, gamma-ray or beta-ray energy and maximum permissible concentration in air (MPC), which are taken from isotope table. The spontaneous decay table has the data of decay mode and branching ratio. The transmutation table has the data of transmutation process, produced nuclide and etc.. The neutron cross-section table stores the data with 42-energy group covering from thermal neutron energy to 15MeV.

The supplemental tables are three kinds of spontaneous decay, decay mode, gamma energy and beta or alpha. These tables play the roles due to aid the retrieval and the calculation of decay heat. Both tables are related by a certain unique key mutually.

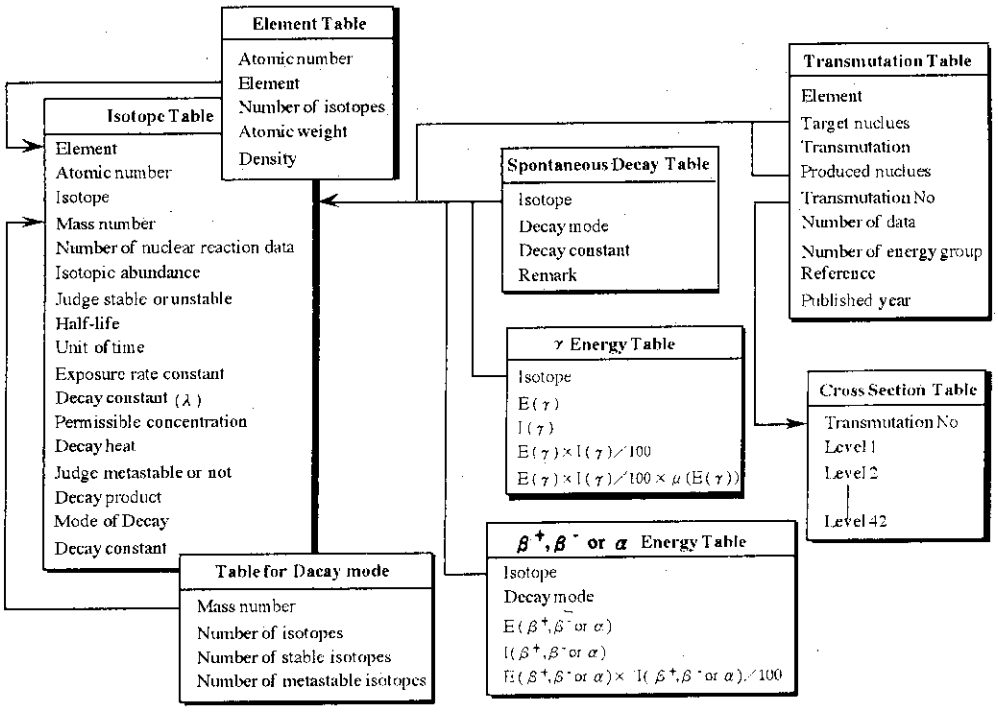

Fig. 1 Data structure of the database for nuclear reaction.

3. Functions and user-interface

3.1 Functions

Fig. 2 shows opening main menu screen of the database. This database has four retrieval functions of nuclear reaction process, properties of radioactive isotope, spontaneous decay of each isotope and decay of produced nuclides after nuclear reaction. We can understand qualitatively the behavior of nuclear reaction such as the transmutation or decay.

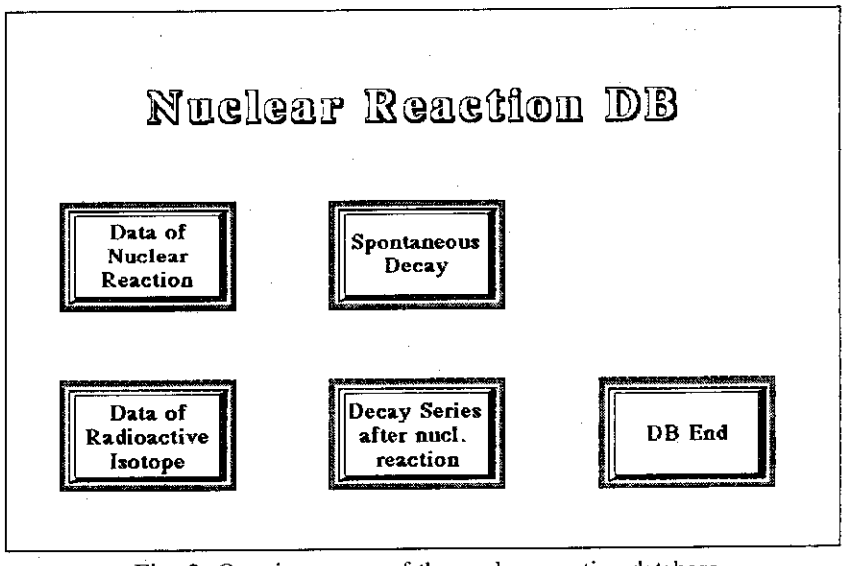

Fig..2 Opening screen of the nuclear reaction database.

3.2 User-interface for retrieval data

After choosing one of four functions on opening screen, various folders corresponding to the function appear as shown Fig. 3,4,5,6.

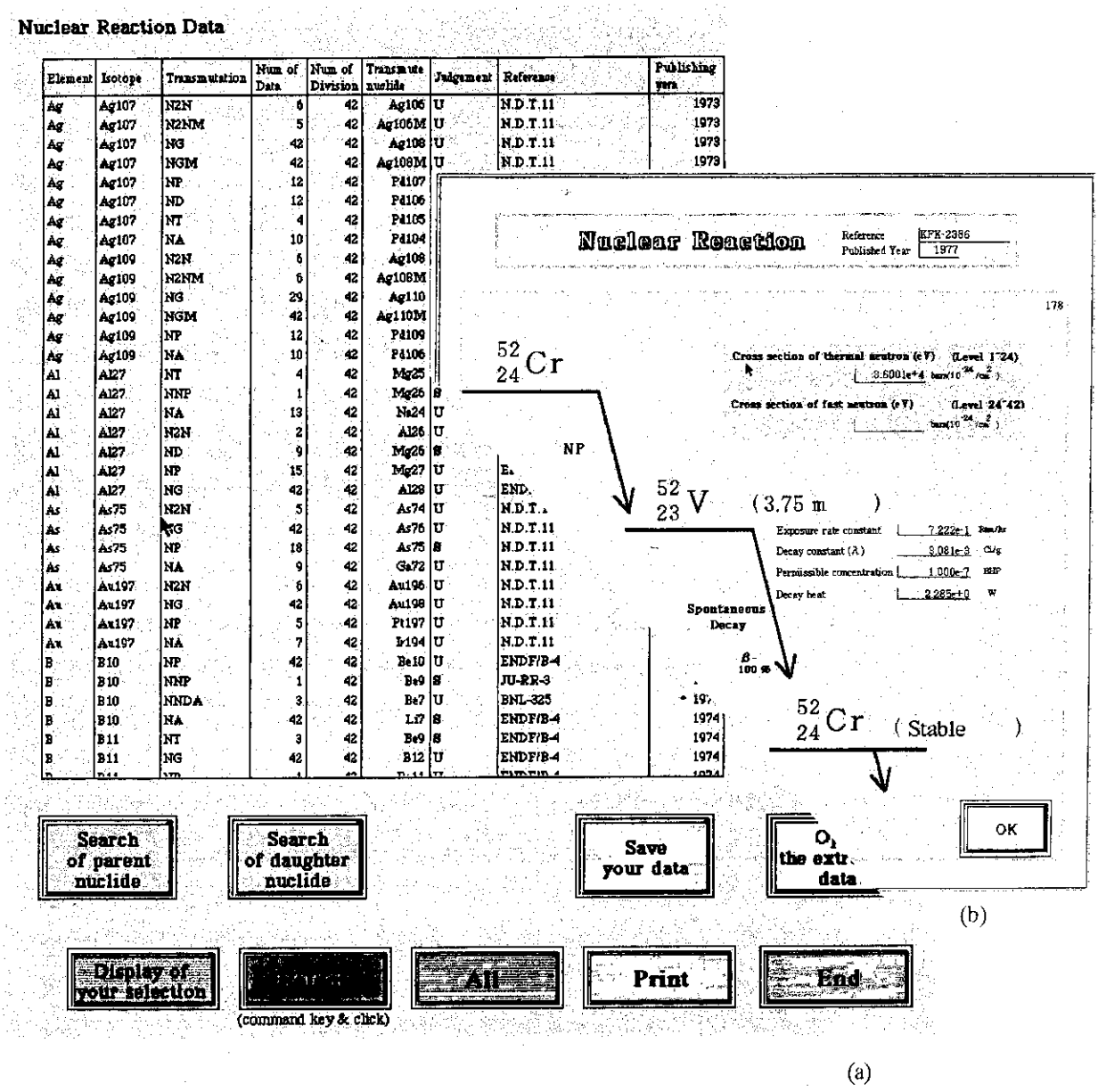

Fig. 3 Retrieval folders of records on nuclear reaction.
(a) : List of records, (b) : Transmutation and decay process.

Fig 3 indicates the retrieval folders of records on nuclear reaction. List screen displays a listing of 843 records of nuclides produced by nuclear reaction in the folder, as shown Fig. 3(a) and then by pressing the button of "parent nuclides", it is possible to view the contents of a nuclear reaction process as shown Fig. 3(b). Fig 4 indicates the retrieval folders of records on isotope properties. The list screen displays a listing of 3517 records of isotopes properties in folder, as shown Fig. 4(a). By selecting the desired isotope, it is possible to view the contents of properties of a isotope, as shown Fig. 4(b). Fig. 5 shows the retrieval folders of records on spontaneous decay. If the isotope is designated by the input of a mass number using the folder as shown Fig. 5(a), the spontaneous decay records of the radio isotope is obtained, as shown Fig. 5(b). Fig. 6 shows the retrieval folders of records on decay and transmutation processes after nuclear reaction. If the isotope is designated by the input of a element using the folder as shown Fig. 6(a), the decay of the produced nuclide and steps of transmutation is obtained, as shown Fig. 6(b).

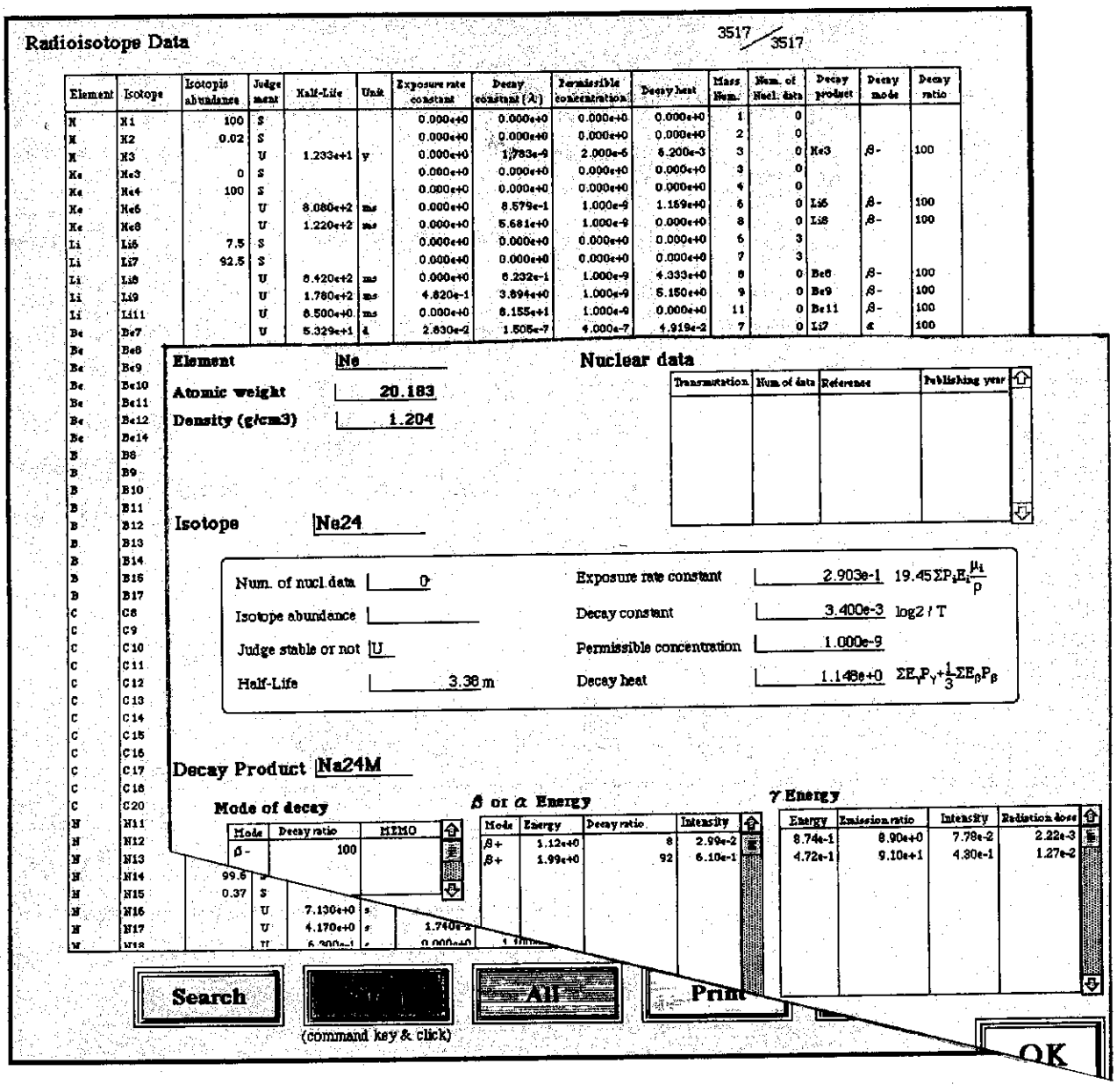

(a) (b)

Fig. 4 Retrieval folders of records on isotope properties.
(a) : List of records, (b) : Various properties of a isotope.

The user-interface (i.e. folder) of the database performs an important role either useful system or not. Using this user-interface, end-user can easily obtain the necessary nformation by the easy operation for retrieving, because a screen provided with pop-up and pull down menu, is employed to be mainly operated by micro-mouse in addition to keyboard.

4.Example of system operation

Type 316 stainless steel is used as the structural material of the fuel sub-assemblies in the sodium cooled fast breeder reactors. This steel is regarded as a candidate material for blanket structures of the fusion reactors. However it is required that materials should have a high resistance against swelling and low radioactivation under the high-energy neutron irradiation environment such as in fusion reactors. Ferritic 9Cr1WVTa steel is also being considered as an alternate candidate structural material to type 316 stainless steel [3]. An amount of He formation and radioactivity under neutron irradiation of both steels will be evaluated as an example of application of the present simulation system.

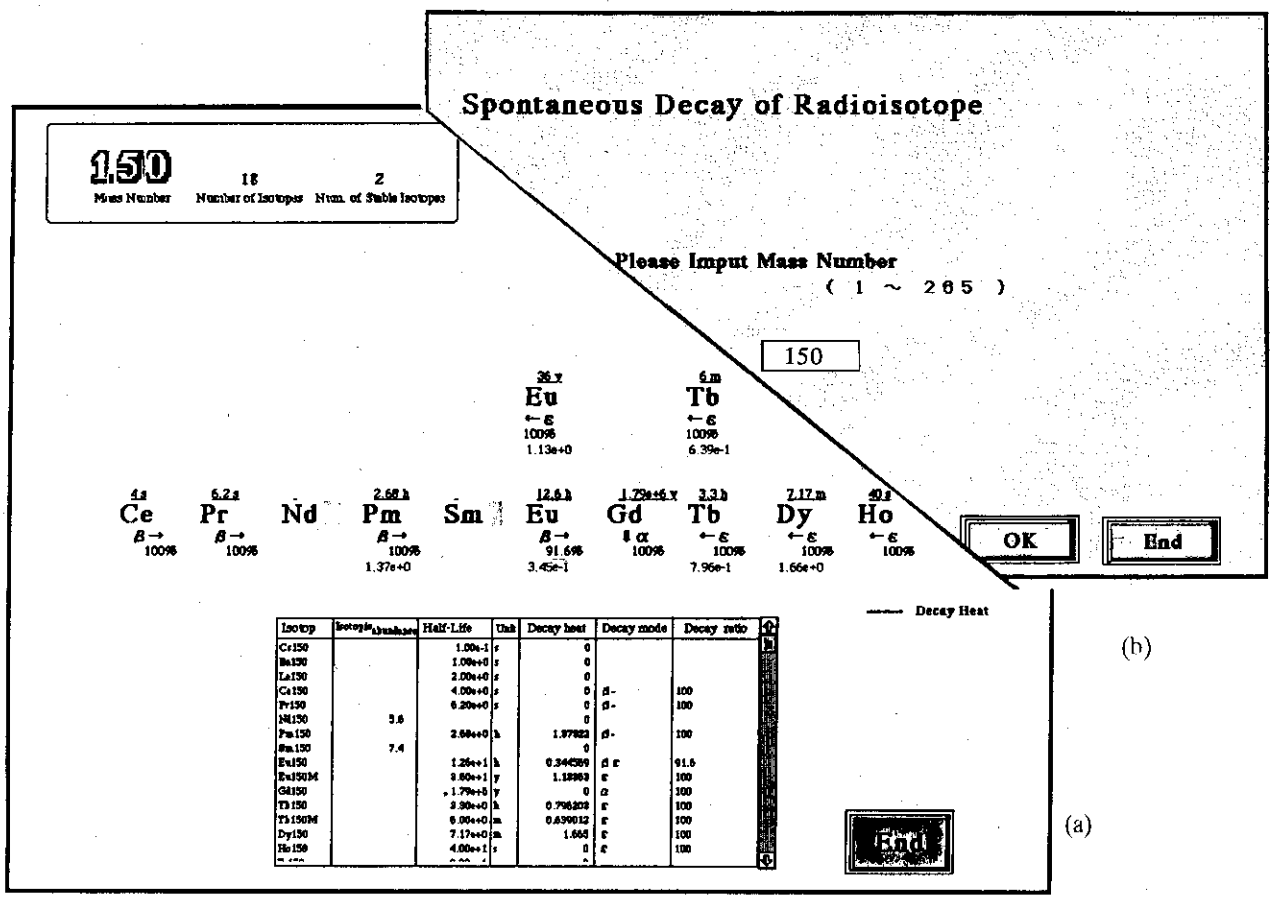

Fig. 5 Retrieval folders of records on spontaneous decay.
(a): Spontaneous decay of designated mass number, (b): Folder for input of a mass number.

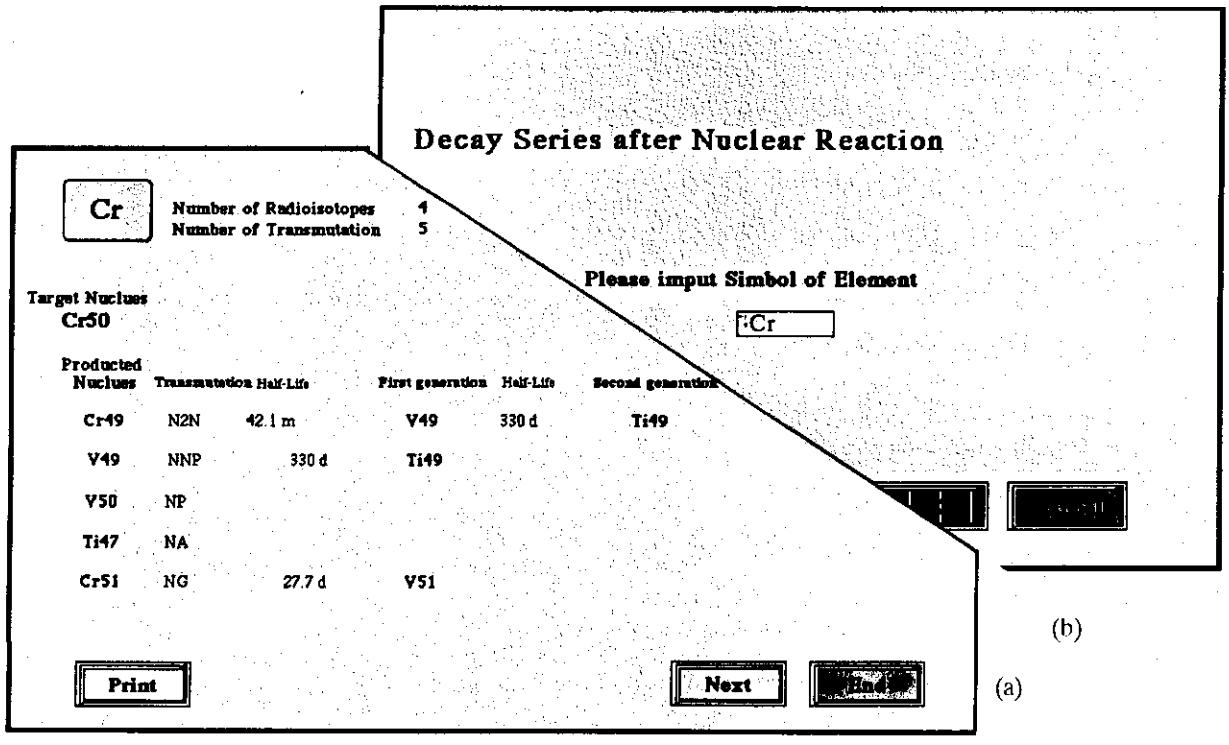

Fig. 6 Retrieval folders of records on decay after nuclear reaction and steps of transmutation.
(a): decay and steps of transmutation, (b): Folder for input of a mass number.

Table 1 Results of retrieval for long half-life on the products of nuclear reaction of the first step caused by neutron irradiation to both type 316 stainless and ferritic steel.

(a) Compositional atom of type 316 stainless steel (Fe,Cr,Ni,Ti,C,Mn,Si, S,P,O,N,B)

Element	Isotope	Reaction	Product	Half-life	Unit	Reference	Year
B	B10	NP	Be10	1.6000e+6	y	ENDF/B-4	1974
C	C13	NG	C14	2.7300e+3	y	ENDF/B-3	1970
C	C13	NA	Be10	1.6000e+6	y	N.D.T.11	1973
N	N14	NP	C14	2.7300e+3	y	ENDF/B-4	1974
FE	FE54	NG	Fe55	2.7000e+0	y	ENDF/B-4	1974
FE	FE54	NNP	Mn53	3.7000e+6	y	N.D.T.11	1973
FE	FE56	N2N	Fe55	2.7000e+0	y	N.D.T.11	1973
NI	NI58	NG	Ni59	7.5000e+4	y	ENDF/B-4	1974
NI	NI58	NA	Fe55	2.7000e+0	y	KFK-2386	1977
NI	NI60	NP	Co60	5.2690e+0	y	ENDF/B-4	1974
NI	NI60	N2N	Ni59	7.5000e+4	y	N.D.T.11	1973
NI	NI61	NNP	Co60	5.2690e+0	y	N.D.T.11	1973
NI	NI62	NG	Ni63	1.0000e+2	y	ENDF/B-4	1974
NI	NI64	N2N	Ni63	1.0000e+2	y	N.D.T.11	1973
CU	CU63	NA	Co60	5.2690e+0	y	ENDF/B-4	1974
CU	CU63	NP	Ni63	1.0000e+2	y	N.D.T.11	1973
MO	MO92	NG	Mo93	3.5000e+3	y	N.D.T.11	1973
MO	MO92	NP	Nb92	3.2000e+7	y	N.D.T.11	1973
MO	MO92	NNP	Nb91	1.0000e+4	y	BNL-325	1976
MO	MO94	NP	Nb94	2.0000e+4	y	N.D.T.11	1973
MO	MO94	N2N	Mo93	3.5000e+3	y	N.D.T.11	1973
MO	MO95	NNP	Nb94	2.0000e+4	y	N.D.T.11	1973
MO	MO96	NA	Zr93				

(b) Compositional atom of ferritic 9Cr1WVTa steel (Fe,Cr,W,V,Ta, C,Mn,Si,S,P,O,N,B)

Element	Isotope	Reaction	Product	Half-life	Unit	Reference	Year
B	B10	NP	Be10	1.6000e+6	y	ENDF/B-4	1974
C	C13	NG	C14	2.7300e+3	y	ENDF/B-3	1970
C	C13	NA	Be10	1.6000e+6	y	N.D.T.11	1973
N	N14	NP	C14	2.7300e+3	y	ENDF/B-4	1974
O	O17	NA	C14	2.7300e+3	y	N.D.T.11	1973
FE	FE54	NG	Fe55	2.7000e+0	y	ENDF/B-4	1974
FE	FE54	NNP	Mn53	3.7000e+6	y	N.D.T.11	1973
FE	FE56	N2N	Fe55	2.7000e+0	y	N.D.T.11	1973
TA	TA181	N3N	Ta179	1.8200e+0	y	ENDF/B-4	1974

Using the nuclide database, the possibility of large amount of He formation and radioactivity in the candidate materials can be easily evaluated qualitatively. The possibility of He formation is known by retrieving cross section size of (n, alpha) reaction on compositional atoms of materials. The radioactivity is known by retrieving half-life of transmuted products of compositional atoms of material. Table 1 shows transmuted products with half-life of more than one year in type 316 and ferritic steel. These result suggest that type 316 stainless steel has more radioactive nuclides and is radioactivated more easily than ferritic 9Cr-1WVTa steel under neutron irradiation. It is found that this system will be frequently used by nuclear material scientists as a material information tool, if this system is jointed to networking system such as "Data-Free-Way"[1]~[3].

5. Conclusion

Using the nuclide database, the possibility of large amount of He formation and radioactivity in the candidate materials can be easily evaluated qualitatively. The possibility of He formation is known by retrieving cross section size of (n, alpha) reaction on compositional atoms of materials. The radioactivity is known by retrieving half-life of transmuted products of compositional atoms of material. Transmuted products with half-life of longer than one year in type 316 and ferritic steel. These result suggest that type 316 stainless steel has more radioactive nuclides and radioactivated more easily than ferritic 9Cr-1WVTa steel for reduced activation under neutron irradiation .

Reference

[1] Fujita M., Kurihara Y., Nakajima H., Yokoyama N., Ueno F., Kano S., Iwata S., Proc. Int. Conf.on Computer Applications to Materials Science and Engineering, 1992 p81-84 (Yokohama, Japan)

[2] Nakajima H., Yokoyama N., Ueno F., Kano S., Fujita M., Kurihara Y. and Iwata S., J. Nucl. Mater. vol.212-215 (1994) p.1171-1714.

[3] Ueno F., Kano S., Iwata S.,Fujita M., Kurihara Y., Nakajima H., Yokoyama N. and Iwata S., J. Nucl. Sci. Technol, vol.31(1994) p.1314-1334.

3. 39 World Wide Web of JAERI Nuclear Data Center

Tsuneo Nakagawa

Nuclear Data Center
Japan Atomic Energy Research Institute
Tokai-mura, Naka-gun, Ibaraki-ken 319-11

The Nuclear Data Center at Japan Atomic Energy Research Institute is distributing the information on nuclear data by using World Wide Web. Available are various types of evaluated nuclear data (graphs, tables, numerical data files), a chart of nuclides, and information on published papers, Japanese Nuclear Data Committee.

1. Introduction

The World Wide Web (WWW) on the Interenet is a very powerful tool for information exchange. Experimental operation of a WWW server of the JAERI Nuclear Data Center (NDC/WWW) started in February 1995. Then, the server was opened to members of Japanese Nuclear Data Committee (JNDC) in March 1995. From April 1995, it has been operated without any access limitations. The URL's (Uniform Resource Locator) of Home Pages of NDC/WWW are

http://cracker.tokai.jaeri.go.jp/index.html (English Home Page)
http://cracker.tokai.jaeri.go.jp/index_J.html (Japanese Home Page)

Figure 1 shows the English Home Page. In this paper, information available from NDC/WWW as of December 1995 is described.

2. General Information

1) What's New on this Server

This is a list of important events happened to NDC/WWW excluding continuos update of information, for example, on publications, meetings.

2) Introduction of Nuclear Data Center

JAERI Nuclear Data Center is briefly explained on the basis of its brochure.

3) Japanese Nuclear Data Committee

Japanese Nuclear Data Committee (JNDC) is a domestic committee consisting of about 145 people working for nuclear data or nuclear energy. On the Japanese page of JNDC, there are lists of its meetings and minutes of working group meetings.

4) Publications

Recent reports published from the Nuclear Data Center and JNDC are listed. Abstracts and a list of contents are shown by clicking "Abstract". Copies of these reports are available upon request to the Nuclear Data Center by e-mail.

3. Nuclear Data

1) Downloading of numerical data

The evaluated nuclear data libraries of JENDL-3.2[1] (original files and point-wise files constructed at 0 K and 300 K), JENDL special purpose files and JNDC FP Decay Data File can be downloaded from this page. Almost all of the files are compressed by gzip.

Additional documents available from the Japanese page of Nuclear Data are explanation of ENDF format, a list of evaluated nuclear data libraries available from JAERI Nuclear Data Center.

2) Tables of Nuclear Data

The following data are shown in a table form:

1. Nuclear mass recommended by Audi and Wapstra[2],
2. Spin and parity, half life taken from ENSDF[3],
3. Cross sections at 0.0253 eV and 14 MeV, resonance integral, ^{235}U fission spectrum average cross sections, 30-keV Maxwellian spectrum average capture cross sections calculated from JENDL-3.2.

First a list of elements is shown, then by clicking one of element names a list of data for Items 1 and 2 is shown with pointers to Item 3. The data of Item 3 are given to the nuclides whose data are given in JENDL-3.2. Figure 2 is an example of the tables of Item 3.

3) Chart of the Nuclides

The chart of the nuclides was made from the experimental data which were compiled by Horiguchi[4]. The half-life of nuclei which have no experimental data was calculated by Tachibana et al.[5] A whole chart is divided into 27 parts. Each part of the chart was created by a program using a gif creation program package of gd1.1.1[6]. Figure 3 is the chart around ^{235}U. By clicking the box of each nuclide, detailed information on the nuclide is listed; mass excess, half-life, γ rays, and pointers to the tables of cross sections (the same as item 3 of Tables of Nuclear Data) and to cross-section graphs.

4) Periodic tables of elements

This is a list of pointers to periodic tables of elements made by various institutes in the world.

5) Cross-section Graphs

Cross-section graphs made from JENDL-3.2 have been prepared for 340 nuclei in the following three types:

Type 1: the total, elastic and inelastic scattering, capture and fission cross sections in the energy range from 0.01 eV to 20 MeV.

Type 2: the same quantities as Type 1, but averaged in 1/4 lethargy intervals.

Type 3: threshold reaction cross sections.

These graphs are created in the form of gif and jpeg files. An example of Type 1 graphs is given in Fig. 4.

It is also possible to make cross-section graphs by using ENDFPLOT developed by Chang[7]. ENDFPLOT has flexibility to specify the nuclide name, reaction types and an energy range of incident neutrons. Since several nuclei and reaction types can be specified at a time, superimpose of cross-section data can be easily made. Figure 5 shows an example of input and Fig.6 the ^{235}U fission cross section written by ENDFPLOT. Available evaluated cross-section data for ENDFPLOT are JENDL-3.2 and JENDL Dosimetry file at a time of December 1995.

6) Others

Information on JENDL (JENDL-1, JENDL-2, JENDL-3.1 and JENDL-3.2), JENDL special purpose files, libraries for applications (group constants), and JNDC FP Decay Data File is

available.

4. Codes for Nuclear Data

This is a page for nuclear data related computer programs. For the moment, there is a list of links to various WWW documents on computer programs in the world.

5. Others

1) International Meetings on Nuclear Data

International conferences and symposiums related to nuclear data are listed and their announcements are linked from this list.

2) Other WWW servers related to Nuclear Data

Many WWW servers related to nuclear data are linked from this page including OECD/NEA Data Bank, BNL National Nuclear Data Center and IAEA Nuclear Data Section.

3) JNDC Mailing List (JNDCmail)

JNDCmail is a mailing list among nuclear data researchers and users in Japan. Articles posted to JNDCmail are automatically listed up here. The articles are written in Japanese.

6. Conclusion

Through the experience for about a year, it has been found that the WWW is a very convenient way of information exchange. So far, a lot of nuclear data information (numerical data, graphs, etc.) became available from our WWW server. They will be continuously updated, and new information will be included.

Any comments on JAERI NDC/WWW should be sent to
www-admin@cracker.tokai.jaeri.go.jp.

References

1) T.Nakagawa, et al.: J. Nucl. Sci. Technol., 32, 1259 (1995)
2) G.Audi and A.H.Wapstra: Nucl. Phys. A595, 409-480 (1995).
3) Evaluated Nuclear Structure Data File, a computer file of evaluated experimental nuclear structure data maintained by the National Nuclear Data Center, Brookhaven National Laboratory.
4) Y.Horiguchi: private communication (1995)
5) T.Tachibana, et al.: Prog. Theor. Phys., 84, 641 (1990).
6) T. Boutell: http://siva.cshl.org/gd/gd.html, the Quest Protein Database Center, Cold Spring Harbor Labs, USA (1995).
7) Chang: private communication (1995).
See also a WWW document at http://hpngp01.kaeri.re.kr/CoN/endfplot_help.html

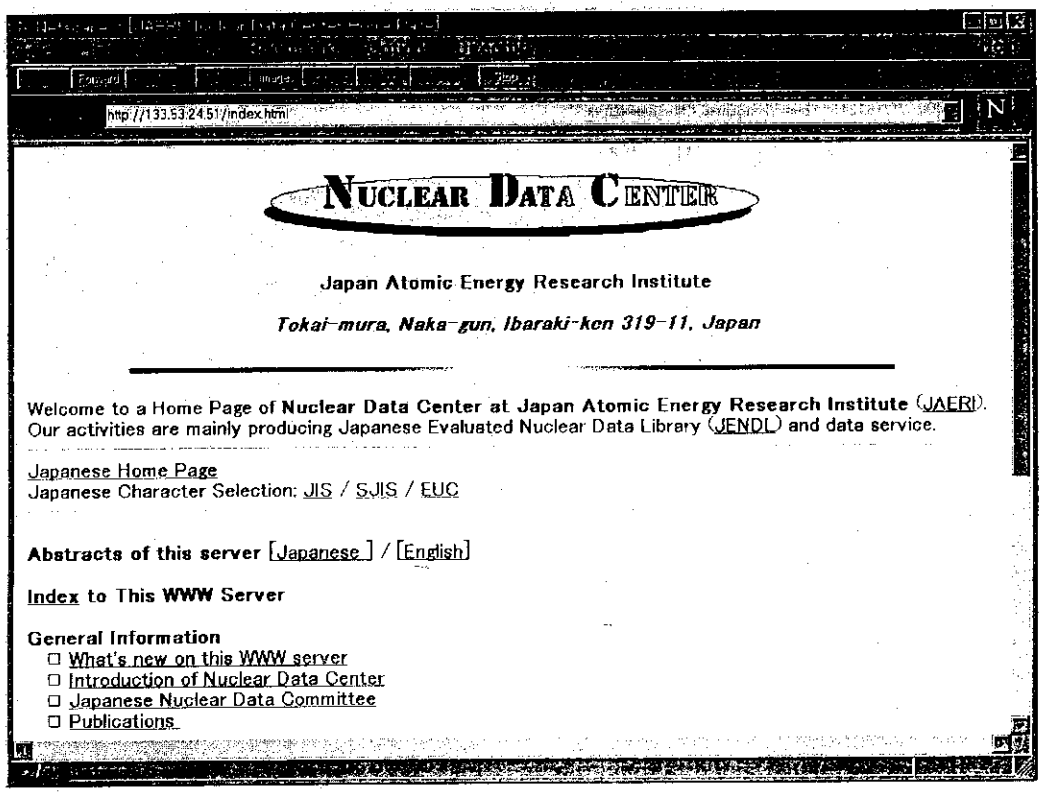

Fig. 1 JAERI Nuclear Data Center Home Page

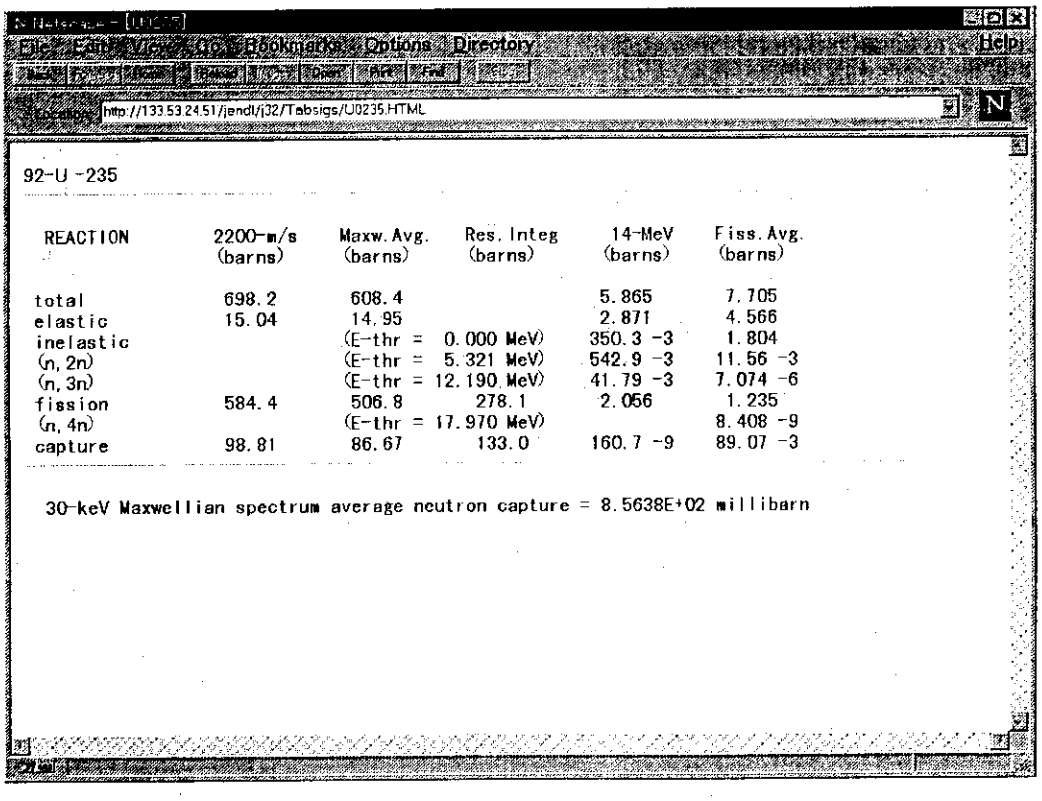

Fig. 2 An example of "Table of nuclear data" (^{235}U)

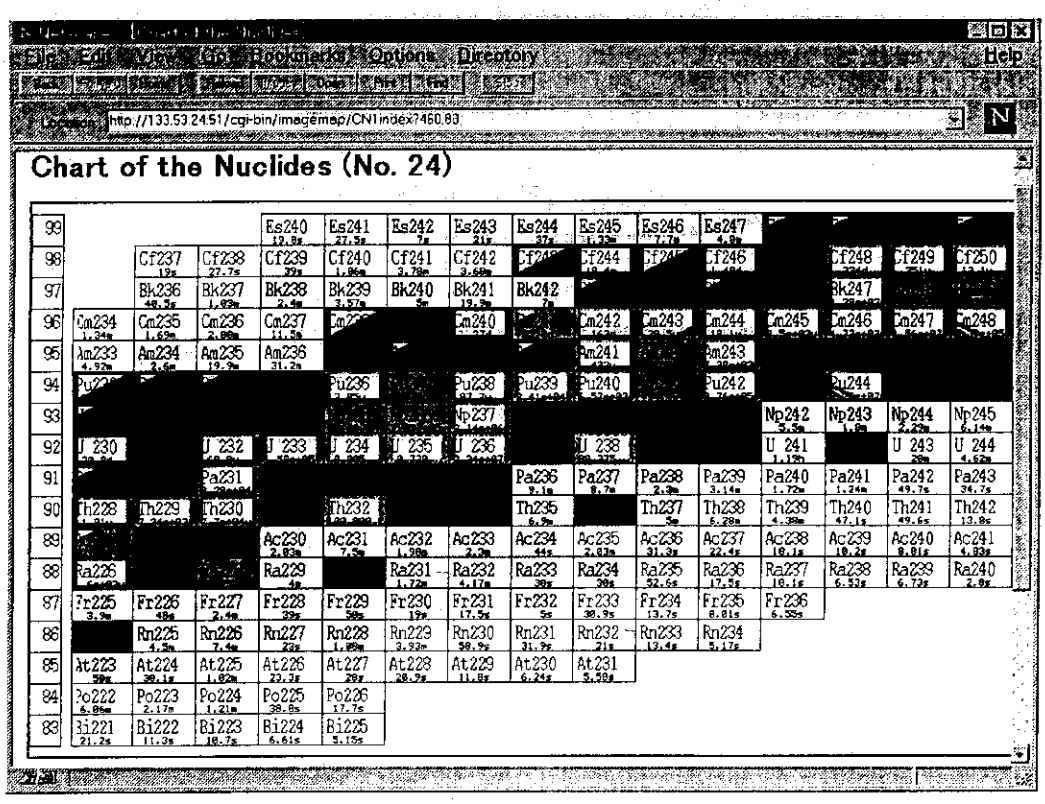

Fig. 3 Chart of nuclide (around ^{235}U)

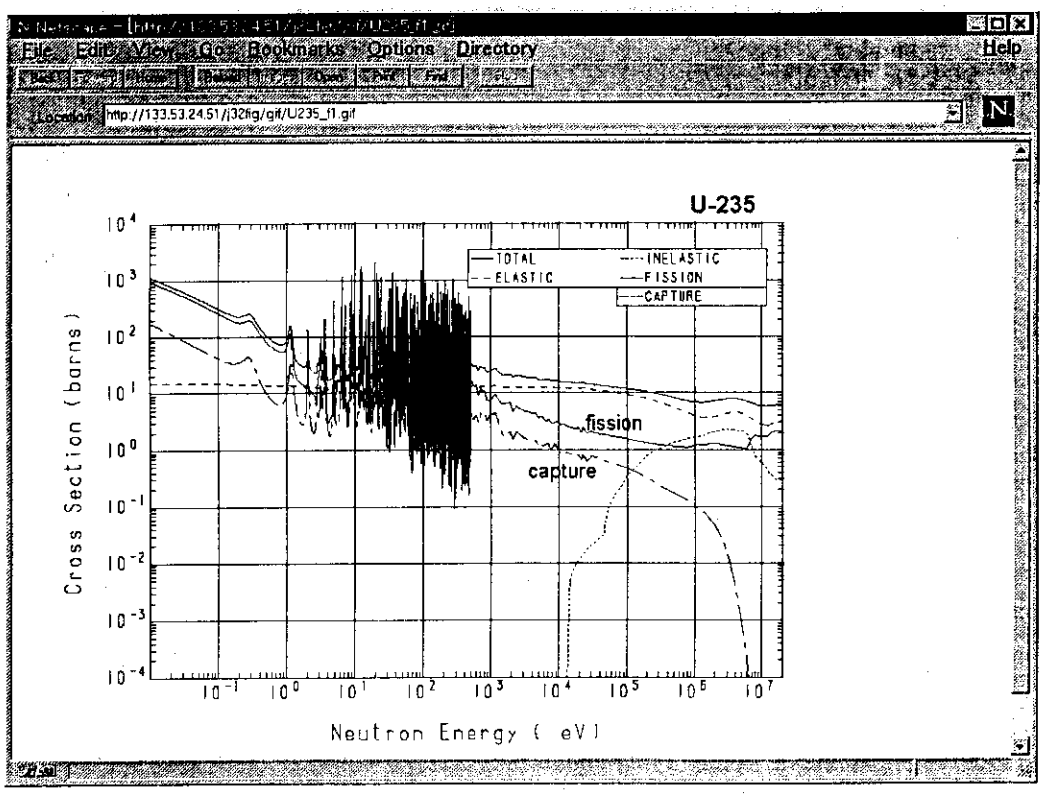

Fig. 4 Type 1 cross-section graph of ^{235}U

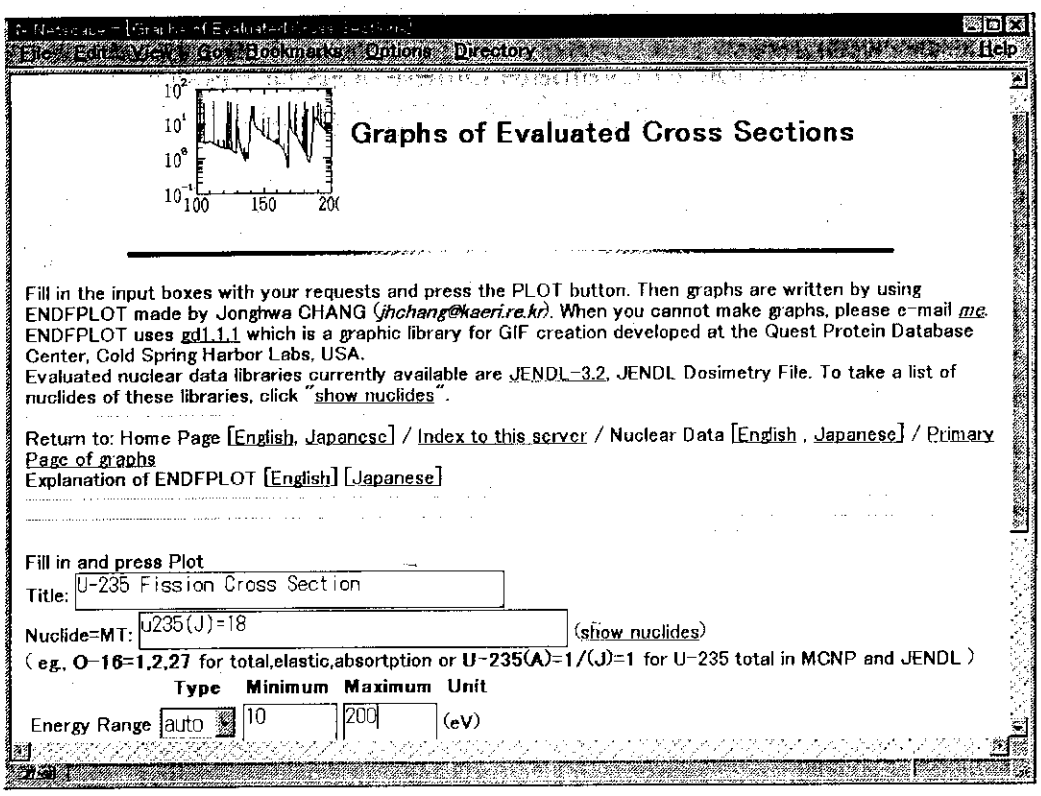

Fig. 5 An example of ENDFPLOT (input)

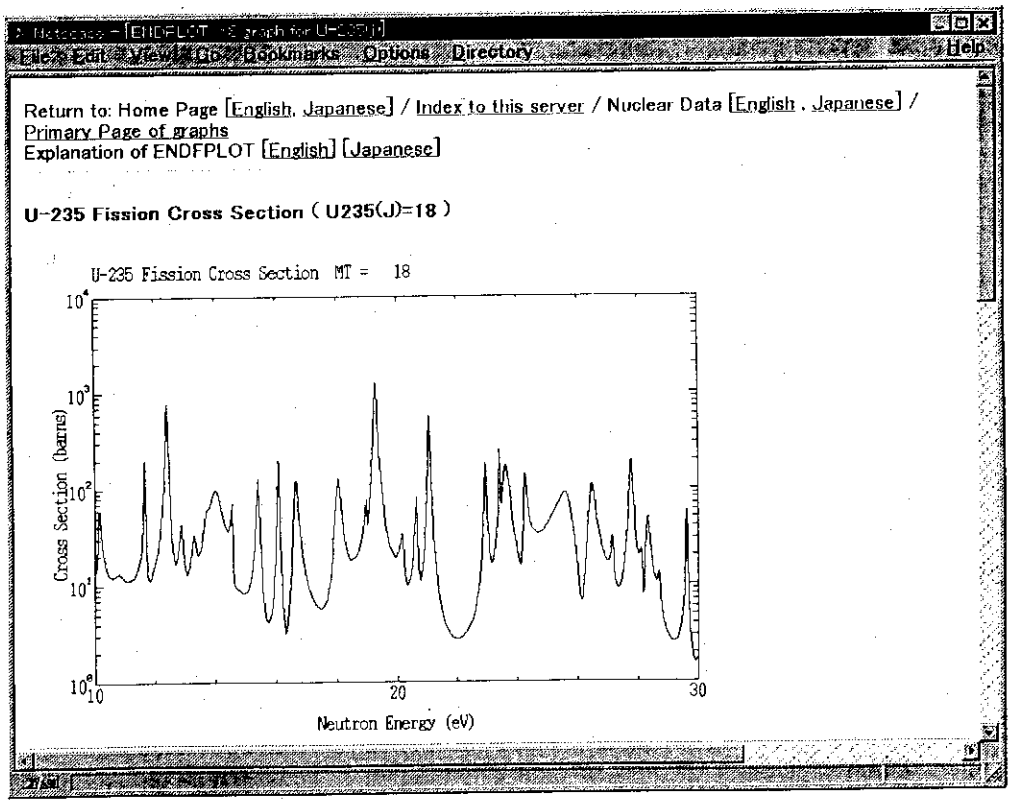

Fig.6 ^{235}U fission cross section

3.40 A Simple Method to Evaluate Differences of Fission Yields from Various Fissioning Systems

Kazuhiro OYAMATSU[a] and Mitsuyuki SAGISAKA[b]
a) Department of Energy Engineering and Science, Nagoya University
Furo-cho, Chikusa-ku, Nagoya 464-01
b) Department of Nuclear Engineering, Nagoya University
Furo-cho, Chikusa-ku, Nagoya 464-01

A simple general method is proposed to give a measure of the difference of two data sets. In this method, we utilize an analogue of the overlap integral of two wave functions in quantumn mechanics. The method is applied to evaluate the difference in the fission yield between a fissioning system and the thermal fission of ^{235}U because the yield determines the necessary the decay data in the summation calculation. It is found that the decay data required for Th, Am, Cm, Cf, Es and Fm isotopes are substantially different from those for major actinides. This method is also applied to evaluate the difference between nuclear data libraries ENDF/B-VI and JNDC version 2. It is found that there are a substantial difference in values of the decay constants and a slight difference in the yield data while the decay energies are almost equal.

1. Introduction

Thanks to many studies in the last two decades, results of the summation calculations of the aggregate decay heat power agrees well with the measured decay powers at cooling times between 2 and 10^4 (s) in the cases of burst fissions, as far as major actinide fissiles, such as ^{235}U, ^{238}U, ^{239}Pu and ^{241}Pu, are concerned. Because the measurements have been performed for only several fissioning systems in the limited range of the cooling time, we have to rely on the summation calculations in processing minor actinide fissiles. Then, it is necessary to examine its prediction power at other cooling times and/or for other fissioning systems. The basic input data for the summation calculation are the yield and decay data of fission products. The fission yield determines the necessary decay data required in the summation calculation. Since the yield depends on the fissioning system, only a porttion of the nuclear data in the library is tested by the actual decay heat measurements. Therefore the maturity of the nuclear data library can not be judged only from the success of the summation calculations for several fissioning systems in the limitted range of the cooling times.

Our group has been evaluating the prediction power of the summation calculation with the present nuclear data library for various fissioning system. On one hand, Ohta et al. [1] performed the conventional uncertainty analysis of the summation calculations with the evaluated nuclear data in ENDF/B-VI [2]. On the other hand, we here try to evaluate (1) the extent of the extrapolation to fissioning systems without actual decay heat measurements and (2) the difference between nuclear data libararies. The extent of the extrapolation is examined by evaluating the difference in the fission yield between a fissioning system and the thermal neutron induced ^{235}U fission in order to clarify how much data are newly required in the summation calculations for minor actinide fissiles. The difference between nuclear data libraries are examined by comparing values of the yield and decay data in two major nuclear data laibraries.

In Sec. 2, we propose a simple method to measure the difference between two data sets. The analyses in the subsequent sections are performed with this method. In Sec. 3, we compare the yields of various fissioning systems, which are available in ENDF/B-VI. In Sec.

4, we compare the yield and decay data of ENDF/B-VI and JNDC Version 2 [3]. Section 5 is devoted to discussion.

2. Definition of Similarity

We propose a simple method to give a measure of the difference between two data set. In this method, we utilize an analogue of the overlap integral of two wave functions, ϕ_1 and ϕ_2, in quantumn mechanics:

$$\frac{\langle\phi_1|\phi_2\rangle}{\sqrt{\langle\phi_1|\phi_1\rangle\langle\phi_2|\phi_2\rangle}} . \qquad (1)$$

Although it is applicable to any two data sets, we start with the case of the independent yields of two fissioning systems. Let us write two sets of independent yield values from two fissioning systems as two N-dimensional vectors:

$$\boldsymbol{y} = \left(y_1, y_2, y_3, \ldots, y_N\right), \quad \boldsymbol{y}' = \left(y'_1, y'_2, y'_3, \ldots, y'_N\right), \qquad (2)$$

where y_i (y'_i) means the independent yield of the nuclide i of one (another) fissioning system. We define "similarity" as

$$\mu = \frac{\boldsymbol{y}\cdot\boldsymbol{y}'}{|\boldsymbol{y}||\boldsymbol{y}'|} = \frac{\sum_{i=1}^{N} y_i \cdot y'_i}{\sqrt{\sum_{i=1}^{N}(y_i)^2 \sum_{j=1}^{N}(y'_j)^2}} , \qquad (3)$$

which gives the ratio of the component of $\boldsymbol{y}'$ parallel to the vector $\boldsymbol{y}$. Note that the similarity μ is identical with the direction cosine ($\cos\theta$) of the two vectors as shown in Fig. 1.

The deviation from the value μ=1 (θ=0) gives a measure of the difference in the fission yield between the two fissioning system. In the extreme cases,

μ=1 when $\boldsymbol{y}$ and $\boldsymbol{y}'$ are the same,

and μ=0 when they are perpendicular (completely different).

The value μ is not very sensitive to the rotation angle θ in Fig. 1 because for a small θ,

$$\mu = \cos\theta \approx 1 - \theta^2/2 . \qquad (4)$$

Although the meaning of the μ value is somewhat ambiguous, in this paper, we use the tentative criteria in Table 1.

3. Difference of Independent Fission Yields from Various Fissioning Systems (ENDF/B-VI)

We compare independent fission yields from various fissioning systems given in ENDF/B-VI. Specifically, the vector $\boldsymbol{y}$ in Eq. (2) is taken as the independent yield from a fissioning system while $\boldsymbol{y}'$ is that from the thermal neutron fission of ^{235}U. The calcualted μ values are depicted in Fig. 2. In this figure, the abbreviations T, F and H stand for fissions induced by thermal, fission and high-energy neutrons, respectively. We see that the fission yield depends much on the fissioning system. This means that the decay data required for fissions of minor actinides are much different from those used for fissions of major actinides such as ^{235}U, ^{239}Pu.

Table 1. Tentative criteria

μ	θ (°)	degree of difference
0.95	18	slightly different
0.9	26	different
less than 0.8	37	substantially different

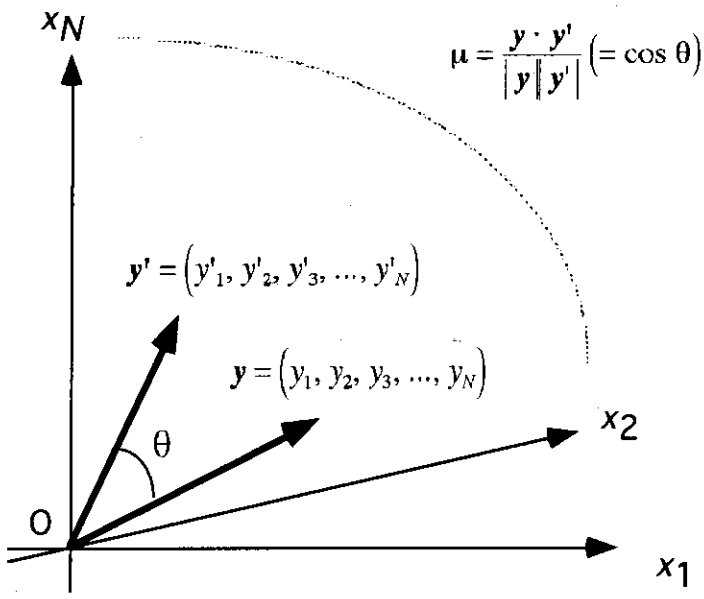

Fig. 1 Definition of simirarity μ.

4. Comparison between ENDF/B-VI and JNDC Version 2

In this section, we compare the yield and decay data in ENDF/B-VI with those in JNDC version 2. Since the number of fission product nuclides are different in these libraries (886 nuclides in ENDF/B-VI and 1227 in JNDC version 2), care must be taken in the following analyses.

4.1. Independent Fission Yield Values

For fission products whose data are not available in ENDF/B-VI, the yield values in ENDF/B-VI are taken to be zero:

$$y_{\mathrm{JNDC2}} = \left(y_{1,\mathrm{J}}, y_{2,\mathrm{J}}, \cdots, y_{886,\mathrm{J}}, y_{887,\mathrm{J}}, \cdots, y_{1227,\mathrm{J}}\right),$$

$$y_{\mathrm{ENDF/B-VI}} = \left(y_{1,\mathrm{E}}, y_{2,\mathrm{E}}, \cdots, y_{886,\mathrm{E}}, 0, \ldots, 0\right). \qquad (5)$$

The similarity μ is calculated for each fissioning system in order to measure the difference between the two libraries.. The comparison is made for 20 fissioning systems because the fission yields from only 20 fissioning systems are available in JNDC version 2. As shown in Fig. 3, the difference is relatively small for all fissioning systems probably because the sources of the yield values are almost the same [4]. However, we see slight differences for some fissioning systems especially for high-energy neutron fissions. These difference, which is considered to stem from the difference in the number of fission product nuclides in the libraries, may cause some effects in the summation calculations probably at short cooling times.

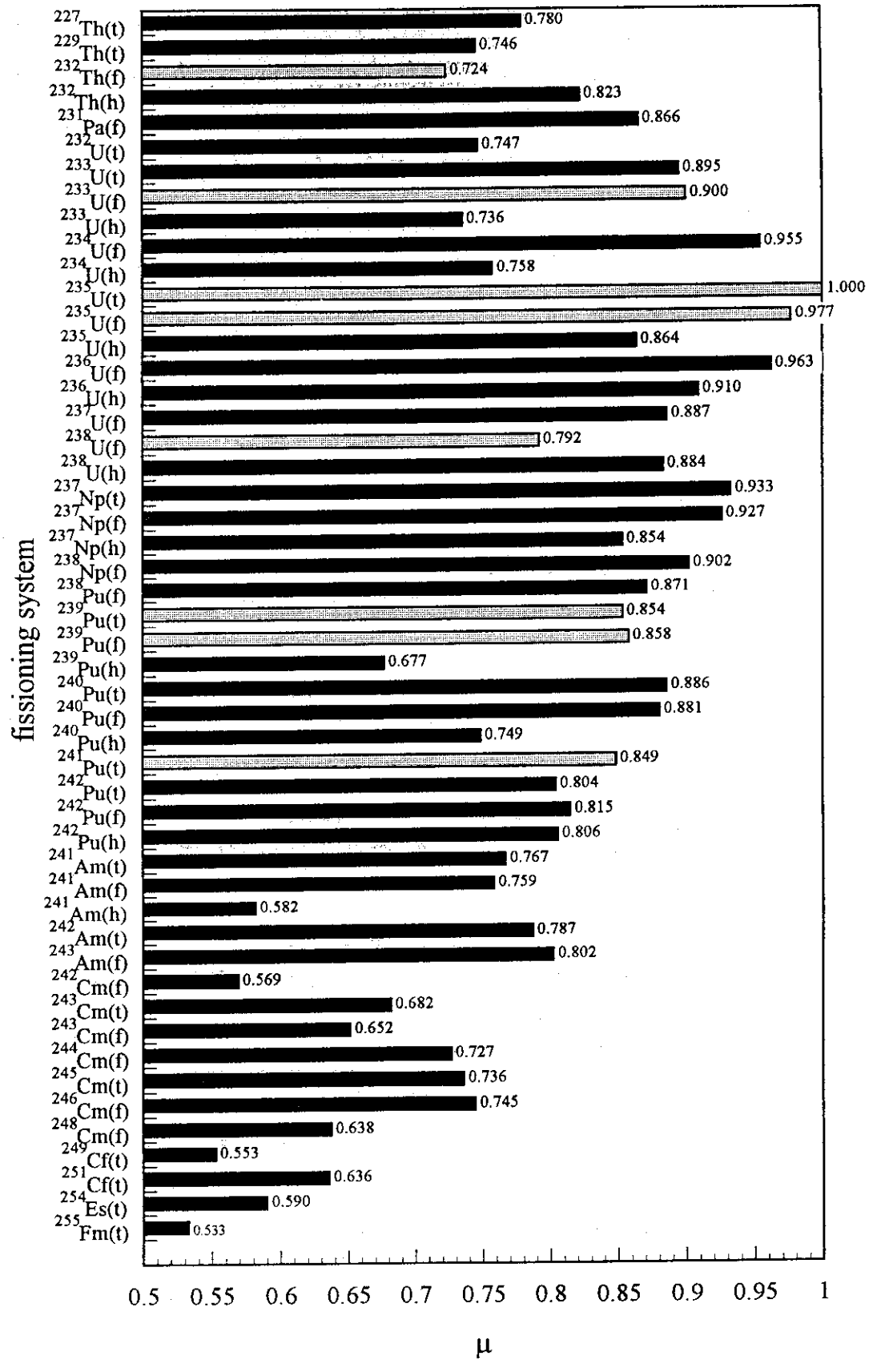

Fig.2. Difference in the independent fission yield

4.2. Difference in Decay Constants, Decay Energies and Q Values

As for the comparison of decay constants, decay energies and Q values, we neglect fission products which are not available in ENDF/B-VI. For example, we consider the following two vectors

$$\lambda_{JNDC2} = \left(\lambda_{1,J}, \lambda_{2,J}, \cdots, \lambda_{886,J}\right), \quad \lambda_{ENDF/B-VI} = \left(\lambda_{1,E}, \lambda_{2,E}, \cdots, \lambda_{886,E}\right) \qquad (6)$$

for the comparison of the decay constant in the two libraries. Are shown in Table 2, the differences in the decay energies and Q values are small. However, there is a noticable difference in the decay constant between the two libraries. Probably this difference originates mainly from the choices of the methods to estimate the decay constant values of very neutron-rich nuclides. Because the decay constant values of these nuclides are often larger by an order of 2 or 3 from those of the other nuclides, the μ value for the decay constant is supposed to be rather underestimated. Nevertheless, this difference in the decay constant may cause significant effects at short cooling times though it will not be a serious problem at sufficiently long cooling times.

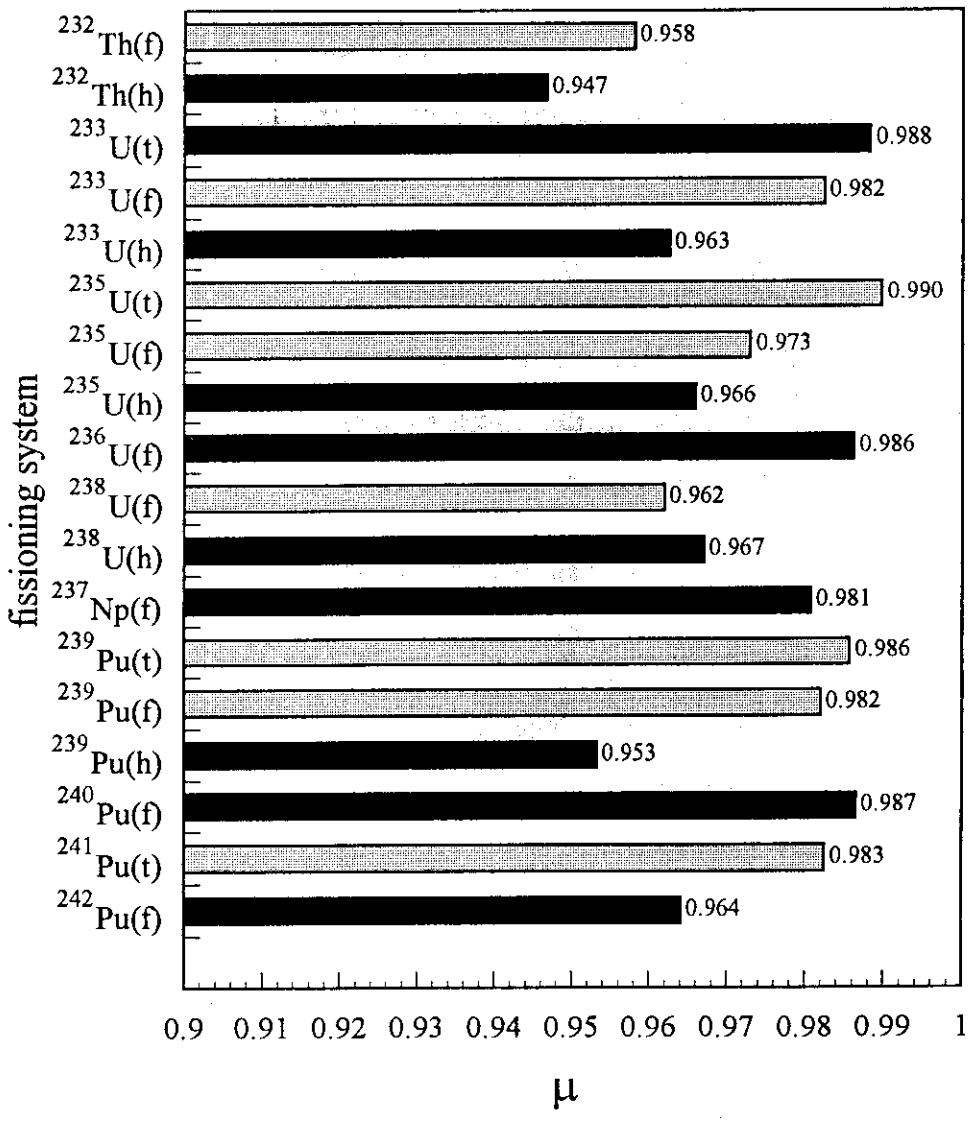

Fig. 3. Differnce in the independent fission yield between ENDF/B-VI and JNDC version 2.

Table 2. Comparison of decay data in ENDF/B-VI and JNDC version 2

λ	E_β	E_γ	Q
0.838	0.997	0.994	0.995

5. Discussion

We have tried to access the maturity of the present nuclear data libraries required in the summation calculation of the aggregate decay heat power from fission products. We have utilized the similarity μ which is defined as an analogue of the overlap integral in quantum mechanics. We have obtained the following conclusions from our simple analysis;

(a) For fissons of Th, Am, Cm, Cf, Es and Fm isotpoes and high-energy fissions of any nuclides, we need decay data of substantially different fission products which are not required for thermal or fast-reactor fissions of major actinides such as ^{235}U and ^{239}Pu.

(b) There are no significant differences in the decay energies E_β and E_γ as well as Q values between JNDC version 2 and ENDF/B-VI.

(c) However, values of the decay constant in the two libraries are substantially different. Together with the difference in number of nuclides in the libraries, the difference in the decay constants may cause a significant discrepancy in the calculated decay heat power at a short cooling time.

The definition of similarity μ have some ambiguity. Since the value of the independent yield, y_i, is the probability to the nuclide i as a fission product, the corresponding amplitude, $\sqrt{y_i}$, may be taken as a component of the vector:

$$\boldsymbol{y} = \left(\sqrt{y_1}, \sqrt{y_2}, \sqrt{y_3}, \cdots, \sqrt{y_N}\right). \tag{7}$$

We have also tried this case and obtained similar results. Therefore the ambiguity in the definition does not change the above conclusion.

The simple method described in this paper can be used to examine the difference between nuclear libraries in more detail. Specifically, we have started to scrutinize the cooling time dependence of the decay heat power from a specific nuclide in the summation calculation with JNDC version 2, ENDF/B-VI and JEF2.2. This will provide us with a differential test of the decay heat calculations and will be reported elsewhere.

Acknowledgements

The authors express their sincere gratitudes to late Prof. K. Tasaka for his continual encouragement until his death on the 14th of Feburary, 1995. They also thank Dr. T. Yoshida for stimulating discussion, and Dr. J. Katakura for his help in obtaining nuclear data.

References

[1] Ohta, H., Oyamatsu, K.and Tasaka, K.:"A Simple Method for Evaluation of Uncertainties in Fission Product Decay Heat Summation Calculations", JAERI Conf (this volume).

[2] see, for example, Katakura, J. and England, J.R.:"Augmentation of ENDF/B Fission Product Gamma-Ray Spectra by Calculated Spectra", LA-12125-MS(1991).

[3] Tasaka, K., Katakura, J., Ihara, H., Yoshida, T., Iijima, S., Nakashima, R., Nakagawa, T., and Takano, H.:"JNDC Nuclear Data Library of Fission Products - 2nd Version", JAERI 1320 (1988).

[4] Yoshida, T., private communication.